



United States
Environmental Protection
Agency

EPA/600/R-16/152 | September 2016 | www.epa.gov/research

Dispersant Effectiveness, In-Situ Droplet Size Distribution and Numerical Modeling to Assess Subsurface Dispersant Injection as a Deepwater Blowout Oil Spill Response Option *and* Evaluation of Oil Fluorescence Characteristics to Improve Forensic Response Tools



Office of Research and Development
National Risk Management Research Laboratory
Land Remediation and Pollution Control Division

IAA No. E12PG00037

Final Report

Dispersant Effectiveness, In-Situ Droplet Size Distribution and Numerical Modeling to Assess
Subsurface Dispersant Injection as a Deepwater Blowout Oil Spill Response Option
and
Evaluation of Oil Fluorescence Characteristics to Improve Forensic Response Tools

Submitted to:

Bureau of Safety and Environmental Enforcement

Submitted by:

Robyn N. Conmy, Ph.D.

U.S. Environmental Protection Agency, Office of Research and Development
26 W. Martin Luther King Drive, Cincinnati, OH 45268
*Tel: 513-569-7090, Fax: 513-569-7620, Email: conmy.robyn@epa.gov

Thomas King, M.Sc.; Brian Robinson, M.Sc; Scott Ryan, M.Sc; Youyu Lu, Ph.D.;

Department of Fisheries and Oceans Canada, Bedford Institute of Oceanography
1 Challenger Drive, Dartmouth, Nova Scotia, Canada B2Y 4A2
Tel: 902-426-4172, Tom.King@mar.dfo-mpo.gc.ca

Mary Abercrombie, M.Sc.

University of South Florida, College of Marine Science
140 7th Ave South, St. Petersburg, FL 33701
*Tel: 727-553-1140, Email: mabercrombie@marine.usf.edu

Michel Boufadel, Ph.D.

New Jersey Institute of Technology, Civil and Environmental Engineering
University Heights, Newark, NJ 07102
Tel: 973-596-5657, Email: michel.boufadel@njit.edu

Haibo Niu, Ph.D.

Dalhousie University, Department of Engineering
PO Box 550, Truro, N.S. Canada
Tel: 902-893-6714, Email: haibo.niu@dal.ca

September 30, 2016

Notice/Disclaimer

The U.S. Environmental Protection Agency (EPA), through its Office of Research and Development, along with the Department of Fisheries and Oceans Canada (DFO Canada) conducted the research described herein. This report contains scientific observations from a series of subsurface oil injection experiments and high resolution fluorescence analyses which were funded from the Bureau of Safety and Environmental Enforcement (BSEE). It has been subjected to peer and administrative review through the EPA, DFO Canada and BSEE, and has been approved for publication as an EPA document, thus the information provided here should not be parsed. Approval does not signify that the contents reflect the views of the U.S. EPA, DFO Canada, or BSEE, nor does the mention of trade names or commercial products constitute endorsement or recommendation for use.

Forward

The U.S. Environmental Protection Agency (US EPA) is charged by Congress with protecting the Nation's land, air, and water resources. Under a mandate of national environmental laws, the Agency strives to formulate and implement actions leading to a compatible balance between human activities and the ability of natural systems to support and nurture life. To meet this mandate, US EPA's research program is providing data and technical support for solving environmental problems today and building a science knowledge base necessary to manage our ecological resources wisely, understand how pollutants affect our health, and prevent or reduce environmental risks in the future.

The National Risk Management Research Laboratory (NRMRL) within the Office of Research and Development (ORD) is the Agency's center for investigation of technological and management approaches for preventing and reducing risks from pollution that threaten human health and the environment. The focus of the Laboratory's research program is on methods and their cost-effectiveness for prevention and control of pollution to air, land, water, and subsurface resources; protection of water quality in public water systems; remediation of contaminated sites, sediments and ground water; prevention and control of indoor air pollution; and restoration of ecosystems. NRMRL collaborates with both public and private sector partners to foster technologies that reduce the cost of compliance and to anticipate emerging problems. NRMRL's research provides solutions to environmental problems by: developing and promoting technologies that protect and improve the environment; advancing scientific and engineering information to support regulatory and policy decisions; and providing the technical support and information transfer to ensure implementation of environmental regulations and strategies at the national, state, and community levels.

Cynthia Sonich-Mullin, Director
National Risk Management Research Laboratory

Abstract

The 2010 Deepwater Horizon oil spill highlighted the need for better understanding the interaction of dispersants and crude oil during high-pressure releases. This report summarizes a study to assess the operational performance of subsurface injection dispersant use on high-pressure releases within a flume tank. Dispersion experiments were conducted using South Louisiana Crude, Alaskan North Slope Crude and Intermediate Fuel Oil 120 oils, with Corexit 9500 and Finasol OSR 52 dispersants and four dispersant-to-oil ratios (DOR 0, 1:20, 1:100, 1:200) at warm and cold temperatures. *In situ* plume dispersion was monitored for particle concentration and Droplet Size Distribution (DSD; LISST-100X), and fluorescence intensity. Samples were collected for Total Petroleum Hydrocarbons and Benzene-Toluene-Ethylbenzene-Xylene concentrations. Empirical data was subsequently used as input variables to refine numerical models of droplet size formation (VDROP-J, JETLAG and Modified Weber Number). This project also generated a fluorescence library of 25 oil types to expand community knowledge base on optical signatures as a function of oil type. In general, the addition of dispersant decreased the oil Volume Mean Diameter (VMD), creating smaller droplets. Dispersions at DOR =1:20 yielded VMD <70 μm and exhibited bimodal DSD, suggesting that produced droplets would likely remain dispersed in the presence of mixing energy. Water temperature did not appear to influence the droplets for lighter crude oils. DSD results suggest a separation of particles within the plume. *In situ* fluorescence was found to be a reliable proxy for oil concentration. These findings have implications for the fate and transport of oil plumes-both for spill response monitoring and numerical modeling.

Acknowledgements

The research presented in this report was funded by the Bureau of Safety and Environmental Enforcement (BSEE) through Interagency Agreement E12PG00037. Efforts were partially supported by the U.S. Environmental Protection Agency - Office of Research and Development (EPA ORD) and the Department of Fisheries Oceans Canada – Bedford Institute of Oceanography (DFO-BIO). This work was a highly collaborative effort and the authors would like to thank all of the contributors. The numerical modeling components are contributions by collaborators Dr. Michel Boufadel and Feng Gao (New Jersey Institute of Technology) and Dr. Haibo Niu and Linlu Weng (Dalhousie University). The high-resolution fluorescence component is a contribution of Mary Abercrombie (University of South Florida). A special thanks to all of the DFO and BDR Contracting staff who made the tank experiments possible: Patrick Toole, Claire McIntyre, Cody Sherren, Jennifer Mason, Peter Thamer, Gary Wohlgeschaffen, Susan Cobanli, and Rod Doane.

Table of Contents

Notice/Disclaimer.....	iii
Forward.....	iv
Abstract.....	v
Acknowledgements.....	vi
List of Figures.....	ix
List of Tables.....	xv
Acronyms and Abbreviations.....	xvi
Executive Summary.....	xvii
Task A.1 Introduction & Relevance.....	1
Task A.2 Experimental Methods.....	5
A.2.1 Flume Tank Description, Flow Calibration, and Operation.....	5
A.2.2 Waste Water Treatment.....	8
A.2.3 Subsurface Oil Injection System.....	8
A.2.4 Submersible Sensor Deployment.....	12
A.2.5 VOC Air Monitoring.....	14
A.2.6 Discrete Water Sample Collection.....	14
A.2.7 Oil and Dispersant Samples.....	14
A.2.8 Experimental Design – Core and Complimentary Experiments.....	16
A.2.9 Submersible Sensor Calibration Experiments.....	17
A.2.10 Submersible Fluorometer and LISST Data Processing.....	18
A.2.11 Analytical Chemistry Analysis.....	20
A.2.12 Numerical Modeling Methods.....	21
TASK A.3 RESULTS.....	22
A.3.1 ANS Dispersion Effectiveness.....	22
A.3.2 IFO 120 Dispersion Effectiveness.....	36
A.3.3 SLC Dispersion Effectiveness.....	46
A.3.4 Gas Condensate Dispersion Effectiveness.....	51
A.3.5 Tank Dilution Series Fluorescence Measurements.....	53
A.3.6 VOC Air Monitoring.....	58
A.3.7 VDROF-J and JETLAG Numerical Plume Modeling.....	68

A.3.8 Weber Number Scaling Numerical Plume Modeling	70
Task B.1 Introduction & Relevance	72
Task B.2 Experimental Methods.....	81
B.2.1 Sample Preparation.....	81
B.2.2 Artificial Seawater Protocol	81
B.2.3 Dispersed Oil in Seawater Protocol.....	81
B.2.4 Spectrophotometric Analysis	82
Task B.3 Results & Discussion	86
B.3.1 Oil Fluorescence Properties	86
B.3.2 Fluorescence as a Function of Chemistry.....	99
B.3.3 Flume Tank and Baffled Flask EEM Comparison	110
B.3.4 PARAFAC Modeling	112
DOR 0.....	114
DOR 1:100	119
DOR 1:20	123
PARAFAC Summary	126
References.....	128
Appendices (Separate Document)	132
APPENDIX A – Experiment Logs	132
APPENDIX B – Analytical Chemistry Results.....	132
APPENDIX C – Jet Release LISST Oil Droplet Size Distribution Histograms	132
APPENDIX D – Jet Release LISST Oil Droplet Size Distribution Time Series Contours	132
APPENDIX E – Submersible Fluorescence Time Series	132
APPENDIX F – Excitation Emission Matrix Contours	239
APPENDIX G – VDROD-J and JETLAG Numerical Plume Modeling Report	265
APPENDIX H – Weber Number Scaling Numerical Plume Modeling Report.....	293

List of Figures

Figure 1. Photos of subsurface oil injection at the BIO flume tank showing the formation of the subsurface oil plume. Note that the background grid size is 1.5 cm x 1.5 cm.

Figure 2. Photo of the DFO BIO flume tank (top) and cross-section of the tank showing the high-flow manifolds used to generate horizontal water currents (not to scale).

Figure 3. Schematic diagram showing the location of the subsurface injector and *in situ* instrumentation submerged within the tank.

Figure 4A. Photo of the pressurized oil vessel used to hold the oil for the subsurface release.

Figure 4B. Schematic diagram of the pressurized oil vessel for subsurface oil release system in the flume tank.

Figure 5. LISST DSD and VMD (left panels) and time series of concentration and particle size (right panels) for ANS and Corexit 9500 warm water treatments. From top to bottom, DOR = 0, 1:200, 1:100, 1:20.

Figure 6. LISST DSD and VMD (left panels) and time series of concentration and particle size (right panels) for ANS and Corexit 9500 cold water treatments. From top to bottom, DOR = 0, 1:200, 1:100, 1:20.

Figure 7. *In situ* submersible fluorescence time series of sub-injection plume of ANS and Corexit 9500 warm water (left panels) and cold water (right panels) treatments. From top to bottom, DOR = 0, 1:200, 1:100, 1:20.

Figure 8. Downstream LISST DSD and VMD (left panels) and time series of concentration and particle size (right panels) for ANS and Corexit 9500 warm water treatments. From top to bottom, DOR = 0, 1:200, 1:100, 1:20.

Figure 9. Downstream LISST DSD and VMD (left panels) and time series of concentration and particle size (right panels) for ANS and Corexit 9500 cold water treatments. From top to bottom, DOR = 0, 1:200, 1:100, 1:20.

Figure 10. LISST DSD and VMD (left panels) and time series of concentration and particle size (right panels) for ANS and Finasol OSR 52 warm water treatments. From top to bottom, DOR = 1:200, 1:100, 1:20. Refer back to Figure 5 for ANS DOR = 0.

Figure 11. *In situ* submersible fluorescence time series of sub-injection plume of ANS and Finasol OSR 52 warm water treatments. From top to bottom, DOR = 1:200, 1:100, 1:20.

Figure 12. Downstream LISST DSD and VMD (left panels) and time series of concentration and particle size (right panels) for ANS and Finasol OSR 52 warm water treatments. From top to bottom, DOR = 1:200, 1:100, 1:20. Refer back to Figure 6 for ANS DOR = 0.

Figure 13. LISST DSD with TPC for ANS with Corexit 9500 and Finasol OSR 52 warm water treatments. DOR = 0 (top panel); DOR = 1:20 experiments are middle and bottom panels.

Figure 14. LISST DSD with TPC (Total Particle Concentration) for DOR = 1:20 experiments of ANS and Corexit 9500 treatments. Water temperatures increase from top to bottom panels.

Figure 15. LISST TPC (Total Particle Concentration) for DOR = 1:20 experiments of ANS and Corexit 9500 treatments as a function of water temperature.

Figure 16. LISST DSD and VMD (left panels) and time series of concentration and particle size (right panels) for IFO 120 and Corexit 9500 warm water treatments. From top to bottom, DOR = 0, 1:200, 1:100, 1:20.

Figure 17. LISST DSD and VMD (left panels) and time series of concentration and particle size (right panels) for IFO 120 and Finasol OSR 52 warm water treatments. From top to bottom, DOR = 1:200, 1:100, 1:20. Refer to Figure 16 for IFO 120 DOR = 0.

Figure 18. Downstream LISST DSD and VMD (left panels) and time series of concentration and particle size (right panels) for IFO 120 and Corexit 9500 warm water treatments. From top to bottom, DOR = 0, 1:200, 1:100, 1:20.

Figure 19. Downstream LISST DSD and VMD (left panels) and time series of concentration and particle size (right panels) for IFO 120 and Finasol OSR 52 warm water treatments. From top to bottom, DOR = 0, 1:200, 1:100, 1:20. Refer to Figure 18 for ANS DOR = 0.

Figure 20. LISST DSD with TPC for IFO 120 with Corexit 9500 and Finasol OSR 52 treatments at warm temperatures. DOR = 0 (top panel); DOR = 1:20 experiments are middle and bottom panels.

Figure 21. LISST DSD and VMD (left panels) and time series of concentration and particle size (right panels) for IFO 120 and Corexit 9500 cold water treatments. From top to bottom, DOR = 0, 1:200, 1:100, 1:20.

Figure 22. Downstream LISST DSD and VMD (left panels) and time series of concentration and particle size (right panels) for IFO 120 and Corexit 9500 cold water treatments. From top to bottom, DOR = 0, 1:200, 1:100, 1:20.

Figure 23. LISST DSD and VMD for IFO 120 (top; DOR = 1:100) and ANS (bottom; DOR = 1:200) with Corexit 9500 during cold water treatments.

Figure 24. LISST DSD and VMD (left panels) and time series of concentration and particle size (right panels) for SLC and Corexit 9500 warm water treatments. From top to bottom, DOR = 0, 1:200, 1:100, 1:20.

Figure 25. Downstream LISST DSD and VMD (left panels) and time series of concentration and particle size (right panels) for SLC and Corexit 9500 warm water treatments. From top to bottom, DOR = 0, 1:200, 1:100, 1:20.

Figure 26. LISST DSD with TPC for SLC with Corexit 9500 treatments at warm temperatures. DOR = 0 (top panel); DOR = 1:20 experiments are bottom panels.

Figure 27. *In situ* submersible fluorescence time series of sub-injection plume of SLC and Corexit 9500 warm water treatments. From top to bottom, DOR = 0, 1:200, 1:100, 1:20.

Figure 28. LISST DSD and VMD (top panels), time series of concentration and particle size (middle panels), and fluorescence time series (bottom panels) for Gas Condensate and Corexit 9500 warm water treatments. Left panels are DOR = 0 and right panels are DOR = 1:20.

Figure 29. Calibration lines for fluorometer response vs TPH concentrations.

Figure 30. Calibration lines for fluorometer response vs BTEX concentrations.

Figure 31. Total Particle Concentration and fluorescence time series for ANS crude oil with Corexit 9500 dispersant.

Figure 32. VOC results for subsurface injection experiments (cold water season) using Alaska North Slope crude oil and four treatment conditions (no dispersant, DOR 1:200, DOR 1:100, DOR 1:20). Replicate treatments represented by light blue, dark blue and green colored lines.

Figure 33. VOC results for subsurface injection experiments (warm water season) using Alaska North Slope crude oil and four treatment conditions (no dispersant, DOR 1:200, DOR 1:100, DOR 1:20). Corexit 9500 was used as the treating agent. Replicate treatments represented by light blue, dark blue and green colored lines.

Figure 34. VOC results for subsurface injection experiments (warm water season) using Alaska North Slope crude oil and four treatment conditions (no dispersant, DOR 1:200, DOR 1:100, DOR 1:20). Finasol OSR 52 was used as the treating agent. Replicate treatments represented by light blue, dark blue and green colored lines.

Figure 35. VOC results for subsurface injection experiments (cold water season) using IFO 120 and four treatment conditions (no dispersant, DOR 1:200, DOR 1:100, DOR 1:20). Corexit 9500 was used as the treating agent. Replicate treatments represented by light blue, dark blue and green colored lines.

Figure 36. VOC results for subsurface injection experiments (warm water season) using IFO 120 and four treatment conditions (no dispersant, DOR 1:200, DOR 1:100, DOR 1:20). Corexit 9500 was used as the treating agent. Replicate treatments represented by light blue, dark blue and green colored lines.

Figure 37. VOC results for subsurface injection experiments (warm water season) using IFO 120 and three treatment conditions (DOR 1:200, DOR 1:100, DOR 1:20). Finasol OSR 52 was used as the treating agent (note – these treatments were not tested in triplicate).

Figure 38. VOC results for subsurface injection experiments using gas condensate and two treatment conditions (no dispersant, DOR 1:20). Corexit 9500 was used as the treating agent.

Figure 39. VOC results for subsurface injection experiments using Sweet Louisiana Crude oil and four treatment conditions (no dispersant, DOR 1:200, DOR 1:100, DOR 1:20). Corexit 9500 was used as the treating agent.

Figure 40. Fluorescence peaks of S. Louisiana sweet crude dispersed in ppb QSE (Quinine Sulfate Equivalents). Symbols represent Fluorescence Intensity Ratio (FIR) locations and the Center Wavelength (CWL) reported by sensor manufacturers. Bandwidths (BW) are not shown.

Figure 41. Twenty-five oil samples stored in glass bottles.

Figure 42. Trypsinizing baffled flasks containing dispersed oil in artificial seawater (top) and corresponding samples removed from each flask, ready for spectrofluorometric analysis.

Figure 43. Alaska North Slope dispersed oil in artificial seawater at DOR 1:20 with locations of $F_{\max1}$, $F_{\max2}$, $F_{\max3}$ and $F_{\max4}$ indicated. Note that maximum fluorescence intensity at $F_{\max3}$ is mostly obscured by masking of second order Rayleigh scattering.

Figure 44. Photographs of pre-analysis samples and corresponding example EEMs of Type I (left) and II (right) oils; DOR = 1:20 for Arabian Light (light oil, API gravity > 31.1°), Mesa (medium oil, API gravity 22.3 – 31.1°) and heavy oils (IFO 40 and Santa Clara, API gravity < 22.3°).

Figure 45. $F_{\max1}$ fluorescence for Light Oils (API gravity > 31°), in order of increasing density: 1. Scotian Shelf Condensate, 2. Federated, 3. Brent, 4. MC252—Discoverer Enterprise, 5. Hibernia, 6. MC252—generic, 7. Terra Nova, 8. Gullfaks, 9. Arabian Light. Note discrepancy in Scotian Shelf Condensate fluorescence pattern (circled) from that of all other Light Oils. It's particularly unusual that fluorescence intensity at highest DOR is lower than that at DORs 1:200 and 1:100.

Figure 46. $F_{\max1}$ fluorescence for Heavy Oils (API gravity < 22.3°), in order of increasing density: 1. Santa Clara, 2. IFO 40, 3. Cold Lake Dilbit, 4. Access Western Blend Dilbit, 5. Hondo, 6. IFO 120, 7. IFO 180, 8. Belridge Heavy, 9. IFO 300. Note discrepancy in Intermediate Fuel Oils (circled) from that of all other Heavy Oils.

Figure 47. For all oil types at DOR 0, total concentration of 2-ring, 3-ring, and 4-ring PAHs (µg/L) against fluorescence intensity (RU) at $F_{\max1}$ (top), and against $F_{\max2}$ (bottom). Strong linear correlation exists between 2-ring PAHs and $F_{\max1}$ fluorescence, but little to no correlation between 3-ring or 4-ring PAHs and $F_{\max1}$ fluorescence intensity (top). Strong linear correlation also exists between 2-ring PAHs and $F_{\max2}$, but no correlation between 3-ring PAHs or 4-ring PAHs and $F_{\max2}$ (bottom).

Figure 48. For all oil types at DOR 0, total concentration of 2-ring, 3-ring, and 4-ring PAHs (µg/L) against fluorescence intensity (RU) at $F_{\max3}$ (top), and against $F_{\max4}$ (bottom). Strong linear correlation exists between 3-ring and 4-ring PAHs and both $F_{\max3}$ and $F_{\max4}$ fluorescence; however, only moderate correlation exists between 2-ring PAHs and $F_{\max3}$ and $F_{\max4}$ fluorescence intensity.

Figure 49. For all oil types at DOR 1:20, total concentration of 2-ring, 3-ring, and 4-ring PAHs (µg/L) against fluorescence intensity (RU) at $F_{\max1}$ (top), and against $F_{\max2}$ (bottom). A moderate logarithmic correlation is exhibited between 2-ring PAHs and fluorescence intensity (RU) at $F_{\max1}$ and a weaker correlation between 2-ring PAHs and $F_{\max2}$, but no correlation exists between 3-ring or 4-ring PAHs and fluorescence intensity at either $F_{\max1}$ or $F_{\max2}$.

Figure 50. For all oil types at DOR 1:20, total concentration of 2-ring, 3-ring, and 4-ring PAHs ($\mu\text{g/L}$) against fluorescence intensity (RU) at $F_{\text{max}3}$ (top), and against $F_{\text{max}4}$ (bottom). A strong logarithmic correlation is exhibited between 2-ring PAHs and fluorescence intensity at $F_{\text{max}3}$. Moderate correlations exist between 3-ring PAHs and $F_{\text{max}3}$ as well as between 2-ring PAHs and $F_{\text{max}4}$. However, only a weak logarithmic correlation exists between 4-ring PAHs and fluorescence intensity at $F_{\text{max}3}$, and there is no correlation between 3-ring or 4-ring PAHs and $F_{\text{max}4}$.

Figure 51. Chemical Dispersibility Ratio (CDR) vs. decreasing oil density (top) and Fluorescence Dispersibility Ratio (FDR) vs. decreasing oil density (bottom) show only a weak correlation between chemistry and oil density, and a moderate correlation between fluorescence and oil density. With the removal of the data point for Scotian Shelf Condensation, correlation between fluorescence and oil density improves to $R^2 = 0.71$.

Figure 52. Fluorescence Dispersibility Ratio (FDR) vs. Chemical Dispersibility Ratio (CDR) shows weak correlation between these two ratios.

Figure 53. South Louisiana Crude MC252 EEMS from BFT (left panels) and tank experiments (right Panels) for DOR = 0, 1:100 and 1:20.

Figure 54. Example of split half validation for the 6-component model of 25 oil types at DOR 0 showing individual fit of data splits (Set 1, left; and Set 2, right) compared to overall model for Mode 2 (top) and Mode 3 (bottom) loadings.

Figure 55. Mode 3 Loadings (Excitation) and Mode 2 Loadings (Emission) for all 25 oil types—DOR0 using 6-component model. Note difference in x-axis scales. Although components are tightly spaced, all appear as separate and distinct peaks.

Figure 56. Variation per Component shows Component 1 accounted for >20% to 40% (unique fit and fit) of the data, while Component 2-contributed 5-10% (unique fit and fit) and Components 3-6 accounted for 5% or less of the data, respectively. While Component 6 accounted for a very low percentage of the data, the 6-component model was still a better fit to the data than the 5-component model.

Figure 57. EEM views of the six components of PARAFAC model for 25 oil types at DOR 0. Component #1: $F_{\text{max}} = \text{Ex } 224\text{nm}/\text{Em } 335\text{nm}$; Component #2: $F_{\text{max}} = \text{Ex } 230\text{nm}/\text{Em } 340\text{nm}$; Component #3: $F_{\text{max}} = \text{Ex } 239\text{nm}/\text{Em } 363\text{nm}$; Component #4: $F_{\text{max}} = \text{Ex } 218\text{nm}/\text{Em } 290 \text{ nm}$; Component #5: $F_{\text{max}} = \text{Ex } 221\text{nm}/\text{Em } 322\text{nm}$; Component #6: $F_{\text{max}} = \text{Ex } 260\text{nm}/\text{Em } 474\text{-}511\text{nm}$.

Figure 58. Mode 3 Loadings (Excitation) and Mode 2 Loadings (Emission) for all 25 oil types—DOR 1:100 using 5-component model. Note difference in x-axis scales. Although components are tightly spaced, all appear as separate and distinct peaks.

Figure 59. Variation per Component shows Component 1 accounted for >35% to almost 50% (unique fit and fit) of the data, while Components 2-5 accounted for 5% or less of the data, respectively.

Figure 60. EEM views of the five components of PARAFAC model for 25 oil types at DOR 1:100. Component #1: $F_{\max} = \text{Ex } 224\text{nm}/\text{Em } 335\text{nm}$; Component #2: $F_{\max} = \text{Ex } 254\text{-}266\text{nm}/\text{Em } 455\text{-}501\text{nm}$; Component #3: $F_{\max} = \text{Ex } 230\text{nm}/\text{Em } 344\text{nm}$; Component #4: $F_{\max} = \text{Ex } 242\text{nm}/\text{Em } 363 \text{ nm}$; Component #5: $F_{\max} = \text{Ex } 218\text{nm}/\text{Em } 290\text{nm}$.

Figure 61. Mode 3 Loadings (Excitation) and Mode 2 Loadings (Emission) for all 25 oil types—DOR 1:20 using 5-component model. Note difference in x-axis scales. Effect of full dispersion appears to broaden and shift emission peaks to longer wavelengths.

Figure 62. Variation per Component shows Component 1 accounted for 25 to 30% of the data (unique fit and fit) while Component 2 has increased to >10% to 25% (unique fit and fit) of the data. Contribution from Component 3 and 4 have increased, as well.

Figure 63. EEM views of the five components of PARAFAC model for 25 oil types at DOR 1:20. Component #1: $F_{\max} = \text{Ex } 224\text{nm}/\text{Em } 335\text{nm}$; Component #2: $F_{\max} = \text{Ex } 233\text{-}266\text{nm}/\text{Em } 432\text{-}450\text{nm}$; Component #3: $F_{\max} = \text{Ex } 230\text{-}242\text{nm}/\text{Em } 501\text{-}520\text{nm}$; Component #4: $F_{\max} = \text{Ex } 233\text{nm}/\text{Em } 349\text{nm}$; Component #5: $F_{\max} = \text{Ex } 218\text{nm}/\text{Em } 290\text{nm}$.

List of Tables

Table 1. List of hydrocarbon fluorometers used in this study. QSDE and PAH represent quinine sulfate dihydrate and petroleum aromatic hydrocarbons, respectively.

Table 2. Water sample collection strategy for the core and complimentary experiments. TPH and BTEX represent Total Petroleum Hydrocarbons and Benzene-Toluene-Ethylbenzene-Xylene, respectively.

Table 3. Physical and chemical property measurements of the oils used in this study.

Table 4. Step-wise sensor calibration experiment parameters.

Table 5. Calibration equations for the submersible fluorometers. Data in this report have fluorescence signal in the manufacturer recommended units.

Table 6. Summary of maximum VOC concentrations at the various treatment conditions tested in this study. Results are for only for warm water experiments.

Table 7. Sensor specifications as listed from manufacturers. Wavelengths listed as Center Wavelengths (CWL) with Full Width at Half Max (FWHM) and Bandpass (BP). Standards used are QS (Quinine Sulfate Dihydrate), NDD Salt (Naphthalene Disulfonic Disodium) and PTSA Salt (Pyrenetetrasulfonic Acid Tetrasodium) (From Conmy et al., 2014b).

Table 8. List of oil samples used for EEM analyses. Oils separated by API (American Petroleum Institute) gravity.

Table 9. EEM fluorescence and chemical characteristics. Refer to Supplemental Table A for full table.

Table 10. Individual hydrocarbon compounds reported as Total Alkanes, Total 2-ring, 3-ring and 4-ring PAHs.

Acronyms and Abbreviations

ADV	Acoustic Doppler Velocimetry
ANS	Alaskan North Slope
BIO DFO	Bedford Institute of Oceanography Dept. of Fisheries and Oceans Canada
BSEE	Bureau of Safety and Environmental Enforcement
BTEX	Benzene-Toluene-Ethylbenzene-Xylene
CRRC	Coastal Response Research Center
DCM	Dichloromethane
DE	Dispersion Effectiveness
DOR	Dispersant to Oil Ratio
DSD	Droplet Size Distribution
DWH	Deepwater Horizon
EEMS	Excitation Emission Matrix Spectroscopy
EPA	U.S. Environmental Protection Agency
GC-FID	Gas Chromatography-Flame Ionization Detector
GC-MS	Gas Chromatography Mass Spectrometry
GoM	Gulf of Mexico
IFO 120	Intermediate Fuel Oil 120
LISST	Laser In Situ Scattering Transmissometry
NEBA	Net Environmental Benefit Analyses
NJIT	New Jersey Institute of Technology
NRDA	Natural Resource Damage Assessments
NRT	National Response Team
OMA	Oil-Mineral Aggregate
PARAFAC	Parallel Factor Analysis
PSC	Particle Size Concentration
SLC	South Louisiana Crude
STP	Standard Temperatures and Pressures
TPC	Total Particle Concentration
TPH	Total Petroleum Hydrocarbons
UAC	Unified Area Command
VMD	Volume Mean Diameter
VOC	Volatile Organic Compounds
WG-50	Wave Gauges

Executive Summary

This report summarizes two projects covered under an Interagency Agreement between the Bureau of Safety and Environmental Enforcement (BSEE) and the U.S. Environmental Protection Agency (EPA) in collaboration with the Bedford Institute of Oceanography, Department of Fisheries and Oceans Canada (BIO DFO), New Jersey Institute of Technology (NJIT) and Dalhousie University. Both projects dovetail together in addressing the ability to differentiate physical from chemical dispersion effectiveness using dispersed oil simulations within a flume tank for improving forensic response monitoring tools. This report is split into separate Tasks based upon the two projects funded by BSEE:

- 1) Dispersant Effectiveness, In-Situ Droplet Size Distribution and Numerical Modeling to Assess Subsurface Dispersant Injection as a Deepwater Blowout Oil Spill Response Option.
- 2) Evaluation of Oil Fluorescence Characteristics to Improve Forensic Response Tools.

TASK A: Dispersant Effectiveness, In-Situ Droplet Size Distribution and Numerical Modeling to Assess Subsurface Dispersant Injection as a Deepwater Blowout Oil Spill Response Option.

The main objectives of work under Task A were to evaluate high velocity subsurface releases of physically and chemically dispersed oil using a flow-through wave (flume) tank. This project addressed three issues: (1) performance evaluation of dispersants for subsurface injection into sub-sea blowouts, (2) tracking, modeling, and predicting the movement and spread of the deepwater plume and oil surfacing from deepwater blowouts, and (3) evaluating the influence of dispersant applications in reducing the concentration of volatile organic compounds emanating from the water surface. Oil dispersion experiments were conducted in the flume tank at the Department of Fisheries and Oceans Canada, Bedford Institute of Oceanography (DFO BIO), which is equipped with an underwater oil release system to simulate a high-pressure release of oil (akin to a deepwater blowout). Subsea plume simulations were generated with a pressurized underwater oil release system adapted from existing technology developed by Masutani and Adams (2000). To mitigate wall effects and to generate oil droplets

in the size range observed at depth during the Gulf of Mexico Deepwater Horizon (GoM DWH) oil spill, a high flow-rate of oil (3.8 L/min) was released through a small diameter nozzle (2.4 mm). Although it is impossible to simulate in the tank the extreme hydrostatic pressures that exist at 1500 m water depth, underwater high-pressure release of crude oil can be simulated with and without dispersant addition. The researchers also recognize that the shallow nature of the tank does not allow for investigating the rise velocity of the droplets that would be observed in a long (~1500m) water column. Rather, the tank allows for gathering data on the differences in droplet size and distribution during physical and chemical dispersion (akin to that observed during DWH) and for observing the vertical and horizontal movement of the droplets. Although results cannot be directly scaled or translated to a deepwater spill in the ocean, results are still useful for understanding the formation and movement of oil droplets under varying oil and dispersant type, dispersant amount and water temperature.

A total of 48 core and 24 complimentary flume tank experiments were conducted to evaluate the effectiveness of dispersant injection and attenuation of the plume as a function of oil type (US EPA reference oils: Alaskan North Slope (ANS) pipeline blend for a light-medium crude, IFO 120 for a heavy refined product and South Louisiana Crude (SLC) for a light crude, and also a gas condensate), chemical dispersant type (Corexit 9500 and Finasol OSR 52), dispersant-to-oil ratio (DOR of 0, 1:20, 1:100, and 1:200; corresponding to DOR concentrations of 0, 5, 1, and 0.5%) and water temperature (< 10 °C for low temperature and > 10 °C for higher temperature). Experiments were conducted at a fixed horizontal current flow rate of 1 cm/s (~ 1/8th of deep water flow rates in the GoM). Faster current was not permissible as it would have resulted insufficient time for collection of *in situ* measurements and discrete samples. Experiments were conducted using oil at 80 °C, although this is lower than the reservoir temperatures for the DWH Macondo wellhead (estimated at 130°C), this is as high as the experimental design would allow for safety reasons given the limits of the pressurized canister.

Time series dispersion effectiveness was evaluated by measuring dispersed oil concentrations from samples collected in the flume tank, and via *in situ* droplet size distribution analysis and fluorescence measurements. Discrete samples were collected for oil chemical analysis of Total

Petroleum Hydrocarbons (TPH) using gas chromatography coupled to a flame ionization detector (GC-FID) and the analysis of Benzene-Toluene-Ethylbenzene-Xylene (BTEX) via gas chromatography mass spectrometry (GC-MS), employed to quantify oil concentration and partitioning of hydrocarbon compounds in seawater.

The produced Droplet Size Distribution (DSD) was determined by using Laser *In-Situ* Scattering and Transmissometry instruments (LISST-100X, type C; Sequoia Scientific Inc. Seattle, WA) to track the full range diameters of chemically and physically dispersed oil droplets. Larger oil droplets, whether physically or chemically dispersed, may be capable of coalescing and rising to the surface under less energetic mixing conditions. The LISST measures particle size and outputs the concentration of particles in 32 logarithmically spaced size bins between 2.5 to 500 μm , thus facilitating a comparison between natural (physical) and chemical dispersion efficiency of crude oil. All submersible sensors were operated with real-time data acquisition throughout each experiment. *In situ* fluorescence was monitored real-time using two Chelsea Technologies Group AquaTrackas (crude and refined oil types), one Sea Bird – Wet Labs Inc. ECO (gelbstoff type), two Turner Designs Inc. Cyclops (crude and refined oil types) and one GMBH Trios (hydrocarbon type) fluorometers. Many of the fluorescence sensors used in this study are the same models employed to track the subsea plume during the DWH oil spill and confirm dispersion effectiveness. Sensors used in this work are also ones provided as examples in the National Response Team (NRT) *Subsea Dispersant Monitoring and Assessment Interim Guidance* Document, that states “the Risk Plan should use a properly calibrated oil-specific fluorometer (e.g., Chelsea UV AQUAtracka, Turner Designs Cyclops, Wet Labs ECO, or equivalent oil-specific instrument) to enable ongoing improvements in sampling”.

Also monitored during experiments was the level of Volatile Organic Compounds (VOC) above the air-water interface of the tank using a handheld photo-ionization detector based meter to evaluate concentrations from the perspective of worker safety. Cautioned are the implications of these shallow water tank results, however as the short vertical water column did not allow for any stripping or dissolving of volatile compounds into the water column as would be expected during a deepwater oil release. Correlations between *in situ* fluorescence data,

droplet size distribution, total particle concentration, and oil chemistry serve as inputs to the modeling activities of this project.

Oil droplet size distribution (DSD) data from this study is essential for the improvement of oil spill trajectory and ocean circulation modeling processes to predict the fate and transport of subsurface plumes and surface oil slick movement. This has implications for improving the scientific and response community's understanding on the impacts of dispersant application at depth, ultimate fate of subsurface dispersed oil plumes and potential natural resource damages. Recent advancements in the use of numerical modelling have allowed oil droplet size predictions resulting from a subsurface release. Several different mathematical approaches have been used to determine how oil would behave flowing out of an orifice at high pressure. This includes the modified Weber Number technique (Johansen et al., 2013) and the VDROP-J model (Zhou et al., 2014) to predict oil droplet breakup taking into account oil viscosity and interfacial tension. However, there is a limited amount of large scale real world data to help validate the output of these models. This study provided the opportunity to further test these techniques through the use of several different oil types and treatment conditions. Additional results from the numerical modelling using data obtained from tank experiments are presented in Appendix G, with Part 1 using the modified Weber Number and Part 2 using VDROP.

The premise for this research is that the evaluation and efficacy of chemical dispersants at depth will differ dramatically from conventional use of chemical dispersants for treating surface oil slicks. This is due to difference in mixing energy, where for surface slicks is provided mainly through naturally occurring surface waves and currents, particularly breaking waves. Monitoring of DSD is essential in differentiating between chemically and physically dispersed oil. Tank observations using underwater injection experiments provide evidence of stable dispersion that may be expected during subsea dispersant injection. Larger oil droplets, whether physically or chemically dispersed, may be capable of coalescing and rising to the surface under less energetic mixing conditions. The experimental results from this work demonstrate the chemical dispersion of oil into small droplets and help to predict the

likelihood of coalescence and resurfacing of oil. Results of the project provide spill responders with critical information on the utility of subsurface dispersant application as an oil spill response option and the modeling capabilities that are available to predict oil trajectory during deep water blowouts. Both assist decision-making regarding countermeasures.

TASK B: Evaluation of Oil Fluorescence Characteristics to Improve Forensic Response Tools.

This project addresses the evaluation of oil fluorescence characteristics and sensor performance for improving response tools used to inform oil spill countermeasure decision-making. Fluorescence has long been used as ‘one tool in the toolbox’ for surface spills and used to supplement visual confirmation during response efforts. Recent oil and gas production in extremely remote locations brings an increased risk of spills in under-the-ice and/or deep-sea environments. For releases in these environs, responders will be evermore reliant on submersible sensors for plume tracking when the human eye cannot be employed. As such, the oil spill community has identified the need for better characterization of spilled oil by fluorometers.

Submersible fluorometers deployed during the 2010 DWH oil spill highlighted the challenges in ensuring selection of the optimum sensor configuration as fluorescence peaks occur over a wide nanometer range, vary in shape and wavelength position, are dependent on oil type due to chemical differences, and are affected by the addition of dispersants. This project addresses these concerns through the following objectives: (1) Characterization of oil optical properties as a function of oil type, DOR and concentration; (2) Generation of a comprehensive Excitation Emission Matrix Spectroscopy, or Matrices (EEMs) library that will be subjected to advanced statistical analyses for identification of wavelength regions best suited for oil detection; and (3) Evaluation of sensor performance through a series of experiments in a flume tank capable of static and flow-through operations, where sensor data will be validated with chemical and optical analyses.

A series of bench-scale dispersed oil-in-seawater experiments were conducted on 25 oils at 4 dispersant-to-oil ratios (DORs) using Corexit 9500 chemical dispersant. Analysis of the resulting 3D fluorescence EEMs show oil-specific results as well as differing effects of dispersant and DORs. Results will inform the identification of optimum oil detection wavelengths in the marine environment as well as confirmation of the chemical effectiveness of dispersant application. Samples were prepared using baffled flasks to physically disperse the oil within seawater. The effect of dispersant on oil-specific fluorescence is shown, where shifts in intensity and peak wavelengths were observed. Results were compared to chemistry results of oil components.

Results of the laboratory EEMs analysis were compared to EEMs collected under Task A of this project to compare the applicability of baffled flask fluorescence to large scale mixing experiments in the flume tank.

Given recent advances with *in situ* fluorometers, enabling detection at lower UV-wavelengths, these findings help to discern wavelength regions influenced by dispersed oil within seawater, improve the interpretation of fluorescence data, and inform decision-making by responders. Findings from this project will serve to improve confidence in field data, filling operational gaps and formulating operational guidelines.

Findings: Tasks A and B

Overall findings from both tasks of this project include:

1. Addition of either Corexit 9500 or Finasol OSR 52 chemical dispersants to Alaskan North Slope (ANS), IFO 120 and South Louisiana Crude (SLC) oils decreased the Volume Mean Diameter (VMD) and shifted the DSD to smaller droplets. In general, Corexit 9500 produced smaller droplets compared to Finasol OSR 52.
2. Dispersions created without chemical dispersants or DOR = 1:200 yielded VMD larger than 70 μm and exhibited unimodal DSD. Dispersions created with DOR = 1:20 yielded VMD between 2.5 to 70 μm size range with a bimodal distribution. This suggests that produced droplets from a DOR = 1:20 dispersant injection with ANS would likely

remain dispersed in the presence of mixing energy given the larger proportion of small droplet sizes observed.

3. Particle size analyses near the injection release (LISST Release) exhibited larger VMD compared to those generated further downstream from release in the tank (LISST Downstream) indicating a shift from larger to smaller droplets within the plume, with and without the presence of dispersant during the 12 minute experiments for ANS and SLC oils. This effect was not always observed with the heavier IFO 120 oil because small droplets were less predominant for this heavier oil.
4. For ANS, dispersion with $< 70 \mu\text{m}$ droplet VMD was observed for the DOR = 1:20 treatments at both cold and warm water temperatures. Water temperature did not appear to influence the DSD or VMD for this lighter crude oil. However, a temperature effect was observed on the Total Particle Concentration (TPC), where lower temperatures were coincident with fewer particles dispersed within the plume for a given volume of oil injected.
5. The addition of Corexit 9500 or Finasol OSR 52 to IFO 120 during warm temperature experiments resulted in a shift in DSD and a decrease in VMD; however bimodal distribution was not achieved and even DOR = 1:20 did not yield VMD less than $70 \mu\text{m}$ in most cases. At cold water temperatures, lower droplet sizes were not observed with the addition of dispersant, where DOR = 1:20 remained well above $200 \mu\text{m}$. This suggests that dispersant addition to this oil at cold or warm temperatures would not yield droplet sizes that would likely remain in suspension.
6. For experiments conducted at water temperatures less than 5°C , The LISST particle size analyzed yielded unexpected DSD where even a unimodal distribution was not measured. Chemistry and *in situ* fluorescence data indicate that the oil was in fact dispersed adequately. This suggests operational problems with the LISST below 5°C , even though it is within the operating temperature of the LISST (manufacturer manual). Additional testing of the cold water temperature limits of the sensor is recommended.

7. SLC oil was more dispersible compared to ANS for treatments with and without chemical dispersant. Bimodal distribution was observed during DOR = 1:20 and some DOR = 1:100 experiments indicating that the jet release of this particular oil into warm water produced smaller droplets than the ANS.
8. *In situ* fluorescence serves as a good proxy for oil concentration during the subsurface injection experiments. Given the experimental design, fluorescence is better suited for correlation with particle size analysis and concentration. Heterogeneity of the produced plumes and the short time scale of experiments (~12 min) led to difficulties in correlations between the plume particle size analyses and chemistry results. This is in part due to discrete samples representing 15 second averages as opposed to instantaneous measures given by fluorometers and particle size analyzers.
9. VOC air monitoring was conducted above the tank at two horizontal locations during experiments. The gas condensate exhibited the highest surface VOC concentrations, followed by ANS and SLC which exhibited similar values. Lowest concentrations were observed for IFO 120 experiments. High VOC concentrations in the air were usually accompanied by lower BTEX concentrations in the water. For all oils tested, the addition of chemical dispersants (DOR = 1:20) resulted in a reduction in VOC concentrations within air compared to experiments without dispersant near the jet release location above the tank.
10. Computer programs for jet hydrodynamics, droplet size distribution, and movement of oil droplets within the jet/plume were employed where developed models were calibrated to experimental data obtained from the oil jet experiments in the flume tank. The models VDROP-J and JETLAG were used to predict the streamwise velocity and the holdup along the centerline of the plume, where both models were in agreement, implying that VDROP-J is capable of predicting the average droplet size distribution in the plume. In the absence of dispersant, the model VDROP-J predicted the oil DSD measured by the LISST. In the presence of dispersant, the VDROP-J model captured the overall trend of the DSD, but was challenged in capturing the peak in droplet concentration observed for 5 microns. The observed peak is could be due to tip-

streaming (when high DORs oil droplets shed filaments from their edges resulting in smaller droplets), and VDROD-J does not yet have a module for this component.

11. The Modified Weber Number approach developed by SINTEF is a recent and promising approach for predicting DSD. Previously, the method has been validated solely by a light crude oil. For this project, median droplet diameters (d_{50}) and the relative droplet size (d_{50}/D) were calculated based on the measured droplet sizes obtained from the tank experiments, and the relations between d_{50}/D and modified Weber number, Reynolds number, and oil concentration were quantified. Results demonstrate that chemical dispersants tested here reduced the droplet size of ANS in both cold and warm temperatures and that dispersants tested here are more effective in reducing droplet size with ANS compared to IFO 120. A two-step Rosin-Rammler approach was found to better predict the droplet size distribution in the empirical data as indicated by higher regression coefficients.
12. Fluorescence EEMs were generated for 25 oil types under varying DOR. Oils could be separated into two categories based on dispersibility; where light, medium and heavy oils were found in each category. Fluorescence peaks are chemistry dependent and were well correlated with Total Petroleum Hydrocarbon (TPH) and Benzene-Toluene-Ethylbenzene-Xylene (BTEX) concentrations. EEMs generated from tank and Baffled Flask Test (BFT) experiments were in agreement with respect to fluorescence peak position and Fluorescence Intensity Ratio (FIR) values as an indication of dispersion effectiveness.

Task A.1 Introduction & Relevance

The 2010 Deepwater Horizon (DWH) oil spill in the Gulf of Mexico has highlighted the pressing need for a better understanding of the interaction of chemical dispersants and crude oil at ocean depth. Early in the blowout release, partial emulsification of oil was observed as it rose to the surface from 1500-m depth, and surface slicks were not continuous (JAG report, 2010). A decision was made to inject dispersants directly at the release point as a possible means to increase efficiency of dispersion and to potentially reduce the amount of dispersant needed if applied at the air-sea interface (CRRC Report, 2010). Large quantities of chemical dispersant were applied via subsurface injection and traditional spraying from aircraft onto the surface oil slick (Oil Budget Calculator, 2010). At a Coastal Response Research Center (CRRC) workshop to discuss the use of subsurface chemical dispersants as an oil spill response option, recommendations to the RRT (Regional Response Teams) by spill response and research expert attendees were made on potential advantages of subsurface dispersant injection given the rate of continuous oil release and preliminary evidence of the dispersant efficacy from the DWH spill (CRRC, 2010). Potential advantages of this application included the fact that the fresh (unweathered) oil was considered well suited for dispersion, operators were able to inject the dispersant directly into the oil stream thereby maximizing dispersant/oil contact, sufficient control of DOR (Dispersant-to-Oil Ratio) could be maintained, injection may minimize the need for surface dispersant application because of reduced oil surfacing and optimized subsurface application would likely promote formation of smaller, more stable droplets of oil, enhancing biodegradation (Lee et al., 2009).

As recommended by the interagency Unified Area Command (UAC) and on-site emergency spill response coordinators, a large-scale environmental monitoring program was implemented to detect and characterize dispersed oil based on field data and plume modeling outputs. This allowed for tracking the subsurface oil plume emanating from the blowout wellhead. Droplet Size Distribution (DSD) analysis using the LISST-100X Laser *in-situ* Scattering and Transmissometry System (Sequoia Scientific Inc. Seattle, WA) and fluorescence intensity from

submersible fluorometers were used as an indication of Dispersion Effectiveness onboard the research vessels, where particle concentrations were monitored to evaluate oil dispersion (presence of small droplets $\leq 70 \mu\text{m}$) based on previous studies for surface dispersant applications (Li et al., 2009b). Data analysis of the monitoring samples provided sound evidence of the presence of oil-bearing small particles both in surface waters and in the subsurface plume (JAG report, 2010). Furthermore, a negative correlation between subsurface dispersant injection and low molecular weight compounds in surface waters was observed. In contrast, a strong positive correlation was observed in the subsurface. These results suggest that subsurface dispersant use may have promoted the formation of small oil droplets in the deep sea. This would likely enhance the natural weathering and dissolution of oil in the water column, thus suppressing the presence of oil organic compounds in surface waters.

Although subsurface *in situ* dispersants were used to counter a deepwater spill blowout, much uncertainty still exists in terms of the DE (Dispersion Effectiveness) with this type of application. For example, assumptions of the optimal DOR are based on empirical data mostly obtained from bench-scale experimental protocols that have been designed for testing at standard temperatures and pressures (STP), whereas conditions at a wellhead on the ocean floor or anywhere along a riser beneath the ocean surface could be significantly different. Hence, DOR for direct injection needs to be better understood. Although theoretical analyses and experiments suggest that jet breakup of the oil is insensitive to the absolute value of system hydrostatic pressure for incompressible liquid-liquid systems (Masutani and Adams, 2000), the effects of several ambient environmental factors on subsurface dispersant effectiveness, including high release pressure, high oil temperature, low water temperature, and the presence of methane and suspended sediments in the oil plume and/or surrounding water column remain to be clarified. Improved understanding on the influence of these factors on DE and the interaction of crude oil and chemical dispersant under a range of turbulent regimes at depth is required for informed decision-making for future subsurface dispersant use.

For evaluating chemical dispersion effectiveness, standard laboratory tests are inherently limited in simulating real field operational performance due to space constraints that are critical for transport and dilution efficiency (NRC, 2005). To address the need to evaluate chemical dispersion effectiveness under more realistic oceanographic and environmental conditions, a meso-scale wave tank capable of generating breaking and regular non-breaking wave conditions is currently in operation at the Bedford Institute of Oceanography (BIO), Dartmouth, Nova Scotia. This tank facility has been used previously to characterize the tank hydrodynamics and the efficacy of several oil dispersant formulations on dispersion of different oil types, including fresh and weathered crude oils and heavy fuel oils under breaking wave conditions (Figure 1) (Lee et al., 2009; Li et al., 2008; Wickley-Olsen et al., 2007). Mathematical modeling and experimental measurements have been used in the characterization of the fluid dynamics of the flume tank. In modeling, computer fluid dynamics software packages have been used to conduct numerical simulation of the fluid field and transport phenomena of the flume tank under both non-breaking and breaking wave conditions. Experimentally, wave gauges (WG-50) have been used to monitor wave profiling throughout the flume tank under various hydrodynamic conditions. Acoustic Doppler Velocimetry (ADV) has been employed to evaluate the *in situ* instantaneous three-dimensional velocity distribution, which is used to compute the velocity gradients and energy dissipation rates (ϵ) in the tank. Using this facility, previous experiments have assessed chemical dispersant effectiveness as a function of energy dissipation rate and particle size distribution (Li et al., 2009a) and demonstrated that the effectiveness of a dispersant is strongly dependent on wave conditions, dispersant type, and oil type (Lee et al., 2009). A strong correlation has been established between dispersion effectiveness and *in-situ* droplet size distribution within the hydrodynamic regime, particularly energy dissipation rate, under a variety of non-breaking wave and breaking wave conditions (Li et al., 2008; Li et al., 2009a). The flume tank has also been operated in flow-through mode to accommodate the effects of underwater currents on dispersion and dilution of oil (Li et al., 2009b; Li et al., 2010). Experiments have also shown the reliability of fluorescence measurements as a proxy for oil concentration within physically and chemically dispersed oil (Conmy et al., 2014). Experimental studies have also been conducted

to better understand oil-mineral aggregate (OMA) formation and the influence of mineral fines on the physical and chemical dispersion of oil (Lee et al., 2009).

This report summarizes results from a project that addresses the operational performance of subsurface injection dispersant use on high pressure releases of oil within the flume tank. Developed methods were focused on monitoring subsurface oil transport by outfitting a new high-flow flume tank at the Department of Fisheries and Oceans Canada (DFO) Bedford Institute of Oceanography (BIO) facility with a new underwater high flow rate oil injection system. In this way, the efficiency of chemical dispersion during high pressure releases within the tank can be quantitatively evaluated and compared to experiments with physical dispersion (without dispersant addition). This work has implications for field response options. To this end, the **objectives** of this work were to:

- 1) Refine existing equipment, technologies, and methodologies for subsurface dispersant application evaluation and monitoring by measuring dispersed oil concentration, fluorescence, and *in situ* oil droplet size distribution,
- 2) Evaluate effects of water temperature and dispersant type on dispersion efficacy and dispersed oil droplet size distribution of oil at high temperatures,
- 3) Evaluate dispersion effectiveness (DE) as a function of oil type and dispersant-to-oil ratio (DOR) for subsurface dispersant injection,
- 4) Assess the effect of dispersant application on the VOC concentration in air above the air-sea interface of the flume tank,
- 5) Integrate droplet size distribution into deepwater blowout transport/behavior models to enable prediction of the dispersed oil droplets under high flow subsurface release velocities.

During the DWH spill, small droplet ($d \leq 70\mu\text{m}$) concentrations were monitored to aid in evaluating oil dispersion efficiency. The particle size and distribution data obtained from the field monitoring program during the DWH oil spill had a significant role in supporting emergency oil spill response operations, fate and transport modeling, and impact assessment.

Findings from this study will have significant implications in further supporting emergency response operations, spill transport models and assessments for future deepwater spills.

Task A.2 Experimental Methods

A.2.1 Flume Tank Description, Flow Calibration, and Operation

Oil dispersion experiments were conducted in the flow-through flume tank at BIO. The BIO flume tank is rectangular shaped with dimensions of 32 m in length x 2 m in height x 0.6 m in width, with an operational water height of 1.65 m. It was fabricated with carbon steel (3/16") and the interior and exterior surfaces are coated with a marine epoxy paint finish to reduce corrosion while operating under marine conditions. Two sets of manifolds consisting of five inflow and outflow pipes (each constructed of 4" PVC pipe and equipped with a ball valve so that the flow rate can be controlled) are fixed (1.1 m from the outer edges) at both ends of the tank (Figure 2). Two high flow centrifugal pumps (Magnetex 3575 Series, 3" suction, 4" discharge, 600 gpm, Houston, TX), one connected to the inflow manifold and the second connected to the outflow manifold provide a flow-through system used to generate horizontal water currents in the tank. A fiberglass holding tank is used to supply seawater for the system to ensure that a constant flow rate is maintained.

Seawater was obtained from the Bedford Basin, which is directly adjacent to the tank. Two smaller pumps (5 HP Pacer S Series Centrifugal Pump, 110 gpm, Lancaster, PA) were used to pull seawater (~50 cm below the surface) through a 3" suction hose from the Basin. A foot valve was installed at the end of the hose to maintain prime water in the line between fillings. Prior to entering the tank, the seawater was filtered through high-flow polypropylene bag filters (5 µm and 25 µm, Atlantic Purification, Dartmouth, NS).

During normal operations, the flume tank (31,500 L) and holding tanks (25, 000 L) were filled with filtered seawater. A stainless steel baffle was mounted (~0.5 m) in front of the influent manifold to control current flow. Flow gauges on the influent and effluent lines were

monitored and valve adjustments were made to obtain a balanced flow rate, and so that the operational volume was maintained throughout the experiment. Water current velocities were measured at various depths and locations in the tank using an ADV (Nortek Vectrino+, Boston, MA) and the flow rates adjusted until the horizontal water current velocities (3.5 cm/s) were consistent at all measured depths.

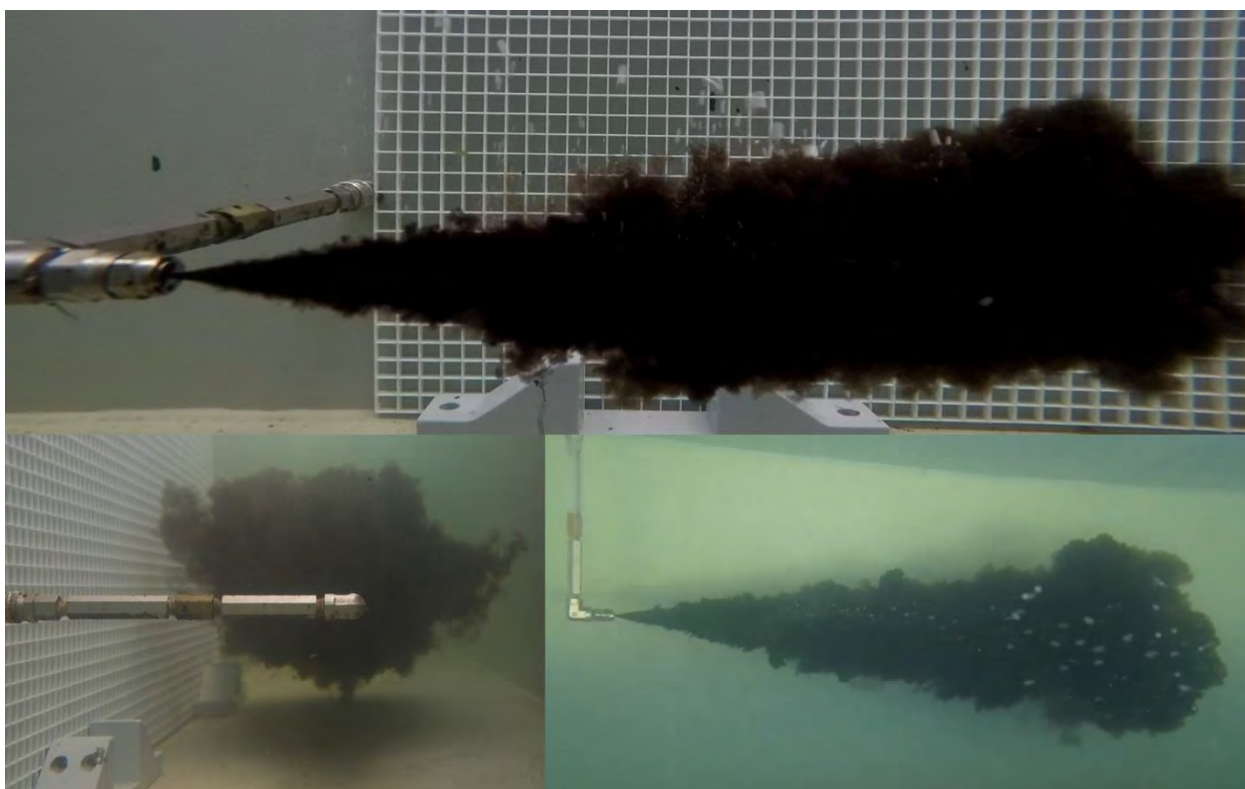


Figure 1. Photos of subsurface oil injection at the BIO flume tank showing the formation of the subsurface oil plume. Note that the background grid size is 1.5 cm x 1.5 cm.



Figure 2. Photo of the DFO BIO flume tank (top) and cross-section of the tank showing the high-flow manifolds used to generate horizontal water currents (not to scale).

A.2.2 Waste Water Treatment

Oil absorbent pads (New Pig, Tipton, PA) are used to manually remove oil from the water surface. The remaining water in the tank is removed by pumping it through an effluent pipe that discharges the waste water over layers of polypropylene PomPom Oil-Mops (New Pig, Tipton, PA) that filter the waste water by removing any remaining insoluble oil prior to discharging it back into the Bedford Basin. Water samples are collected from the treated effluent and the PomPom's are changed if total petroleum hydrocarbon concentrations exceed the minimum guidelines (10 ppm) for wastewater discharge in Canada. Pads and Oil-Mops are discarded as oily waste disposal.

A.2.3 Subsurface Oil Injection System

A custom (engineered in-house) subsurface oil injection system was used to generate dispersed oil plumes in the tank (Figure 3). Briefly, the system consists of a 2 L stainless steel pressure vessel that rests in a support rack. A series of valves and pressure gauges are connected to the pressure vessel. The assembled system is fastened to the outer wall of the tank by way of a quick connect bulkhead fitting. From the same location inside the tank, the fitting connects the outer assembly to a nozzle (2.4 mm inner diameter), which extends mid-width perpendicular to the tank wall (20 cm off the bottom and 9 m downstream from the inflow manifold) and is angled at the tip, so as to direct the discharge plume downstream. Given the shallow nature of the tank, this release setup enabled using the horizontal length of the tank to capture the plume movement.

For each experiment, oil or oil/dispersant premix is added to the pressure vessel (Figure 4A) in order to reduce the influence of any additional confounding factor of mixing effectiveness. Inside the pressure vessel is a copper coil that is connected to a water bath to permit the oil to be heated to 80°C, which takes 30 minutes. Although lower than the estimated oil temperature during the DWH release (~130°C), this is the highest temperature permissible in the pressure vessel to avoid risk of explosion. The vessel is then pressurized (40 psi for ANS, SLC and Condensate; 60 psi for IFO 120) with compressed Nitrogen. A ball valve connected to

the pressure vessel is manually opened and oil is released through the subsurface nozzle into the flume tank (Figure 4B). The release time and total volume (determined by mass) of oil injected are recorded. After each experiment, the entire subsurface injector system was cleaned by flushing repeatedly with toluene, acetone and fresh water until no visible oil remained prior to next experiment.

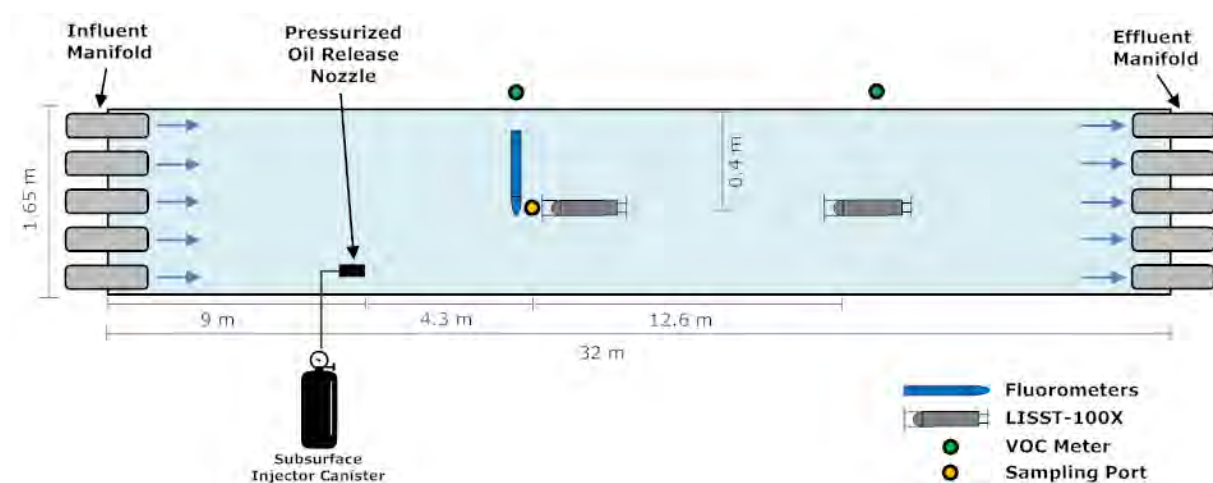


Figure 3. Schematic diagram showing the location of the subsurface injector and *in situ* instrumentation submerged within the tank.



Figure 4A. Photo of the pressurized oil vessel used to hold the oil for the subsurface release.

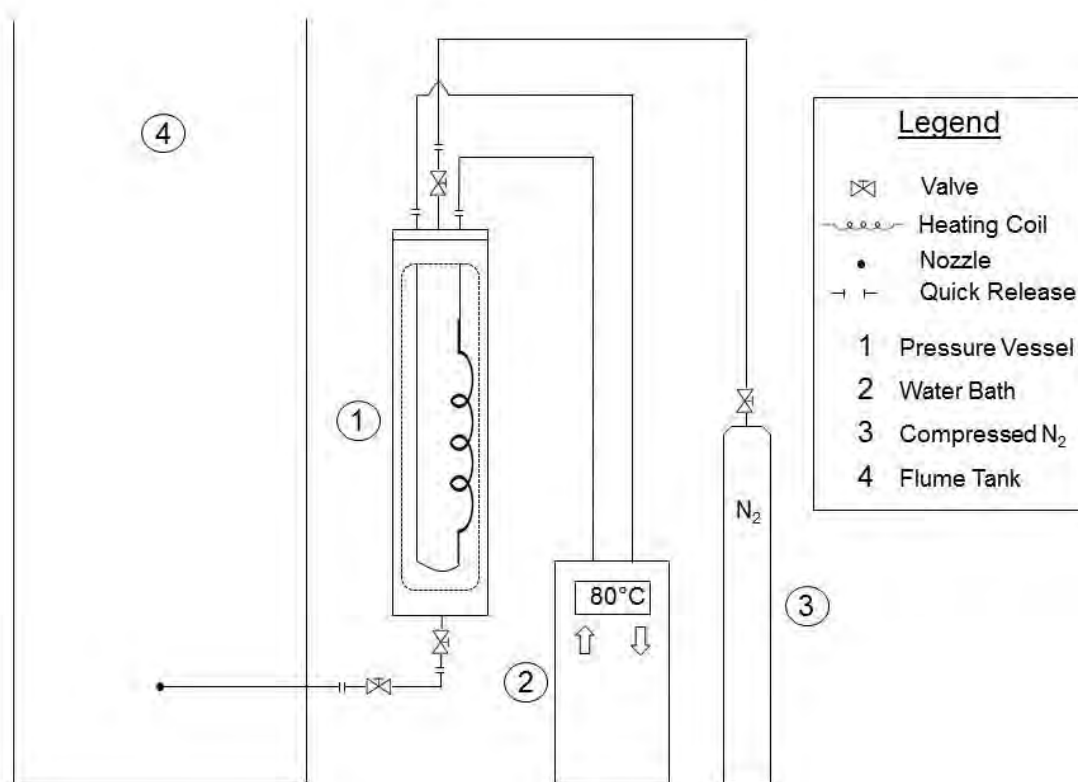


Figure 4B. Schematic diagram of the pressurized oil vessel for subsurface oil release system in the flume tank.

A.2.4 Submersible Sensor Deployment

Fluorescence- A total of six hydrocarbon fluorometers that are used worldwide during oil spill response were evaluated during this study (Table 1). The fluorometers were mounted on an aluminum frame located 4.3 m from the oil release point with their UV windows and at a depth of 0.4 m. The instruments were attached to a crosspiece support bar, so that they were all located the same distance downstream from the oil release point with the UV window pointed directly down at the bottom of the tank.

Table 1. List of hydrocarbon fluorometers used in this study. QSDE and PAH represent quinine sulfate dihydrate and petroleum aromatic hydrocarbons, respectively.

Instrument	Excitation/Emission wavelengths and Units
Chelsea UV AQUAtracka (Refined)	239/360nm, µg/L Perylene
Chelsea UV AQUAtracka (Crude)	239/440nm, µg/L Carbazole
Turner Designs Cyclops (Fine Oil)	254/350nm, Volts
Turner Designs Cyclops (Crude Oil)	365/510nm, Volts
Sea Bird – WET Labs ECO-FLU	370/460nm, µg/L QSDE
GmbH Trios	254/360nm, µg/L PAH

Several different data acquisition systems were used to control and collect data from the *in situ* fluorometers. The GmbH Trios was operated by the manufacturer's power supply and data acquisition system using the MSDA_DE software, which provided a real-time display of the signal intensity in calibrated units of µg/L PAH. The sampling rate was set at one reading every five seconds and raw data was saved as a comma delimited (.csv) file. The two Turner instruments were connected to a Databank Handheld Datalogger (Turner Designs, Sunnyvale, CA), which powered both instruments and recorded data at a sampling rate of 1 reading every

3 seconds. The datalogger auto-gain feature cycles through settings of 1x, 10x, and 100x depending on the signal intensity. Raw data was recorded as signal intensity in mV and was offloaded from the datalogger via USB connection to a laptop and saved as a text (.txt) file. The Sea Bird - WET Labs and Chelsea instruments were connected to a custom-built power supply and data acquisition system (Pace Scientific XR5-SE datalogger; Mooresville, NC), which collected data from the instruments at a sampling rate of one reading per second. The signal was recorded internally on the datalogger and then sent via wireless connection to a laptop in real-time display. Raw data was recorded as signal intensity in mV and offloaded as a .txt file.

Particle Size Analysis - Oil droplet size was measured *in situ* using two LISST-100X particle size analyzers (Sequoia Scientific, Seattle, WA). The instrument measures particle sizes in the range of 2.5 – 500 μm in 32 logarithmically spaced bins. The first LISST was located immediately after the aluminum frame supporting the fluorometer package at a distance of 5.1 m from the oil release point and the second LISST was located at 16.9 m from the oil release point and both at a depth of 0.4 m (Figure 3). Placement was informed by the numerical modeling team of this project to maximize oil droplet detection without saturating the instrument. Both instruments were connected via a 20 m cable to laptops running the LISST-SOP data acquisition software (version 5). Prior to the start of each experiment, a background scatter file of the seawater quality in the tank was generated and used later to subtract from the final experimental data file. The instruments were operated in real-time mode with a sample acquisition rate of one measurement every three seconds.

Supplemental Measures - Weather conditions (air temperature, wind speed, wind direction, humidity, rainfall) for all experiments were recorded using a Vantage VUE Weather station (Davis Instruments, Hayward, CA). Water temperature and salinity were measured using a YSI handheld probe. Underwater video of oil droplets and the transport of the plume were captured using a GoPro Hero4 digital camera, as well as a Sony RX100 III digital camera with underwater housing.

A.2.5 VOC Air Monitoring

Surface volatile organic compound (VOC) concentrations were monitored using handheld ToxiRAE Pro PID portable gas detectors (RAE Systems, San Jose, CA). Two detectors were used for each experiment, and they were positioned 0.4 m above the water surface at distances of 5.1 and 16.9 m from the oil release point (Figure 3). The detectors were calibrated using a certified 25 ppm benzene calibration gas (AirLiquide, Dartmouth, NS) according to the manufacturer's recommended procedure. Instrument drift was checked periodically against the calibration gas and recalibrated if necessary. During the experiments, the handheld meters were set to datalogging mode, which recorded VOC concentrations as ppm of benzene every three seconds. This data was offloaded and saved as a .txt file for processing.

A.2.6 Discrete Water Sample Collection

Water samples for chemical analysis were collected at various time points throughout the experiments (Table 2). Three ¼" stainless steel tubes were attached to the aluminum fluorometer frame, so that the end of the tube was located at the same depth as the instrument UV windows (0.4 m). These were attached via peroxide cured silicon tubing (Cole Parmer, Vernon Hills, IL) to a Masterflex L/S multi-channel digital peristaltic pump (Cole Parmer, Vernon Hills, IL) which flowed to a three-way valve system. When the valve was set to bypass mode, the water in the lines was continuously primed and flowing, so it could instantaneously be switched to sample mode to allow for sample collection. The pump flow rate was set to approximately 120 mL/min, and all tubing was flushed with clean seawater for 5 minutes prior to the start of any experiment. Tubing was replaced on an as needed basis. Water samples from the effluent manifolds were also collected through a 1" sampling valve at the exit of effluent pipe prior to it entering the treatment system.

A.2.7 Oil and Dispersant Samples

Four different hydrocarbon products were tested in this study to cover a range of viscosity and physico-chemical characteristics: Two crude oils, a fuel oil, and a gas condensate. Samples of Alaska North Slope crude oil (ANS) and Intermediate Fuel Oil 120 (IFO 120) were obtained from

BSEE. Sweet Louisiana Crude was obtained from NOAA. Gas Condensate was obtained from Exxon Mobil and originated from the Sable Offshore Energy Project. Physical properties of the samples (Table 3) were measured using an Anton Paar SVM 3000 Stabinger Viscometer (Anton Paar, Saint Laurent, QC). Supplies of chemical dispersants (Corexit 9500 and Finasol OSR 52) were purchased from the manufacturers.

Table 2. Water sample collection strategy for the core and complimentary experiments. TPH and BTEX represent Total Petroleum Hydrocarbons and Benzene-Toluene-Ethylbenzene-Xylene, respectively.

Time (min)	TPH (Tank)	TPH (Effluent)	BTEX (Tank)	BTEX (Effluent)	Fluorometry (Tank)	Fluorometry (Effluent)
Background	X		X		X	
T = 0	X	X	X			
T = 0.5	X					
T = 1.0	X		X		X	
T = 1.5	X					
T = 2.0	X	X	X		X	
T = 2.5	X					
T = 3.0	X		X			
T = 3.5	X					
T = 4.0	X	X	X	X		
T = 4.5	X					
T = 5.0	X		X	X		
T = 6.0	X	X	X	X		
T = 8.0	X	X	X	X		X
T = 10.0	X	X	X	X		
T = 12.0	X	X	X	X		
Total # Samples/Expt	16	7	11	5	3	1
Total # of Samples Analyzed	TPH – 1725 BTEX – 1200 Fluorometry – 300					

Table 3. Physical and chemical property measurements of the oils used in this study.

Oil Type	Measurement Temperature (°C)	Density (g/mL)	Kinematic Viscosity (centistokes)	BTEX Content (%)
Alaska North Slope (ANS)	50	0.8529	6.4	2.3
	40	0.8600	8.3	
	25	0.8704	13.1	
	15	0.8777	18.9	
Intermediate Fuel Oil (IFO 120)	50	0.9345	134.0	0.2
	40	0.9411	240.3	
	25	0.9515	781.4	
	15	0.9587	2481.5	
Gas Condensate (CND)	50	0.7247	0.4	13.4
	15	0.7466	0.5	
Sweet Louisiana Crude (SLC)	50	0.8219	3.2	2.4
	40	0.8291	4.0	
	25	0.8733	5.8	
	15	0.8473	8.2	

A.2.8 Experimental Design – Core and Complimentary Experiments

Both the flume tank and holding tanks were filled with filtered seawater as described above. Seawater temperature and salinity were recorded using a handheld probe (YSI Incorporated, Yellow Springs, OH). After the flume tank was filled, the *in situ* instrumentations including the fluorometers, LISSTs, and VOC meters were positioned in desired locations as indicated previously. The subsurface oil release system was filled with oil or oil/dispersant premix, which was heated to operating temperature. The water supply lines leading to the high flow pumps

were primed and the inflow and outflow pumps were started. The system was run in recirculation mode for 10 minutes to allow current flow to stabilize in the flume tank. At a set time point prior to oil injection (5 minutes), data-logging on all instruments was started and background seawater samples were collected. After the oil was injected into the tank, the real-time readout of the fluorometer signal was monitored. Once the first spike in signal intensity was observed (usually after 2 minutes based on the fluorometer signal readout), a stopwatch was started and the first chemistry samples were collected. At this point the high flow system was switched from recirculation mode to flow through, which diverted the water flow into the effluent treatment system instead of returning it to the holding tank. The experiment ran for 12 minutes, at which point the high flow pumps were turned off and the instrument data acquisition was stopped. The tank was cleaned and drained as described above. Tank and instruments were cleaned using Big Orange Degreaser (Zep Superior Solutions, Atlanta, GA), to prevent any potential contamination between experiments. Instrument windows were cleaned using disposable alcohol wipes (Bausch and Lomb, Vaughan, ON). Water samples were returned to the lab and stored at 4°C.

A.2.9 Submersible Sensor Calibration Experiments

The calibration experimental setup was similar to the core and complimentary experiments, except that the oil was added in a step-wise (tank dilution series measurements) fashion to the flume tank as shown in Table 4. Calibration experiments were conducted in such a way to create a series of known concentrations of dispersed oil in the flume tank. Predetermined amounts of oil and dispersant (Corexit 9500) premix were added to the tank (Alaska North Slope, ANS, crude was used at a DOR of 1:20) using the subsurface injector.

The flume tank was operated in recirculation mode and oil/dispersant premix injections occurred every 45 minutes, which provided a sufficient time for the dispersed oil concentrations to stabilize in the tank (previous testing of this system showed that hydrocarbon concentrations in the tank are homogenous after 45 minutes of recirculation). The recirculation of water in the tank provided sufficient mixing energy to allow small droplets

generated by the subsurface injector to remain dispersed in the water column. *In situ* instrumentation was located at the same locations as all other experiments. Water samples were collected at 45 minute time intervals after each oil addition.

Upon reaching homogeneity in the tank (i.e. 45 minutes after each oil addition), the average fluorometric intensity signal collected over a 4 minute time period was calculated. Fluorometers were calibrated to manufacturer suggested units using factors provided. Triplicate water sample analysis results for Total Petroleum Hydrocarbons (TPH) and Benzene-Toluene-Ethylbenzene-Xylene (BTEX) were averaged that correspond with the same time points. Fluorescence and chemistry averages were regressed to generate calibration curves of TPH and BTEX vs signal intensity for oil additions ranging from 1 to 18 ppm. Higher variability at low concentrations resulted in the exclusion of some data points in the regression calculation.

A.2.10 Submersible Fluorometer and LISST Data Processing

Raw LISST data files were processed using a statistically-based quality control script written using the R statistical package (www.r-project.org). In summary, this script identifies and removes “Over Range” samples (defined as 0 $\mu\text{L/L}$ across all particle size bins) and outliers. Outliers are defined as any reading that is greater than the moving mean (5 data points before and after the targeted time point) of the dataset multiplied by four times the standard deviation (over the same interval as the moving mean). Due to the potential for one or more extreme outliers to skew both the moving mean and standard deviation calculations for points around them, this outlier detection routine is run iteratively, excluding previously flagged points, until no more outliers are detected. Once these QC steps have been performed, the script calculates a number of parameters from the data such as Total Particle Concentration (TPC), Volume Mean Diameter (VMD), and Particle Size Concentration (PSC). It then goes on to detect the plume curve (if present) and time-normalizes the data based on that location. Data are presented as Droplet Size Distribution (DSD). Plots presented include data 2 minutes before and 8 minutes after the start of the plume curve. Data from the Downstream LISST were normalized so that the plume began at $t = 5$ min in order to visually convey that the plume was

detected in the tank roughly 3 min after detection by the LISST further upstream near point of injection release.

Similar to the LISST data, a script was used to detect outliers in data collected from the *in situ* fluorometers. Curve detection was then performed and the data was time-normalized to include 2 minutes of data before, and 8 minutes of data after the start of the plume curve. The baseline of the plume curve was then calculated using data points observed in the first minute preceding the start of the curve and this baseline was subtracted from the data. Finally, factory calibration factors were applied to the data values for each instrument before plotting.

Table 4. Step-wise sensor calibration experiment parameters.

Oil Addition #	Mass of Oil Added for each Addition (g)	Cumulative Oil Concentration in Tank (mg/L)
1	9.45	0.3
2	9.45	0.6
3	12.6	1
4	63	3
5	94.5	6
6	189	12
7	189	18

A.2.11 Analytical Chemistry Analysis

Total Petroleum Hydrocarbon (TPH) Analysis - The method used for extraction and processing of TPH samples was developed by DFO in-house (Cole et al., 2007; King et al., 2015). Water samples were collected in pre-weighed 125 mL amber glass bottles and filled to approximately 90 mL. Sample bottles were weighed and a mass difference was used to determine the total volume of the collected water sample. The samples were immediately stored at 4°C until ready for further processing. Within 24 hrs of collection, 10.0 mL of dichloromethane (DCM) was added to each sample. The samples were shaken by hand for 30 seconds, and then placed on a Wheaton R2P roller (Wheaton, Millville, NJ) set at 9 rpm. After 18 hours on the roller, a Pasteur pipette was used to transfer the DCM solvent layer into a pre-weighed 15 mL graduated centrifuge tube. The solvent was then evaporated under a gentle stream of nitrogen using an N-Evap (Organomation, Berlin, MA) and topped up with DCM to a final volume of 1.00 mL. The solvent extract was transferred into an auto-sampler vial and stored at -20°C for GC-FID analysis.

Sample extracts (1 µL) were injected using an Agilent 7683 auto-sampler into an Agilent 7890B GC, using splitless injection set to oven track mode (2°C higher than the oven temperature program). The column used for separations was a Supelco MDN-5s 30 m × 250 µm × 0.25 µm (length × i.d. × film thickness). Hydrogen was used as a carrier gas with a flow rate of 3.0 mL/min. The GC oven is programmed to an initial oven temperature of 35°C, held for 2 min, followed by an increase to 320°C at 20°C/min, and held at 320°C for 10 min, with a total run time of 26.25 min. The GC flame ionization detector (FID) was operated at 320°C with the hydrogen flow set at 30 mL/min and the air flow set at 400 mL/min. An eight point calibration was generated using standards prepared from the appropriate crude oil stock that was used to generate the TPH samples (e.g. ANS, IFO 120, SLC or Gas Condensate). Peak quantification was performed using relative response factors. Routinely the method of extraction was tested for efficiency by a spike and recovery study. Typically, a mean percent recovery of >90% was calculated from filtered seawater spiked with crude oil. Lab and field blanks were incorporated in the method.

BTEX Analysis - EPA Method 8240 (purge and trap) was modified by running a gas chromatograph/mass spectrometer in selected ion monitoring mode to include ethylbenzene (Cole et al., 2007). To summarize, water samples for BTEX (benzene, toluene, ethylbenzene and [m,p & o] xylene) analysis were collected in 40 mL purge and trap vials. The vials were spiked with 40 µL of 6N HCl to serve as a preservative, so that they can be stored at 4°C for up to 14 days.

The purge and trap system was a Teledyne Tekmar Stratum PTC purge and trap concentrator equipped with a Tenax/silica gel/charcoal trap. The auto-sampler was a Teledyne Tekmar Aquatek 70-vial unit. The auto-sampler transferred a 5 mL aliquot of sample into the purge and trap chamber, where it was purged with helium for 11 minutes. During this process, the volatiles were trapped on the Tenax trap and then desorbed at 225°C for 2 min. The desorbed gases enter a heated transfer line connected to the Agilent 6890 GC injector and subsequently proceed to the GC column (Supelco MDN-5s 30 m × 250 µm × 0.25 µm length × i.d. × film thickness).

The GC oven was programmed at an initial oven temperature of 50°C, held for 8 min, followed by an increase to 280°C at 40°C/min, and held at 280°C for 2 min, for a total run time of 18 min. The gases exiting the GC column were detected by an Agilent 5973 mass selective detector (MS) used in selective ion mode (SIM) monitoring for six ions: 77, 78, 91, 92, 105 and 106 amu. BTEX standards were prepared in 40 mL purge and trap vials. Samples and standards were analyzed using this method, along with sample blanks and duplicate samples.

A.2.12 Numerical Modeling Methods

Refer to Appendices G and H for numerical modeling components.

TASK A.3 RESULTS

The overarching objective for this project was to evaluate the operational performance of the subsurface injection of dispersants during deepwater blowouts. Presented here are the results from a series of flume tank subsurface injection experiments where dispersion effectiveness was evaluated via response monitoring tools (fluorescence and particle size analyzers), discrete water sample chemistry analysis and VOC air monitors. The logs for all experiments conducted can be found in Appendix A. Corresponding chemistry results for each experiment are tabulated in Appendix B.

A.3.1 ANS Dispersion Effectiveness

Injection experiments were conducted using ANS crude oil, chemically dispersed with Corexit and Finasol. Regardless of warm ($\geq 11^{\circ}\text{C}$) or cold ($5.4 - 10.7^{\circ}\text{C}$) water temperatures, the addition of the two tested dispersant lowers the VMD of ANS and shifts the DSD to smaller droplets within the plume. An example of this trend is shown in Figures 5 and 6. Note that LISST histogram plots have constrained Y-axes; thus lines that extend slightly above the top of the plot area represent values that were truncated. Histograms in these figures correspond to time points at the leading edge of the plume (~2-3 min from oil release). Contour plot X-axis represents experiment elapsed time. Plots for triplicate experiments for each treatment are shown in Appendices C and D. All plots represent data from the LISST positioned closest to the jet release (denoted as Jet Release LISST throughout the document) and in close proximity to the submersible fluorometers. Histograms represent the particle concentration for a given size class (Y axes). Contour plots represent the 10 minute time series of the plume, where colored contours represent the particle concentration (normalized to max value for comparison purposes), Y axes represent the droplet sizes in μm and X axes are time in minutes. Time is elapsed time since oil injection into the tank. These contours allow for ascertaining how the DSD shifts over the duration of the release. A second LISST positioned further downstream of release (denoted as Downstream LISST throughout the document) allows for comparing the evolution of the plume in space and time since release of the plume. For warm temperature experiments, there is a slight decrease in VMD

for DOR = 1:200 and 1:100 (Corexit) compared to the no-dispersant treatment (DOR = 0), in this case $\sim 130\ \mu\text{m}$ down to $\sim 80\ \mu\text{m}$ (exact numbers are within text of the figures). A large shift in DSD is observed for the DOR 1:20 treatment, where VMD is $\sim 10\ \mu\text{m}$. The cold water treatments exhibit this same trend, where VMD is $\sim 10\ \mu\text{m}$ for the DOR = 1:20 treatment (Figure 6). *In situ* submersible fluorescence from multiple fluorometers was recorded during experiments. Example time series for each dispersant and temperature treatment are shown in Figure 7 and illustrate the impact of dispersant at DOR = 1:20 in the plume. With DORs of 0, 1:200 and 1:100, the plumes tend to exhibit a spike in fluorescence shortly after release (within 2 min), and then a sharp decline in signal that is brought to extinction by 4 minutes. For DOR = 1:20, however, the signal remains elevated and with variability for up to 6 minutes. This indicates that more oil is remaining submerged in the plume for a longer time period. Time series fluorescence plots for triplicate experiments for each treatment are shown in Appendix E.

The Downstream LISST positioned further from the jet release and the fluorometers serves as an indication of plume evolution through the tank. Plots of the Downstream LISST DSD and VMD for all dispersant treatments for warm and cold water experiments are shown in Figures 8 and 9, respectively. Comparing these to the LISST results near the jet release illustrates the decrease in Total Particle Concentration (TPC; represents the maximum concentration for the entire plume) as the plume disperses through the tank (note the change of Y axis scale). Also evident is a shift to smaller particles for all DOR treatments as the plume moves through the tank. Where the decrease in TPC suggests plume dilution in the tank, the DSD shift to smaller particles suggests that within each experiment larger droplets were removed from the plume within 6 minutes of the oil release, most likely rising to the surface of the tank.

Warm water experiments conducted with ANS and Finasol OSR 52 dispersant also yield a shift in DSD towards smaller VMD for DOR = 1:20 (Figure 10). However the shift is smaller than that observed with Corexit 9500 (Figure 5), with lowest VMD on the order of $\sim 50\text{-}60$

μm . DOR = 1:200 and 1:100 treatments exhibited spikes in fluorescence signal that taper off within 3 minutes of oil release (Figure 11). Fluorescence for DOR = 1:20 Finasol OSR 52 treatments exhibited a decrease in intensity at ~ 4 minutes which is faster than that for treatments with Corexit 9500. The Downstream LISST exhibited a similar shift in DSD and TPC that was observed with Corexit 9500 treatments (Figures 12 and 13).

Water temperatures for experiments ranged between 5.4 – 20.8 °C. In general there was no clear trend on the influence of temperature on DSD, VMD fluorescence intensity, or oil concentrations for the time series for DOR = 0, 1:200 or 1:100 treatments. This suggests that water temperature has little effect on the dispersibility of ANS (80 °C oil temperature) when released as a jet with little or no exposure to chemical dispersant (in this case the pre-mixing process prior to release). In contrast, DOR = 1:20 experiments showed a decrease in total particle concentration (TPC) with decreasing temperature even though no effect was observed on DSD for the two temperatures. Figure 14 shows three examples of this effect, where TPC values for each DOR = 1:20 experiment increase as a function of temperature (Figure 15). It is important to note that for all treatments using ANS, the experiment at the lowest temperature (SubANS-10R; 5.4 °C) exhibited anomalous dispersion compared to the other DOR = 1:200 treatments (Appendices C and D). Because this occurred in only one experiment out of 33 experiments with ANS, it is difficult to ascribe a cause for this other than an improper jet release of oil.

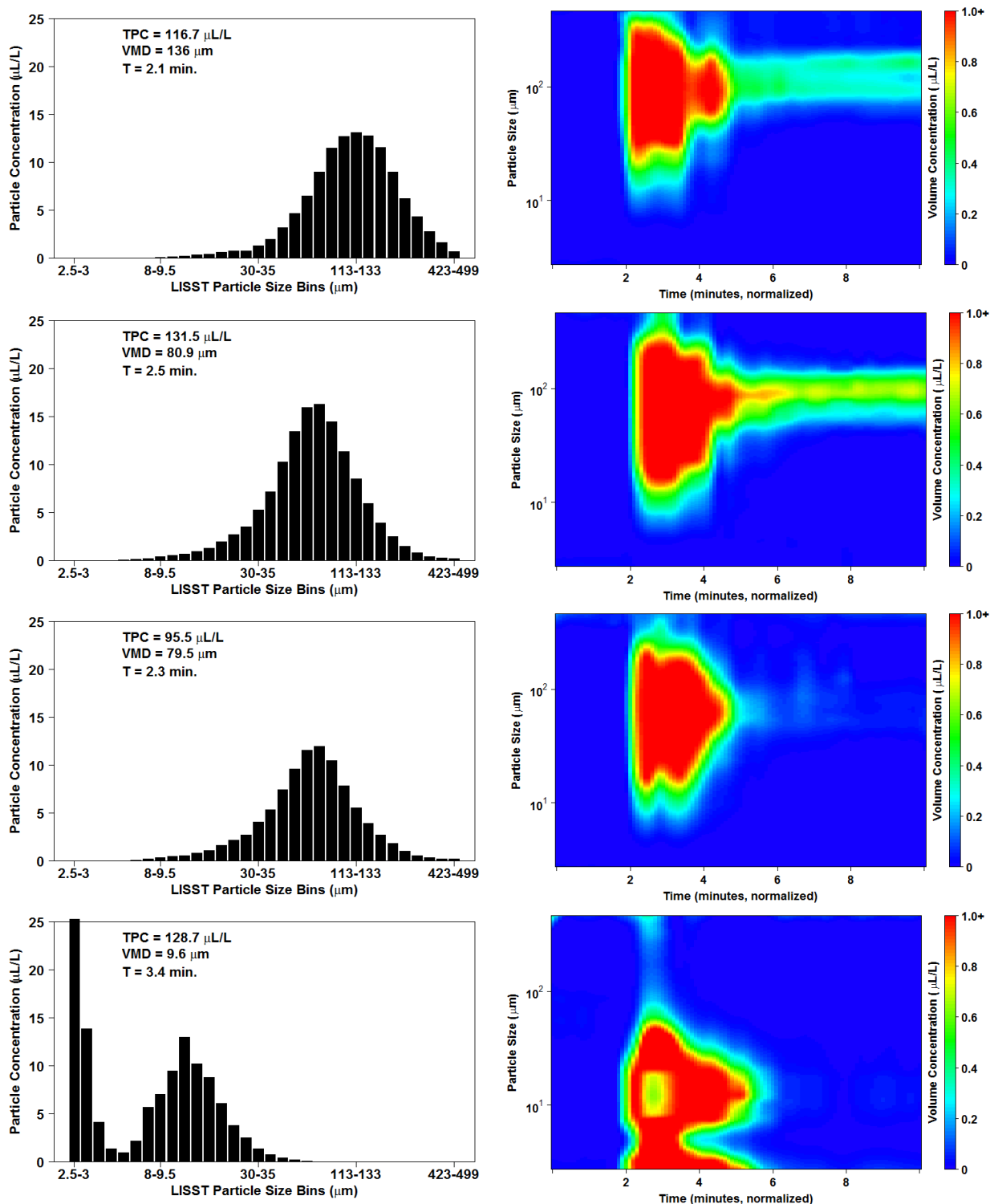


Figure 5. LISST DSD and VMD (left panels) and time series of concentration and particle size (right panels) for ANS and Corexit 9500 warm water treatments. From top to bottom, DOR = 0, 1:200, 1:100, 1:20.

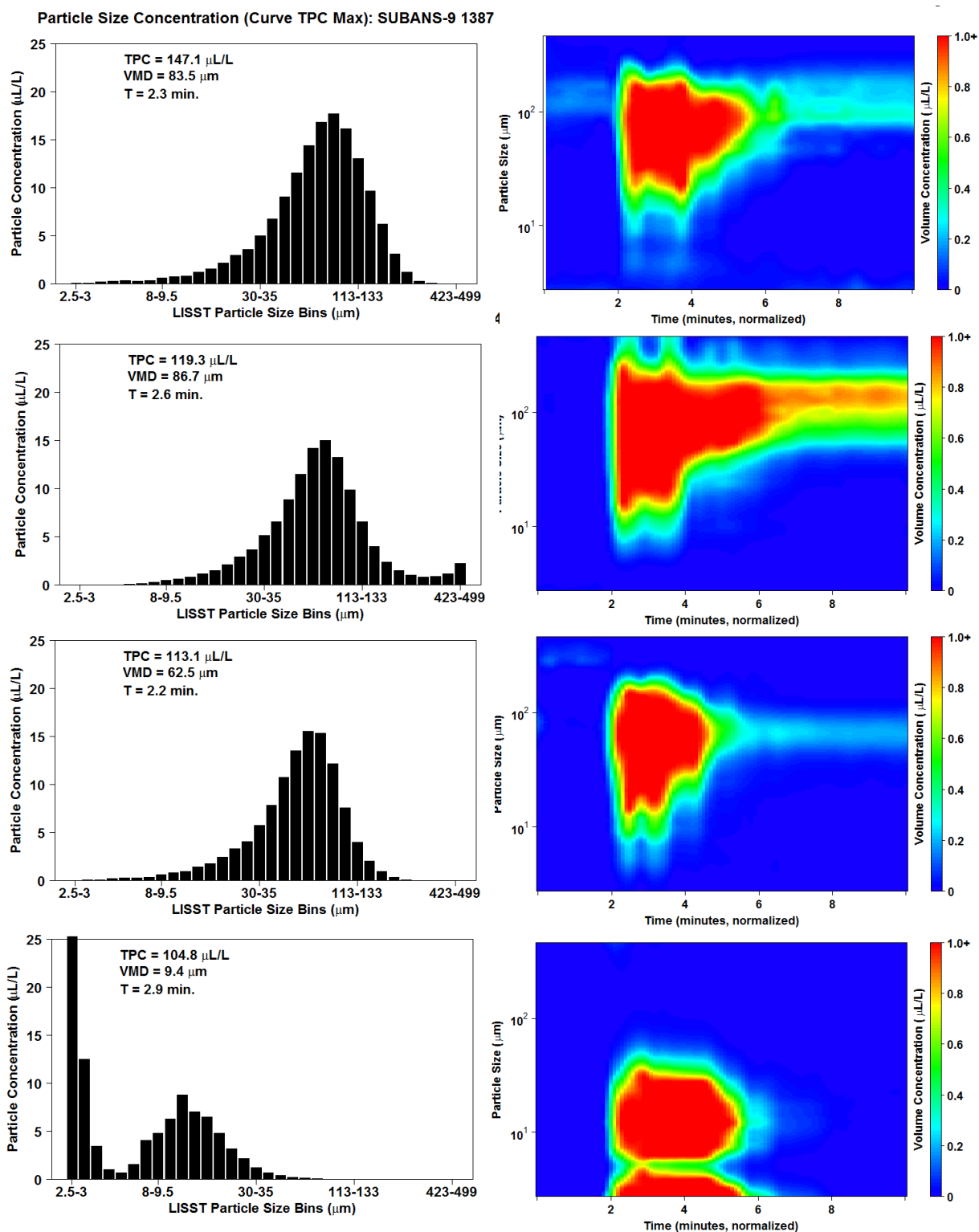


Figure 6. LISST DSD and VMD (left panels) and time series of concentration and particle size (right panels) for ANS and Corexit 9500 cold water treatments. From top to bottom, DOR = 0, 1:200, 1:100, 1:20.

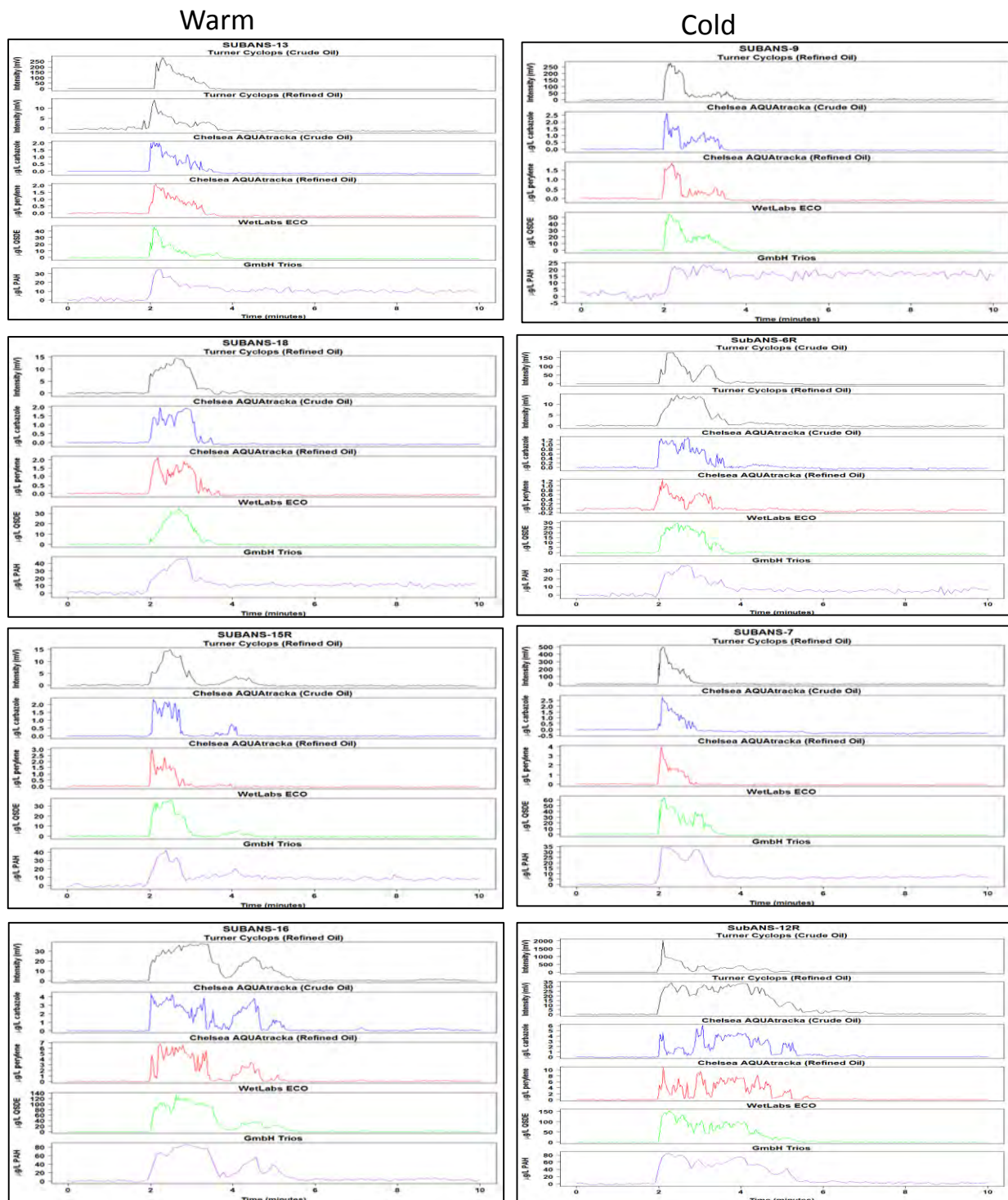


Figure 7. *In situ* submersible fluorescence time series of sub-injection plume of ANS and Corexit 9500 warm water (left panels) and cold water (right panels) treatments. From top to bottom, DOR = 0, 1:200, 1:100, 1:20.

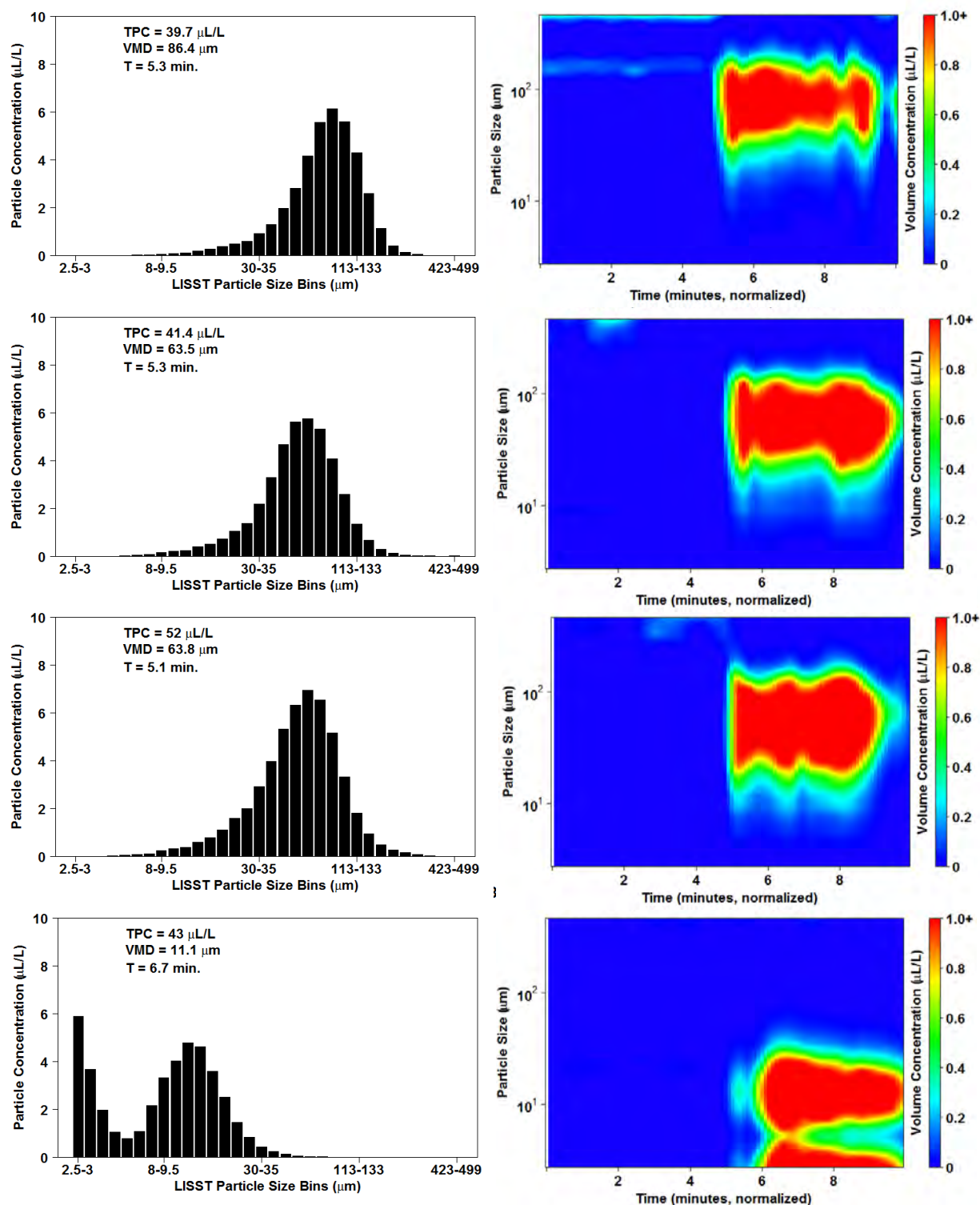


Figure 8. Downstream LISST DSD and VMD (left panels) and time series of concentration and particle size (right panels) for ANS and Corexit 9500 warm water treatments. From top to bottom, DOR = 0, 1:200, 1:100, 1:20.

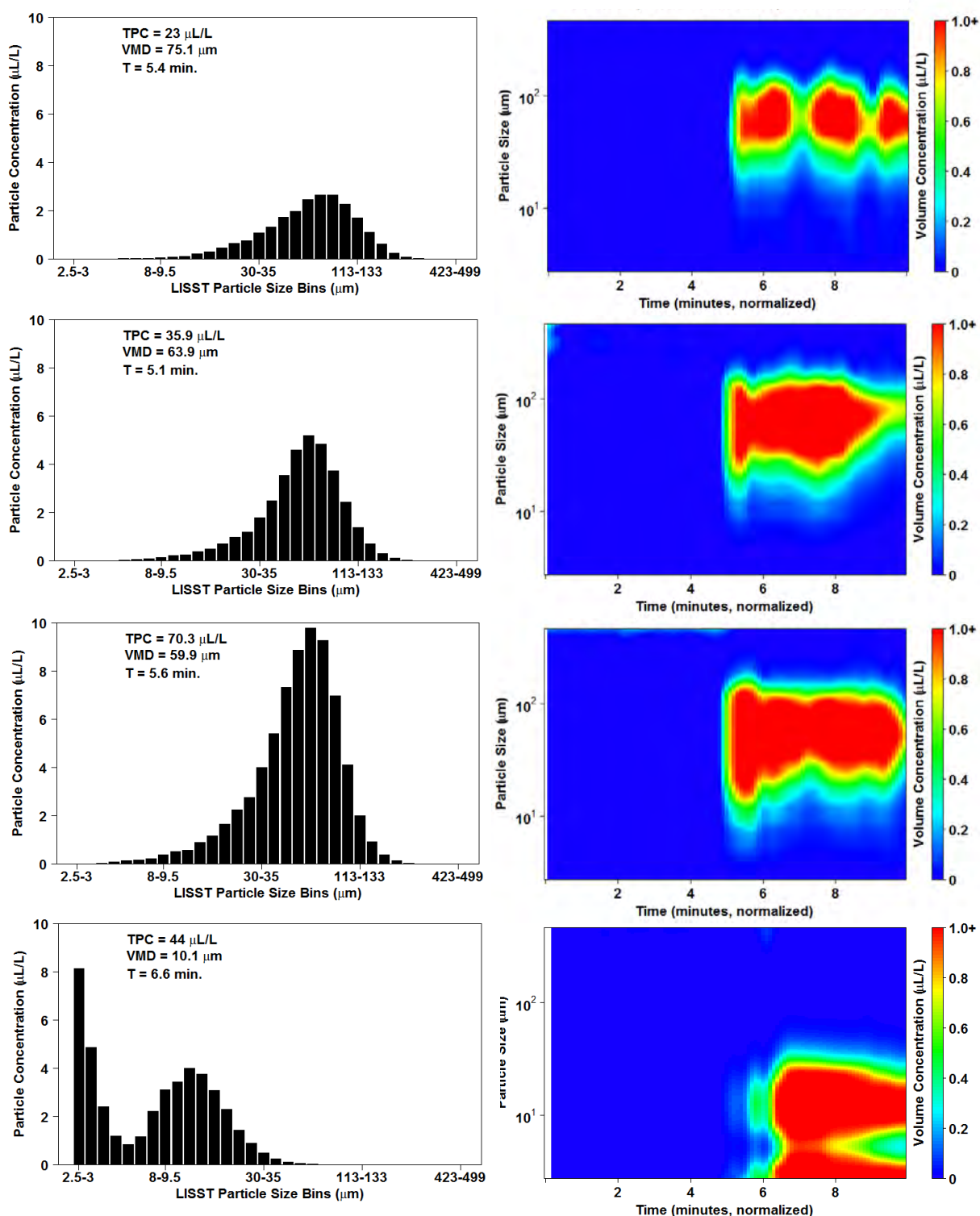


Figure 9 Downstream LISST DSD and VMD (left panels) and time series of concentration and particle size (right panels) for ANS and Corexit 9500 cold water treatments. From top to bottom, DOR = 0, 1:200, 1:100, 1:20.

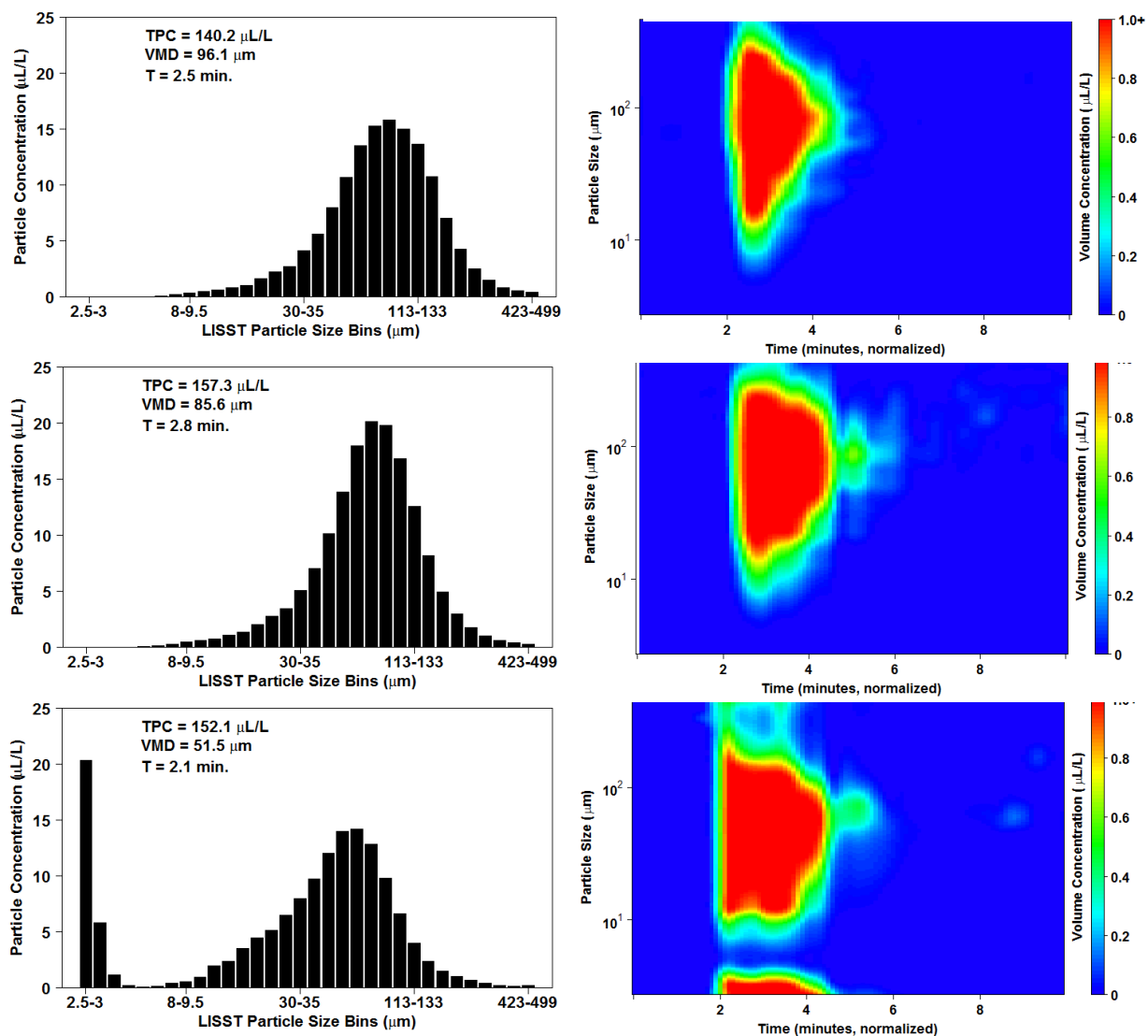


Figure 10. LISST DSD and VMD (left panels) and time series of concentration and particle size (right panels) for ANS and Finasol OSR 52 warm water treatments. From top to bottom, DOR = 1:200, 1:100, 1:20. Refer back to Figure 5 for ANS DOR = 0.

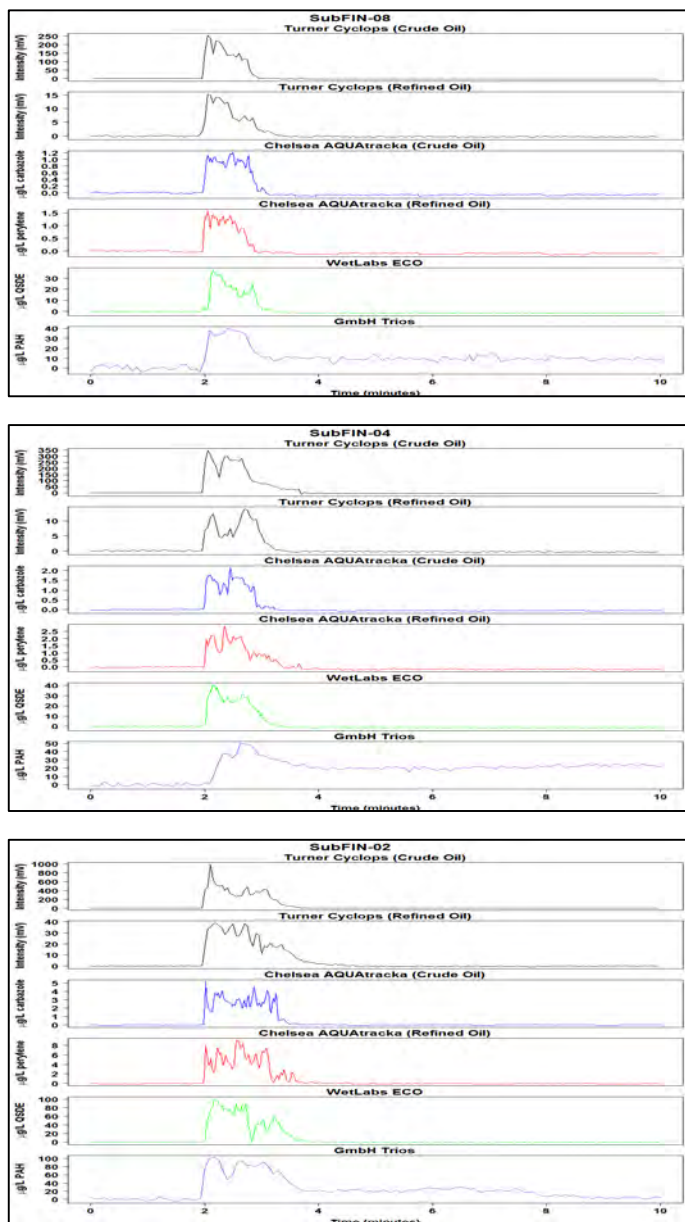


Figure 11. *In situ* submersible fluorescence time series of sub-injection plume of ANS and Finasol OSR 52 warm water treatments. From top to bottom, DOR = 1:200, 1:100, 1:20.

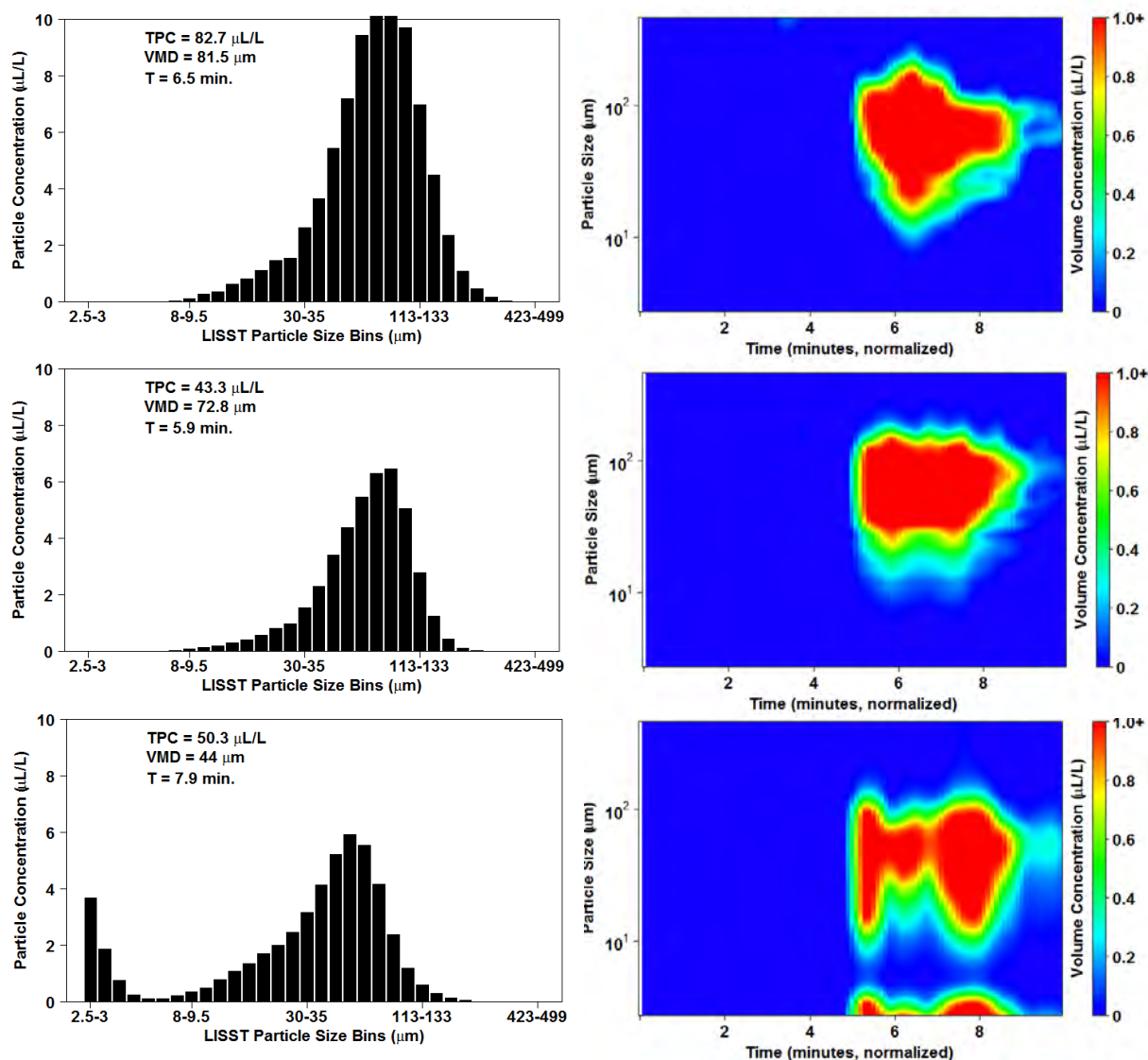


Figure 12. Downstream LISST DSD and VMD (left panels) and time series of concentration and particle size (right panels) for ANS and Finasol OSR 52 warm water treatments. From top to bottom, DOR = 1:200, 1:100, 1:20. Refer back to Figure 6 for ANS DOR = 0.

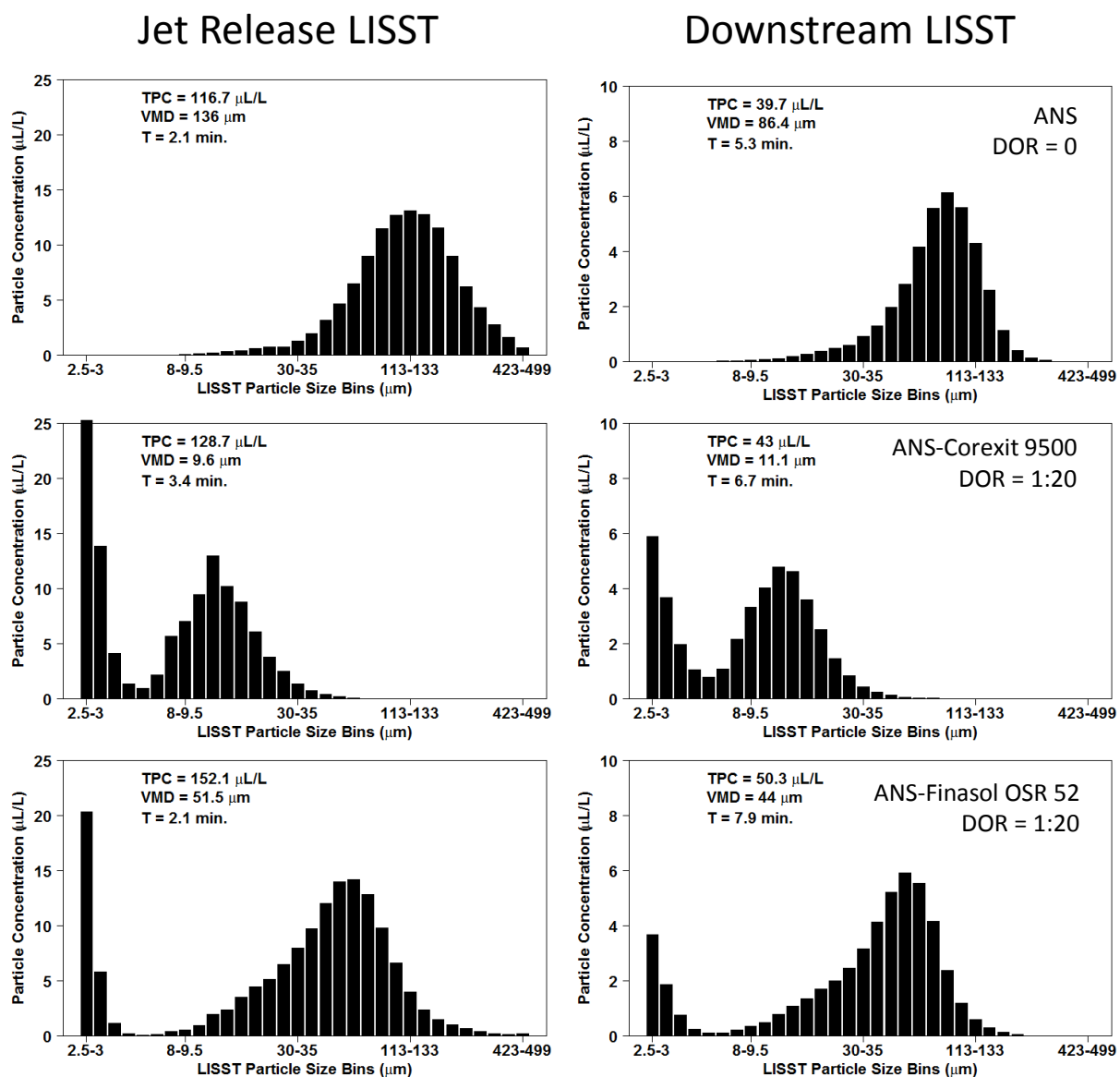


Figure 13. LISST DSD with TPC for ANS with Corexit 9500 and Finasol OSR 52 warm water treatments. DOR = 0 (top panel); DOR = 1:20 experiments are middle and bottom panels.

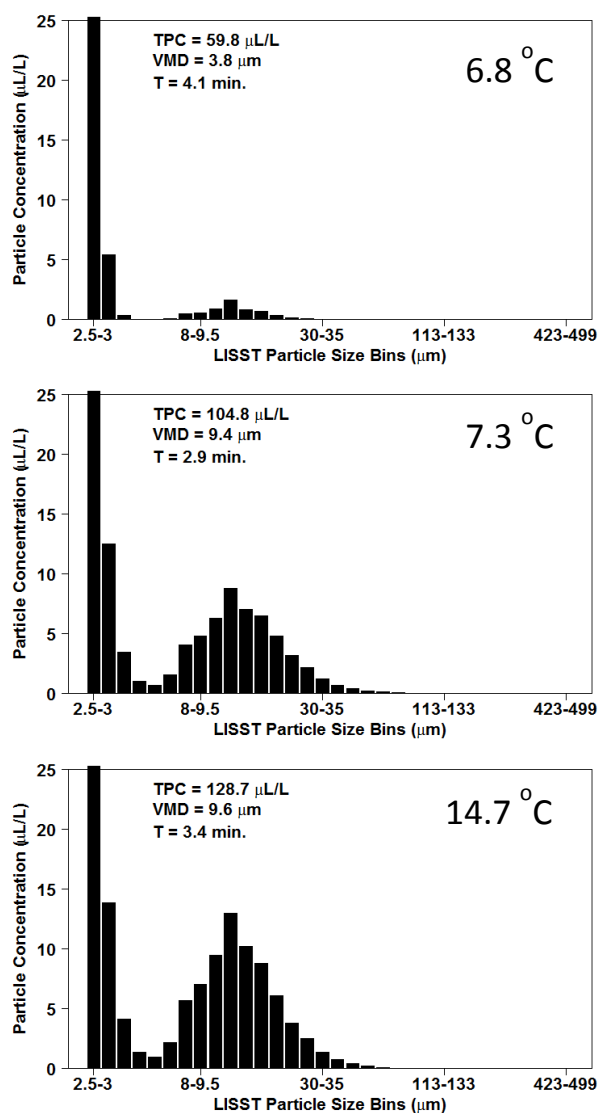


Figure 14. LISST DSD with TPC (Total Particle Concentration) for DOR = 1:20 experiments of ANS and Corexit 9500 treatments. Water temperatures increase from top to bottom panels.

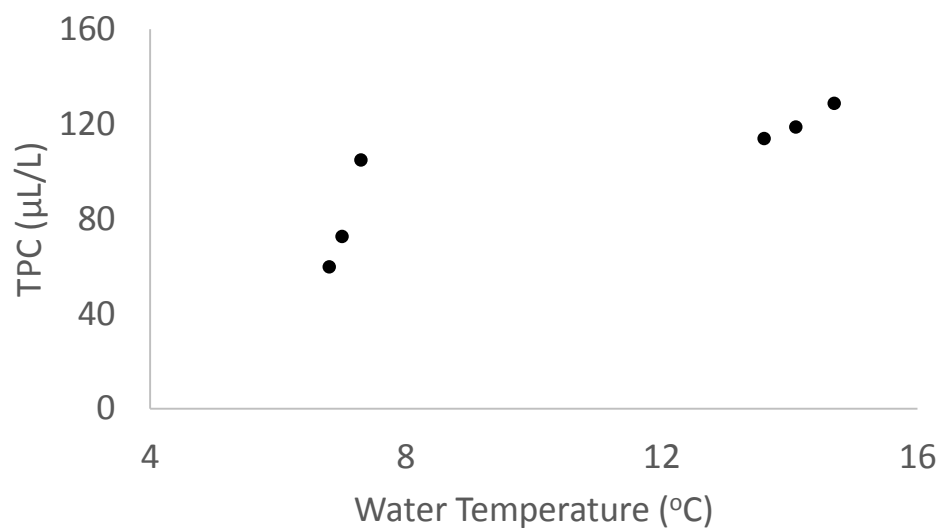


Figure 15. LISST TPC (Total Particle Concentration) for DOR = 1:20 experiments of ANS and Corexit 9500 treatments as a function of water temperature.

A.3.2 IFO 120 Dispersion Effectiveness

Injection experiments were conducted using Intermediate Fuel Oil (IFO 120), chemically dispersed with Corexit 9500 and Finasol OSR 52. For warm water experiments, temperatures ranged between 13.5 – 16 °C for treatments with Corexit 9500 and between 17.5 – 20.3 °C for treatments with Finasol OSR 52. In the DOR = 0, 1:200 and 1:100 treatments using Corexit 9500, VMD typically remained > 200 µm (Figure 16). VMD values were smaller for DOR = 1:20 treatments (~66-120 µm), indicating a shift in DSD, but to a lesser extent than the shift observed for ANS experiments. Fluorescence data exhibited scatter and noise in the signal for all but the DOR = 1:20 treatments (Appendix E). A similar trend in DSD, VMD and fluorescence signal was observed for IFO 120 exposed to Finasol OSR 52 at warm temperatures (Figure 17), where DOR = 1:200, 1:100 and 1:20 exhibited VMD values of 376.5, 209.5 and 125.8 µm, respectively. Unlike experiments with ANS, which is less viscous and dense, IFO 120 exposed to dispersant tended to result in larger oil droplets for a given amount of dispersant added. Comparing the results of IFO 120 with the two dispersants is challenging because no triplicate experiments were conducted for Finasol OSR 52 treatments, as the latter treatments were add-on experiments and not central to the project. In general, from the data collected, Finasol OSR 52 yielded higher VMD for a given DOR compared to Corexit 9500 at warm temperatures. As with ANS, the Downstream LISST measured a decrease in TPC and shift to smaller droplet sizes as the plume moved through the tank for all treatments, but to a lesser extent with DOR = 1:20 (Figures 18, 19 and 20).

For cold water experiments using IFO 120 exposed to Corexit 9500, temperatures ranged between (4.9 – 7.5 °C). At these colder temperatures a shift in DSD and VMD was not as apparent (Figure 21). For DOR = 0, 1:200 and 1:100 VMD typically remained > 223 µm but was as high as 344 µm. The DOR = 1:20 treatment exhibited VMD of 178-327 µm, suggesting that this oil was not well dispersed at cold temperatures. Fluorescence time series data were noisy for all experiments except the DOR = 1:20 (Appendix E). The Downstream LISST recorded extremely low particle concentrations, further suggesting poor dispersion (Figure 22). During the IFO 120 cold water treatments, one experiment resulted in an anomalous

DSD histogram that was similar to an anomalous one observed during one of the ANS experiments (Figure 23). In both cases, the experiments were conducted at the coldest temperatures during the course of this study (4.9 and 5 °C). Suspected as a possible cause may be the LISST instrument itself. The manual reports that the lower operating temperature for the LISTT-100X is -10 °C. However, the data suggests that our particular unit may have experienced some complications at low temperatures. This is supported by the fact that the fluorescence signal and chemistry data for these experiments indicate no anomalies. Further testing would be needed to confirm the effect of low temperatures on particle size analysis results using our instrument to rule out any potential issues with operating at temperatures between 5 and -10 °C.

One aspect to note with the IFO 120 cold water experiments is that a few of the treatments were conducted at water temperatures of ~12 °C, which overlaps with the temperatures of the warm water group. This was the result of erratic weather patterns that at times were difficult to work around. Thus, when interpreting the temperature data, caution must be exercised for these particular experiments (refer to Appendix A for temperature log), and for the interpretation in this section, they were excluded as they do not represent cold conditions.

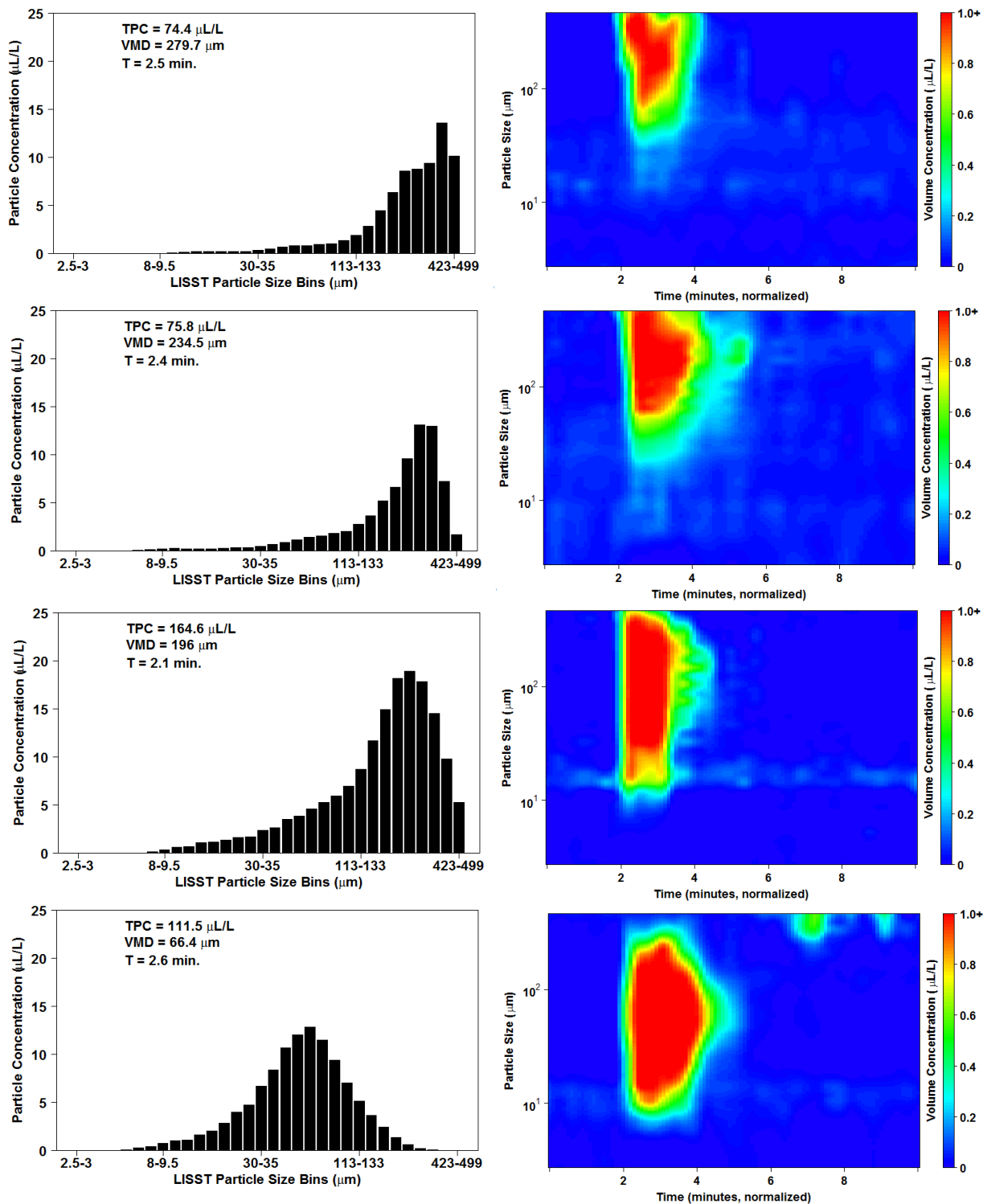


Figure 16. LISST DSD and VMD (left panels) and time series of concentration and particle size (right panels) for IFO 120 and Corexit 9500 warm water treatments. From top to bottom, DOR = 0, 1:200, 1:100, 1:20.

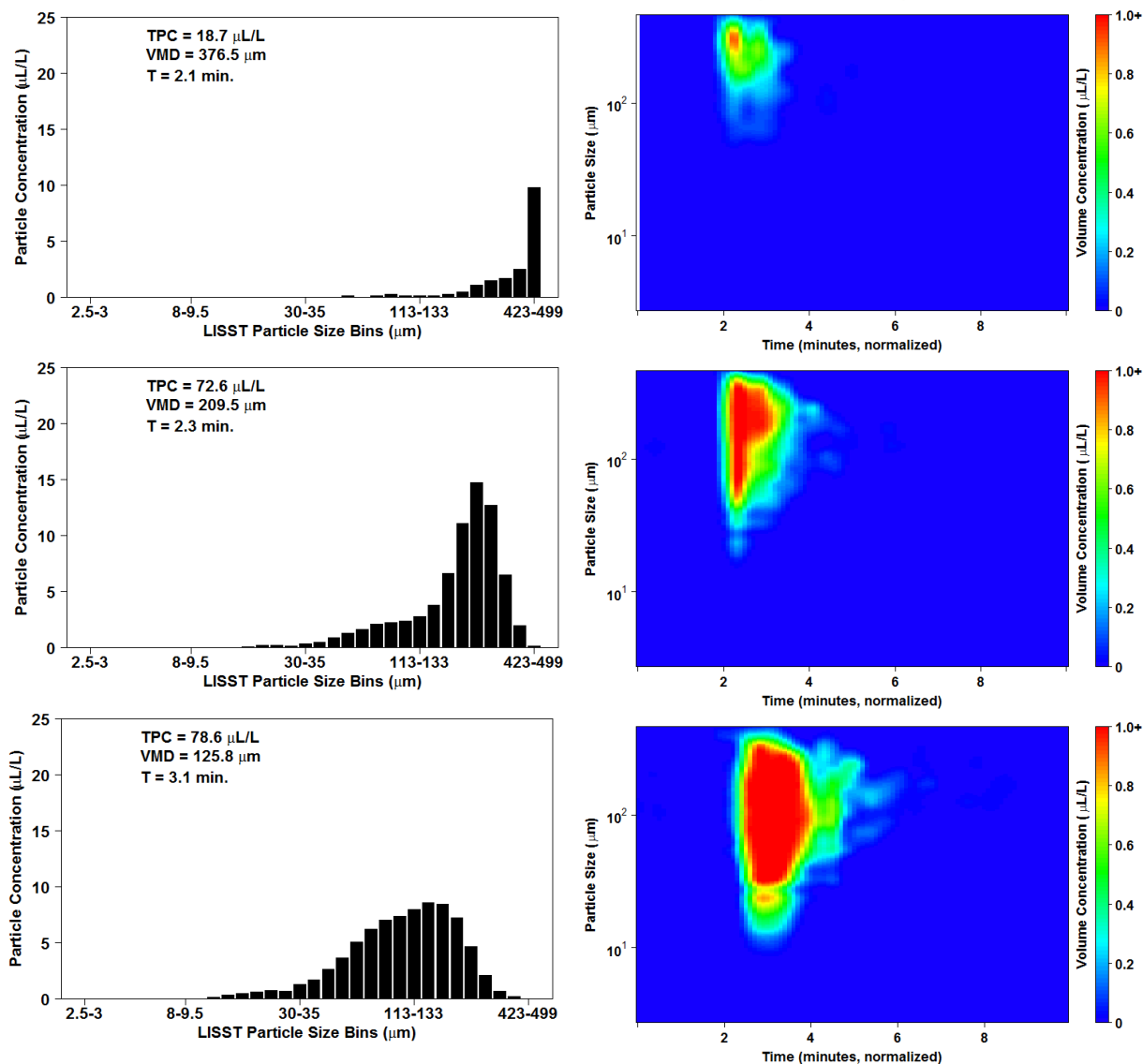


Figure 17. LISST DSD and VMD (left panels) and time series of concentration and particle size (right panels) for IFO 120 and Finasol OSR 52 warm water treatments. From top to bottom, DOR = 1:200, 1:100, 1:20. Refer to Figure 16 for IFO 120 DOR = 0.

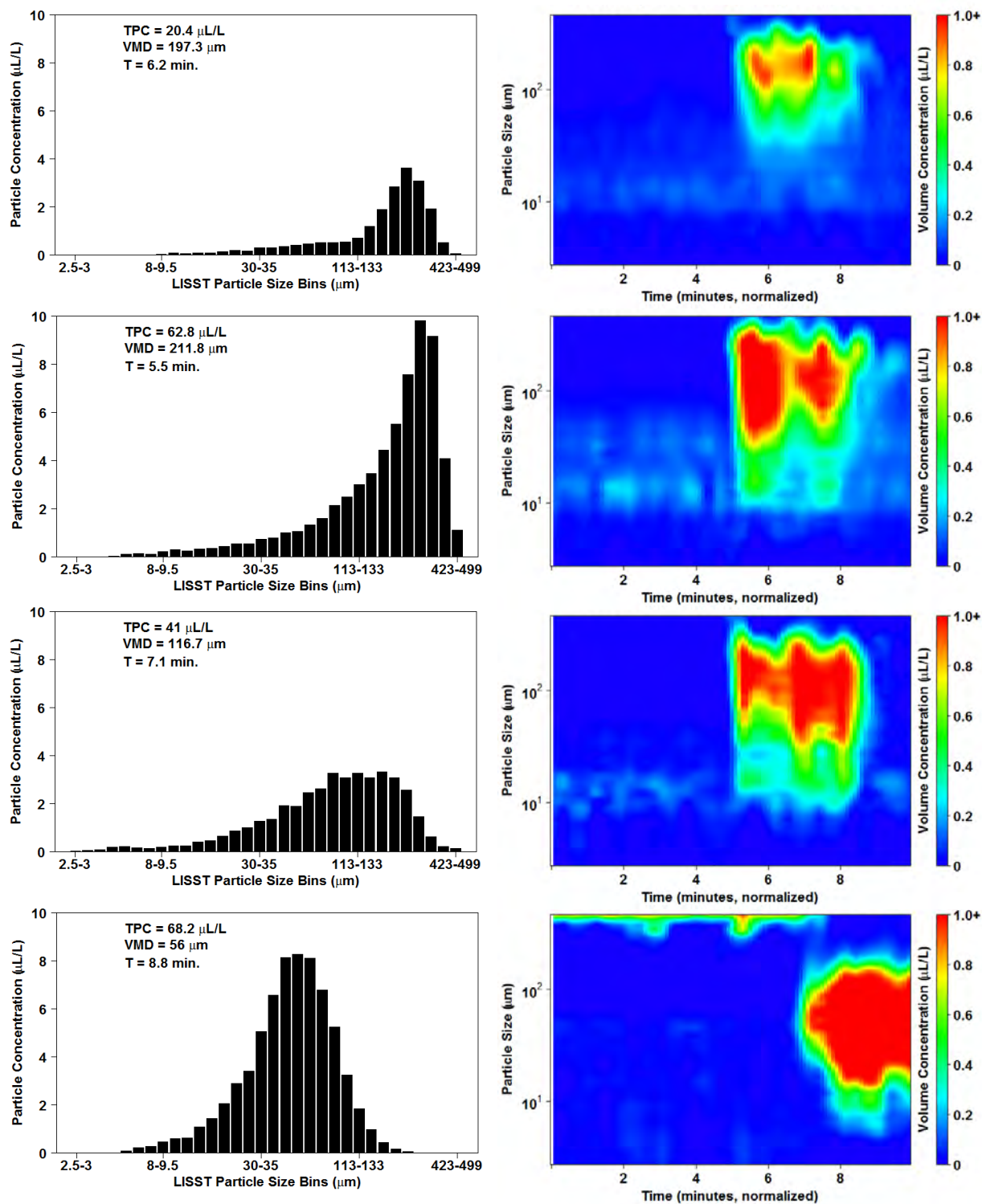


Figure 18. Downstream LISST DSD and VMD (left panels) and time series of concentration and particle size (right panels) for IFO 120 and Corexit 9500 warm water treatments. From top to bottom, DOR = 0, 1:200, 1:100, 1:20.

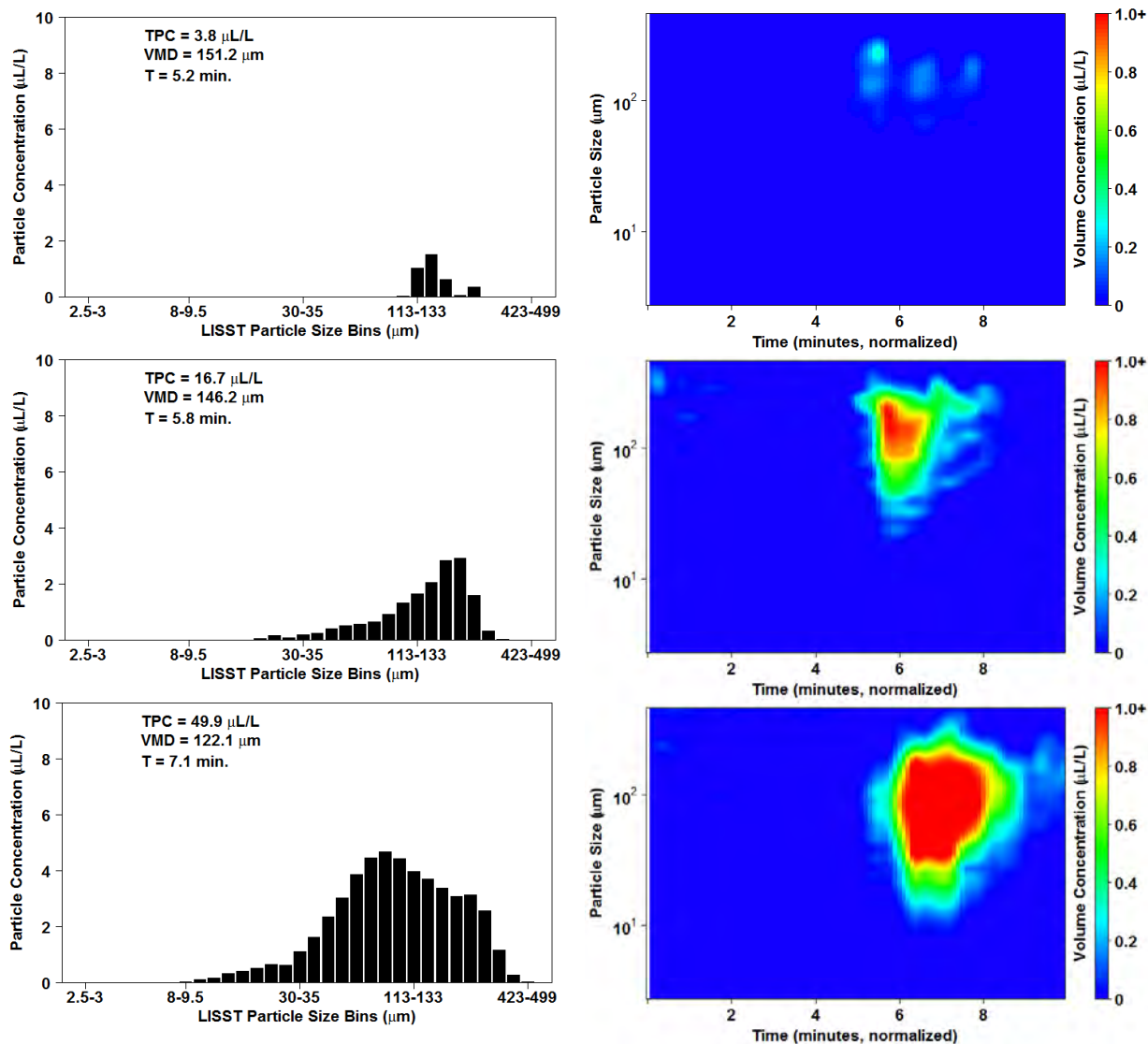


Figure 19. Downstream LISST DSD and VMD (left panels) and time series of concentration and particle size (right panels) for IFO 120 and Finasol OSR 52 warm water treatments. From top to bottom, DOR = 0, 1:200, 1:100, 1:20. Refer to Figure 18 for ANS DOR = 0.

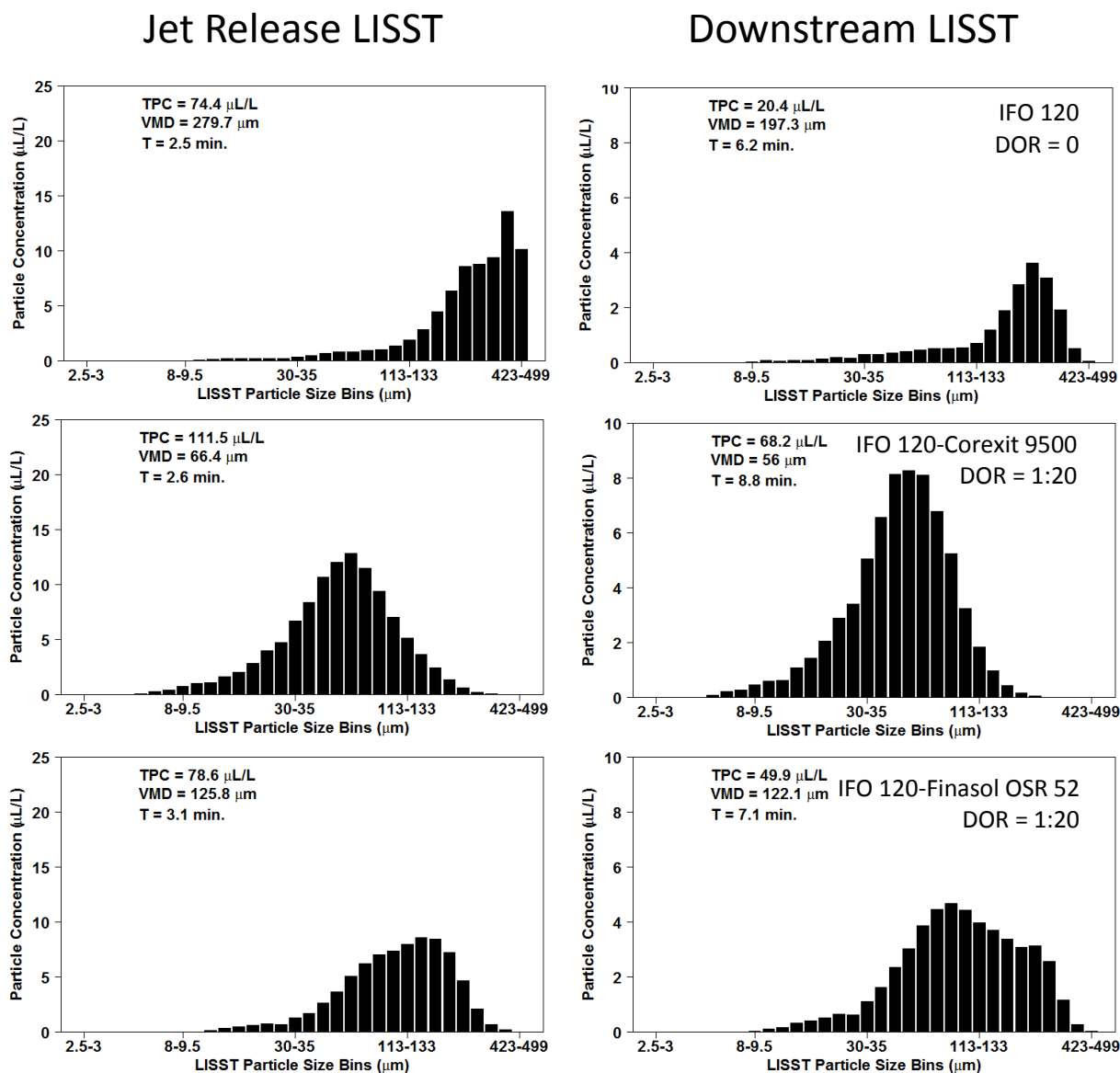


Figure 20. LISST DSD with TPC for IFO 120 with Corexit 9500 and Finasol OSR 52 treatments at warm temperatures. DOR = 0 (top panel); DOR = 1:20 experiments are middle and bottom panels.

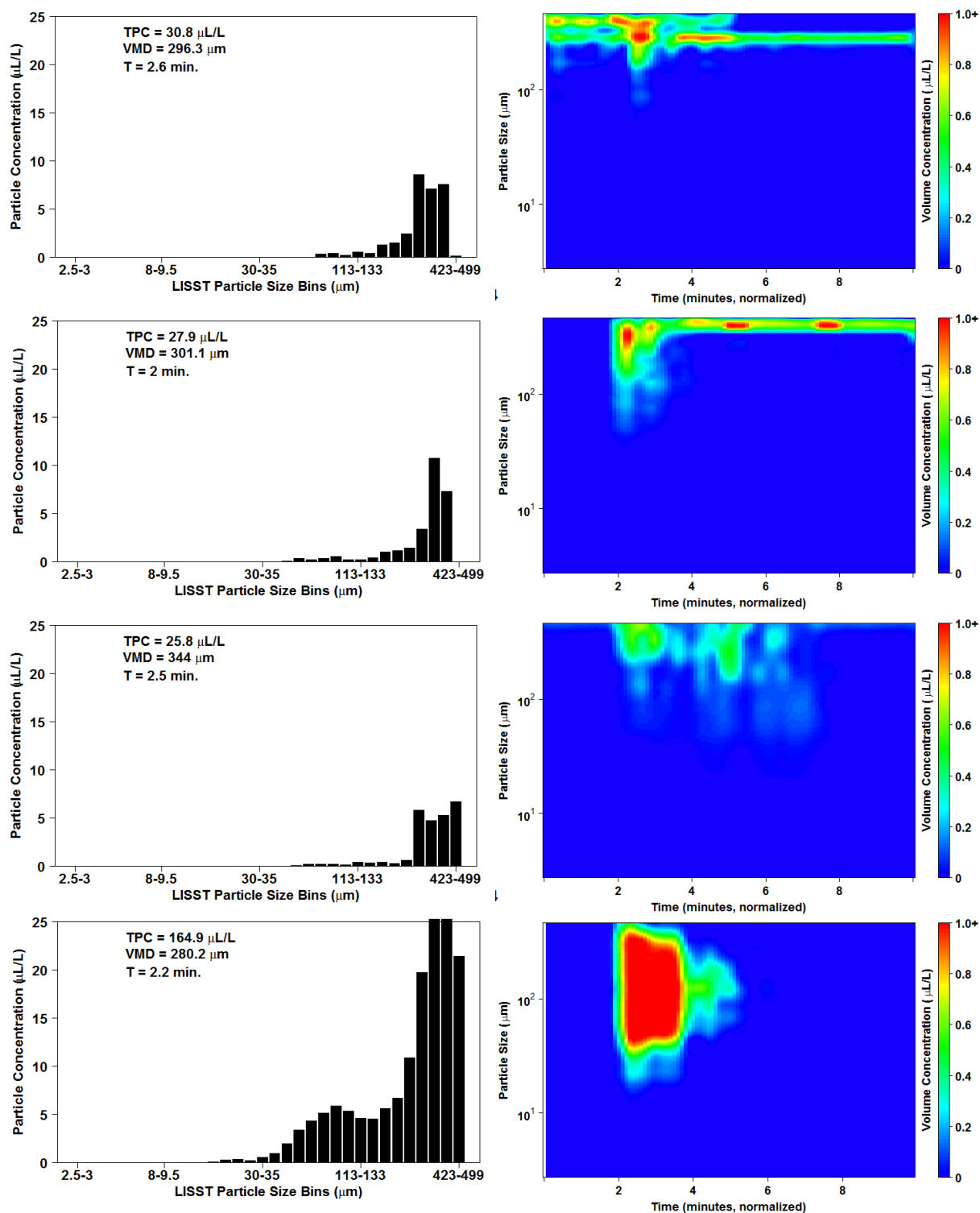


Figure 21. LISST DSD and VMD (left panels) and time series of concentration and particle size (right panels) for IFO 120 and Corexit 9500 cold water treatments. From top to bottom, DOR = 0, 1:200, 1:100, 1:20.

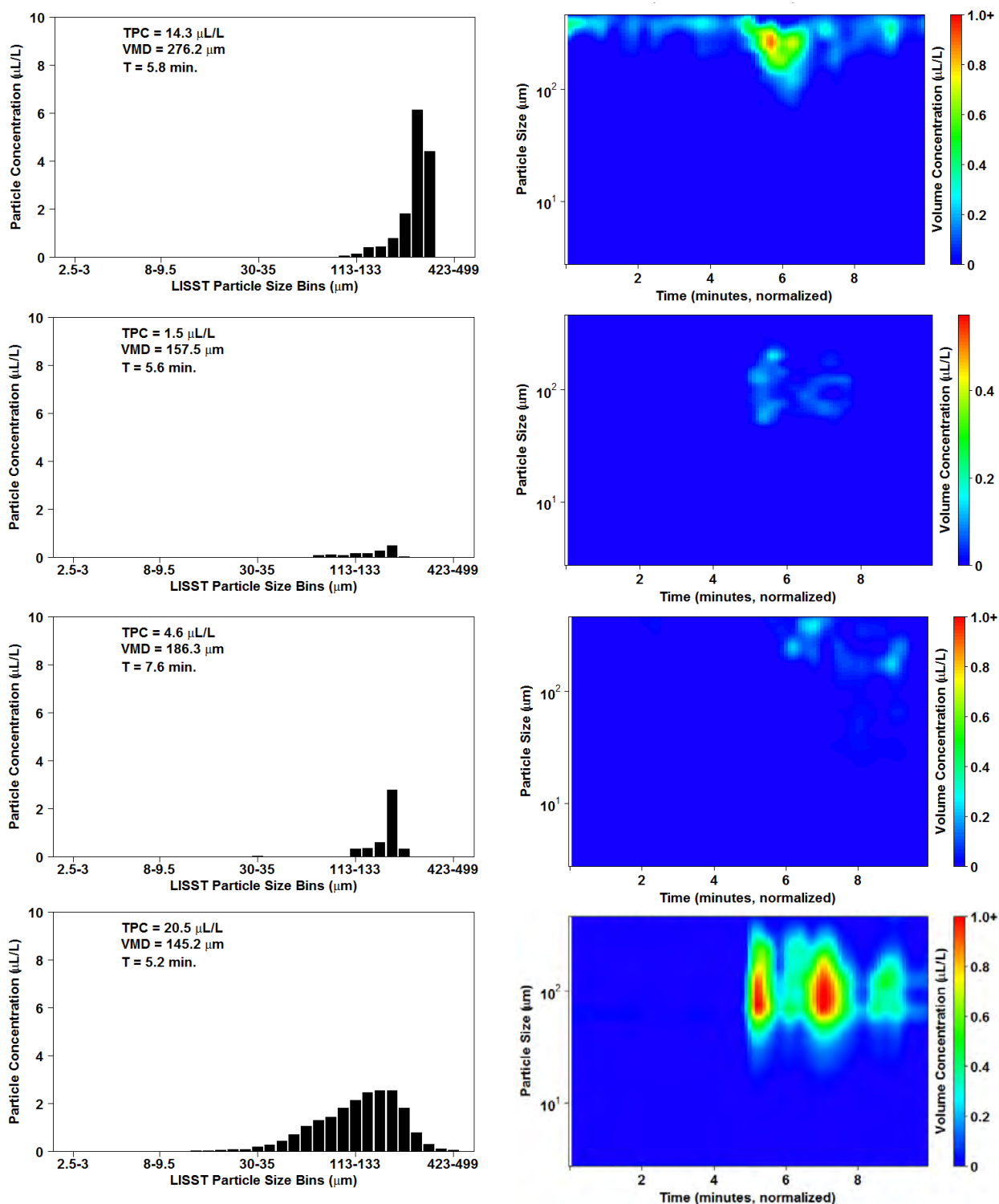


Figure 22. Downstream LISST DSD and VMD (left panels) and time series of concentration and particle size (right panels) for IFO 120 and Corexit 9500 cold water treatments. From top to bottom, DOR = 0, 1:200, 1:100, 1:20.

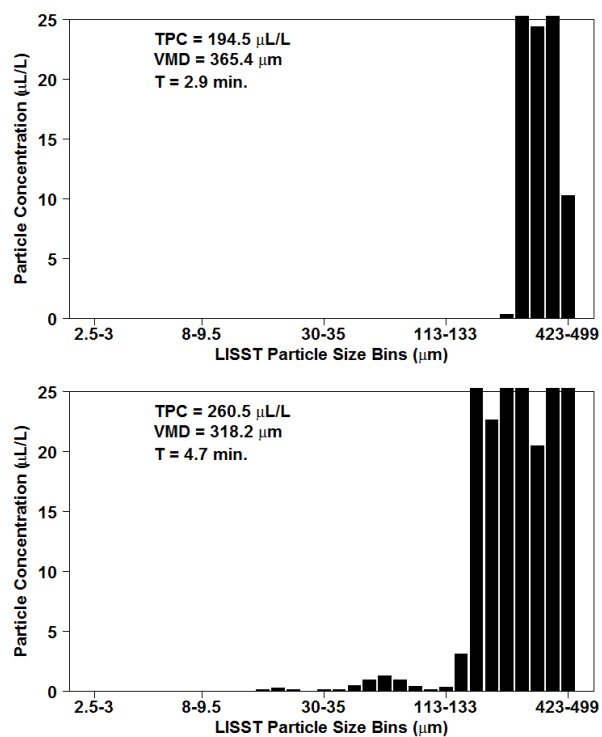


Figure 23. LISST DSD and VMD for IFO 120 (top; DOR = 1:100) and ANS (bottom; DOR = 1:200) with Corexit 9500 during cold water treatments.

A.3.3 SLC Dispersion Effectiveness

Experiments involving South Louisiana Crude (SLC) oil treated with Corexit 9500 were conducted for warm water conditions (16.6 – 19.6 °C) to compare dispersion between ANS and SLC. Experiments with SLC yielded higher TPC values compared to ANS results, most likely the result of slightly larger amounts of oil added to the pressure canister (~25-50 g) due to the lower viscosity of SLC resulting in more oil injected by the injector, so comparisons shouldn't be made regarding TPC. The observed VMD of physically-dispersed SLC oil (neat; DOR = 0; ~123-148 µm) was found to be less than that of ANS (>200 µm). The addition of dispersant yielded a shift in DSD and VMD to smaller particles, where DOR = 1:200 and 1:100 exhibited diameters of ~91-108 µm, and DOR = 1:20 ranged between ~15 -21 µm, as depicted in Figure 24. The Downstream LISST results indicate smaller droplet size as the plume moves through the tank (size fractionation) and a decrease in TPC (plume dilution), further demonstrating this trend for all oils (Figures 25 and 26). The fluorescence data indicates a strong signal with little scatter for up to 4 min in these treatments (Figure 27; Appendix E). Using these results, comparisons can be made to results of SLC with Corexit 9500 from surface plume simulations (oil released into tank via pour in from flask) from Conmy et al., 2014a (and unpublished data) from those experiments. No apparent differences between DSD and VMD for DOR = 0 treatments were found. For DOR = 1:20 VMD values are similar, however, the range of droplet diameters for surface simulations is larger with particles up to 200 µm. In subsurface injection jet experiments the range of diameters is narrower, where particles > 100 µm were not observed. This suggests that the combination of the chemical dispersant tested here, elevated turbulent mixing from the jet release and higher oil temperature of 80 °C yielded smaller droplets. To discern the dominant factor controlling the difference, additional testing would need to be conducted.

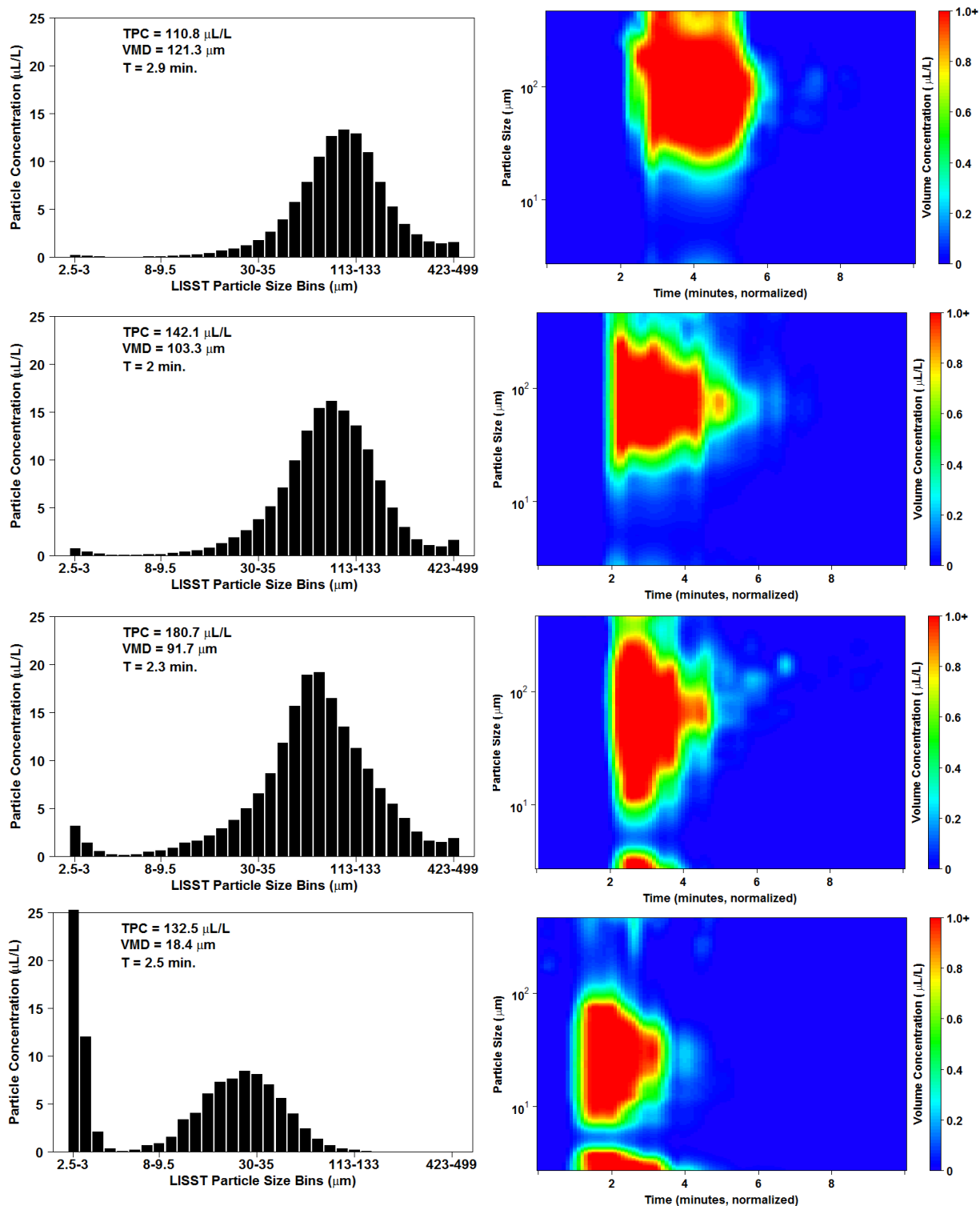


Figure 24. LISST DSD and VMD (left panels) and time series of concentration and particle size (right panels) for SLC and Corexit 9500 warm water treatments. From top to bottom, DOR = 0, 1:200, 1:100, 1:20.

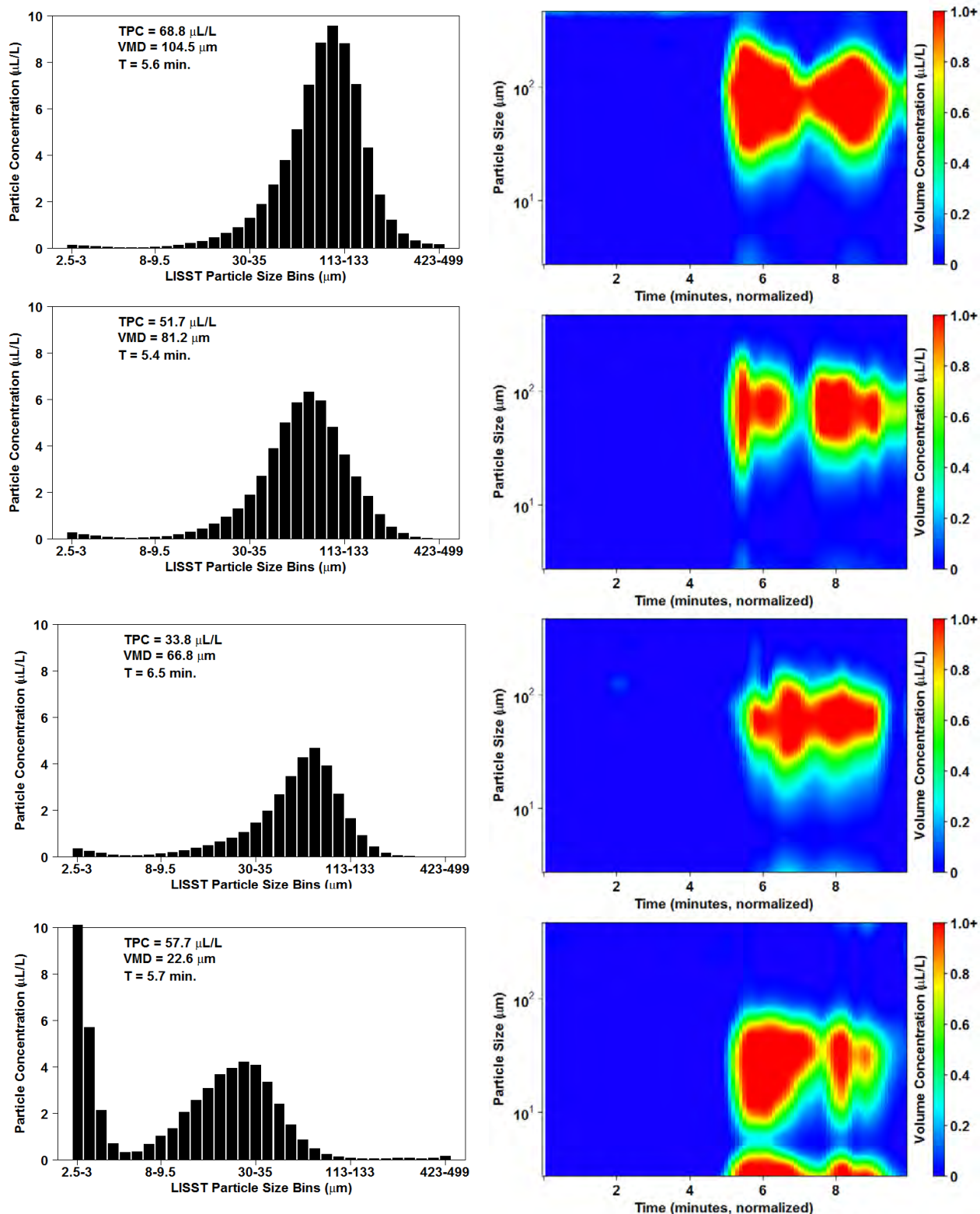


Figure 25. Downstream LISST DSD and VMD (left panels) and time series of concentration and particle size (right panels) for SLC and Corexit 9500 warm water treatments. From top to bottom, DOR = 0, 1:200, 1:100, 1:20.

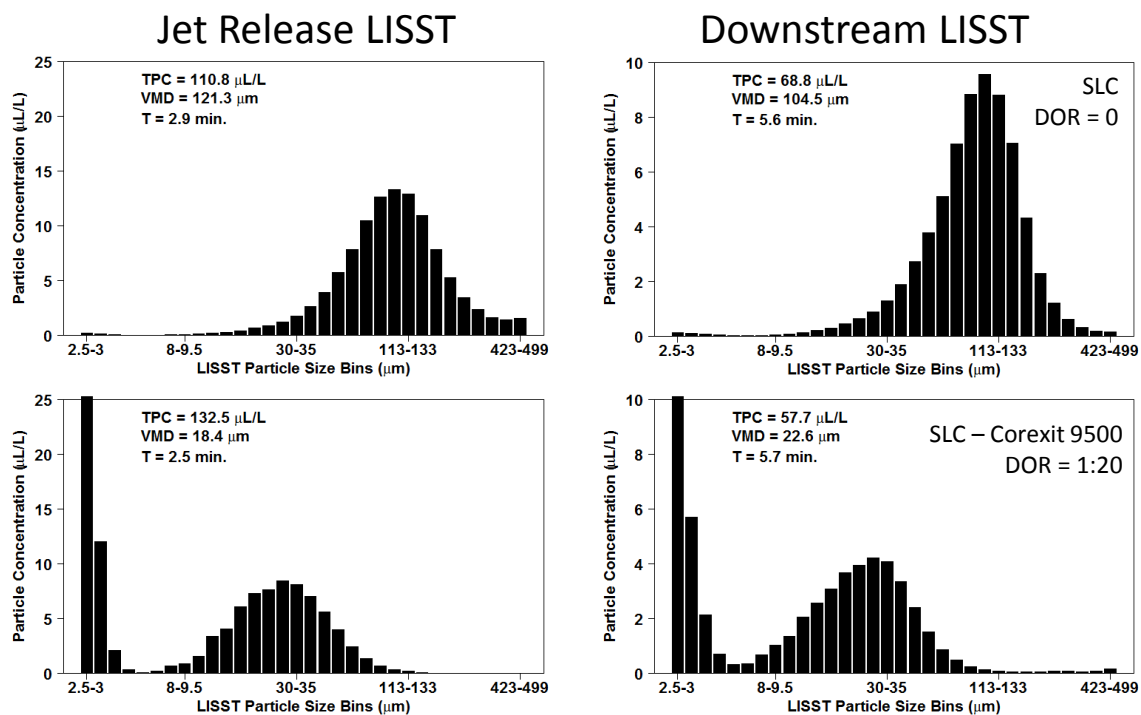


Figure 26. LISST DSD with TPC for SLC with Corexit 9500 treatments at warm temperatures. DOR = 0 (top panel); DOR = 1:20 experiments are bottom panels.

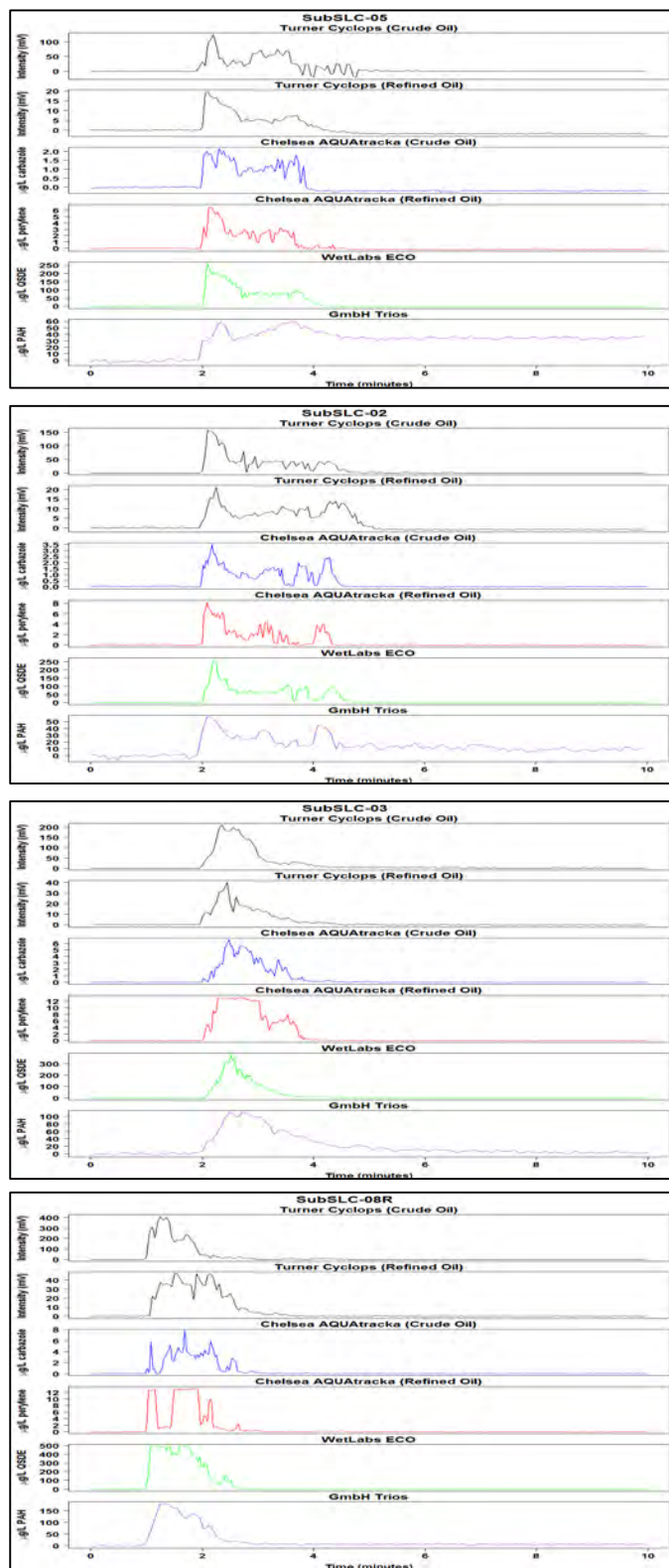


Figure 27. *In situ* submersible fluorescence time series of sub-injection plume of SLC and Corexit 9500 warm water treatments. From top to bottom, DOR = 0, 1:200, 1:100, 1:20.

A.3.4 Gas Condensate Dispersion Effectiveness

Injection experiments were conducted with Gas Condensate and Corexit 9500 for warm water conditions (10 – 12 °C temperature range) and DOR = 0 and 1:20 only. The Gas Condensate consisted of mostly C15 alkanes and lower PAHs (naphthalene and alkylated derivatives). The VMD for Gas Condensate with no dispersant added ranged between ~150 – 215 μm (Figure 28). With the addition of dispersant, VMD for the triplicates were 60.4, 68.2 and 170.4 μm suggesting that dispersant at DOR = 1:20 shifts the DSD to smaller particles for most experiments. Large variability in the triplicates was observed, however at this time there is no clear explanation as to the cause. The corresponding fluorescence data for these treatments indicate a strong signal with little scatter for up to 3 min in both treatments (Figure 28; Appendix E).

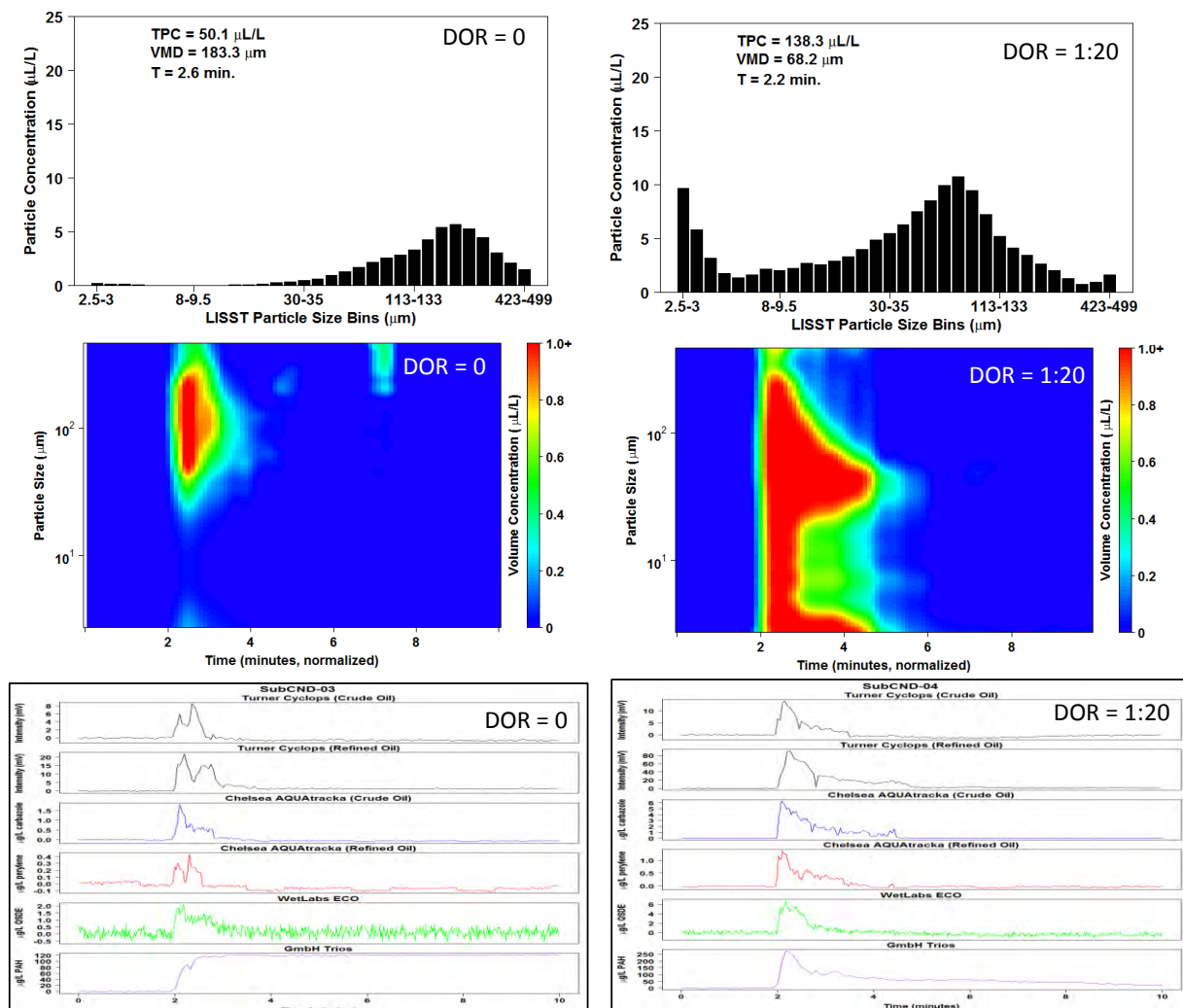


Figure 28. LISST DSD and VMD (top panels), time series of concentration and particle size (middle panels), and fluorescence time series (bottom panels) for Gas Condensate and Corexit 9500 warm water treatments. Left panels are DOR = 0 and right panels are DOR = 1:20.

A.3.5 Tank Dilution Series Fluorescence Measurements

Submersible fluorescence results are presented in units recommended by manufacturers and using calibration factors provided by the manufacturers. Efforts were made to correlate the fluorescence intensity with TPH and / or BTEX concentration but were not possible due to issues inherent with the discrete sample collection. In order to fill bottles for chemical analysis, a 30 second time period was needed. Due to the short time period of the experiments and the heterogeneity of the plume concentration through time (evident from the fluorescence time series), oil concentrations within the bottles represent an average over a 30 second time period that cannot be aligned with the time series data, which are generated on the time scale of seconds. Given this fact, a dilution series within the tank using ANS was conducted to provide a calibration curve for fluorometers to a known concentration of oil in a homogeneous tank akin to Conmy et al., 2014a. Calibration regression results for all submersible fluorometers can be found in Figures 29 and 30 for TPH and BTEX, respectively and regression equations are tabulated in Table 5. Strong correlations between oil concentration and fluorescence intensity were observed, suggesting that fluorescence signal may serve as a proxy for TPH or BTEX at specific time points within the tank. This is an advantage as fluorescence intensity and oil droplet concentrations time series can therefore be calibrated and employed to provide for chemistry estimates that can be correlated with particle / oil droplet concentrations at fine time scales within the tank during experiments. For example, comparing the TPC and fluorescence signature for ANS with and without dispersant illustrates the differences in the oil droplet concentration and dissolved oil during injection experiments and the utility of monitoring both to understanding plume dynamics (Figure 31).

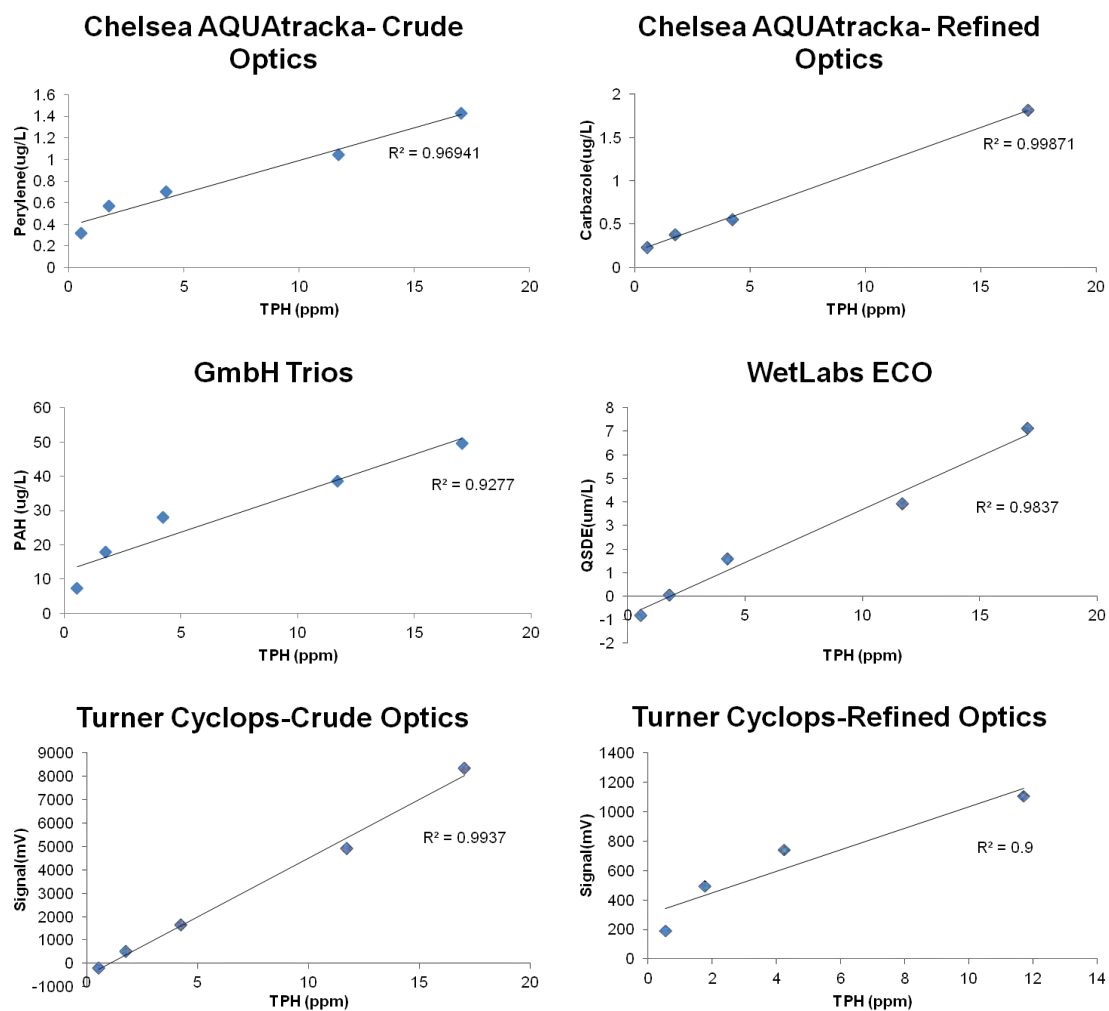


Figure 29. Calibration lines for fluorometer response vs TPH concentrations.

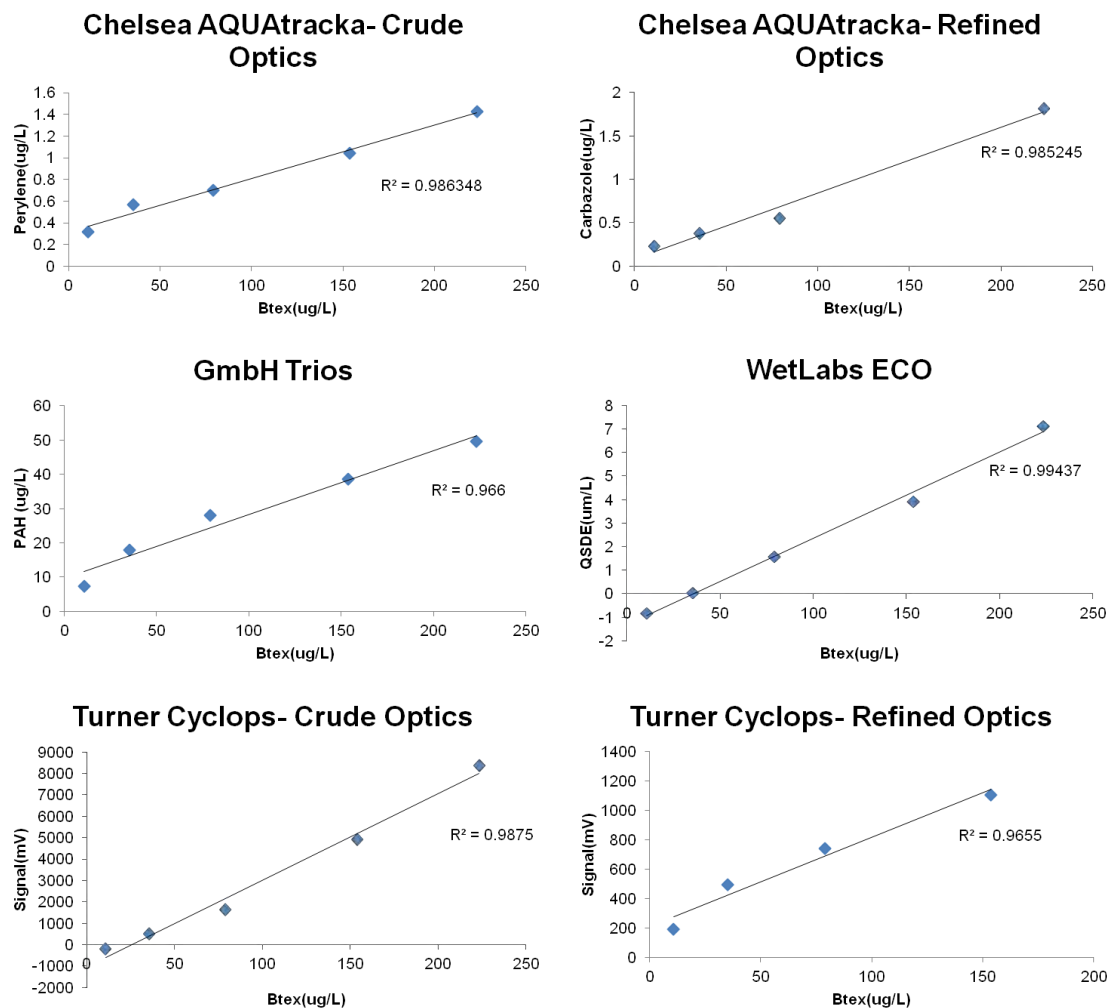


Figure 30. Calibration lines for fluorometer response vs BTEX concentrations.

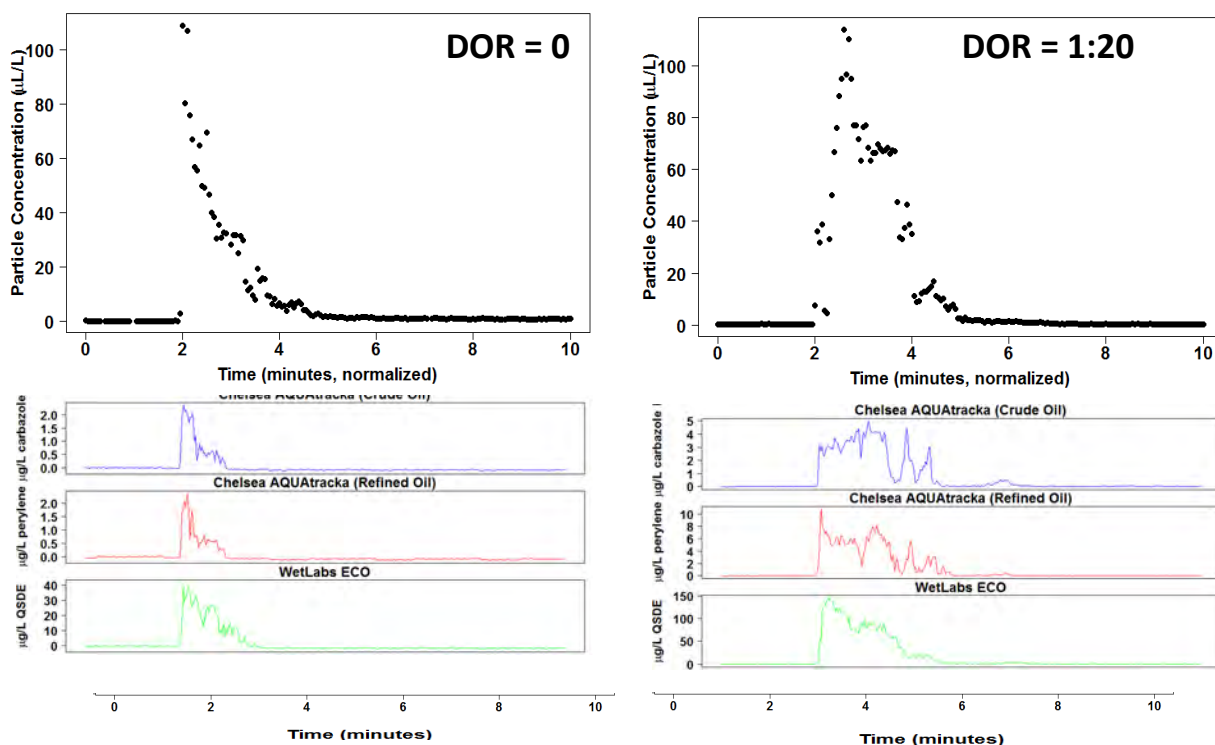


Figure 31. Total Particle Concentration and fluorescence time series for ANS crude oil with Corexit 9500 dispersant.

Table 5. Calibration equations for the submersible fluorometers. Data in this report have fluorescence signal in the manufacturer recommended units.

Instrument	Factory Calibration Standard (units)	TPH Calibration Equation	BTEX Calibration Equation
Chelsea Aquatracka (Crude Optics)	Perylene (ug/L)	$[TPH] = ([Perylene] - 0.3834) / 0.06051$	$[BTEX] = ([Perylene] - 0.3165) / 0.004922$
Chelsea Aquatracka (Refined Optics)	Carbazole (ug/L)	$[TPH] = ([Carbazole] - 0.1804) / 0.09575$	$[BTEX] = ([Carbazole] - 0.08487) / 0.007584$
GmbH Trios	PAH (ug/L)	$[TPH] = ([PAH] - 12.288) / 2.2733$	$[BTEX] = ([PAH] - 9.559) / 0.1871$
Turner Cyclops (Crude Optics)	Signal (mV)	$[TPH] = (Signal + 320.26) / 503.94$	$[BTEX] = (Signal + 1152.2) / 42.429$
Turner Cyclops (Refined Optics)	Signal (mV)	$[TPH] = (Signal - 299.29) / 73.339$	$[BTEX] = (Signal - 212.05) / 6.0593$
Wetlabs ECO	QSDE (uM/L)	$[TPH] = (QSDE - 0.2102) / 0.4362$	$[BTEX] = (QSDE + 0.5403) / 0.03697$

A.3.6 VOC Air Monitoring

For all experiments, the Volatile Organic Compounds (VOC) measurements exhibited higher variability compared to the in water sensor measurements. The installation of a wind curtain along the western side of the tank helped to reduce the prevailing winds coming directly off the water, however the effects of wind were not completely eliminated. The observed variability is likely caused by differences in wind speed and direction both among the triplicate experiments (typically run on the same day), and among the different treatments (which were run over days/weeks). The VOC meters were installed with the air intakes pointing down and were 0.4 m above the water surface at the top edge of the tank. This positioning helped to reduce the effects of wind, given that the tank walls acted as an additional wind blocker.

Two VOC meters were deployed above the tank, but only results from the VOC meter closest to the oil release are presented here (Jet Release VOC meter; the VOC meter directly above the fluorometer rack). Results from the second VOC meter (Downstream VOC meter) installed 11.8 m farther downstream are more variable, both in concentrations between triplicate runs and in the time it takes for airborne VOC concentrations to reach the meter. In general, readings from the second meter showed a broader plume with a lower peak VOC concentration. Due to an instrument malfunction, approximately 17 experiments are missing data from the Downstream VOC meter. All results from the Jet Release VOC meter are presented in Figures 32-39. Note that the Y-axis scale differs depending on the oil type (20 ppm for IFO, 45 ppm for ANS & SLC, 250 ppm for Gas Condensate).

Of the four different hydrocarbon products tested, experiments using the gas condensate exhibited the highest surface VOC concentrations, followed by ANS and SLC which exhibited similar values. The lowest concentrations were observed for IFO 120 experiments. Higher concentrations of VOC in the air were usually accompanied by lower BTEX concentrations in the water for each oil type (analytical chemistry results in Appendix B). Chemistry results from the water column (effluent, listed in Appendix B tables) samples help to verify the findings from the VOC meters. In general, the measured concentrations of BTEX in the effluent water

samples were higher for experiments using dispersant compared to the untreated experiments. The effluent port in the flume tank during normal operation produces a depth integrated water sample which does not draw off the water surface. Therefore, oil that rises to the surface is not drawn into the effluent, and so the tank effluent can be used as a measure of how much oil was dispersed into the water column. Regardless of the oil product tested, the use of chemical dispersants resulted in a reduction in VOC concentrations in the air above the water compared to corresponding experiments without dispersant. These results comparing the mean maximum VOC concentrations (30 second before/after peak readings) measured during each experiment are summarized in Table 6. A general trend was also observed where increasing the DOR resulted in lower surface VOC concentrations near the jet release location. Statistical analysis using ANOVA followed by confidence interval test (Tukey's test) to compare the means found that there were significant differences between VOC readings for ANS at a DOR of 1:20 versus no dispersant (both Corexit and Finasol), as well as significant differences for SLC at a DOR of 1:20 versus no dispersant and DOR 1:100 and 1:200. Caution should be used when extrapolating these results to other spill scenarios, given that this was a shallow water tank so the effects of dissolution of VOCs from oil droplets in a deepwater blowout would not be accounted for in these experiments. Due to wind effects mentioned previously, trends in VOC concentrations above the plume further down the tank could not be established. Further, wind conditions may have contributed to the observed variability in the measurements. The effects of wind on the dilution and transport of VOCs should also be considered during a real world spill scenario, and so the absolute values of VOC concentrations measured in this study should only be used to compare the relative differences between treatments, and should not be used as a guide for worker exposure. Caution must be exercised however in that these results merely represent VOCs that make it to the air-sea interface from a very shallow wave tank. They cannot simulate the dissolution of VOCs into water that would be expected in a deep water column.

Table 6. Summary of maximum VOC concentrations at the various treatment conditions tested in this study. Results are for only for warm water experiments.

	Avg. Peak VOC Concentration (ppm), n = 3				ANOVA
Oil Type	No Dispersant	DOR 1:200	DOR 1:100	DOR 1:20	p-value, $\alpha = 0.05$
ANS (Corexit 9500)	23.07	13.27	12.43	0.13	0.023
ANS (Finasol OSR 52)	23.07	16.56	7.17	2.9	0.024
IFO 120	1.00	0.90	7.37	0.17	0.133
Condensate	121.23	--	--	19.73	0.152
SLC	28.53	27.5	16.75	1.53	0.001

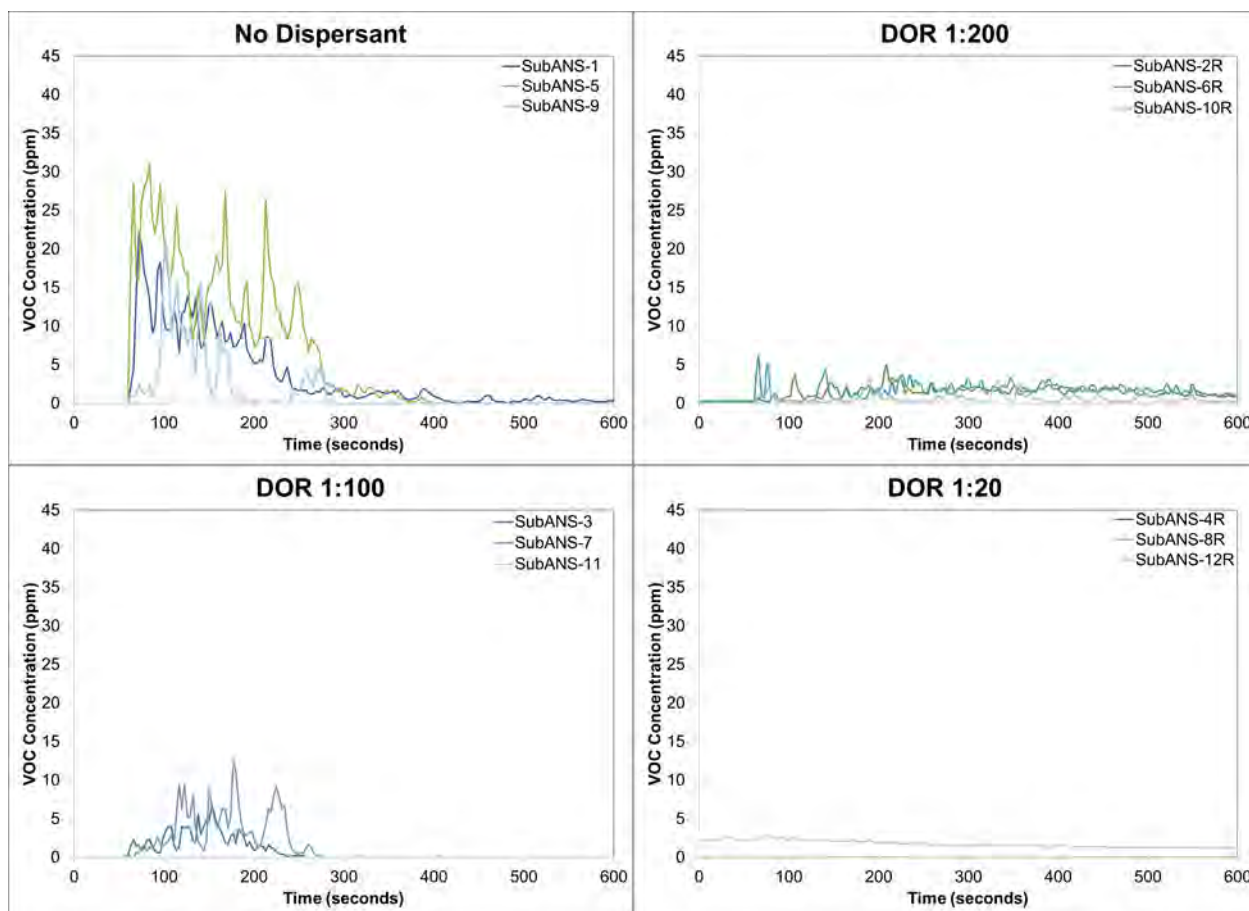


Figure 32. VOC results for subsurface injection experiments (cold water season) using Alaska North Slope crude oil and four treatment conditions (no dispersant, DOR 1:200, DOR 1:100, DOR 1:20). Replicate treatments represented by light blue, dark blue and green colored lines.

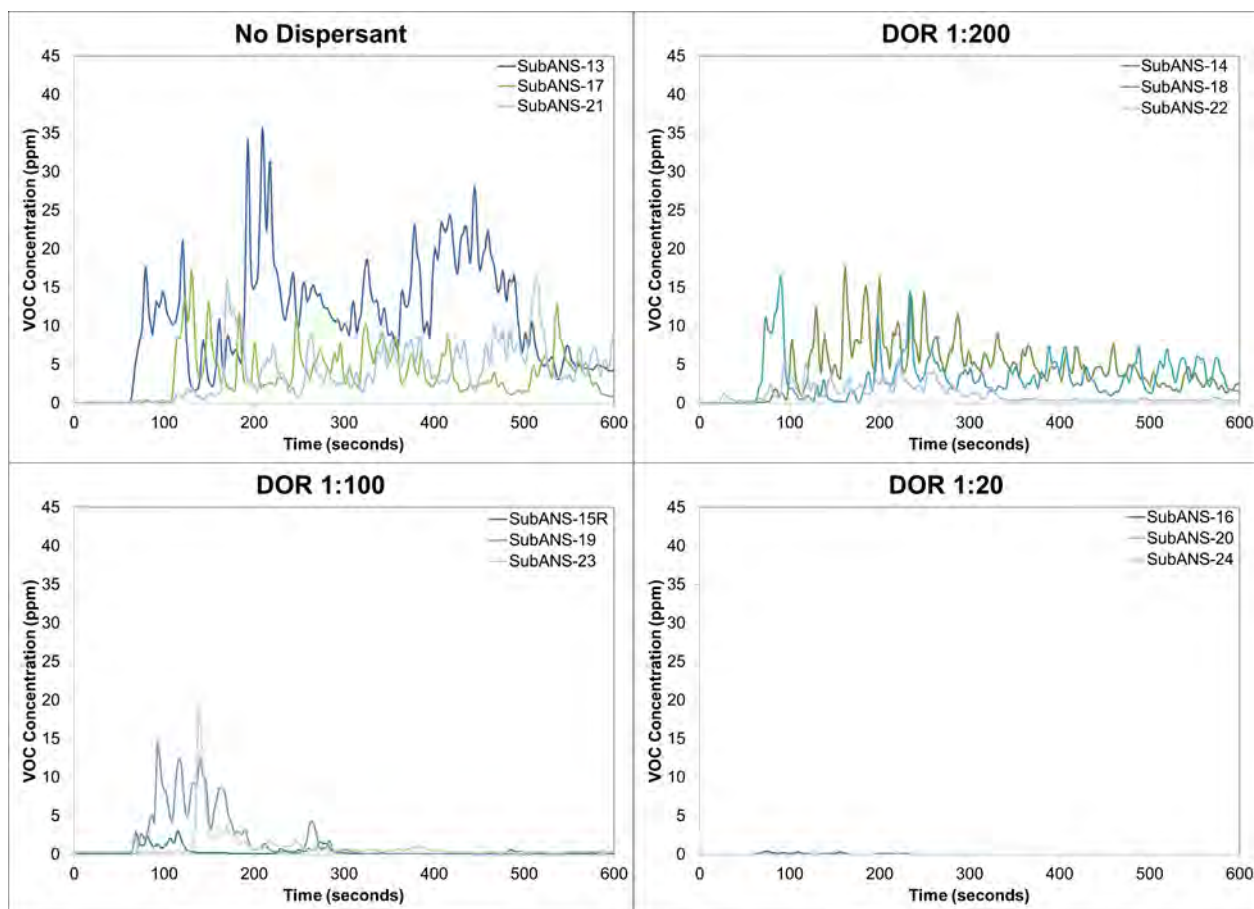


Figure 33. VOC results for subsurface injection experiments (warm water season) using Alaska North Slope crude oil and four treatment conditions (no dispersant, DOR 1:200, DOR 1:100, DOR 1:20). Corexit 9500 was used as the treating agent. Replicate treatments represented by light blue, dark blue and green colored lines.

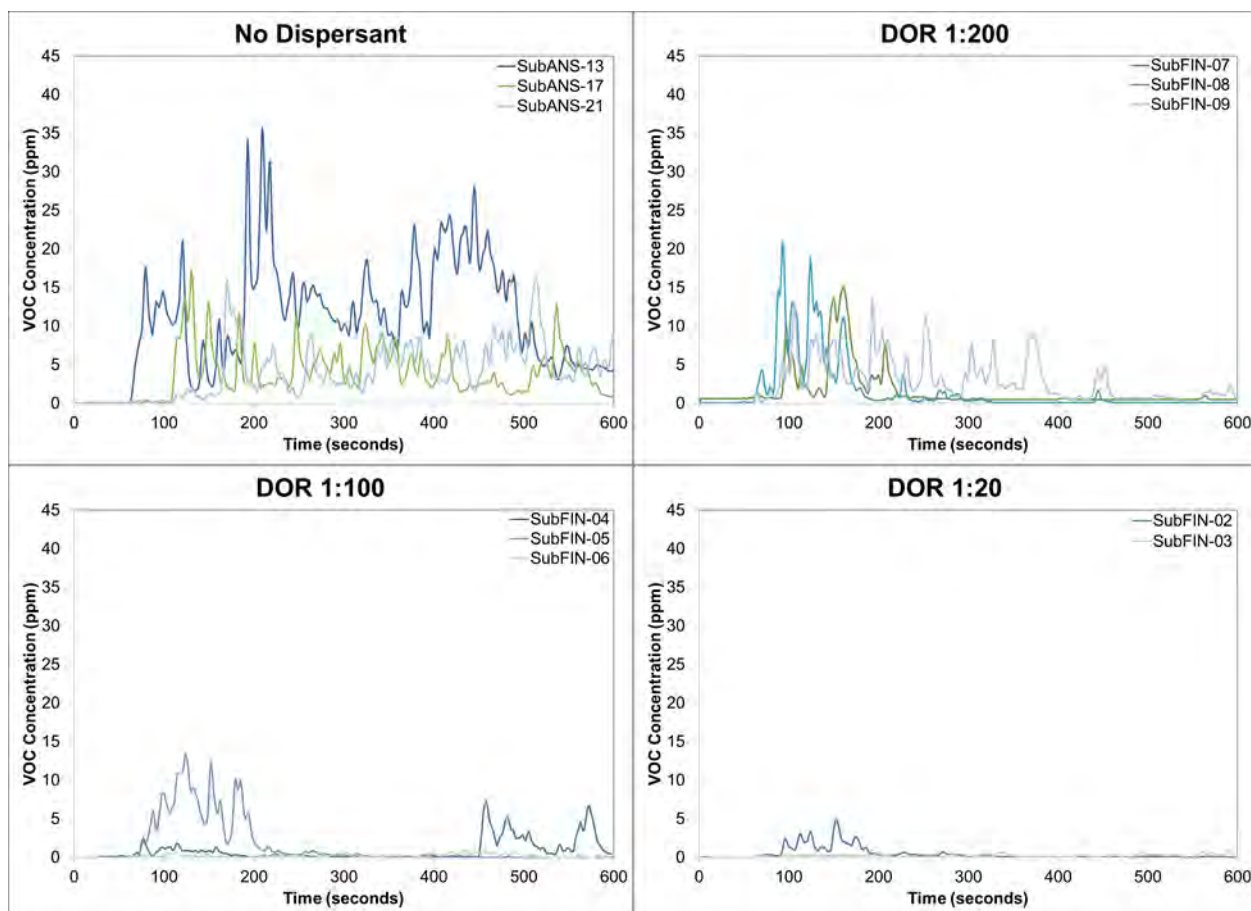


Figure 34. VOC results for subsurface injection experiments (warm water season) using Alaska North Slope crude oil and four treatment conditions (no dispersant, DOR 1:200, DOR 1:100, DOR 1:20). Finasol OSR 52 was used as the treating agent. Replicate treatments represented by light blue, dark blue and green colored lines.

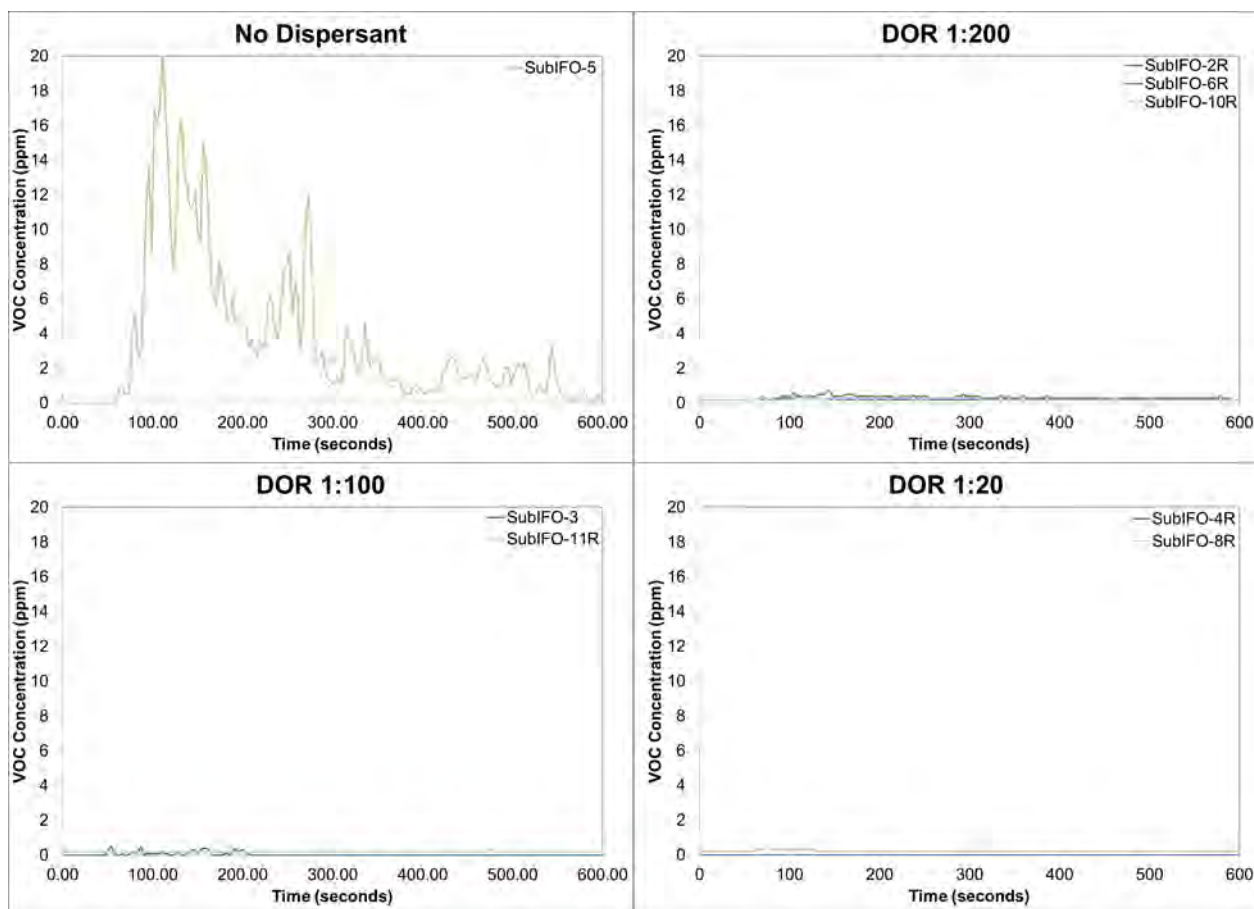


Figure 35. VOC results for subsurface injection experiments (cold water season) using IFO 120 and four treatment conditions (no dispersant, DOR 1:200, DOR 1:100, DOR 1:20). Corexit 9500 was used as the treating agent. Replicate treatments represented by light blue, dark blue and green colored lines.

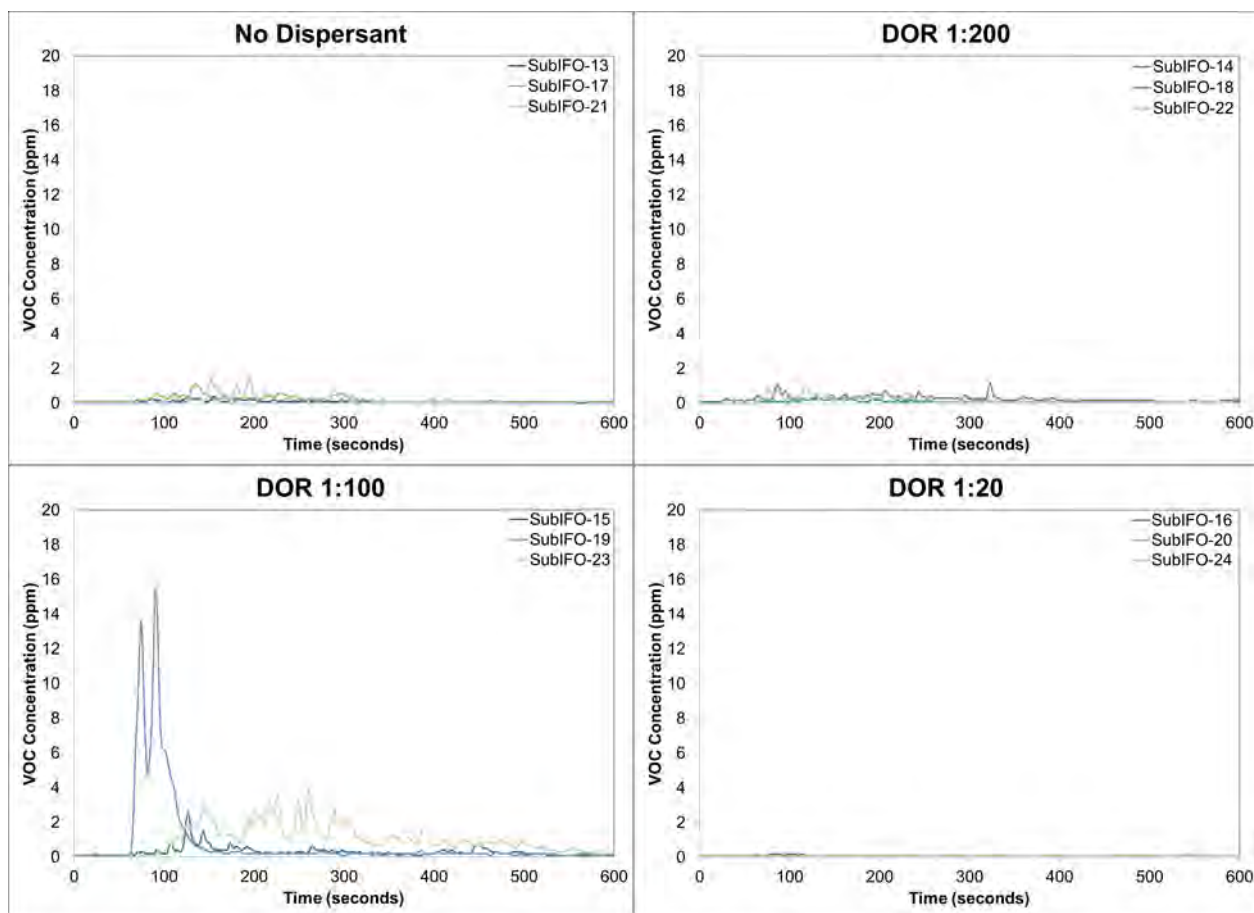


Figure 36. VOC results for subsurface injection experiments (warm water season) using IFO 120 and four treatment conditions (no dispersant, DOR 1:200, DOR 1:100, DOR 1:20). Corexit 9500 was used as the treating agent. Replicate treatments represented by light blue, dark blue and green colored lines.

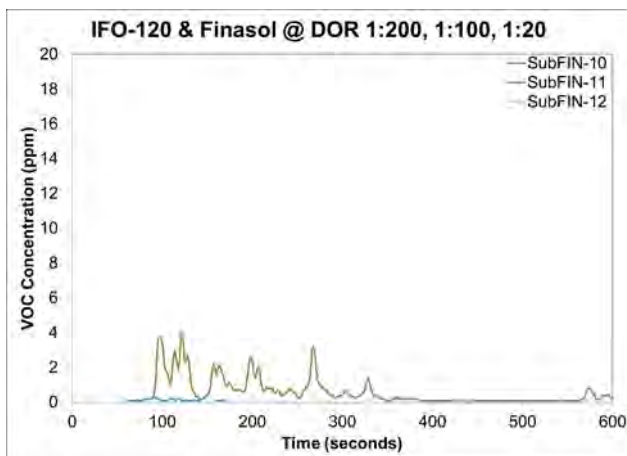


Figure 37. VOC results for subsurface injection experiments (warm water season) using IFO 120 and three treatment conditions (DOR 1:200, DOR 1:100, DOR 1:20). Finasol OSR 52 was used as the treating agent (note – these treatments were not tested in triplicate).

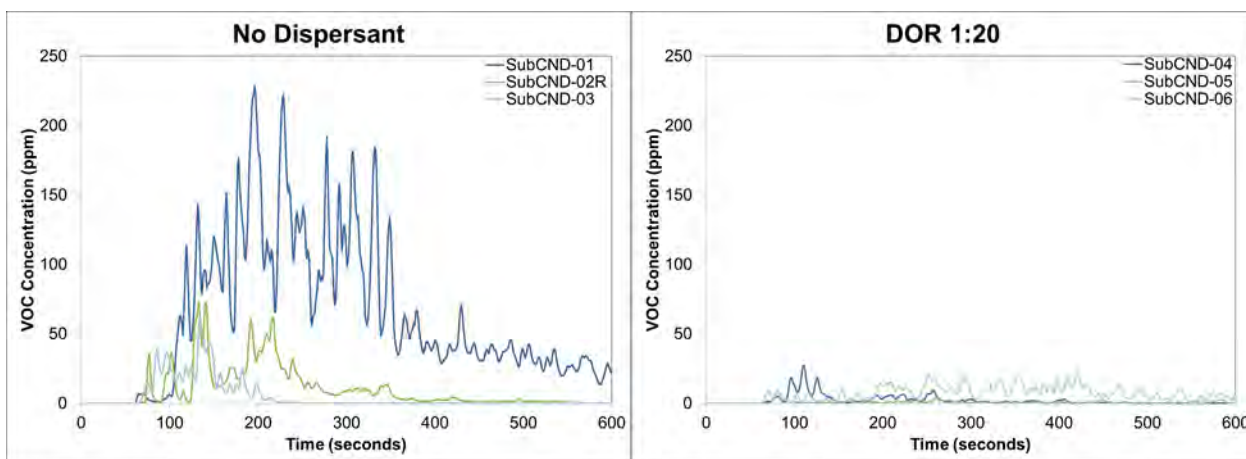


Figure 38. VOC results for subsurface injection experiments using gas condensate and two treatment conditions (no dispersant, DOR 1:20). Corexit 9500 was used as the treating agent.

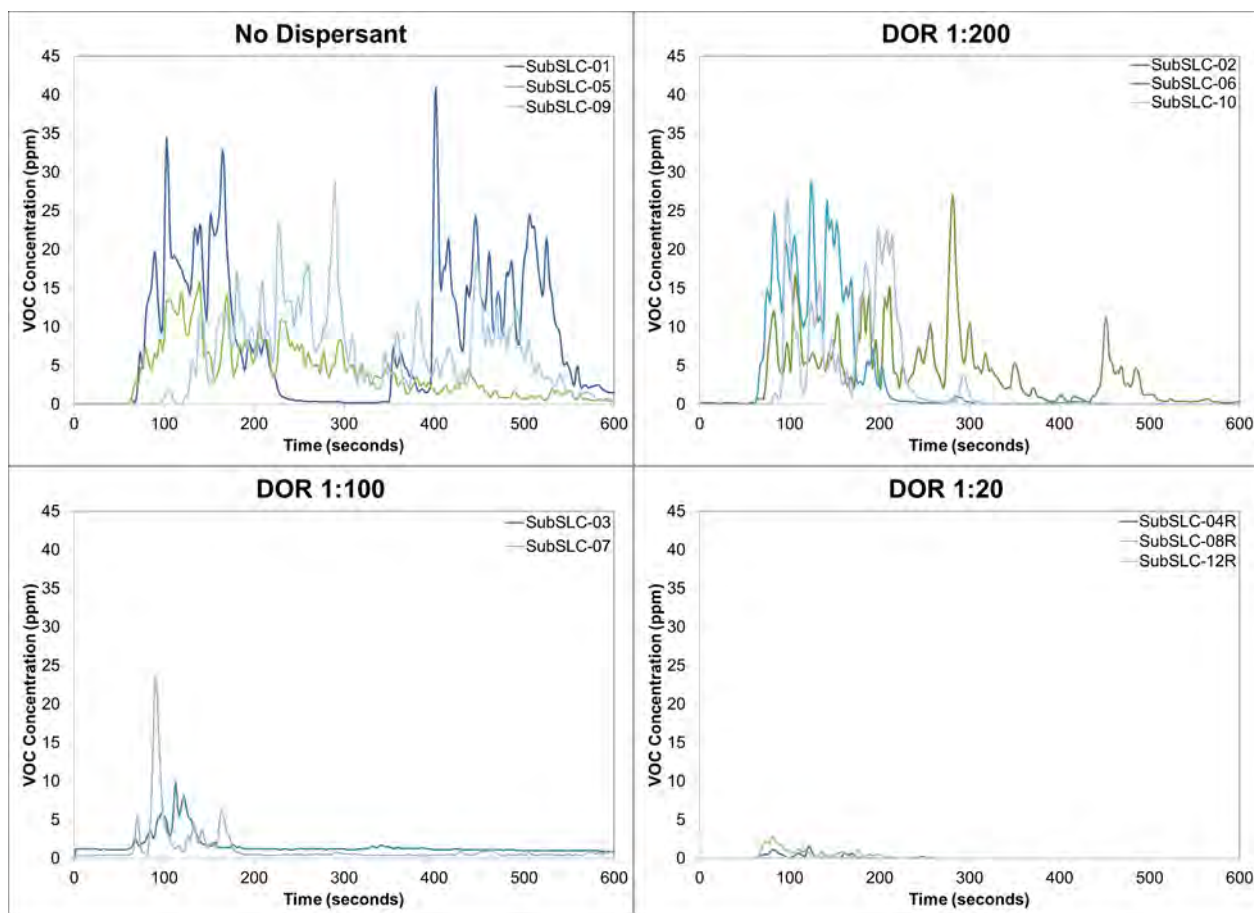


Figure 39. VOC results for subsurface injection experiments using Sweet Louisiana Crude oil and four treatment conditions (no dispersant, DOR 1:200, DOR 1:100, DOR 1:20). Corexit 9500 was used as the treating agent.

A.3.7 VDROP-J and JETLAG Numerical Plume Modeling

Refer to Appendix G for detailed summary of the VDROP-J and JETLAG numerical modeling component along with figures. Modeling the movement of oil released underwater is a challenging task due to limitations in measuring hydrodynamics in an oil-water system. Computational Fluid Dynamics (CFD) models are capable of reproducing the hydrodynamics provided they have sufficient resolution. However, current CFD models cannot predict the droplet size distribution. For this reason, we used a suite of programs to understand jet hydrodynamics, the droplet size distribution, and the movement of oil droplets within the jet/plume. The developed models were calibrated to experimental data of oil jet released underwater in the BIO tank. Based on the properties of the jet (mass flow rate 3.8 L/min through a 2.4 mm orifice), the regime of the jet is atomization, which indicates that the jet would break into small droplets. The models VDROP-J and JETLAG were used to predict the streamwise centerline velocity and the holdup (volume of oil divided by the total volume of fluids in a control volume) along the centerline of the plume, where both models were in agreement. This implies that VDROP-J is adequate to predict the average droplet size distribution in the plume. In the absence of dispersant, the model VDROP-J predicted oil DSD that is very close to that measured by the LISST instrument. However, In the presence of dispersant premixed with the oil, the VDROP-J model captured the overall trend of the DSD, but could not capture the peak in droplet concentration observed at 5 μm . The observed peak is most likely due to tip-streaming (when at high DORs, oil droplets shed filaments from their edges resulting in smaller droplets), and VDROP-J does not have such a module at this time but is considered for future development.

The computational fluid dynamics (CFD) program Fluent (www.ansys.com) was used to model the hydrodynamics of the horizontal jet experiments. The standard $k - \varepsilon$ model was used to model turbulence, and the Volume of Fluid (VOF) was used to model the two phases (oil and water). The profiles of the holdup (ratio of oil volume to total volume), velocity magnitude, eddy diffusivity and turbulent dissipation rate were presented. Findings indicate that the holdup drops sharply with distance from the source to a few percent within 0.50 m from the source, suggesting the occurrence of water entrainment into the plume. A significant reduction

in the energy dissipation rate was also observed, by orders of magnitude along the centerline, starting from 10^4 watt/kg to 10^{-4} watt/kg. Both holdup and energy dissipation values have important consequences on oil droplet breakup and coalescence. The plume exhibited a core of high velocity and high mixing, while the edge of the plume had more or less violent conditions, which is probably due to the entrained water squishing the edges of the plume. The velocity and eddy diffusivity are needed to predict the movement of individual oil droplets. The shape of the plume was circular near the orifice, but became oblate horizontally at a centerline distance of 2.0 m, which is due to both the buoyancy of the whole plume and its inertia. This suggests that the narrow width of the tank (0.60 m) did not affect the jet hydrodynamics (otherwise the jet would be elongated in the vertical). The width of the tank had an effect on the jet dynamics only near the surface as the plume became elongated along the tank near the surface.

The CFD approach has its limitations as it smooths out the edge of the oil jet/plume, and thus does not allow for the formation of large eddies around the plume. Here, large eddy simulations (LES) were used to capture the large eddies where the movement of individual oil droplets employed a lagrangian approach. Water velocity and the eddy diffusivity were used to transport oil droplets, and the effect of individual oil droplet buoyancy and inertia were accounted for. Accounting for the inertia of oil droplets has not been done previously in the oil spill literature. Neglecting the inertia of the droplets results in overestimates of their rise rate as the inertia from a horizontal jet tends to propel the droplet more horizontally, and thus their rise gets delayed also by turbulent mixing. Results suggest that oil droplets with a diameter less than 100 μm would mix uniformly in the plume, while those close to 500 μm would tend to be above the centerline of the plume. This indicates that, when measuring the droplet size distribution using the LISST, the placement of the LISST would not affect the reading of droplets that are less than 100 microns. But the LISST needs to be placed judiciously to capture particles that are 300 to 500 μm , otherwise LISST placement below the centerline would underestimate the actual droplets in that range. In contrast, LISST placement above the centerline does not allow for determining that the concentration values represent the whole cross section of the plume.

A.3.8 Weber Number Scaling Numerical Plume Modeling

Refer to Appendix H for detailed summary of the Weber Number Scaling numerical modeling component. During the Deepwater Horizon oil spill, modeling activities for predicting oil droplet size distribution formed in subsea oil blowouts was critical given their direct influence on the fate and transport of oil in the marine environment. The scientific community's knowledge on droplet size distributions and our capability to predict the distributions are still limited. A recent and promising approach for predicting DSD is the Modified Weber Number approach developed by SINTEF. Thus far, this method has been based on experimental results, validated by a light crude oil (Oseberg Blend crude oil). Here, this approach is validated over a range of oil types (IFO 120 and ANS) using a series of experiments conducted with a subsurface release of oil within the DFO horizontal flow tank.

Based on the measured droplet sizes obtained from the tank experiments, corresponding median droplet diameters (d_{50}) and the relative droplet size (d_{50}/D) were calculated, where D is the nozzle diameter. Accordingly, the relations between d_{50}/D and modified Weber number, Reynolds number, and oil concentration were quantified. With regression analyses, the empirical coefficients for the prediction of droplets size distribution based on the modified Weber number were determined for a certain type of oil (e.g., IFO 120 and ANS). The results indicated that chemical dispersants play an important role in reducing the droplet size of ANS in both cold and warm temperatures. The effectiveness of dispersant in reducing droplet size is higher for ANS compared to IFO 120. There may be thresholds for the dose of chemical dispersant to some oils (e.g., IFO 120) but further data analyses are needed to confirm this. There may also be over dose of dispersant to some oils (e.g., ANS) when the DOR is high, eventually affecting the droplet size distribution. Furthermore, the data indicate that the distributions of the data with $d/d_{50} \leq 1$ and $d/d_{50} > 1$ are significantly varied. Therefore, a two-step Rosin-Rammler approach was introduced to more accurately predict the droplet size distribution. The regression coefficients for the two-step Rosin-Rammler are higher compared to the single step in most cases (Appendix H), indicating the advantage of the proposed two-step Rosin-Rammler approach. It should also be noted that the measured interfacial tension (IFT) for the IFO 120 and ANS with different DORs appear to be significantly different compared

to the measured results from SINTEF for the modified Weber number approach, possibly due to the characteristics of different oils.

Task B.1 Introduction & Relevance

BSEE's *Remote Sensing & Surveillance of Oil Spills* broad agency announcement that funded this work states that "In remote sensing, a sensor other than human vision or conventional photography is used to detect or map oil spills." Thus, although certain remote sensing of oil spills is traditionally linked to detection of oil on the sea surface from above, the scope of the technology can be extended to include the detection of oil in the deep-sea and/or under-the-ice conditions using various sensors, as responders cannot use vision within the water column. As demonstrated during the 2010 Gulf of Mexico Deepwater Horizon (DWH) oil spill, oil detection by fluorescence can enable responders to discern trajectory of plumes and assess effectiveness of dispersant countermeasures (ACT, 2008; Joint Analysis Group Report, 2010). The information gained from such technologies was used to track oil in the water column and inform response strategies to protect natural resources potentially at risk; thus supporting both Net Environmental Benefit Analyses (NEBA) and Natural Resource Damage Assessments (NRDA). To advance the application of this methodology, this project evaluated fluorescence characteristics of various oils with and without dispersants to aid in the selection and refinement of *in situ* sensors for use in oil spill response operations.

The overall objective of this work was to translate oil fluorescence R&D into operational tools for oil spill response. Tabulating information on the optimum fluorescence wavelengths for oil detection as a function of oil type and DOR assists responders selecting sensors and establishing Best Practices for rapid decision making during spill response. The results of this project are timely and can be used in conjunction with the National Response Team (NRT) guidance document, *Environmental Monitoring for Atypical Dispersant Operations: Including Guidance for Subsea Application and Prolonged Surface Application*, for incident-specific decisions concerning monitoring subsea dispersant use (www.nrt.org). It specifically calls upon using oil-specific submersible fluorometers with laboratory and on-board ship analyses using fixed wavelength and scanning spectrofluorometers to enable improvements to monitoring sampling during dispersant application. Findings from this project provide additional scientific information in support of implementing guidance recommendations.

Fluorescence characteristics - All fluorophores (molecules that fluoresce) have characteristic wavelengths for maximum absorption of light and characteristic wavelengths at which they emit light as fluorescence. Absorption and fluorescence can occur at either narrow or wide wavelength ranges depending on the chemistry and complexity of the fluorophores. A variety of naturally occurring fluorescent compounds occur in the ocean, from ones with narrow wavelength ranges with sharp fluorescence peak maxima (pigments, proteins) to complex compounds with wide diffuse peaks over long wavelength ranges, such as the ubiquitous Colored Dissolved Organic Matter (CDOM) or petroleum oils.

Fluorescence characteristics of complex mixtures can overlap if structurally similar compounds are shared. Such is the case with CDOM and the aromatic fraction of crude oils. Both are comprised of a variety of organic molecules and both exhibit complex, three-dimensional EEM spectra. In general, crude oils have a broad excitation peak centered in the ultraviolet spectrum (< 300 nm) and two emission peaks, one centered in the ultraviolet spectrum around 340 nm and a much larger and broader peak in the visible around 445 nm (Bugden et al., 2008). These peaks result from the single ring benzene derivatives and the “polynuclear aromatic” fraction that are particularly susceptible to UV excitation wavelengths. EEMs exhibit distinct fingerprints for different oils as illustrated by previous studies (Bugden et al., 2008; Kepkay et al., 2008).

DWH in situ oil fluorescence - Deployment of submersible fluorometers during the DWH oil spill response illustrated the utility of this forensic tool that enabled large-scale monitoring of oil concentrations to a depth of approximately 1600 m. Co-deployment of the fluorometers alongside other response sensors [Conductivity-Temperature-Depth (CTD), Dissolved Oxygen (DO), Laser *In-Situ* Scattering and Transmissometry (LISST)] from multiple platforms (e.g. profilers) with real-time capabilities improved our understanding of the processes influencing the fate and behavior of the oil in the presence and absence of chemical dispersants. Added to this, extensive water column sampling also involved discrete sample collection for oil particle concentration and size, Total Petroleum Hydrocarbons (TPH), Volatile Organic Carbon (VOC) and other physical, chemical, biological factors. To date, the in-depth reviews by the Joint Analysis Group (JAG) charged with data analysis have found that of all the variables measured, the most

highly correlated in the subsea plume are *in situ* DO and oil fluorescence intensity (Joint Analysis Group Report, 2010). Such a correlation is not unexpected as laboratory tests show that enhanced oxygen utilization can result from microbial respiration in the presence of oil compounds (Venosa et al., 2002b). Beyond the underlying biochemical mechanisms however, likelihood of correlation is increased based on the fact that variables measured *in situ* at high sampling rates are better to capture plume heterogeneity. Hence, the utility of *in situ* fluorescence as a tool was ascertained early in the response due to such correlations, the high temporal and spatial resolution provided by the sensors, and also the advantages afforded by real-time capability compared to discrete analyses.

However, the multitude of submersible fluorometers used in the DWH response called to attention differences in the sensitivity and analytical capability of the instruments used due to differences in configuration of excitation and emission wavelengths, methods of calibration, sensitivity, and correlation to oil concentration (Figure 40, Table7). Many are not customized to capture oil fluorescence peak maxima, rather only a fraction of the signal (Fuller et al., 2003; Conmy et al., 2004 Conmy et al., 2014b). Furthermore, the ability of any fluorescence sensor (laboratory or field submersible) to detect oil is a function of (1) how well the sensor matches the excitation and emission wavelengths of the oil (including bandwidth of the wavelength filters or bandpasses from gratings, (2) the power of the light source, and (3) the sensitivity of the detector.

When tracking in the subsea became necessary early in the response, fluorometers used for detection of CDOM (i.e., WET Labs ECO series) were deployed on the vertical profilers as they were widely available, were capable of full ocean depth deployment and had been previously shown to detect oil in water (Wet Labs, Inc. website, www.wetlabs.com). These sensors typically have light sources that excite at wavelengths slightly longer than peak absorption by hydrocarbons and detect emission in the visible. They employ filters centered on excitation (Ex) and emission (Em) wavelengths at 370 and 460 nm (ExEm_{370/460nm}). Although the center wavelength of the filters does not capture the peak of the oil fluorescence signal, the wide bandwidth of the emission filters (120 nm Full Width at Half Max) and the broad nature of the fluorescence peaks means that CDOM sensors are capable of detecting a large portion of the

visible fluorescence signal. CDOM fluorometers were used to detect oil during the response in part because of their accessibility, but also because these sensors capture some portion of the oil fluorescence peak that occurs at the longer UV wavelengths where CDOM peaks also exist.

To quell questions regarding the ability of the ECO CDOM fluorometer to detect oil in the subsea plume, calibration tests were conducted at Louisiana State University (LSU) using Mississippi Canyon 252 (MC252) source oil. They provided a means to convert raw fluorescence data to Quinine Sulfate Dihydrate Equivalents (QSDE, the standard typically used for CDOM) to ppm of oil (JAG report, 2010). The calibrations were conducted in flasks on orbital shakers at 90 revolutions per minute (rpm), where oil concentrations ranged between 1-50 ppm. Dispersant (Corexit 9500) was added at a DOR of 1:2.5 and 1:25. The response of the fluorometer was linear with respect to oil but varied as a function of DOR, with a quenching of fluorescence in the presence of more dispersant per unit oil. Results of this test indicated that the ECO sensor was a sufficient proxy for oil concentrations greater than 1 ppm (NOAA, 2010). However, as the response continued and after the well was capped, oil concentrations in the subsea plume decreased as well as the magnitude of the fluorescence anomaly due to dilution and degradation of the oil, particularly at further distances from the wellhead. Concern was raised that a fluorometer with higher sensitivity for oil (one with a hydrocarbon-specific configuration) was needed. At that time, Chelsea UV Aquatrackas (ExEm_{239/360nm}) were deployed to track the plume in the far field of the response geographic region with the expectation (and subsequent confirmation) that it would detect fluorescence signal at lower oil concentrations.

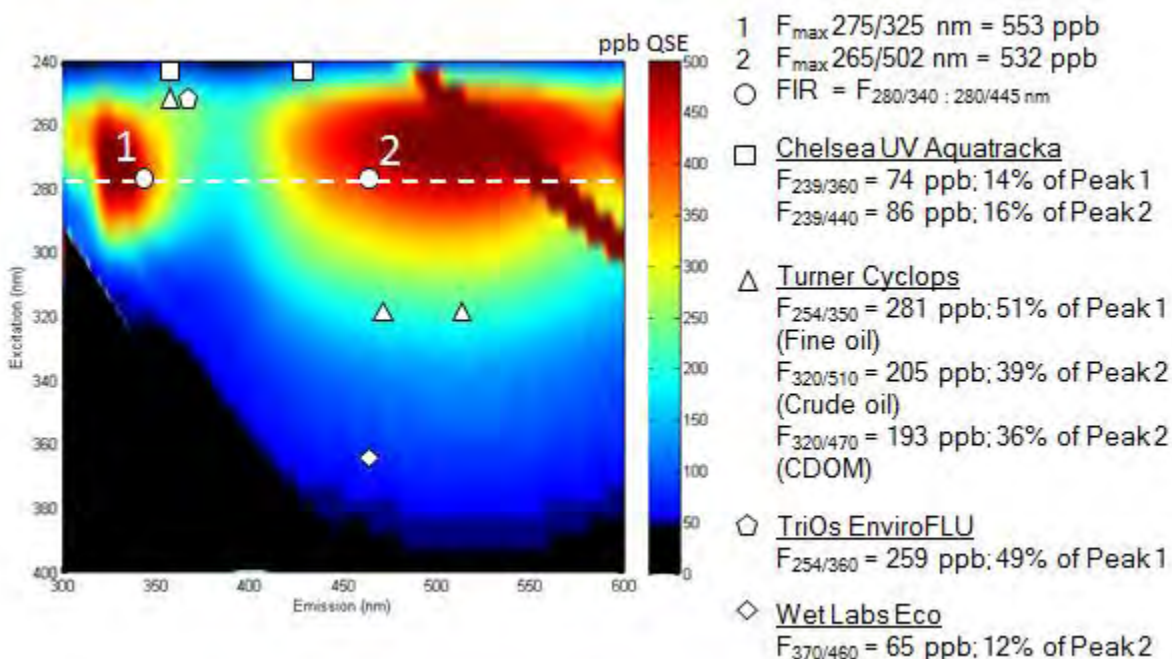


Figure 40. Fluorescence peaks of S. Louisiana sweet crude dispersed in ppb QSE (Quinine Sulfate Equivalents). Symbols represent Fluorescence Intensity Ratio (FIR) locations and the Center Wavelength (CWL) reported by sensor manufacturers. Bandwidths (BW) are not shown.

Table 7. Sensor specifications as listed from manufacturers. Wavelengths listed as Center Wavelengths (CWL) with Full Width at Half Max (FWHM) and Bandpass (BP). Standards used are QS (Quinine Sulfate Dihydrate), NDD Salt (Napthalene Disulfonic Disodium) and PTSA Salt (Pyrenetetrasulfonic Acid Tetrasodium) (From Conmy et al., 2014b).

Manufacturer	Instrument	Light source	Excitation λ (nm)	Emission λ (nm)	Detector	Dynamic Range
Chelsea Technologies Group	UV AQUAtracka	Xenon lamp	239 CWL	360 CWL	PMT	0.001 - 10 $\mu\text{g/L}$ Carbazole
	UV AQUAtracka	Xenon lamp	239 CWL	440 CWL	PMT	0.001 - 10 $\mu\text{g/L}$ Perylene
Seapoint Sensors	SUVF	LED	370, 12 FWHM	440, 40 FWHM	Photodiode	0.1 - 1500 $\mu\text{g/L}$ QS
TriOS, GmbH	EnviroFLU-HC, DS	Xenon lamp	254, 25 FWHM	360, 50 FWHM	Photodiode	0 - 5000 ppb Phenanthren
Turner Designs	Cyclops (Fine oil)	LED	254, 40 nm BP	350, 50 nm BP	Photodiode	0 - 10,000 ppb NDD Salt
	Cyclops (Crude oil)	LED	320, 130 nm BP	510, 180 nm BP	Photodiode	0 - 2700 ppb PTSA Salt
	Cyclops (CDOM)	LED	320, 130 nm BP	470, 60 nm BP	Photodiode	0 - 2500 ppb QS
WetLabs	WetStar	LED	370, 10 FWHM	460, 120 FWHM	Photodiode	0.100 - 1000 ppb QS
	ECO-FLU, triplet, puck	LED	370, 10 FWHM	460, 120 FWHM	Photodiode	0.01 - 500 ppb QS

Post-DWH response sensor tank testing -To address persisting uncertainties regarding sensor performance in the subsea, a team of scientists conducted experiments in May 2011 to study the dynamic range, sensitivity, and response of *in situ* fluorometers to changing excitation or emission properties of fresh and weathered MC252 oil (NOAA Science Box Award, PI: Michelle Wood; Co-PI's from EPA, NOAA, University of South Florida). The experiment was conducted within the flow-through flume tank at the BIO in Dartmouth, Nova Scotia, taking into consideration environmental factors such as wave energy and ocean currents. Experiments included the stepwise addition of oil and dispersant (DOR of 1:25; 0.3 - 12 ppm of MC252 SLC oil) to the flume tank while collecting *in situ* fluorescence and droplet-size distribution data, as well as coincident discrete samples for chemistry and EEM analyses. The flume tank was operated in static mode and each addition of oil and dispersant was allowed to homogenize prior to collecting discrete samples and coincident sensor measurements to calculate the least linear squares regressions. Results indicated that all sensors tested were responsive to changes in MC252 oil concentration regardless of wavelength configuration. Linear response of the WET Labs ECO,

Turner Designs Cyclops and the Chelsea Technologies Group AQUAtrackas sensors as a function of oil concentration was observed, where lowest concentrations were not below the detection limit of any sensor tested (Conmy et al., 2014a). Results demonstrated that all sensors exhibited a wide dynamic range of detection for MC 252 oil and were capable of detecting oil at the lowest concentration (approximately 300 ppb oil), which is significantly lower than the LSU calibration study (1 ppm) and a common misconception during the response (Conmy et al., 2014a). Differences in the detection limit between the studies may be explained by differences in the design, scale and the amount of physical dispersion of the tests, where the tank can provide mixing energies similar to those found in the field.

The 2011 study findings answered critical questions about sensor performance to detecting MC252 oil. However, the experiment highlighted the need for future studies to evaluate sensor performance using a variety of DORs and for multiple oil types. Evident from the DWH spill and post-spill research was that further R&D is needed to transfer knowledge gained through laboratory 3-D Excitation Emission Matrix (EEM) Spectroscopy into practical information for fluorescence tools used during spill response. Fluorescent properties are oil specific and investigating variations in EEMs as function of oil type and dispersant-to-oil ratios better prepares the community in identifying sensors for response options. To that end, the objectives of this project were to:

- I. Generate a comprehensive EEMs database, building upon existing data at the Department of Fisheries and Oceans Canada, to provide fluorescence peak information as a function of oil type, weathering state, concentration and Dispersant-to-Oil Ratios (DORs).
- II. Critically examine the database using advanced statistical methods and models to identify wavelengths best suited for oil monitoring during dispersant application and degradation.
- III. Conduct flume tank experiments to determine submersible sensors capable of providing data comparable to scanning and/or fixed wavelength laboratory fluorometers for rapid deployment during response efforts.

Through this project, a comprehensive EEMs library database was generated covering a wide variety of oils from light to heavy fuel and crude oils and diluted bitumen. Varying DORs (1:20, 1:100, 1:200, 0) and oil concentrations were evaluated as the presence of dispersant alters EEM fingerprints. EEMs were subjected to advanced statistical analyses and models to identify wavelengths best suited for oil monitoring during dispersant application and subsequent tracking. Fluorescence is a non-destructive characterization tool that is routinely used to examine complex organic mixtures (foods, wine, medical compounds, aquatic organic matter, oils). Unlike single compound solutions, they exhibit broad, diffuse peaks that result from overlapping smaller peaks with similar chemistry. Although EEMs can be a substantial source of information on chemical composition and variability amongst samples, the high-dimensionality (intensity by emission by excitation) and nonlinearity of the data equates to difficulties in data interpretation and extraction of practical information as a characterization tool (Bieroza et al., 2010). Therefore, it is difficult to determine which underlying chemical components are responsible for which portion of the fluorescence fingerprint. Combining standard techniques for EEM analysis such as assessment of particular fluorescence peak features including peak height and wavelength position via 'peak picking' with Parallel Factor Analysis (PARAFAC) modeling results in a more comprehensive understanding of the chemical constituents. The use of advanced multivariate analyses such as PARAFAC has gained popularity as an effective means to deconvolve complex, broad peaks into their underlying smaller components (Stedmon et al., 2003; Boehme et al., 2004; Christensen et al., 2005; Stedmon and Bro, 2008). Here, we processed EEMs data with scripts in the N-way toolbox for Matlab (Andersen and Bro, 2000) and SOLO software (Eigenvector, Inc) and used the algorithms to isolate wavelengths to best characterize an oil type. An excellent review of these chemometric techniques and applications is provided in Bieroza et al., 2010. This approach will allow for comparing oil in water mixtures for similarities and contrasting features.

Results were evaluated for the Fluorescence Intensity Ratio (FIR) technique (Bugden et al. 2008; Kepkay et al. 2008). The latter calculates the ratio at $\text{ExEm}_{280/340\text{nm}}$ to $\text{ExEm}_{280/445\text{nm}}$ as an indicator

of oil dispersion. Previous studies at DFO COOGER have shown that dispersed oil fluoresces over two peaks centered on emission wavelengths of 340 nm and 445 nm, at excitation wavelength 280 nm, and that chemical dispersion enhances the emission intensity at 445 nm (Bugden et al. 2008; Kepkay et al. 2008). Postulated is that the fluorescence intensity at ExEm_{280/340nm} represents the dispersion of lower molecular weight aromatic hydrocarbons, while intensity at ExEm_{280/445nm} corresponds to higher molecular weight aromatic compounds.

Finally our work addresses the disconnect that exists between fluorescence research conducted in laboratories and the collection of fluorescence data from submersible sensors. By conducting laboratory-based and tank-based experiments on the same oil type and DOR, comparisons between EEMs can be made across scales. This helps to determine how well the *in situ* sensors are aligned in detecting dispersed oil.

Task B.2 Experimental Methods

B.2.1 Sample Preparation - Twenty-five oil samples from the DFO and EPA stockpiles (covering a wide range of viscosity and oil type) were used for spectrofluorometric testing, where oil characteristics were tabulated for the test oils based on an extensive literature search (Table 8; Supplemental Material A). All glassware used in this study was cleaned to ensure highest analytical integrity including solvent rinsing, deionized water rinsing and baking in a muffle furnace at 450°C where appropriate. Samples were stored in 125mL amber glass bottles with PTFE-lined caps (Figure 41).

B.2.2 Artificial Seawater Protocol - Artificial seawater was used for DOR mixing to avoid interference of fluorophores found in natural seawater with oil fluorescence signal. Fresh artificial seawater was made to salinity of 28 ppt and was prepared in 1 L quantity at the beginning of each experiment by adding Tropic Marin® salts (Appendix A) to 1 L ultrapure water dispensed from a Millipore Milli-Q unit (≤ 4 ppb DOM) into a 1.5 L glass beaker, covering the beaker with aluminum foil, and stirring with a magnetic stir-bar on electric stir plate for 20 minutes at room temperature ($\sim 24^{\circ}\text{C}$).

B.2.3 Dispersed Oil in Seawater Protocol - A series of dispersed-oil-in-seawater experiments were performed using baffled trypsinizing flasks (baffled flasks) with artificial seawater, MC252 oil and Corexit 9500 chemical dispersant (Venosa et al., 2002a). Four petroleum oil / dispersant solutions were prepared for each oil type at the following DORs: 0, 1:20, 1:100, and 1:200. Oil was pipetted into an 8.6 ml amber vial, followed by addition of the appropriate amount of Corexit 9500 chemical dispersant into the vial. Teflon-lined capped vials were shaken by hand for 60 seconds and 10 μL of dispersant / oil mixture was pipetted (Eppendorf positive displacement micropipettes, 1-20 μL) into 100 mL artificial seawater contained in each of three replicate flasks. Flasks were covered with parafilm and placed on a New Brunswick Scientific Innova 2100 platform shaker (orbit = 1.9 cm) for 12 minutes at 200 rpm. Approximately 3.5mL of the resulting dispersed-oil-in-seawater was immediately dispensed through a spigot near the bottom of each flask into three 4.0-mL UV-grade quartz cuvettes, which were immediately covered with Teflon

stoppers to prevent evasion of volatile components during fluorescence analyses (Figure 42). After removal of spectrophotometric samples, additional volumes of sample were removed from the baffled flasks for extraction of total petroleum hydrocarbons (TPH) by dimethylene chloride (DCM). TPH analysis follows the same Gas Chromatography-Mass Spectrometry (GC-MS) method as in Task A of this project.

B.2.4 Spectrophotometric Analysis - A Horiba Scientific AquaLog spectrofluorometer was used to analyze the 25 oil types with varying DOR. A series of analyses were initially performed while varying the instrument's settings (excitation and emission increments, gain setting, integration time) in order to determine optimal settings for the entire experimental protocol. Excitation-Emission Matrices (EEMs) were generated using the following instrument parameters: 200 – 800 nm excitation (3 nm increments), 249 – 828 nm emission range (CCD detector at 534 nm 8 pixel increments), medium gain setting and integration time of 0.1 sec. A quinine sulfate dihydrate dilution series was created consisting of: 0.5N H₂SO₄ solvent; 100 ppm 1° (primary stock) solution; 100 ppb 2° (secondary stock) solution; 1,3,5,10 and 20ppb quinine sulfate solutions. Dilutions were analyzed for fluorescence and used for cross-calibration with instrument software built-in quinine sulfate tool to convert results into Quinine Sulfate Equivalents (QSE) and demonstrate linearity of fluorescence in a dilution series. All data processing and spectral corrections follow the manufacturer's manual. Dilution series with oil concentrations between 1 – 500 ppb were also generated to determine lower detection limits for oils. EEMs are presented in Raman Units (RU).



Figure 41. Twenty-five oil samples stored in glass bottles.

Table 8. List of oil samples used for EEM analyses. Oils separated by API (American Petroleum Institute) gravity.

Light (API >31.1°)	Medium (API 22.3 – 31.1°)	Heavy (API <22.3°)
Arabian Light (32.2°)	Alaska North Slope (29.7°)	Access Western Blend Dilbit (21.3°)
Brent (38.2°)	Alaskan North Slope (10% weathered)	Belridge Heavy (13.6°)
Federated (39.4°)	Heidrun (28.6°)	Cold Lake Dilbit (21.5°)
Gullfaks (32.7°)	Lago (25.0°)	Hondo (19.5°)
Hibernia (35.6°)	Mesa (30.3°)	IFO 40 (21.9°)
MC252—Discoverer Enterprise (37.2°)	Sea Rose (29.8°)	IFO 120 (18.4°)
MC252—generic (35.2°)	Vasconia (26.3°)	IFO 180 (14.1°)
Scotian Shelf Condensate (53.2°)		IFO 300
Terra Nova (33.8°)		Santa Clara(22.1°)

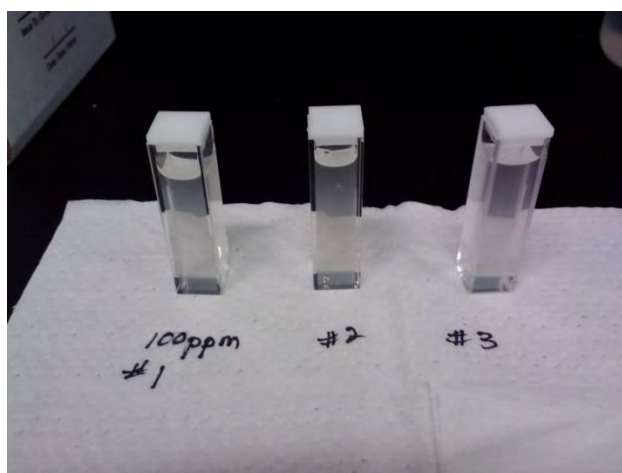


Figure 42. Trypsinizing baffled flasks containing dispersed oil in artificial seawater (top) and corresponding samples removed from each flask, ready for spectrofluorometric analysis.

Task B.3 Results & Discussion

B.3.1 Oil Fluorescence Properties

Four characteristic excitation/emission (Ex/Em) peak locations were identified: $F_{\max1}$ – $F_{\max4}$ (Figure 43) for all 25 oil types at four DORs (Figure 43). The highest intensity peak ($F_{\max1}$) occurred, without exception, at Ex 221-239 nm/Em 335-344 nm and was paired with a blue-shifted, lower intensity peak ($F_{\max2}$) at Ex 215-221 nm/Em 285-308 nm in all oil types. A third broad, low-intensity peak ($F_{\max3}$) was observed at Ex 215-305 nm/Em 418-571 nm, to varying degrees across oil types, corresponding with oil categories determined by API gravity (Table 8). Light crude oils exhibited $F_{\max3}$ fluorescence at all DORs with the exception of Scotian Shelf Condensate. Of note is that Scotian Shelf Condensate appeared physically unlike any of the other light oils: clear in color with apparent very low viscosity. Since viscosity is largely determined by the size and relative weight of component hydrocarbons (Fingas 2011), fewer complex fluorophores would likely be present in this oil type. Fluorescence in the $F_{\max3}$ region was identified at all DORs in only one medium weight oil (Heidrun), and was not present at any DOR in one medium oil (Vasconia). Two medium-weight oils emitted measurable fluorescence in the $F_{\max3}$ region only with full dispersion (Lago and Mesa), while Sea Rose showed fluorescence at DORs 1:100 and 1:20. One medium weight oil, Alaska North Slope (both fresh and 10% weathered), exhibited unusual $F_{\max3}$ behavior, with measureable fluorescence at DOR 0, 1:100 and 1:20, but not at DOR 1:200. Finally, for the heavy weight oils, $F_{\max3}$ was almost completely absent at all DORs, with the exception of fluorescence at DOR 1:20 for Cold Lake Dilbit (Diluted Bitumen) and IFO 40, and across all DORs for one anomalous member of this group—Access Western Blend Dilbit. Dilbit is a mixture of bitumen—essentially a heavy crude oil with API gravity < 10.0°—and a diluent—either a light condensate or naptha (Priaro 2016). The combination of characteristics from both oil types may account for the unusual $F_{\max3}$ fluorescence observed in this oil type. Additionally, Intermediate Fuel Oils (IFOs) are not true crude oils, but marine fuels consisting of a mixture of post-refinery heavy residual oil and refined diesel fuel, which may also help to explain the appearance of $F_{\max3}$ fluorescence in IFO 40. Clearly, the presence of fluorescence in the $F_{\max3}$ region, especially at DOR 1:20, appears to be related to API gravity, and thus to density as well as kinematic viscosity since API gravity = $(141.5/\text{Specific}$

Gravity) – 131.5 (Fingas, 2011). The absence of $F_{\max3}$ region fluorescence in heavy weight oils may be due to retention of energy within the large, complex hydrocarbons which make up the highest density oils. Additionally, the appearance of fluorescence in the $F_{\max3}$ region at highest DORs for the medium weight oils (Lago, Mesa, and Sea Rose) suggests that smaller droplet sizes were created via the dispersion which could lead to a decrease in reabsorption of fluorescence within the oil – water mixture. A fourth region of broad, low-intensity fluorescence ($F_{\max4}$) was identified at Ex 269-291 nm/Em 326-353 nm for all oil types at all DORs. $F_{\max1}$ and $F_{\max4}$ oil-in-water fluorescence regions appear to be analogous to the characteristic colored dissolved organic matter (CDOM) fluorescence regions ‘Ac’ at Ex 260/Em 400-460 and ‘C’ at Ex 320-365/Em 420-470 (Coble, 2014).

In addition to maximum intensity for each fluorescence peak (in RU), full width at half maximum (FWHM) was also recorded. Further, fluorescence intensity at Ex/Em 281/340 and 281/456 nm was recorded to enable calculation of the FIR for all samples. Optimum settings for signal collection on the HORIBA AquaLog necessitated excitation at 3 nm intervals, which accounts for the 1 nm discrepancy from the published FIR wavelengths (Bugden, et al. 2008). Fluorescence intensity at the specified Ex/Em wavelength settings of five off-the-shelf *in situ* fluorometers (Conmy et al., 2014a & b), which were all employed in the response to the DWH spill, was recorded. Those wavelengths were also adjusted slightly to compensate for signal collection intervals on the HORIBA AquaLog. Selected results are presented in Table 9 along with results of chemical analyses, and complete fluorescence results are included as a Supplemental Table A. EEM contour ‘fingerprint’ plots for all oils, which characterize each oil type and illustrate the effect of dispersant on the fluorescence properties, are presented in Appendix F. The ability to identify oil source can be useful in the prevention and abatement of oil spill pollution. To that end, efforts to determine characteristic fluorescence fingerprints have existed since the 1970s (Frank, 1978) and have received renewed attention with the advent of improved fluorescence detection systems (Bugden, 2008).

Intensity of $F_{\max1}$ was consistently strong across oil types, with no ambiguity in peak location. The observed Ex/Em range of significant fluorescence intensity was fairly narrow with FWHM of only

37-50 nm, and little to no change in peak location with increasing DOR. However, Six of the nine light oil types, but just one of the seven medium oil types and one of the nine heavy oil types¹ displayed this slight increase (approximately 4.5 nm) in FWHM with maximum dispersion (DOR 1:20). One medium weight oil (Lago) and one heavy oil (Access Western Blend Dilbit) showed the same slight increase in FWHM at both DORs 1:100 and 1:20. The impact of applying the Inner Filter Effect correction tool (IFE) to fluorescence intensity was also calculated for $F_{\max 1}$. This correction utilizes the measured absorbance of the sample to correct for fluorescence emitted by fluorophores within the sample, but re-absorbed within the sample itself. Of note is that application of the IFE resulted in only a small magnification of the fluorescence signal at DORs 0, 1:200 and 1:100 for all oil types; however, there was a clear delineation between two categories of oil types at DOR 1:20: Oil Type I, with IFE effect > 2.5 and Oil Type II, with IFE effect < 2.5 (Table 9). This appears to be due to the increase in optical density, and thus absorbance, possibly caused by interaction between Corexit 9500 and well dispersed Type I oils. Photographs of four representative pre-analysis samples, along with the resulting EEMs of oil type are shown in Figure 44 to illustrate the difference in fluorescence between the types regardless of being a light, medium or heavy crude oil.

Due to variation from laboratory to laboratory, and even differences in instrument to instrument performance from the same manufacturer, it is necessary to convert fluorescence intensity “raw counts” to a standardized unit for useful reporting purposes. Traditionally, the fluorescence community has utilized a dilution series of quinine sulfate dihydrate in weak acid to convert instrument output to Quinine Sulfate Equivalents (QSE) (Coble, 1996). However, in recent years the alternate method of reporting in Raman Units (RU) has gained favor (Murphy et al., 2010). Due to inherent properties of water molecules, the Raman scatter peak is a reliable feature which can be used through collecting a scan of ultra-pure water at the beginning of each day, and then using the ratio of raw counts to the area under the curve of the Raman peak (approximately 381-426 nm) to convert fluorescence to RU. As the Quinine Sulfate SRM is no longer available from

¹ Increase of approximately 4.5 nm in FWHM in $F_{\max 1}$ seen in light oils Arabian Light, Brent, Federated, Gullfaks, Hibernia, and Terra Nova; in medium oil Mesa; and in heavy oil IFO 120 at DOR 1:20.

NIST (National Institute of Standards and Technology), we have reported results in RU and offer a conversion factor to QSE using the highest quality quinine sulfate dihydrate readily available.

Overall, $F_{\max1}$ intensity ranged from a minimum of 39.58 RU (Access Western Blend Dilbit DOR 0) to 3090.23 RU (IFO 120 DOR 1:100). Since all of the Intermediate Fuel Oils and the Scotian Shelf Condensates showed unusual fluorescence profiles which tended to skew the results for the aforementioned reasons (Figures 45 and 46), these will be eliminated from the remaining discussion. $F_{\max1}$ intensity within Type I oils ranged from 357.62 RU (Arabian Light DOR 1:200) to 1998.60 RU (MC252 Discoverer Enterprise DOR 1:20), while the range in Type II Oils was the overall low of 39.58 previously mentioned to a high of 1098.90 (Heidrun DOR 1:20).

While the excitation wavelength of maximum intensity for $F_{\max2}$ remained relatively consistent, the emission wavelength varied within, as well as among, oil types. The occurrence of double and triple peaks, as well as minor sub-peaks, within the $F_{\max2}$ region was fairly common. It was sometimes difficult to distinguish the $F_{\max2}$ peak from the shoulder of a very strong $F_{\max1}$ peak, especially at higher DORs. For this reason, determination of the true FWHM was sometimes problematic. For $F_{\max2}$ intensity, Type I Oils ranged from 63.95 RU (Brent DOR 1:200) to 437.32 RU (MC252 Discoverer Enterprise DOR 1:20), and Type II Oils ranged from 25.07 RU (Belridge Heavy DOR 0) to 164.07 RU (Heidrun DOR 1:20).

For oil types exhibiting an $F_{\max3}$ peak, it was most apparent at the highest DOR (1:20) and some oils exhibited a strong $F_{\max3}$ peak across all DORs (e.g., Brent, Federated). However, for those oils the $F_{\max3}$ peak at DOR 1:20 was significantly blue shifted (peak moved to lower wavelengths) from the $F_{\max3}$ location observed at lower DORs. FWHM of the $F_{\max3}$ peak was much greater than that of any other peak (145-283 nm), with the exception of the three lower DORs of Access Western Blend Dilbit (52-56 nm). Identification of highest $F_{\max3}$ intensity proved somewhat problematic as it tended to lay within the second order Rayleigh region, a band of high intensity light resulting from scattering by water molecules. The edge of highest intensity could also lie in this region, so determination of the true FWHM was also problematic for many oil types. Traditionally, second order Rayleigh is eliminated by simply masking this region (10-12 nm). Although algorithms have been developed to model the character of fluorescence peaks lying within (Zepp, et al. 2004;

Bahram, et al. 2006), assumptions about the linearity of fluorescence must be made, and the true signal behavior cannot be known. For this reason, as our goal was to identify signals which could also be detected by *in situ* instruments, the decision was made to identify the maximum fluorescence intensity lying outside of the second order Rayleigh region rather than to try to interpolate the data.

As previously mentioned, $F_{\max 3}$ intensity was not always present, and it was observed far more often in Type I Oils with a range of 2.64 RU (Arabian Light DOR 1:200) to 744.69 (MC252 Discoverer Enterprise DOR 1:20). Only four of the Type II Oils exhibited $F_{\max 3}$ peaks and these ranged from 2.45 RU (Access Western Blend Dilbit DOR 0) to 174.93 RU (Heidrun DOR 1:20).

As with $F_{\max 2}$, the $F_{\max 4}$ region sometimes contained double peaks. Unique spectral shapes for this region were also observed, especially in higher-density oils such as Access Western Blend Dilbit, Belridge Heavy, and Cold Lake Dilbit. FWHM ranged from 27 nm to 73 nm, for all oil types but one. The exception was Access Western Blend Dilbit, with FWHM of 77-110. Intensity at $F_{\max 4}$ ranged from 33.53 RU (Arabian Light DOR 1:200) to 231.86 RU (MC252 Discoverer Enterprise DOR 1:20) in Type I Oils and from 4.93 RU (Access Western Blend Dilbit DOR 0) to 116.97 RU (Heidrun DOR 1:20) in Type II Oils.

Results of the concentration dilution series showed that the HORIBA AquaLog was consistently capable of detecting dispersed oil in artificial seawater in the three oil types tested (Alaska North Slope, IFO 120, and MC252 Discoverer Enterprise) at all four DORs down to at least 50 ppb. However, detecting dispersed oil below 100 ppb necessitated increasing the integration time to 10 sec. per scan in order to collect sufficient data, which resulted in a total analysis time of approximately 30 minutes for each sample. Since the HORIBA AquaLog scans from high to low wavelengths and much of the fluorescence signal from petroleum resides in the UV region, photobleaching of the sample as well as temperature effects certainly may have impacted these results.

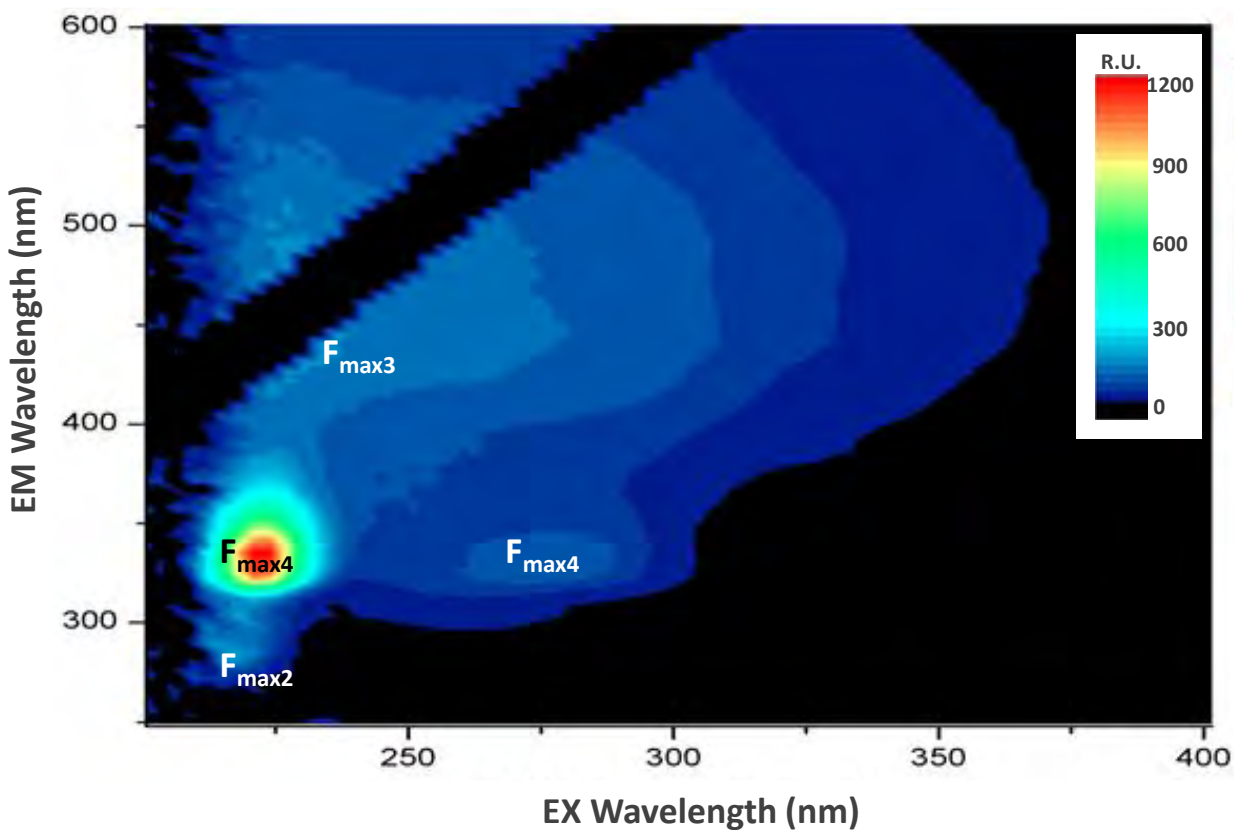


Figure 43. Alaska North Slope dispersed oil in artificial seawater at DOR 1:20 with locations of F_{max1} , F_{max2} , F_{max3} and F_{max4} indicated. Note that maximum fluorescence intensity at F_{max3} is mostly obscured by masking of second order Rayleigh scattering.

Table 9. EEM fluorescence and chemical characteristics. Refer to Supplemental Table A for full table.

Type I Oils		F_{\max}^1 (RU)	IFE	FIR	Alkanes ($\mu\text{g/L}$)	2-ring PAHs ($\mu\text{g/L}$)	3-ring PAHs ($\mu\text{g/L}$)	4-ring PAHs ($\mu\text{g/L}$)
Alaska North Slope	0	697.07	1.16	21.59	375	145	15	8
	1:200	715.01	1.15	35.41				
	1:100	839.60	1.32	6.59				
	1:20	1171.63	3.33	0.88	3019	477	89	65
Alaska North Slope (10% weathered)	0	812.97	1.19	21.70	545	182	19	14
	1:200	831.70	1.21	21.70				
	1:100	828.06	1.28	9.08				
	1:20	1109.51	3.01	0.91	3312	499	99	74
Arabian Light	0	400.42	1.18	7.29	733	113	11	12
	1:200	357.62	1.07	11.61				
	1:100	426.82	1.26	2.70				
	1:20	701.75	4.19	0.39	6004	571	71	103
Brent	0	646.18	1.15	7.59	1068	162	21	12
	1:200	660.37	1.16	6.65				
	1:100	708.16	1.37	1.97				
	1:20	1098.42	3.05	0.68	5954	456	97	58
Federated	0	574.35	1.14	3.70	1921	197	41	30
	1:200	607.97	1.21	2.01				
	1:100	645.28	1.37	0.94				
	1:20	1223.17	4.37	0.36	6501	488	129	87
Gulfaks	0	937.00	1.24	5.79	762	326	47	26
	1:200	934.42	1.27	5.57				
	1:100	933.08	1.35	3.24				
	1:20	1524.21	3.73	0.71	1943	642	107	60
Hibernia	0	938.08	1.24	6.91	2289	296	39	24
	1:200	951.49	1.34	3.22				
	1:100	978.62	1.47	1.69				
	1:20	1812.41	4.02	0.49	6095	541	94	59
MC252 (Discoverer Enterprise)	0	998.50	1.27	5.01	1578	300	50	30
	1:200	1009.18	1.37	3.06				
	1:100	1085.54	1.48	1.22				
	1:20	1998.60	4.76	0.39	3992	482	101	68
MC252 (generic)	0	857.35	1.24	4.42	1468	231	36	21
	1:200	877.78	1.25	3.56				
	1:100	964.02	1.57	0.95				
	1:20	1795.13	4.73	0.40	5093	511	113	67

Type I Oils	DOR	F_{\max}^1 (RU)	IFE	FIR	Alkanes ($\mu\text{g/L}$)	2-ring PAHs ($\mu\text{g/L}$)	3-ring PAHs ($\mu\text{g/L}$)	4-ring PAHs ($\mu\text{g/L}$)
MESA	0	757.84	1.19	18.14	1388	234	34	24
	1:200	806.76	1.22	11.97				
	1:100	745.17	1.26	6.44				
	1:20	1107.09	2.77	1.04	4088	439	85	62
Sea Rose	0	1145.29	1.28	9.80	1583	285	35	19
	1:200	1223.98	1.33	7.59				
	1:100	1236.63	1.55	2.18				
	1:20	1973.55	3.56	0.71	5903	601	120	70
Terra Nova	0	665.50	1.16	6.93	1038	168	18	11
	1:200	719.72	1.22	3.79				
	1:100	821.24	1.37	1.47				
	1:20	1380.34	3.76	0.40	5608	463	77	50

Type II Oils	DOR	F_{\max}^1 (RU)	IFE	FIR	Alkanes ($\mu\text{g/L}$)	2-ring PAHs ($\mu\text{g/L}$)	3-ring PAHs ($\mu\text{g/L}$)	4-ring PAHs ($\mu\text{g/L}$)
Access Western Blend Dilbit	0	39.58	1.02	11.41	93	15	4	10
	1:200	46.52	1.02	11.62				
	1:100	49.84	1.03	8.54				
	1:20	60.19	1.08	1.13	258	40	17	37
Belridge Heavy	0	118.69	1.07	4.90	42	31	21	30
	1:200	161.75	1.08	5.22				
	1:100	140.96	1.07	4.62				
	1:20	147.09	1.12	3.30	44	49	35	52
Cold Lake Dilbit	0	120.61	1.05	18.92	155	74	20	22
	1:200	120.65	1.05	17.33				
	1:100	125.85	1.06	11.50				
	1:20	133.15	1.17	1.92	368	160	50	57
Heidrun	0	902.69	1.28	4.50	382	337	55	43
	1:200	909.47	1.26	6.22				
	1:100	964.31	1.33	3.74				
	1:20	1098.90	2.19	0.77	684	524	96	79
Hondo	0	283.04	1.09	18.38	412	76	8	2
	1:200	312.27	1.08	15.38				
	1:100	274.80	1.07	17.44				
	1:20	288.01	1.07	16.33	319	67	7	1
IFO-40	0	1173.91	1.20	27.94	1324	408	152	168
	1:200	1246.63	1.22	47.73				
	1:100	1338.56	1.25	35.74				
	1:20	1458.79	2.29	4.57	4354	1033	475	561
IFO-120	0	3030.69	1.68	109.67	343	607	88	49
	1:200	2903.21	1.61	101.83				
	1:100	3090.23	1.65	85.76				
	1:20	2527.73	1.67	34.32	840	885	212	118
IFO-180	0	1263.05	1.22	33.67	866	410	235	320
	1:200	1394.42	1.23	36.08				
	1:100	1703.55	2.37	36.31				
	1:20	1532.99	1.63	12.19	2933	1189	797	1095
IFO-300	0	720.55	1.11	61.26	446	216	79	188
	1:200	443.51	1.14	25.85				
	1:100	465.91	1.07	45.70				
	1:20	661.50	1.10	39.81	366	183	65	157
Lago	0	352.22	1.07	12.13	1289	114	32	18

Type II Oils	DOR	F_{\max}^1 (RU)	IFE	FIR	Alkanes ($\mu\text{g/L}$)	2-ring PAHs ($\mu\text{g/L}$)	3-ring PAHs ($\mu\text{g/L}$)	4-ring PAHs ($\mu\text{g/L}$)
	1:200	398.40	1.13	11.73				
	1:100	367.75	1.12	8.88				
	1:20	453.10	1.75	0.92	4221	258	88	51
Santa Clara	0	157.30	1.05	25.93	209	27	1	0
	1:200	147.55	1.05	22.73				
	1:100	154.98	1.08	18.26				
	1:20	169.39	1.12	6.97	1196	72	9	3
Scotian Shelf Condensate	0	946.52	1.15	40.62	447	125	2	0
	1:200	1408.59	1.44	53.68				
	1:100	1487.16	1.53	58.06				
	1:20	1337.98	1.50	47.65	1057	216	4	0
Vasconia	0	844.93	1.15	34.56	2550	317	98	59
	1:200	828.37	1.16	44.43				
	1:100	835.62	1.17	34.09				
	1:20	935.79	1.67	3.41	4402	467	164	95

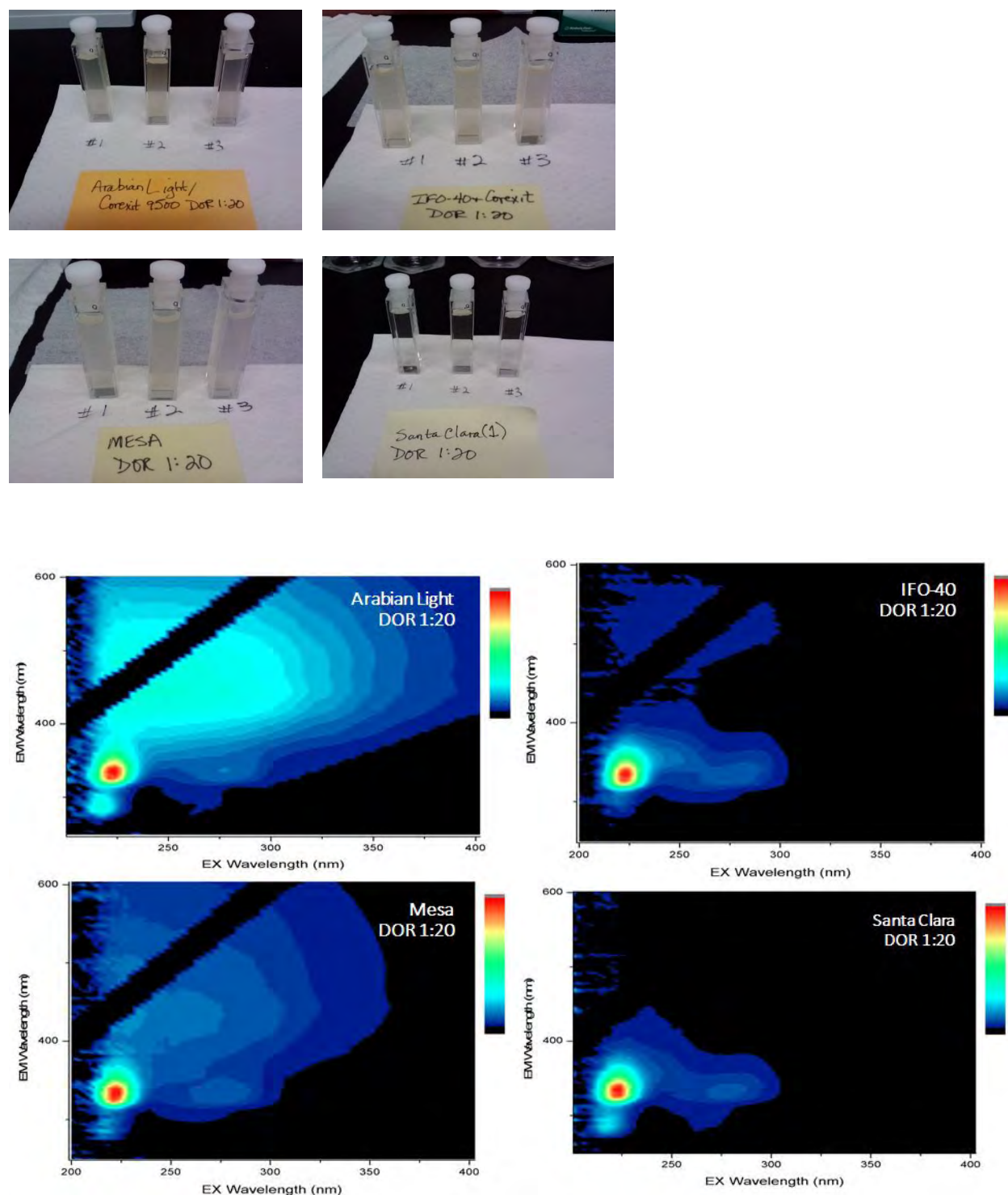


Figure 44. Photographs of pre-analysis samples and corresponding example EEMs of Type I (left) and II (right) oils; DOR = 1:20 for Arabian Light (light oil, API gravity > 31.1°), Mesa (medium oil, API gravity 22.3 – 31.1°) and heavy oils (IFO 40 and Santa Clara, API gravity < 22.3°).

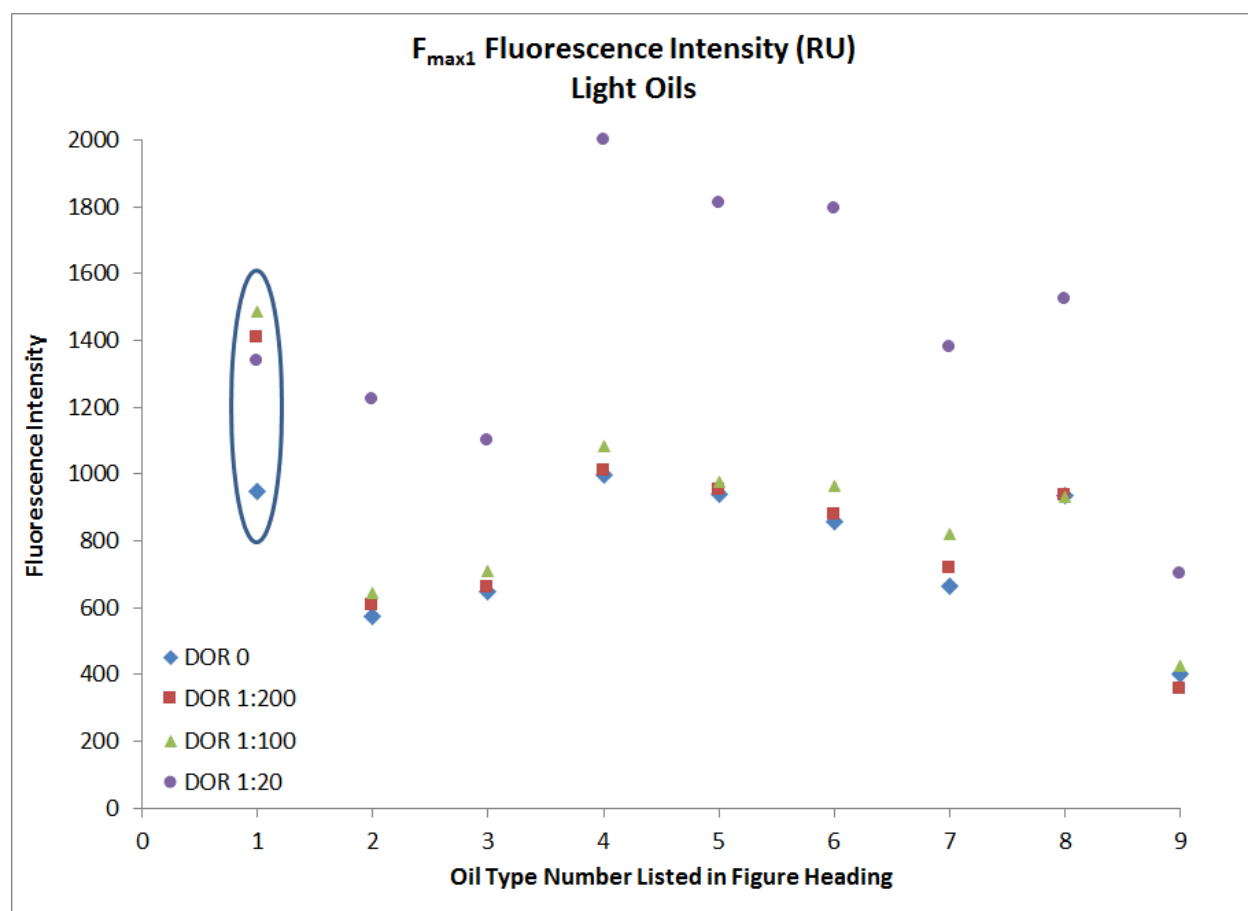


Figure 45. F_{max1} fluorescence for Light Oils (API gravity > 31°), in order of increasing density: 1. Scotian Shelf Condensate, 2. Federated, 3. Brent, 4. MC252—Discoverer Enterprise, 5. Hibernia, 6. MC252—generic, 7. Terra Nova, 8. Gulfaks, 9. Arabian Light. Note discrepancy in Scotian Shelf Condensate fluorescence pattern (circled) from that of all other Light Oils. It's particularly unusual that fluorescence intensity at highest DOR is lower than that at DORs 1:200 and 1:100.

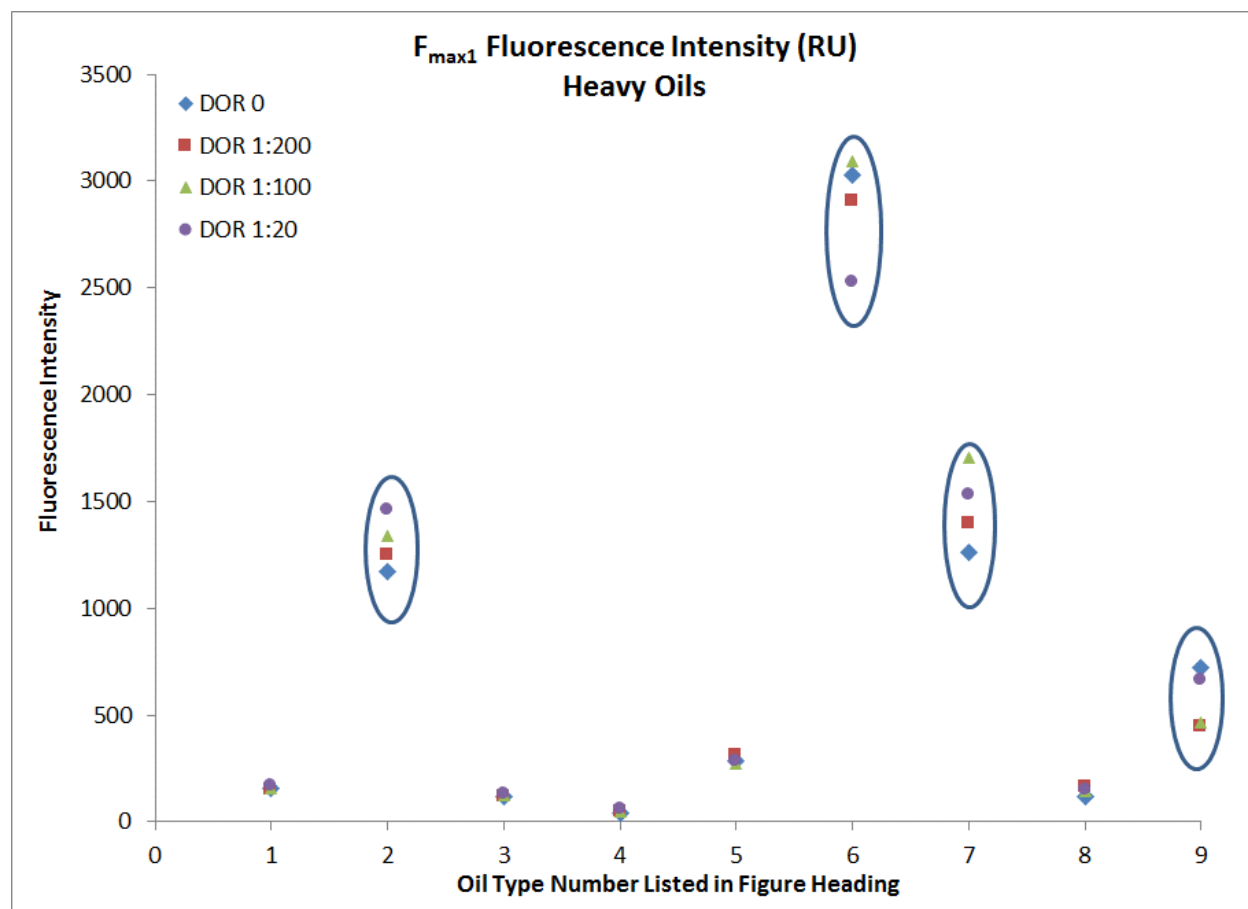


Figure 46. F_{max1} fluorescence for Heavy Oils (API gravity < 22.3°), in order of increasing density: 1. Santa Clara, 2. IFO 40, 3. Cold Lake Dilbit, 4. Access Western Blend Dilbit, 5. Hondo, 6. IFO 120, 7. IFO 180, 8. Belridge Heavy, 9. IFO 300. Note discrepancy in Intermediate Fuel Oils (circled) from that of all other Heavy Oils.

B.3.2 Fluorescence as a Function of Chemistry

Samples of dispersed oil in artificial seawater (DOR 0 and DOR 1:20 for each oil type), extracted into methylene chloride were analyzed via GC-MS. Total alkanes, 2-ring, 3-ring, and 4-ring PAHs (see Table 10 for list of hydrocarbons in each class) were each plotted against $F_{\max1}$, $F_{\max2}$, $F_{\max3}$, and $F_{\max4}$ (Figures 47-50). Results showed highest correlation at DOR 0 between total 3-ring PAHs and fluorescence intensity at $F_{\max3}$ and $F_{\max4}$ (Figure 48) followed by that of 2-ring PAHs and fluorescence intensity at $F_{\max1}$ and $F_{\max2}$ (Figure 47) and between 4-ring PAHs and fluorescence intensity at $F_{\max3}$ and $F_{\max4}$ (Figure 48). It is important to note, however, that only 12 of the 25 oil types exhibited any $F_{\max3}$ fluorescence at DOR 0.² These correlations support the fact that larger, more complex PAHs fluoresce at longer emission wavelengths.

For all oils at DOR 1:20, logarithmic relationships rather than linear relationships best modeled all correlations; however, overall these were weaker than those found at DOR 0. Highest correlation was observed between 2-ring PAHs and $F_{\max3}$ intensity (Figure 50), with moderate correlations observed between 2-ring PAHs and fluorescence at $F_{\max1}$ and between 2-ring PAHs and $F_{\max2}$ fluorescence (Figure 49), and between 3-ring PAHs and $F_{\max3}$ fluorescence (Figure 50). Only weak correlations were observed between 2-ring PAHs and fluorescence at $F_{\max2}$ (Figure 49) and between 4-ring PAHs and $F_{\max3}$ fluorescence (Figure 50). Clearly, full dispersion at DOR 1:20 results in widely varying changes in fluorescence intensity across all oil types.

² Oil types exhibiting $F_{\max3}$ fluorescence at DOR 0: Access Western Blend Dilbit, Alaska North Slope (both fresh and 10% weathered), Arabian Light, Brent, Federated, Gullfaks, Heidrun, Hibernia, MC252 (both Discoverer Enterprise and generic), and Terra Nova.

September 2016

Table 10. Individual hydrocarbon compounds reported as Total Alkanes, Total 2-ring, 3-ring and 4-ring PAHs.

Total Alkanes:	Total 2-ring PAHs:	Total 3-ring PAHs	Total 4-ring PAHs:
n-decane	Naphthalene	phenanthrene	pyrene
undecane	Methylnaphthalene	anthracene	methylpyrene
dodecane	Dimethylnaphthalene	methylphenanthrene	dimethylpyrene
tridecane	Trimethylnaphthalene	dimethylphenanthrene	trimethylpyrene
tetradecane	tetramethylnaphthalene	trimethylphenanthrene	tetramethylpyrene
pentadecane	Acenaphthene	tetramethylphenanthrene	naphthobenzothiophene
hexadecane	Acenaphthylene	fluoranthene	methylnaphthobenzothiophene
heptadecane	Fluorene		dimethylNBenzothiophene
2,6,10,14-TMPdecane (pristine)	Methylfluorene		trimethylNBenzothiophene
octadecane	Dimethylfluorene		tetramethylNBenzothiophene
2,6,10,14-TMHdecane (phytane)	Trimethylfluorene		benz[a]anthracene
nonadecane	Dibenzothiophene		chrysene
eicosane	methyldibenzothiophene		methylchrysene
heneicosane	dimethyldibenzothiophene		dimethylchrysene
docosane	trimethyldibenzothiophene		trimethylchrysene
tricosane	tetramethyldibenzothiophene		tetramethylchrysene
tetracosane			benzo[b]fluoranthene
pentacosane			benzo[k]fluoranthene

September 2016

Total Alkanes:	Total 2-ring PAHs:	Total 3-ring PAHs	Total 4-ring PAHs:
hexacosane			benzo[e]pyrene
heptacosane			perylene
octacosane			
n-nonacosane			
tricontane			
n-heneicontane			
dotriacontane			
tritriacontane			
tetratriacontane			
n-pentatriacontane			
17 α (H), 21 β (H)-hopane			
17 β (H), 21 α (H)-hopane			

The effect of DOR 1:20 on dissolved hydrocarbons can also be investigated by taking the ratio of total alkanes + PAHs at DOR 1:20 to total alkanes + PAHs at DOR 0 to yield the Chemical Dispersibility Ratio (CDR). The ratio ranges from between 0.8 for two heavy oils (Hondo and IFO 300) and 7.8 for Arabian Light. Although heavy oils tended to have lower CDRs and light oils tended to have higher ratios, oil density was not correlated with chemical dispersion. For example, the heavy oil Santa Clara (API Gravity 22.1°) had the third highest CDR (5.4), while Scotian Shelf Condensate, by far the lightest oil (API Gravity 46.6°), had a CDR of only 2.2 (Figure 51). The effect of dispersion on fluorescence intensity can be similarly investigated by taking the ratio of F_{max1} fluorescence intensity at DOR 1:20 to that at DOR 0, resulting in the Fluorescence Dispersibility Ratio (FDR). The FDR also shows a general increasing trend with increasing API Gravity, but only a moderate linear correlation ($R^2 = 0.55$). The relationship between CDR and FDR exhibited weak linear correlation ($R^2 = 0.17$) (Figure 52).

All four Intermediate Fuel Oils (IFO 40, IFO 120, IFO 180, and IFO 300) as well as Scotian Shelf Condensate (SSC), showed fluorescence and chemistry anomalies that tended to skew overall results. With respect to SSC, all other light oils (API Gravity < 22.3°) exhibited increasing fluorescence intensity with increasing DOR, culminating in an increase at DOR 1:20; however, SSC showed a decrease in fluorescence intensity at DOR 1:20, dropping to below the level exhibited at DOR 1:200 (Figure 45). Additionally, SSC was the only light oil which exhibited no F_{max3} fluorescence at any DOR. Chemically, SSC is unique, containing a high proportion of 2-ring to 3-ring PAHs—52.2 for DOR 0 and 58.6 for DOR 1:20. With the exception of Santa Clara, with a 2-ring to 3-ring ratio of 31.9 at DOR 0, all other oil types had a ratio of 10 or less at both DOR 0 and DOR 1:20. SSC also contained no 4-ring or 5-ring PAHs, unlike all other oils with the exception of DOR 0 Santa Clara. All Intermediate Fuel Oils fell into the heavy oil group (API Gravity > 31°), in which all other oils showed little to no increase in fluorescence intensity with increasing DOR as well as maximum F_{max1} intensity of just 60-288 RU. The IFOs, however, showed far greater F_{max1} intensity across the board (721-3031 RU) along with clear separation with increasing DOR. Like Scotian Shelf Condensate, IFO 120, IFO 180, and IFO 300 also exhibited a drop in F_{max1} intensity at DOR 1:20; in fact, IFO 120 F_{max1} at DOR 1:20 was actually

17% lower than at DOR 0. These same three IFOs also had the highest overall concentration of PAHs, and all four IFOs were the only oils to contain any anthracene. For all oil types, total alkanes as a function of fluorescence intensity was found to be only loosely correlated, as total concentration increased overall in relation to fluorescence intensity with no clear relationship.

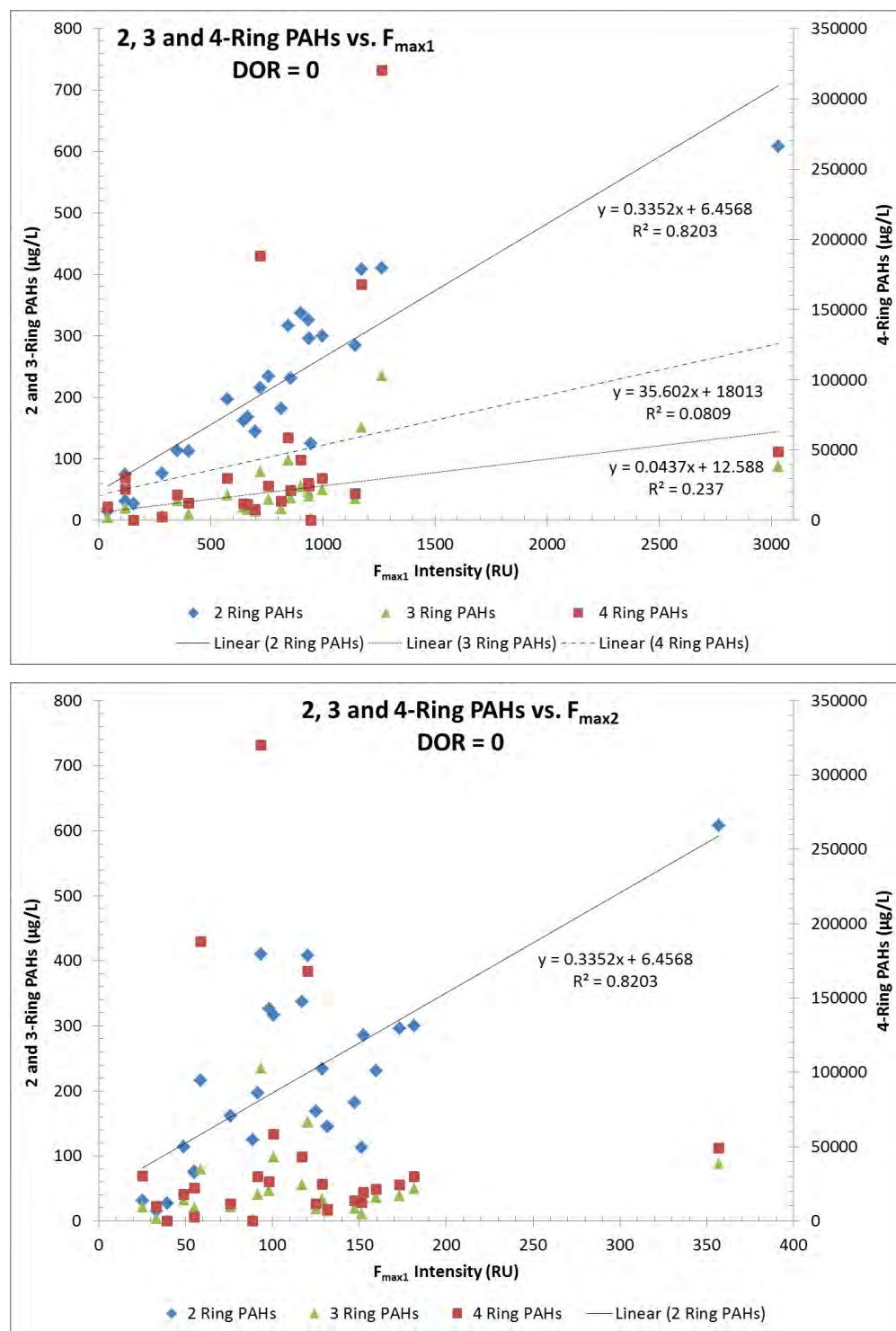


Figure 47. For all oil types at DOR 0, total concentration of 2-ring, 3-ring, and 4-ring PAHs ($\mu\text{g/L}$) against fluorescence intensity (RU) at F_{max1} (top), and against F_{max2} (bottom). Strong linear correlation exists between 2-ring PAHs and F_{max1} fluorescence intensity (top). Little to no correlation exists between 3-ring or 4-ring PAHs and F_{max1} fluorescence intensity (top). Strong linear correlation also exists between 2-ring PAHs and F_{max2} , but no correlation exists between 3-ring PAHs or 4-ring PAHs and F_{max2} (bottom).

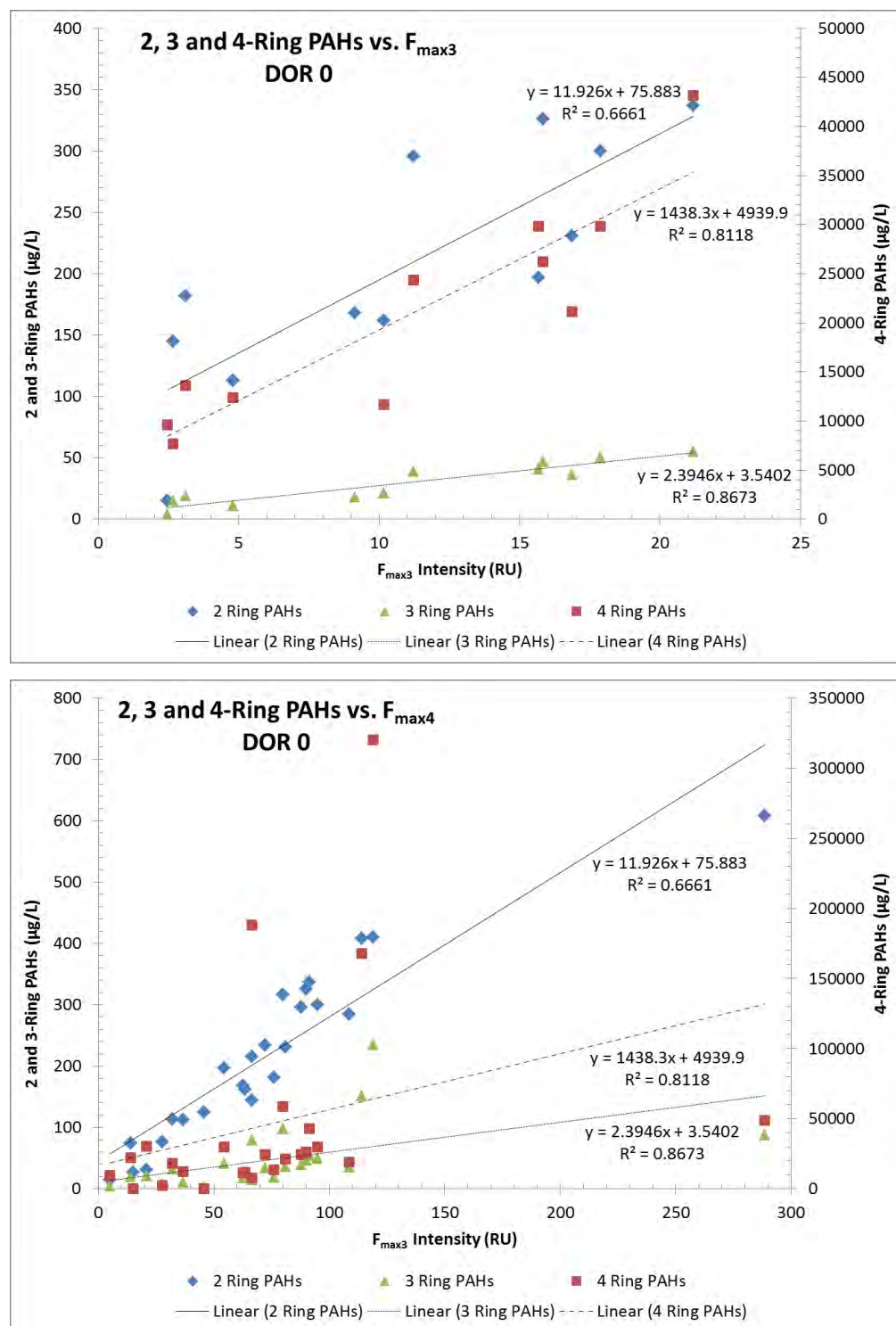


Figure 48. For all oil types at DOR 0, total concentration of 2-ring, 3-ring, and 4-ring PAHs ($\mu\text{g/L}$) against fluorescence intensity (RU) at $F_{\max3}$ (top), and against $F_{\max4}$ (bottom). Strong linear correlation exists between 3-ring and 4-ring PAHs and both $F_{\max3}$ and $F_{\max4}$ fluorescence; however, only moderate correlation exists between 2-ring PAHs and $F_{\max3}$ and $F_{\max4}$ fluorescence intensity.

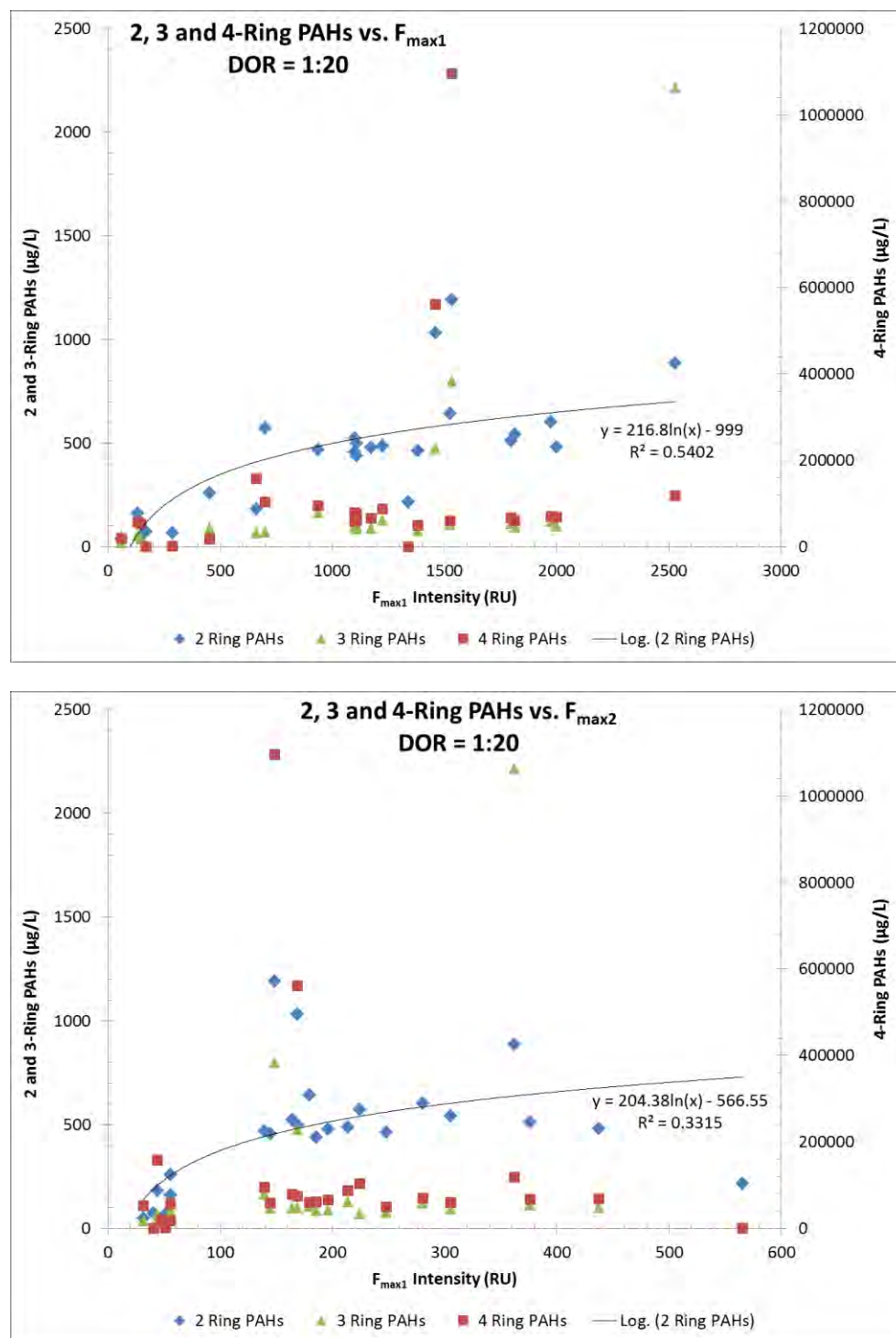


Figure 49. For all oil types at DOR 1:20, total concentration of 2-ring, 3-ring, and 4-ring PAHs (µg/L) against fluorescence intensity (RU) at F_{max1} (top), and against F_{max2} (bottom). A moderate logarithmic correlation is exhibited between 2-ring PAHs and fluorescence intensity (RU) at F_{max1} and a weaker correlation between 2-ring PAHs and F_{max2} , but no correlation exists between 3-ring or 4-ring PAHs and fluorescence intensity at either F_{max1} or F_{max2} .

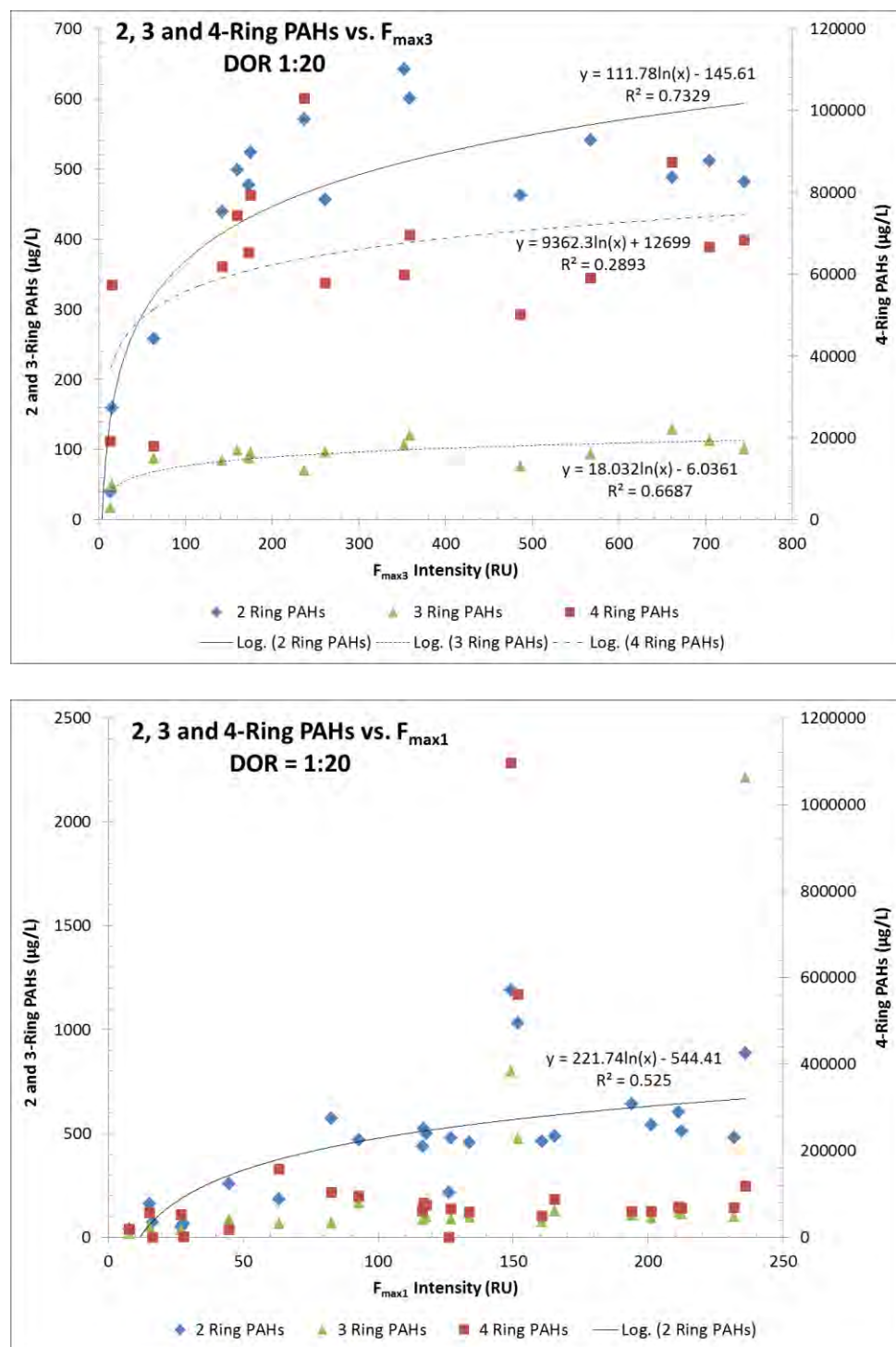


Figure 50. For all oil types at DOR 1:20, total concentration of 2-ring, 3-ring, and 4-ring PAHs ($\mu\text{g/L}$) against fluorescence intensity (RU) at $F_{\max3}$ (top), and against $F_{\max4}$ (bottom). A strong logarithmic correlation is exhibited between 2-ring PAHs and fluorescence intensity at $F_{\max3}$. Moderate correlations exist between 3-ring PAHs and $F_{\max3}$ as well as between 2-ring PAHs and $F_{\max4}$. However, only a weak logarithmic correlation exists between 4-ring PAHs and fluorescence intensity at $F_{\max3}$, and there is no correlation between 3-ring or 4-ring PAHs and $F_{\max4}$.

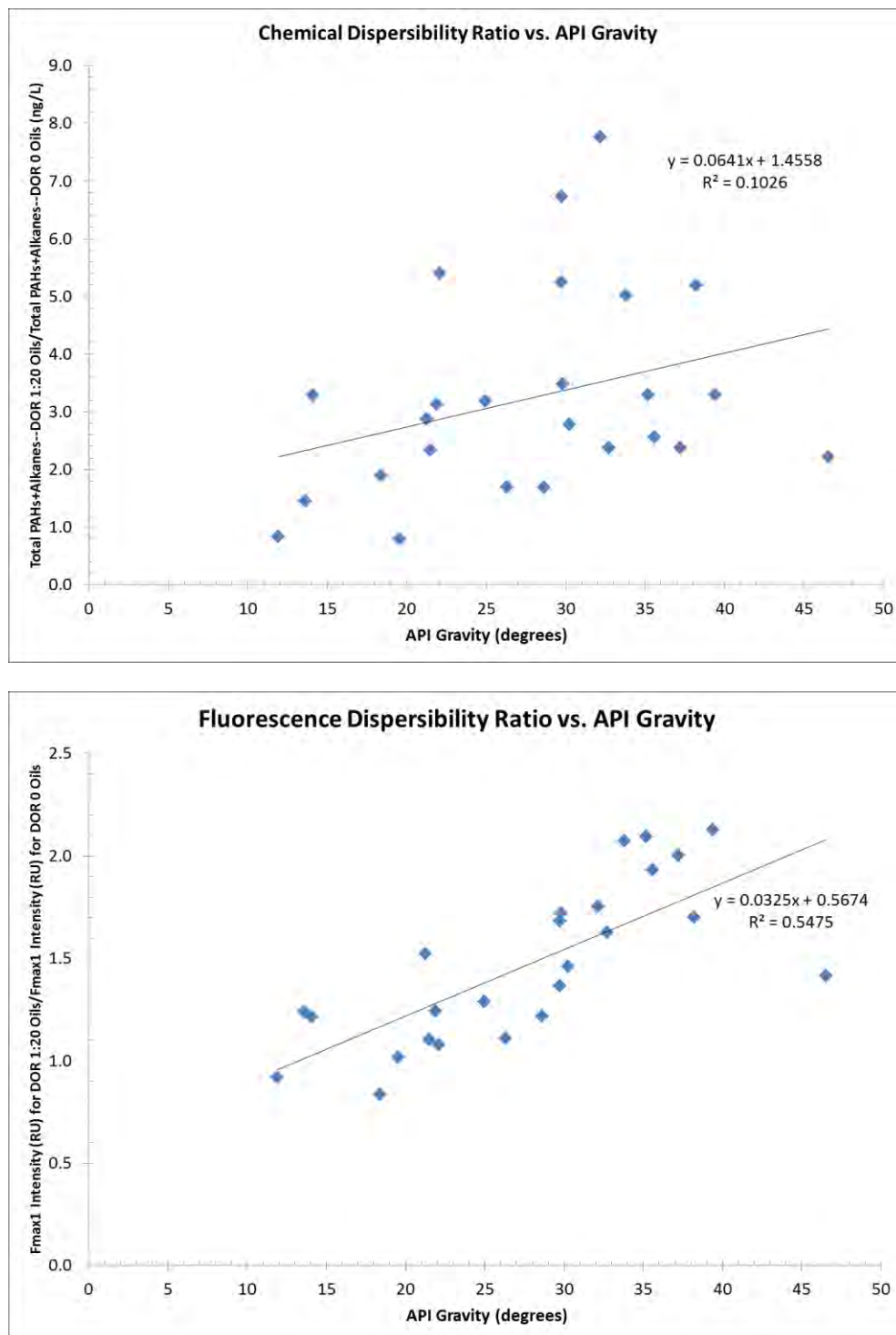


Figure 51. Chemical Dispersibility Ratio (CDR) vs. decreasing oil density (top) and Fluorescence Dispersibility Ratio (FDR) vs. decreasing oil density (bottom) show only a weak correlation between chemistry and oil density, and a moderate correlation between fluorescence and oil density. With the removal of the data point for Scotian Shelf Condensation, correlation between fluorescence and oil density improves to $R^2 = 0.71$.

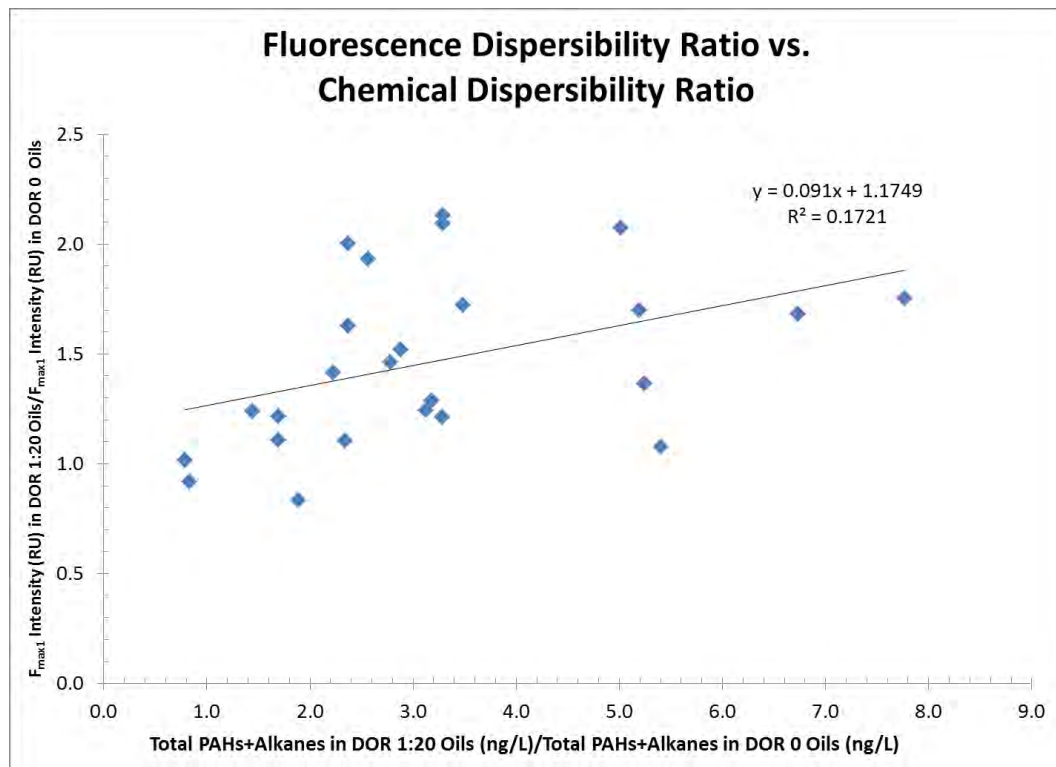


Figure 52. Fluorescence Dispersibility Ratio (FDR) vs. Chemical Dispersibility Ratio (CDR) shows weak correlation between these two ratios.

B.3.3 Flume Tank and Baffled Flask EEM Comparison

In addition to the EEMs generated from the BFT of 25 oil types, EEMS were also generated from the discrete sample collection during the flume tank experiments using South Louisiana Crude oil (SLC) in Task A of this project report. Samples for EEM analysis were collected and immediately analyzed on the same Horiba Aqualog at DFO using identical analysis protocols and data processing. A comparison of SLC MC252 EEMs for varying DOR from the BFT (left) and the flume tank (right) experiments are illustrated in Figure 53. Note that that the contour coloring for the peaks is identical between experiments, but the baseline color varied, where black was used for the BFT EEMs and blue used for tank EEMs, but the appearance of the blue color this is not to be confused with the presence of higher fluorescence in regions away from the peak fluorescence. Fluorescence Intensity Ratios (FIR) were calculated for the tank EEMs and found to be between 7.1 and 9.1 for DOR = 0, 1.3 and 4.3 for DOR = 1:100 and 0.6 and 0.8 for DOR = 1:20. This is follows the findings of Bugden et al., 2008 where a decrease in FIR is observed with the addition of dispersant. It is also consistent with the BFT EEMs which show a 4.9 for DOR = 0 and 0.4 for DOR = 1:20 (Supplemental Table A). These results indicate that FIR can be an indicator of dispersion effectiveness for SLC oil.

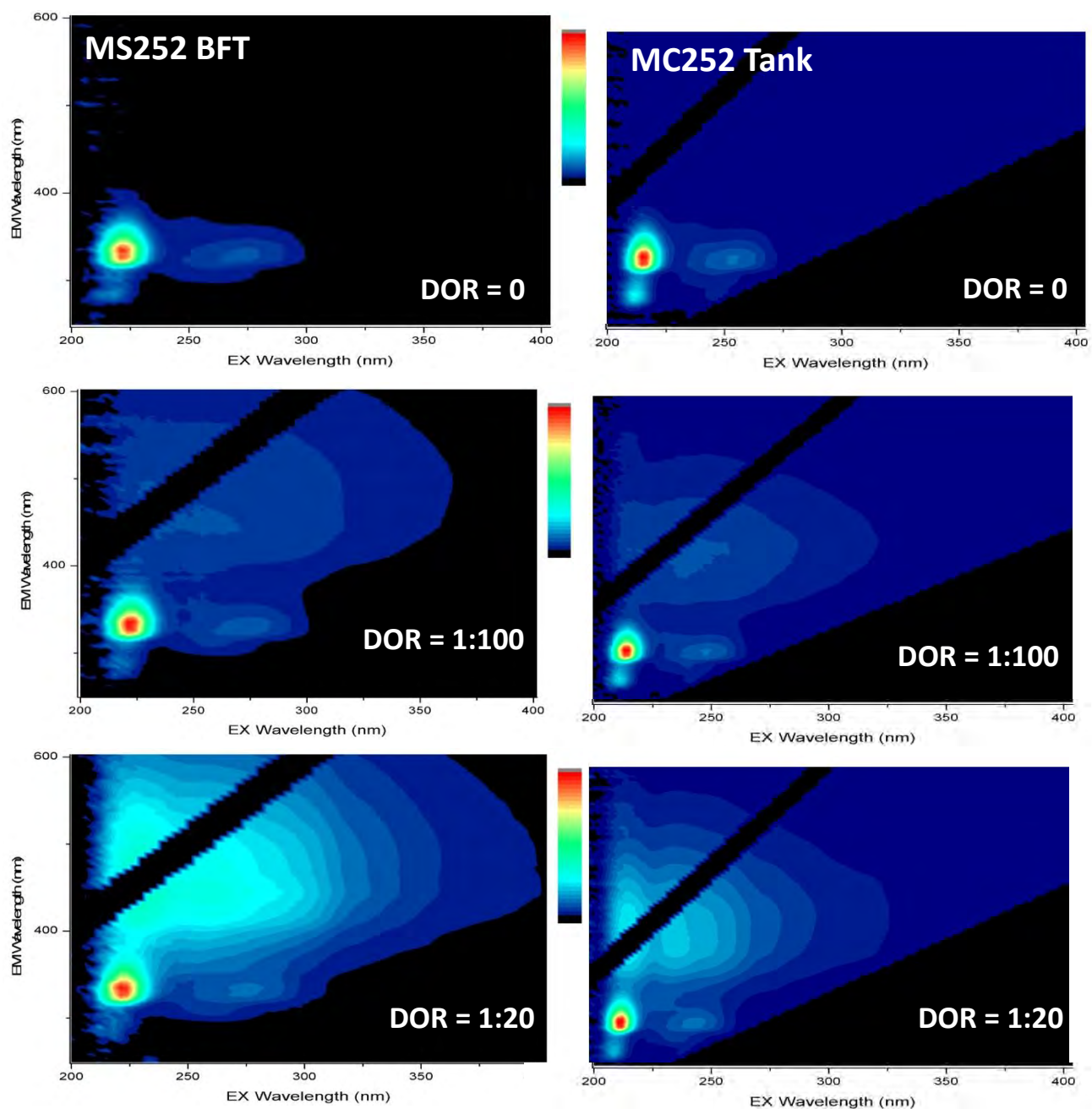


Figure 53. South Louisiana Crude MC252 EEMS from BFT (left panels) and tank experiments (right Panels) for DOR = 0, 1:100 and 1:20.

B.3.4 PARAFAC Modeling

Originally designed to model complexity in the field of psychometrics (Carroll and Chang, 1970; Harshman, 1970), parallel factor analysis (PARAFAC, also known as canonical decomposition or CANDECOMP) was first employed in the analysis of fluorescence data within the next ten years (Appelhof and Davidson, 1981). Over the past twenty years, PARAFAC has been widely embraced by chemometricians and used to tease apart the overlapping fluorescence components of complex chemical mixtures containing fluorescent substances ranging from proteins and pigments to pesticides and PAHs (Andersen and Bro, 2003). More recently, PARAFAC analysis has been used in the analysis of the fate and transport of dispersed oil from the Deepwater Horizon Oil Spill (Mendoza, et al., 2013; Zhou, et al., 2003).

Presented with hundreds of complex fluorescence EEM data sets containing samples, excitation, and emissions; PARAFAC analysis can reduce this to data sets containing samples and intensity at a few important wavelength pairs (Murphy et al., 2014). In the past, this information gathering was often done via time-consuming “peak-picking” whereby EEMs were visually inspected for apparent F_{\max} location, then fluorescence intensity data at that excitation/emission point was copied and pasted into a spreadsheet for further analysis. PARAFAC provides the capability to turn that somewhat qualitative task into a more quantitative exercise; however, careful preparation of the data is critical in order to obtain a meaningful outcome. PARAFAC analysis also allows the consideration of minor fluorescence peaks, which may have been overwhelmed by high-intensity major peaks, but may be no less important in the analysis of EEM results. More importantly, PARAFAC analysis allows for direct comparison to chemical composition upon successful modelling of an EEM data set (Murphy, et al., 2014). The steps that must be undertaken for successful PARAFAC analysis are: (1) assembling the dataset; (2) preprocessing to correct biases, remove scatter and normalize; (3) exploring the dataset to remove possible outliers and develop preliminary models; (4) validating the model by determining the proper number of components and evaluating model fit; (5) interpreting results (Murphy, et al., 2013).

In order to identify connections between the fluorescence profiles and underlying chemical complexity of the 25 oil types in the BFT analysis (Figure 53), PARAFAC analysis was performed

on the fluorescence data. The PLS Toolbox (Eigenvector, Inc.) was used within MATLAB (MathWorks, Inc. 2014b) to accomplish this task. After importing raw data and assembling datasets, three constraints were applied to all samples: normalization, EEM filtering, and non-negativity. Normalization was conducted to compensate for the wide variation in fluorescence intensity across oil types ($F_{\max 1} = 39.6$ RU for Access Western Blend Dilbit to $F_{\max 1} = 3090.2$ RU for IFO 120) in order to prevent samples with high fluorescence intensity values from skewing the model. Further, normalization of maximum intensity to 1 (inf-Norm) was chosen rather than normalization of the entire area of fluorescence (1-Norm) to preserve differences in spectral shape. EEM filtering was applied in order to remove artifacts of the fluorescence analysis process known as first and second order Rayleigh scatter. This was accomplished by interpolating data across those regions (12 nm for first order Rayleigh and 24 nm for second order Rayleigh); zero values were also assigned to sub-Rayleigh wavelengths since fluorescence emission takes place at wavelengths above excitation due to Stokes shift. Raman scatter, the other light-related artifact which must be removed before PARAFAC analysis can be performed, was accomplished as sample analysis was done by subtracting that day's sample blank from each sample. Upon running several PARAFAC test models using 4, 5, 6 and 7-components on a dataset containing the DOR 0 sample from flask #1 of all 25 oil types, data between excitation at 200 nm and 212 nm was excluded. The inherent "noise" typically found at excitation < 240 nm, related to the low intensity of xenon lamps in that region, led to this decision. Excluding data at excitation and emission wavelengths above 680 nm was also employed in order to improve processing results since no fluorescence information of value was contained in that region.

The biggest challenge in PARAFAC modelling is in determining the most appropriate number of component factors. While it is important to ensure separation of all individual factors, it is also critical not to select too many components in order to avoid over-fitting the data. Several ways of doing this are suggested in the PARAFAC tutorial (Bro, 1997): comparison of the resulting factor profiles with background knowledge of expected components, consideration of the residuals, and split half validation of the model. The latter has also been recommended by other researchers (Harshman and Lundy, 1994; Murphy, et al., 2013). Split half analysis is accomplished by dividing the data into two independent subsets and applying the model to each of the subsets.

In theory, if the correct number of components has been selected, the two halves of the data should each fit the model well; however, Murphy cautions that a relatively large data set is necessary in order for this to hold true (2013). Smilde, et al., (2004) also caution that some phenomenon observed within a subset of data may not match the overall model, but instead may just be present in that particular random half of the dataset. Thus, it could be anticipated that split half validation will work better with samples within oil weight subdivisions than with the dataset containing all 25 oil types as a whole. Bro and Kiers (2003) have also advised using core consistency of the model to validate that the correct number of components have been selected. All of these methods were employed for the following analyses by first noting the percentage of data fit by the model, next checking the core consistency of the model, then inspecting residuals, inspecting the loadings for Mode 3 (excitation) and Mode 2 (emission), and inspecting EEMs of each component. Finally, split half analysis was done. In all cases, several models were run with different numbers of components to ensure selection of the most appropriate model.

DOR 0

Initially, a five-component model was fit to the dataset, followed by 4-, 6- and 7-component models. Best overall fit was obtained with the six-component model, which explained 99.504% of the data. Core consistency was 52%, and split half validation was 56.4% (Figure 54). Review of residuals showed they were minimal with random distribution, inspection of plots of Mode 2 and Mode 3 loadings (Figure 55), variation per component (Figure 56), as well as EEMs of individual components (Figure 57) all supported choice of the 6-factor model for best fit.

Similarity measure of splits and overall model 56.4%

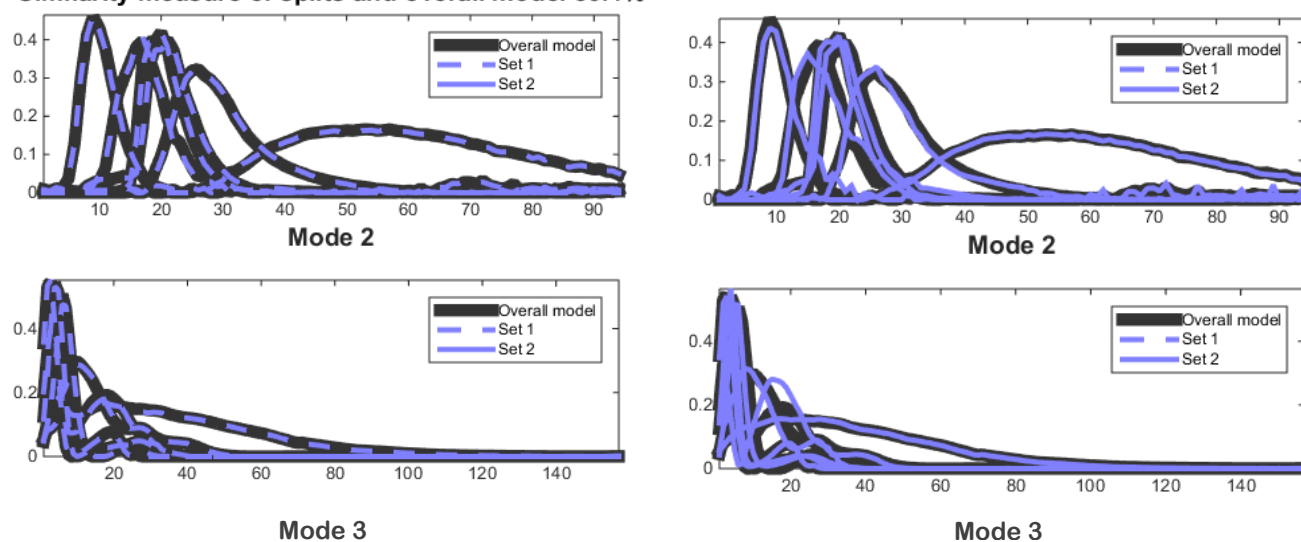


Figure 54. Example of split half validation for the 6-component model of 25 oil types at DOR 0 showing individual fit of data splits (Set 1, left; and Set 2, right) compared to overall model for Mode 2 (top) and Mode 3 (bottom) loadings.

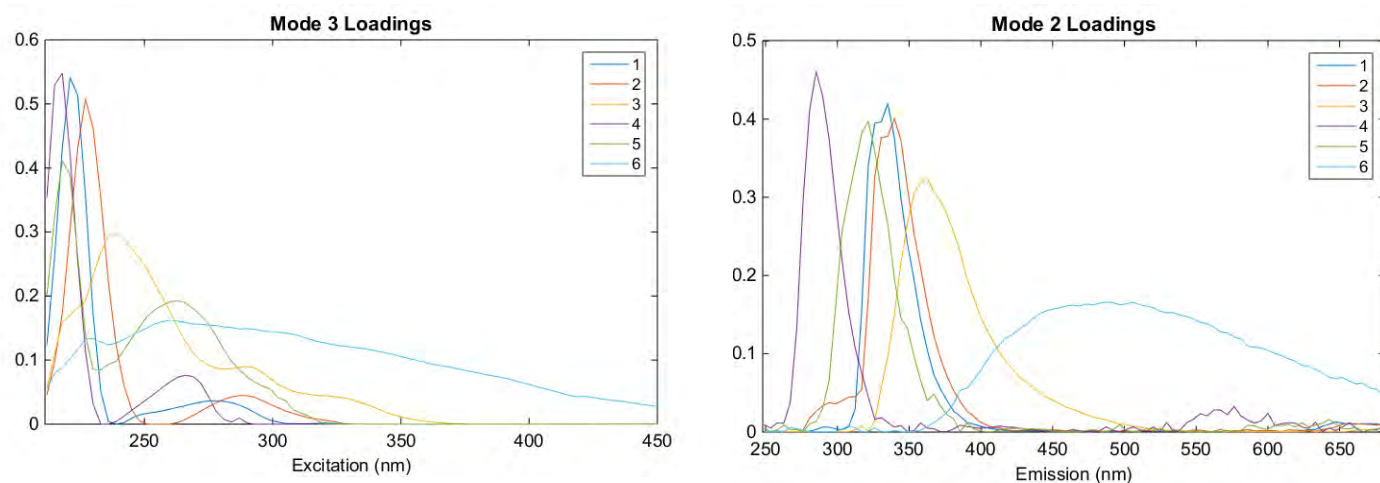


Figure 55. Mode 3 Loadings (Excitation) and Mode 2 Loadings (Emission) for all 25 oil types—DOR0 using 6-component model. Note difference in x-axis scales. Although components are tightly spaced, all appear as separate and distinct peaks.

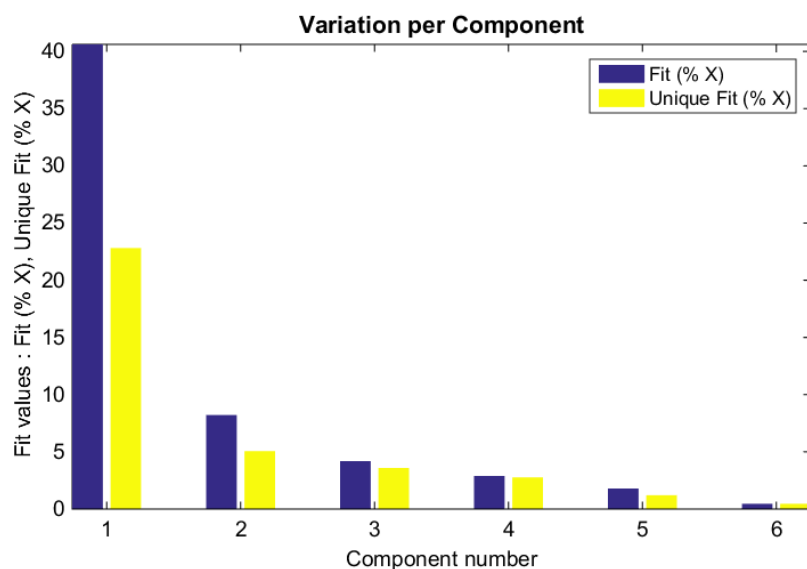


Figure 56. Variation per Component shows Component 1 accounted for >20% to 40% (unique fit and fit) of the data, while Component 2-contributed 5-10% (unique fit and fit) and Components 3-6 accounted for 5% or less of the data, respectively. While Component 6 accounted for a very low percentage of the data, the 6-component model was still a better fit to the data than the 5-component model.

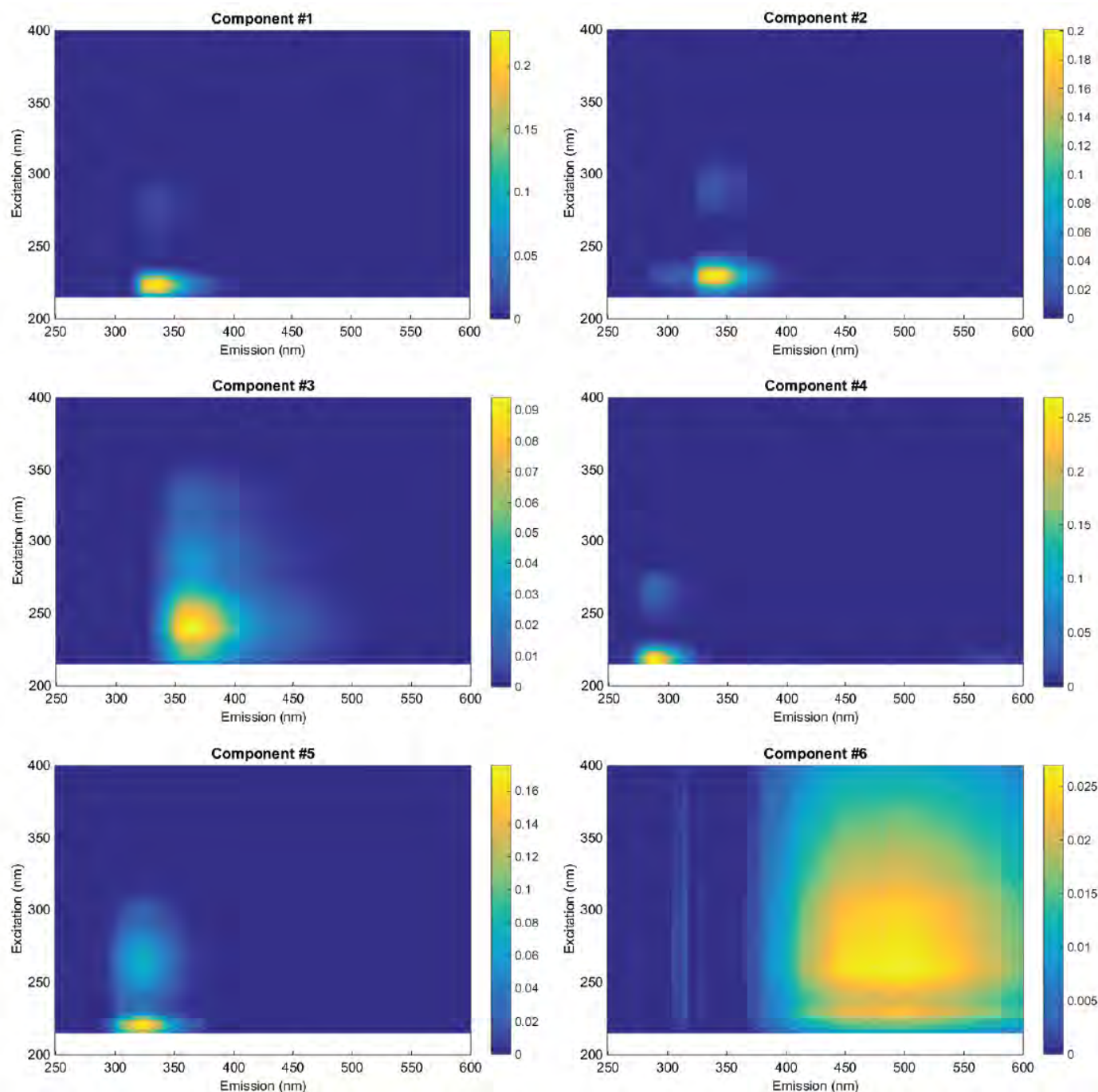


Figure 57. EEM views of the six components of PARAFAC model for 25 oil types at DOR 0. Component #1: F_{\max} = Ex 224nm/Em 335nm; Component #2: F_{\max} = Ex 230nm/Em 340nm; Component #3: F_{\max} = Ex 239nm/Em 363nm; Component #4: F_{\max} = Ex 218nm/Em 290 nm; Component #5: F_{\max} = Ex 221nm/Em 322nm; Component #6: F_{\max} = Ex 260nm/Em 474-511nm.

DOR 1:100

A six-component model was fit to the dataset containing all 25 oil types at DOR 1:00 since that was the best fit for the DOR 0 dataset, followed by a 7-component model, which returned an error warning that two or more components may be fitting the same feature, as well as core consistency <0%. Finally, a 5-component model was fit to the dataset. Interestingly, for the DOR 1:100 dataset, the 5-component model proved to be the best fit, explaining 99.353% of the data with core consistency of 72% and split half validation of 75.8%. Residuals were minimal and randomly distributed, and visual inspection of loadings (Figure 58), variation per component (Figure 59) and component EEMs (Figure 60) led to acceptance of the 5-component model.

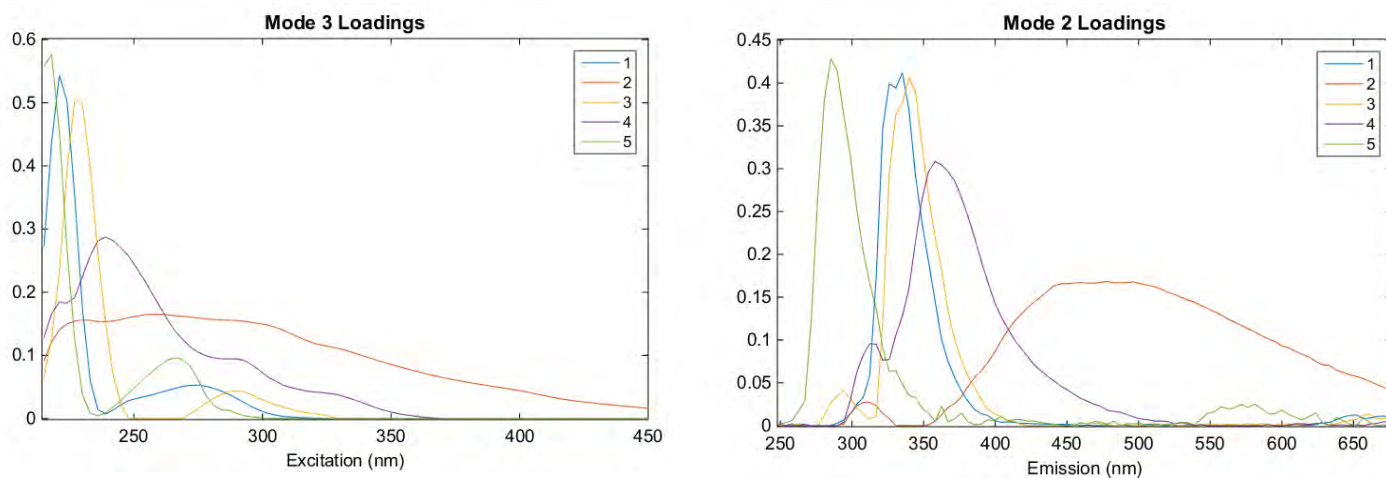


Figure 58. Mode 3 Loadings (Excitation) and Mode 2 Loadings (Emission) for all 25 oil types—DOR 1:100 using 5-component model. Note difference in x-axis scales. Although components are tightly spaced, all appear as separate and distinct peaks.

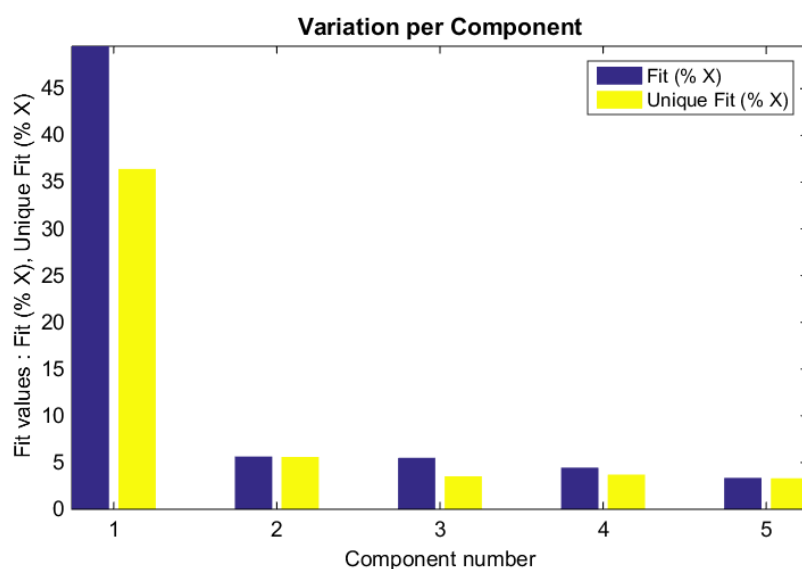


Figure 59. Variation per Component shows Component 1 accounted for >35% to almost 50% (unique fit and fit) of the data, while Components 2-5 accounted for 5% or less of the data, respectively.

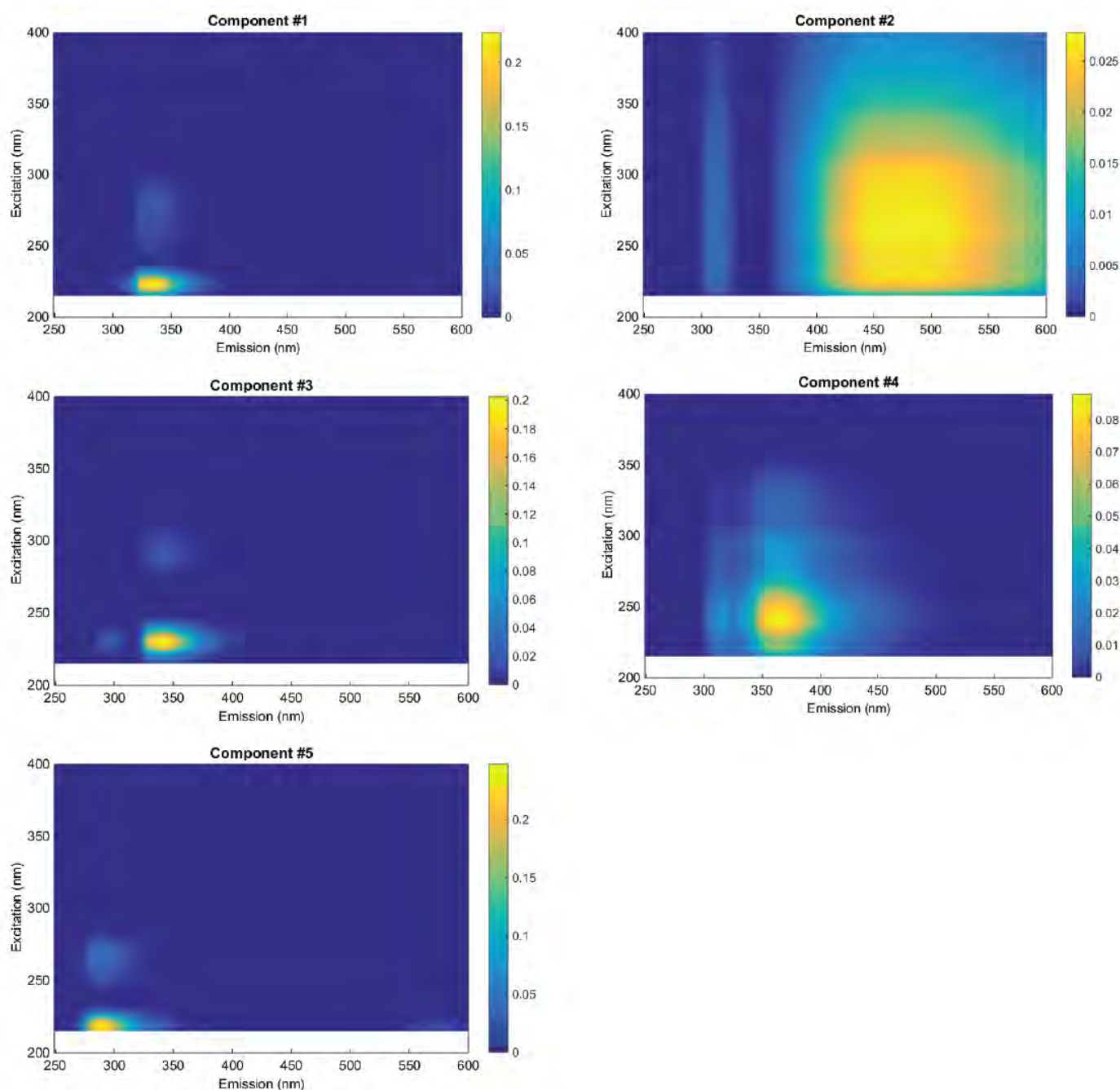


Figure 60. EEM views of the five components of PARAFAC model for 25 oil types at DOR 1:100. Component #1: F_{\max} = Ex 224nm/Em 335nm; Component #2: F_{\max} = Ex 254-266nm/Em 455-501nm; Component #3: F_{\max} = Ex 230nm/Em 344nm; Component #4: F_{\max} = Ex 242nm/Em 363 nm; Component #5: F_{\max} = Ex 218nm/Em 290nm.

DOR 1:20

Once again, a six-component was fit to the dataset containing all 25 oil types at DOR 1:20; however, an error message warning that two or more components may be fitting the same data was displayed, and the core consistency was <0%. Fitting a 5-component model to the data, however, resulted in 98.891% of the data explained by the model as well as core consistency of 84% and a split half validation of 84%. Overall, residuals were minimal and randomly distributed; however, residuals appeared to occur at somewhat higher wavelengths than at other DORs. Visual inspection of loadings (Figure 60), variation per component (Figure 62), and component EEMS (Figure 63) led to final acceptance of the 5-component model.

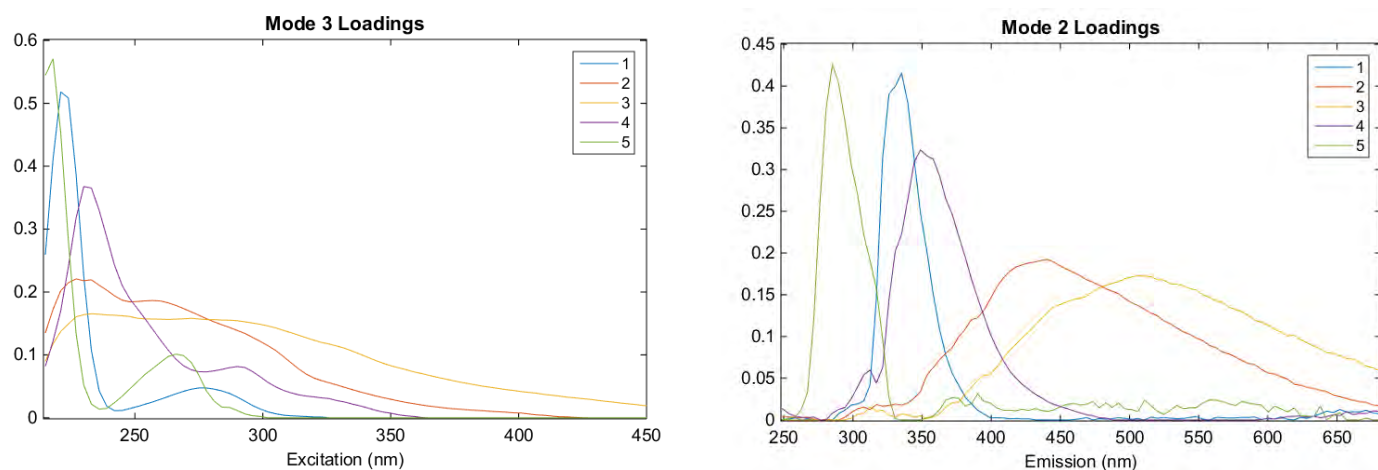


Figure 61. Mode 3 Loadings (Excitation) and Mode 2 Loadings (Emission) for all 25 oil types—DOR 1:20 using 5-component model. Note difference in x-axis scales. Effect of full dispersion appears to broaden and shift emission peaks to longer wavelengths.

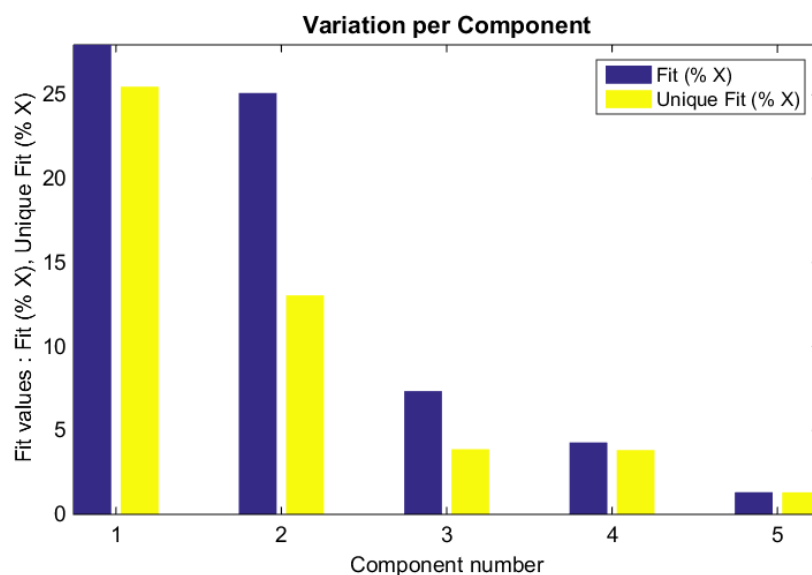


Figure 62. Variation per Component shows Component 1 accounted for 25 to 30% of the data (unique fit and fit) while Component 2 has increased to >10% to 25% (unique fit and fit) of the data. Contribution from Component 3 and 4 have increased, as well.

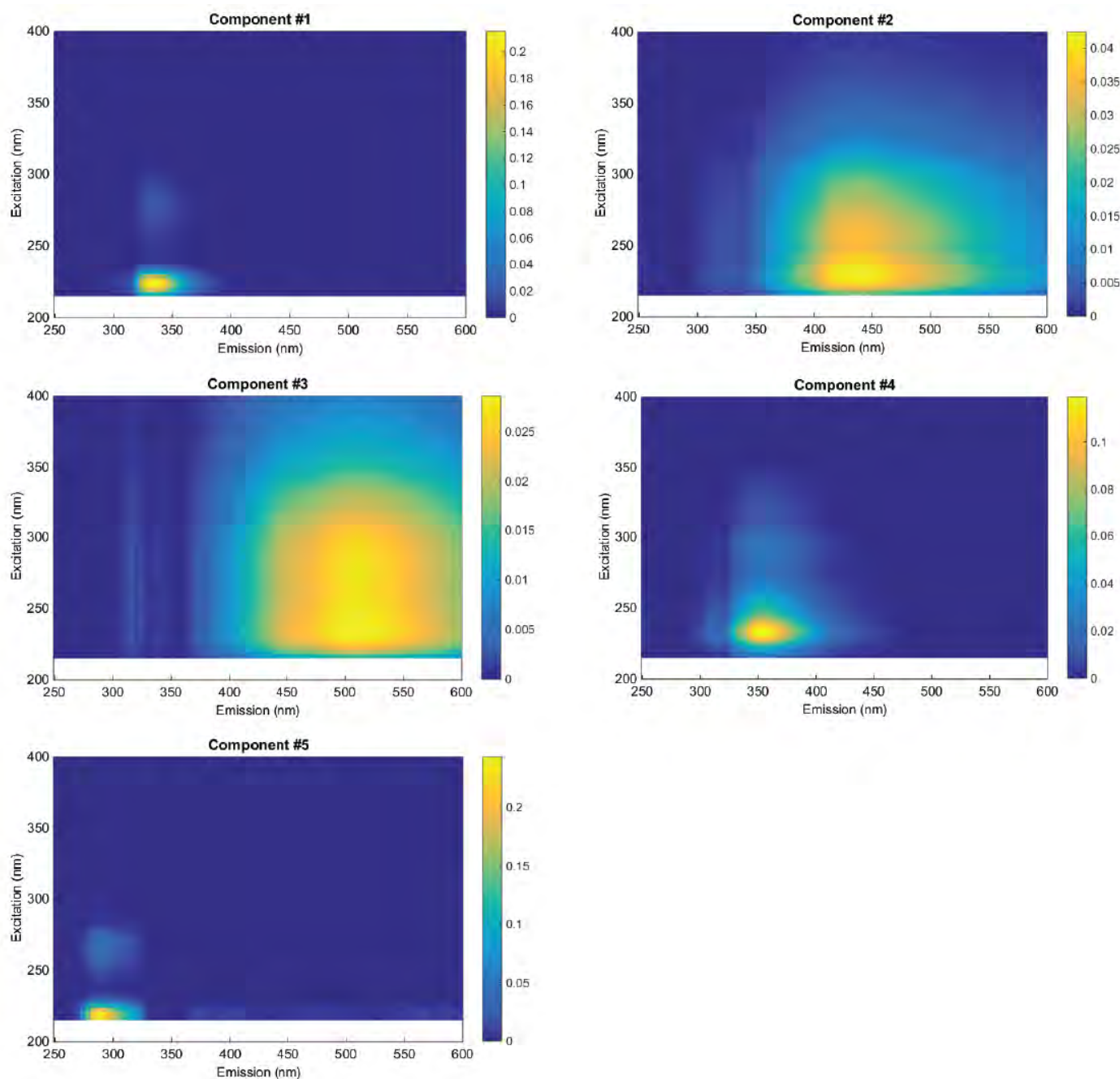


Figure 63. EEM views of the five components of PARAFAC model for 25 oil types at DOR 1:20. Component #1: F_{\max} = Ex 224nm/Em 335nm; Component #2: F_{\max} = Ex 233-266nm/Em 432-450nm; Component #3: F_{\max} = Ex 230-242nm/Em 501-520nm; Component #4: F_{\max} = Ex 233nm/Em 349nm; Component #5: F_{\max} = Ex 218nm/Em 290nm.

PARAFAC Summary

PARAFAC analysis of EEM datasets for the 25 oil types at DOR 0, DOR 1:100 and DOR 1:20 show interesting changes in fluorescence intensity with increasing dispersion. However, we see a decrease in distinct components from six at DOR 0 to five at DOR 1:100 and 1:20. From analysis of plots of Mode 3 (Excitation) and Mode 2 (Emission) Loadings, it appears that increased dispersion results in a broadening and shift to longer emission wavelengths as well as in a larger contribution of fluorescence intensity at higher wavelengths. Upon examination of the EEMs of each component, several other patterns emerge. Even with the minimal dispersion at DOR 1:100, contribution to the overall model from a broad fluorescence peak which provided the least contribution to the overall model at DOR 0—Component #6—became second in importance at DOR 1:100, albeit with a contribution to the model of only about 5%. Upon full dispersion at DOR 1:20, this broad, high-wavelength peak retained importance to the model of approximately 5-7%; however, another broad, but slightly lower wavelength peak appeared as Component #2 with 12-25% contribution to the overall model. Throughout the entire analysis, Component #1 at Ex 224nm/Em 335nm remained the most important contribution to the model, which confirms this fluorescence region as the best target for detecting oil in the marine environment. However, since the region represented by Component #2 in the DOR 1:20 dataset becomes a major contribution to the model only upon effective dispersion, the FIR ratio (Bugden et al., 2008) can be used to track this important parameter.

The MC252 oil samples used for these analyses, both ones collected onboard the Discoverer Enterprise during DWH and the generic version provided by BP, are classified as light, sweet crude based on density and sulfur content. Overall, oil types range from light to heavy due to the proportion of n-alkanes and cyclo-alkanes vs. aromatic hydrocarbon compounds, while sulfur content determines the rank of sweet (<1%) vs. sour (>1%). These characteristics arise from kerogen source and reservoir maturity (Tissot and Welty, 1978). The 25 oils analyzed in the BFT cover a wide range of light to heavy oil types, as well as a range of sulfur content. Oil fluorescence phenomena arise from the presence of π -bonding in C=C bonds, leading to highest fluorescence intensity from polycyclic aromatic hydrocarbons (Ryder, 2005), with fluorescence intensity tending to increase with increasing molecular weight (Mendoza, et al., 2013). However, the

presence of fluorescence quenching species, as well as energy transfer between complex molecules, complicates the isolation of compound-specific fluorescence in crude oil analysis. Fluorescence research has shown that heavy oils generally have broad, weak fluorescence while lighter oils have narrower, more intense emission bands (Steffens and Landulfo, 2010). Due to the hundreds, if not thousands, of complex hydrocarbons present in crude oils, characterization of fluorescence arising from specific PAH molecules would not be useful. However, PARAFAC analysis of these 25 oil types has shown that it is possible to use fluorescence characterization in specific wavelength regions for detection of non-dispersed vs. dispersed oil across a wide variety of oil types.

The well depth of the MC252 oil source is by far the deepest of all our 25 oil type sources (approximately 1600 m); however, a number of other oil types were sourced from offshore well locations. These include the light oils Brent and Gullfaks from the North Sea (140-230 m water depth) as well as Hibernia, Scotian Shelf Condensate and Terra Nova from offshore eastern Canada (12-100 m water depth). Intermediate weight oils Heidrun from the Norwegian Sea (350 m water depth) and Sea Rose from off the coast of Newfoundland, Canada (100 m water depth) as well as the heavy oil Hondo from offshore California (260 m water depth) were also included in this study. The intermediate weight Alaskan North Shore, both fresh and 10% weathered, would be representative of oil which may be sourced from offshore Alaska in the future. Additionally, with the presence of approximately 3,000 platforms in the U.S. Gulf of Mexico (BOEM, 2016), understanding the characterization of non-dispersed and dispersed MC252 oil will certainly aid in preparedness for the possibility of future oil spill events in that region.

References

Alliance for Coastal Technologies Report (2008) Hydrocarbon sensors for oil spill prevention and response. Ref # [UMCES]CBL08-095, 28 pp.

Andersen, C. M., R. Bro (2003) Practical aspects of PARAFAC modeling of fluorescence excitation-emission data. *J. Chemom.*, 17:200-217.

Appelhof, C.J., and E.R. Davidson (1981) Strategies for Analyzing Data from Video Fluorometric Monitoring of Liquid Chromatographic Effluents. *J. Anal. Chem.* 53:2053-2056.

Bahram, M., et al. (2006). "Handling of Rayleigh and Raman scatter for PARAFAC modeling of fluorescence data using interpolation." *Journal of Chemometrics* 20(3-4): 99-105.

Bierozza, M., A. Baker, J. Bridgeman (2010) Classification and calibration of organic matter fluorescence data with multiway analysis methods and artificial neural networks: an operational tool for improved drinking water treatment. *Envirometrics*, 22: 256-270.

Boehme, J.R., P.G. Coble, R.N. Conmy (2004) Examining CDOM fluorescence variability using principal component analysis: seasonal and regional modeling of three-dimensional fluorescence in the Gulf of Mexico. *Marine Chemistry*, 89:3-14.

Bro, R. (1997) PARAFAC. Tutorial and applications. *Chemometrics and Intelligent Laboratory Systems*. 38:149-171.

Bro, R., and H.A.L. Kiers (2003) A new efficient method for determining the number of components in PARAFAC models. *J. Chemometrics* 17:274-286.

Bugden, J.B.C., C.W. Yeung, P.E. Kepkay, K. Lee (2008) Application of ultraviolet fluorometry and EEMS to fingerprint oil and chemically dispersed oil in seawater. *Marine Pollution Bulletin*, 56(4): 677-85.

CRRC Report (2010) Coastal Response Research Center Deepwater Horizon Dispersant USE Meeting Report, May 26-27, 2010, 108 pp.

Carroll, J.D. and J.-J. Chang (1970) Analysis of Individual Differences in Multidimensional Scaling via an N-Way Generalization of "Eckart-Young" Decomposition. *Psychometrika* 35:283-319.

Christensen, A.B. Hansen, J. Mortensen, O. Andersen (2005) Characterization and matching of oil samples using fluorescence and PARAFAC. *Anal. Chem.*, 77:2210-17.

Coble, P.G. (1996) Characterization of marine and terrestrial DOM in seawater using EEM spectroscopy. *Mar. Chem.*, 51: 325-346.

Coble, P.G. (2014) Aquatic Organic Matter Fluorescence. In *Aquatic Organic Matter Fluorescence*. Coble, P.G., Lead, L., Baker, A., Reynolds, D.M. and Spencer, R.G.M., Eds., Cambridge University Press, pp. 75-122.

Cole, M.G., T. King, K. Lee (2007) Analytical technique for extracting hydrocarbons from water using sample container as extraction vessel in combination with a roller apparatus. *Anal. Chem.*, 77: 2210-17.

Conmy, R.N., P.G. Coble and C.E. Del Castillo (2004) Calibration and performance of the WetLabs' SAFire *in situ* fluorometer using seawater. *Contin. Shelf Res.*, 24: 431-42.

Conmy, R. N., et al. (2014a) Submersible Optical Sensors Exposed to Chemically Dispersed Crude Oil: Wave Tank Simulations for Improved Oil Spill Monitoring. *Environ Sci Technol* 48(3): 1803-1810.

Conmy, R.N., C.E. Del Castillo, B. Downing, R.F. Chen (2014b) Calibrations and Quality Control of *In situ* Sensors. In: *Fluorescence Applications in Aquatic Science*. Eds: A. Baker & P.G. Coble, Cambridge Univ. Press, 31 pp.

Fingas, M. (2011) Introduction to Oil Chemistry and Properties. In *Oil Spill Science and Technology*; Fingas, M., Eds; Elsevier. pp. 51-59.

Frank, U. (1978) A Review of Fluorescence Spectroscopic Methods for Oil Spill Source Identification. *Toxicological and Environment Chemistry Rev.*, 2:163-185.

Fuller, C.B., J.S. Bonner, C.A. Page, G. Arrambide, M.C. Sterling, Jr., T. Ojo (2003) Field instruments for real time in-situ crude oil concentration measurements. A Conrad Blucher Institute, Texas A&M Corpus Christi Report, 10 pp.

Harshman, R.A. (1970) Foundations of the PARAFAC procedure: Models and conditions for an "explanatory" multimodal factor analysis. *UCLA Working Papers in Phonetics* 16:1-84.

Harshman, R.A. and M.E. Lundy (1994) PARAFAC: Parallel factor analysis. *Computational Statistics & Data Analysis* 18:39-72.

Johansen, O., et al. (2013) Droplet breakup in subsea oil releases - Part 2: Predictions of droplet size distributions with and without injection of chemical dispersants. *Marine Pollution Bulletin* 73(1): 327-335.

Joint Analysis Group Report (2010) Review of Data to Examine Subsurface Oil in the Vicinity of DWH MC-252, May 19-June 19, 2010; 29 pp.

Kepkay, P., W. Young, J.B.C. Bugden, Z. Li, K. Lee (2008) Ultraviolet fluorescence spectroscopy (UVFS): A new means of determining the effectiveness of chemical dispersants on oil spills. *International Oil Spill Conference*. API, Washington D.C., Savannah, GA, pp. 639-44.

King, T.L., B. Robinson, C. McIntyre, P. Toole, S. Ryan, F. Saleh, M.C. Boufadel, K. Lee (2015) Fate of surface spills of cold lake blend diluted bitumen treated with dispersant and mineral fines in a wave tank. In: *Environmental Engineering Science*, Vol. 32, No. 3, 01.03.2015, p. 250-261.

Lee, K., Li, Z., Boufadel, M.C., Venosa, A.D. and Scott Miles, M. (2009) Wave tank studies on dispersant effectiveness as a function of energy dissipation rate and particle size distribution. Final report submitted to NOAA/CRRC/UNH. Pp67+ appendix.

Li, Z., Lee, K., King, T., Boufadel, M.C. and Venosa, A.D., (2008) Oil droplet size distribution as a function of energy dissipation rate in an experimental wave tank 2008 International Oil Spill Conference. American Petroleum Institute, Washington D.C., Savannah, GA, pp. 621-626.

Li, Z., Lee, K., King, T., Boufadel, M.C. and Venosa, A.D., (2009a) Evaluating Chemical Dispersant Efficacy in an Experimental Wave Tank: 2, Significant Factors Determining *In Situ* Oil Droplet Size Distribution. *Environmental Engineering Science*, 26(9): 1407-1418.

Li, Z., Lee, K., King, T., Boufadel, M.C. and Venosa, A.D., (2009b) Evaluating crude oil chemical dispersion efficacy in a flow-through wave tank under regular non-breaking wave and breaking wave conditions. *Marine Pollution Bulletin*, 58: 735-744.

Li, Z., Lee, K., King, T., Boufadel, M.C. and Venosa, A.D., (2010) Effects of temperature and wave conditions on chemical dispersion efficacy of heavy fuel oil in an experimental flow-through wave tank. *Marine Pollution Bulletin*, In Press, Corrected Proof.

Li, Z., K. Lee, T. King, P.E. Kepkay, O. Mikkelsen, C. Pottsmith (2011) Monitoring dispersed oil droplet size distribution at the GOM Deepwater Horizon spill site. *International Oil spill Conference Proceedings*, March 2011.

Masutani, S.M., E.E. Adams (2000) *Experimental Study of Multiphase Plumes with Application to Deep Ocean Oil Spills*, Final Report to U.S. Dept. of the Interior, Minerals Management Service, Contract No., 1435-01-98-CT-30946.

Mendoza, W.G., D.D. Riemer, R.G. Zika (2013) Application of fluorescence and PARAFAC to assess vertical distribution of subsurface hydrocarbons and dispersant during the Deepwater Horizon oil spill. *Environmental Science Processes & Impacts* 15:1017-1030.

Murphy, K. R., et al. (2010). "Measurement of Dissolved Organic Matter Fluorescence in Aquatic Environments: An Interlaboratory Comparison." *Environ Sci Technol* 44(24): 9405-9412.

Murphy, K. R., C.A. Stedmon, D. Graeber, R. Bro (2013) Fluorescence Spectroscopy and multi-way techniques, PARAFAC. *Anal. Methods*, 5: 6557-6566.

Murphy, K.R., Bro, R., Stedmon, C.A. (2014) Chemometric Analysis of Organic Matter Fluorescence. In: *Aquatic Organic Matter Fluorescence*. Eds: Coble, P.G., Lead, J., Baker, A., Reynolds, D.M., Spencer, R.G.M. Cambridge University Press, pp.339-375.

NOAA Technical Report NOS OR&R 25 (2010): Joint Analysis Group, Deepwater Horizon Oil Spill: Review of Preliminary Data to Examine Subsurface Oil in the Vicinity of MC252, May 19 – June 19, 2010, 168 pp.

Oil Budget Calculator (2010) NOAA Report Oil Budget Calculator: Deepwater Horizon, Federal Interagency Solutions Group, 217 pp.

NRC Report (2005) National Research Council Oil Spill Dispersants: Efficacy and Effects, Washington, DC, 400 pp.

Priaro, M. (2014) A Bitumen and Dilbit Primer. <https://www.behance.net/gallery/16654901/A-BITUMEN-AND-DILBIT-PRIMER> (accessed June 10, 2016).

Rosin, P., E. Rammler (1933) The Laws Governing the Fineness of Powdered Coal. *J. Institute of Fuel*, 7, 29-36.

Ryder, A.G. (2005) Analysis of Crude Petroleum Oils Using Fluorescence Spectroscopy. *Reviews in Fluorescence* 2005 pp. 169-198.

Smilde, A., Bro, R., Geladi, P. (2004) Validation and Diagnostics. In: *Multi-way Analysis with Applications in the Chemical Sciences*. John Wiley & Sons, Ltd. Pp. 145-173

- Stedmon, C.A., S. Markager, R. Bro (2003) Tracing dissolved organic matter in aquatic environments using a new approach to fluorescence spectroscopy. *Mar. Chem.*, 82: 239-54.
- Stedmon, C.A., R. Bro (2003) Characterizing dissolved organic matter fluorescence with parallel factor analysis: a tutorial. *Limnol. Oceanogr. Methods*, 6: 572-579.
- Steffens, J., Landulfo, E., Courrol, L.C., Guardani, R. (2011) Application of Fluorescence to the Study of Crude Petroleum. *J. Fluoresc.* 21:859-864.
- Tissot, B.P. and D.H. Welty (1978) Classification of Crude Oils. In: *Petroleum Formation and Occurrence*. Springer-Verlag, pp. 369-377.
- Venosa, A.D., D.W. King, G.A. Sorial (2002a) The Baffled Flask Test for Dispersant Effectiveness: A Round Robin Evaluation of Reproducibility and Repeatability. *Spill Science & Technology Bulletin*, 7(5-6): 299-308.
- Venosa, A.D., K. Lee, M.T. Suidan, S. Garcia-Blanco, S. Cobanli, M. Moteleb, J.R. Haines, G. Tremblay, M. Hazelwood (2002b) Bioremediation and Biorestitution of a Crude Oil-Contaminated Freshwater Wetland on the St. Lawrence River. *Bioremediation Journal*, 6(3):261-281.
- Wickley-Olsen, E., Boufadel, M.C., King, T., Li, Z., Lee, K., Venosa, A.D. (2007) Regular and breaking waves in wave tank for dispersion effectiveness testing. In: *Proceedings of the 30th Arctic and Marine Oil spill Program (AMOP) Technical Seminar*, Edmonton, AB, Canada. Environment Canada, Ottawa, Ontario, Canada, pp. 161–187.
- Zepp, R. G., et al. (2004). "Dissolved organic fluorophores in southeastern US coastal waters: correction method for eliminating Rayleigh and Raman scattering peaks in excitation-emission matrices." *Marine Chemistry* 89(1-4): 15-3.
- Zhao, L., et al. (2014). "Evolution of droplets in subsea oil and gas blowouts: Development and validation of the numerical model VDROD-J." *Marine Pollution Bulletin* 83(1): 58-69.
- Zhou, Z, Guo, L., Shiller, A.M., Lohrenz, S.E., Asper, V.L., Osburn, C.L. (2003) Characterization of oil components from the Deepwater Horizon oil spill in the Gulf of Mexico using fluorescence EEM and PARAFAC techniques. *Marine Chemistry* 148:10-21.

Appendices

APPENDIX A – Experiment Logs

APPENDIX B – Analytical Chemistry Results

APPENDIX C – Jet Release LISST Oil Droplet Size Distribution Histograms

APPENDIX D – Jet Release LISST Oil Droplet Size Distribution Time Series Contours

APPENDIX E – Submersible Fluorescence Time Series

APPENDIX F – Excitation Emission Matrix Contours

APPENDIX G – VDROD-J and JETLAG Numerical Plume Modeling Report

APPENDIX H – Weber Number Scaling Numerical Plume Modeling Report

APPENDIX A – Experiment Logs for subsurface injection experiments with Alaskan North Slope crude, IFO-120, South Louisiana crude and Gas Condensate.

Table A1. Log sheet for subsurface injection experiments with ANS and Corexit 9500 for cold water temperatures.

Experiment ID	Date	Oil Type	Oil Amount (g)	Dispersant-to-Oil Ratio DOR	Oil Temp. °C	Seawater Temp. °C	Air Temp. °C	Salinity ppt	Oil Injection Time seconds	Injection Pressure psi	Weather Conditions
SubANS-1	22-May-14	ANS	208.0	0	80	11.4	11.0	28.1	4	40	Calm
SubANS-2R	02-Dec-14	ANS	290.5	1:200	80	6.4	0.0	27.7	5	40	clear/windy
SubANS-3	23-May-14	ANS	284.5	1:100	80	11.2	14.0	28.0	5	40	Clear, calm
SubANS-4R	03-Dec-14	ANS	287.2	1:20	80	6.8	0.5	28.6	5	40	breezy
SubANS-5	26-May-14	ANS	279.3	0	80	8.4	9.0	28.6	5	40	Overcast
SubANS-6R	02-Dec-14	ANS	335.0	1:200	80	6.1	-2.0	27.7	5	40	light wind
SubANS-7	30-May-14	ANS	276.3	1:100	80	8.5	17.0	29.1	5	40	Clear, calm
SubANS-8R	03-Dec-14	ANS	297.2	1:20	80	7.0	4.5	28.8	5	40	rainy/breezy
SubANS-9	02-Jun-14	ANS	281.4	0	80	9.7	17	29.1	5	40	Clear, calm
SubANS-10R	17-Dec-14	ANS	344.5	1:200	80	5.4	2.0	26.5	5	40	calm
SubANS-11	06-Jun-14	ANS	276.8	1:100	80	10.7	14.0	29.0	5	40	Overcast
SubANS-12R	03-Dec-14	ANS	295.7	1:20	80	7.3	6.5	28.8	5	40	rain
Averages			288.0			8.2	7.8	28.3			

Table A2. Log sheet for subsurface injection experiments with IFO-120 and Corexit 9500 for cold water temperatures.

Experiment ID	Date	Oil Type	Oil Amount (g)	Dispersant-to-Oil Ratio DOR	Oil Temp. °C	Seawater Temp. °C	Air Temp. °C	Salinity ppt	Oil Injection Time seconds	Injection Pressure psi	Weather Conditions
SubIFO-1R	17-Dec-14	IFO-120	253.6	0	80	4.9	1.0	25.9	10	60	calm
SubIFO-2R	04-Dec-14	IFO-120	208.2	1:200	80	6.7	6.0	28.1	7	60	windy
SubIFO-3	20-Jun-14	IFO-120	213.9	1:100	80	13.2	12.4	27.9	7	62	Partly cloudy, windy
SubIFO-4R	05-Dec-14	IFO-120	219.6	1:20	80	5.6	-3.5	29.3	10	30	sunny calm
SubIFO-5	17-Jun-14	IFO-120	275.1	0	80	12.0	20.0	28.7	7	62	Clear, calm
SubIFO-6R	04-Dec-14	IFO-120	215.6	1:200	80	6.6	5	27.4	8	60	windy
SubIFO-7R	10-Dec-14	IFO-120	239.3	1:100	80	7.5	9.0	28.4	8	60	heavy rain/wind
SubIFO-8R	05-Dec-14	IFO-120	243.3	1:20	80	5.4	-3.5	28.4	10	60	sunny breezy
SubIFO-9	17-Jun-14	IFO-120	359.6	0	80	12.7	20.3	29.0	7	62	Clear, sunny
SubIFO-10R	04-Dec-14	IFO-120	221.7	1:200	80	6.6	4.5	27.2	8	60	windy
SubIFO-11R	17-Dec-14	IFO-120	N/A	1:100	80	4.9	0.5	25.8	10	60	calm
SubIFO-12R	10-Dec-14	IFO-120	204.8	1:20	80	6.8	7.0	29.5	9	60	rain/wind
Averages			241.3			7.7	6.6	28.0			

Table A3. Log sheet for subsurface injection experiments with ANS and Corexit 9500 for warm water temperatures.

Experiment ID	Date	Oil Type	Oil Amount (g)	Dispersant-to-Oil Ratio DOR	Oil Temp. °C	Seawater Temp. °C	Air Temp. °C	Salinity ppt	Oil Injection Time seconds	Injection Pressure psi	Weather Conditions
SubANS-13	05-Sep-14	ANS	303.7	0	80	17.7	19.0	29.4	5	40	sunny
SubANS-14	08-Sep-14	ANS	295.2	1:200	80	16.0	18.0	29.8	5	40	sunny
SubANS-15R	10-Sep-14	ANS	304.3	1:100	80	13.8	16.5	30.0	5	40	cloudy, calm
SubANS-16	10-Sep-14	ANS	291.9	1:20	80	14.7	19.0	30.0	5	40	partly sunny
SubANS-17	05-Sep-14	ANS	299.6	0	80	18.1	23.5	29.5	5	40	sunny, calm
SubANS-18	08-Sep-14	ANS	297.7	1:200	80	16.2	19.0	29.7	5	40	sunny
SubANS-19	09-Sep-14	ANS	283.4	1:100	80	15.3	18.5	29.9	5	40	sunny, calm
SubANS-20	11-Sep-14	ANS	289.6	1:20	80	14.1	16.0	30.0	5	40	overcast, calm
SubANS-21	08-Sep-14	ANS	297.1	0	80	15.1	14.5	29.8	5	40	sunny
SubANS-22	09-Sep-14	ANS	281.8	1:200	80	14.2	14.0	30.0	5	40	cloudy, calm
SubANS-23	10-Sep-14	ANS	284.4	1:100	80	13.4	16.0	30.1	5	40	partly cloudy
SubANS-24	11-Sep-14	ANS	285.8	1:20	80	13.6	17.5	30.0	5	40	sunny, calm
Average			292.9			15.2	17.6	29.9			

Table A4. Log sheet for subsurface injection experiments with IFO-120 and Corexit 9500 for warm water temperatures.

Experiment ID	Date	Oil Type	Oil Amount (g)	Dispersant-to-Oil Ratio DOR	Oil Temp. °C	Seawater Temp. °C	Air Temp. °C	Salinity ppt	Oil Injection Time seconds	Injection Pressure psi	Weather Conditions
SubIFO-13	12-Sep-14	IFO-120	256.8	0	80	14.9	18.5	29.9	7	60	Sunny, breezy
SubIFO-14	15-Sep-14	IFO-120	279.0	1:200	80	13.5	14.0	30.0	8	60	Sunny, breezy
SubIFO-15	16-Sep-14	IFO-120	336.2	1:100	80	14.0	12.0	30.0	8	60	sunny, calm
SubIFO-16	17-Sep-14	IFO-120	315.9	1:20	80	14.7	14.0	29.9	7	60	Clear, calm
SubIFO-17	12-Sep-14	IFO-120	293.3	0	80	14.7	20.0	30.0	8	60	sunny, windy
SubIFO-18	15-Sep-14	IFO-120	331.8	1:200	80	13.8	16.5	30.0	8	60	cloudy, breezy
SubIFO-19	16-Sep-14	IFO-120	353.8	1:100	80	14.7	14.0	30.0	7	60	overcast, calm
SubIFO-20	17-Sep-14	IFO-120	345.6	1:20	80	15.2	18.0	29.9	7	60	Sunny, breezy
SubIFO-21	12-Sep-14	IFO-120	303.6	0	80	15.2	20.0	30.0	8	60	sunny, windy
SubIFO-22	15-Sep-14	IFO-120	363.3	1:200	80	14.0	16.5	30.0	8	60	cloudy
SubIFO-23	16-Sep-14	IFO-120	352.6	1:100	80	14.7	16.5	30.0	7	60	overcast, calm
SubIFO-24	17-Sep-14	IFO-120	380.0	1:20	80	16.0	20.0	30.0	7	60	sunny, calm
Average			326.0			14.6	16.7	30.0			

Table A5. Log sheet for subsurface injection experiments with Gas Condensate and Corexit 9500 for warm water temperatures.

Experiment ID	Date	Oil Type	Oil Amount (g)	Dispersant-to-Oil Ratio DOR	Oil Temp. °C	Seawater Temp. °C	Air Temp. °C	Salinity ppt	Oil Injection Time seconds	Injection Pressure psi	Weather Conditions
SubCND-01	15-Jun-15	Condensate	169.3	None	ambient	10.0	20.5	27.4	4	40psi	Clear, calm
SubCND-02R	17-Jun-15	Condensate	299.8	None	ambient	11.1	17.2	27.8	6	40psi	Windy, partly sunny
SubCND-03	16-Jun-15	Condensate	328.6	None	ambient	10.0	14.5	28.5	6	40psi	Overcast
SubCND-04	16-Jun-15	Condensate	308.9	1:20	ambient	10.8	17.0	28.4	6	40psi	Overcast, breezy
SubCND-05	17-Jun-15	Condensate	308.7	1:20	ambient	11.9	16.5	26.7	6	40psi	Windy
SubCND-06	17-Jun-15	Condensate	301.8	1:20	ambient	11.6	17.0	27.2	6	40psi	Windy, partly sunny
SubCND-07	15-Jun-15	None	-	None	-	10.0	20.5	27.4	5	40psi	Clear, calm
Average			288.4			11.5	18.4	27.5			

Table A6. Log sheet for subsurface injection experiments with ANS and Finasol OSR 52 for warm water temperatures.

Experiment ID	Date	Oil Type	Oil Amount (g)	Dispersant-to-Oil Ratio DOR	Oil Temp. °C	Seawater Temp. °C	Air Temp. °C	Salinity ppt	Oil Injection Time seconds	Injection Pressure psi	Weather Conditions
SubFIN-01	09-Jul-15	ANS	275.6	1:20	80	16.6	17.5	26.9	5	40psi	Sunny
SubFIN-02	09-Jul-15	ANS	279.7	1:20	80	17.4	23.5	27.2	5	40psi	Sunny
SubFIN-03	17-Jul-15	ANS	268.4	1:20	80	16.8	24.0	28.3	5	40psi	Sunny, breezy
SubFIN-04	13-Jul-15	ANS	251.4	1:100	80	17.0	24.0	27.8	5	40psi	Sunny, calm
SubFIN-05	13-Jul-15	ANS	261.7	1:100	80	18.6	27.5	27.6	5	40psi	Sunny, calm
SubFIN-06	13-Jul-15	ANS	258.0	1:100	80	20.8	30.0	27.5	5	40psi	Sunny, calm
SubFIN-07	15-Jul-15	ANS	283.0	1:200	80	14.2	19.0	28.7	5	40psi	Foggy
SubFIN-08	15-Jul-15	ANS	264.8	1:200	80	17.5	23.5	28.0	5	40psi	Sunny
SubFIN-09	17-Jul-15	ANS	267.9	1:200	80	17.0	22.0	28.0	5	40psi	Sunny
Average			267.8			17.3	23.4	27.8			

Table A7. Log sheet for subsurface injection experiments with IFO-120 and Finasol OSR 52 for warm water temperatures.

Experiment ID	Date	Oil Type	Oil Amount (g)	Dispersant-to-Oil Ratio DOR	Oil Temp. °C	Seawater Temp. °C	Air Temp. °C	Salinity ppt	Oil Injection Time seconds	Injection Pressure psi	Weather Conditions
SubFIN-10	30-Jul-15	IFO-120	131.6	1:200	80	17.5	15.0	28.0	6	60psi	Light fog
SubFIN-11	30-Jul-15	IFO-120	264.9	1:100	80	18.7		26.2	6	60psi	Sunny, calm
SubFIN-12	30-Jul-15	IFO-120	297.5	1:20	80	20.3	27.5	25.9	6	60psi	Sunny
Average			231.3			18.8	21.3	26.7			

Table A8. Log sheet for subsurface injection experiments with SLC and Corexit 9500 for warm water temperatures.

Experiment ID	Date	Oil Type	Oil Amount (g)	Dispersant-to-Oil Ratio DOR	Oil Temp. °C	Seawater Temp. °C	Air Temp. °C	Salinity ppt	Oil Injection Time seconds	Injection Pressure psi	Weather Conditions
SubSLC-01	23-Jul-15	MC252	317.3	0	80	16.6	18.0	27.7	6	40psi	Calm, overcast
SubSLC-02	24-Jul-15	MC252	315.2	1:200	80	17.0	19.5	28.1	6	40psi	Sunny, calm
SubSLC-03	27-Jul-15	MC252	317.5	1:100	80	16.9	17.5	28.5	6	40psi	Light rain
SubSLC-04	28-Jul-15	MC252	317.1	1:20	80	17.4	18.5	27.6	6	40psi	Rain
SubSLC-05	23-Jul-15	MC252	322.0	0	80	17.0	24.5	27.8	6	40psi	Sunny, calm
SubSLC-06	24-Jul-15	MC252	319.5	1:200	80	17.1	23.0	28.1	6	40psi	Sunny
SubSLC-07	27-Jul-15	MC252	322.9	1:100	80	17.0	18.5	28.5	6	40psi	Rain
SubSLC-08	28-Jul-15	MC252	318.0	1:20	80	17.8	18.5	27.2	6	40psi	Drizzle, breezy
SubSLC-09	23-Jul-15	MC252	329.4	0	80	17.2	24.5	27.9	6	40psi	Sunny
SubSLC-10	24-Jul-15	MC252	325.2	1:200	80	17.1	23.5	28.4	6	40psi	Overcast
SubSLC-11	27-Jul-15	MC252	330.6	1:100	80	17.0	18.5	28.0	6	40psi	Rain
SubSLC-12	28-Jul-15	MC252	321.1	1:20	80	18.1	21.0	27.3	6	40psi	Windy, drizzle
Average			321.3			17.2	20.5	27.9			

APPENDIX B – Analytical TPH and BTEX analytical chemistry values for each experiment time point.

Table B1. Total Petroleum Hydrocarbon (TPH) and Benzene-Toluene-Ethylbenzene-Xylene (BTEX) values for subsurface injection experiments of ANS with Corexit 9500 for warm water experiments. TPH method detection limit is < 1 ppm, represented by 0 in top table. Effluent samples are represented with # E in time column.

Time (min)	TPH (ppm) DOR = 0			TPH (ppm) DOR = 1:200			TPH (ppm) DOR = 1:100			TPH (ppm) DOR = 1:20		
	SUBANS13	SUBANS17	SUBANS21	SUBANS14	SUBANS18	SUBANS22	SUBANS15R	SUBANS19	SUBANS23	SUBANS16	SUBANS20	SUBANS24
0	0	0	0	0	1	0	Data missing	0	0	0	0	1
2	37	0	127	72	84	67		32	46	34	8	41
2.5	174	253	359	237	132	128		159	65	72	60	113
3	57	149	60	98	177	97		103	159	82	77	44
3.5	24	35	60	11	17	40		25	31	27	62	49
4	2	8	146	4	2	15		1	5	7	5	13
4.5	0	1	14	1	2	3		0	2	20	1	3
5	0	0	34	0	0	1		0	0	4	0	1
5.5	0	0	36	0	0	0		0	0	1	0	0
6	0	0	7	0	0	0		0	0	0	1	2
6.5	0	0	3	0	0	1		1	0	0	1	0
7	0	0	4	0	0	0		1	0	1	1	0
8	0	0	3	0	0	0		0	0	0	0	0
10	0	0	1	0	0	0		0	0	0	1	0
12	0	0	1	0	0	0		0	0	1	0	0
14	0	0	1	0	0	0		0	0	0	0	0
2 E	0	0	0	0	0	0		0	0	0	0	0
4 E	0	0	0	0	0	0		0	0	0	0	0
6 E	0	0	2	0	0	0		0	0	0	0	0
8 E	7	37	12	19	6	10		15	16	32	18	17
10 E	12	13	5	11	23	13		21	25	19	18	29
12 E	8	5	4	8	18	10		5	10	6	7	5
14 E	3	3	3	4	11	4		2	3	3	3	2

Time (min)	BTEX (ppb) DOR = 0			BTEX (ppb) DOR = 1:200			BTEX (ppb) DOR = 1:100			BTEX (ppb) DOR = 1:20		
	SUBANS13	SUBANS17	SUBANS21	SUBANS14	SUBANS18	SUBANS22	SUBANS15R	SUBANS19	SUBANS23	SUBANS16	SUBANS20	SUBANS24
0	0	0	0	2	3	1	Data missing	0	0	2	0	2
2	0	0	744	106	16	312		16	124	88	0	13
3	161	1333	920	1218	2063	1447		791	1161	1529	1445	636
4	14	248	1883	94	65	346		45	127	140	262	209
5	2	15	514	10	15	21		7	14	72	9	22
6	6	6	317	8	7	5		6	4	15	19	23
7	2	2	102	6	6	4		8	3	7	12	3
8	4	1	92	5	6	3		3	2	4	9	3
10	1	1	59	4	5	2		3	2	4	11	2
12	3	4	39	3	5	2		3	2	4	4	2
14	3	1	31	3	4	2		3	1	4	3	2
6 E	0	0	71	1	1	3		2	0	5	0	1
8 E	37	107	195	255	145	178		331	312	517	408	393
10 E	37	50	122	193	278	349		379	322	232	267	298
12 E	27	77	88	152	232	168		74	163	107	108	76
14 E	75	10	59	87	109	62		32	44	48	49	27

Table B2. Total Petroleum Hydrocarbon (TPH) and Benzene-Toluene- Ethylbenzene -Xylene (BTEX) values for subsurface injection experiments of ANS with Corexit 9500 for cold water experiments. TPH method detection limit is < 1 ppm, represented by 0 in top table. Effluent samples are represented with # E in time column.

Time (min)	TPH (ppm) DOR = 0			TPH (ppm) DOR = 1:200			TPH (ppm) DOR = 1:100			TPH (ppm) DOR = 1:20		
	SUBANS1	SUBANS5	SUBANS9	SUBANS2R	SUBANS6R	SUBANS10R	SUBANS3	SUBANS7	SUBANS11	SUBANS4R	SUBANS8R	SUBANS12R
0	0	0	0	1	0	0	0	1	0	0	0	1
2	214	17	132	70	109	201	5	189	106	2	25	301
2.5	66	0	48	150	192	110	269	87	88	79	160	114
3	7	0	60	131	83	3	18	18	37	71	46	42
3.5	1	0	4	35	27	5	34	2	7	44	5	29
4	1	0	1	3	10	4	1	1	2	11	6	34
4.5	1	0	0	2	13	2	1	0	0	15	3	10
5	1	0	0	2	4	1	0	0	0	4	3	4
5.5	0	0	0	1	2	1	0	0	0	1	2	1
6	0	0	1	1	1	0	0	0	0	0	5	1
6.5	0	0	0	0	0	1	0	0	0	0	3	1
7	0	0	0	0	0	1	0	0	0	0	1	0
8	0	0	0	0	0	1	0	0	0	0	1	0
10	0	0	0	0	0	1	0	0	0	0	0	0
12	0	0	0	0	0	0	0	0	0	0	0	0
14	0	0	0	0	0	1	0	0	0	0	0	0
2 E	0	0	0	0	0	1	0	0	0	0	0	0
4 E	0	0	0	0	0	1	0	0	0	0	0	0
6 E	0	0	0	0	0	20	0	0	1	0	0	1
8 E	7	8	4	16	19	32	13	4	12	4	4	12
10 E	6	0	4	5	34	8	5	9	11	23	13	23
12 E	6	1	5	7	17	5	10	6	4	12	10	12
14 E	2	1	2	13	4	5	5	1	2	5	14	6

Time (min)	BTEX (ppb) DOR = 0			BTEX (ppb) DOR = 1:200			BTEX (ppb) DOR = 1:100			BTEX (ppb) DOR = 1:20		
	SUBANS1	SUBANS5	SUBANS9	SUBANS2R	SUBANS6R	SUBANS10R	SUBANS3	SUBANS7	SUBANS11	SUBANS4R	SUBANS8R	SUBANS12R
0	1	1	3	0	1	0	1	1	1	0	1	5
2	940	1303	2604	0	638	774	1	2488	1937	19	18	52
3	123	341	1437	1599	1143	274	350	566	1034	1046	470	570
4	5	11	36	109	133	200	52	21	69	163	63	469
5	3	5	13	52	71	18	11	7	13	145	66	72
6	3	4	8	6	16	7	7	6	7	11	100	21
7	2	3	7	3	6	14	4	5	6	8	16	12
8	2	3	7	3	4	8	4	4	5	5	8	7
10	1	3	5	3	3	3	3	3	4	4	3	5
12	1	3	5	2	2	2	4	3	3	2	3	5
14	1	2	5	2	2	3	2	3	3	2	2	4
6 E	no sample	no sample	no sample	0	0	898	no sample	no sample	no sample	5	17	73
8 E	no sample	no sample	no sample	295	348	418	no sample	no sample	no sample	150	121	232
10 E	no sample	no sample	no sample	338	417	185	no sample	no sample	no sample	360	216	336
12 E	no sample	no sample	no sample	170	215	128	no sample	no sample	no sample	205	186	163
14 E	no sample	no sample	no sample	95	no sample	78	no sample	no sample	no sample	78	197	58

Table B3. Total Petroleum Hydrocarbon (TPH) and Benzene-Toluene- Ethylbenzene -Xylene (BTEX) values for subsurface injection experiments of ANS with Finasol OSR 52 for warm water experiments. TPH method detection limit is < 1 ppm, represented by 0 in top table. Effluent samples are represented with # E in time column.

Time (min)	TPH (ppm) DOR = 1:200			TPH (ppm) DOR = 1:100			TPH (ppm) DOR = 1:20		
	SUBFIN-07	SUBFIN-08	SUBFIN-09	SUBFIN-04	SUBFIN-05	SUBFIN-06	SUBFIN-01	SUBFIN-02	SUBFIN-03
0	0	1	16	7	1	0	0	1	0
2	68	42	13	84	9	24	84	38	17
2.5	147	164	111	214	123	66	113	150	206
3	78	28	106	116	109	67	97	122	197
3.5	35	24	59	113	99	48	22	113	109
4	22	2	5	6	16	26	8	17	6
4.5	4	2	13	15	17	9	9	18	31
5	2	0	4	7	13	6	3	10	18
5.5	0	0	4	4	8	4	1	4	12
6	2	0	1	2	3	3	1	4	4
6.5	0	0	1	2	2	2	1	3	2
7	0	0	0	1	2	0	1	2	1
8	1	0	0	1	2	2	1	2	1
10	0	0	0	2	2	0	1	1	0
12	0	0	0	0	1	1	1	1	1
14	0	0	0	0	1	0	0	1	0
2 E	0	0	0	0	1	0	1	2	0
4 E	0	0	0	1	0	0	1	1	0
6 E	0	0	0	2	1	1	1	1	1
8 E	18	25	15	22	17	24	20	12	21
10 E	23	9	11	20	23	18	21	19	16
12 E	6	5	6	6	10	6	7	13	11
14 E	2	2	4	3	3	4	3	5	5

Time (min)	BTEX (ppb) DOR = 1:200			BTEX (ppb) DOR = 1:100			BTEX (ppb) DOR = 1:20		
	SUBFIN-07	SUBFIN-08	SUBFIN-09	SUBFIN-04	SUBFIN-05	SUBFIN-06	SUBFIN-01	SUBFIN-02	SUBFIN-03
0	0	1	0	0	2	1	1	6	2
2	81	187	0	28	1	1	0	28	1
3	894	908	1056	1063	766	535	585	1203	1937
4	467	238	304	527	337	305	439	530	589
5	201	45	36	144	224	78	95	143	184
6	11	13	21	37	50	22	24	47	59
7	16	10	15	16	17	10	9	16	19
8	9	8	8	8	9	6	4	8	12
10	6	6	5	1	6	4	3	5	8
12	3	5	4	3	5	3	2	4	5
14	4	5	2	5	3	2	2	3	5
6 E	0	3	0	0	0	0	0	0	1
8 E	390	444	287	464	312	413	380	229	287
10 E	385	192	253	331	373	308	365	327	261
12 E	119	123	132	105	148	129	115	183	188
14 E	58	66	68	51	51	65	52	68	87

Table B4. Total Petroleum Hydrocarbon (TPH) and Benzene-Toluene- Ethylbenzene -Xylene (BTEX) values for subsurface injection experiments of IFO 120 with Corexit 9500 for warm water experiments. TPH method detection limit is < 1 ppm, represented by 0 in top table. Effluent samples are represented with # E in time column.

Time (min)	TPH (ppm) DOR = 0			TPH (ppm) DOR = 1:200			TPH (ppm) DOR = 1:100			TPH (ppm) DOR = 1:20		
	SUBIFO13	SUBIFO17	SUBIFO21	SUBIFO14	SUBIFO18	SUBIFO22	SUBIFO15	SUBIFO19	SUBIFO23	SUBIFO16	SUBIFO20	SUBIFO24
0	6	4	0	0	0	0	3	2	1	0	0	1
2	16	69	151	87	20	108	187	162	202	27	159	103
2.5	56	155	117	87	55	113	81	414	344	129	171	127
3	35	43	32	14	16	411	58	30	101	110	4	107
3.5	31	9	16	10	11	8	6	1	4	45	1	4
4	4	8	2	4	18	5	2	0	1	15	1	2
4.5	3	3	0	2	10	5	8	1	0	4	0	0
5	8	4	1	2	5	0	1	1	0	2	1	1
5.5	4	7	0	4	5	0	1	0	0	0	0	0
6	5	2	0	2	2	0	1	0	1	1	1	1
6.5	0	1	1	2	1	0	1	1	0	0	0	0
7	0	2	1	2	0	0	1	1	0	1	0	0
8	0	2	1	1	0	0	0	0	1	0	0	0
10	0	1	0	1	0	0	1	0	0	0	0	0
12	0	1	1	1	0	0	0	0	0	0	1	0
14	0	0	1	0	0	0	0	0	1	0	0	1
2 E	0	0	0	1	0	0	0	0	0	0	0	0
4 E	0	0	0	0	lost	0	0	0	0	0	0	0
6 E	0	0	0	0	0	0	0	1	0	0	0	0
8 E	3	15	9	4	2	13	3	17	15	2	40	51
10 E	5	39	21	5	13	22	10	15	46	13	25	31
12 E	2	15	4	6	8	7	7	5	14	30	7	7
14 E	1	4	2	1	3	2	2	3	3	1	3	4

Time (min)	BTEX (ppb) DOR = 0			BTEX (ppb) DOR = 1:200			BTEX (ppb) DOR = 1:100			BTEX (ppb) DOR = 1:20		
	SUBIFO13	SUBIFO17	SUBIFO21	SUBIFO14	SUBIFO18	SUBIFO22	SUBIFO15	SUBIFO19	SUBIFO23	SUBIFO16	SUBIFO20	SUBIFO24
0	0	0	3	0	0	2	0	1	1	0	2	2
2	11	9	68	98	0	138	166	6	89	4	123	15
3	40	111	42	40	32	75	144	102	277	64	22	163
4	5	37	1	3	26	5	3	2	4	5	1	5
5	1	1	1	8	9	1	0	2	2	0	1	2
6	1	1	1	3	1	1	0	2	2	0	1	2
7	0	0	1	3	1	1	0	1	2	0	1	2
8	0	0	1	0	1	1	0	1	2	0	1	2
10	0	0	1	0	1	1	0	2	2	0	1	2
12	1	0	1	0	1	1	0	1	2	0	1	2
14	0	0	1	0	1	1	0	1	2	0	1	2
6 E	0	0	1	0	1	1	0	17	1	0	1	2
8 E	8	5	20	8	7	31	11	28	40	20	62	69
10 E	7	18	27	10	27	32	19	16	33	51	25	36
12 E	2	6	8	4	11	11	10	11	19	11	8	15
14 E	0	1	1	1	6	4	2	4	6	3	5	7

Table B5. Total Petroleum Hydrocarbon (TPH) and Benzene-Toluene- Ethylbenzene -Xylene (BTEX) values for subsurface injection experiments of IFO 120 with Corexit 9500 for cold water experiments. TPH method detection limit is < 1 ppm, represented by 0 in top table. Effluent samples are represented with # E in time column.

Time (min)	TPH (ppm) DOR = 0			TPH (ppm) DOR = 1:200			TPH (ppm) DOR = 1:100			TPH (ppm) DOR = 1:20		
	SUBIFO1R	SUBIFO5	SUBIFO9	SUBIFO2R	SUBIFO6R	SUBIFO10R	SUBIFO3	SUBIFO7R	SUBIFO11R	SUBIFO4R	SUBIFO8R	SUBIFO12R
0	0	0	2	1	2	1	5	0	1	1	0	1
2	111	118	210	30	12	1	110	1	36	7	2	28
2.5	50	165	55	15	14	30	135	28	29	11	107	69
3	3	32	7	4	1	35	10	19	2	2	81	39
3.5	3	2	1	1	2	11	3	5	1	6	36	10
4	1	1	1	1	1	2	1	5	1	4	2	2
4.5	1	1	1	1	0	1	1	10	1	2	2	2
5	1	1	1	0	1	1	1	7	1	1	2	1
5.5	1	0	1	0	0	1	1	4	0	1	1	1
6	0	0	1	0	0	0	1	3	1	1	1	1
6.5	1	0	1	1	0	0	1	3	0	2	1	0
7	1	0	2	1	0	1	1	4	1	1	1	1
8	1	0	1	0	0	0	1	1	1	1	1	0
10	1	0	1	1	0	1	1	1	1	0	1	1
12	0	1	1	0	1	0	1	1	1	1	1	1
14	1	1	1	1	0	0	1	1	0	1	1	0
2 E	0	0	0	0	0	1	0	0	1	0	0	0
4 E	0	0	0	0	1	1	1	1	1	0	1	1
6 E	2	0	0	1	1	1	1	1	0	0	1	0
8 E	4	4	13	0	2	0	2	0	2	5	2	1
10 E	1	6	15	1	3	3	5	2	1	2	10	9
12 E	1	5	5	1	1	1	2	2	1	2	7	4
14 E	0	2	3	0	1	1	1	2	1	1	1	2

Time (min)	BTEX (ppb) DOR = 0			BTEX (ppb) DOR = 1:200			BTEX (ppb) DOR = 1:100			BTEX (ppb) DOR = 1:20		
	SUBIFO1R	SUBIFO5	SUBIFO9	SUBIFO2R	SUBIFO6R	SUBIFO10R	SUBIFO3	SUBIFO7R	SUBIFO11R	SUBIFO4R	SUBIFO8R	SUBIFO12R
0	1	0	0	0	0	1	0	0	0	0	2	0
2	3	73	277	20	30	1	22	1	7	0	225	7
3	6	53	10	1	1	32	20	25	4	4	164	94
4	1	1	1	0	0	2	1	4	0	5	14	3
5	1	0	1	0	0	2	0	15	0	0	4	1
6	1	1	1	0	0	2	0	2	0	0	2	0
7	1	1	0	0	0	2	0	8	0	0	2	0
8	1	1	0	0	0	2	0	1	0	0	2	0
10	1	0	0	0	0	2	0	1	0	0	2	0
12	1	0	0	0	0	2	0	0	0	0	2	0
14	1	0	0	0	0	2	0	0	0	0	2	0
6 E	14	no sample	no sample	0	0	1	no sample	0	0	0	2	0
8 E	5	no sample	no sample	1	4	1	no sample	1	5	5	8	1
10 E	1	no sample	no sample	2	1	5	no sample	3	1	2	27	16
12 E	1	no sample	no sample	1	0	2	no sample	6	0	1	11	6
14 E	1	no sample	no sample	0	0	2	no sample	4	0	1	3	0

Table B6. Total Petroleum Hydrocarbon (TPH) and Benzene-Toluene- Ethylbenzene -Xylene (BTEX) values for subsurface injection experiments of IFO 120 with Finasol OSR 52 for warm water experiments. TPH method detection limit is < 1 ppm, represented by 0 in top table. Effluent samples are represented with # E in time column.

Time (min)	TPH (ppm) DOR = 1:200 SUBFIN-10	TPH (ppm) DOR = 1:100 SUBFIN-11	TPH (ppm) DOR = 1:20 SUBFIN-12
0	1	2	0
2	45	55	3
2.5	14	170	181
3	10	14	117
3.5	3	19	46
4	2	4	9
4.5	2	3	2
5	1	3	3
5.5	0	2	2
6	2	1	2
6.5	1	2	2
7	1	1	0
8	1	2	1
10	1	2	0
12	1	0	0
14	1	0	1
2 E	1	2	2
4 E	1	1	1
6 E	0	0	0
8 E	1	8	11
10 E	0	5	28
12 E	0	3	9
14 E	0	2	4

Time (min)	BTEX (ppb) DOR = 1:200 SUBFIN-10	BTEX (ppb) DOR = 1:100 SUBFIN-11	BTEX (ppb) DOR = 1:20 SUBFIN-12
0	0	1	0
2	17	22	10
3	24	59	180
4	1	11	6
5	1	2	1
6	0	1	1
7	0	1	1
8	0	1	0
10	0	1	0
12	0	1	0
14	0	1	0
6 E	0	1	0
8 E	3	20	46
10 E	4	9	53
12 E	1	4	16
14 E	0	2	8

Table B7. Total Petroleum Hydrocarbon (TPH) and Benzene-Toluene- Ethylbenzene -Xylene (BTEX) values for subsurface injection experiments of SLC with Corexit 9500 for warm water experiments. TPH method detection limit is < 1 ppm, represented by 0 in top table. Effluent samples are represented with # E in time column.

Time (min)	TPH (ppm) DOR = 0			TPH (ppm) DOR = 1:200			TPH (ppm) DOR = 1:100			TPH (ppm) DOR = 1:20		
	SUBSLC-01	SUBSLC-05	SUBSLC-09	SUBSLC-02	SUBSLC-06	SUBSLC-10	SUBSLC-03	SUBSLC-07	SUBSLC-11	SUBSLC-04	SUBSLC-08	SUBSLC-12
0	1	3	2	3	0	1	0	0	2	2	3	1
2	48	13	100	6	3	4	8	26	11	2	4	1
2.5	156	140	130	130	110	195	262	119	171	22	56	32
3	105	120	106	75	29	111	164	100	60	120	130	131
3.5	52	109	104	87	20	38	122	45	22	85	93	115
4	48	111	40	45	28	8	30	16	8	69	55	42
4.5	9	29	39	56	10	4	13	7	6	57	23	18
5	2	10	22	17	9	3	3	4	13	28	12	9
5.5	4	3	10	14	4	2	3	2	6	10	6	4
6	3	3	3	7	3	2	1	3	7	6	3	2
6.5	2	3	4	3	0	1	1	2	4	3	2	2
7	1	0	4	3	2	2	2	2	2	2	2	2
8	1	1	2	3	0	1	2	2	1	3	2	1
10	1	1	2	3	0	1	1	1	2	2	1	1
12	1	0	1	1	0	1	1	0	1	2	1	1
14	0	0	2	3	2	1	1	1	1	2	1	1
2 E	2	1	1	1	0	1	0	0	1	2	1	1
4 E	2	2	1	2	0	1	1	0	1	2	1	1
6 E	1	1	1	1	0	1	1	0	1	2	1	2
8 E	13	12	11	16	12	14	4	5	7	8	11	17
10 E	11	9	5	10	7	12	13	17	17	12	13	17
12 E	10	12	8	11	10	7	9	9	12	15	11	13
14 E	8	5	6	9	4	2	7	4	6	9	7	6

Time (min)	BTEX (ppb) DOR = 0			BTEX (ppb) DOR = 1:200			BTEX (ppb) DOR = 1:100			BTEX (ppb) DOR = 1:20		
	SUBSLC-01	SUBSLC-05	SUBSLC-09	SUBSLC-02	SUBSLC-06	SUBSLC-10	SUBSLC-03	SUBSLC-07	SUBSLC-11	SUBSLC-04	SUBSLC-08	SUBSLC-12
0	2	6	3	1	2	2	1	1	4	0	1	8
2	141	1	523	0	2	12	54	359	6	0	1	3
3	1082	1268	1161	1046	578	1794	2058	1518	590	2455	1038	708
4	316	1507	721	664	457	464	923	668	77	1128	494	890
5	58	74	548	380	317	87	124	91	152	118	110	65
6	17	59	44	199	129	23	60	40	136	34	42	35
7	17	24	31	49	32	14	25	14	55	17	20	16
8	10	19	21	28	15	8	21	9	15	7	9	10
10	8	13	15	9	7	7	7	6	19	6	8	8
12	6	12	13	6	6	6	6	4	0	4	5	7
14	6	12	11	5	6	5	4	4	5	3	5	6
6 E	0	0	0	0	1	0	6	0	1	0	5	1
8 E	337	335	212	252	396	344	140	249	224	371	337	220
10 E	263	371	174	240	199	323	265	444	394	6	392	197
12 E	207	296	276	211	335	190	210	225	264	371	258	343
14 E	136	130	185	184	113	64	162	110	147	136	146	222

Table B8. Total Petroleum Hydrocarbon (TPH) and Benzene-Toluene- Ethylbenzene -Xylene (BTEX) values for subsurface injection experiments of Gas Condensate with Corexit 9500 for warm water experiments. TPH method detection limit is < 1 ppm, represented by 0 in top table. Effluent samples are represented with # E in time column.

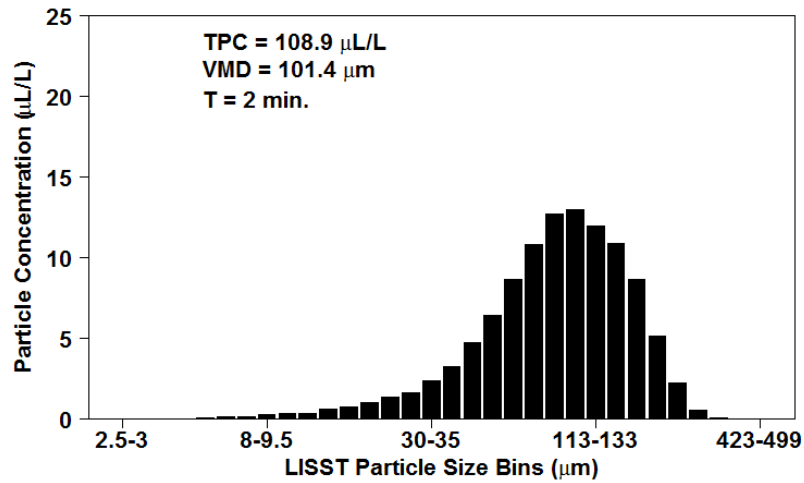
Time (min)	TPH (ppm) DOR = 0			TPH (ppm) DOR = 1:20		
	SUBCND-01	SUBCND-02R	SUBCND-03	SUBCND-04	SUBCND-05	SUBCND-06
0	0	0	0	0	0	0
2	4	41	29	76	50	25
2.5	4	12	12	32	102	42
3	2	1	3	17	35	5
3.5	0	2	0	9	2	26
4	0	2	0	2	3	2
4.5	0	1	0	4	5	0
5	0	1	0	0	4	0
5.5	0	1	0	1	9	0
6	0	0	0	0	7	0
6.5	0	1	0	0	2	0
7	0	0	0	0	0	0
8	0	0	0	0	3	0
10	0	0	0	0	2	1
12	0	1	0	0	2	0
14	0	0	0	0	1	0
2 E	0	0	0	0	0	0
4 E	0	0	0	0	1	0
6 E	0	0	0	0	0	0
8 E	1	1	2	5	3	4
10 E	0	1	1	9	3	5
12 E	0	1	0	8	4	7
14 E	0	1	0	3	5	3

Time (min)	BTEX (ppb) DOR = 0			BTEX (ppb) DOR = 1:20		
	SUBCND-01	SUBCND-02R	SUBCND-03	SUBCND-04	SUBCND-05	SUBCND-06
0	1	4	4	5	1	13
2	998	2326	4041	6345	4418	1298
3	706	186	772	3665	2618	1261
4	41	741	72	323	1104	532
5	19	28	36	46	1195	252
6	18	99	25	28	962	35
7	15	27	22	18	355	40
8	11	29	17	15	863	26
10	11	29	12	11	186	27
12	6	18	15	9	269	24
14	6	12	7	7	371	17
6 E	1	3	324	336	61	8
8 E	322	228	579	834	462	683
10 E	282	174	205	1393	553	853
12 E	90	135	86	1012	633	848
14 E	43	84	34	459	636	520

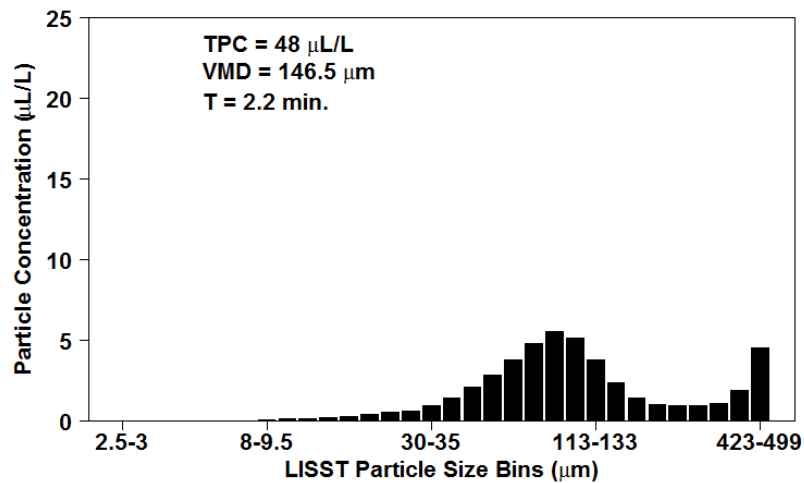
APPENDIX C – Jet Release LISST Oil Droplet Size Distribution Histograms*

**Note that LISST histogram plots have constrained Y-axes, thus lines which extend slightly above the top of the plot area represent values which were truncated.*

Particle Size Concentration (Curve TPC Max): SUBANS-1 1387



Particle Size Concentration (Curve TPC Max): SUBANS-5 1387



Particle Size Concentration (Curve TPC Max): SUBANS-9 1387

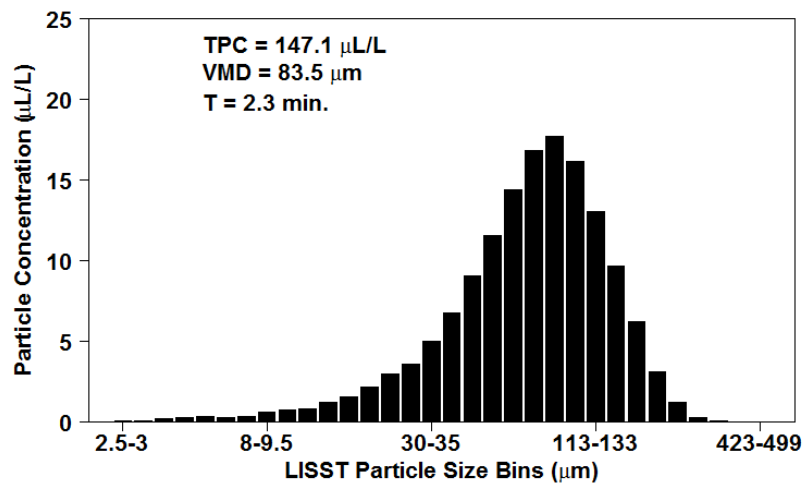
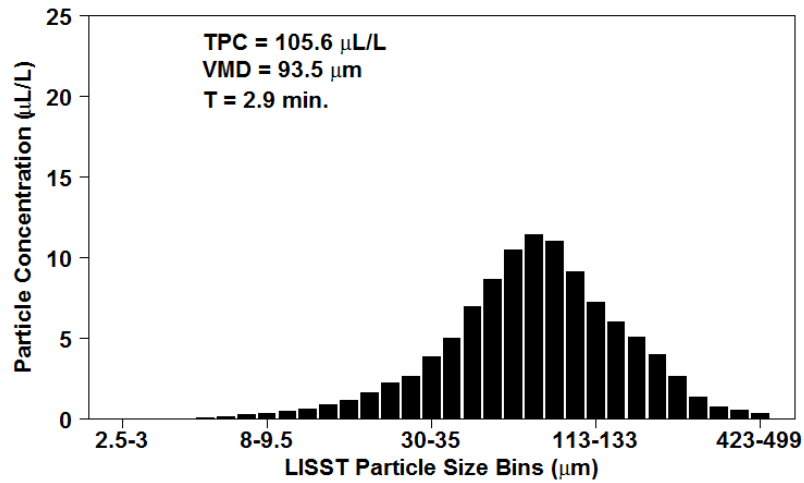
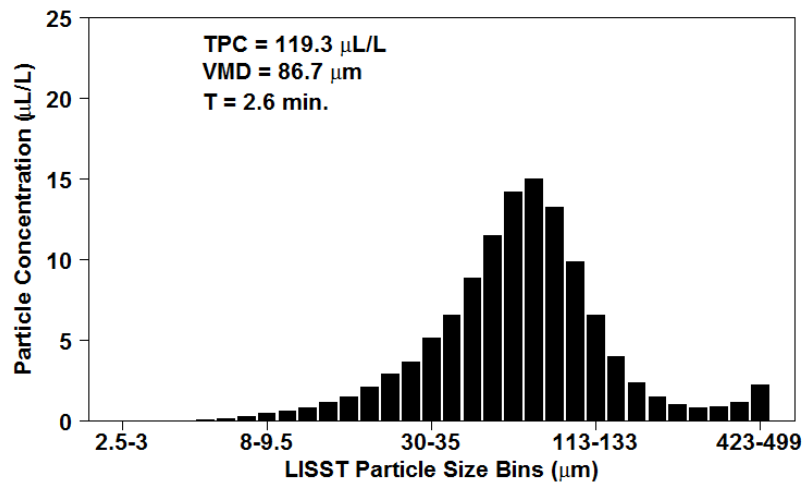


Figure C1. LISST DSD plot for ANS, no dispersant, cold water experiments.

Particle Size Concentration (Curve TPC Max): SubANS-2R 1174



Particle Size Concentration (Curve TPC Max): SubANS-6R 1174



Particle Size Concentration (Curve TPC Max): SubANS-10R 1174

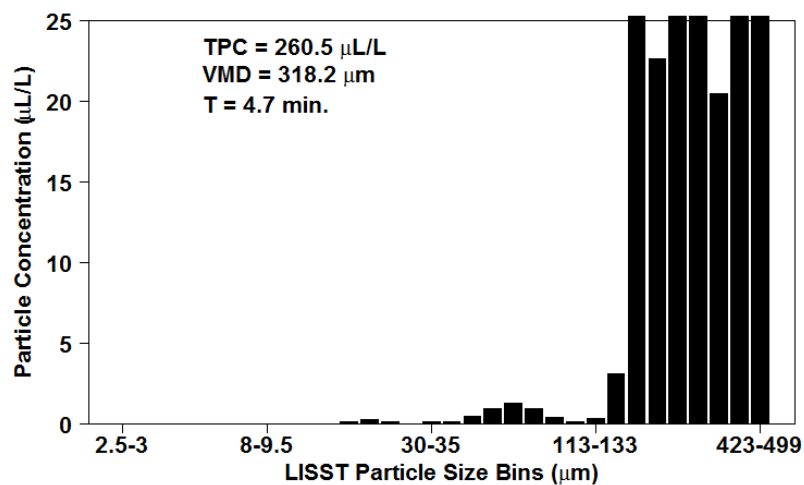
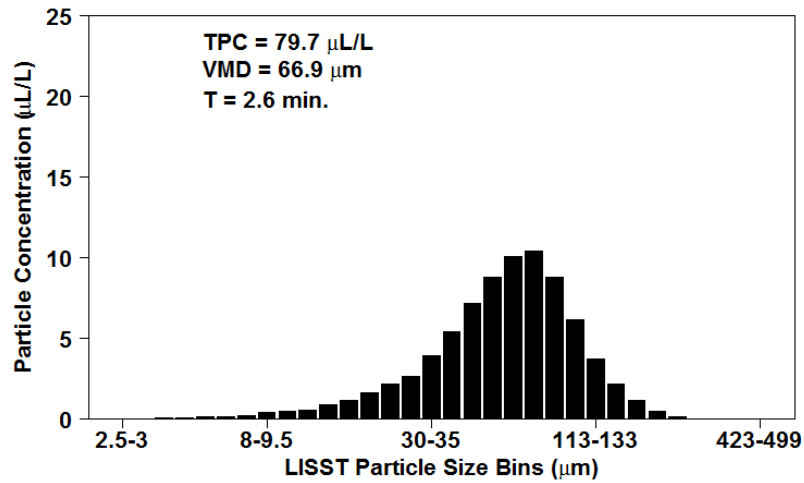
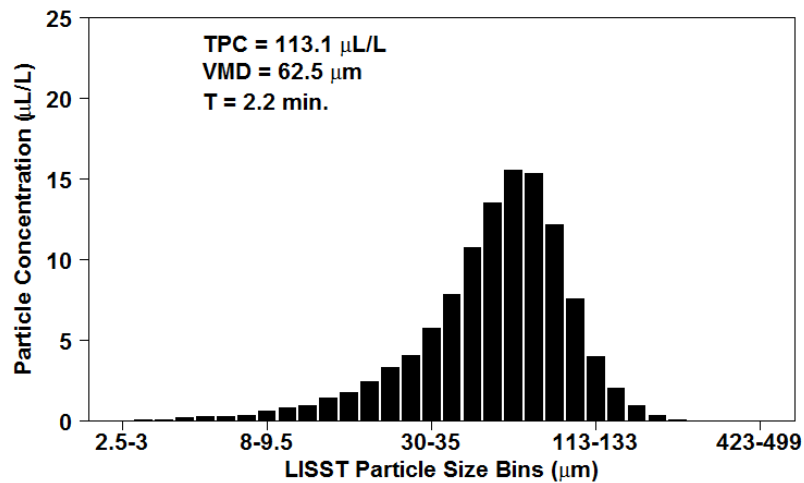


Figure C2. LISST DSD plot for ANS, DOR 1:200 (Corexit 9500), cold water experiments.

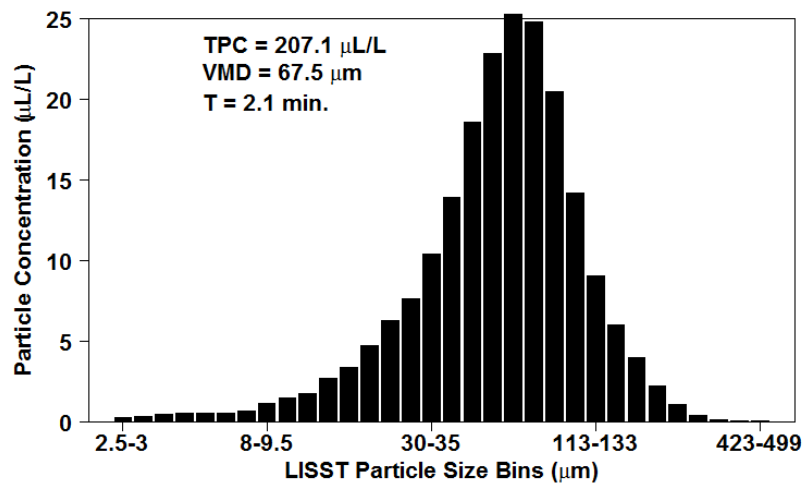
Particle Size Concentration (Curve TPC Max): SUBANS-3 1387



Particle Size Concentration (Curve TPC Max): SUBANS-7 1387



Particle Size Concentration (Curve TPC Max): subans-11 1387



FigureC3. LISST DSD plot for ANS, DOR 1:100 (Corexit 9500), cold water experiments.

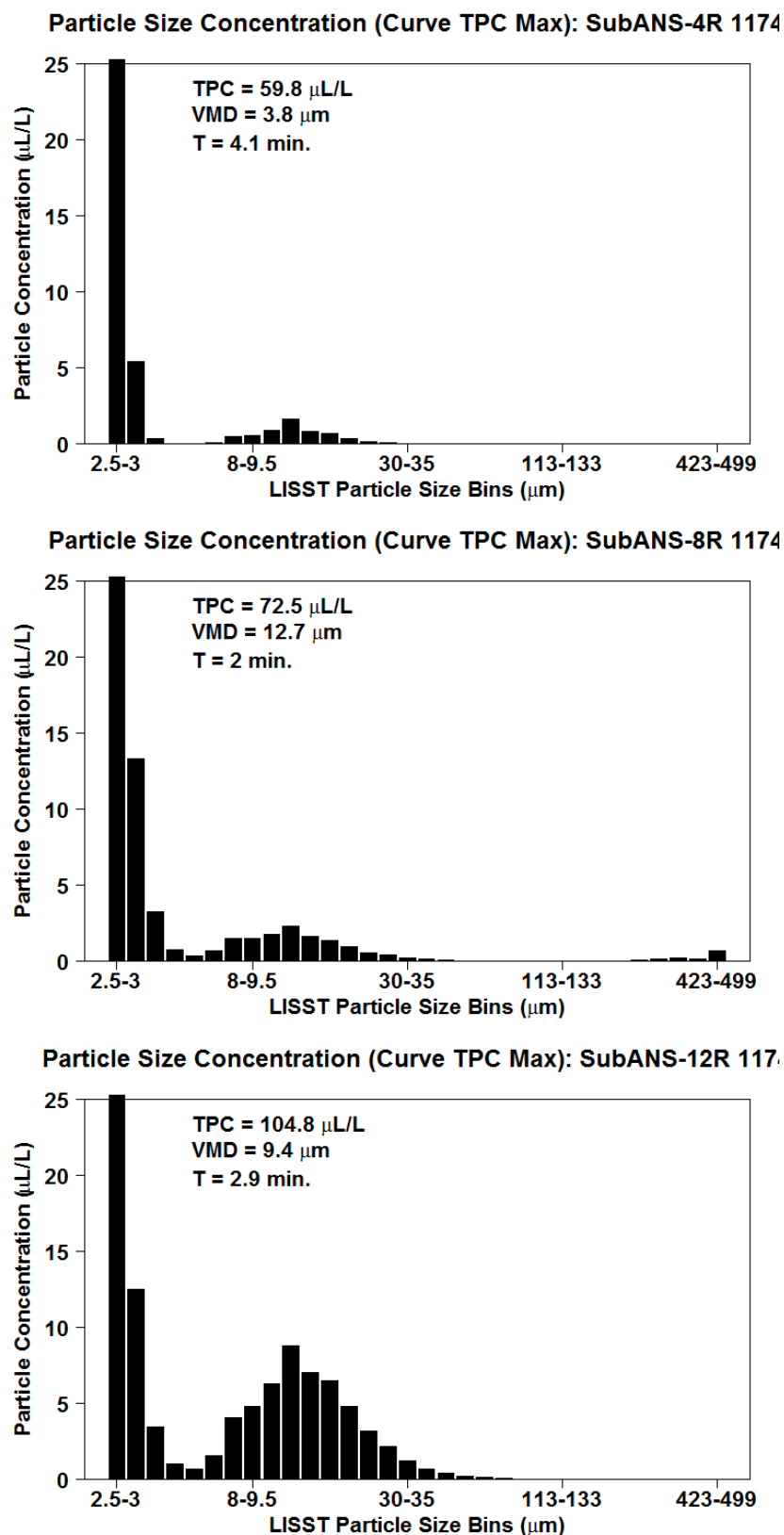


Figure C4. LISST DSD plot for ANS, DOR 1:20 (Corexit 9500), cold water experiments.

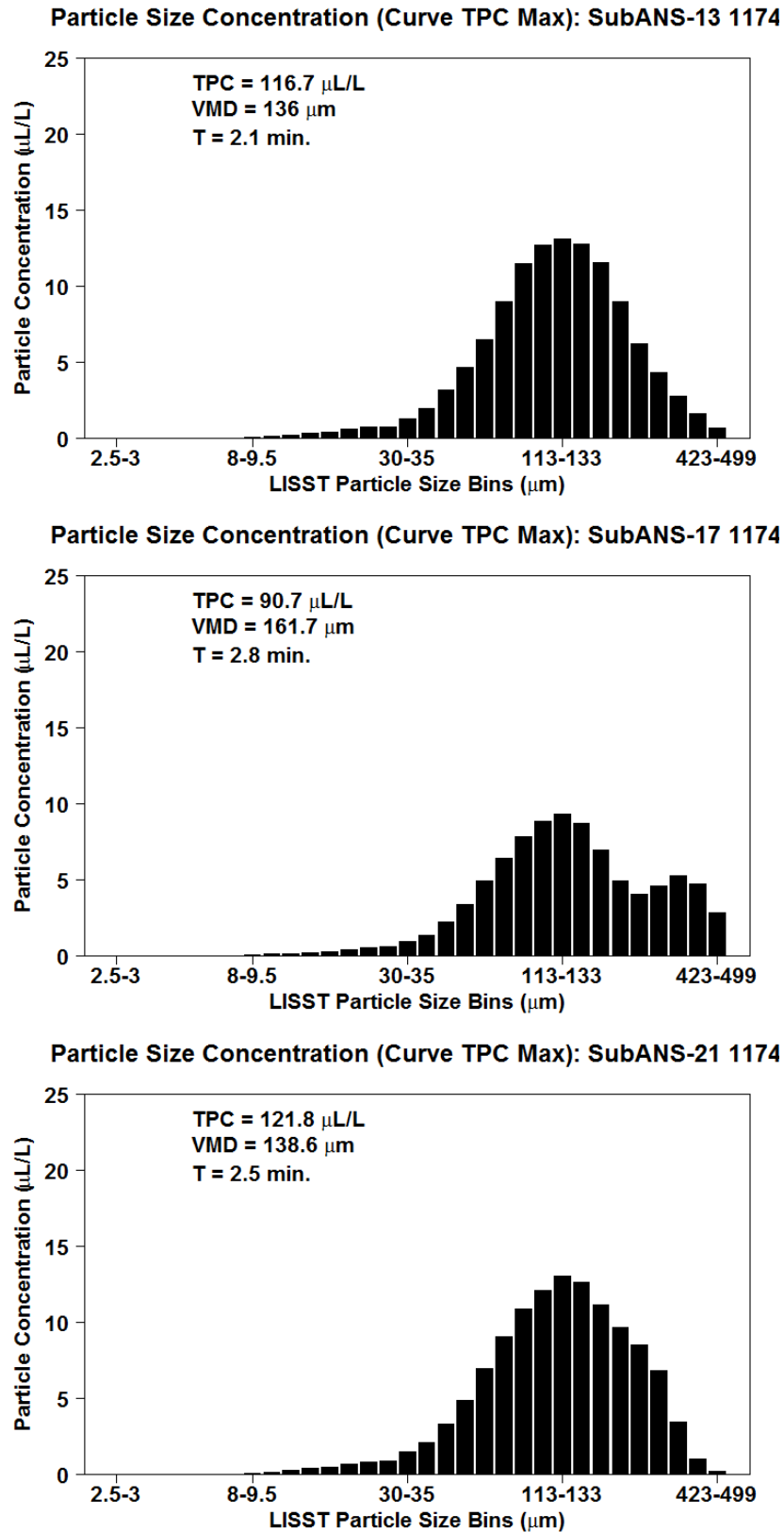


Figure C5. LISST DSD plot for ANS, DOR 0 (Corexit 9500), warm water experiments.

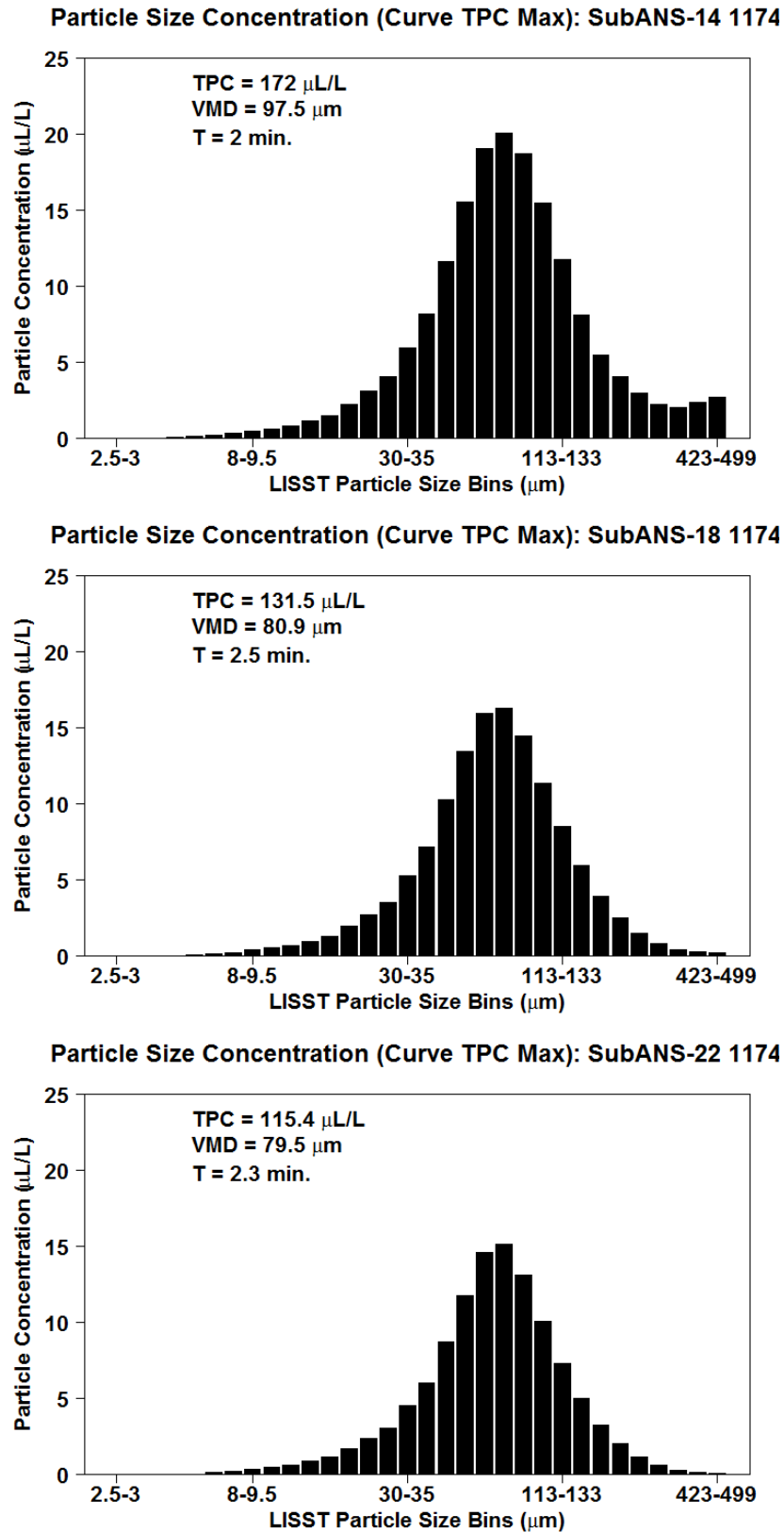
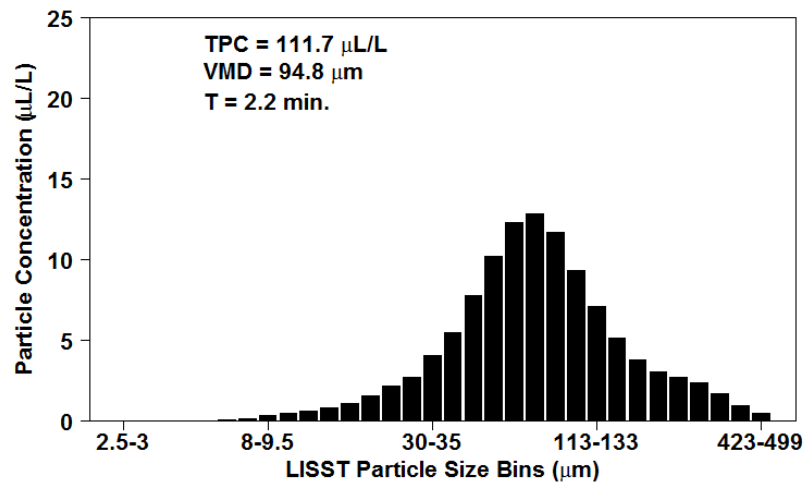
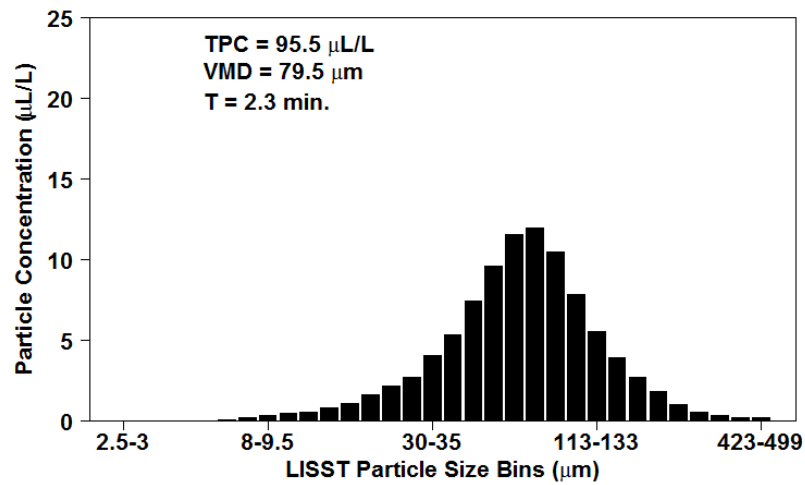


Figure C6. LISST DSD plot for ANS, DOR 1:200 (Corexit 9500), warm water experiments.

Particle Size Concentration (Curve TPC Max): SubANS-15R 117.



Particle Size Concentration (Curve TPC Max): SubANS-19 1174



Particle Size Concentration (Curve TPC Max): SubANS-23 1174

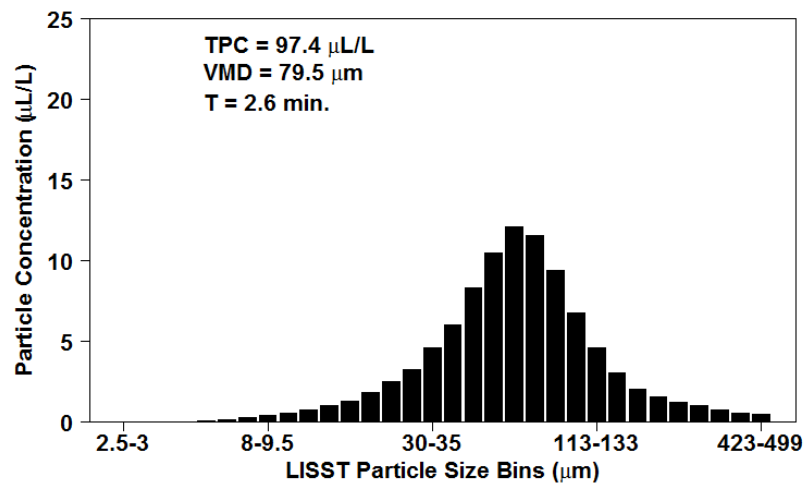


Figure C7. LISST DSD plot for ANS, DOR 1:100 (Corexit 9500), warm water experiments.

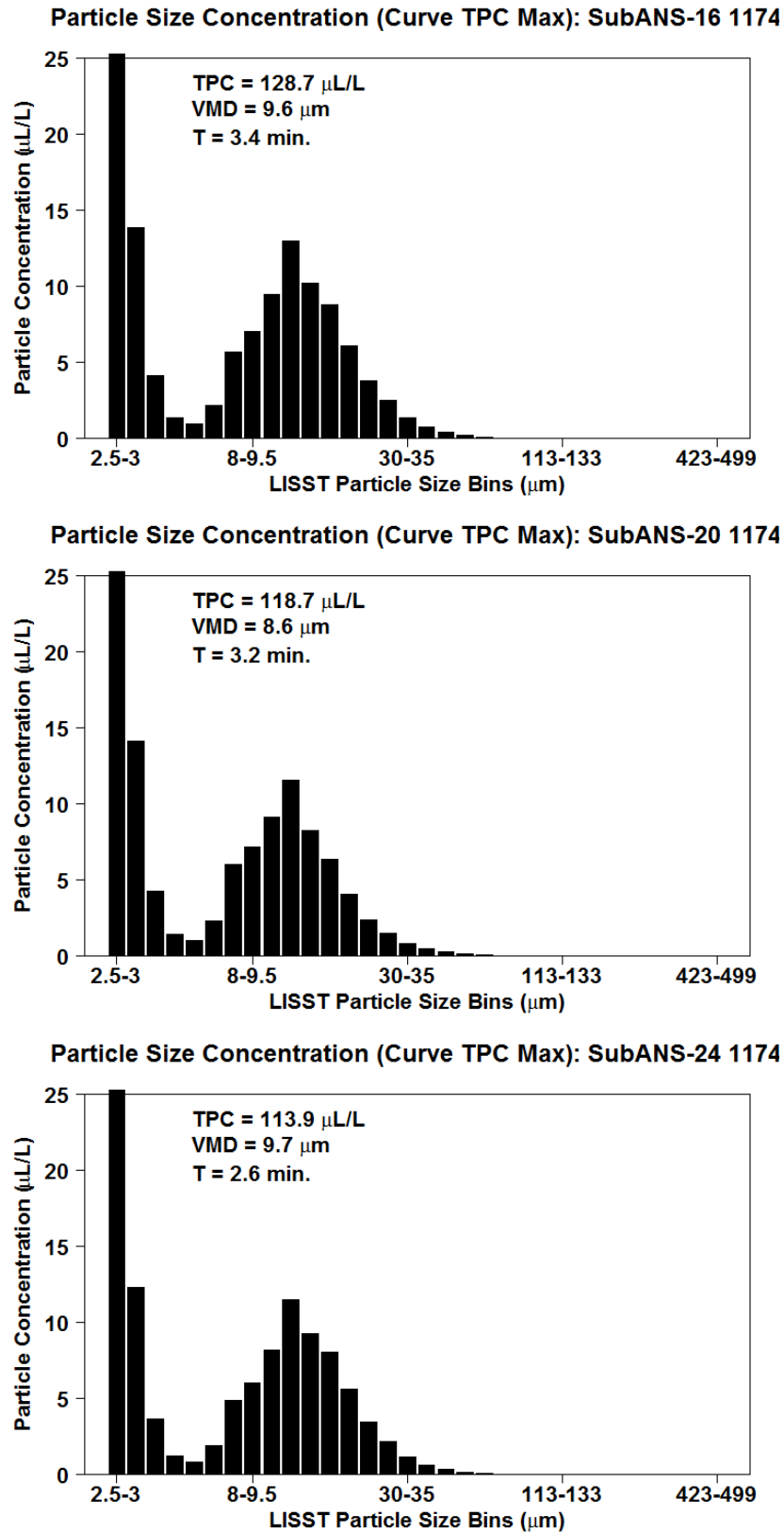


Figure C8. LISST DSD plot for ANS, DOR 1:20 (Corexit 9500), warm water experiments.

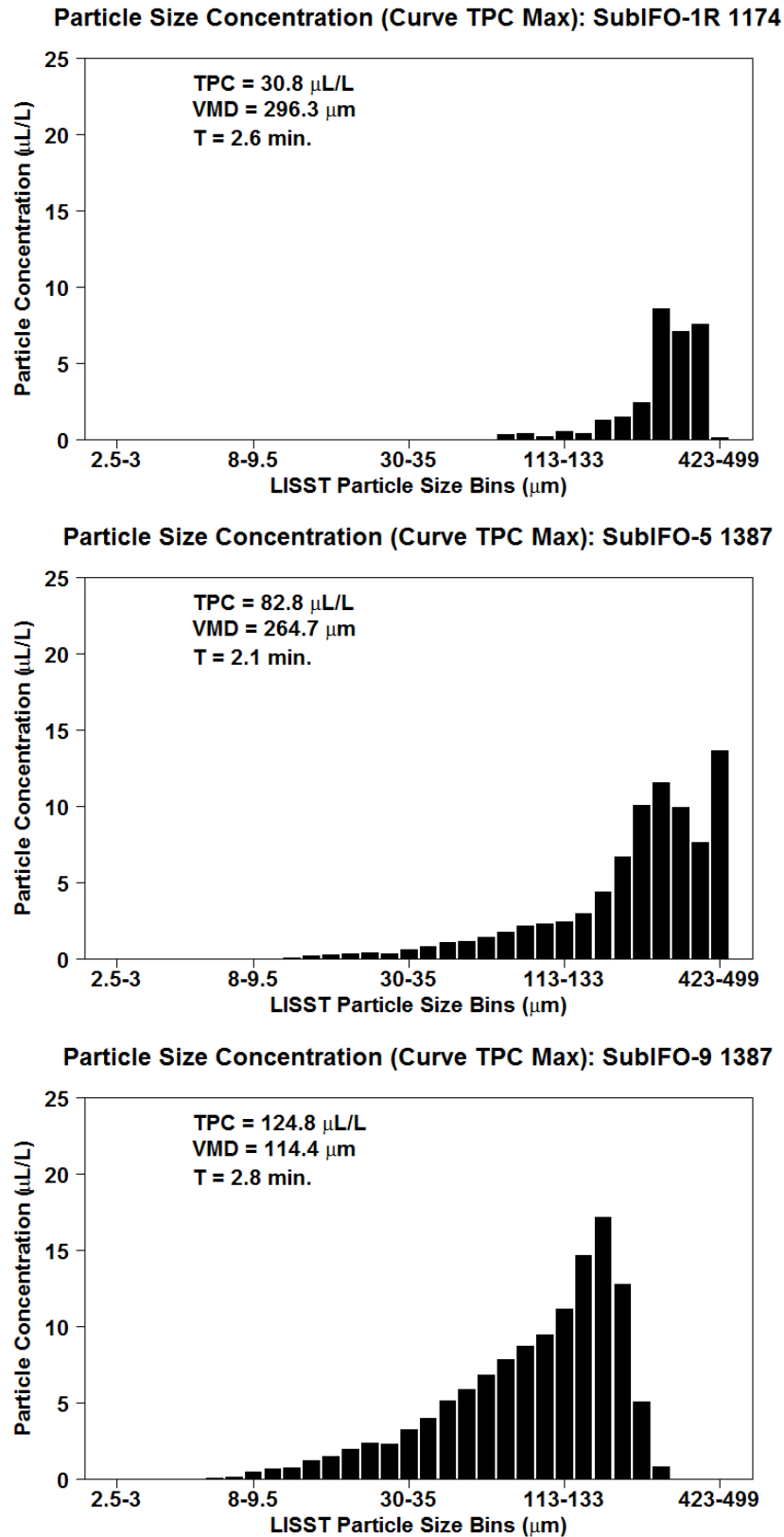


Figure C9. LISST DSD plot for IFO-120, no dispersant, cold water experiments.

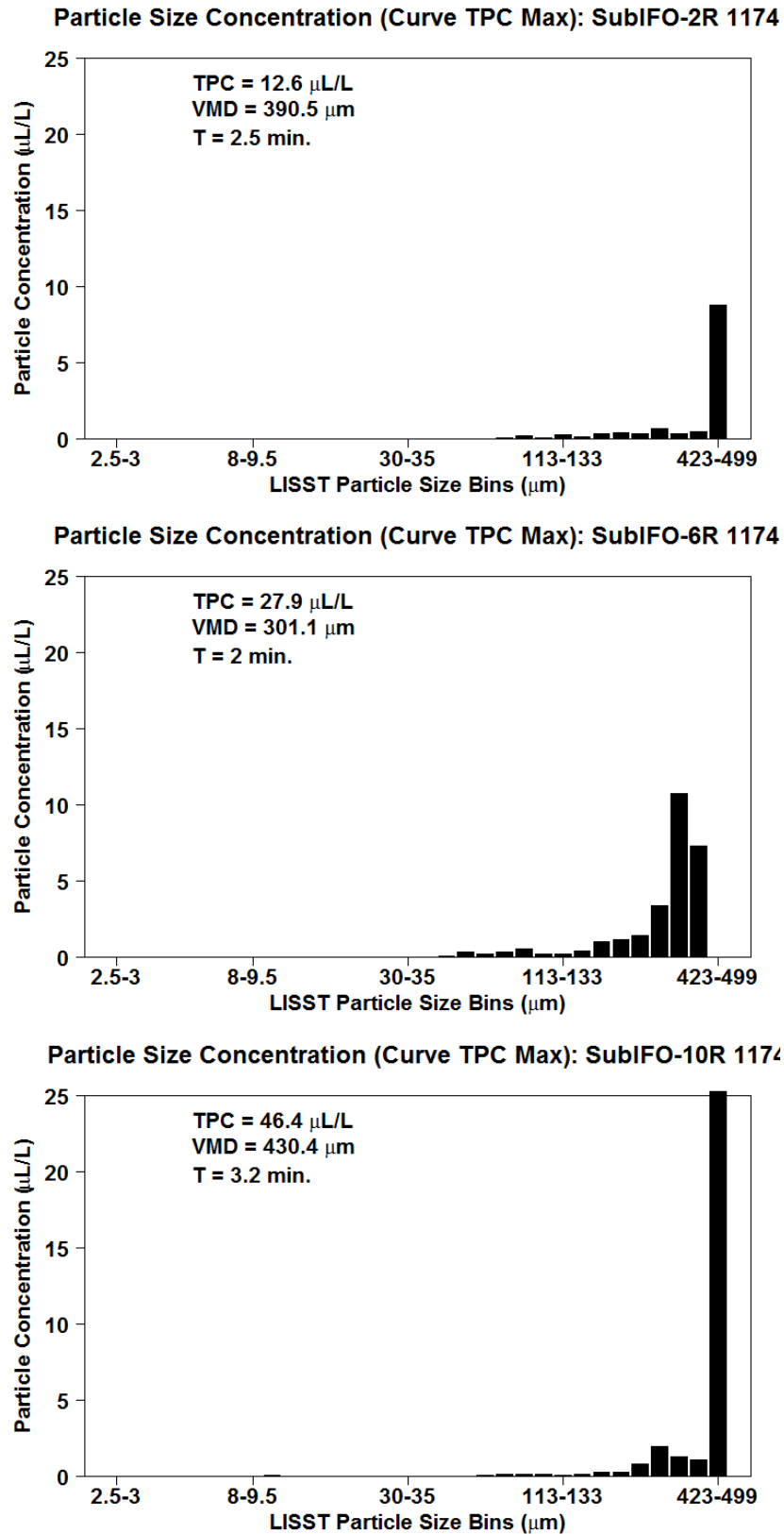


Figure C10. LISST DSD plot for IFO-120, DOR 1:200 (Corexit 9500), cold experiments.

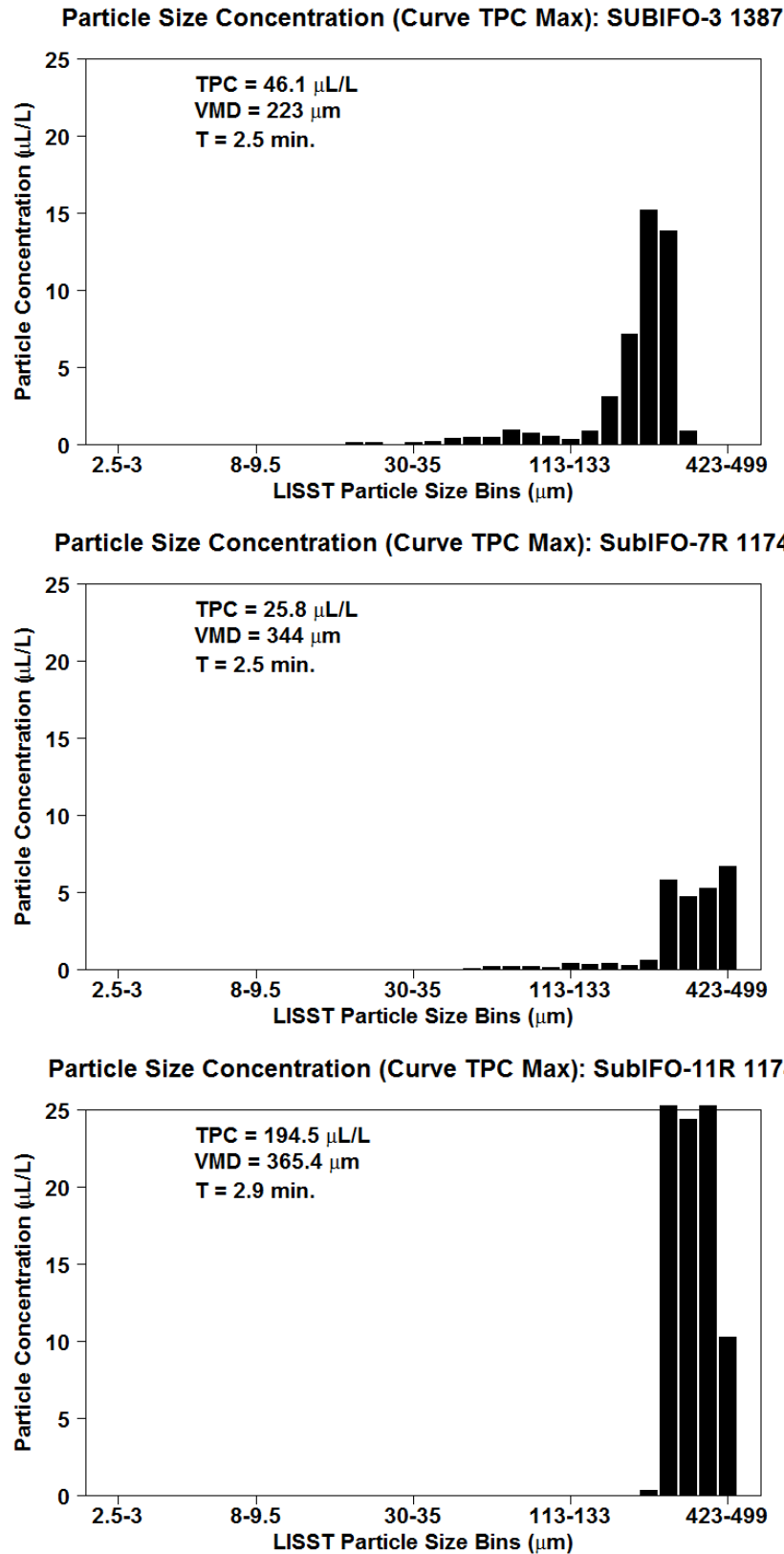


Figure C11. LISST DSD plot for IFO-120, DOR 1:100 (Corexit 9500), cold experiments.

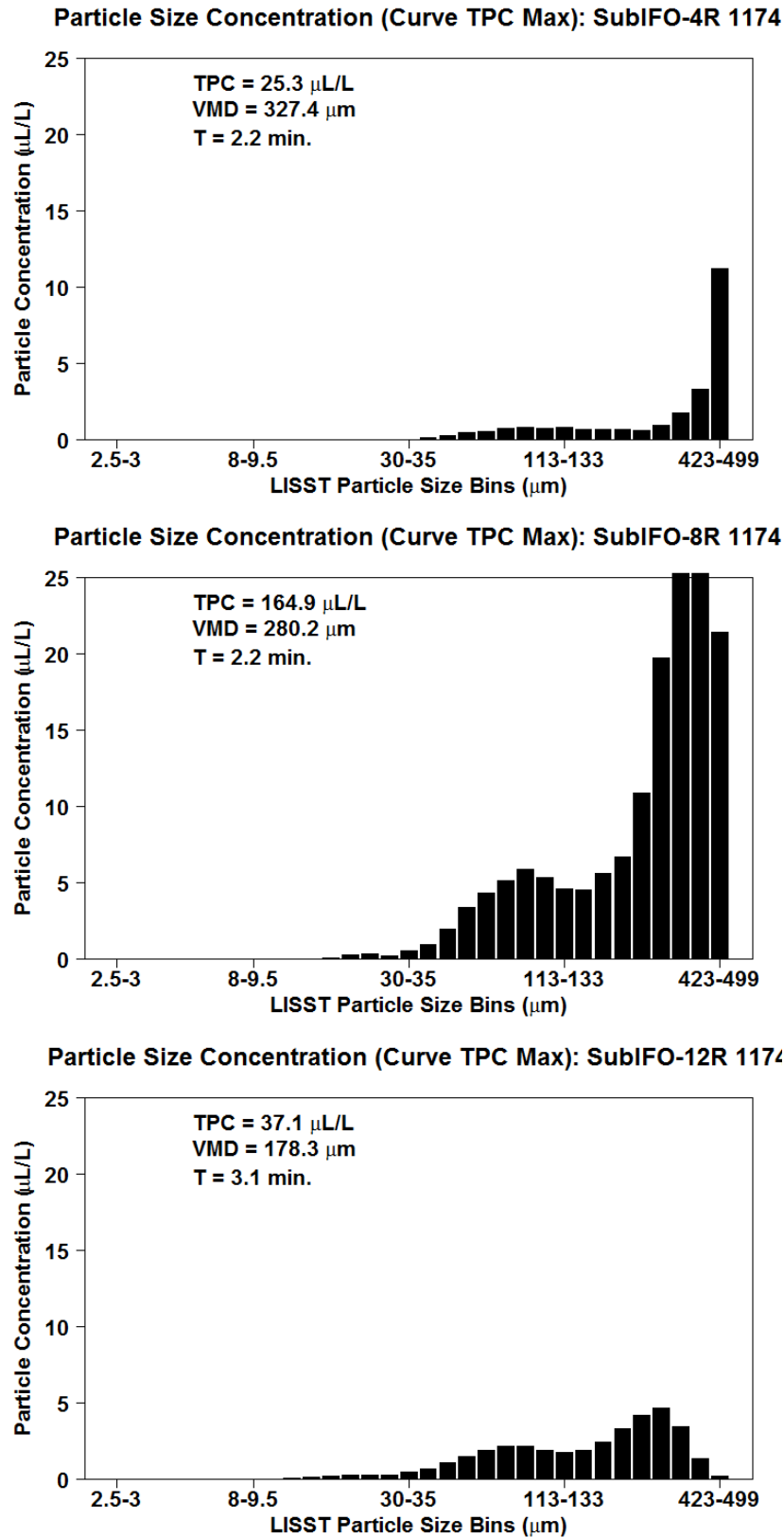
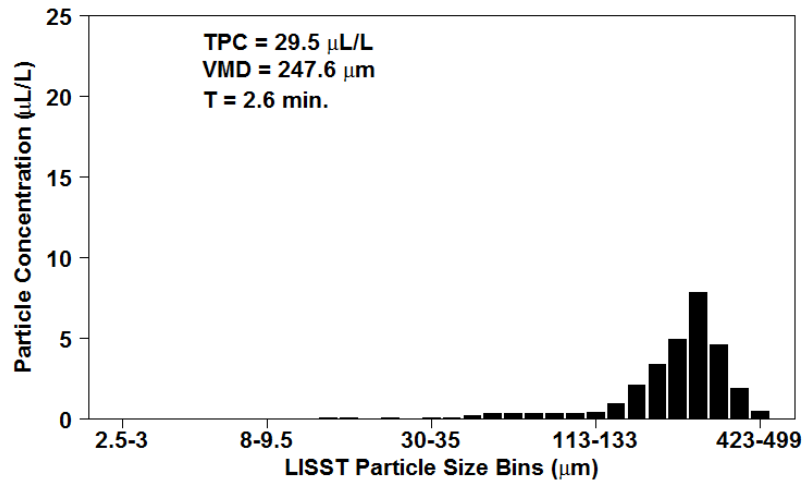
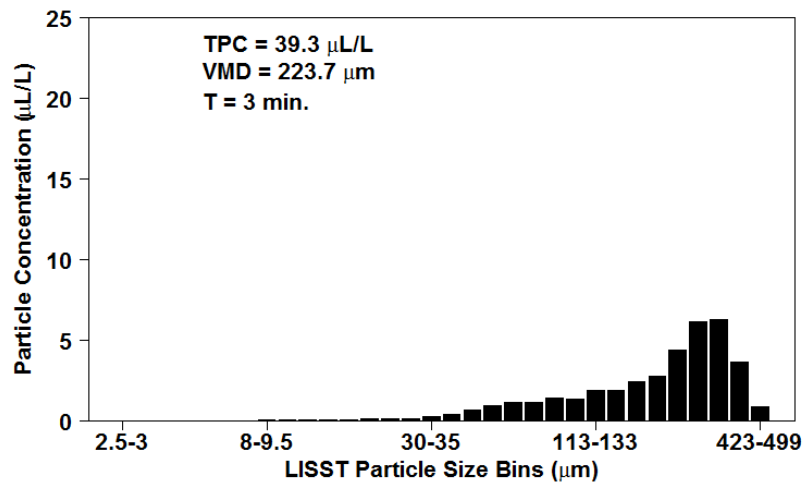


Figure C12. LISST DSD plot for IFO-120, DOR 1:20 (Corexit 9500), cold water experiments.

Particle Size Concentration (Curve TPC Max): SubIFO-13 1174



Particle Size Concentration (Curve TPC Max): SubIFO-17 1174



Particle Size Concentration (Curve TPC Max): SubIFO-21 1174

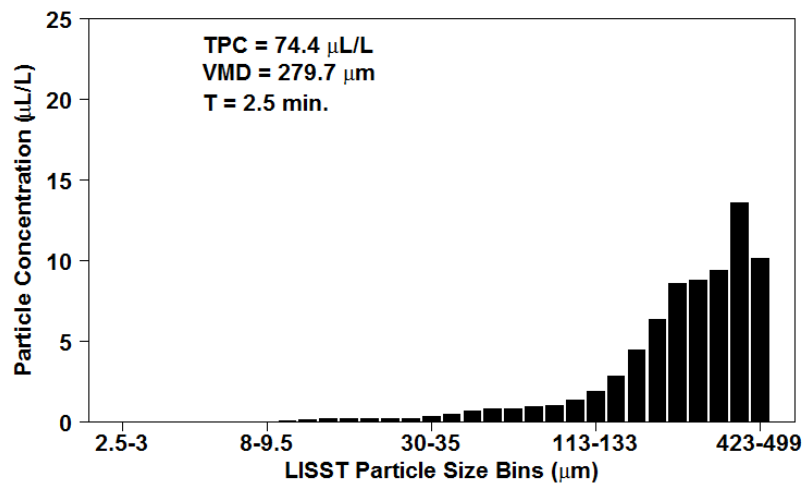


Figure C13. LISST DSD plot for IFO-120, no dispersant, warm water experiments.

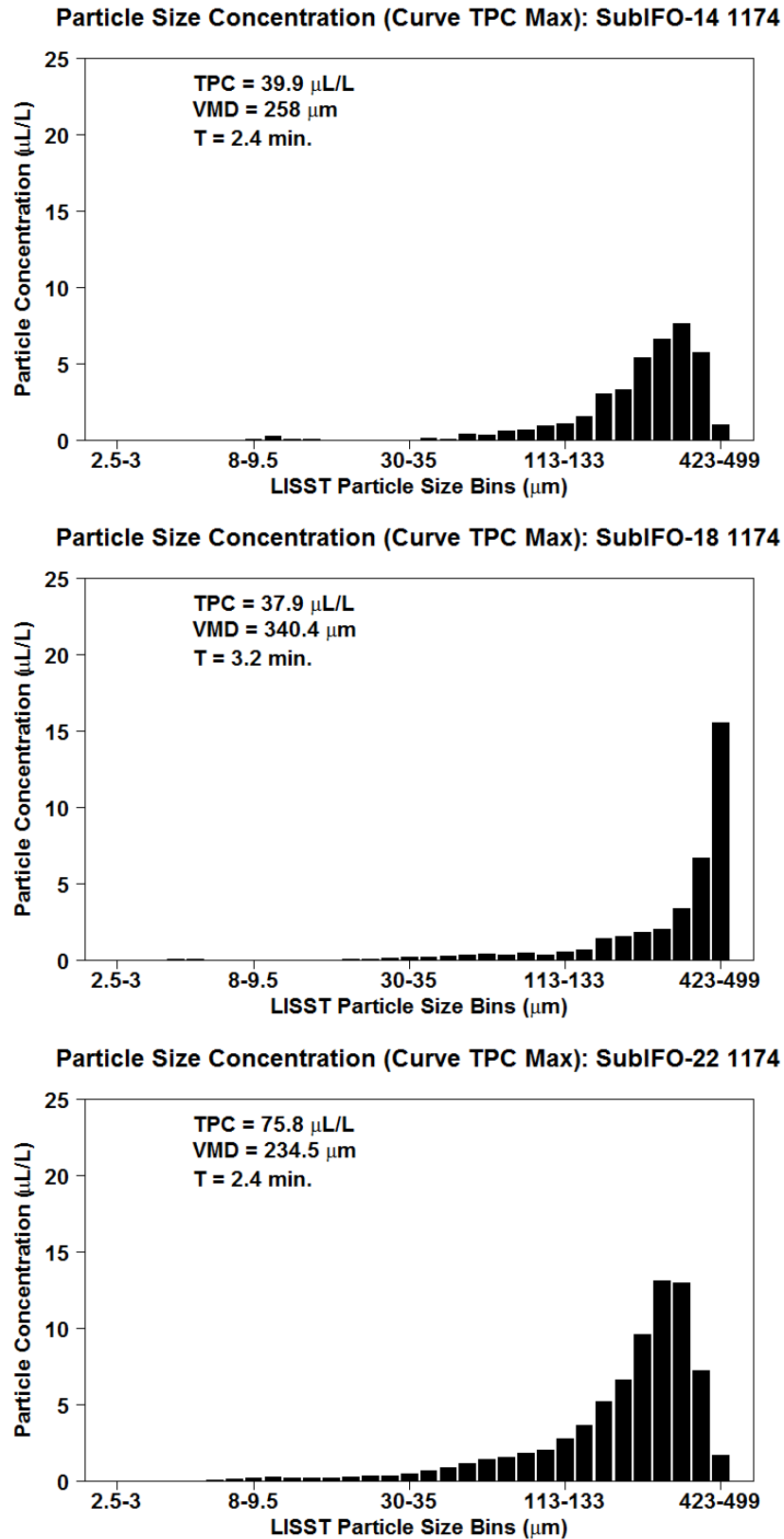


Figure C14. LISST DSD plot for IFO-120, DOR 1:200 (Corexit 9500), warm experiments.

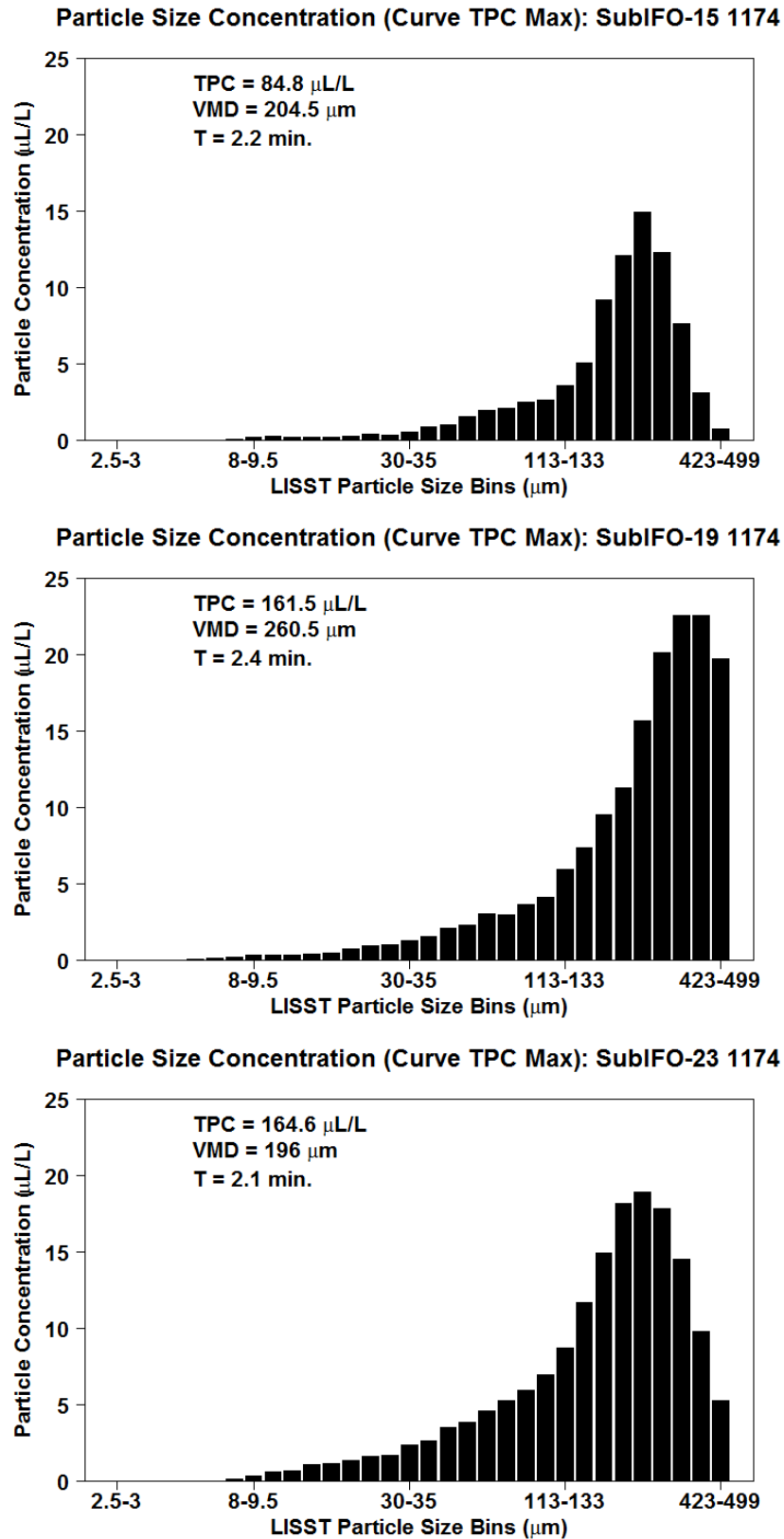
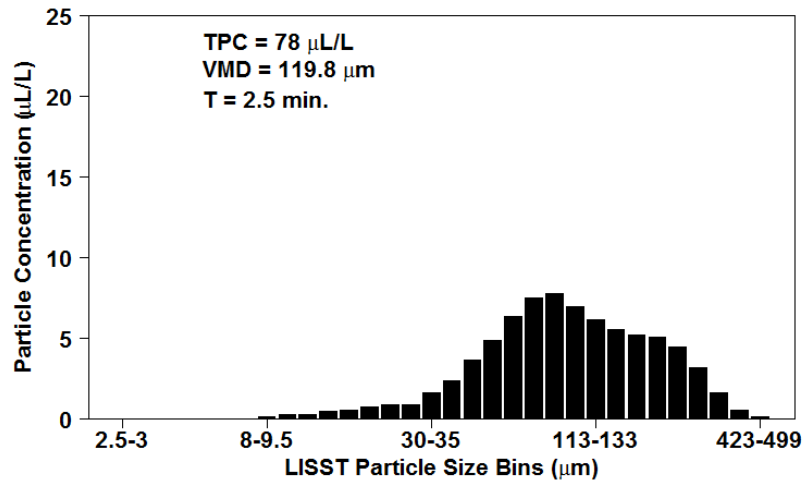
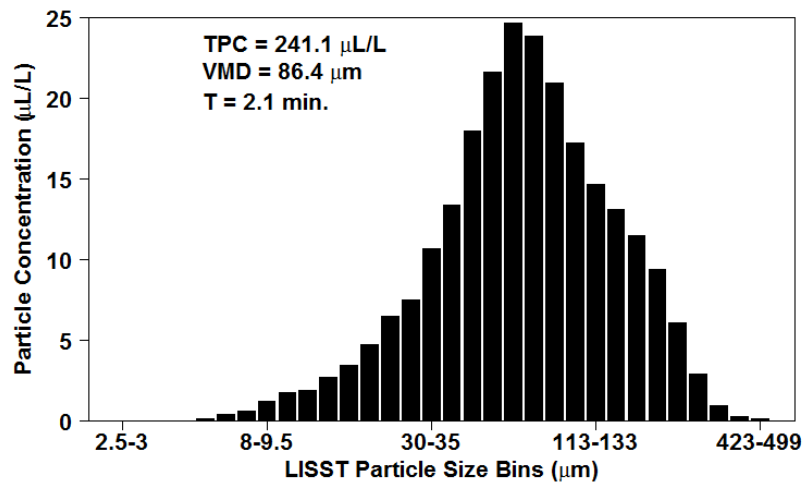


Figure C15. LISST DSD plot for IFO-120, DOR 1:100 (Corexit 9500), warm experiments.

Particle Size Concentration (Curve TPC Max): SubIFO-16 1174



Particle Size Concentration (Curve TPC Max): SubIFO-20 1174



Particle Size Concentration (Curve TPC Max): SubIFO-24 1174

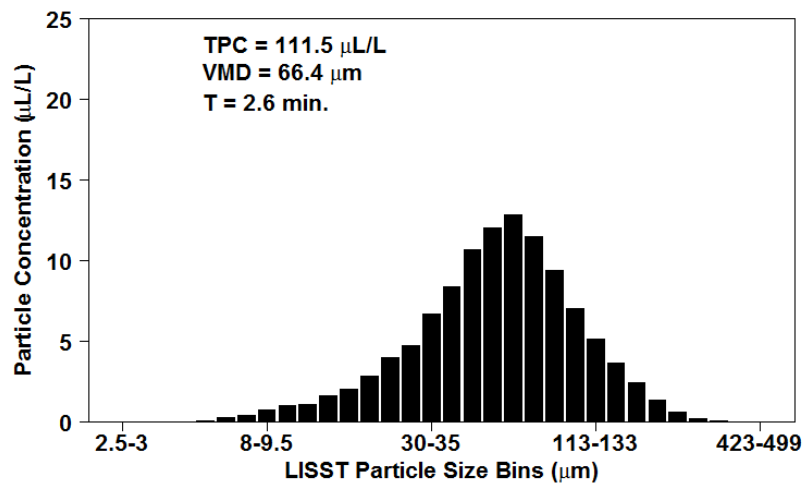


Figure C16. LISST DSD plot for IFO-120, DOR 1:20 (Corexit 9500), warm experiments.

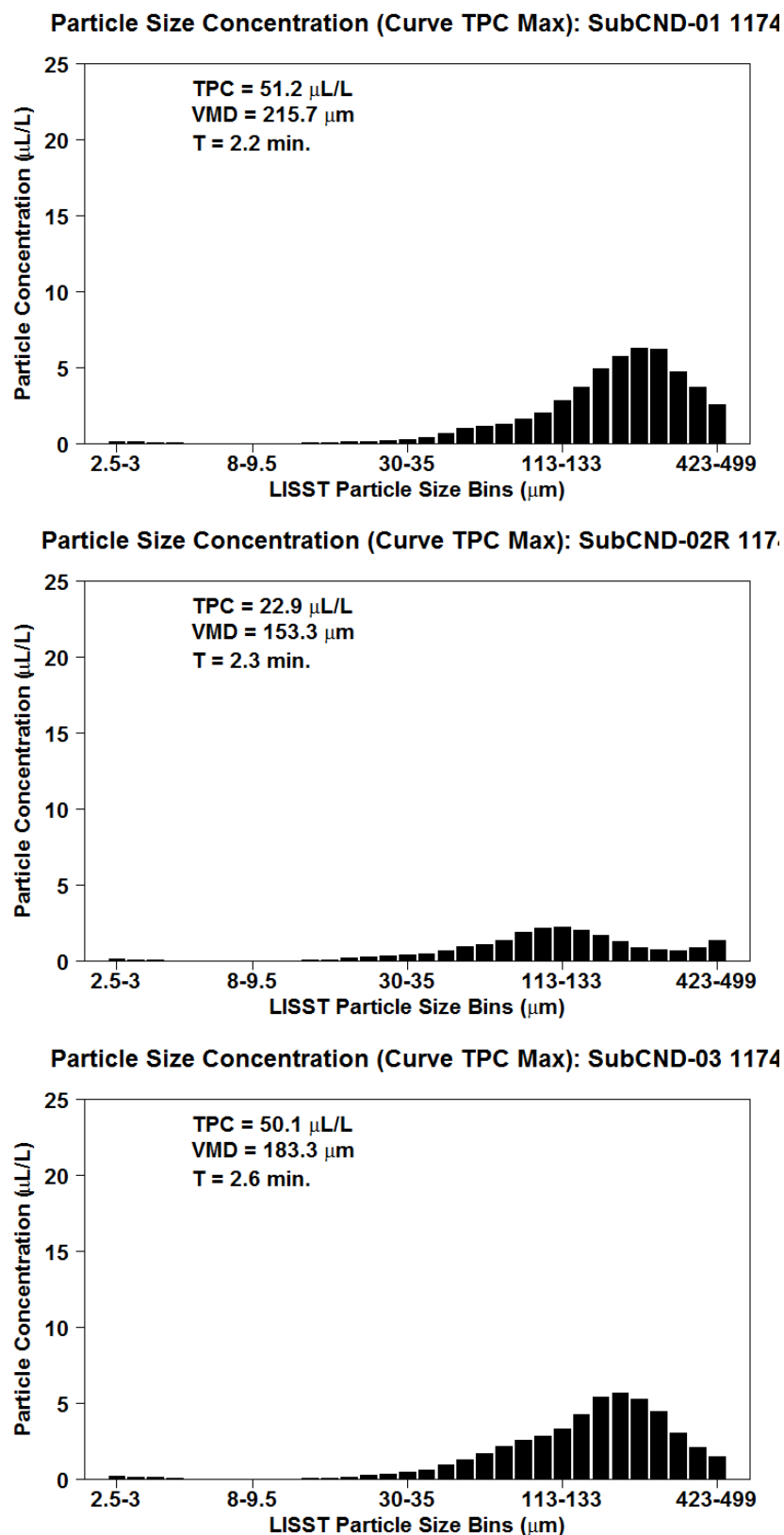


Figure C17. LISST DSD plot for Gas Condensate, no dispersant.

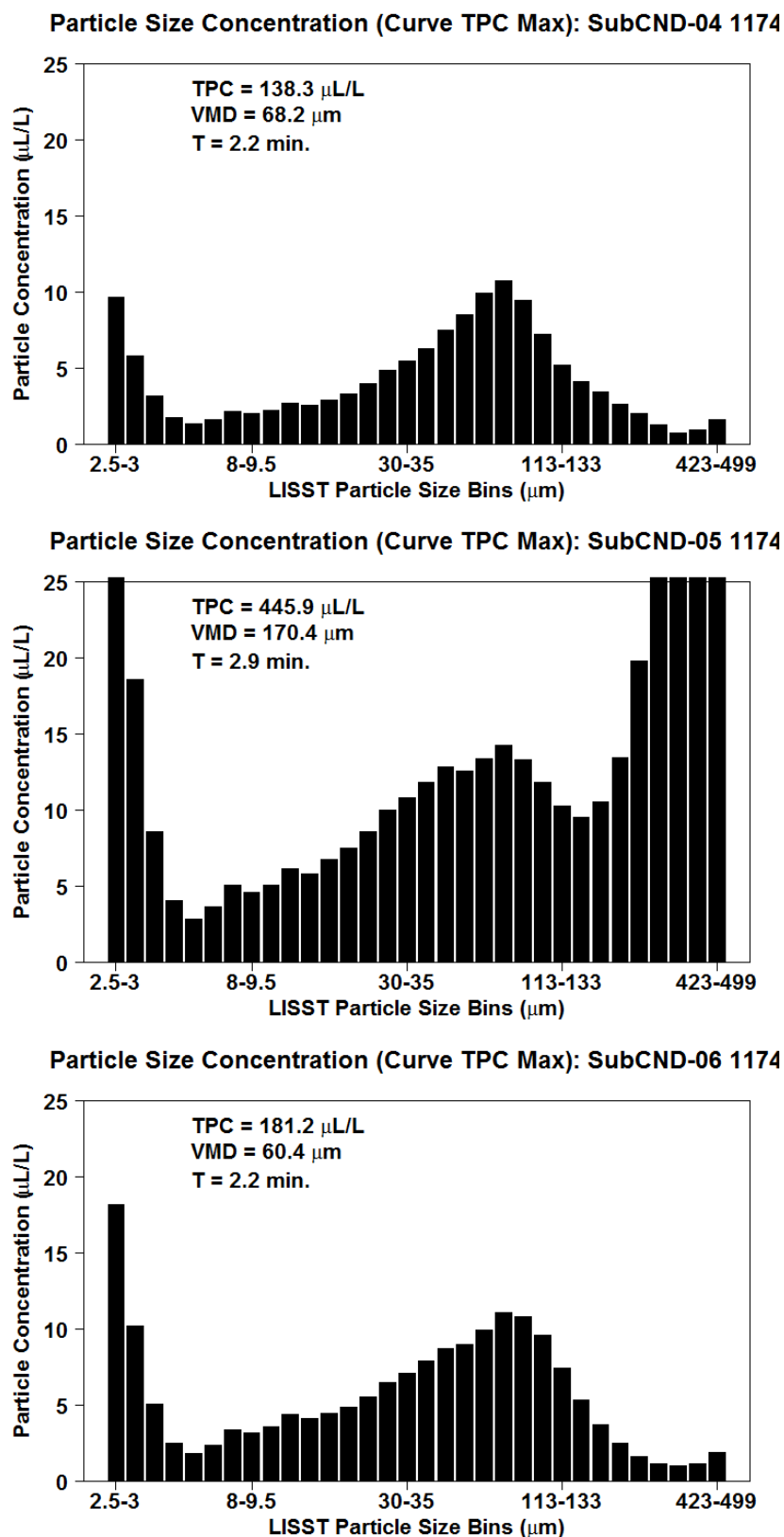


Figure C18. LISST DSD plot for Gas Condensate, DOR 1:20 (Corexit 9500).

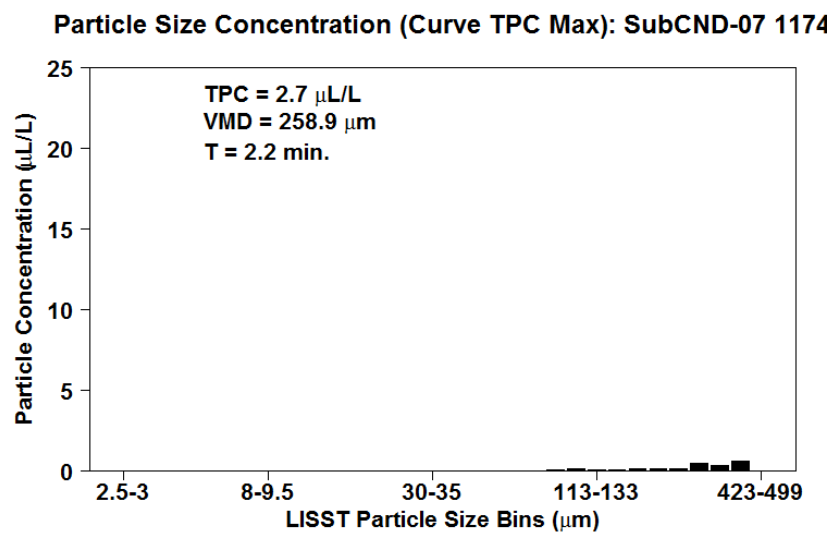
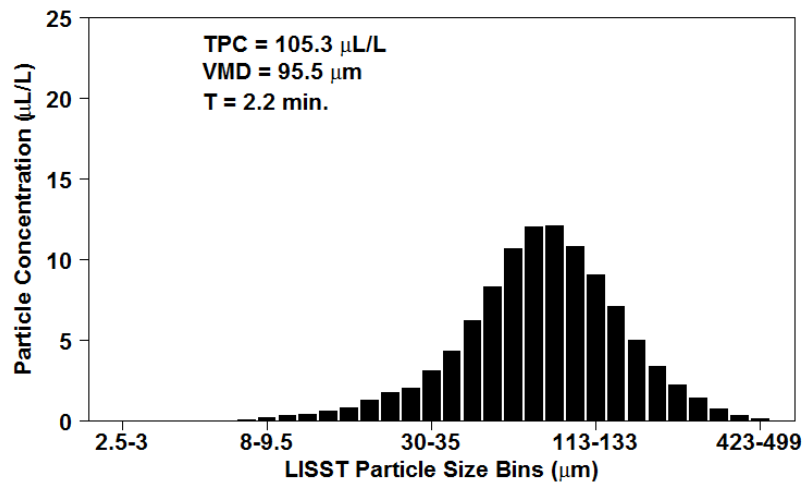
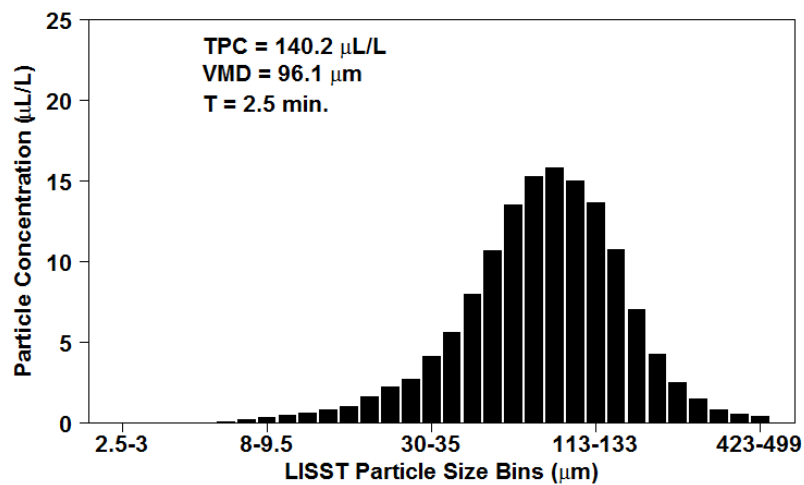
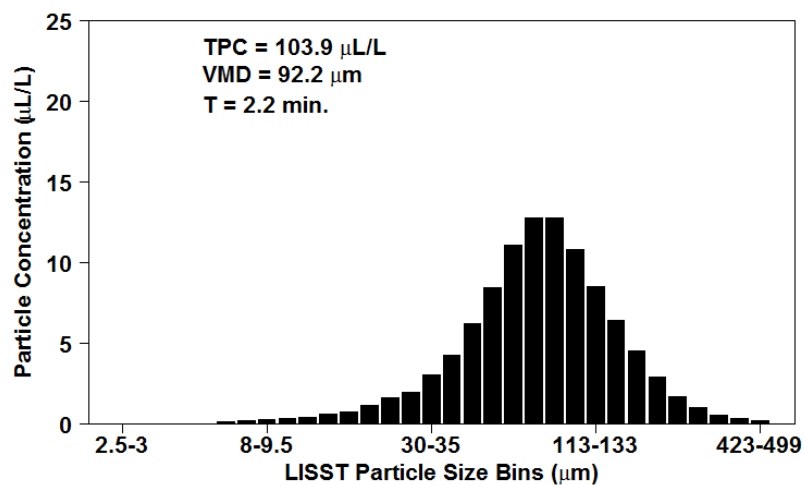
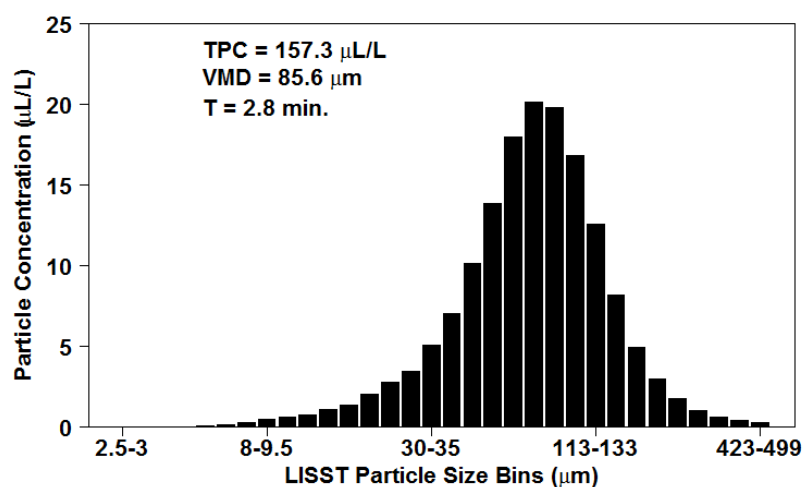


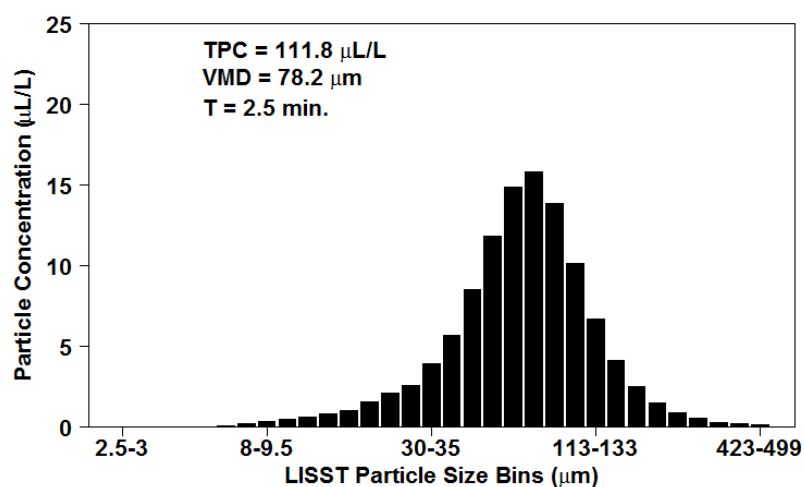
Figure C19. LISST DSD plot for air injection, no dispersant.

Particle Size Concentration (Curve TPC Max): SubFIN-07 1174**Particle Size Concentration (Curve TPC Max): SubFIN-08 1174****Particle Size Concentration (Curve TPC Max): SubFIN-09 1174****Figure C20. LISST DSD plot for ANS, DOR 1:200 (Finasol OSR 52), warm experiments.**

Particle Size Concentration (Curve TPC Max): SubFIN-04 1174



Particle Size Concentration (Curve TPC Max): SubFIN-05 1174



Particle Size Concentration (Curve TPC Max): SubFIN-06 1174

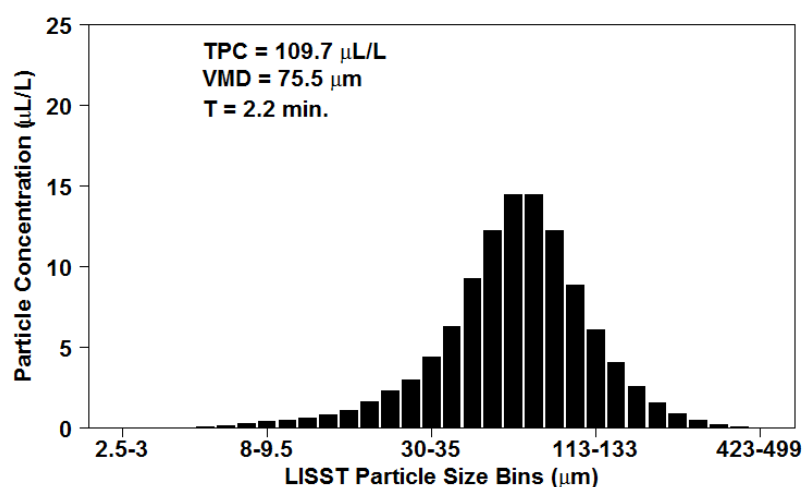


Figure C21. LISST DSD plot for ANS, DOR 1:100 (Finasol OSR 52), warm experiments.

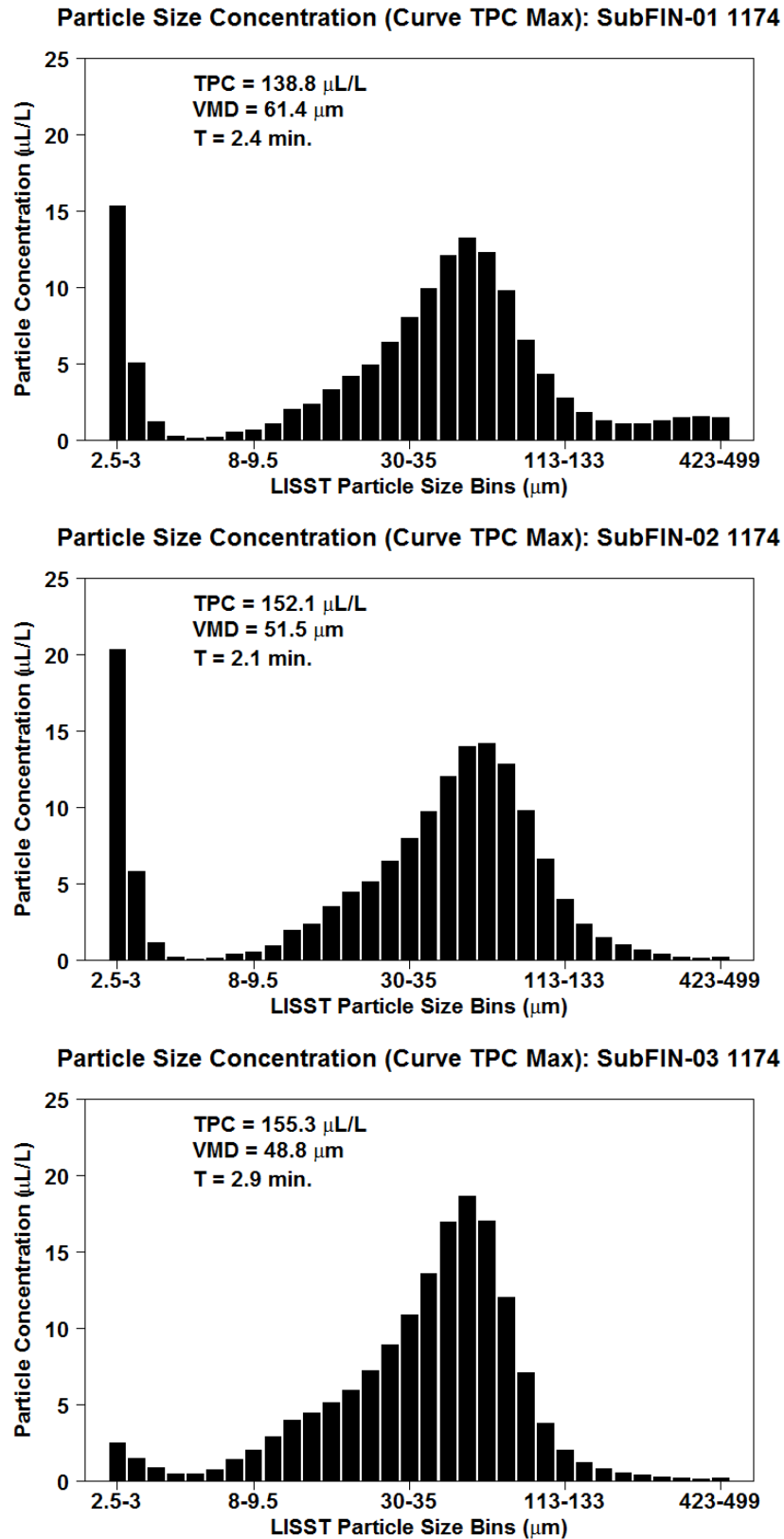


Figure C22. LISST DSD plot for ANS, DOR 1:20 (Finasol OSR 52), warm water experiments.

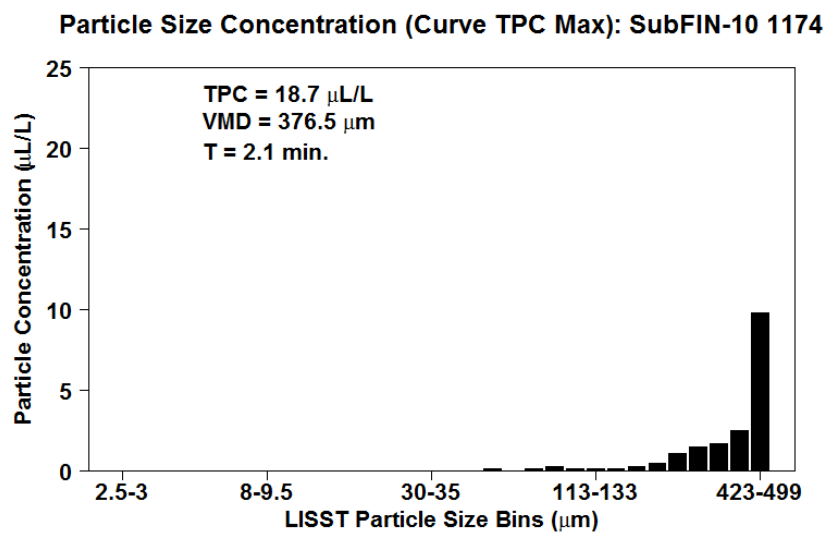


Figure C23. LISST DSD plot for IFO-120, DOR 1:200 (Finasol OSR 52), warm water experiments.

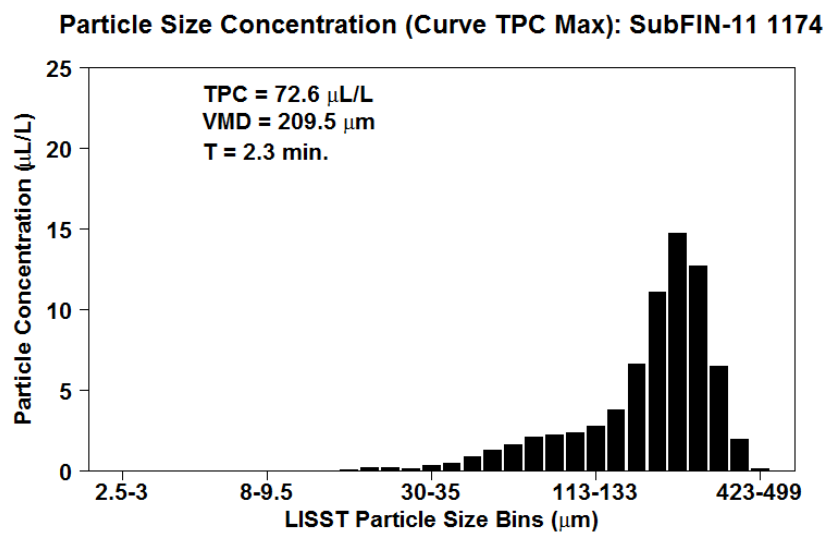


Figure C24. LISST DSD plot for IFO-120, DOR 1:100 (Finasol OSR 52), warm experiments.

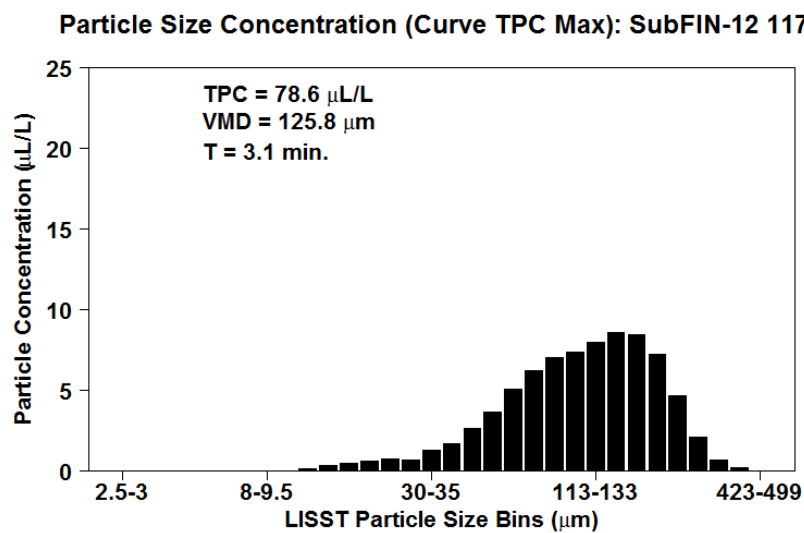


Figure C25. LISST DSD plot for IFO-120, DOR 1:20 (Finasol OSR 52), warm experiments.

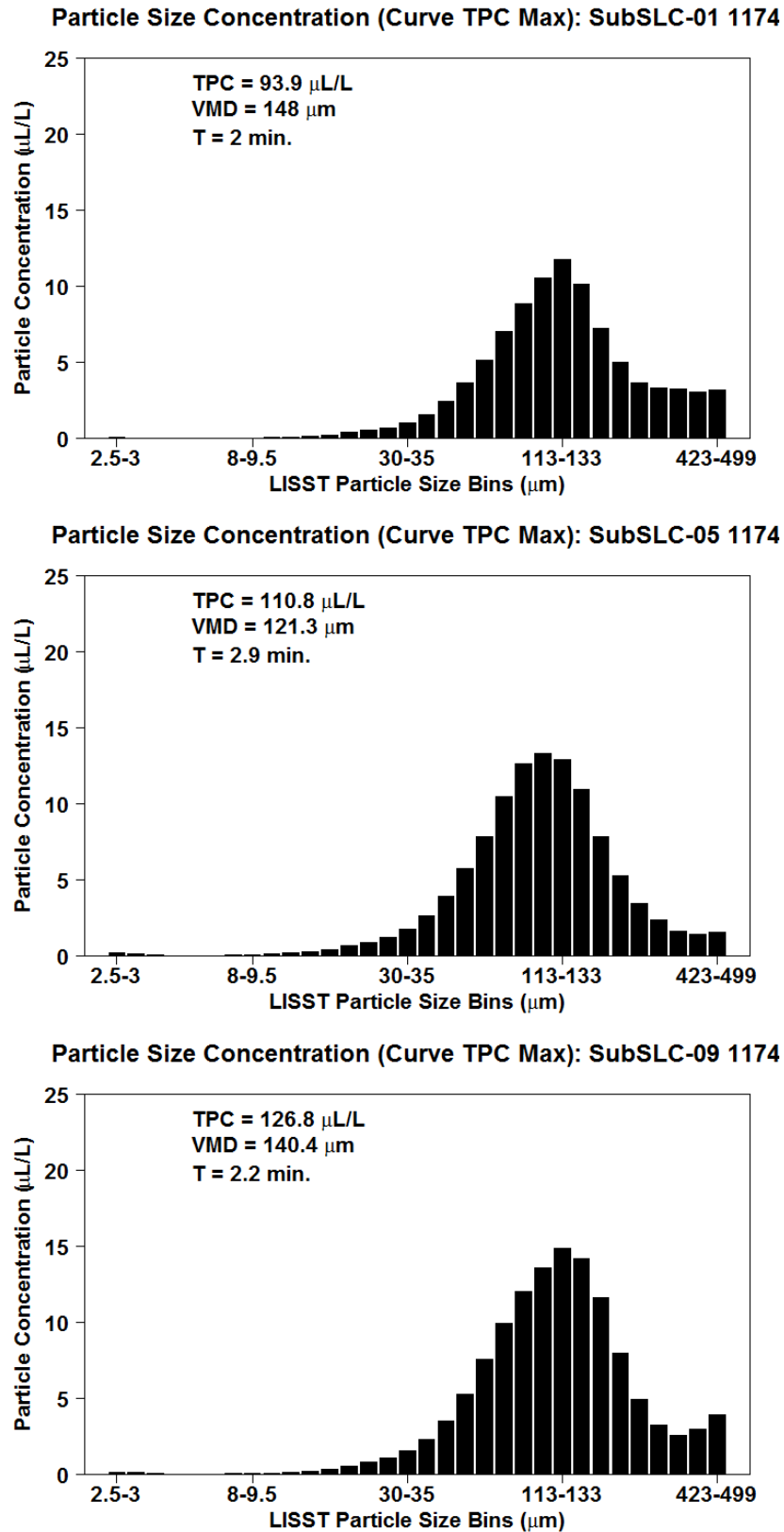


Figure C26. LISST DSD plot for SLC, no dispersant, warm water experiments.

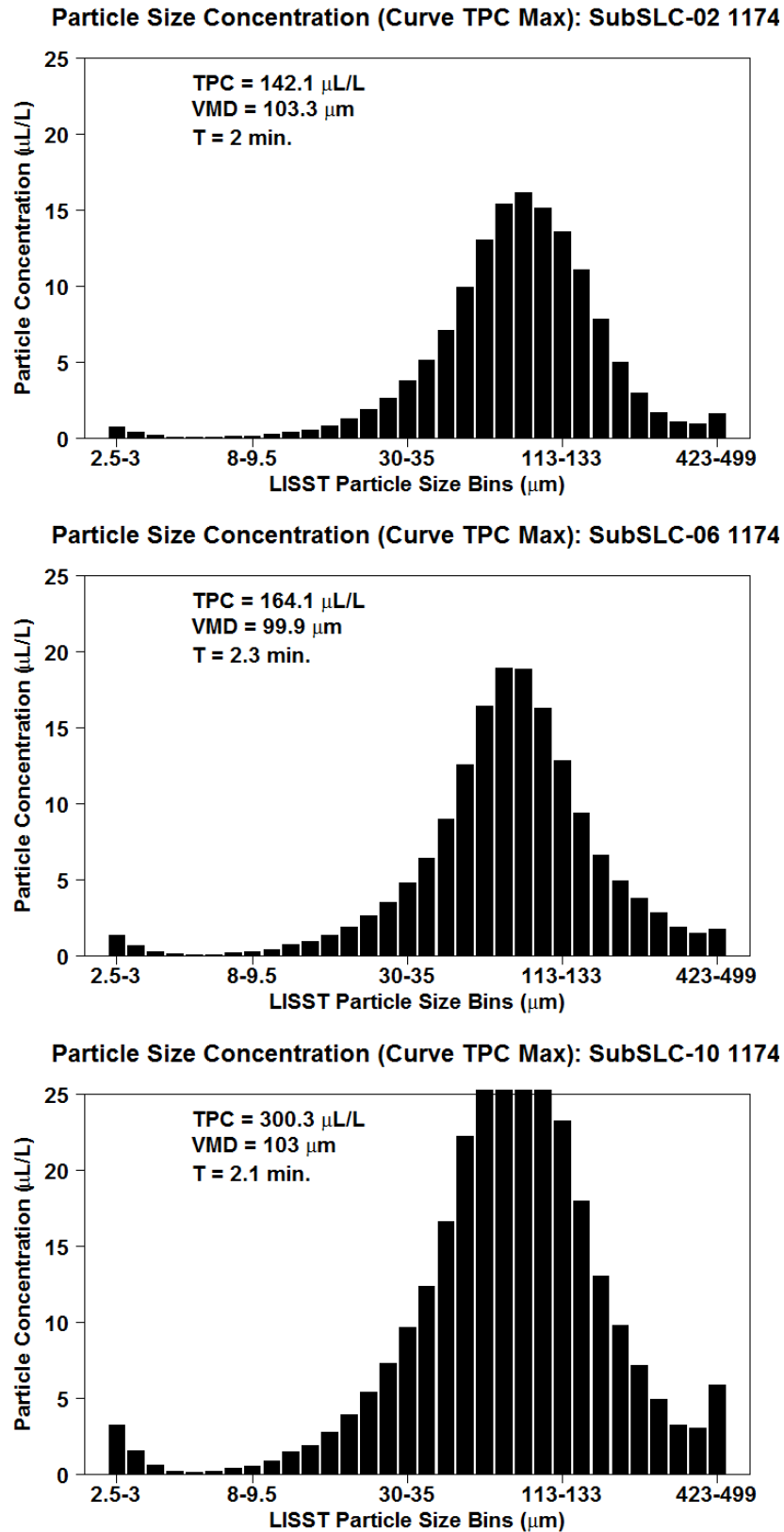


Figure C27. LISST DSD plot for SLC, DOR 1:200 (Corexit 9500), warm water experiments.

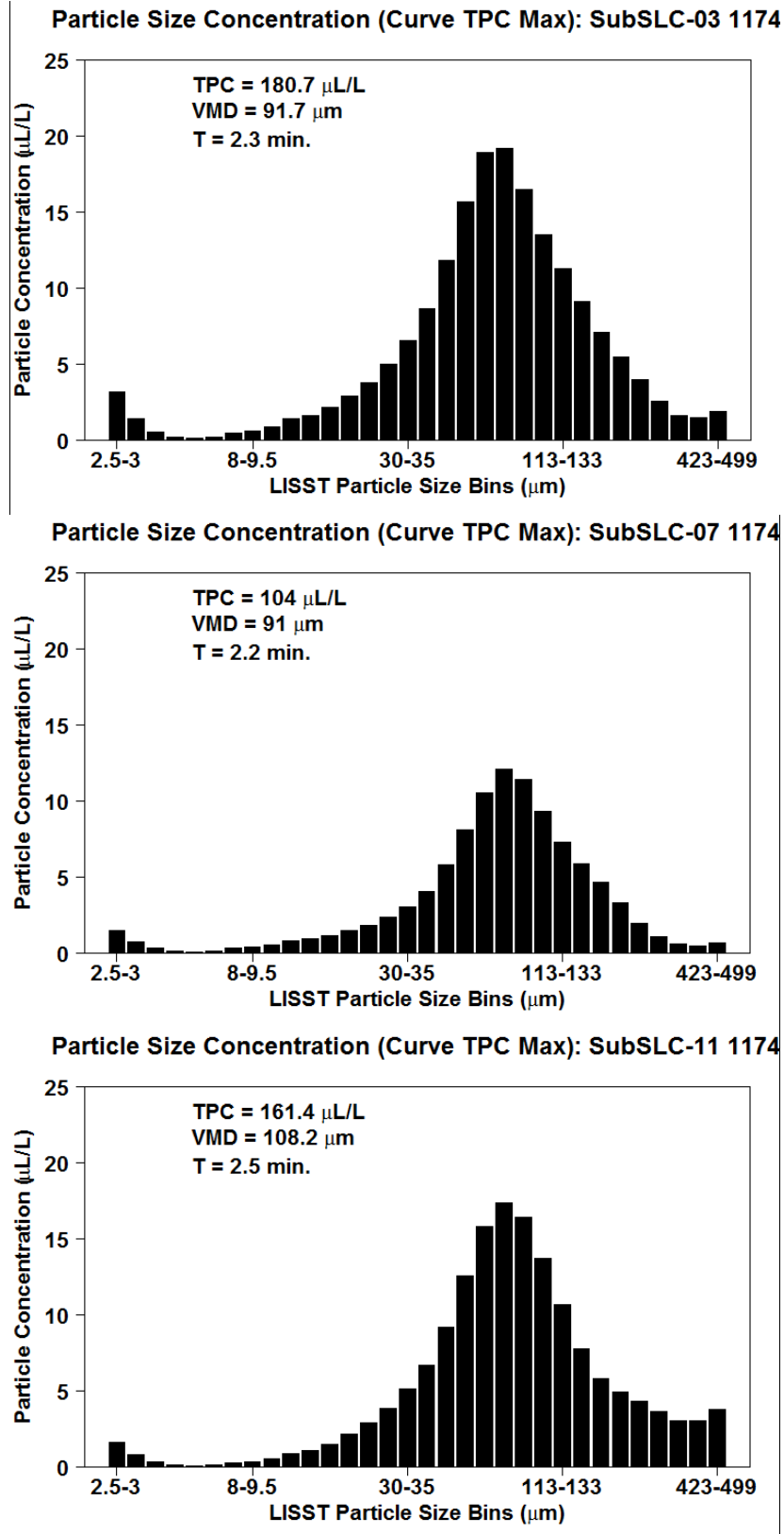
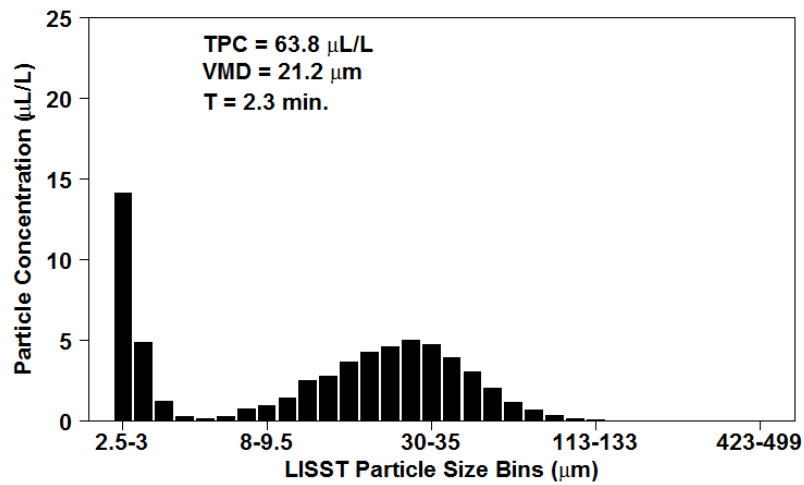
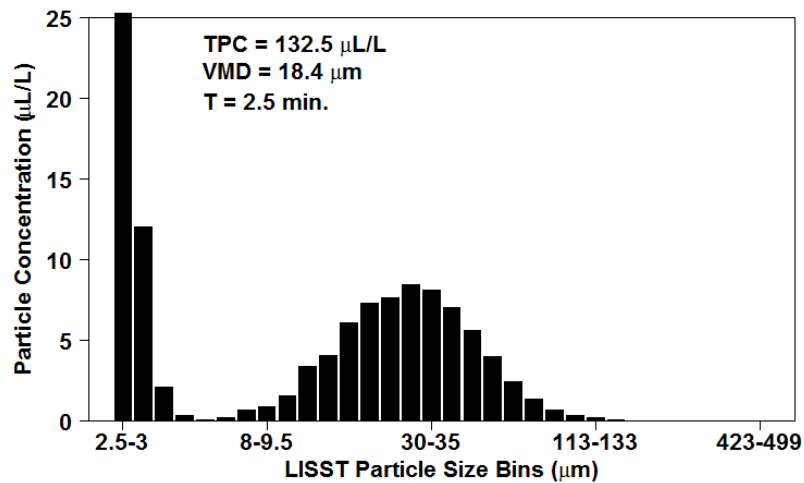


Figure C28. LISST DSD plot for SLC, DOR 1:100 (Corexit 9500), warm water experiments.

Particle Size Concentration (Curve TPC Max): SubSLC-04R 117.



Particle Size Concentration (Curve TPC Max): SubSLC-08R 117.



Particle Size Concentration (Curve TPC Max): SubSLC-12R 117.

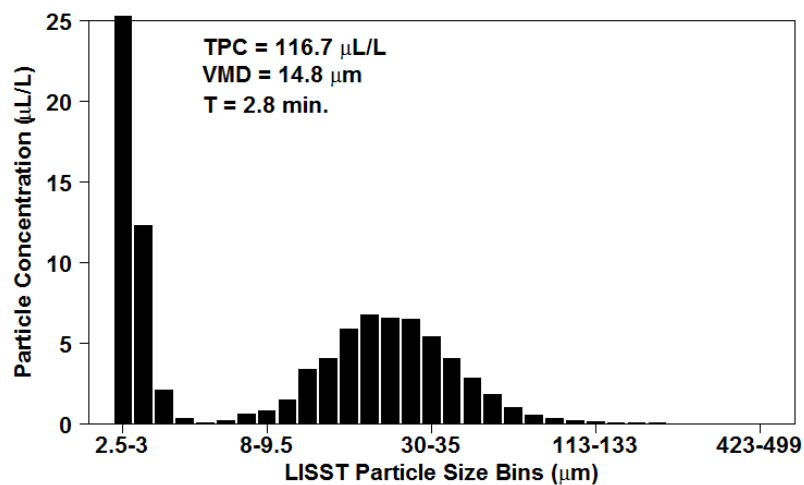


Figure C29. LISST DSD plot for SLC, DOR 1:20 (Corexit 9500), warm water experiments.

APPENDIX D – Jet Release LISST Oil Droplet Size Distribution Time Series Contours

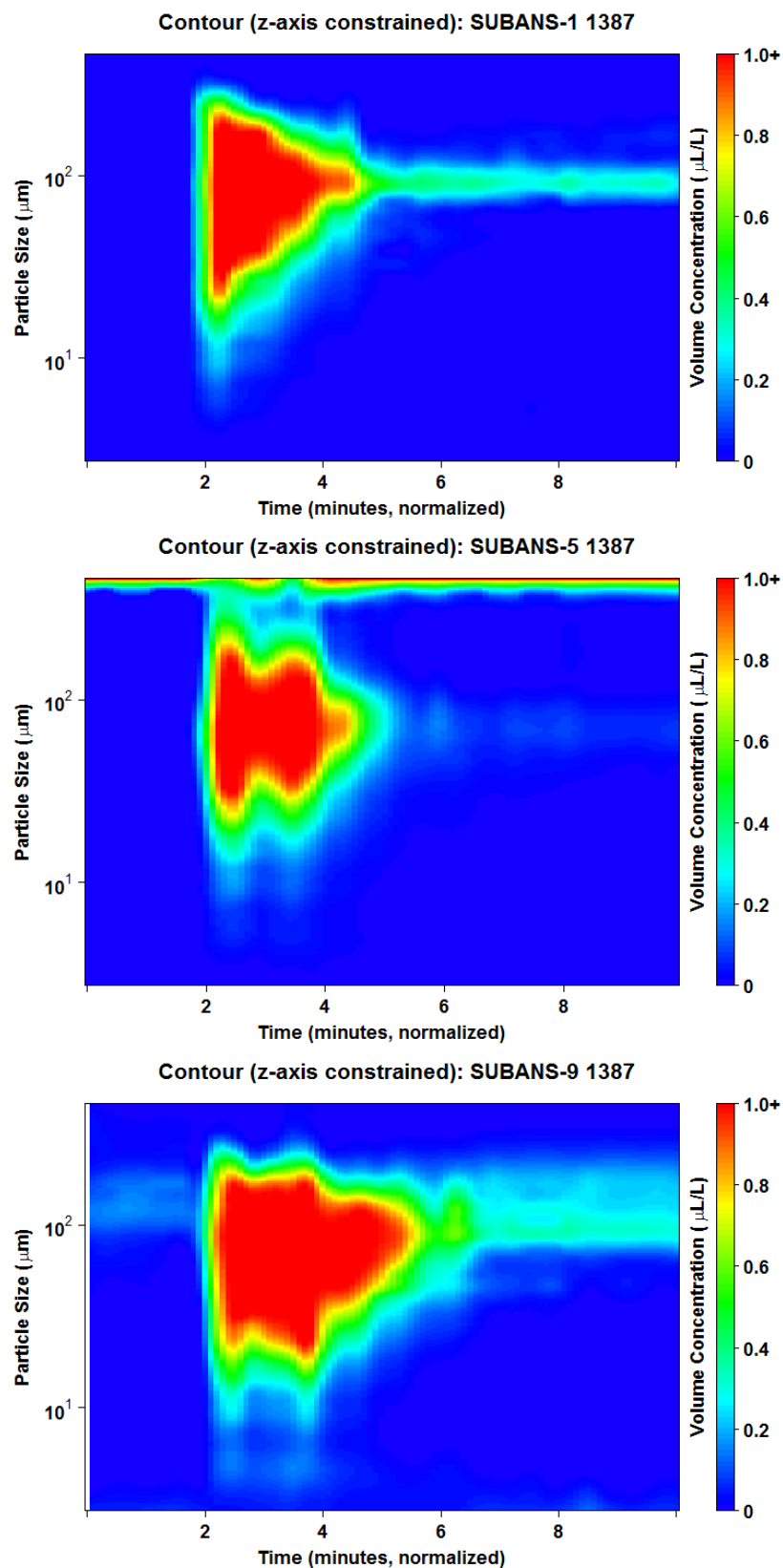
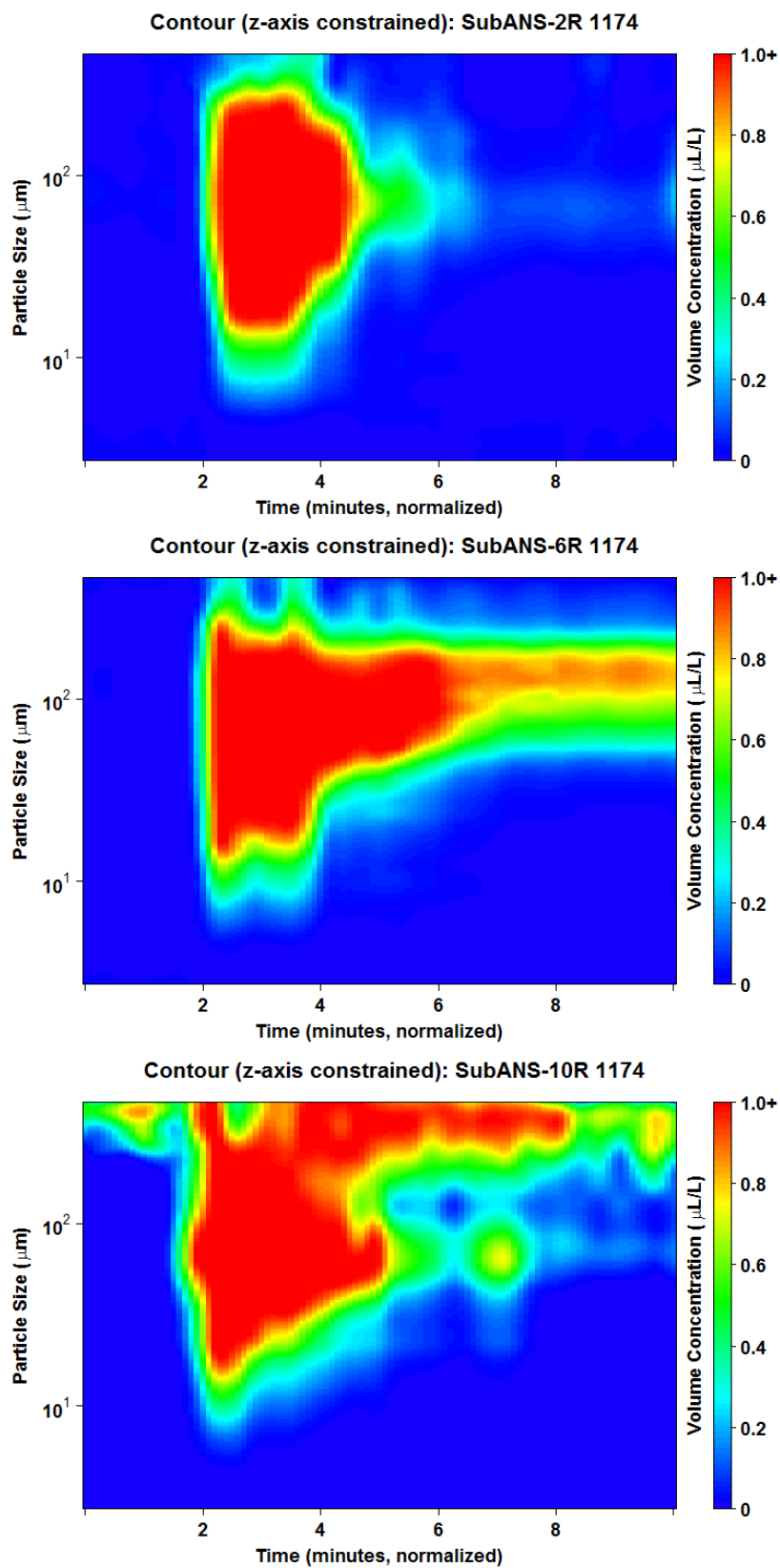


Figure D1. LISST contour plot for ANS, no dispersant, cold water experiments.



FigureD2. LISST contour plot for ANS, DOR 1:200 (Corexit 9500), cold water experiment.

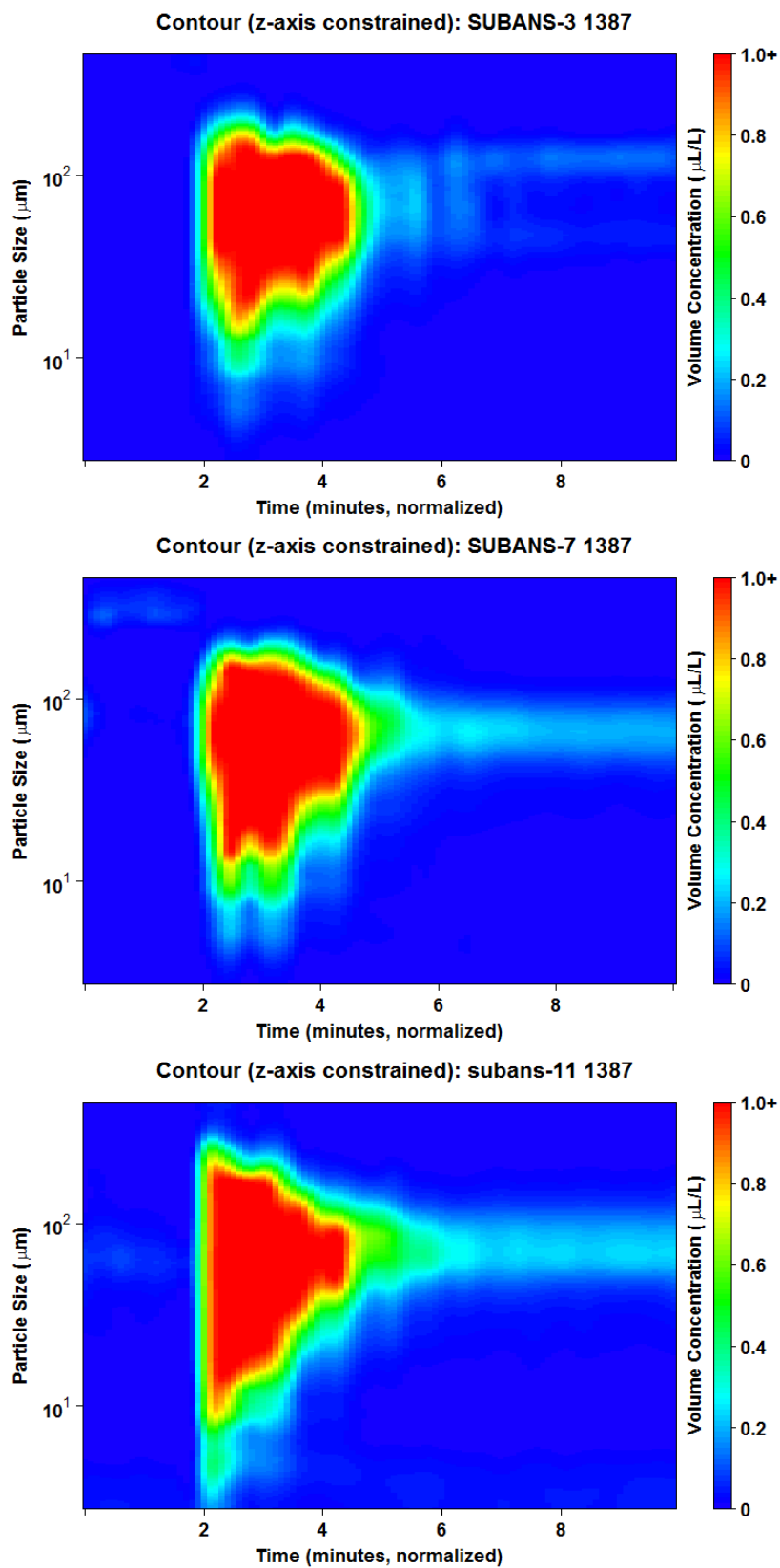


Figure D3. LISST contour plot for ANS, DOR 1:100 (Corexit 9500), cold water experiment.

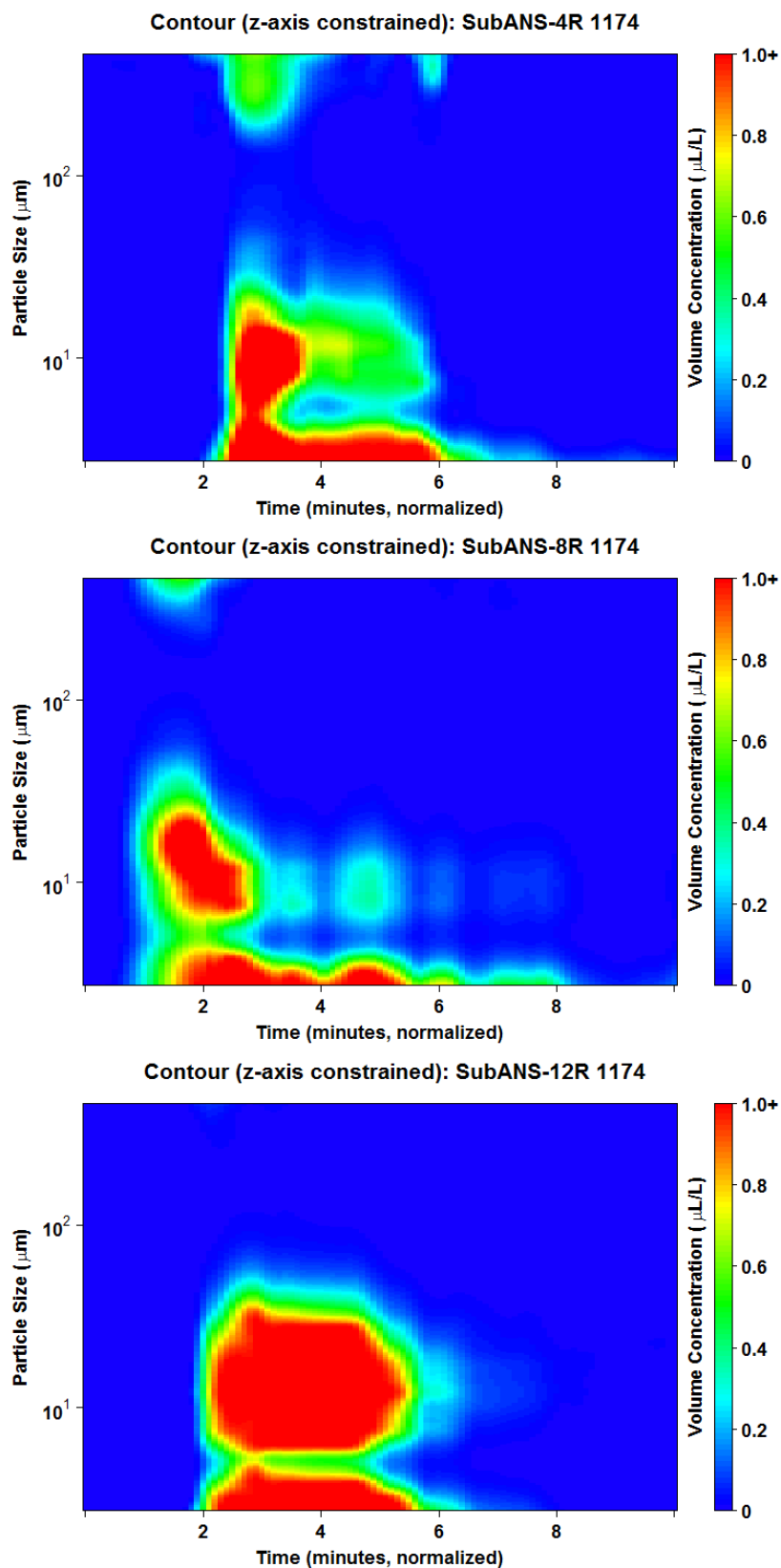


Figure D4. LISST contour plot for ANS, DOR 1:20 (Corexit 9500), cold water experiment.

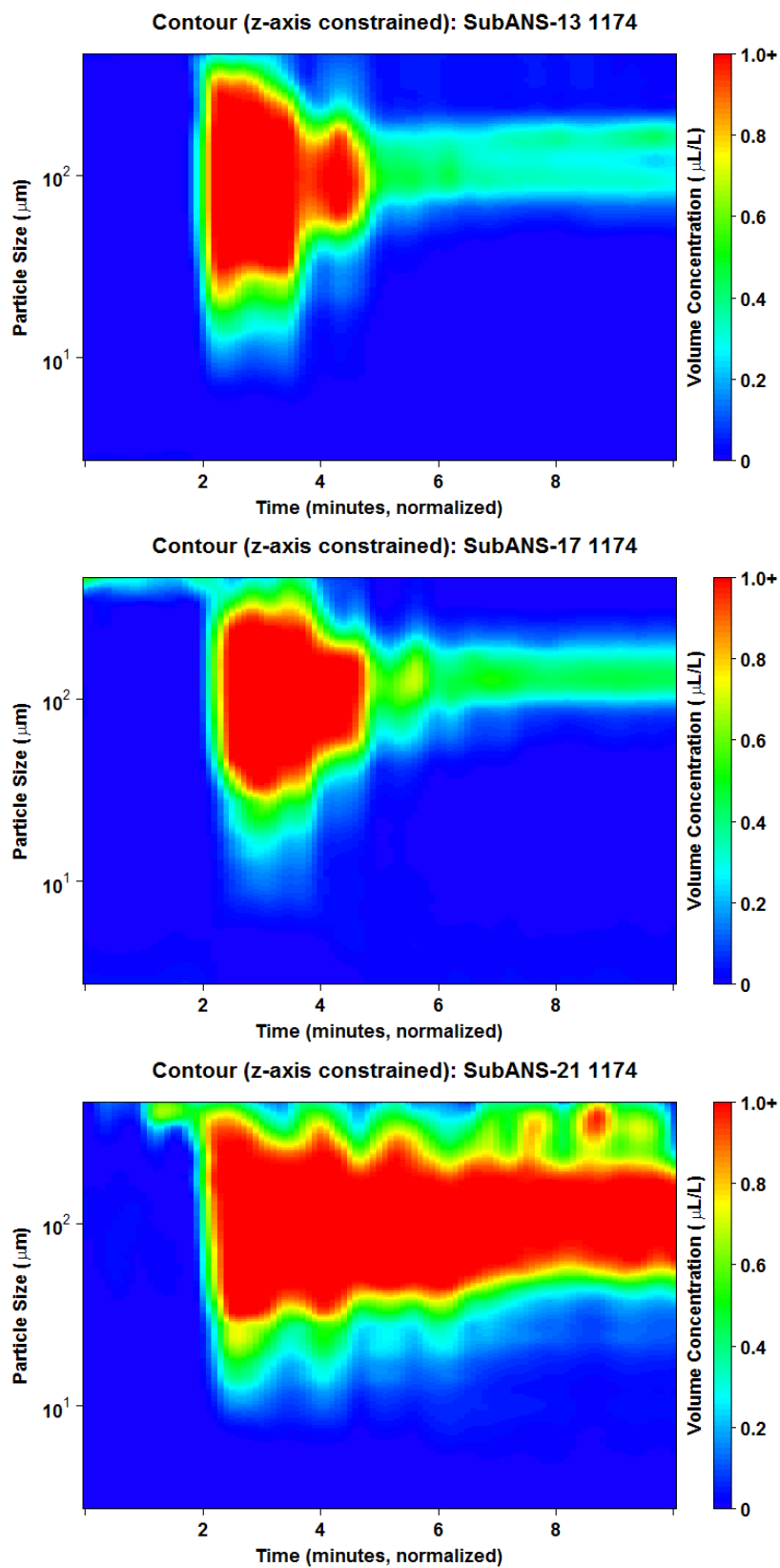


Figure D5. LISST contour plot for ANS, no dispersant (Corexit 9500), warm experiment.

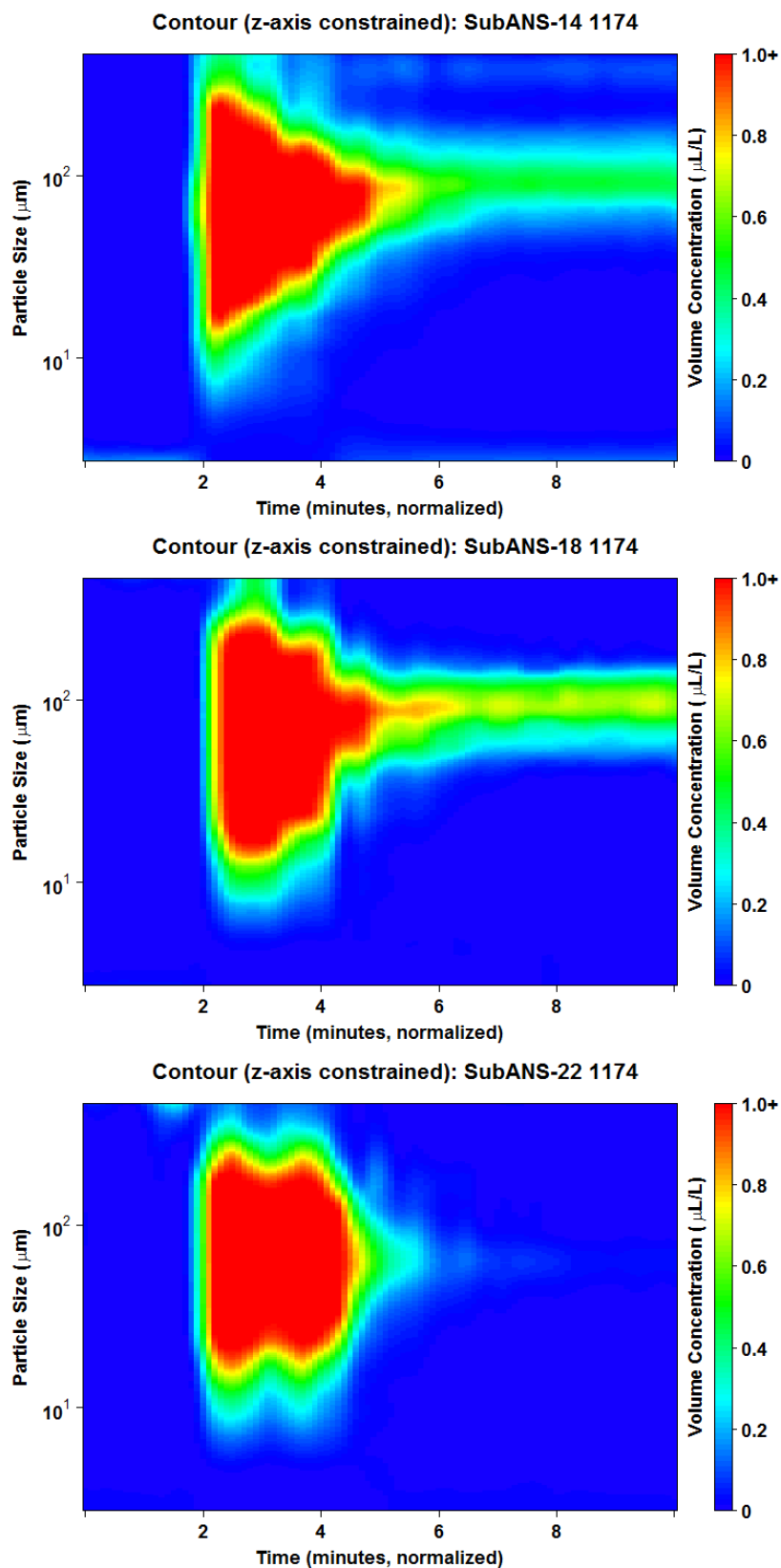


Figure D6. LISST contour plot for ANS, DOR 1:200 (Corexit 9500), warm experiment.

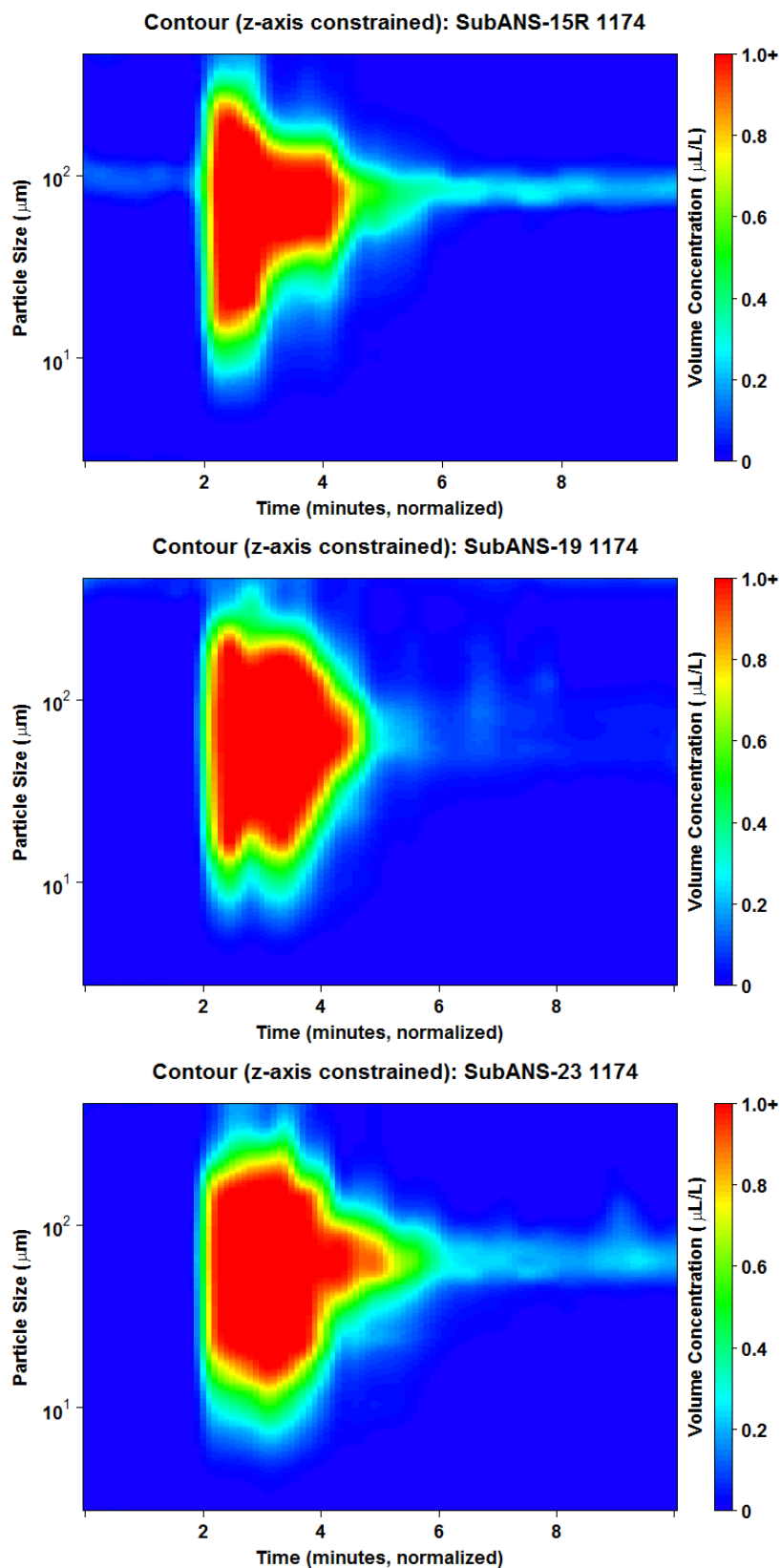


Figure D7. LISST contour plot for ANS, DOR 1:100 (Corexit 9500), warm experiment.

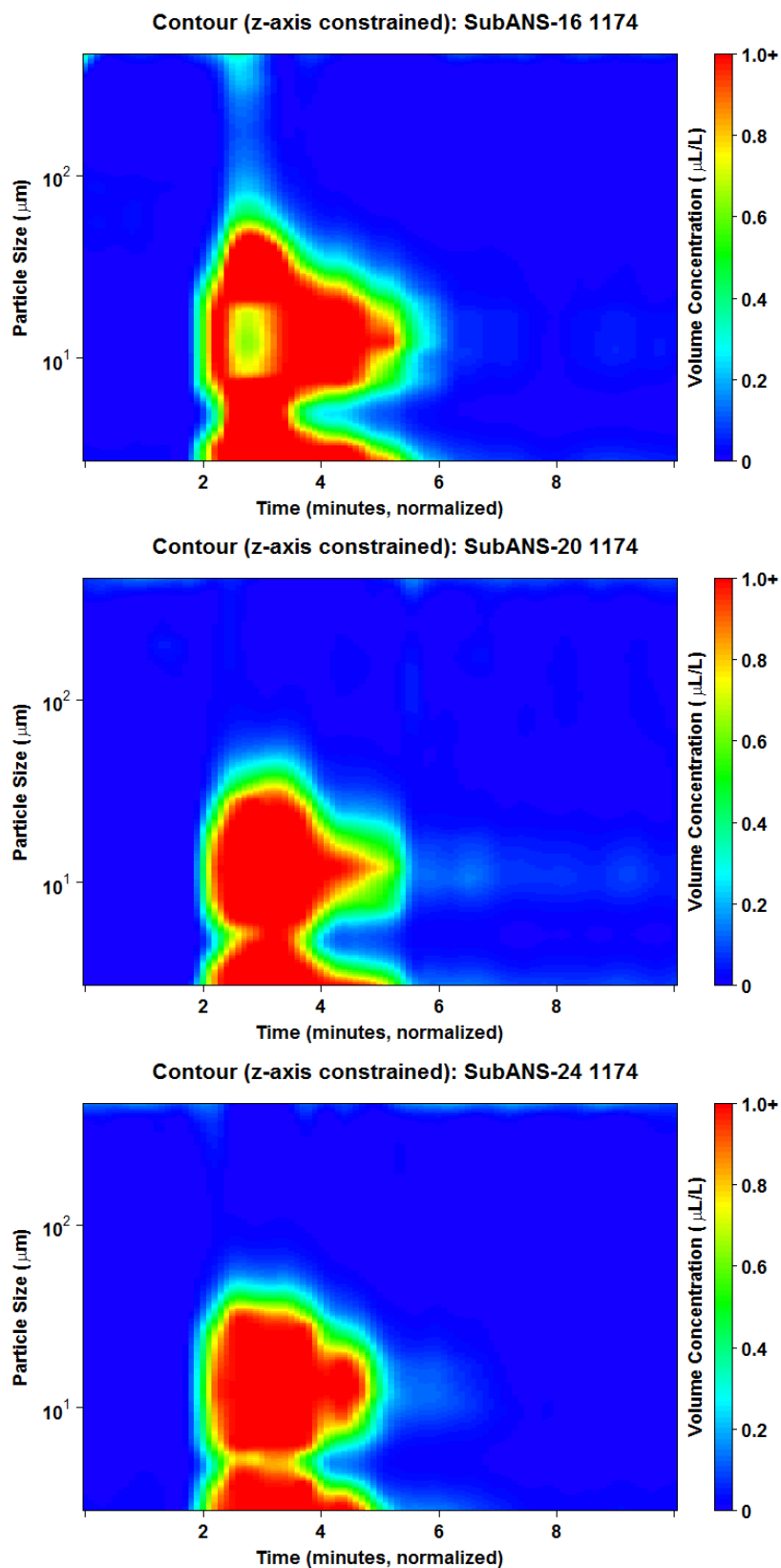


Figure D8. LISST contour plot for ANS, DOR 1:20 (Corexit 9500), warm experiment.

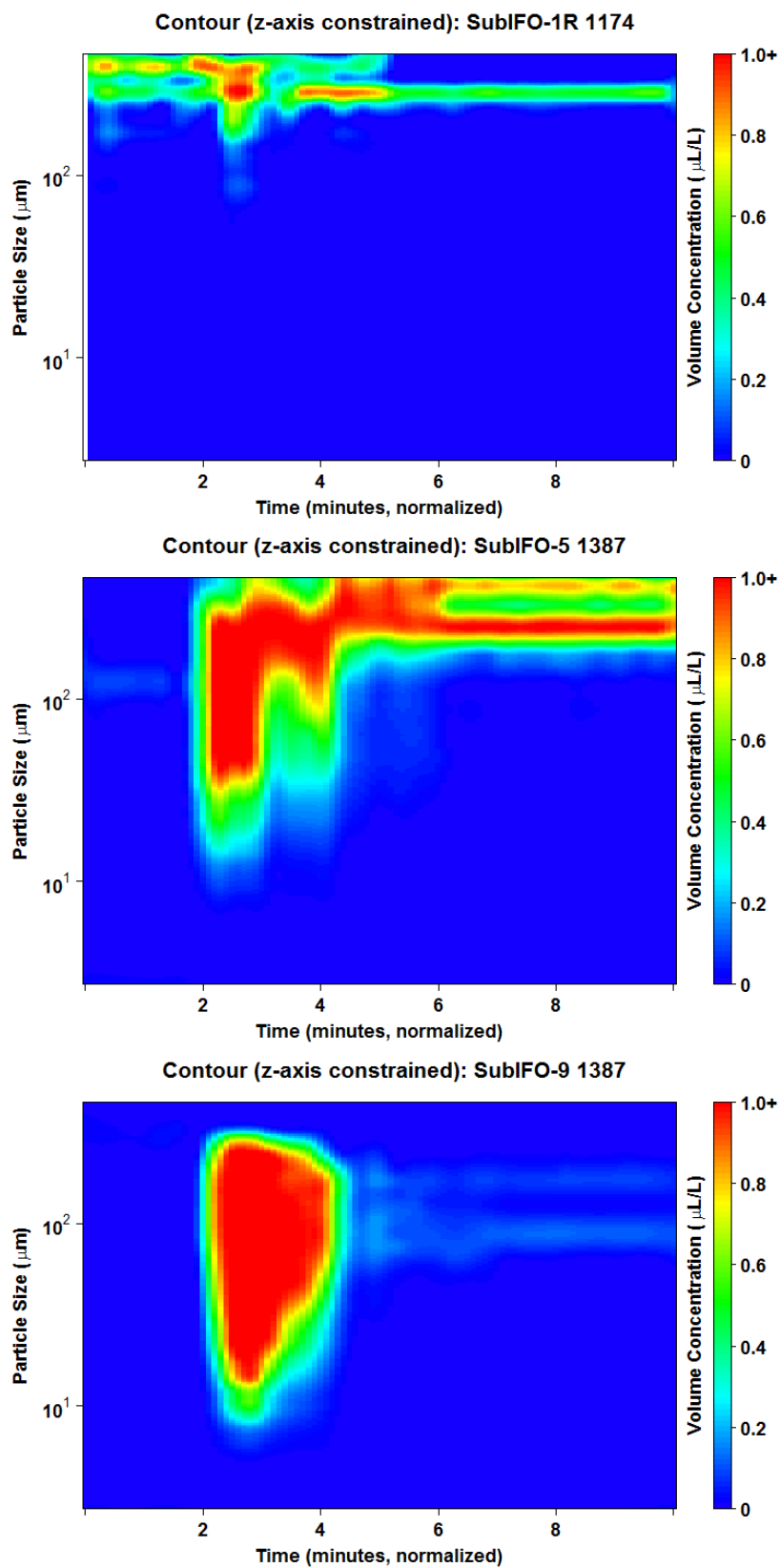


Figure D9. LISST contour plot for IFO-120, no dispersant, cold water experiment.

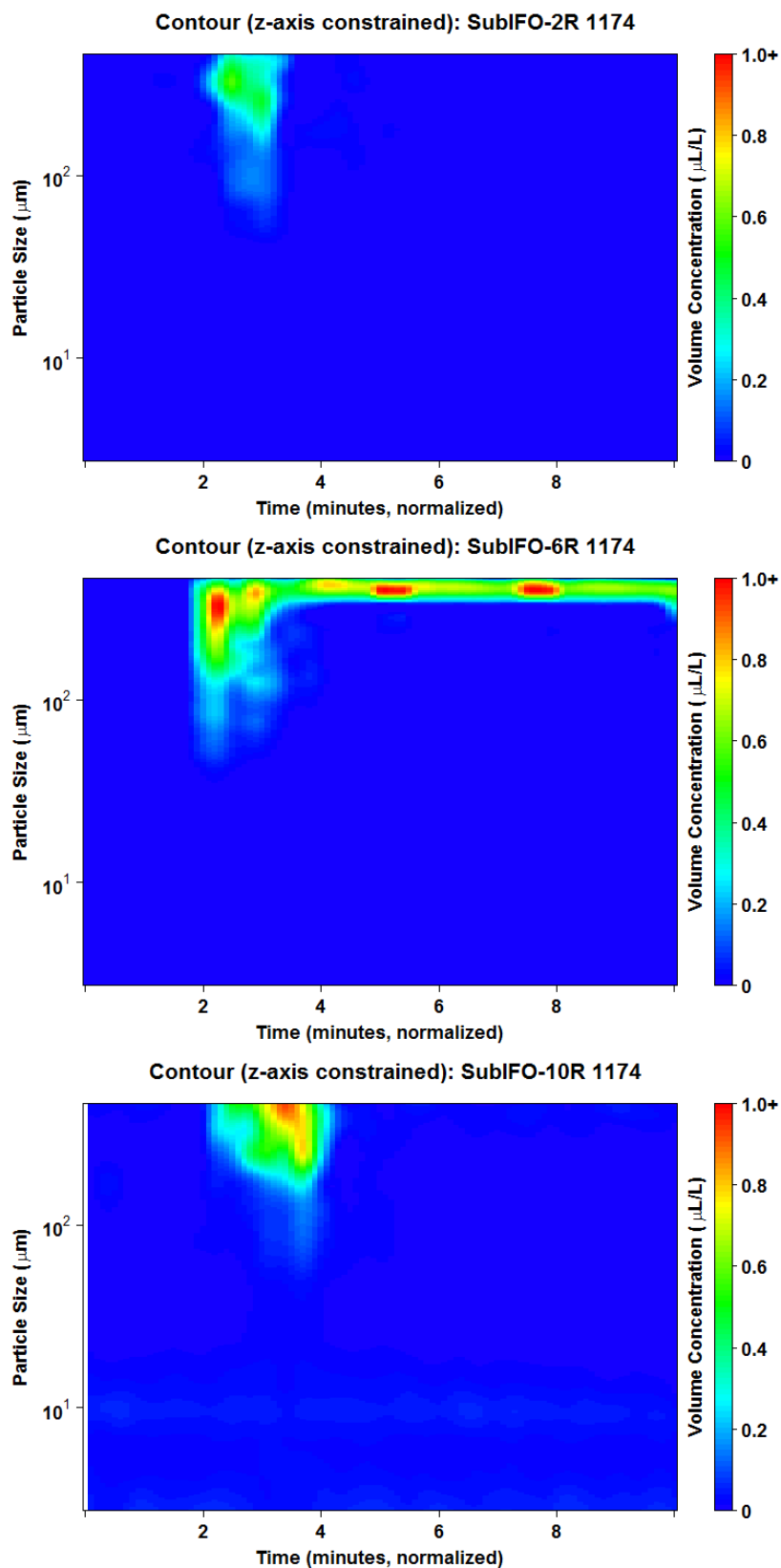


Figure D10. LISST contour plot for IFO-120, DOR 1:200 (Corexit 9500), cold experiment.

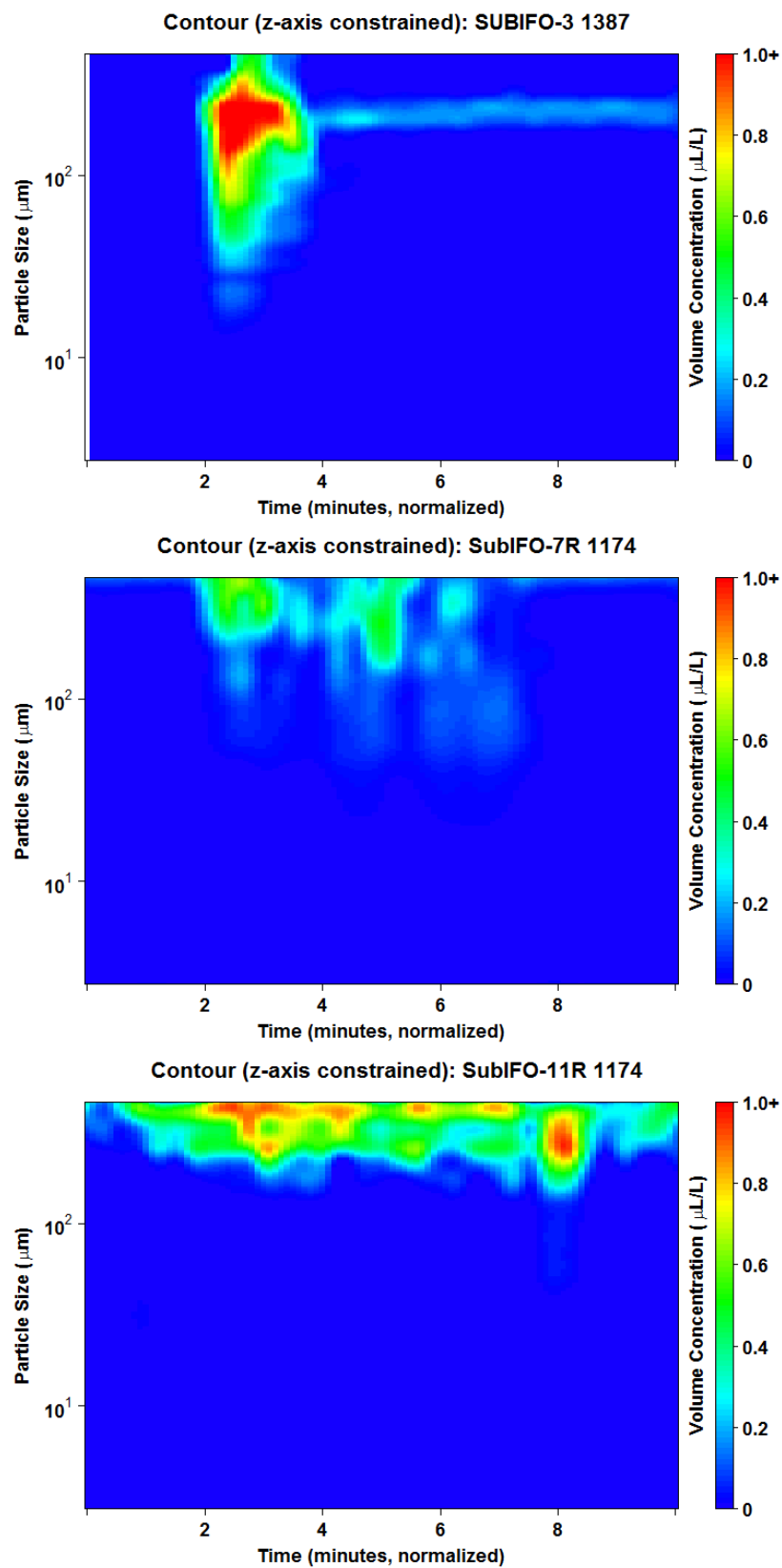


Figure D11. LISST contour plot for IFO-120, DOR 1:100 (Corexit 9500), cold experiment.

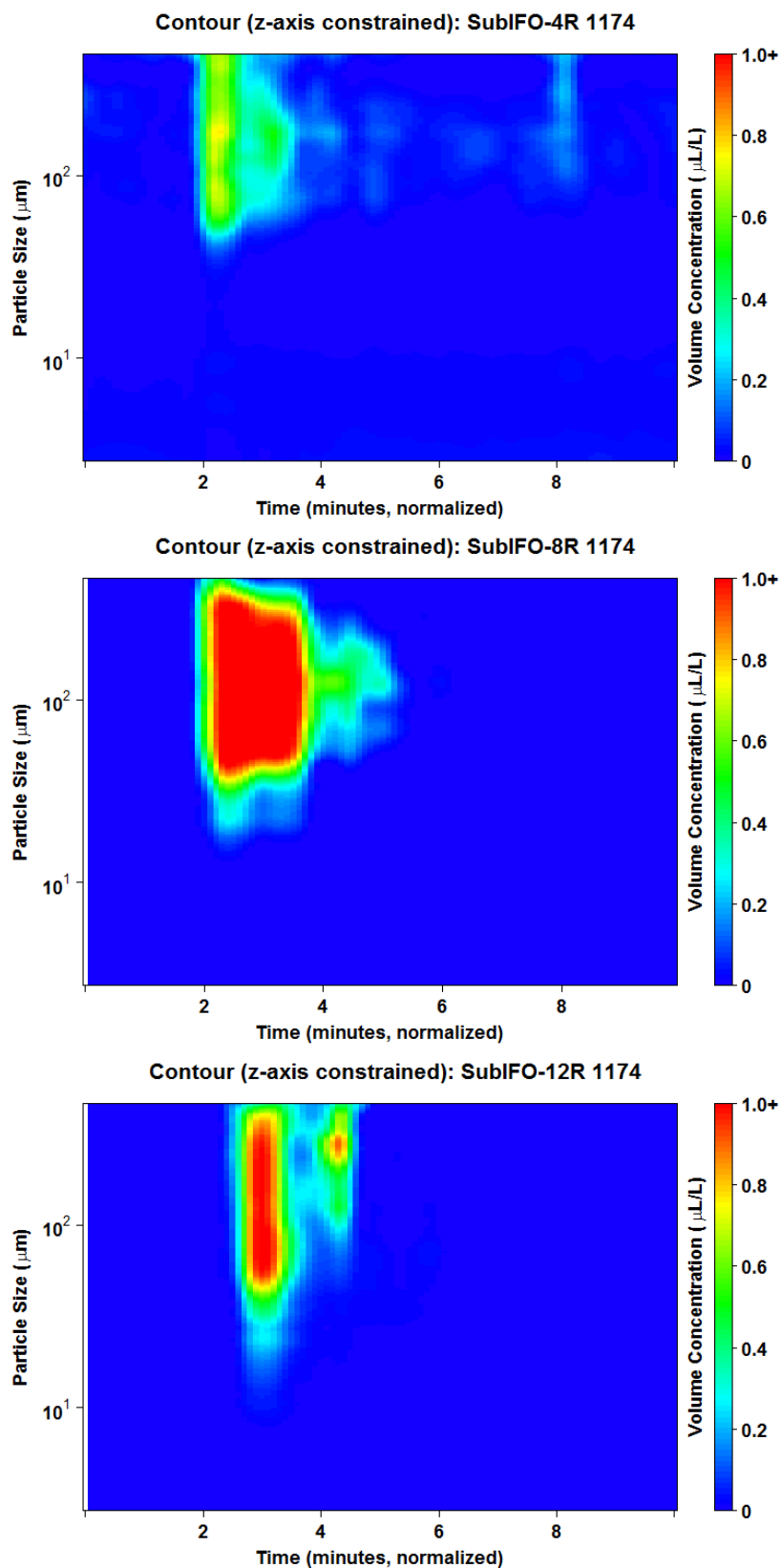


Figure D12. LISST contour plot for IFO-120, DOR 1:20 (Corexit 9500), cold experiment.

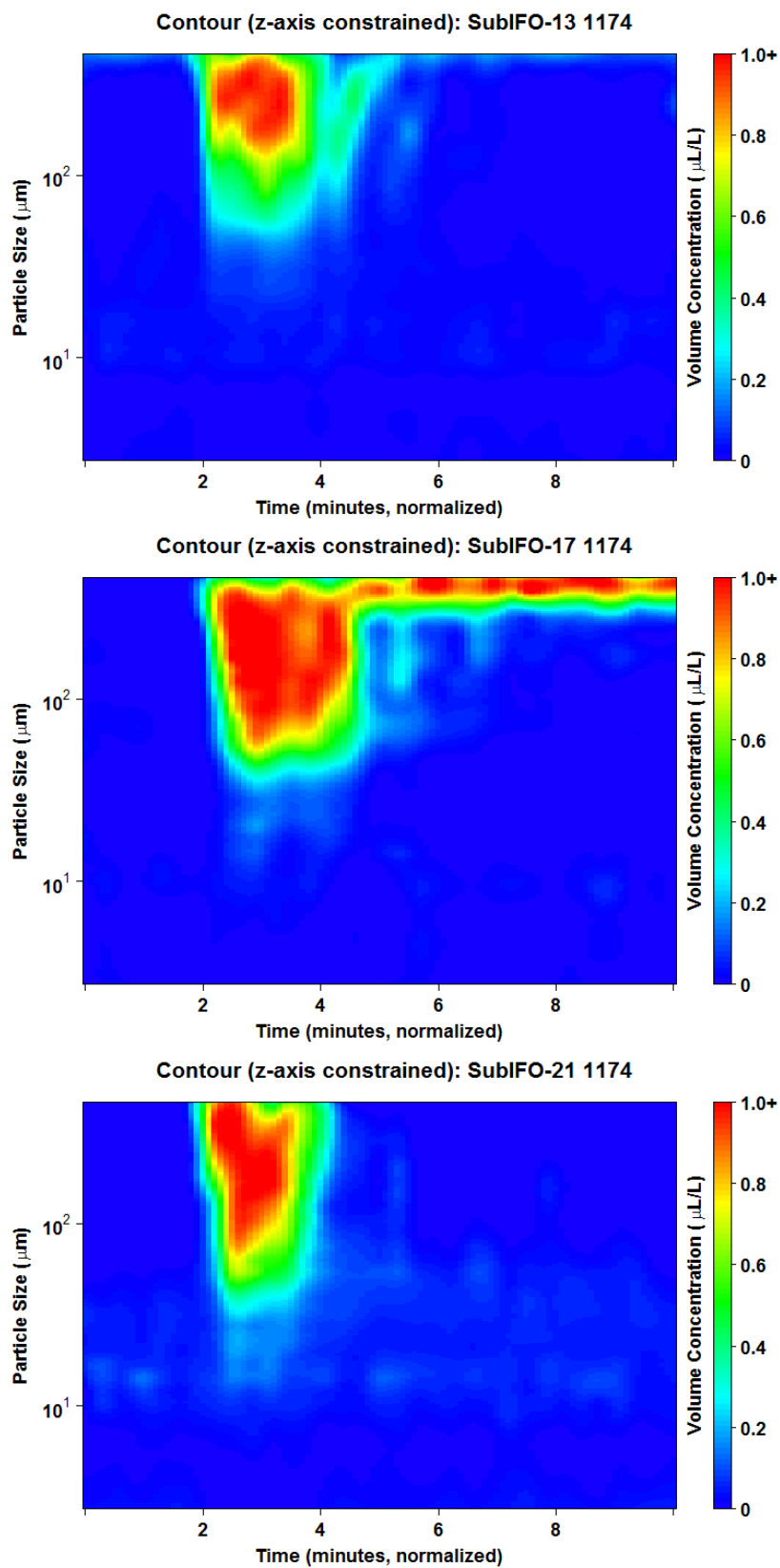


Figure D13. LISST contour plot for IFO-120, no dispersant, warm water experiment.

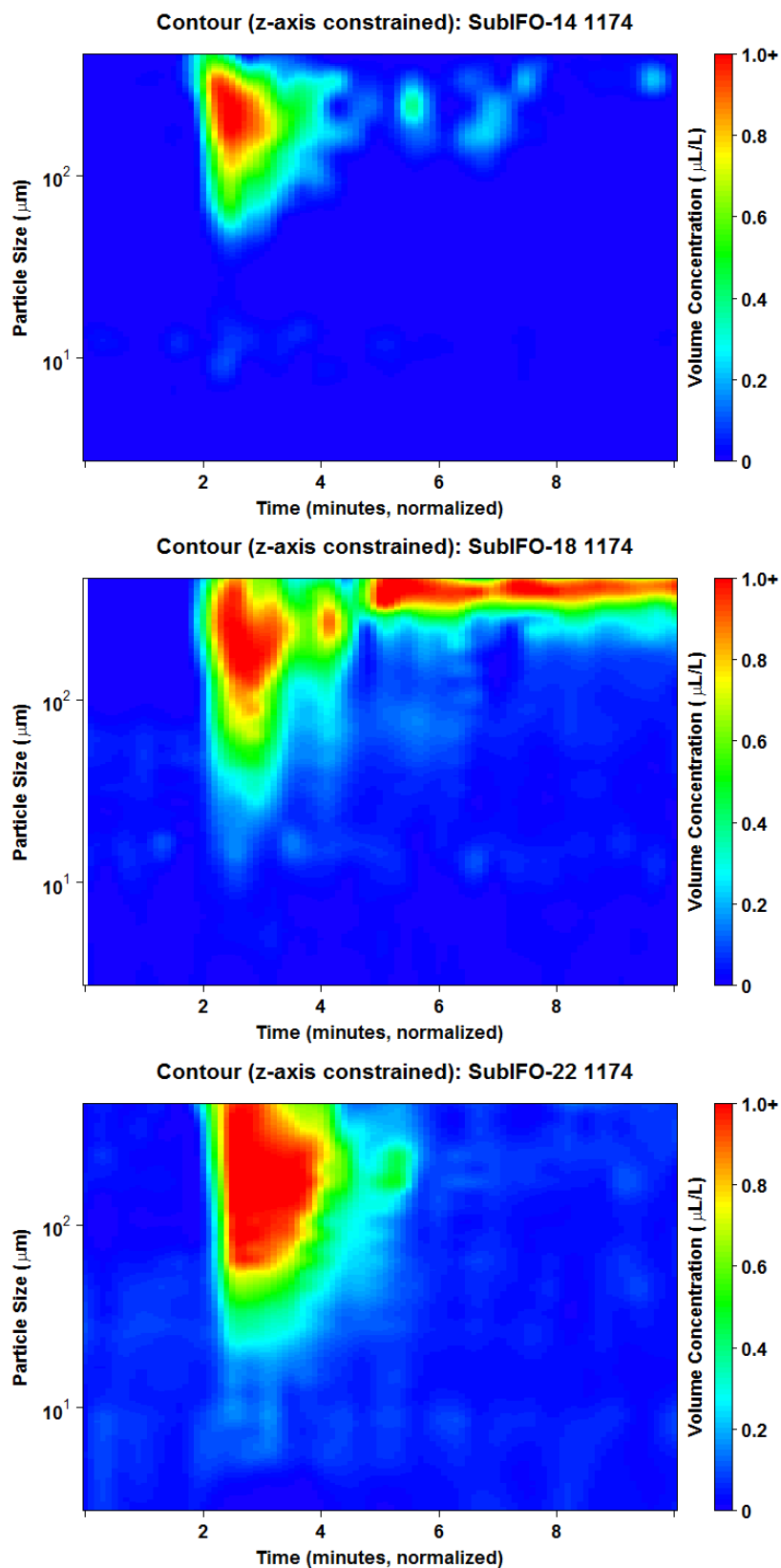


Figure D14. LISST contour plot for IFO-120, DOR 1:200 (Corexit 9500), warm experiment.

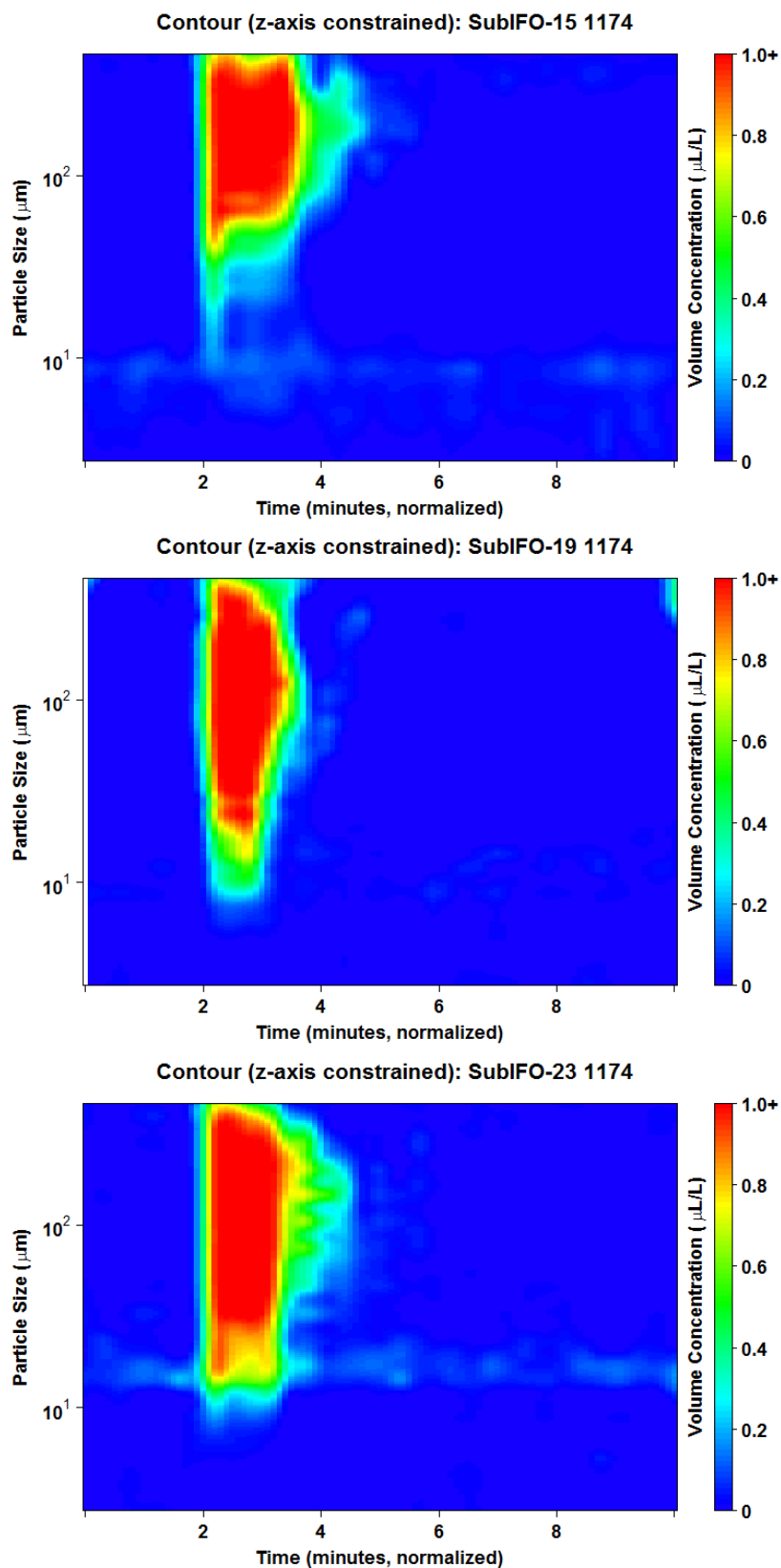


Figure D15. LISST contour plot for IFO-120, DOR 1:100 (Corexit 9500), warm experiment.

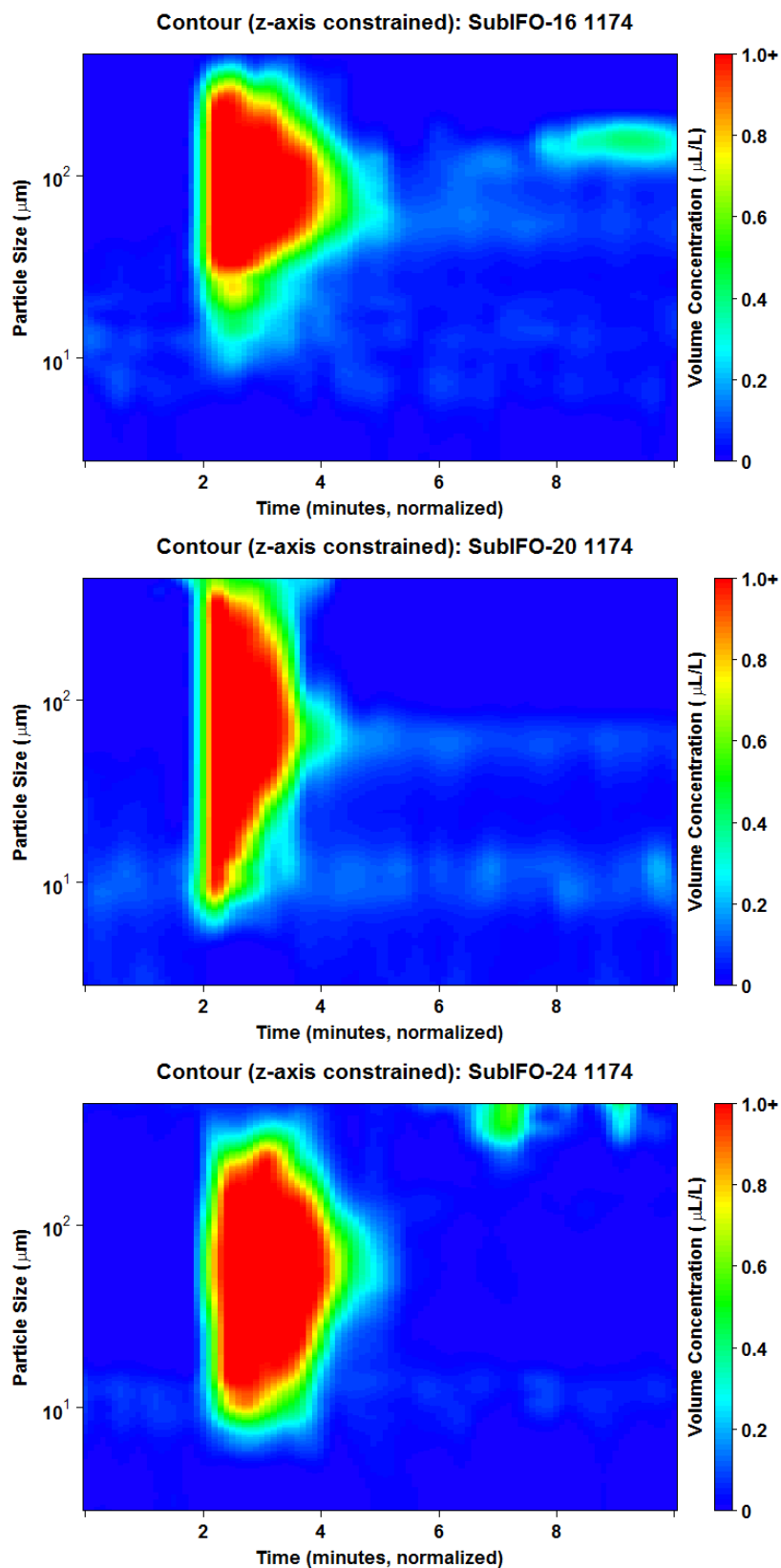


Figure D16. LISST contour plot for IFO-120, DOR 1:20 (Corexit 9500), warm experiment.

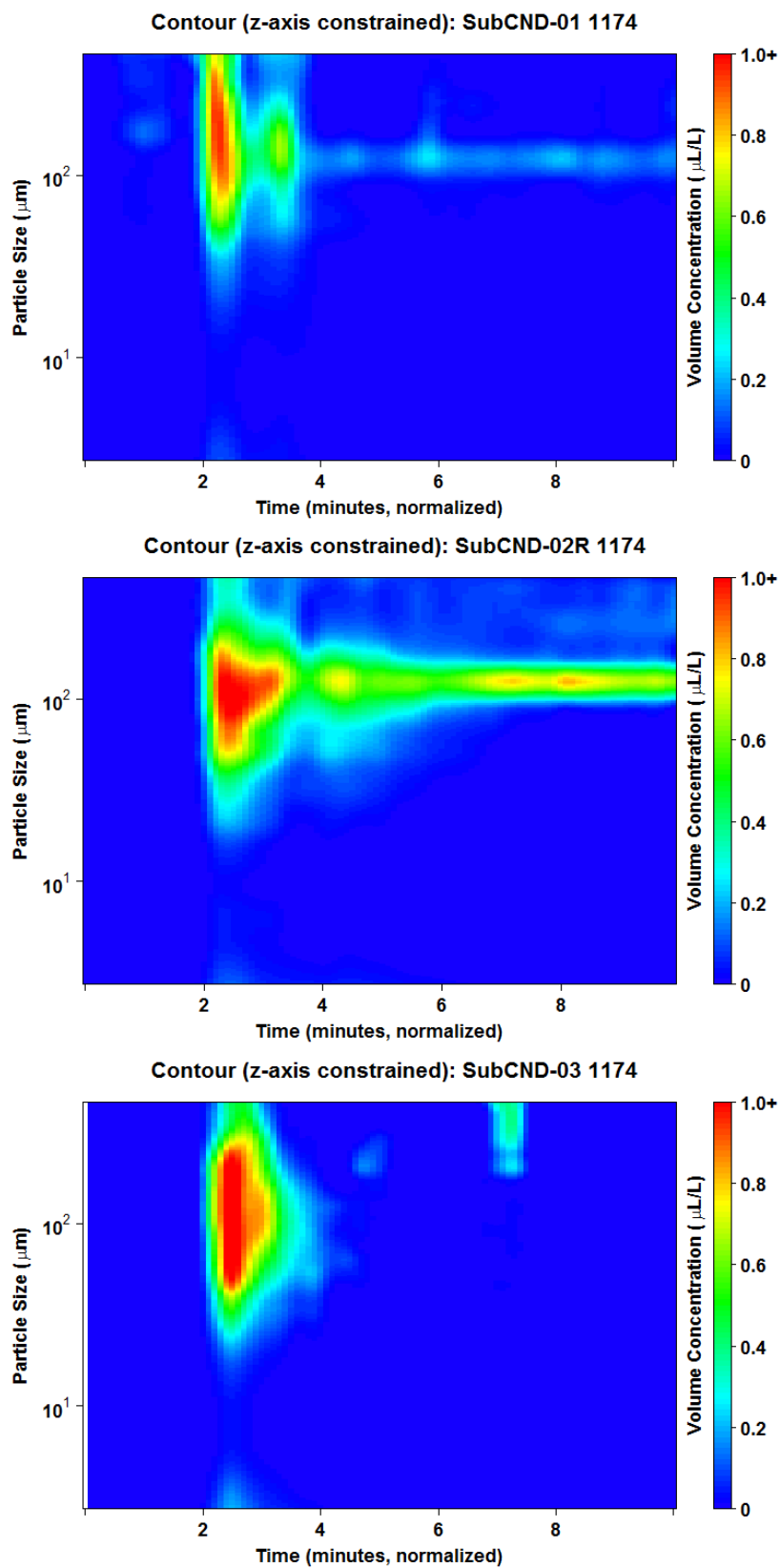


Figure D17. LISST contour plot for Gas Condensate, no dispersant.

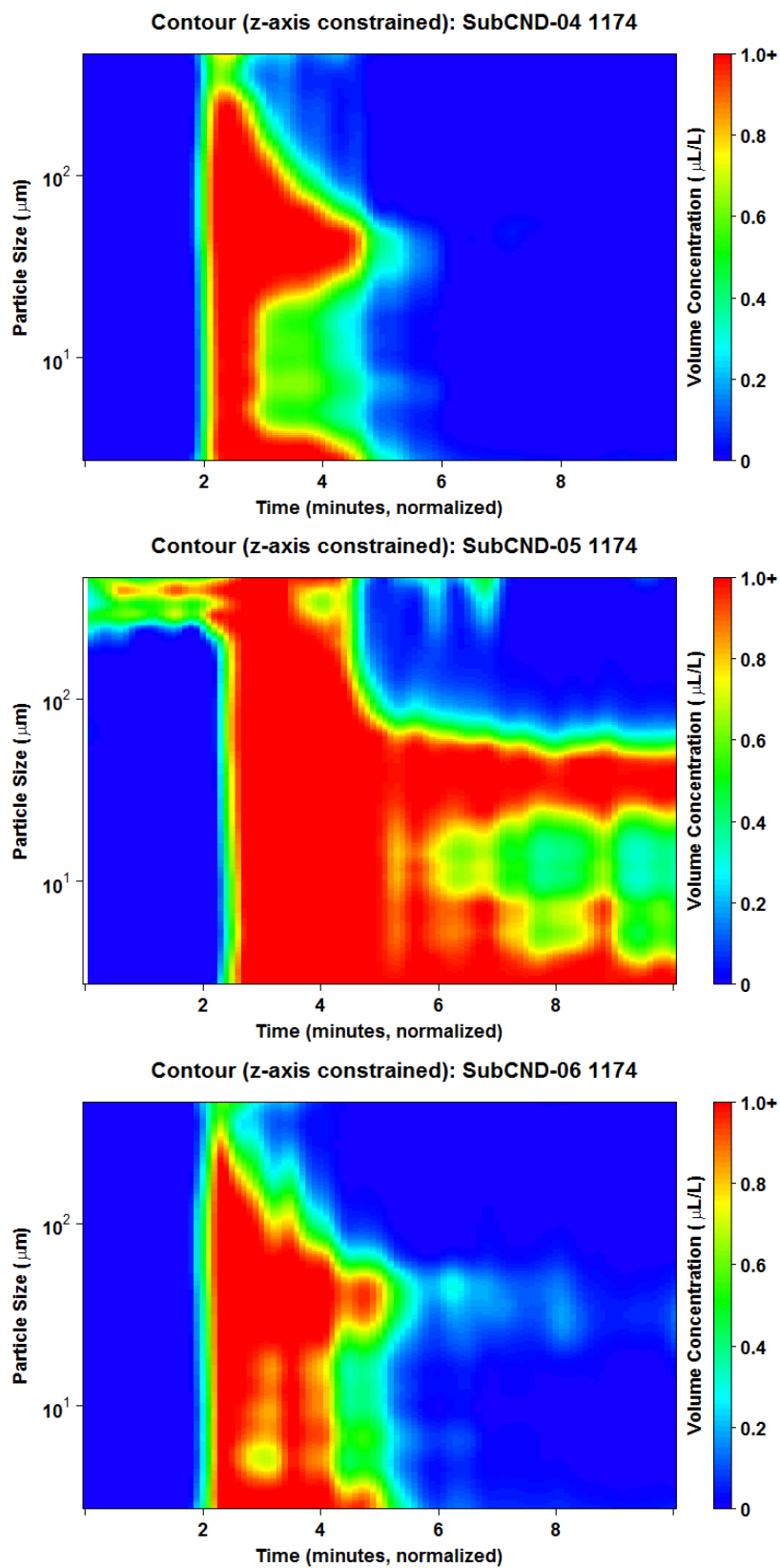


Figure D18. LISST contour plot for Gas Condensate, DOR 1:20 (Corexit 9500).

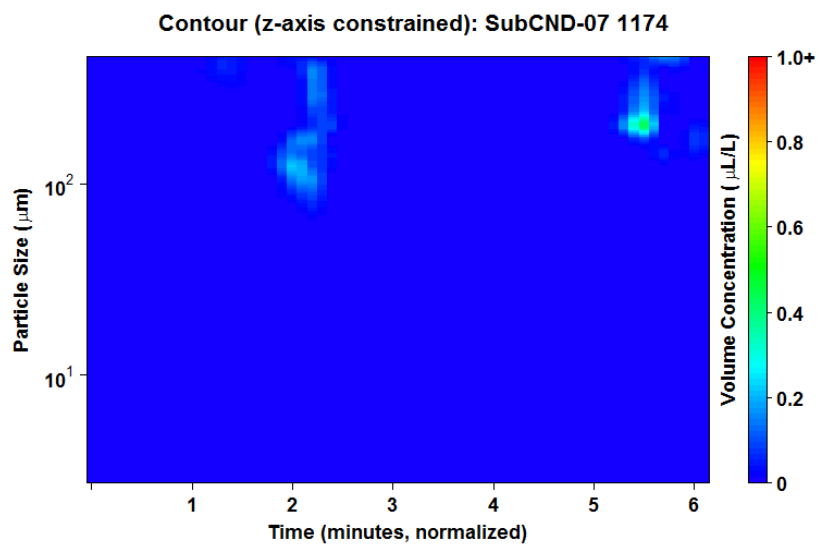


Figure D19. LISST contour plot for air injection, no dispersant.

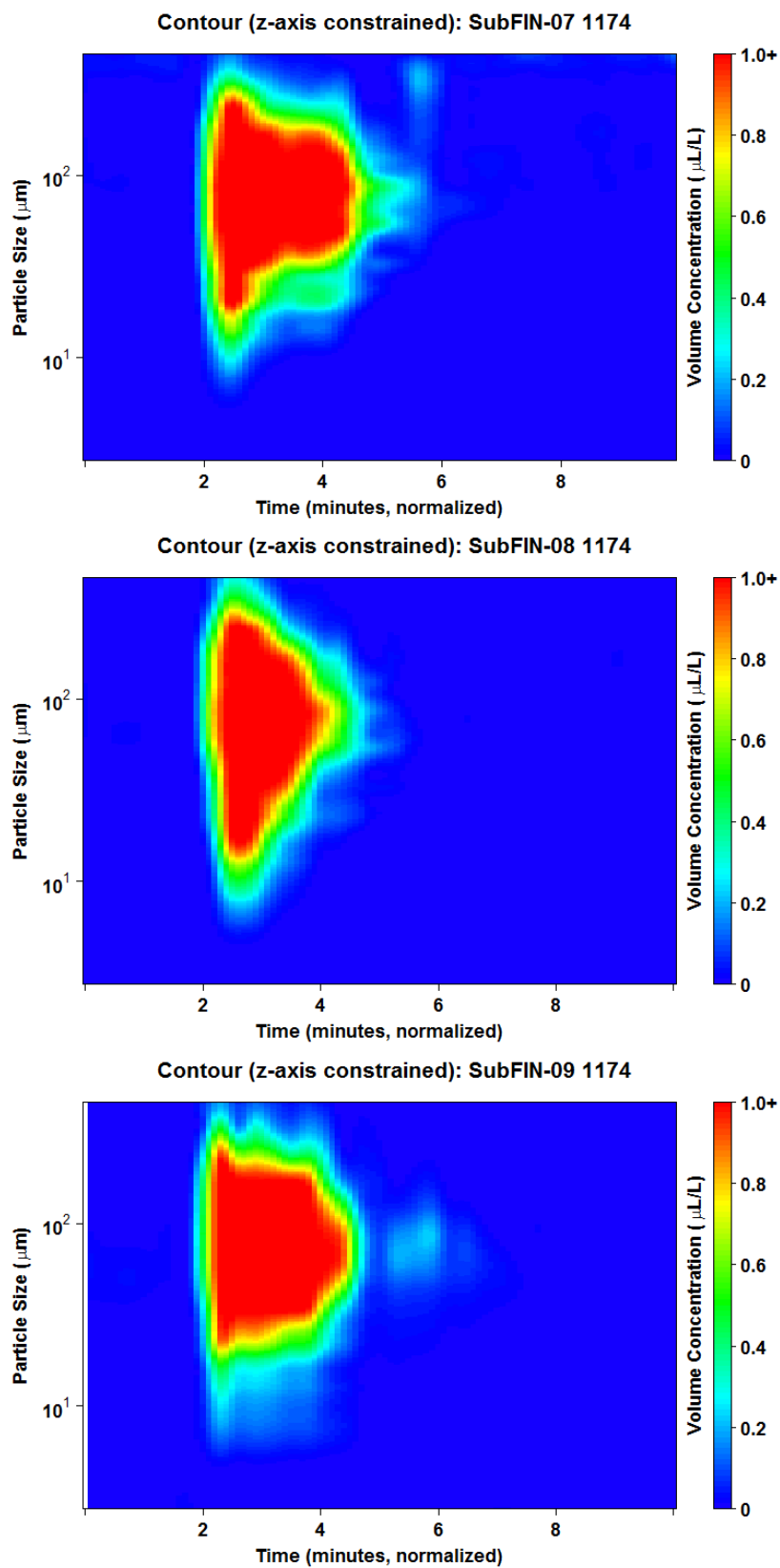


Figure D20. LISST contour plot for ANS, DOR 1:200 (Finasol OSR 52), warm experiment.

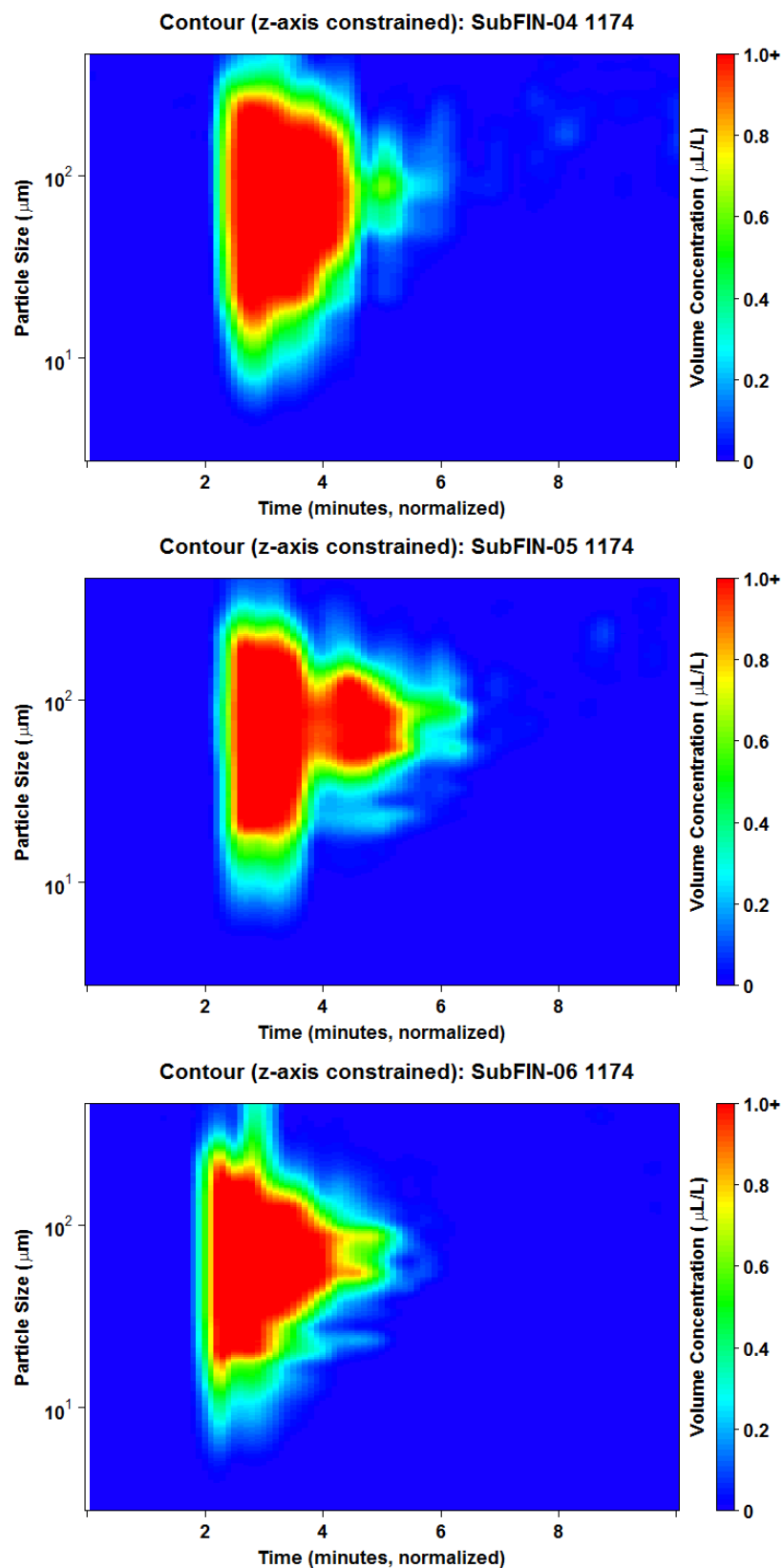


Figure D21. LISST contour plot for ANS, DOR 1:100 (Finasol OSR 52), warm experiment.

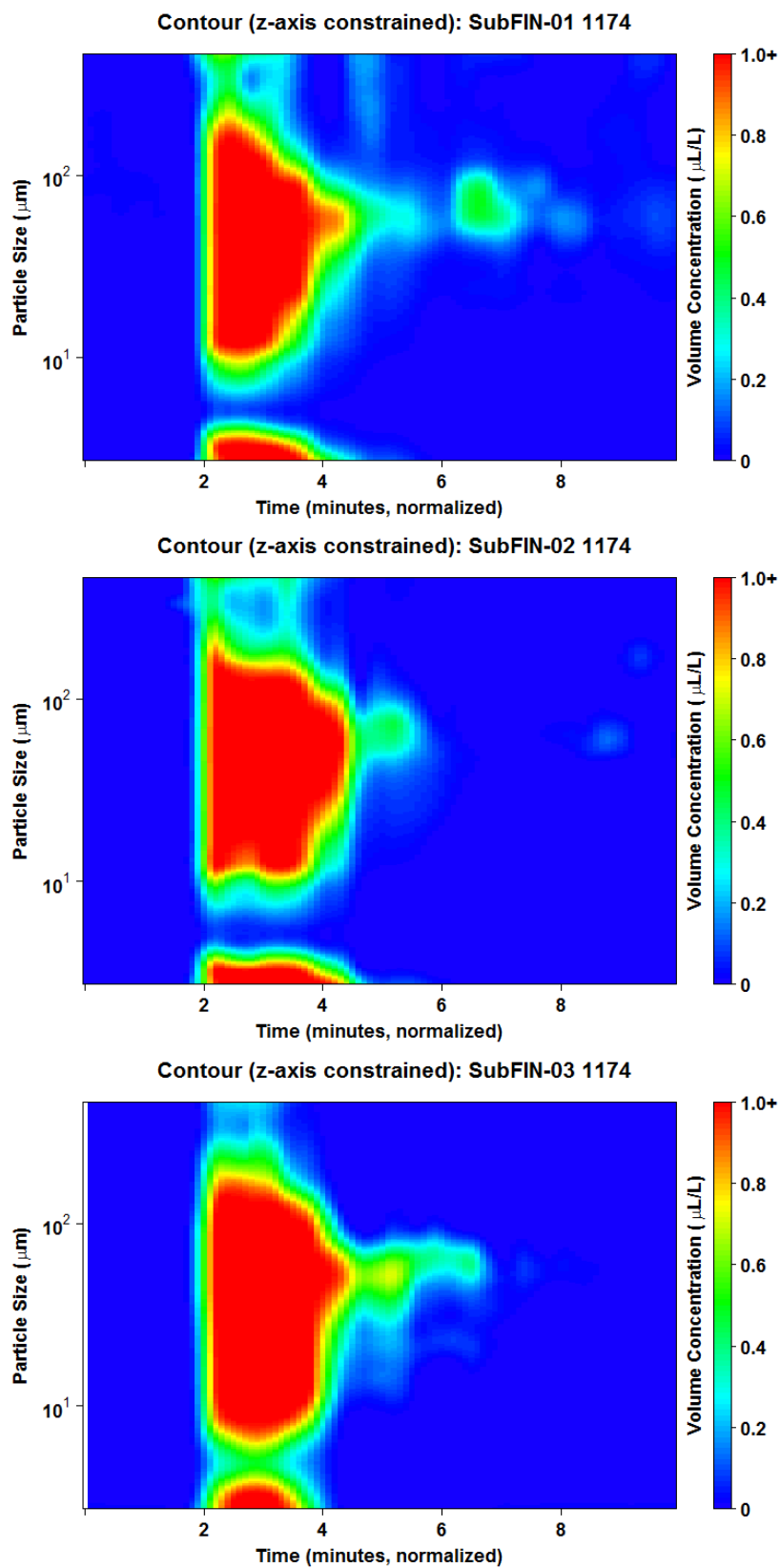


Figure D22. LISST contour plot for ANS, DOR 1:20 (Finasol OSR 52), warm experiment.

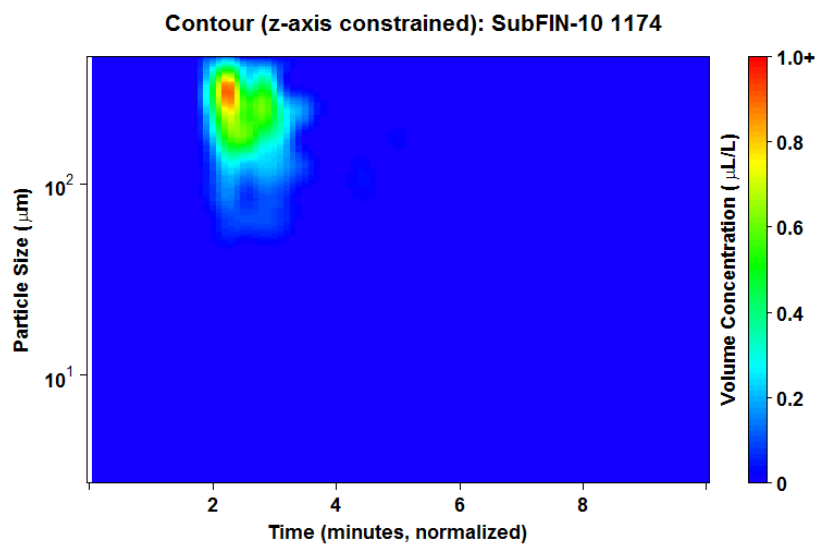


Figure D23. LISST contour plot for IFO-120, DOR 1:200 (Finasol OSR 52), warm experiment.

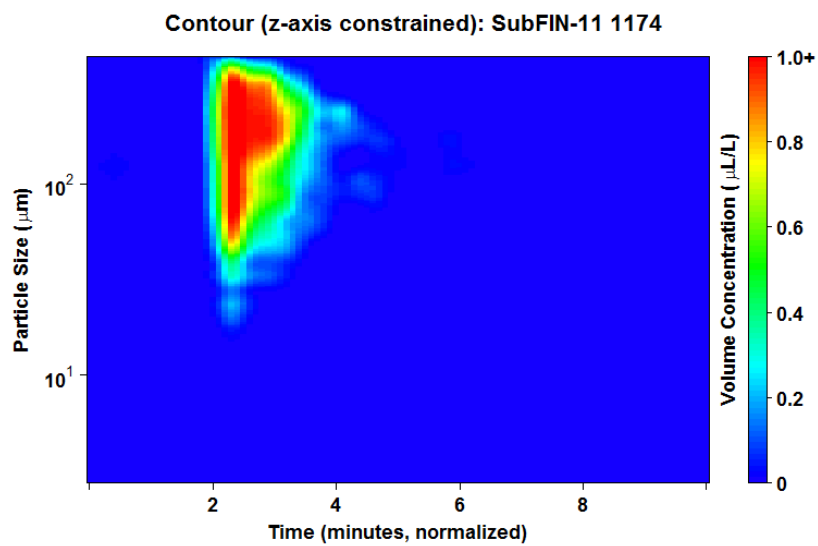


Figure D24. LISST contour plot for IFO-120, DOR 1:100 (Finasol OSR 52), warm experiment.

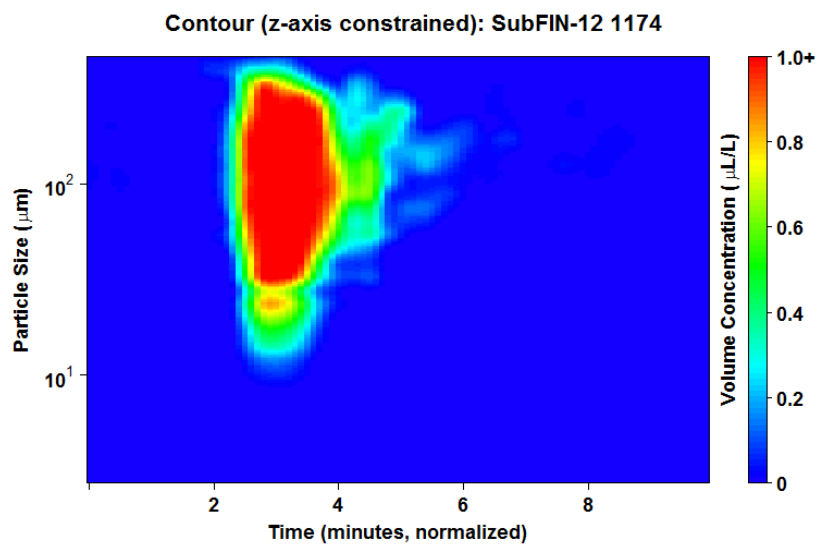


Figure D25. LISST contour plot for IFO-120, DOR 1:20 (Finasol OSR 52), warm experiment.

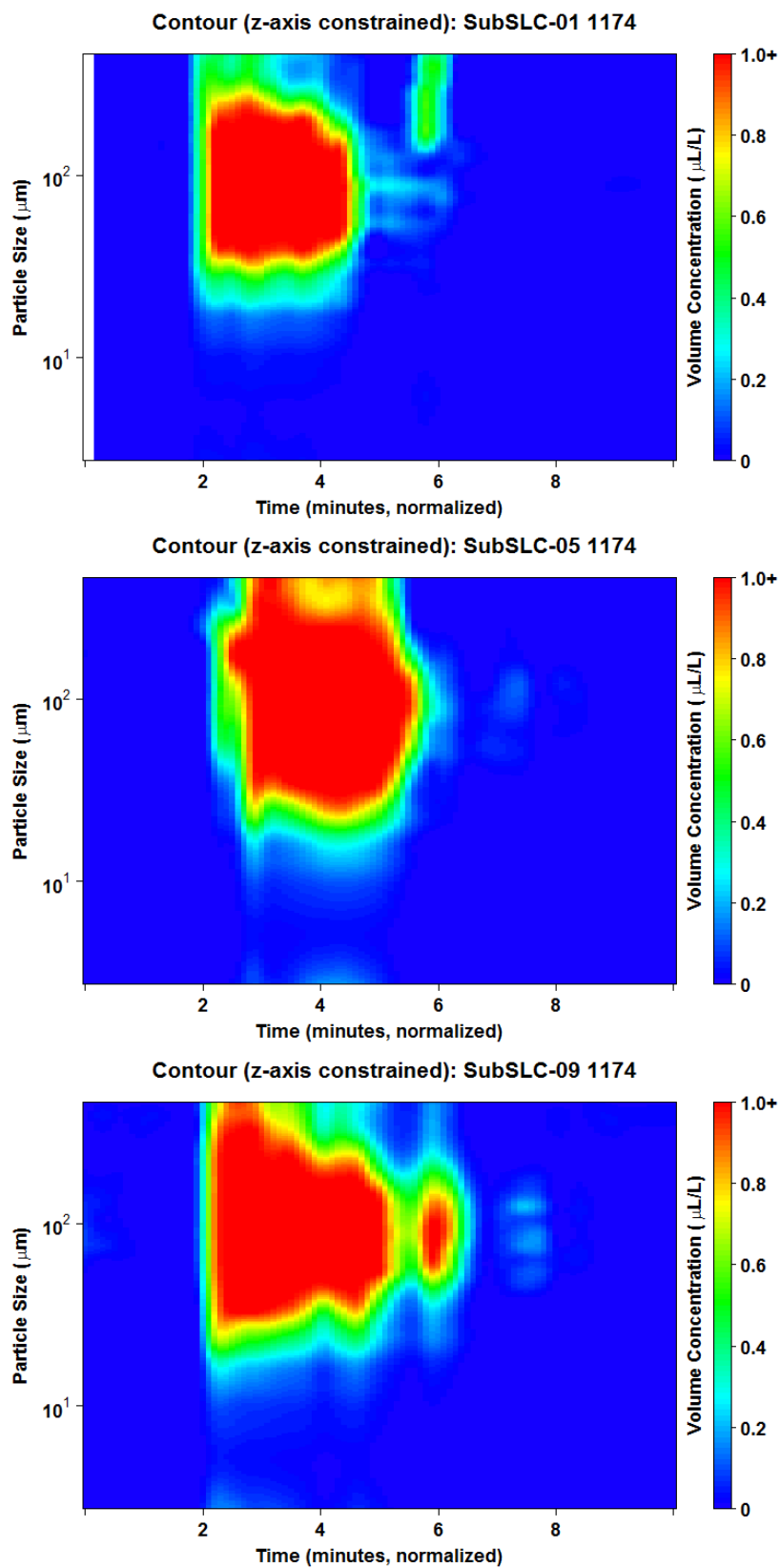


Figure D26. LISST contour plot for SLC, no dispersant, warm water experiment.

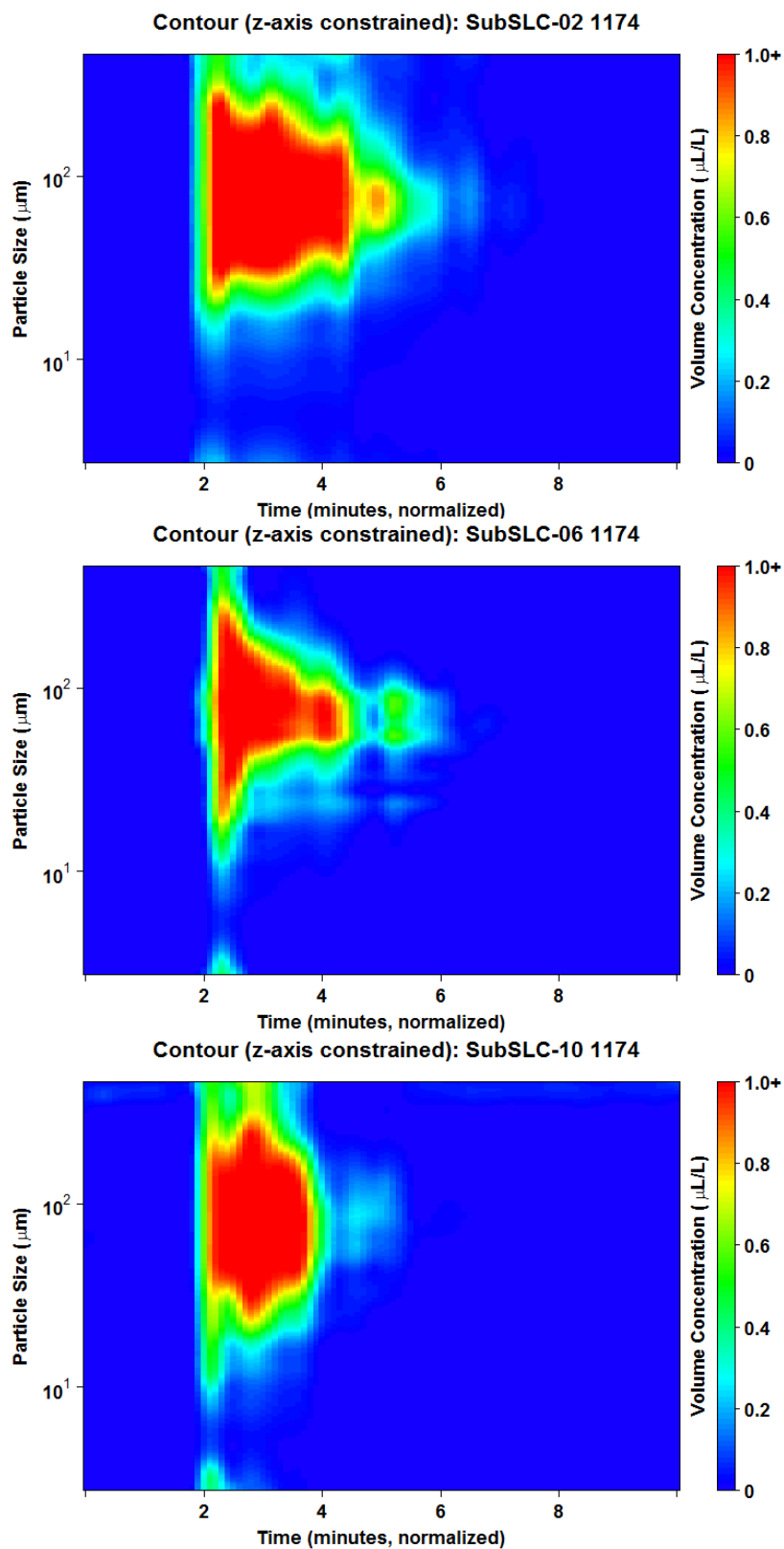


Figure D27. LISST contour plot for SLC, DOR 1:200 (Corexit 9500), warm water experiment.

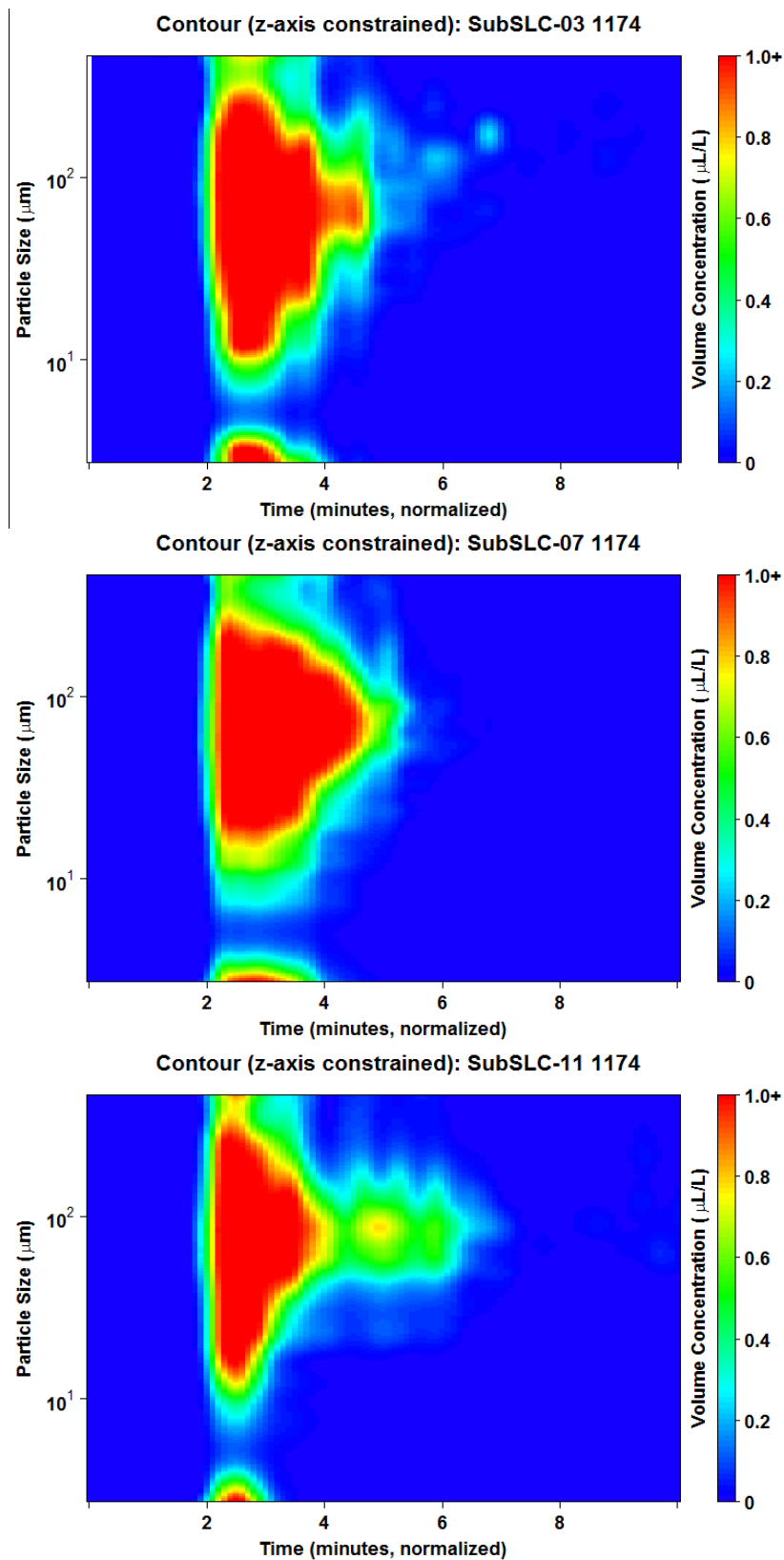


Figure D28. LISST contour plot for SLC, DOR 1:100 (Corexit 9500), warm experiment.

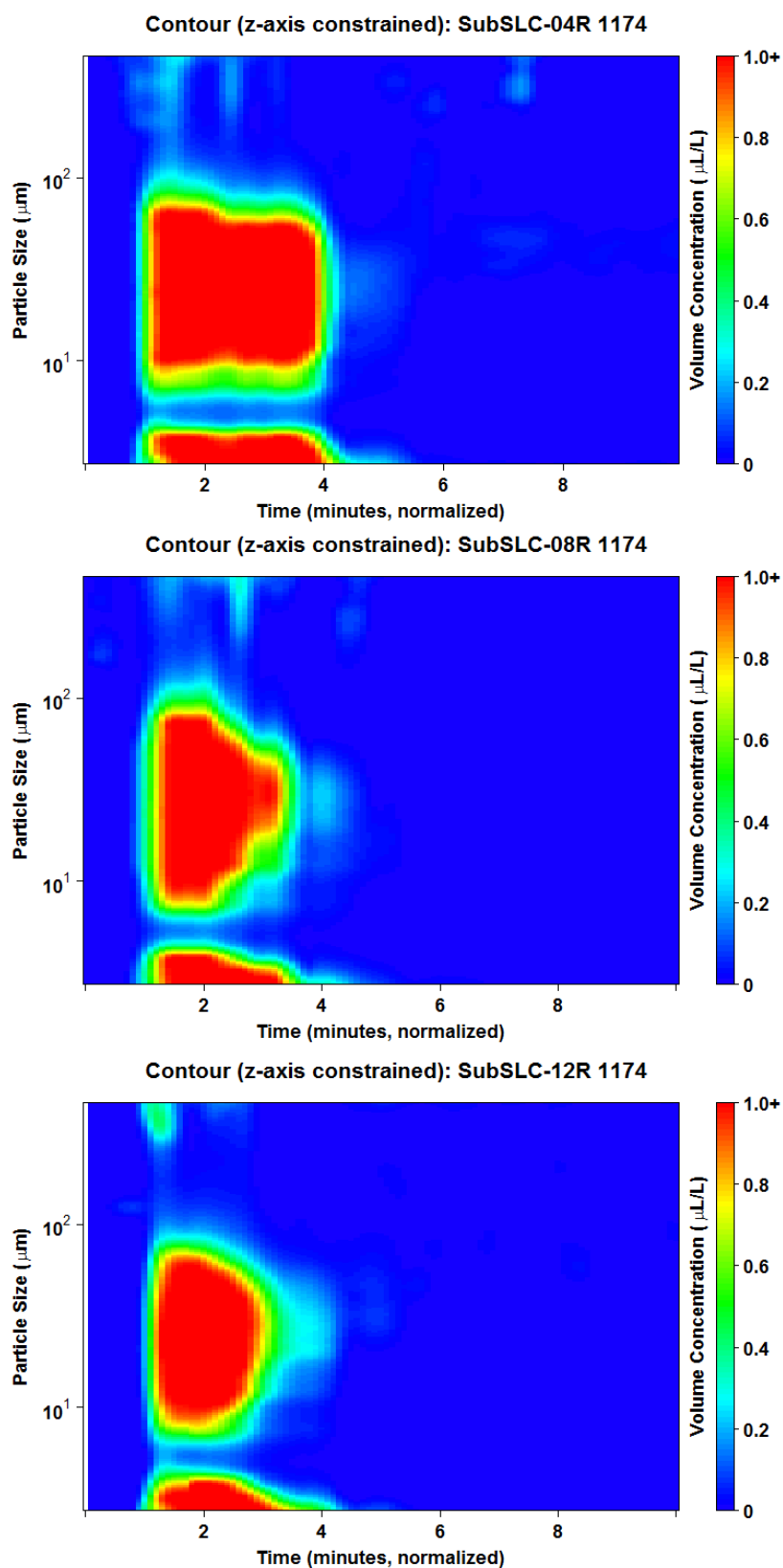


Figure D29. LISST contour plot for SLC, DOR 1:20 (Corexit 9500), warm water experiment.

APPENDIX E – Submersible Fluorescence Time Series

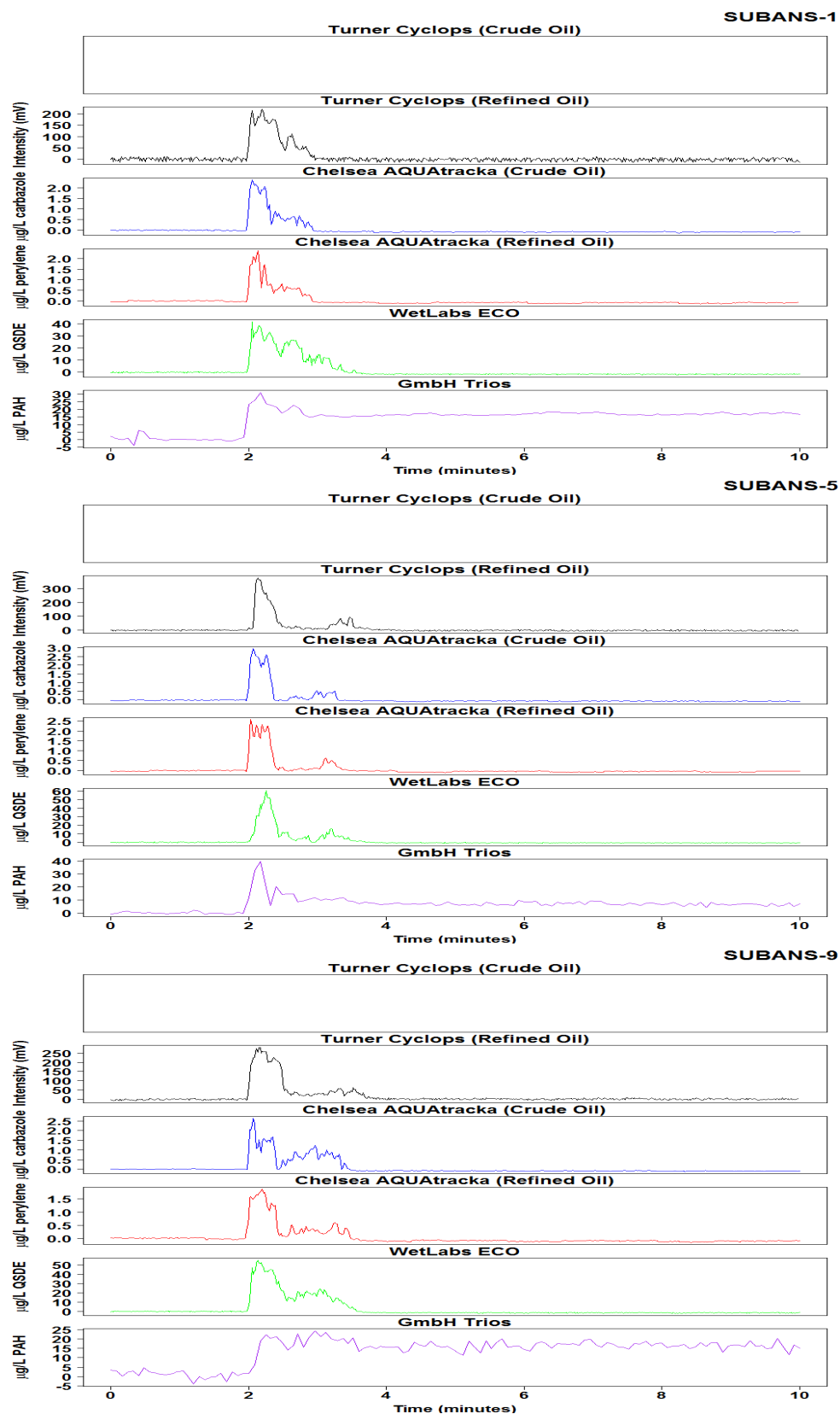


Figure E1. Raw in-situ fluorometer signal for ANS, no dispersant, cold experiment.

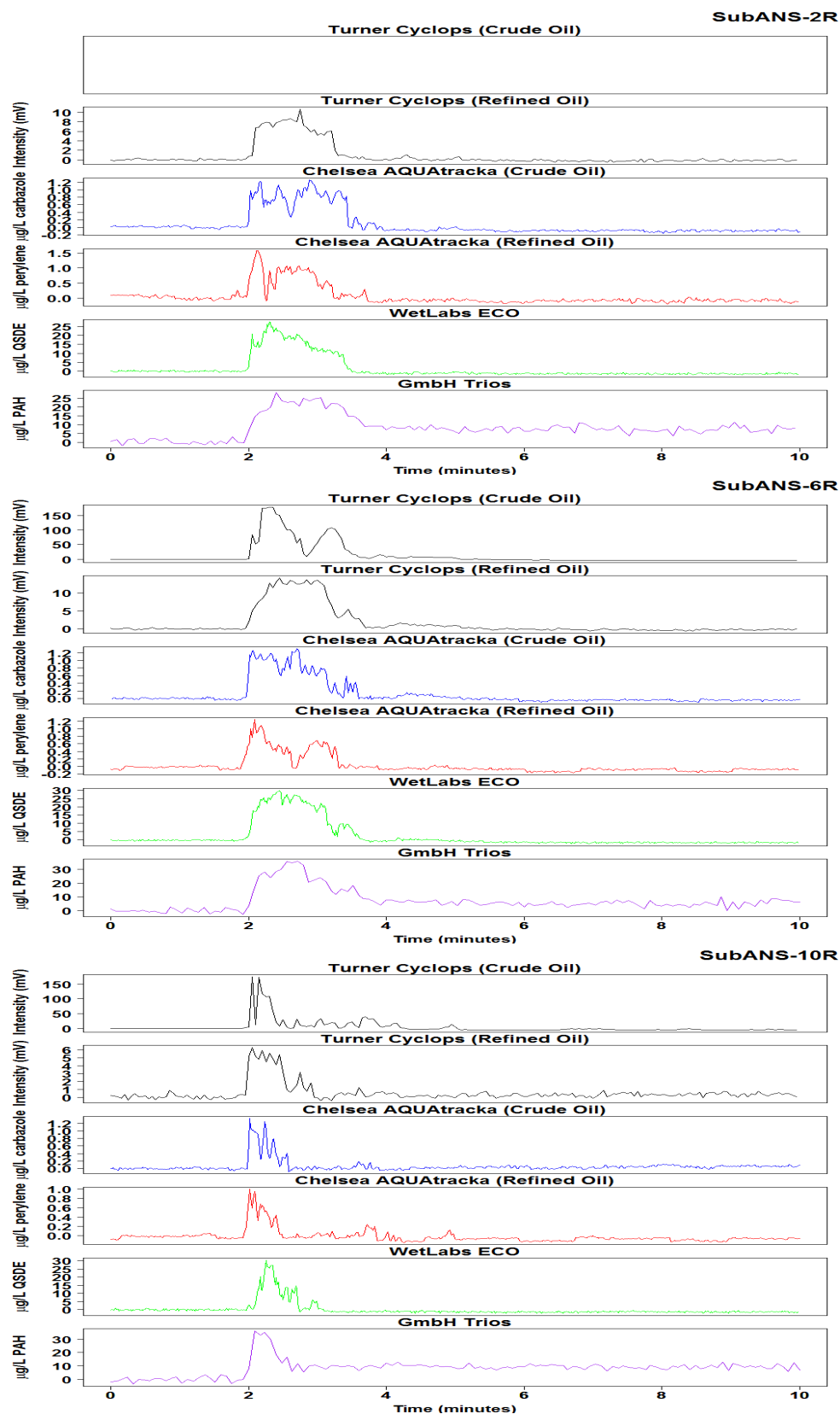


Figure E2. Raw in-situ fluorometer signal for ANS, DOR 1:200 (Corexit 9500), cold expt.

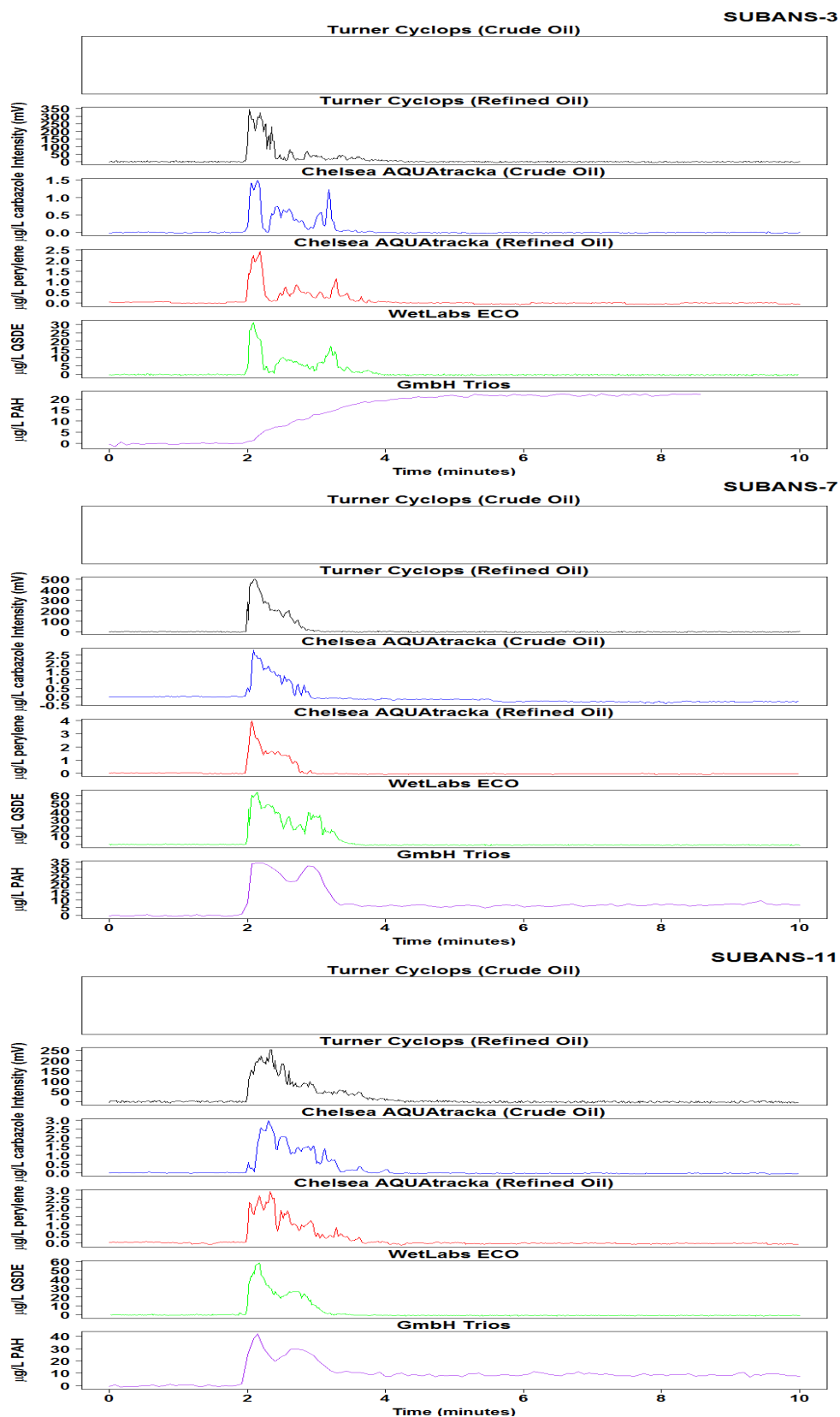


Figure E3. Raw in-situ fluorometer signal for ANS, DOR 1:100 (Corexit 9500), cold expt.

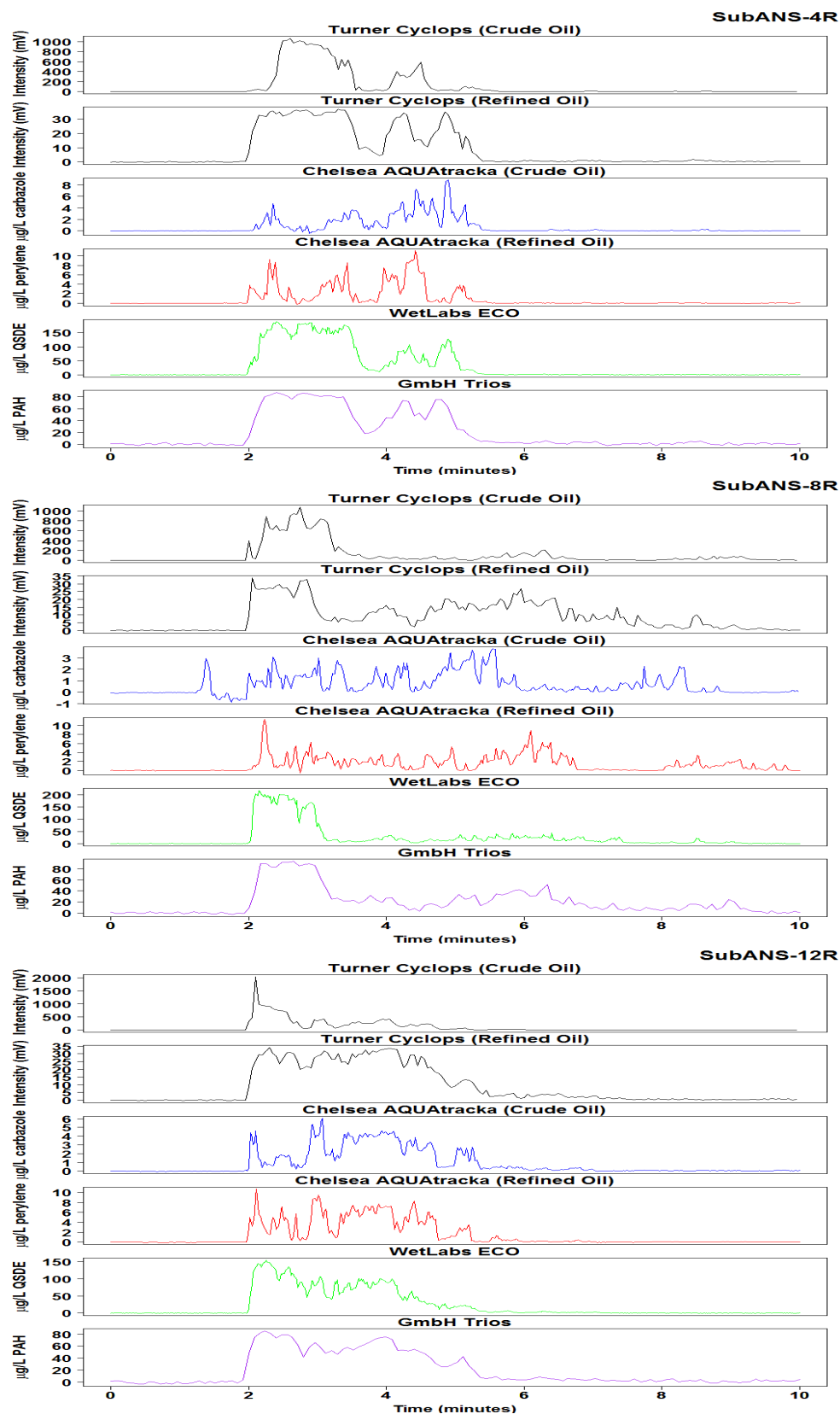


Figure E4. Raw in-situ fluorometer signal for ANS, DOR 1:20 (Corexit 9500), cold expt.

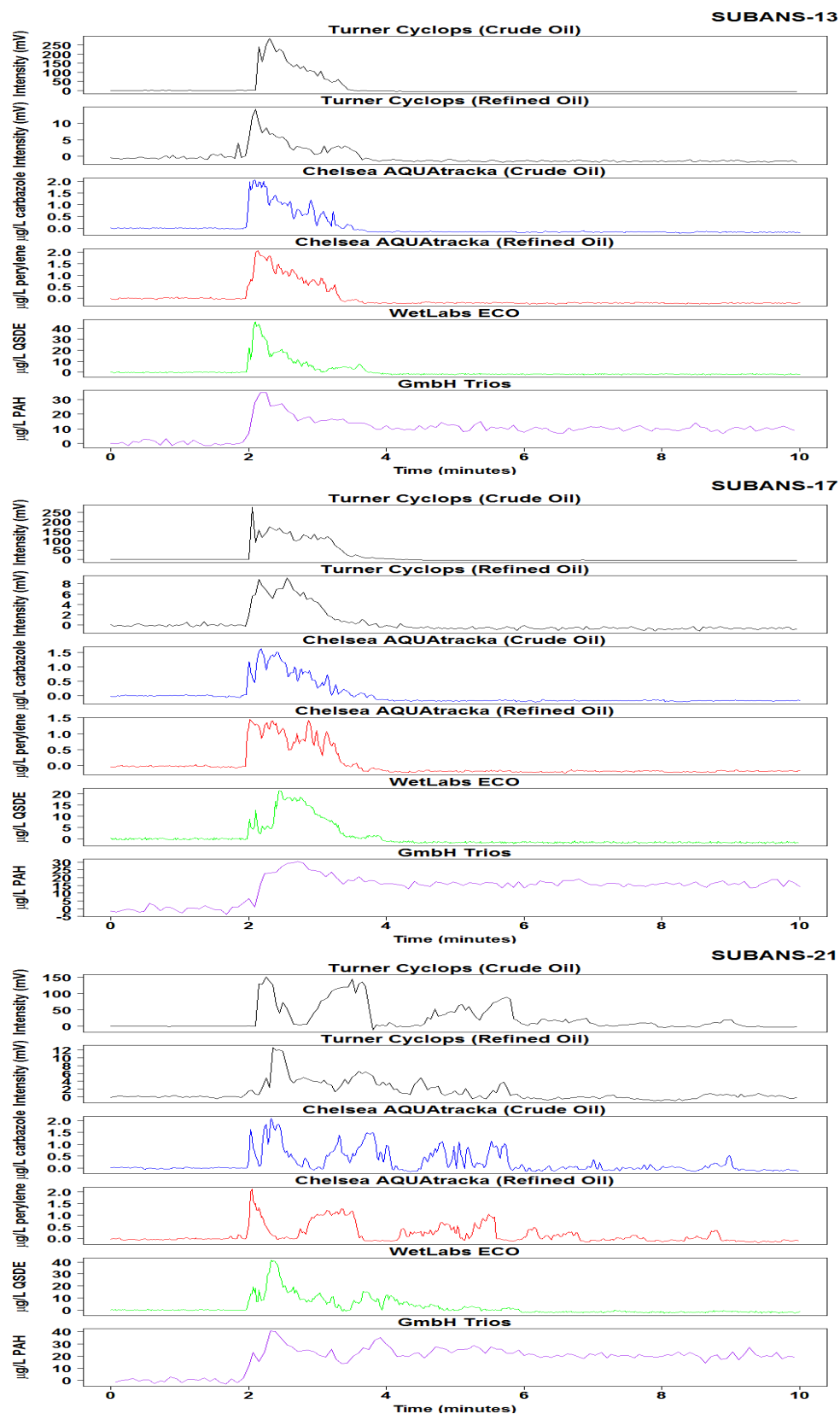


Figure E5. Raw in-situ fluorometer signal for ANS, DOR 0 (Corexit 9500), warm expt.

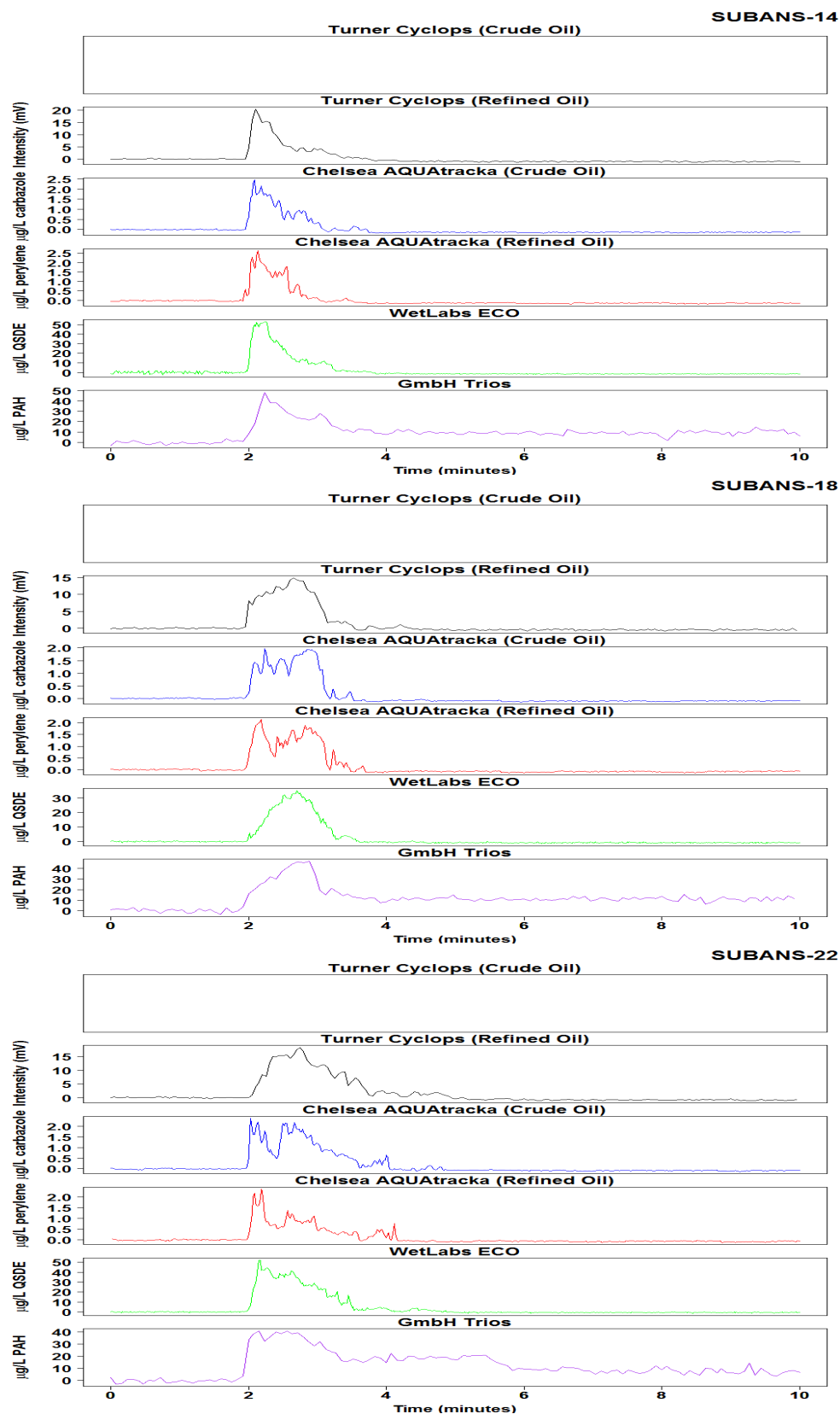


Figure E6. Raw in-situ fluorometer signal for ANS, DOR 1:200 (Corexit 9500), warm expt.

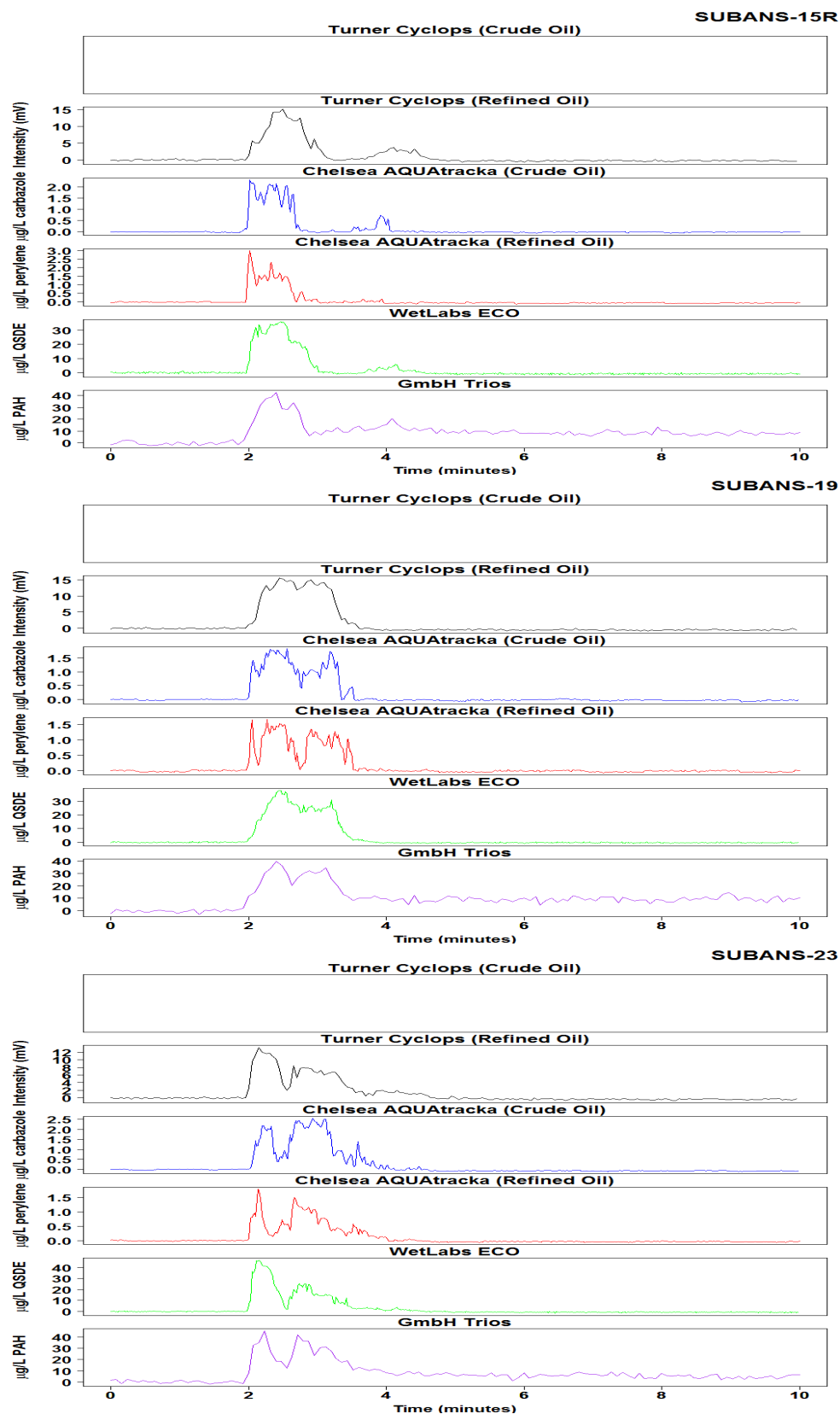


Figure E7. Raw in-situ fluorometer signal for ANS, DOR 1:100 (Corexit 9500), warm expt.

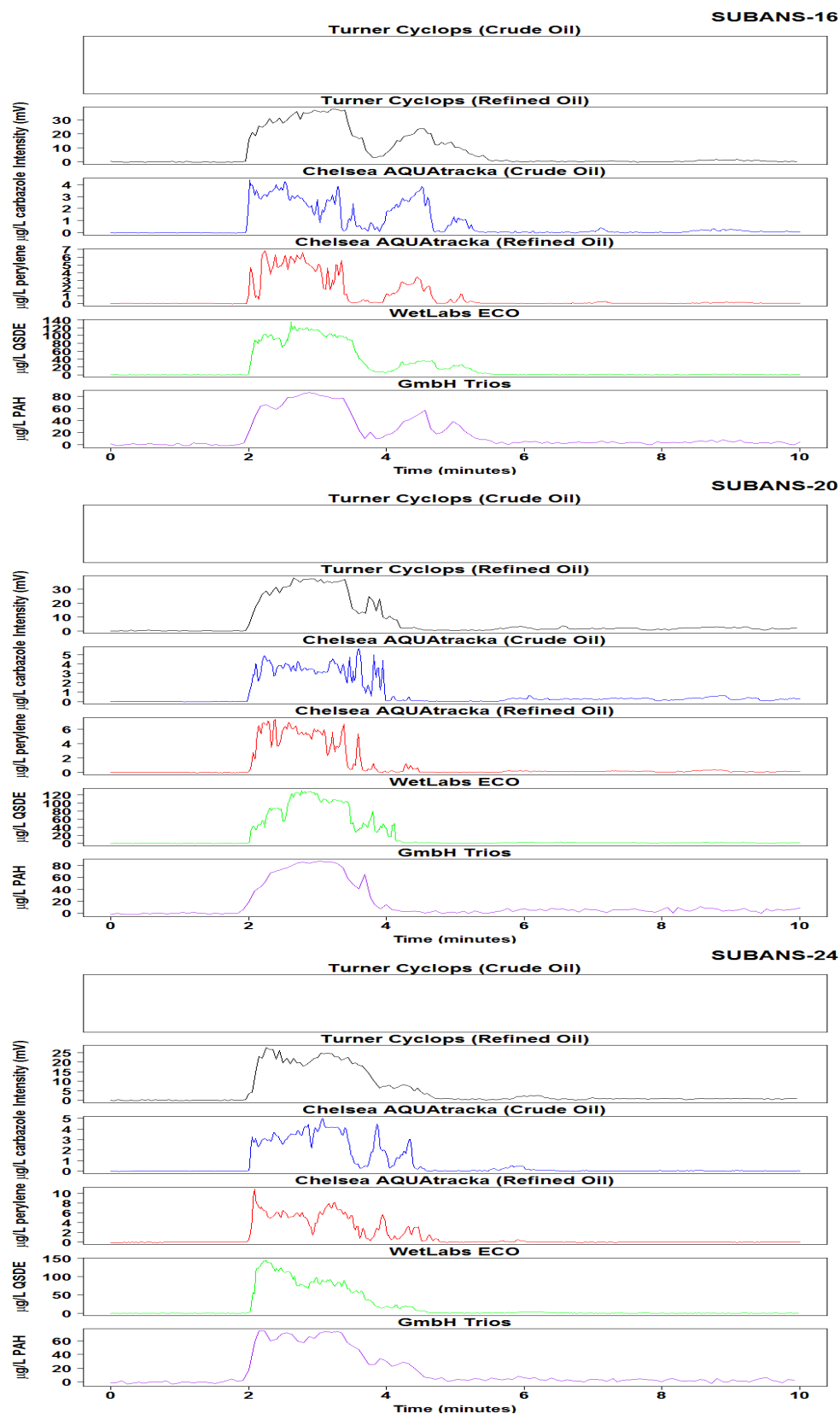


Figure E8. Raw in-situ fluorometer signal for ANS, DOR 1:20 (Corexit 9500), warm expt.

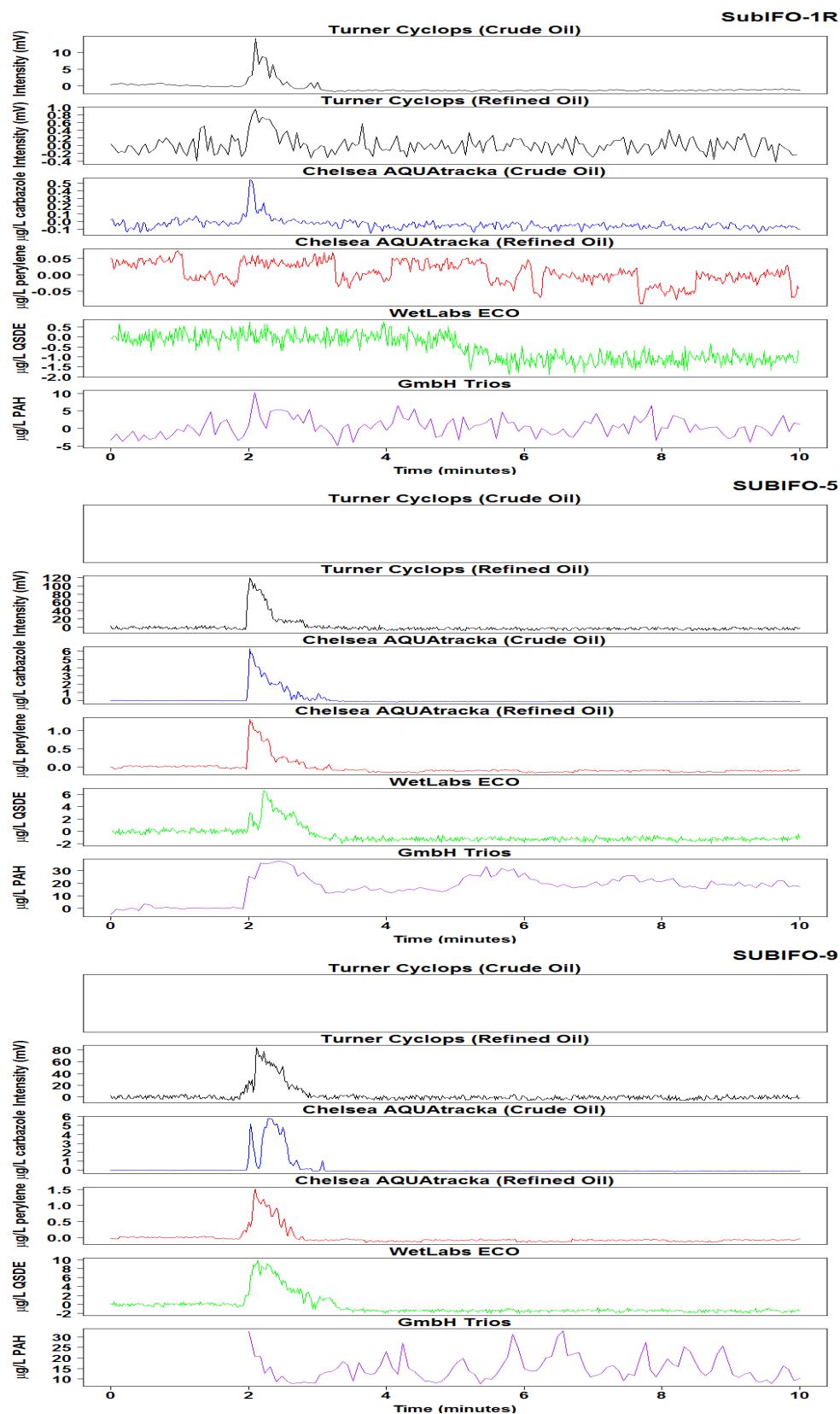


Figure E9. Raw in-situ fluorometer signal, IFO-120, no dispersant, cold water expt.

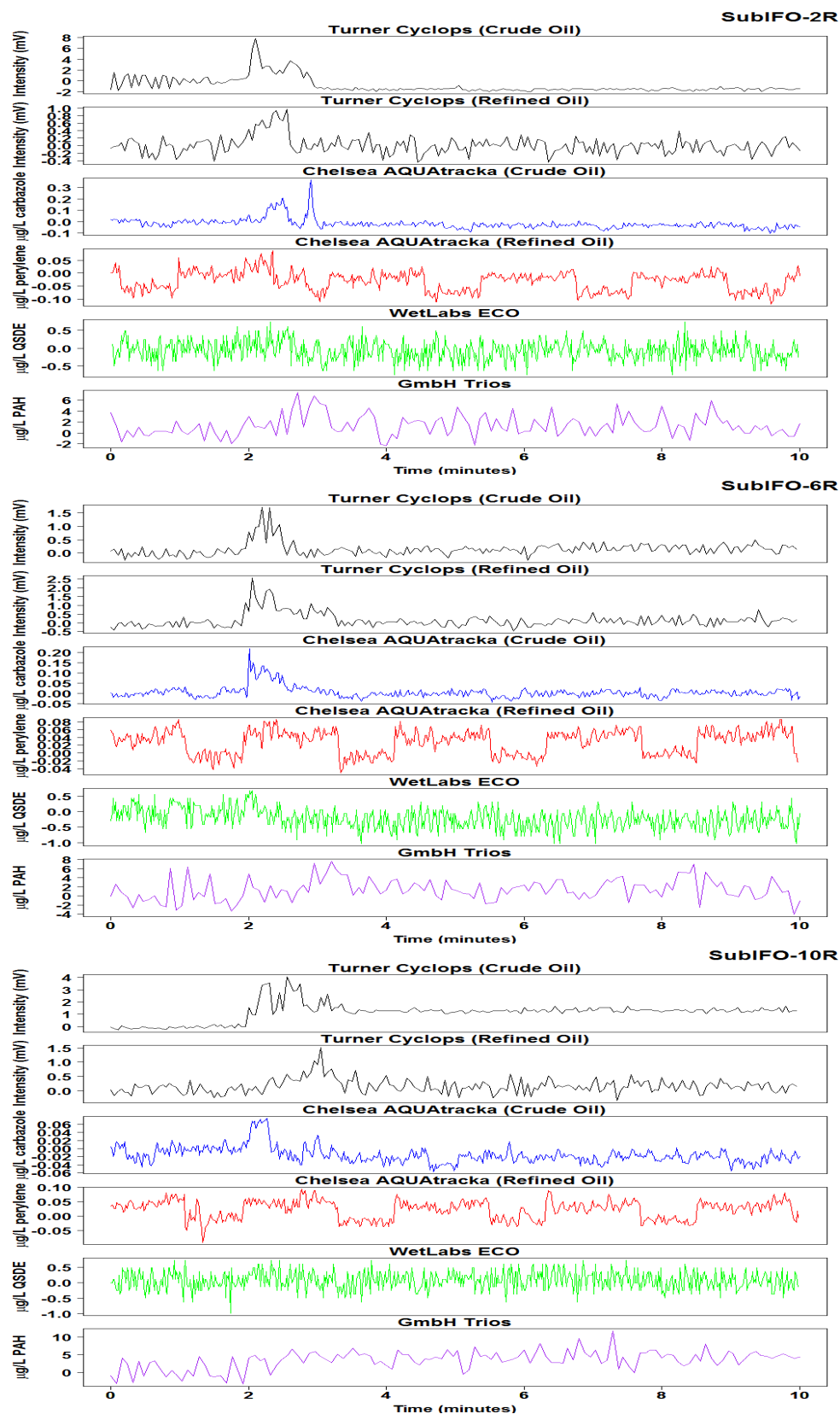


Figure E10. Raw in-situ fluorometer signal, IFO-120, DOR 1:200 (Corexit 9500), cold expt.

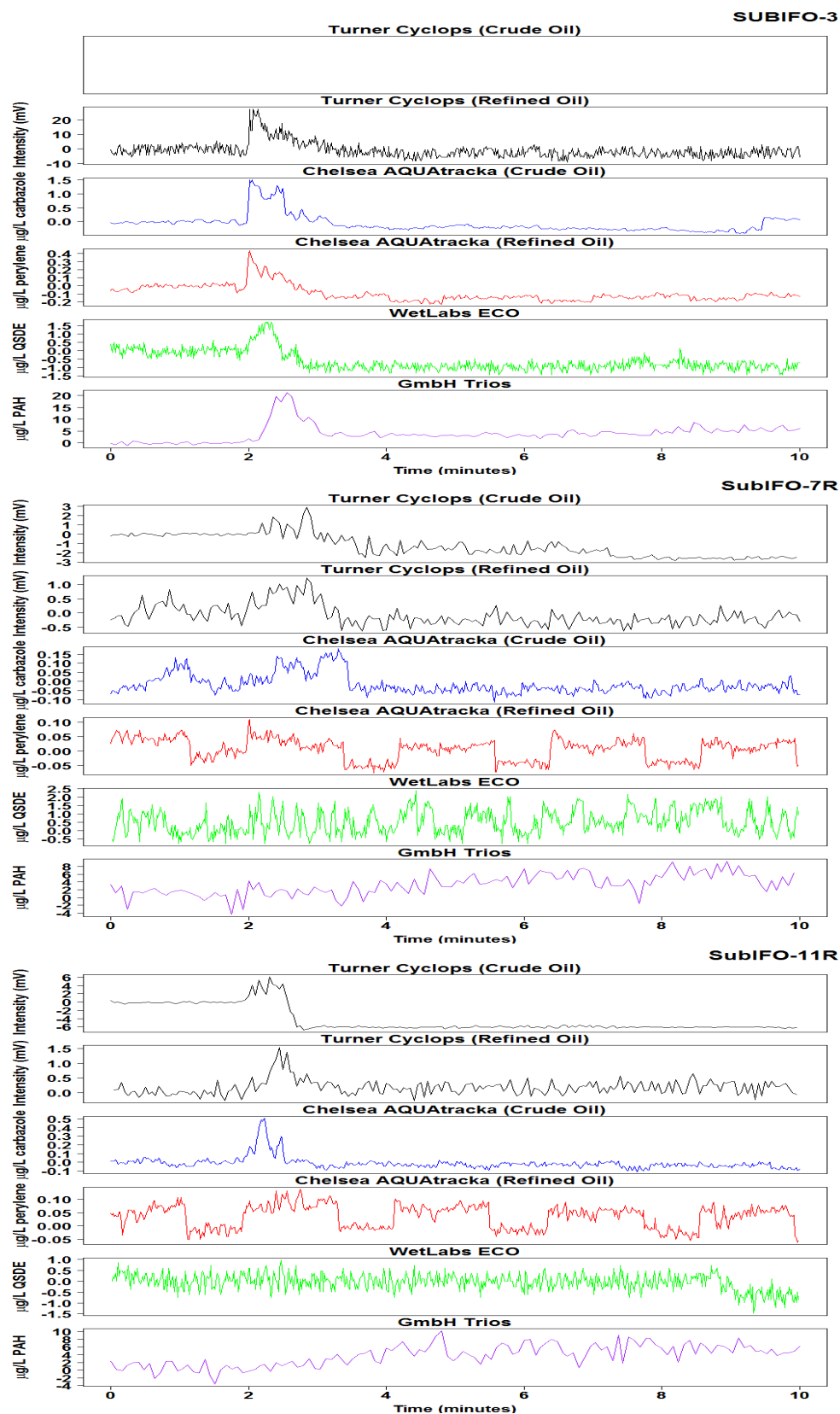


Figure E11. Raw in-situ fluorometer signal, IFO-120, DOR 1:100 (Corexit 9500), cold expt.

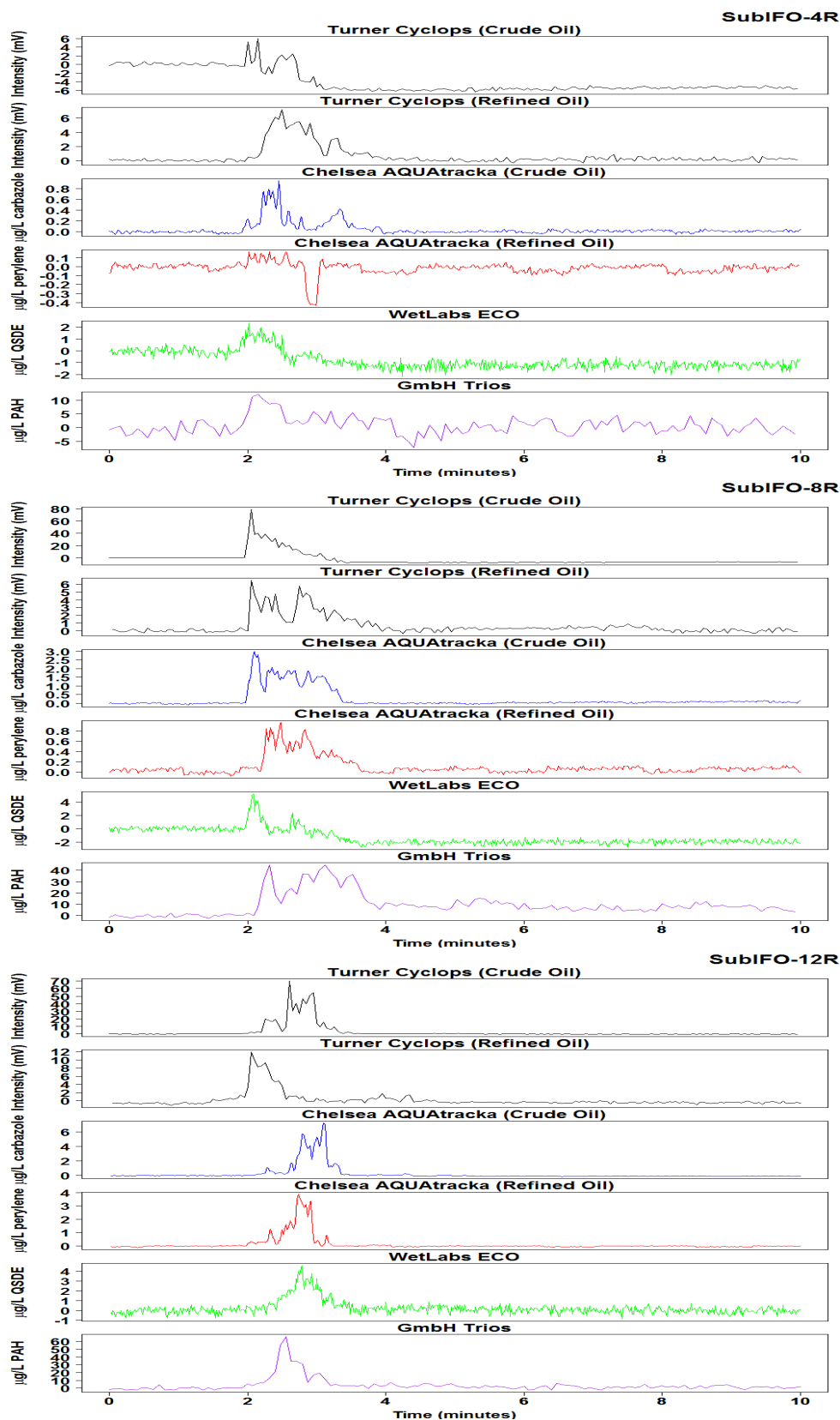


Figure E12. Raw in-situ fluorometer signal, IFO-120, DOR 1:20 (Corexit 9500), cold expt.

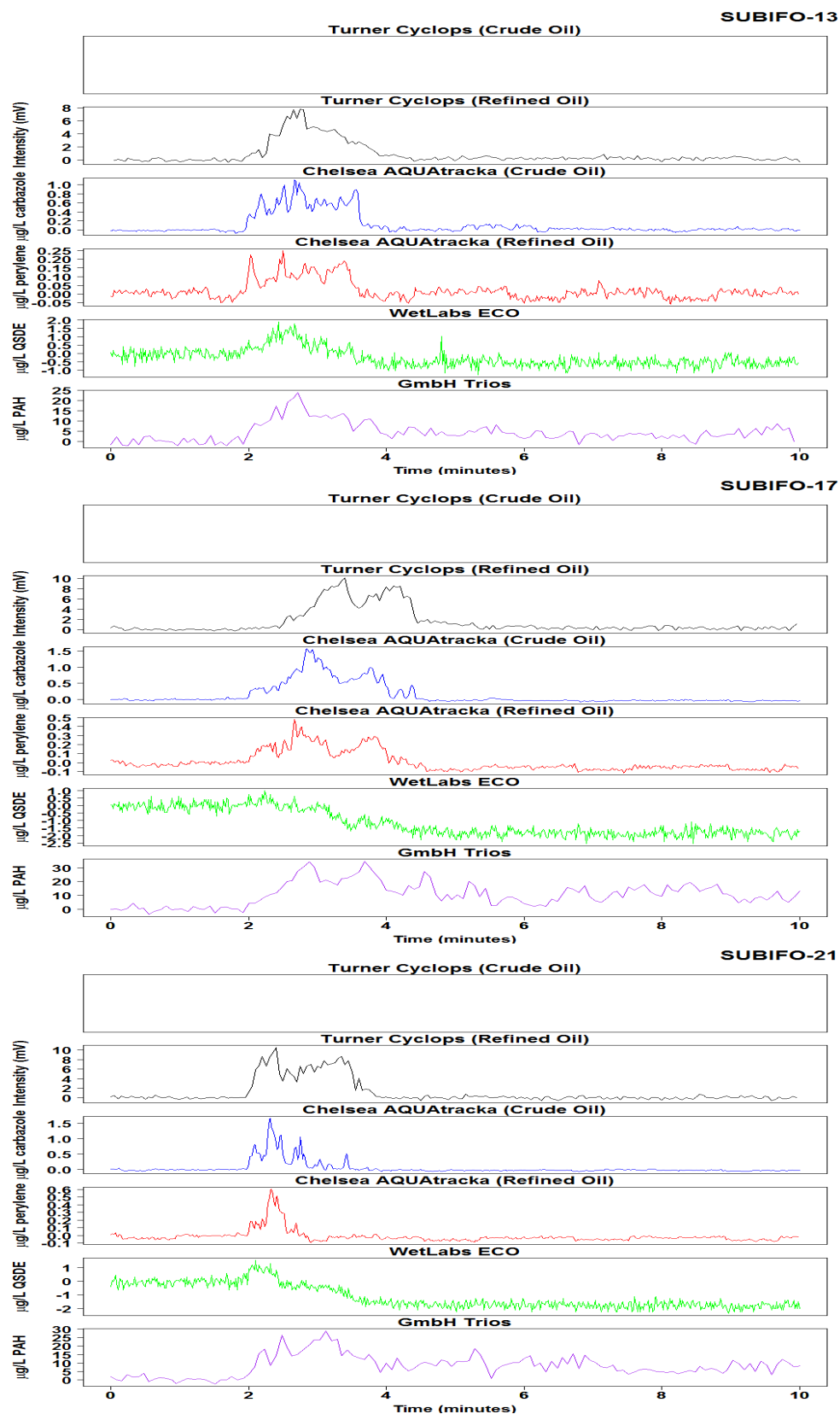


Figure E13. Raw in-situ fluorometer signal for IFO-120, no dispersant, warm water expt.

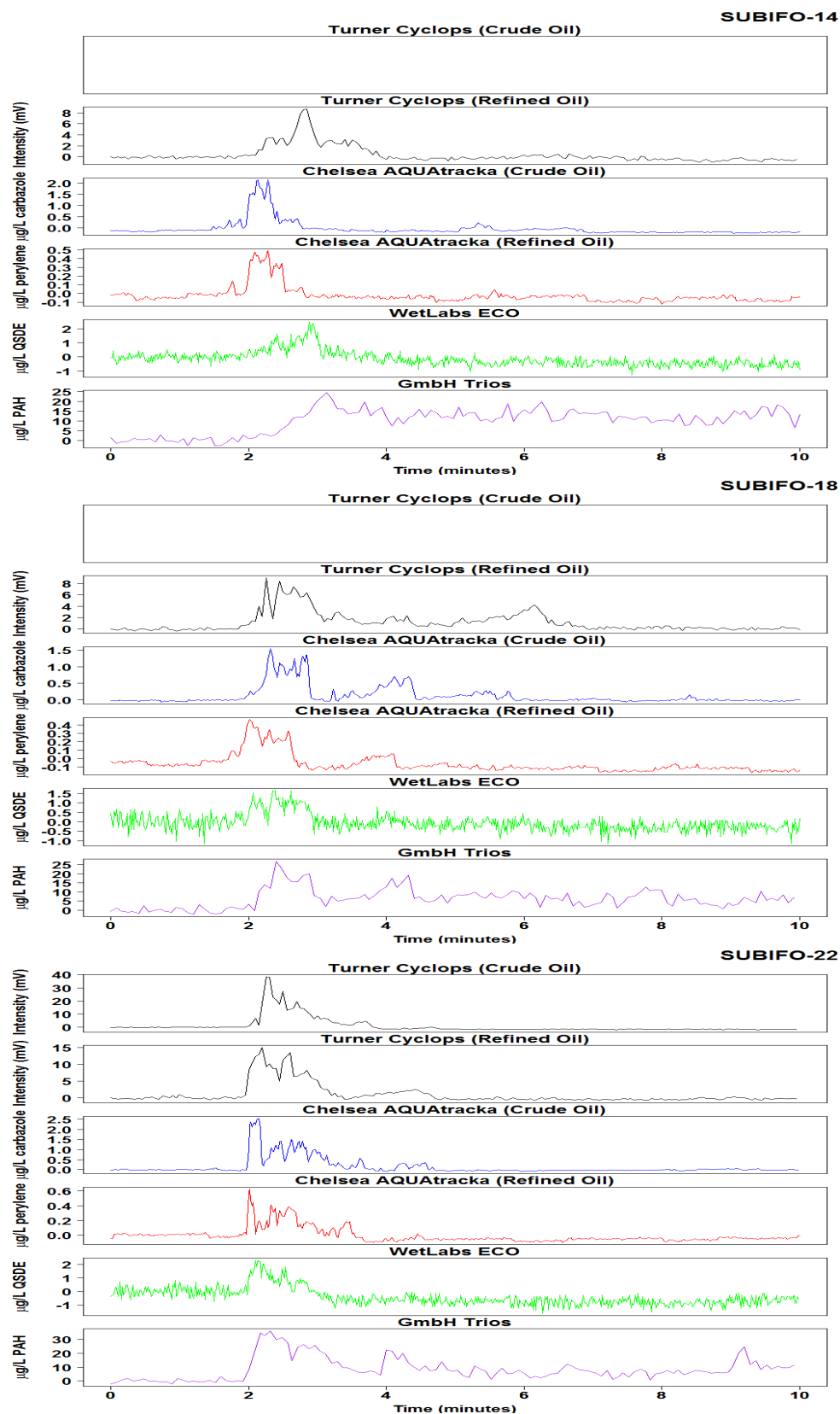


Figure E14. Raw in-situ fluorometer signal, IFO-120, DOR 1:200 (Corexit 9500) warm expt.

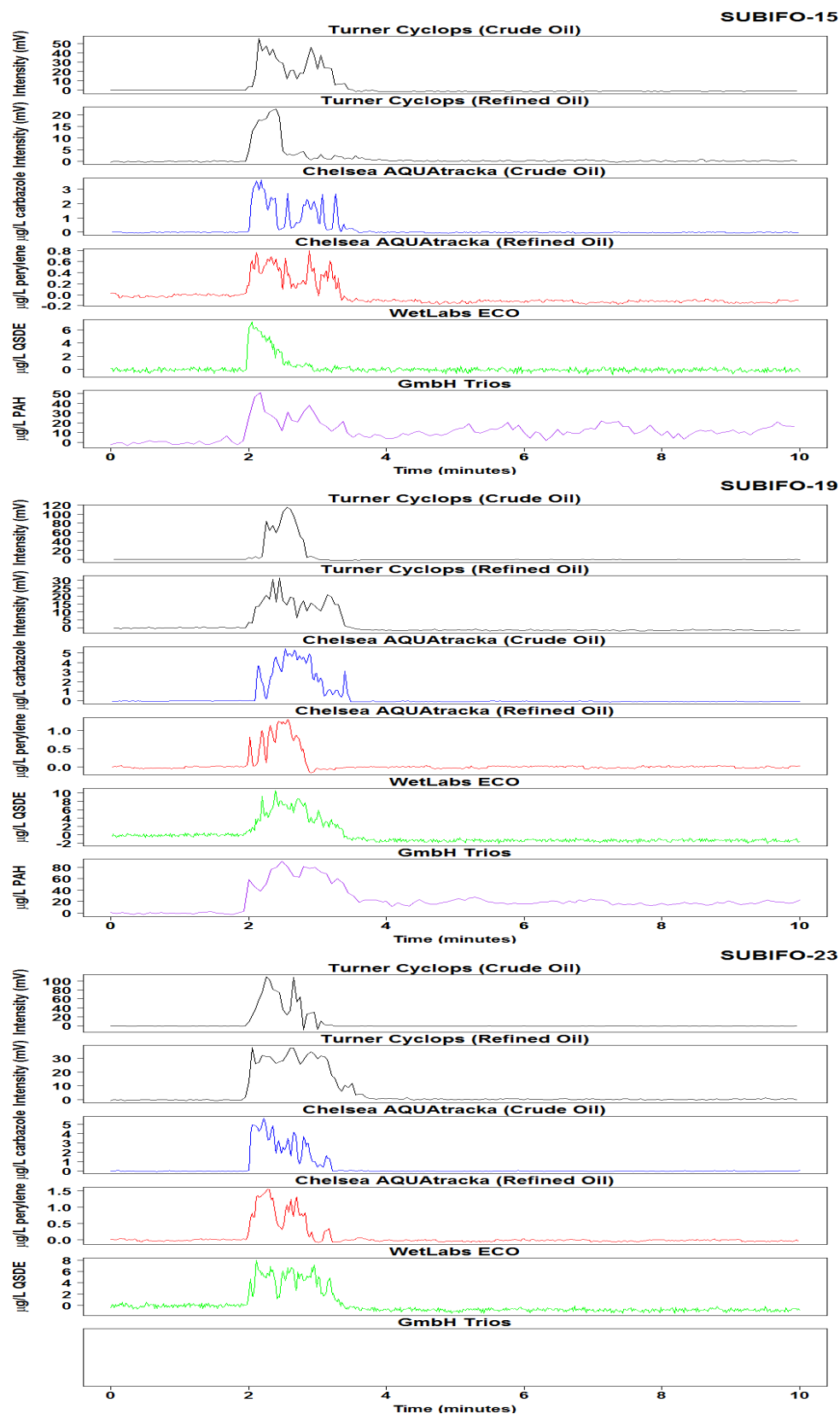


Figure E15. Raw in-situ fluorometer signal, IFO-120, DOR 1:100 (Corexit 9500) warm expt.

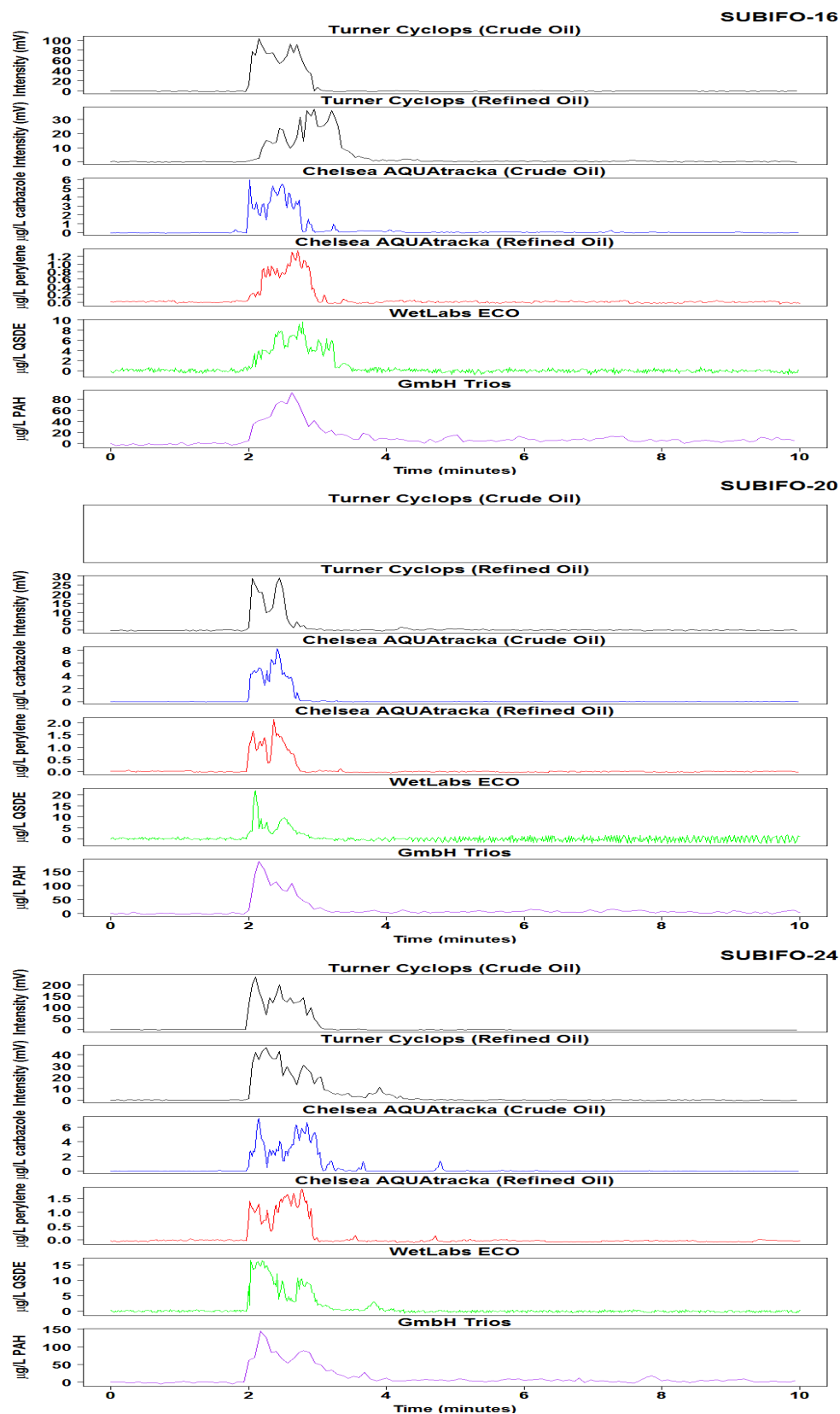


Figure E16. Raw in-situ fluorometer signal, IFO-120, DOR 1:20 (Corexit 9500), warm expt.

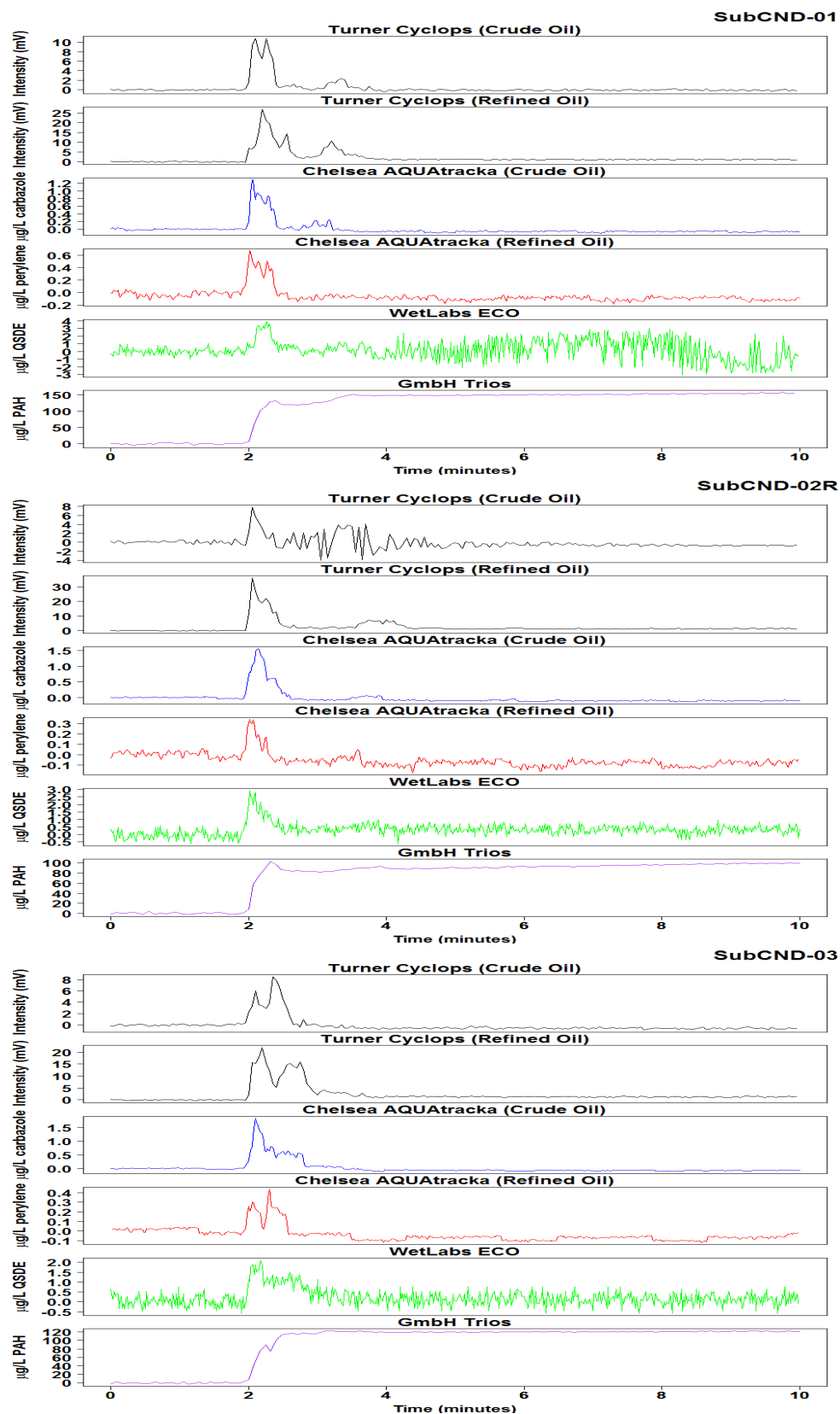


Figure E17. Raw in-situ fluorometer signal for Gas Condensate, no dispersant.

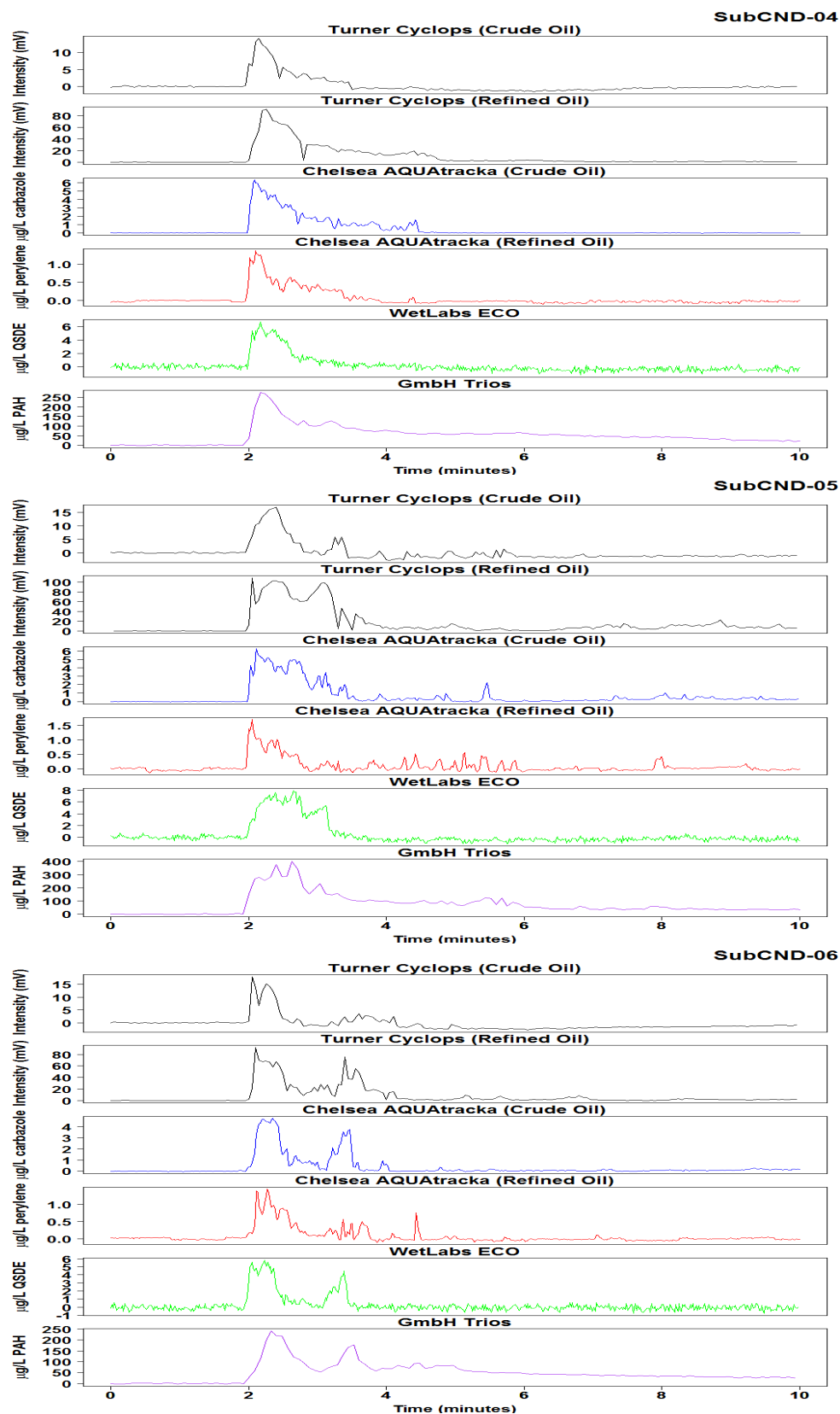


Figure E18. Raw in-situ fluorometer signal for Gas Condensate, DOR 1:20 (Corexit 9500).

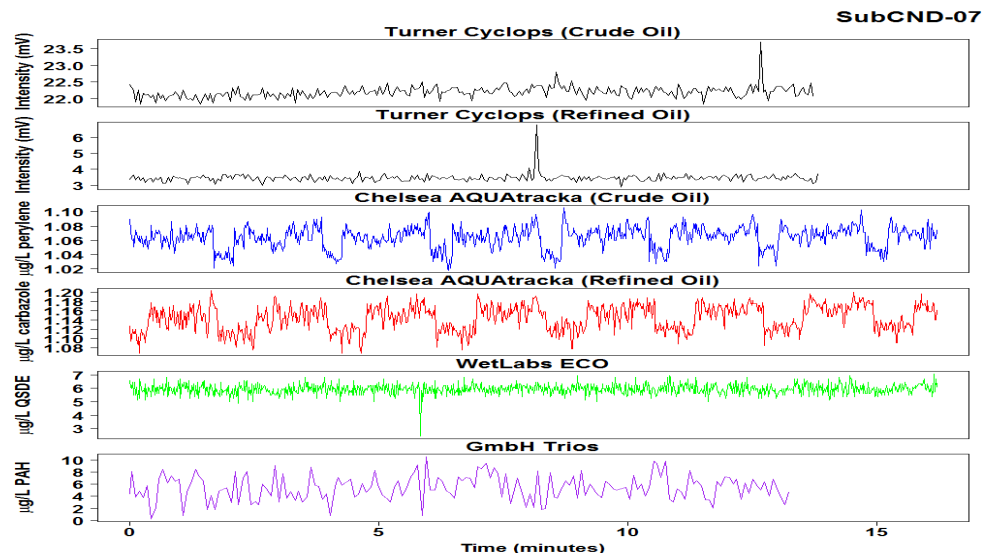


Figure E19. Raw in-situ fluorometer signal for air injection, no dispersant.

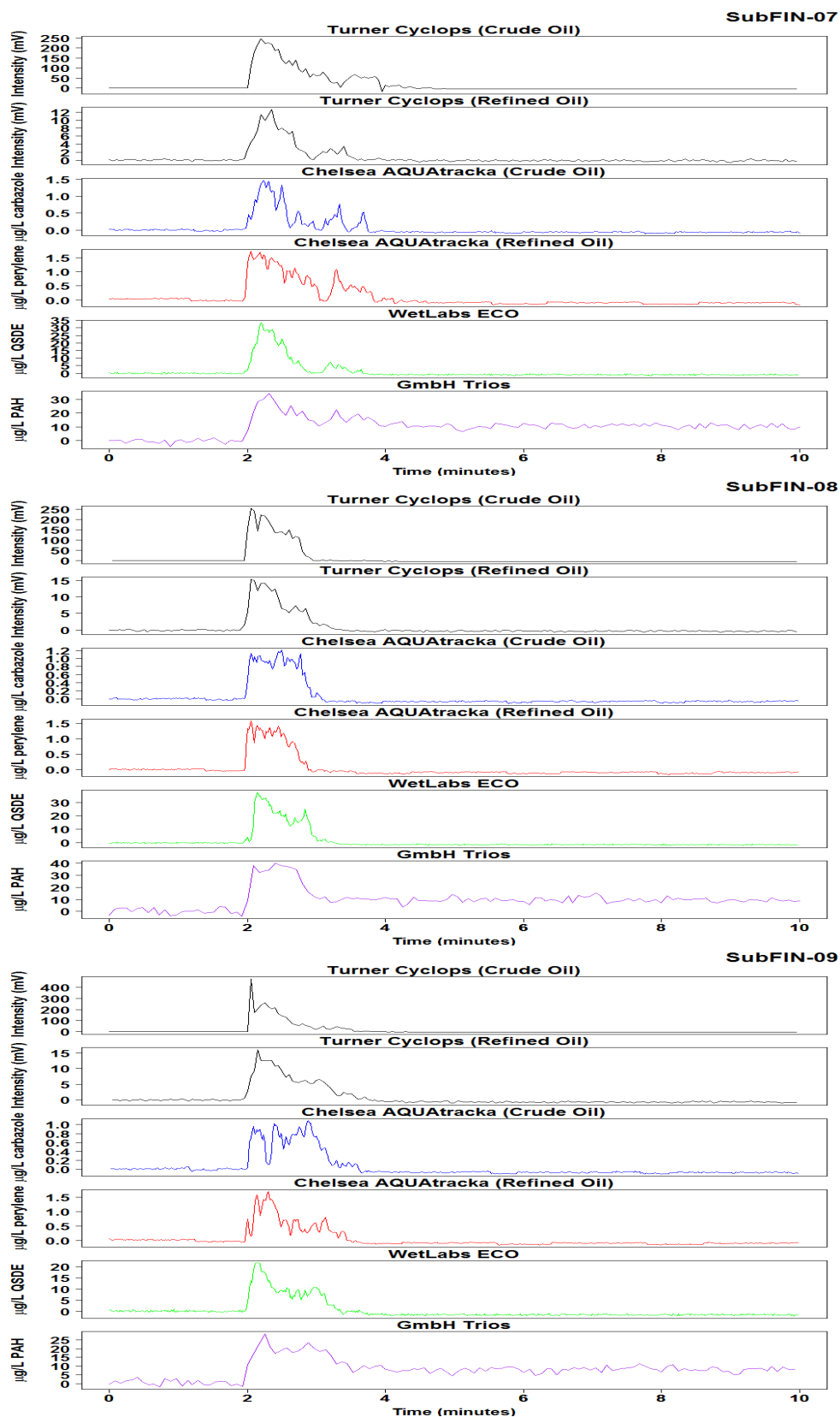


Figure E20. Raw in-situ fluorometer signal, ANS, DOR 1:200 (Finasol OSR 52), warm expt.

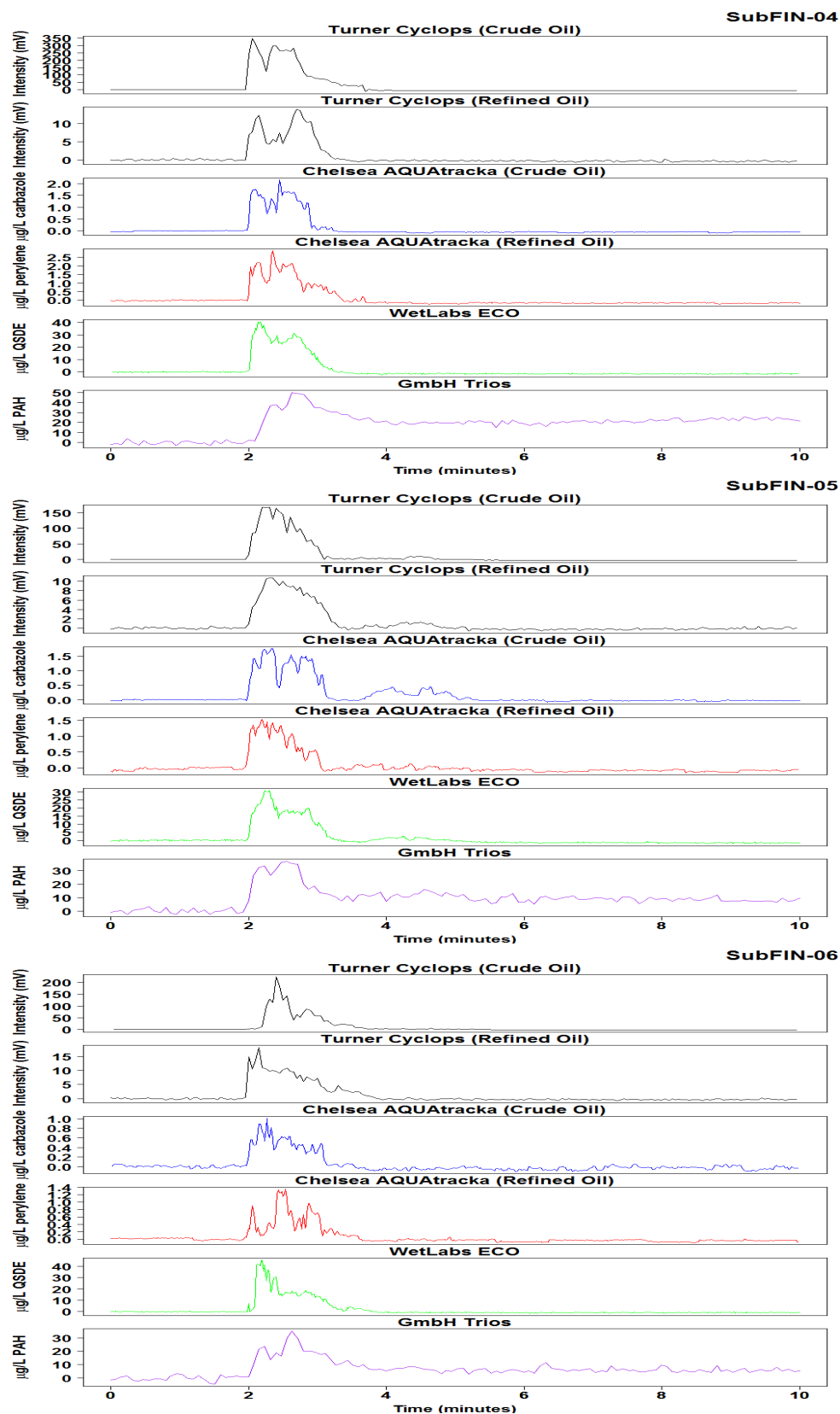


Figure E21. Raw in-situ fluorometer signal ANS, DOR 1:100 (Finasol OSR 52) warm expt.

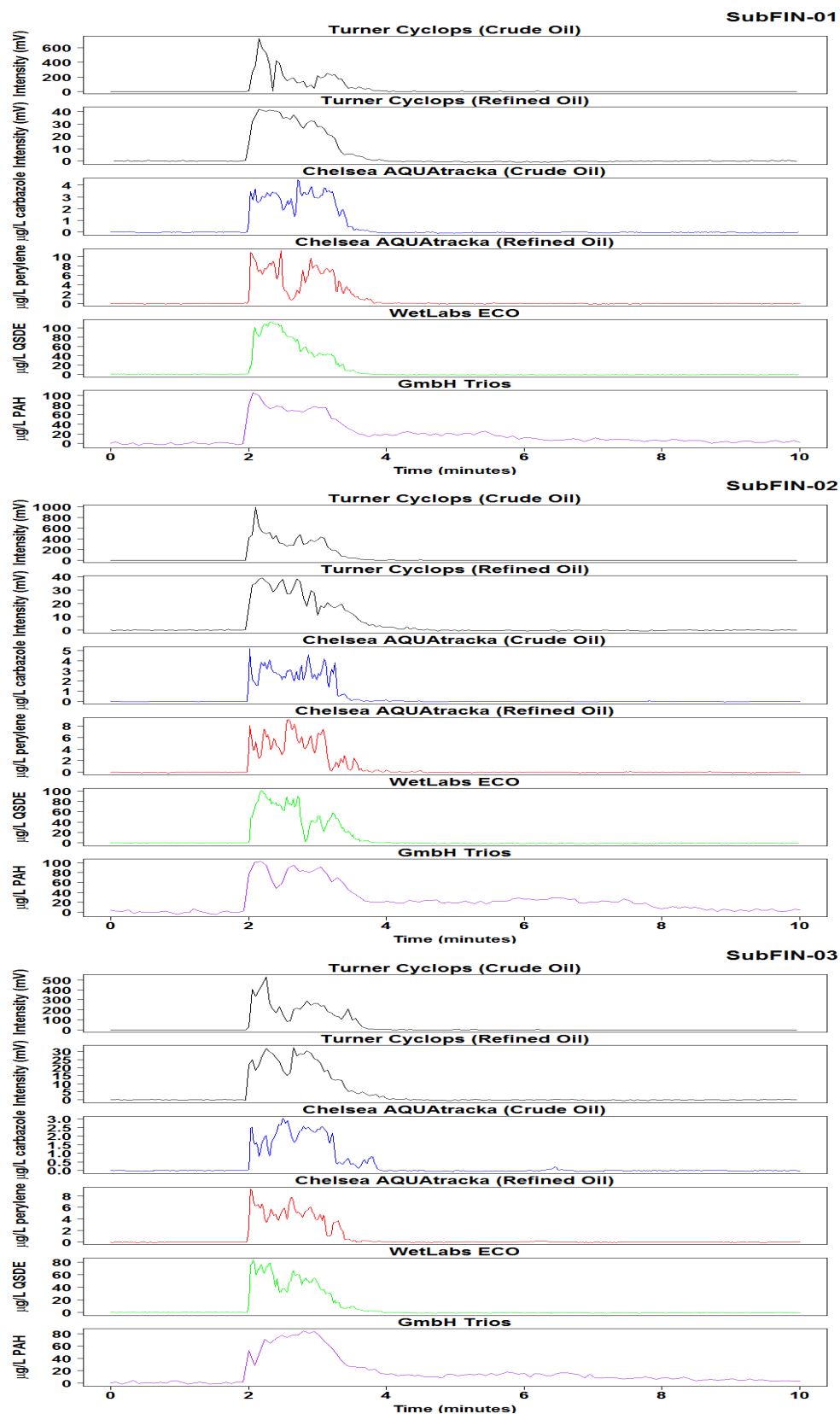


Figure E22. Raw in-situ fluorometer signal for ANS, DOR 1:20 (Finasol OSR 52) warm expt.

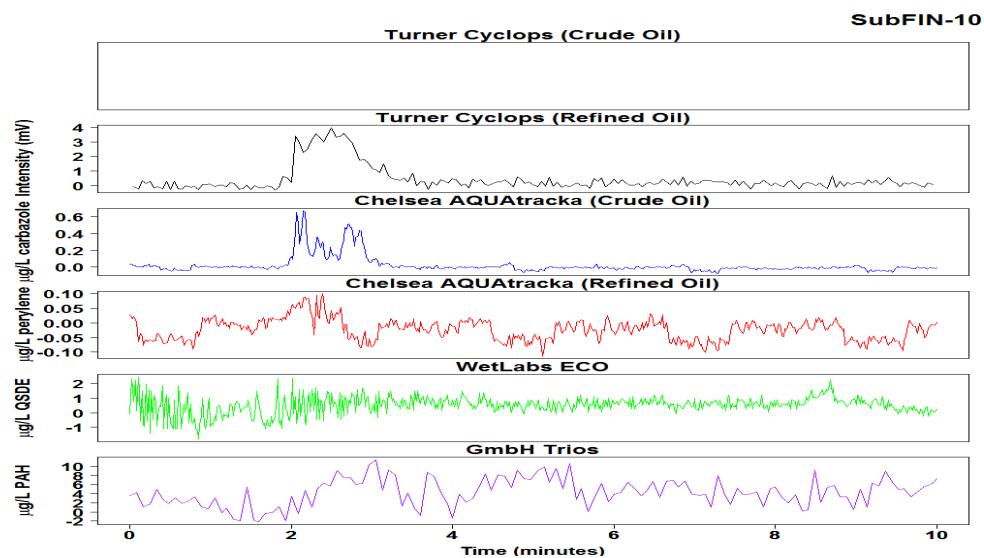


Figure E23. Raw in-situ fluorometer signal for IFO-120, DOR 1:200 (Finasol OSR 52), warm water experiment.

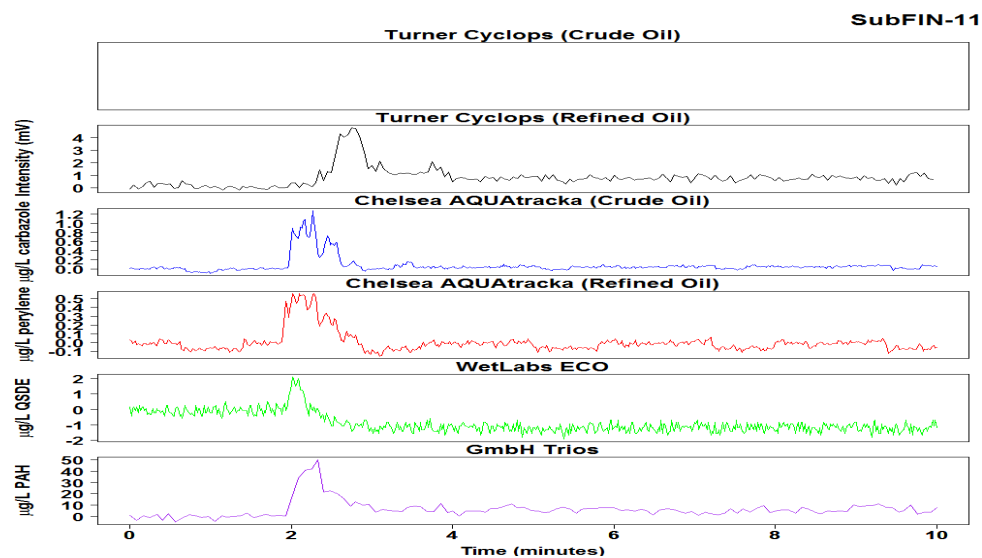


Figure E24. Raw in-situ fluorometer signal for IFO-120, DOR 1:100 (Finasol OSR 52), warm water experiment.

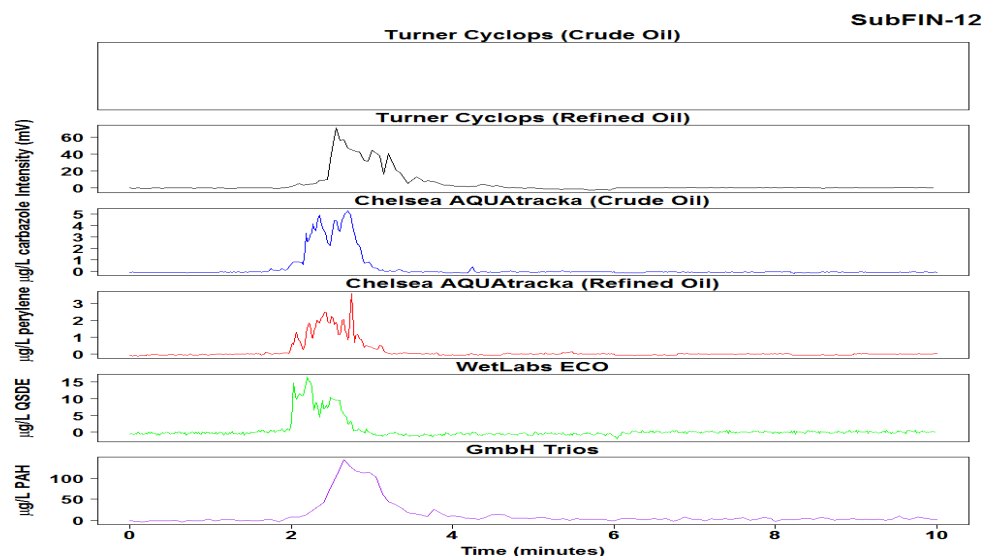


Figure E25. Raw in-situ fluorometer signal IFO-120, DOR 1:20 (Finasol OSR 52) warm expt.

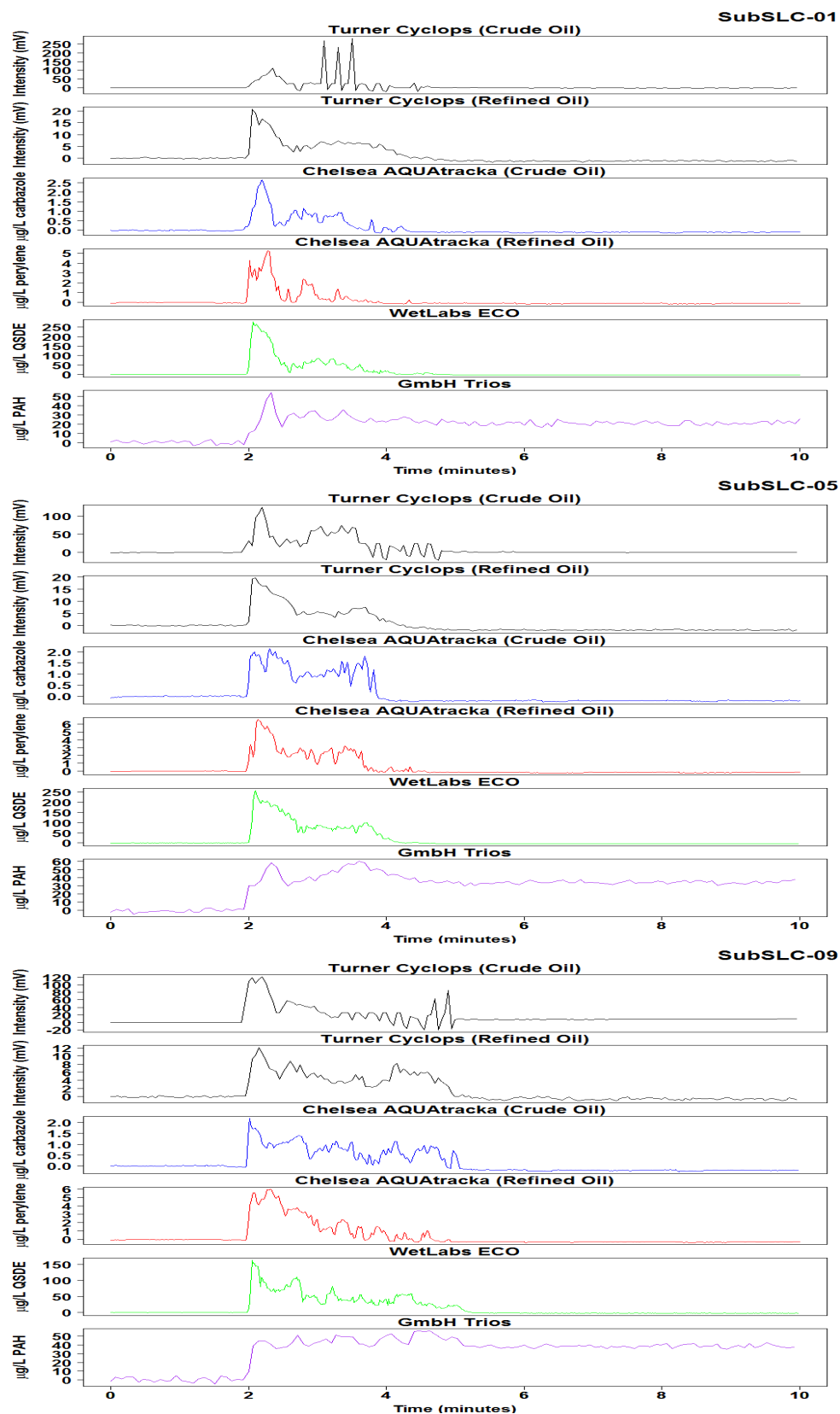


Figure E26. Raw in-situ fluorometer signal for SLC, no dispersant, warm water expt.

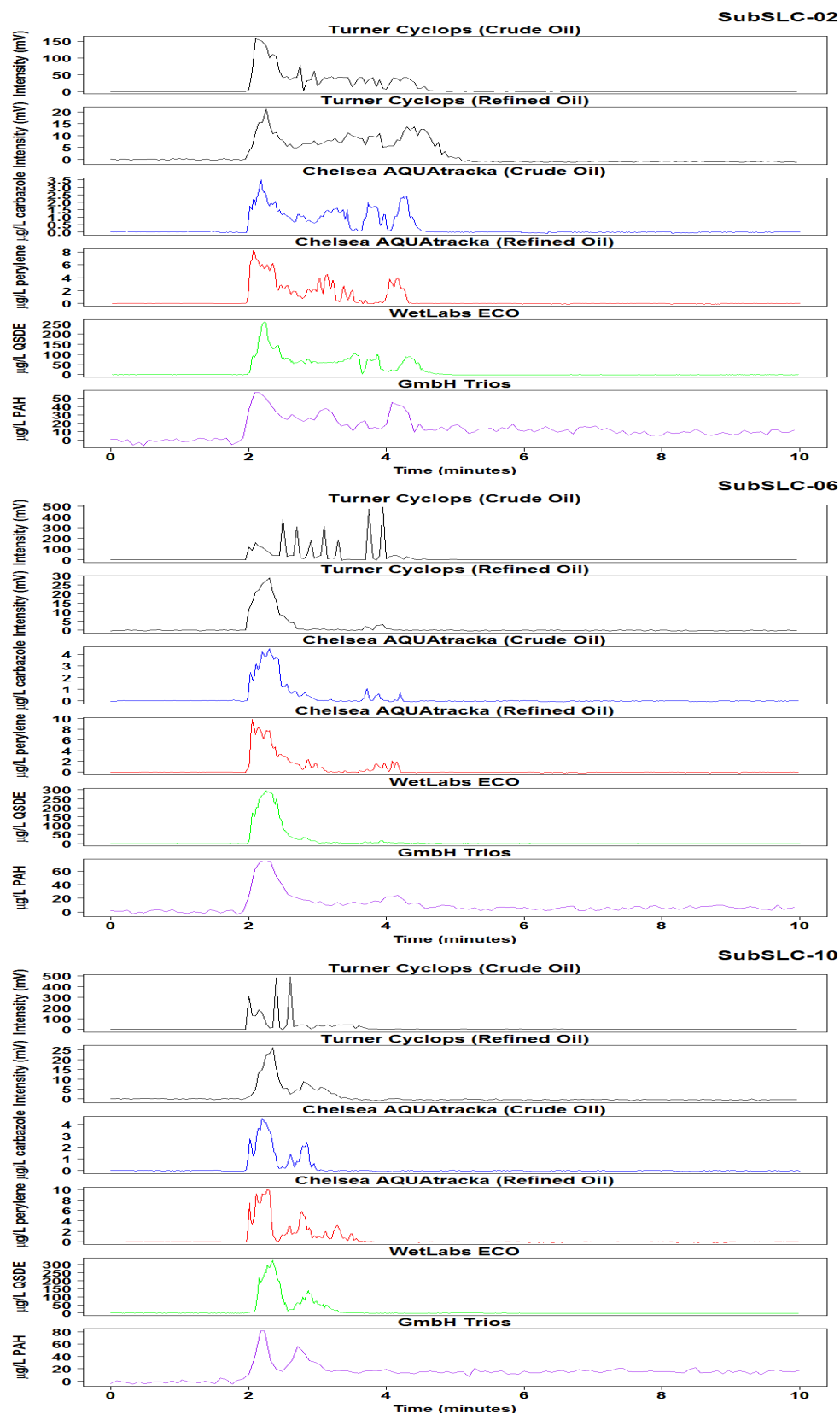


Figure E27. Raw in-situ fluorometer signal for SLC, DOR 1:200 (Corexit 9500), warm expt.

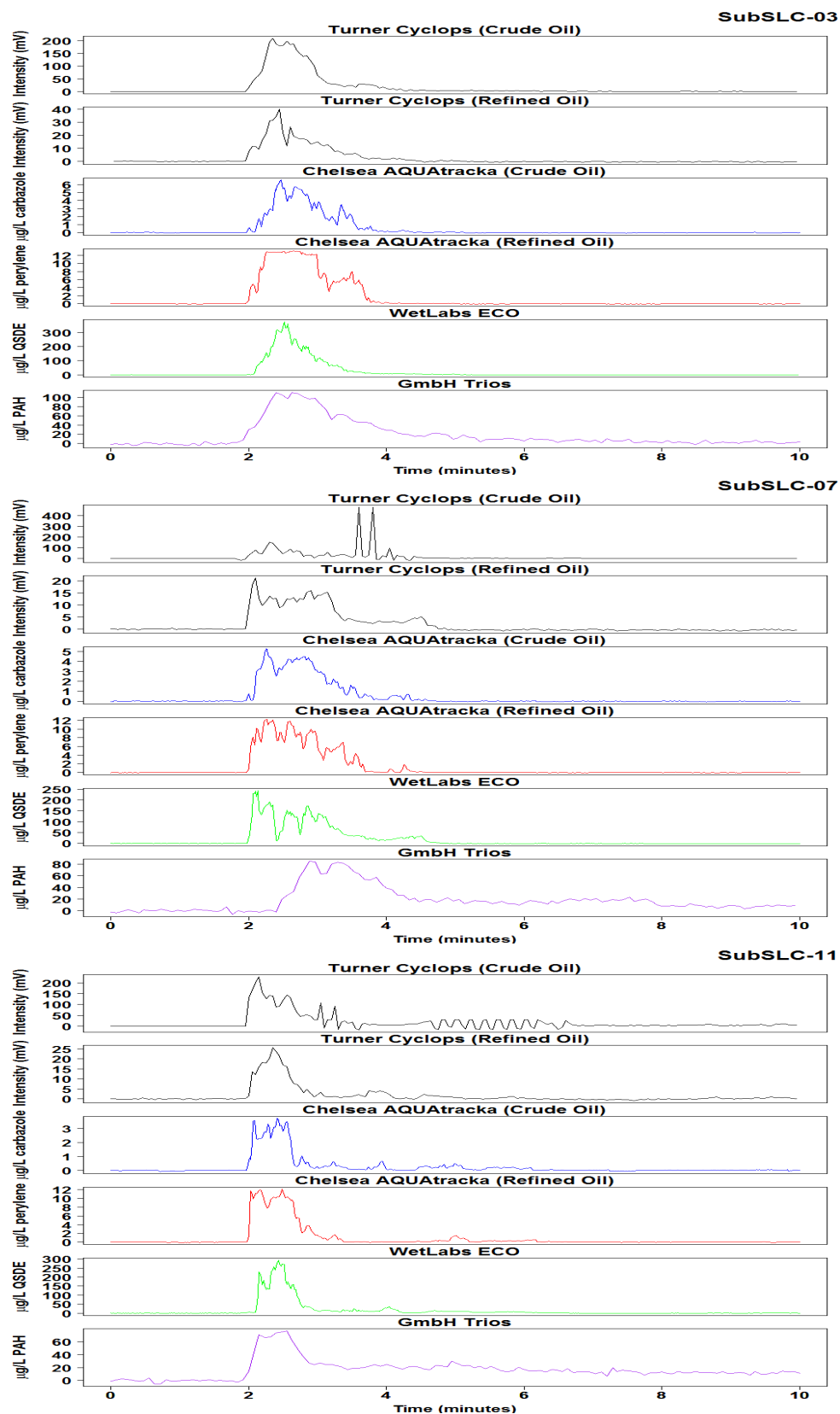


Figure E28. Raw in-situ fluorometer signal for SLC, DOR 1:100 (Corexit 9500), warm expt.

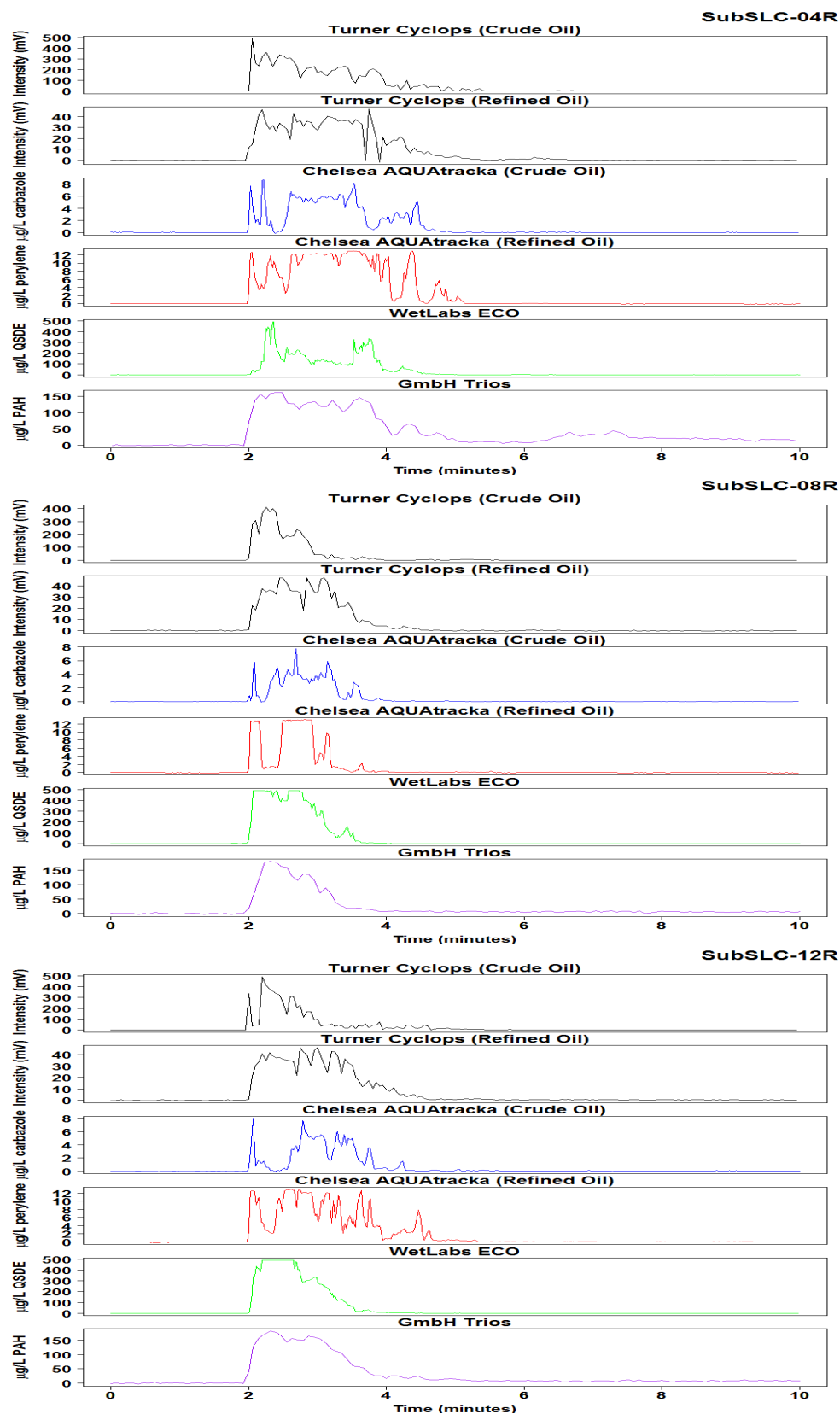


Figure E29. Raw in-situ fluorometer signal for SLC, DOR 1:20 (Corexit 9500), warm expt.

Appendix F – Excitation Emission Matrix Contours

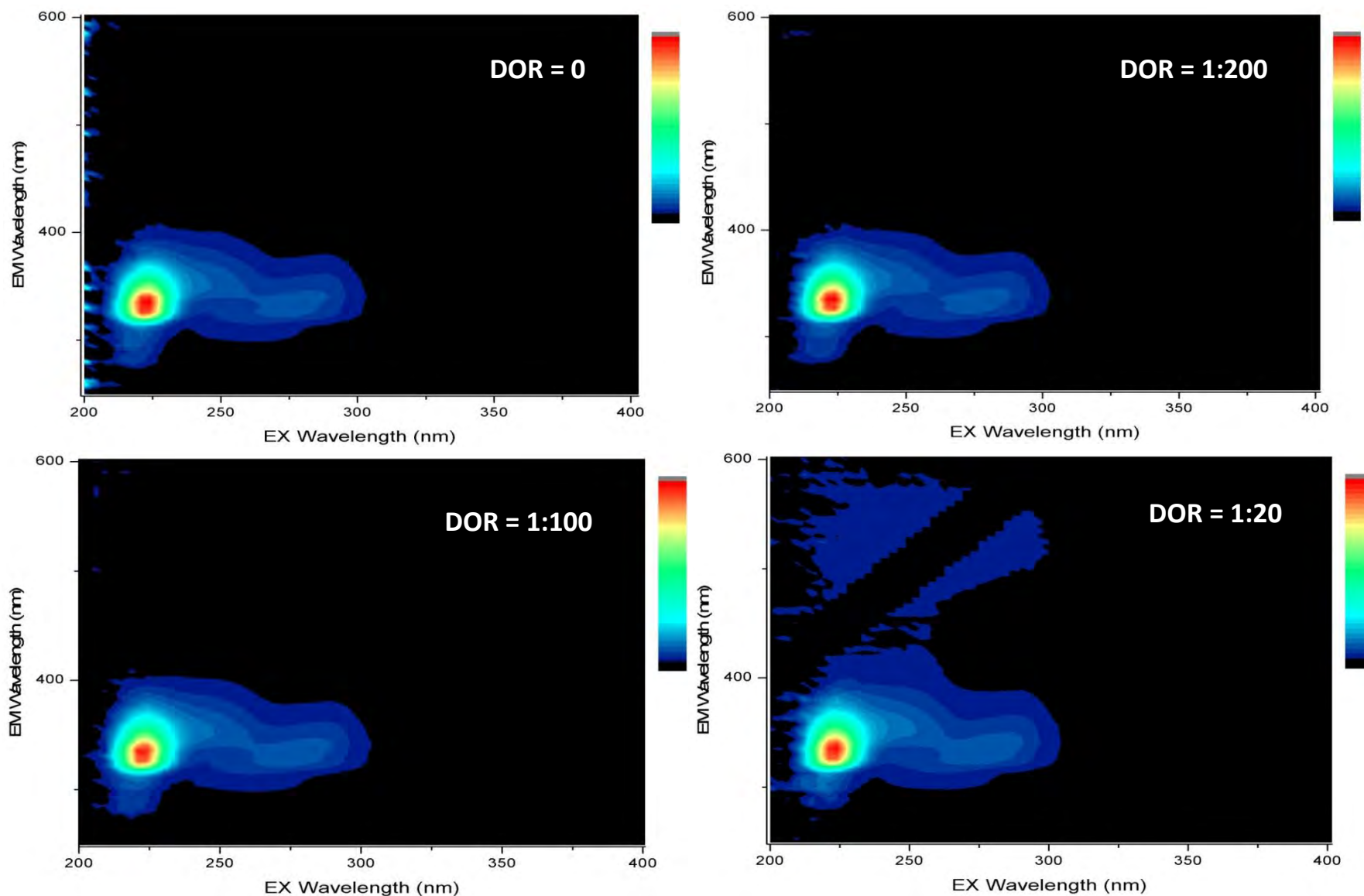


Figure F1. Light Oil Category – IFO-40 oil with dispersant EEMs. Colored contours represent intensity, scaled to maximum fluorescence peak (red).

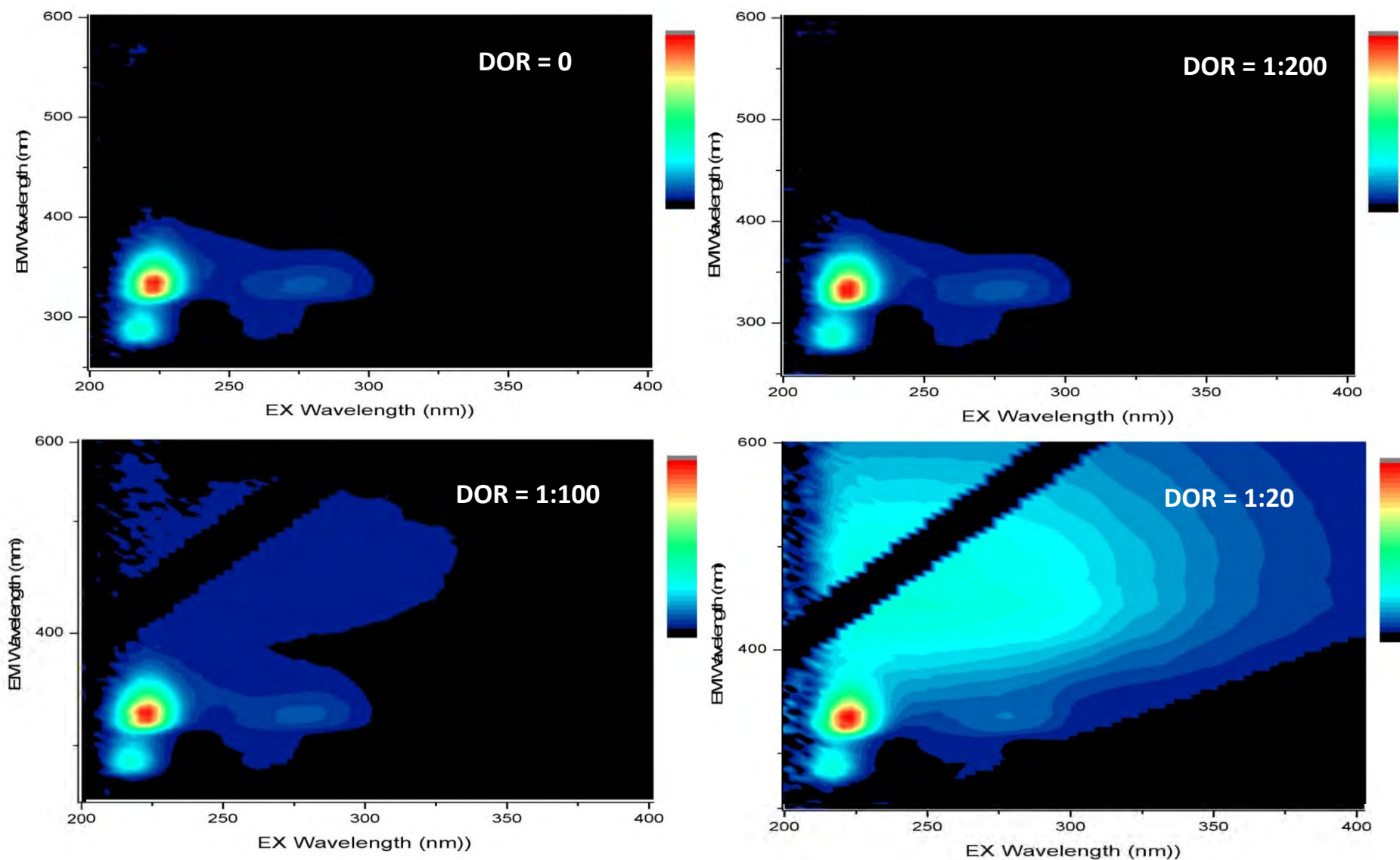


Figure F2. Light Oil Category – Arabian Light crude oil with dispersant EEMs. Colored contours represent intensity, scaled to maximum fluorescence peak (red).

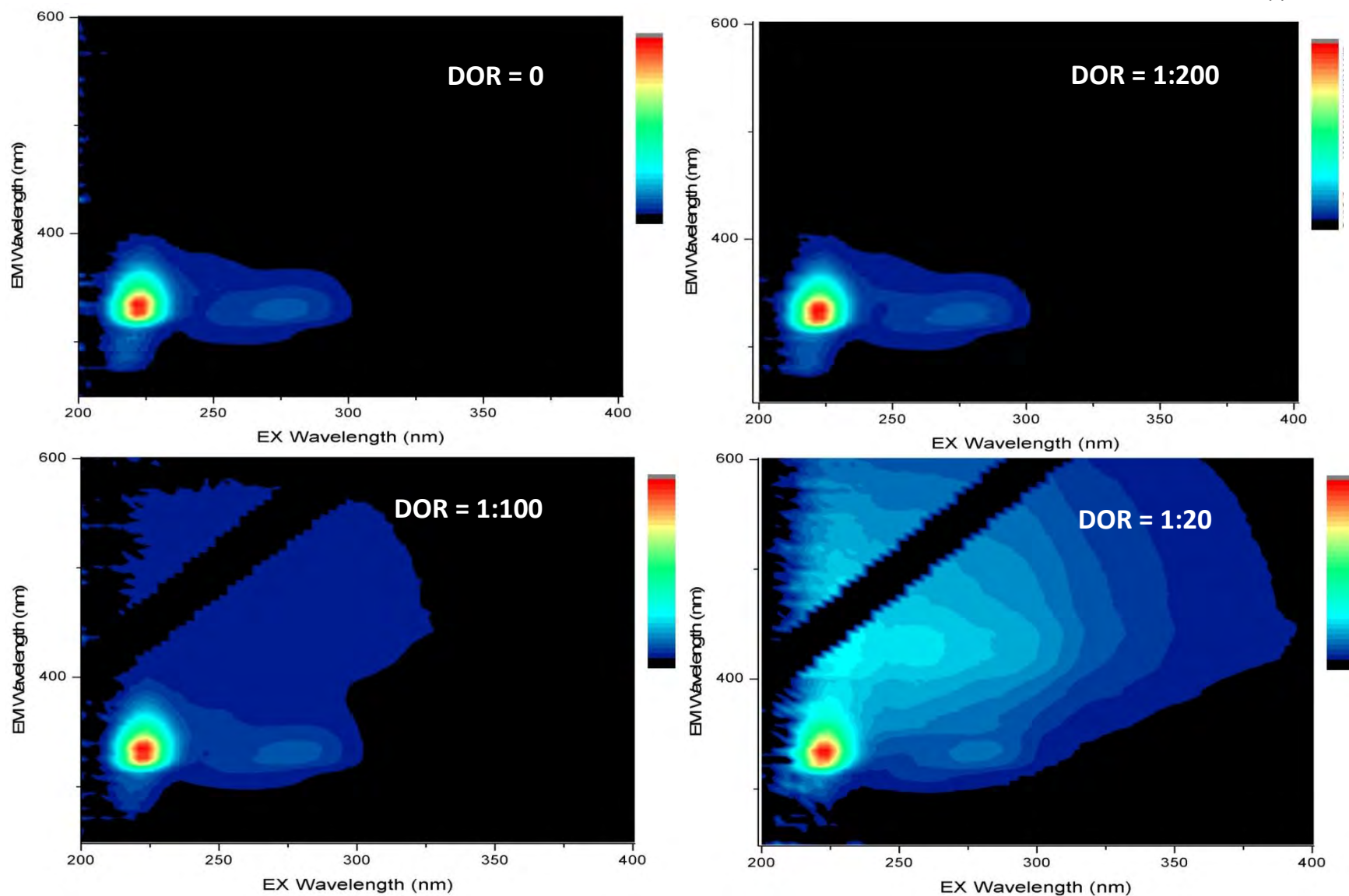


Figure F3. Light Oil Category – Brent crude oil with dispersant EEMs. Colored contours represent intensity, scaled to maximum fluorescence peak (red).

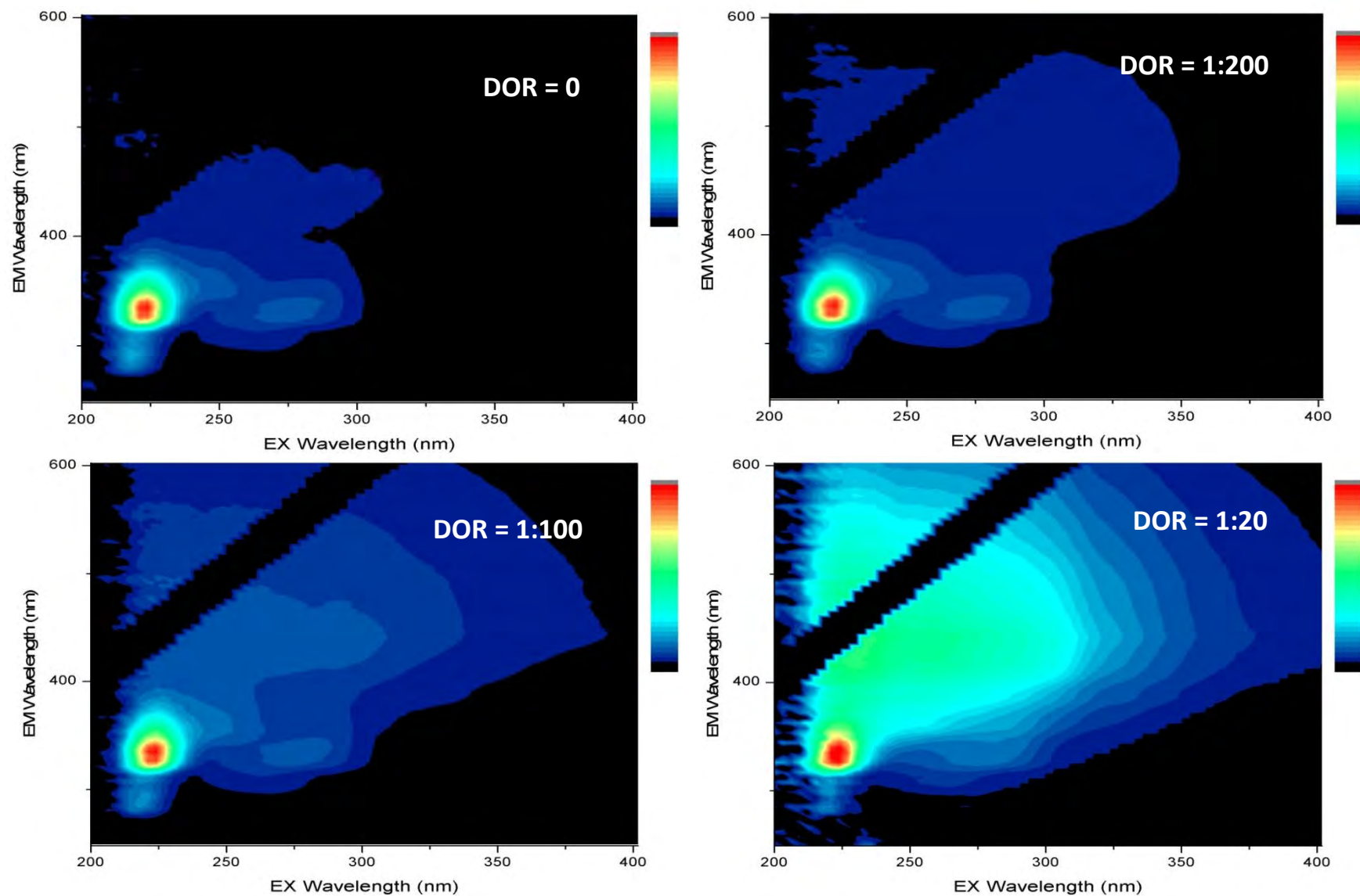


Figure F4. Light Oil Category – Federated crude oil with dispersant EEMs. Colored contours represent intensity, scaled to maximum fluorescence peak (red).

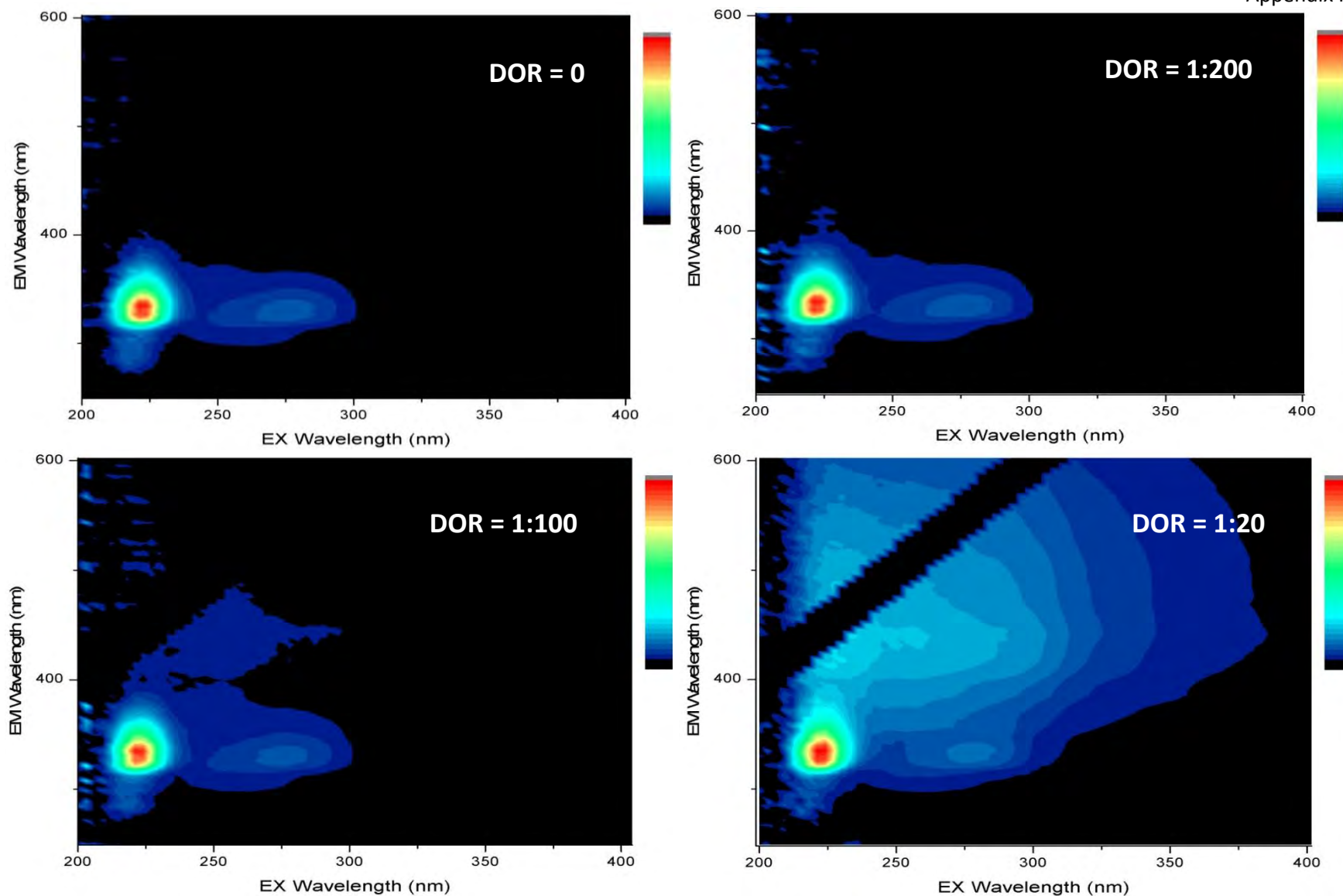


Figure F5. Light Oil Category – Gullfaks crude oil with dispersant EEMs. Colored contours represent intensity, scaled to maximum fluorescence peak (red).

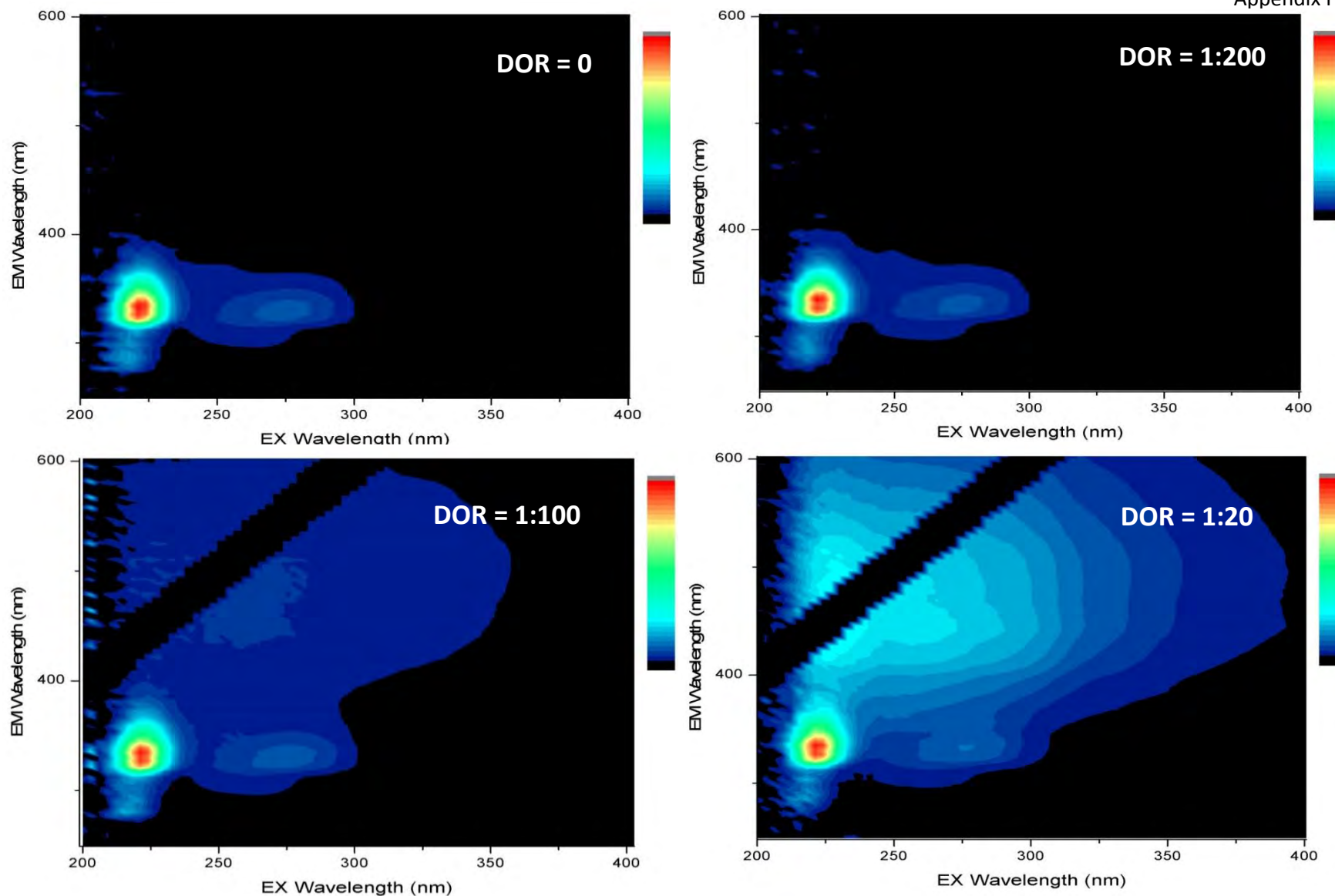


Figure F6. Light Oil Category – Hibernia crude oil with dispersant EEMs. Colored contours represent intensity, scaled to maximum fluorescence peak (red).

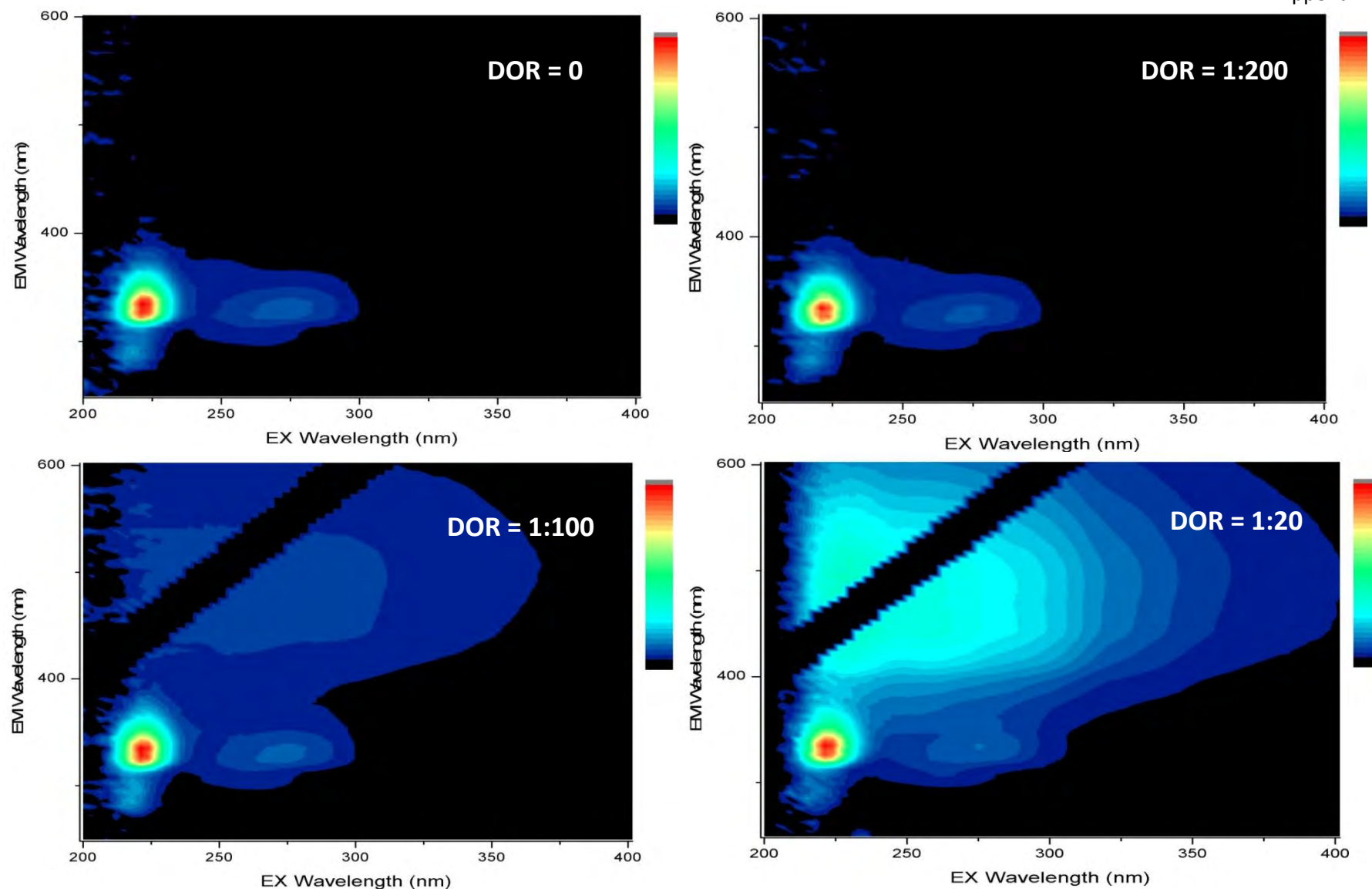


Figure F7. Light Oil Category – MC252 (Discoverer Enterprise) crude oil with dispersant EEMs. Colored contours represent intensity, scaled to maximum fluorescence peak (red).

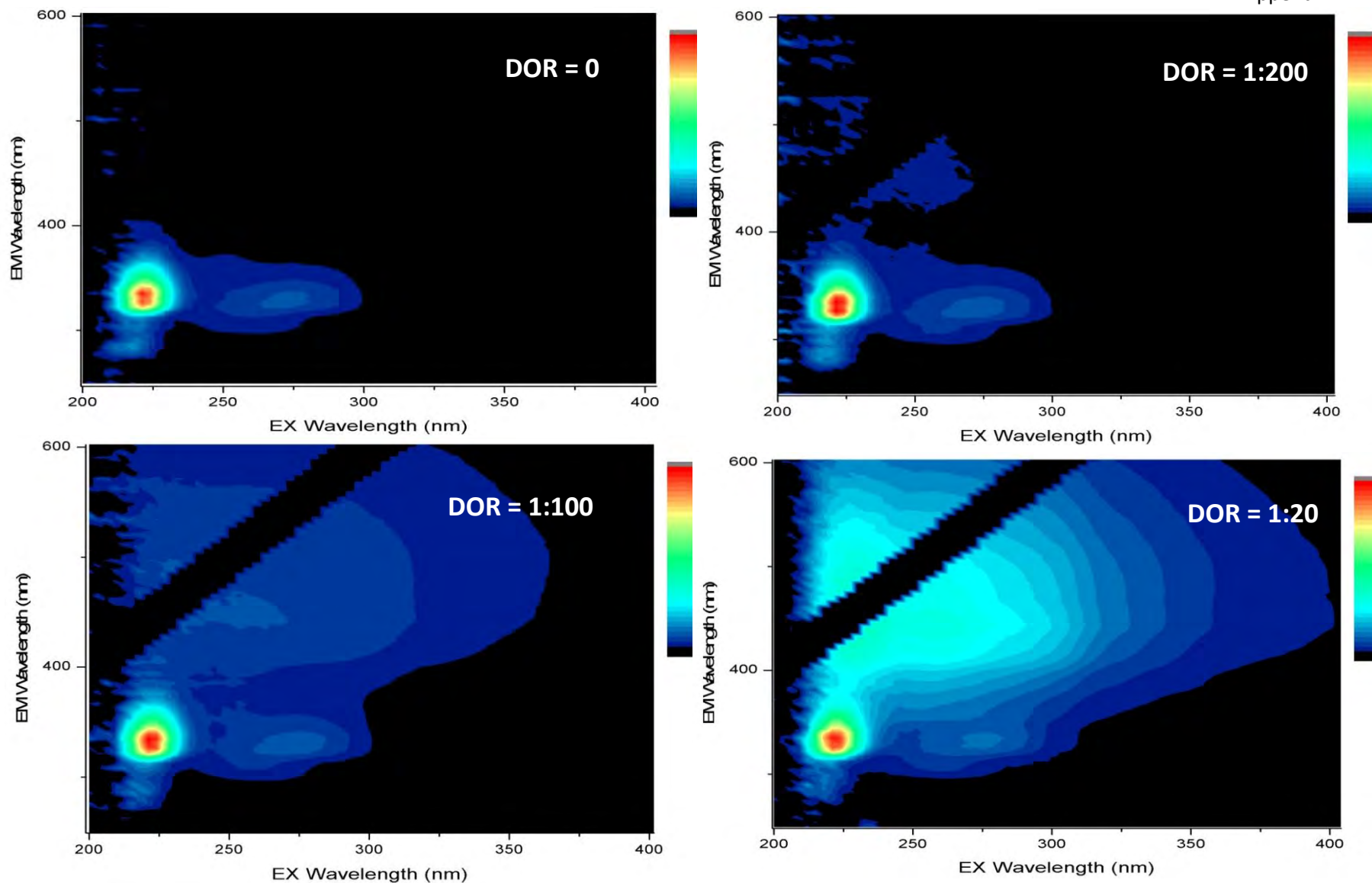


Figure F8. Light Oil Category – MC252 (Generic) crude oil with dispersant EEMs. Colored contours represent intensity, scaled to maximum fluorescence peak (red).

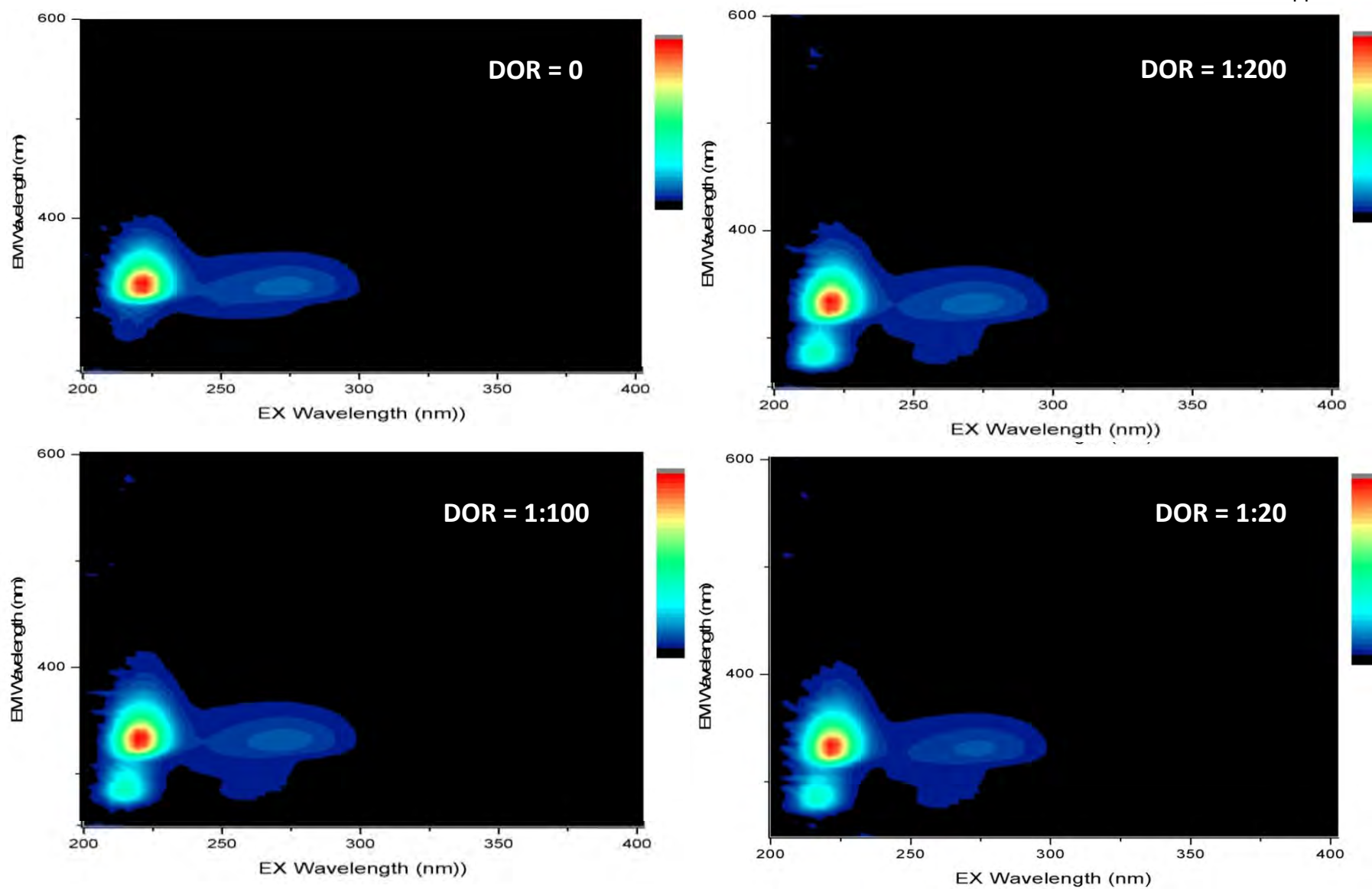


Figure F9. Light Oil Category – Scotian Shelf Condensate crude oil with dispersant EEMs. Colored contours represent intensity, scaled to maximum fluorescence peak (red).

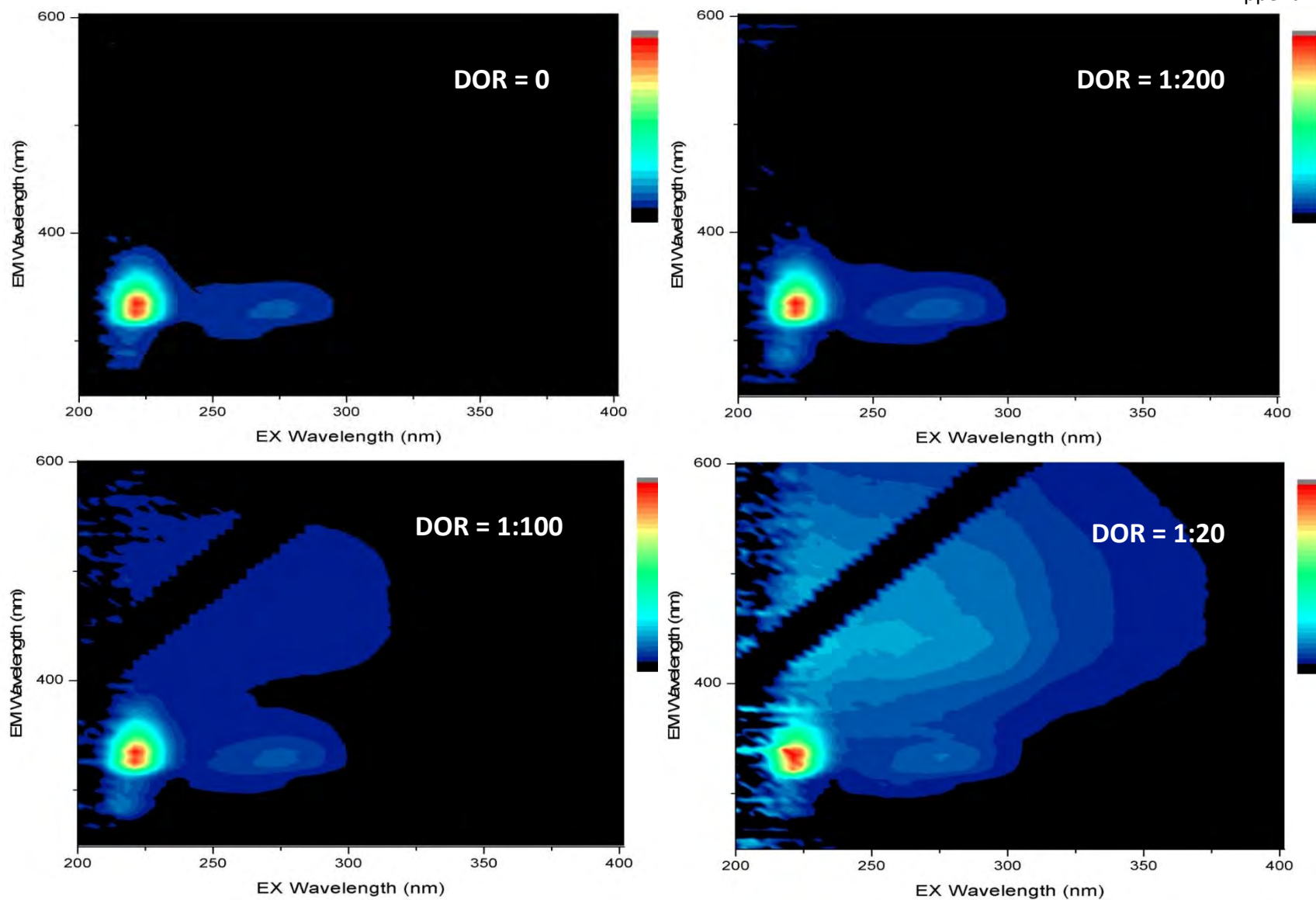


Figure F10. Light Oil Category – Sea Rose crude oil with dispersant EEMs. Colored contours represent intensity, scaled to maximum fluorescence peak (red).

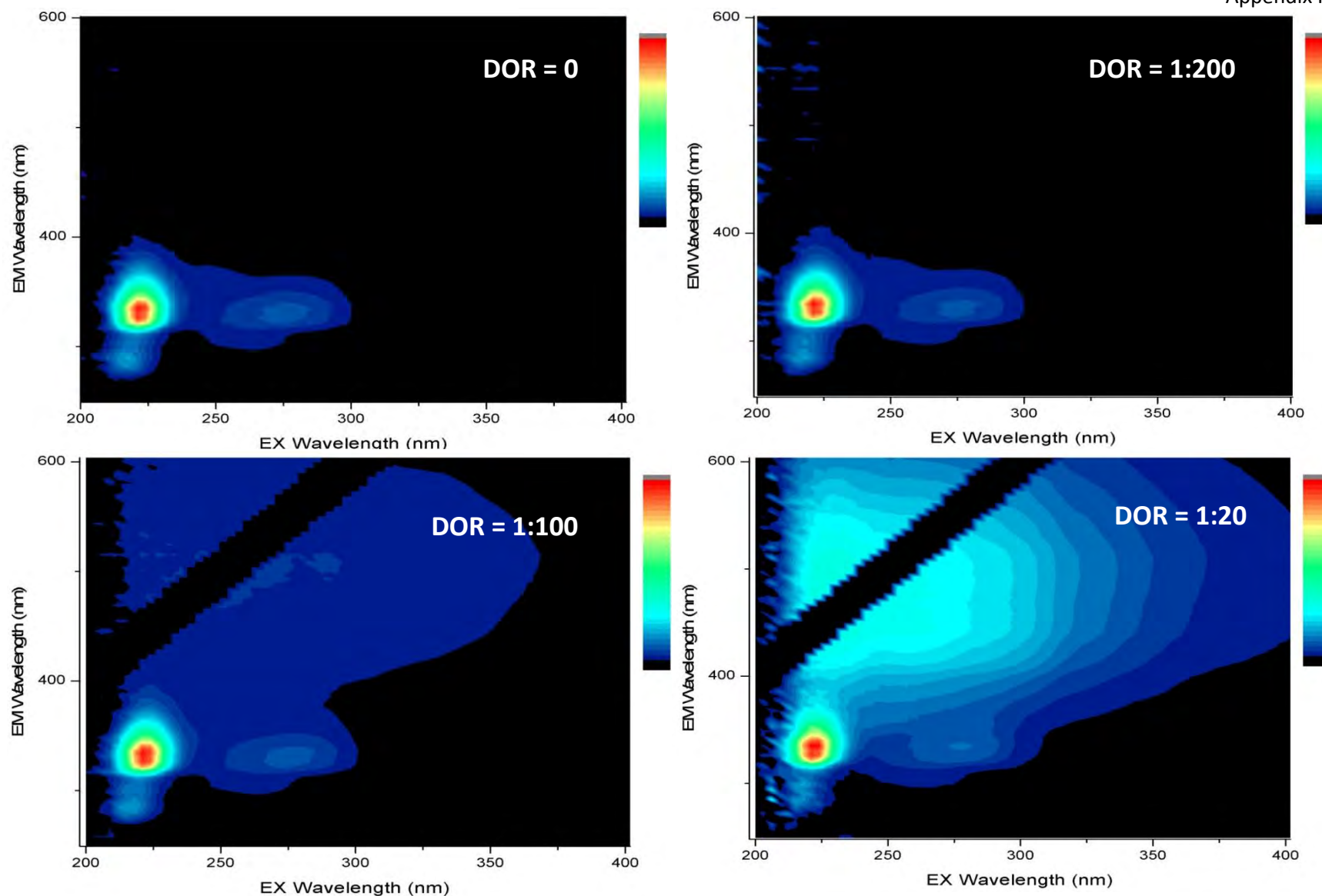


Figure F11. Light Oil Category – Terra Nova crude oil with dispersant EEMs. Colored contours represent intensity, scaled to maximum fluorescence peak (red).

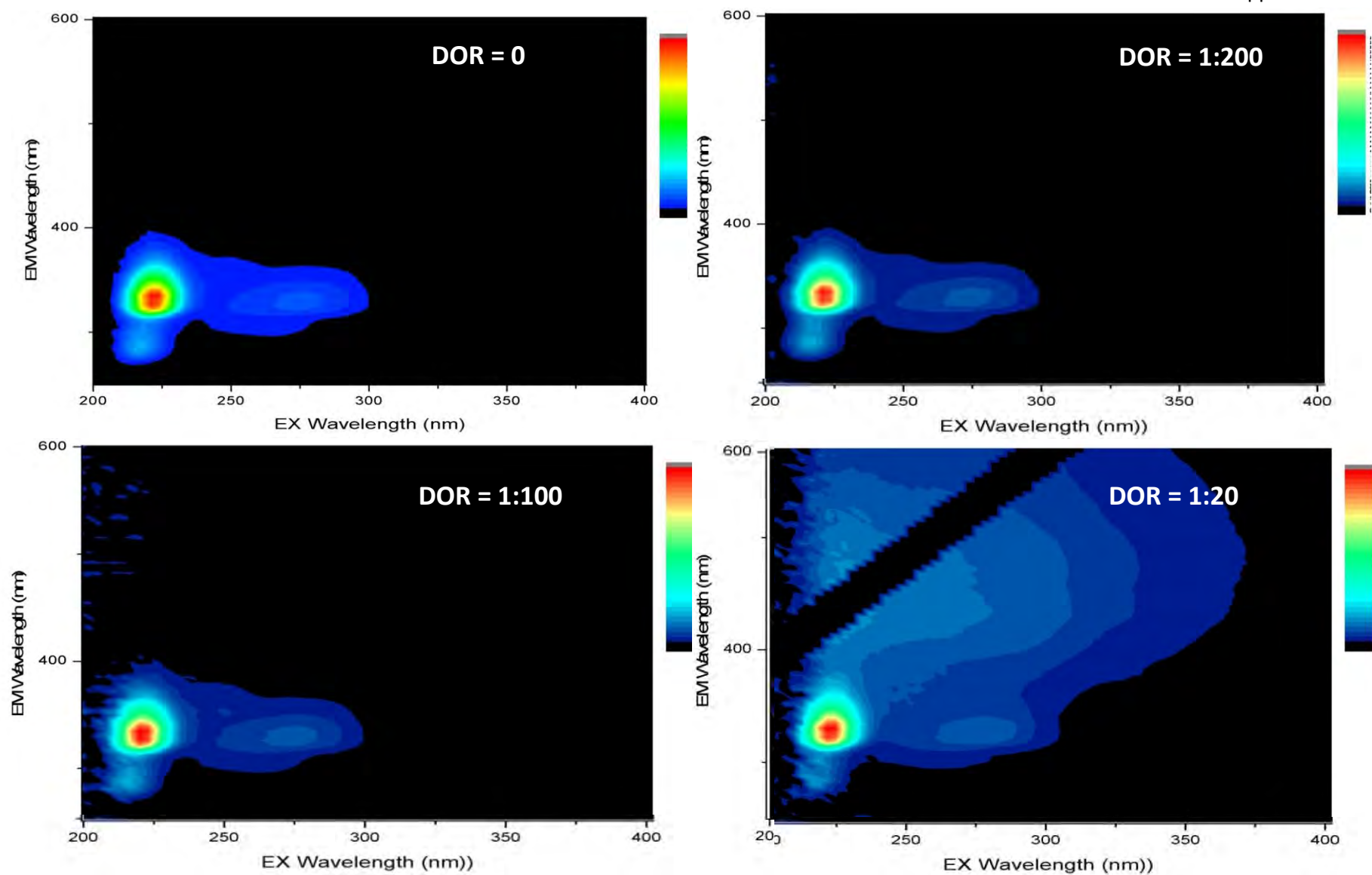


Figure F12. Medium Oil Category - ANS (Alaskan North Slope) crude oil with dispersant EEMs. Colored contours represent intensity, scaled to maximum fluorescence peak (red).

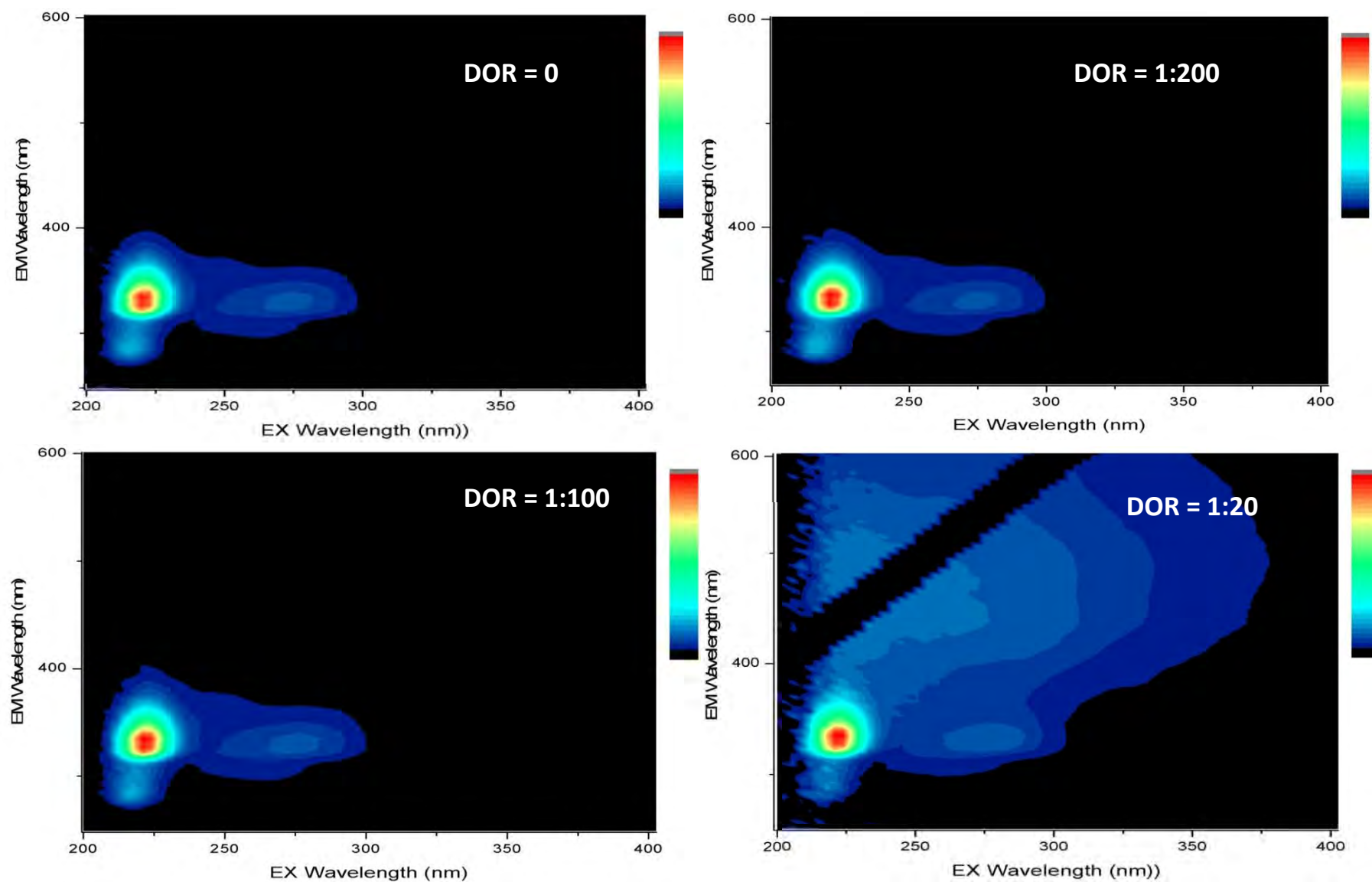


Figure F13. Medium Oil Category - 10% Weathered ANS (Alaskan North Slope) crude oil with dispersant EEMs. Colored contours represent intensity, scaled to maximum fluorescence peak (red).

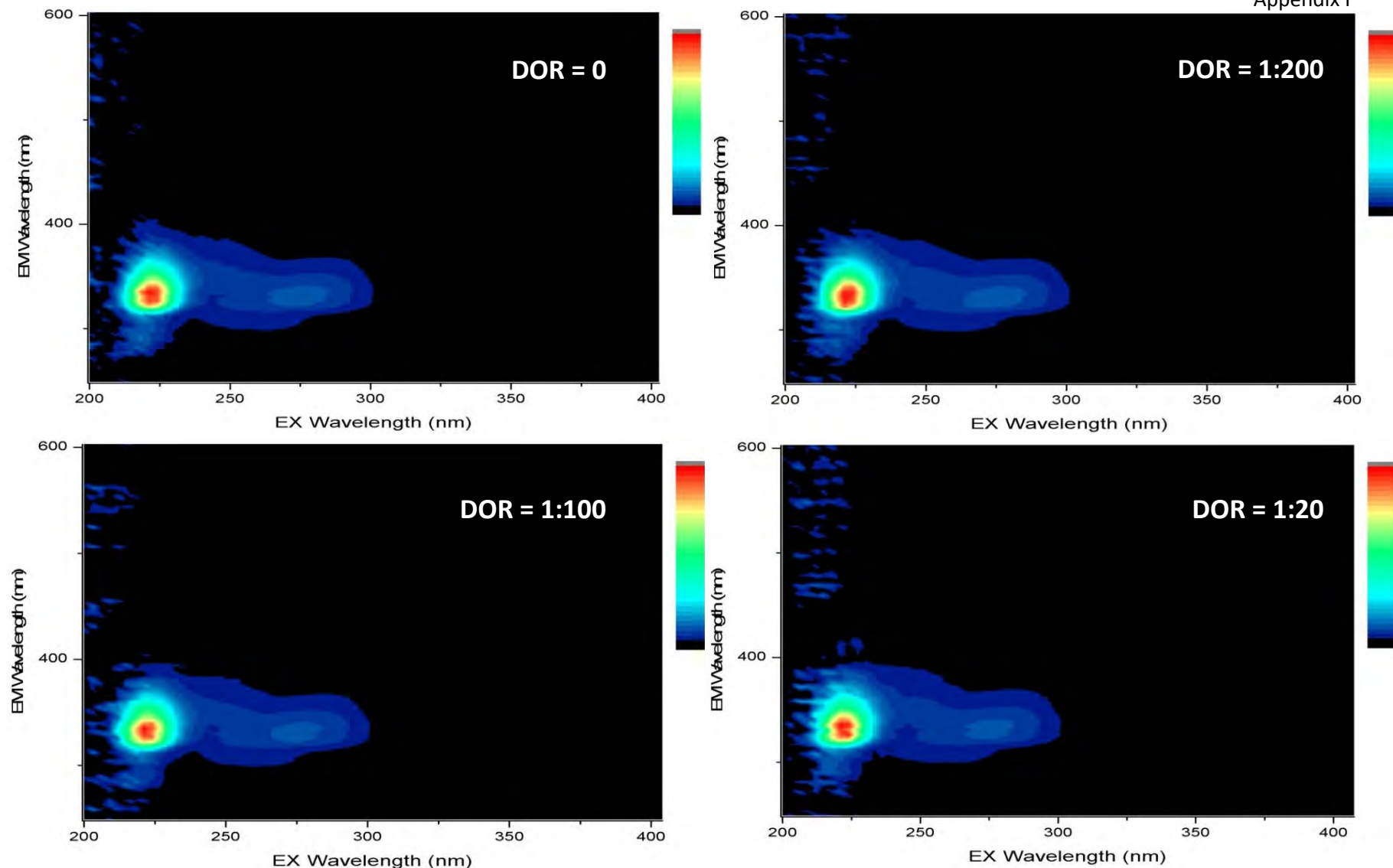


Figure F14. Medium Oil Category – Heavy IFO-120 oil with dispersant EEMs. Colored contours represent intensity, scaled to maximum fluorescence peak (red).

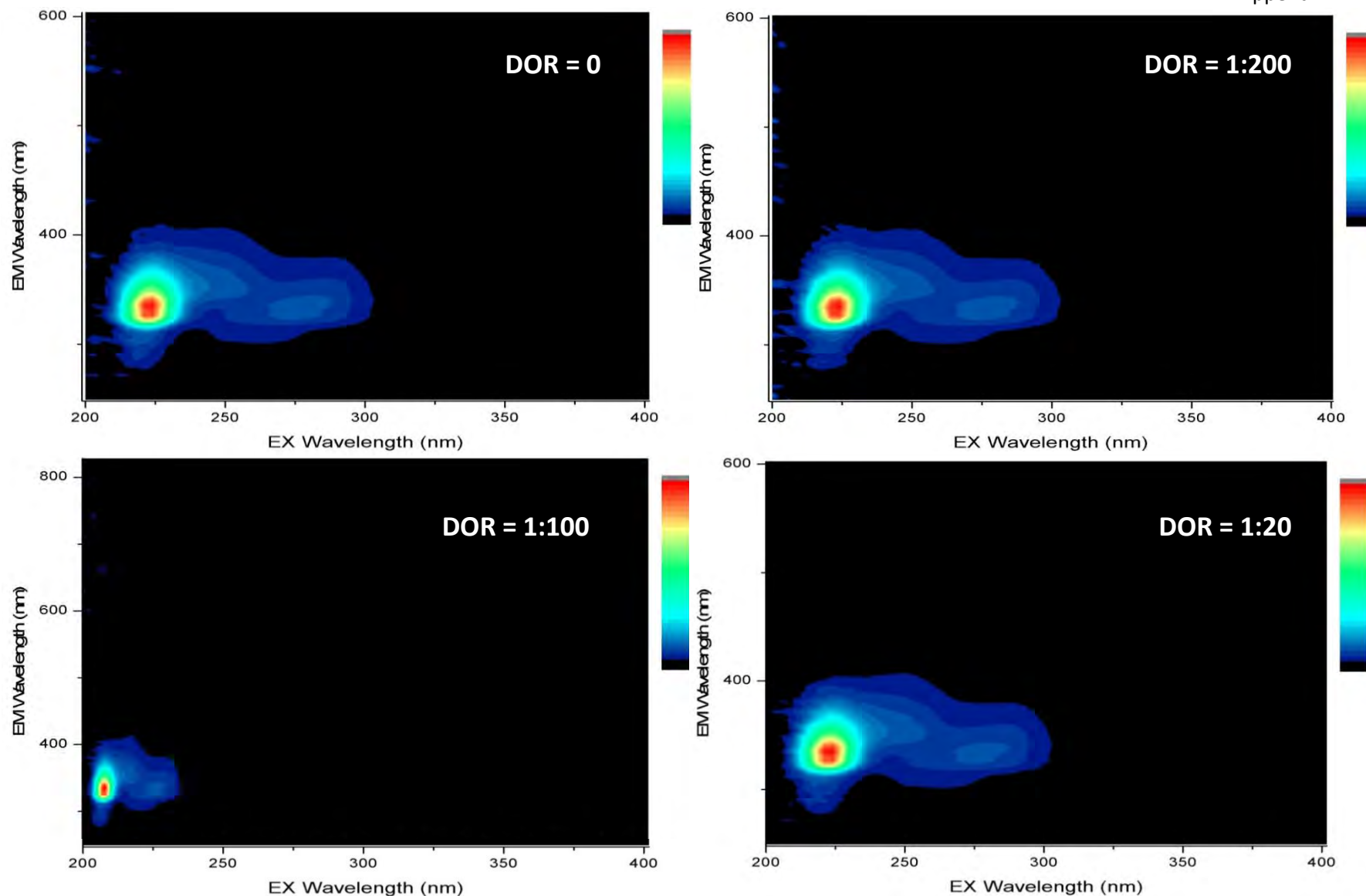


Figure F15. Medium Oil Category - Heavy IFO-180 oil with dispersant EEMs. Colored contours represent intensity, scaled to maximum fluorescence peak (red).

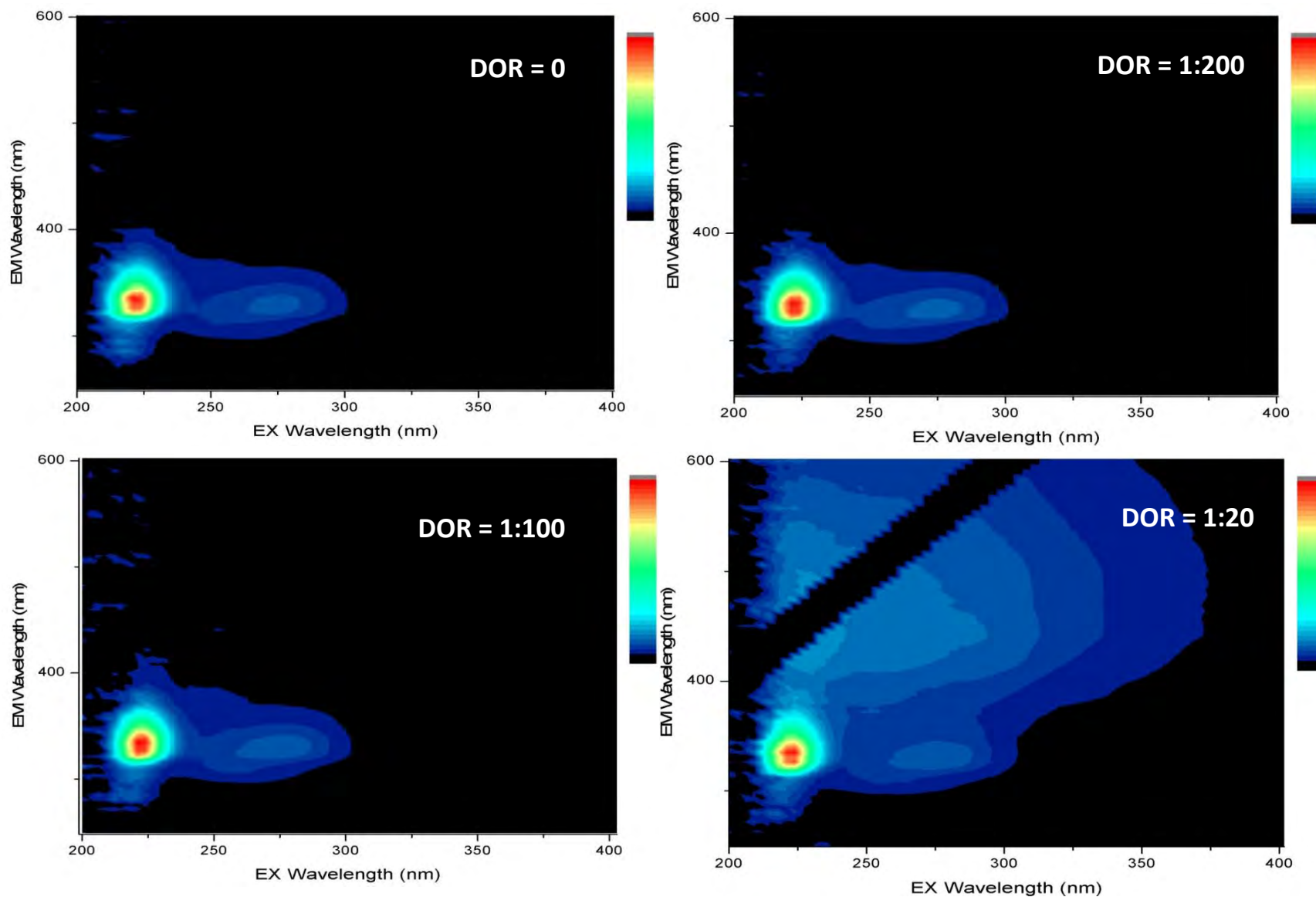


Figure F16. Medium Oil Category - Heidrun crude oil with dispersant EEMs. Colored contours represent intensity, scaled to maximum fluorescence peak (red).

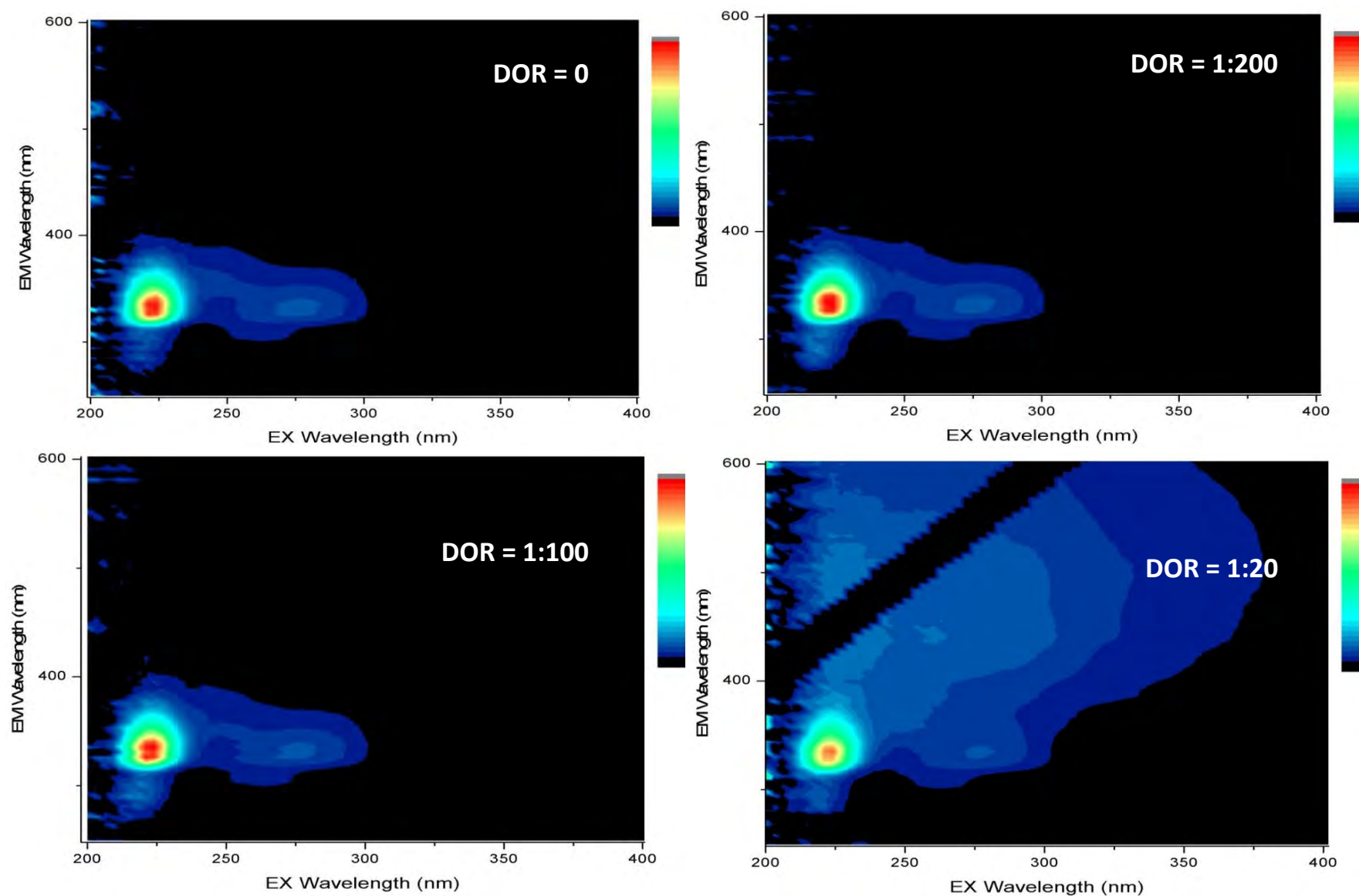


Figure F17. Medium Oil Category - Lago crude oil with dispersant EEMs. Colored contours represent intensity, scaled to maximum fluorescence peak (red).

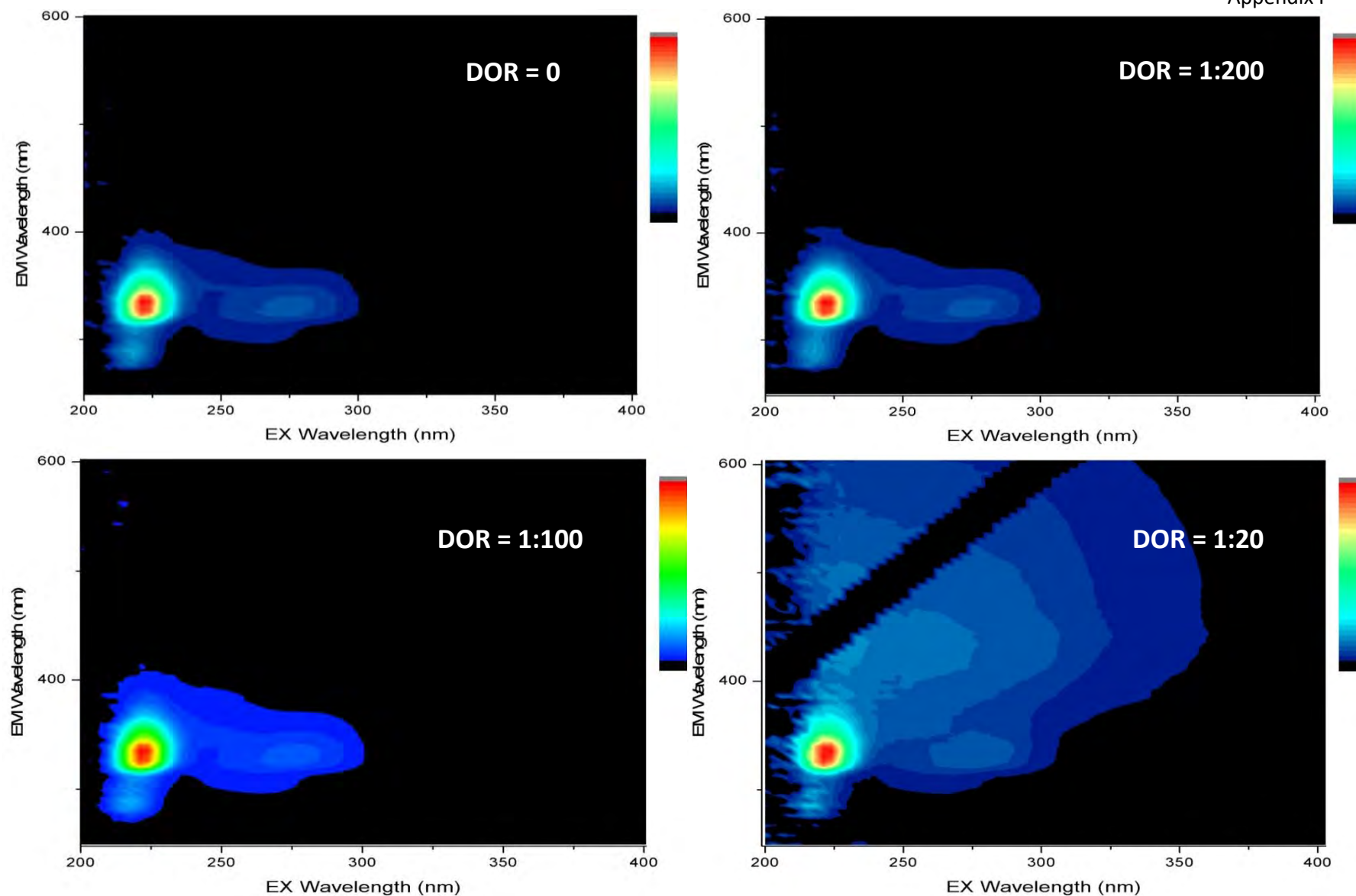


Figure F18. Medium Oil Category - Mesa crude oil with dispersant EEMs. Colored contours represent intensity, scaled to maximum fluorescence peak (red).

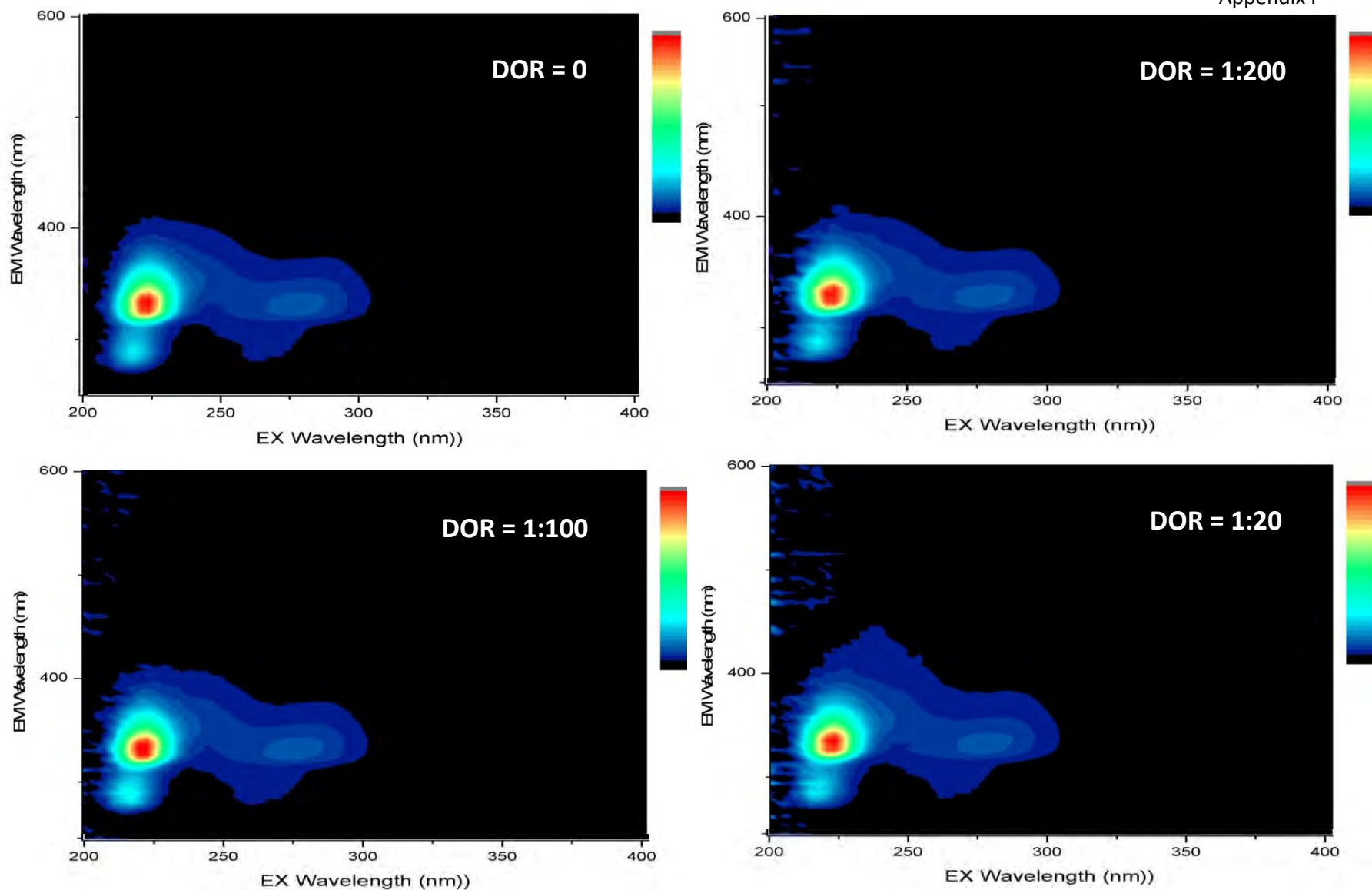


Figure F19. Medium Oil Category – Santa Clara crude oil with dispersant EEMs. Colored contours represent intensity, scaled to maximum fluorescence peak (red).

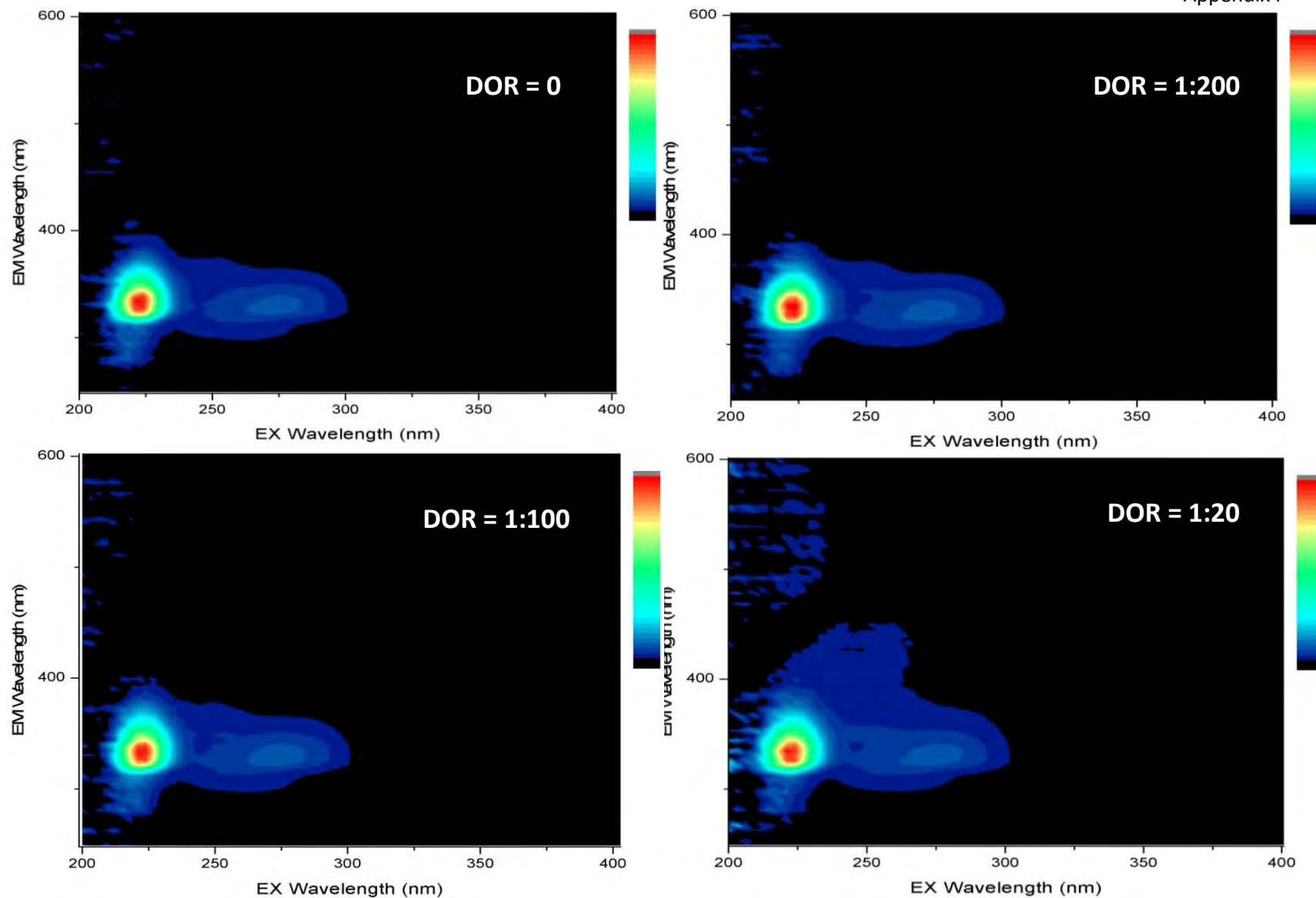


Figure F20. Medium Oil Category - Vasconia crude oil with dispersant EEMs. Colored contours represent intensity, scaled to maximum fluorescence peak (red).

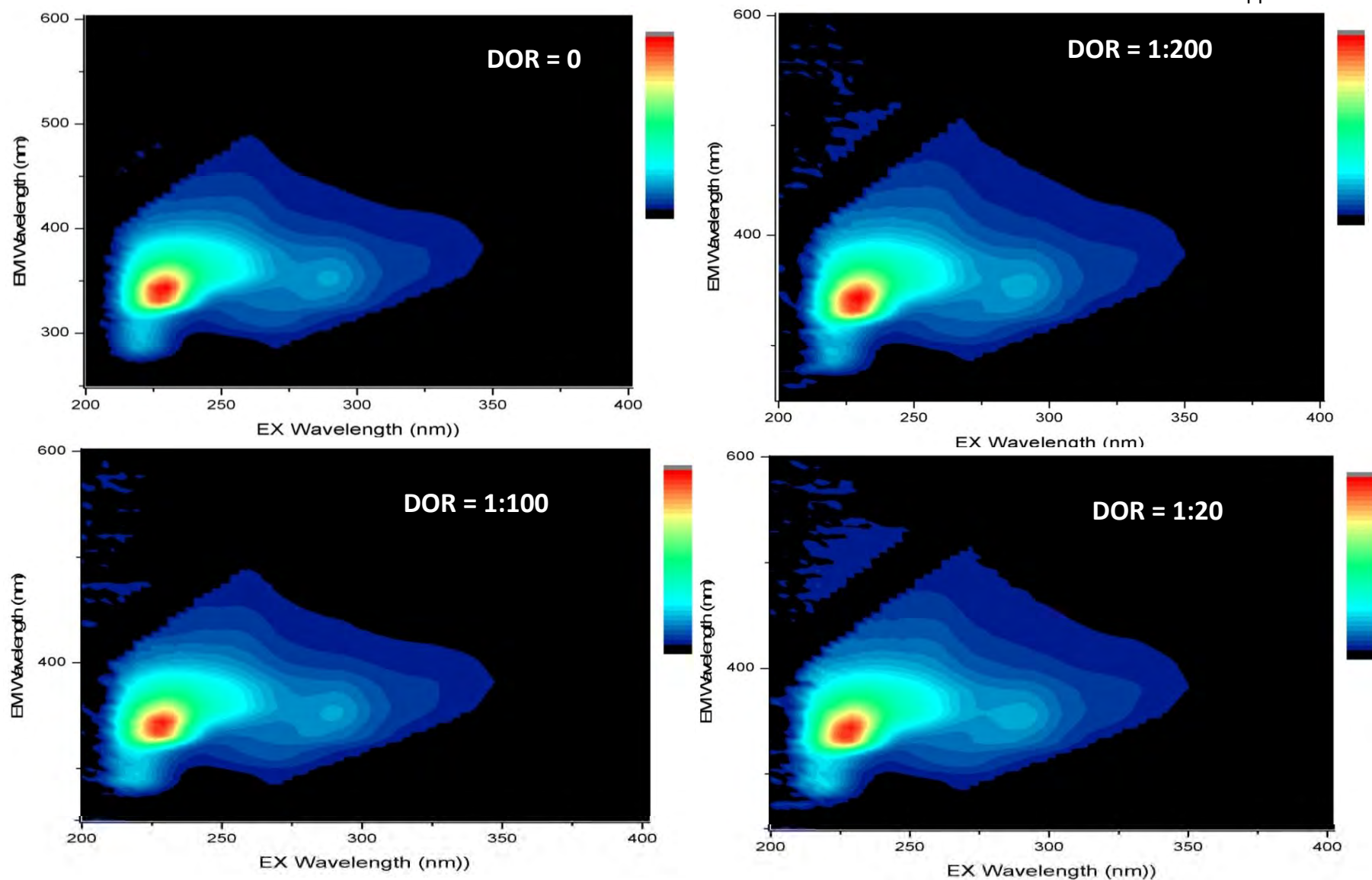


Figure F21. Heavy Oil Category - Belridge crude oil with dispersant EEMs. Colored contours represent intensity, scaled to maximum fluorescence peak (red).

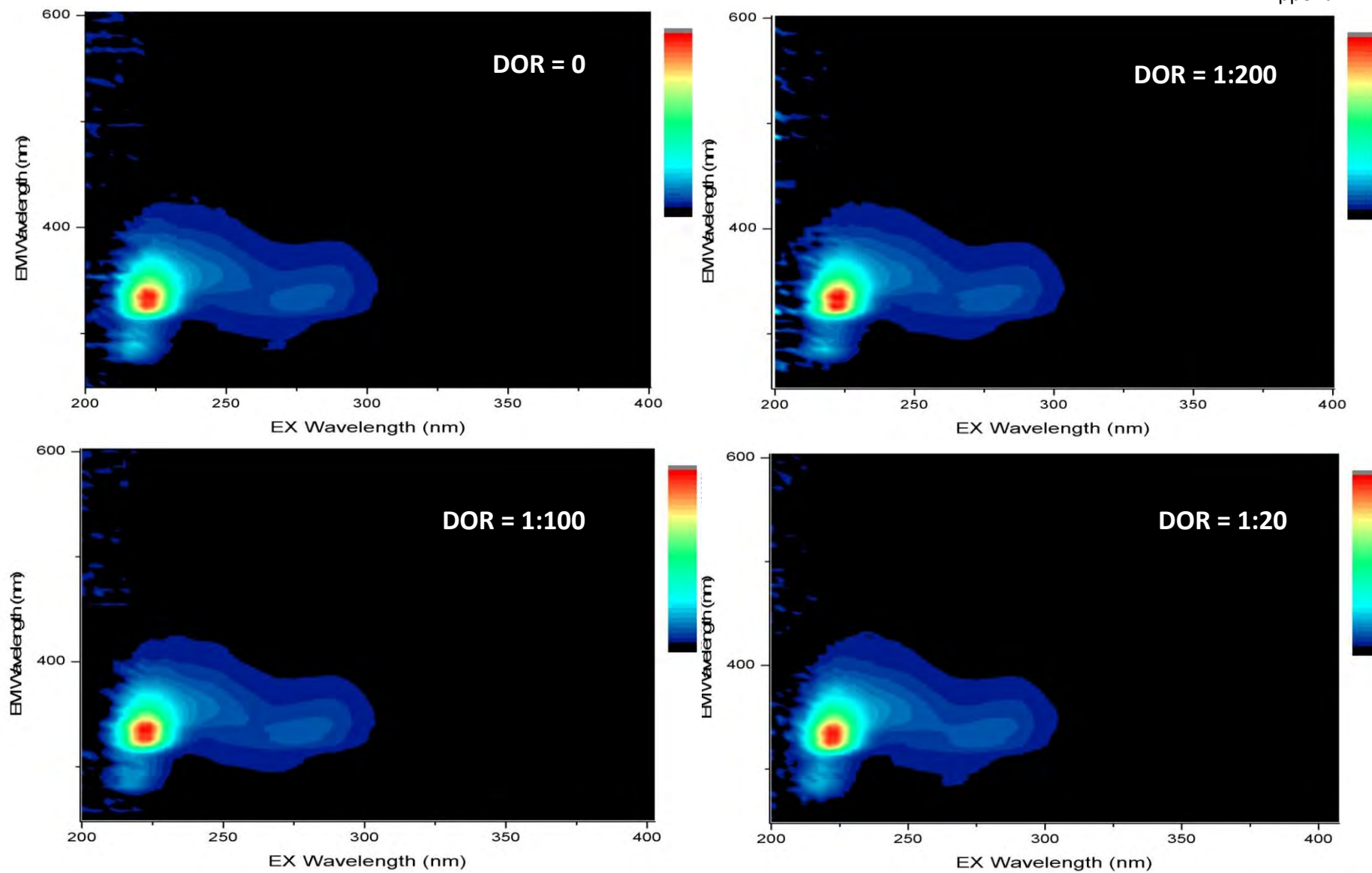


Figure F22. Heavy Oil Category - Hondo crude oil with dispersant EEMs. Colored contours represent intensity, scaled to maximum fluorescence peak (red).

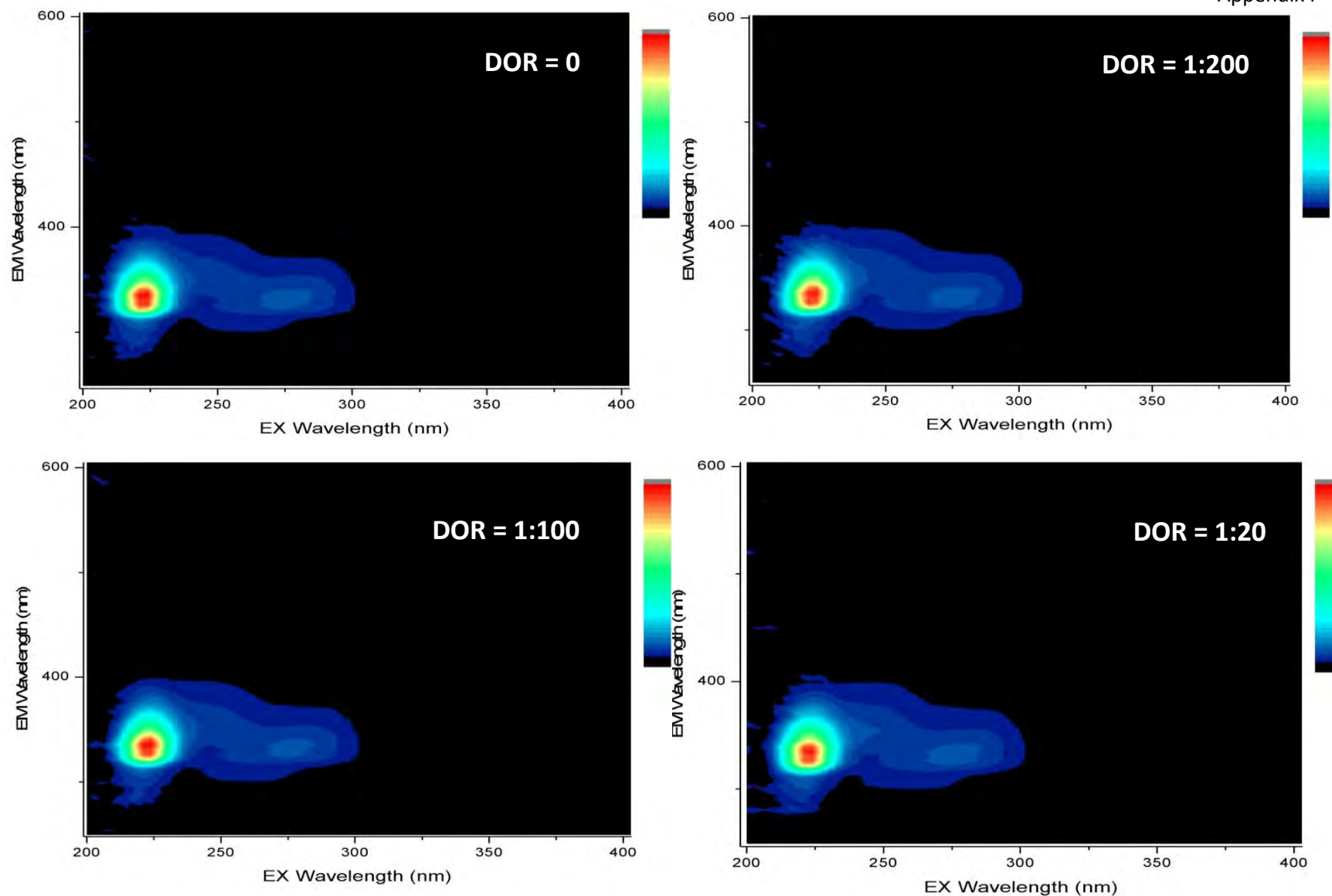


Figure F23. Heavy Oil Category – IFO-300 crude oil with dispersant EEMs. Colored contours represent intensity, scaled to maximum fluorescence peak (red).

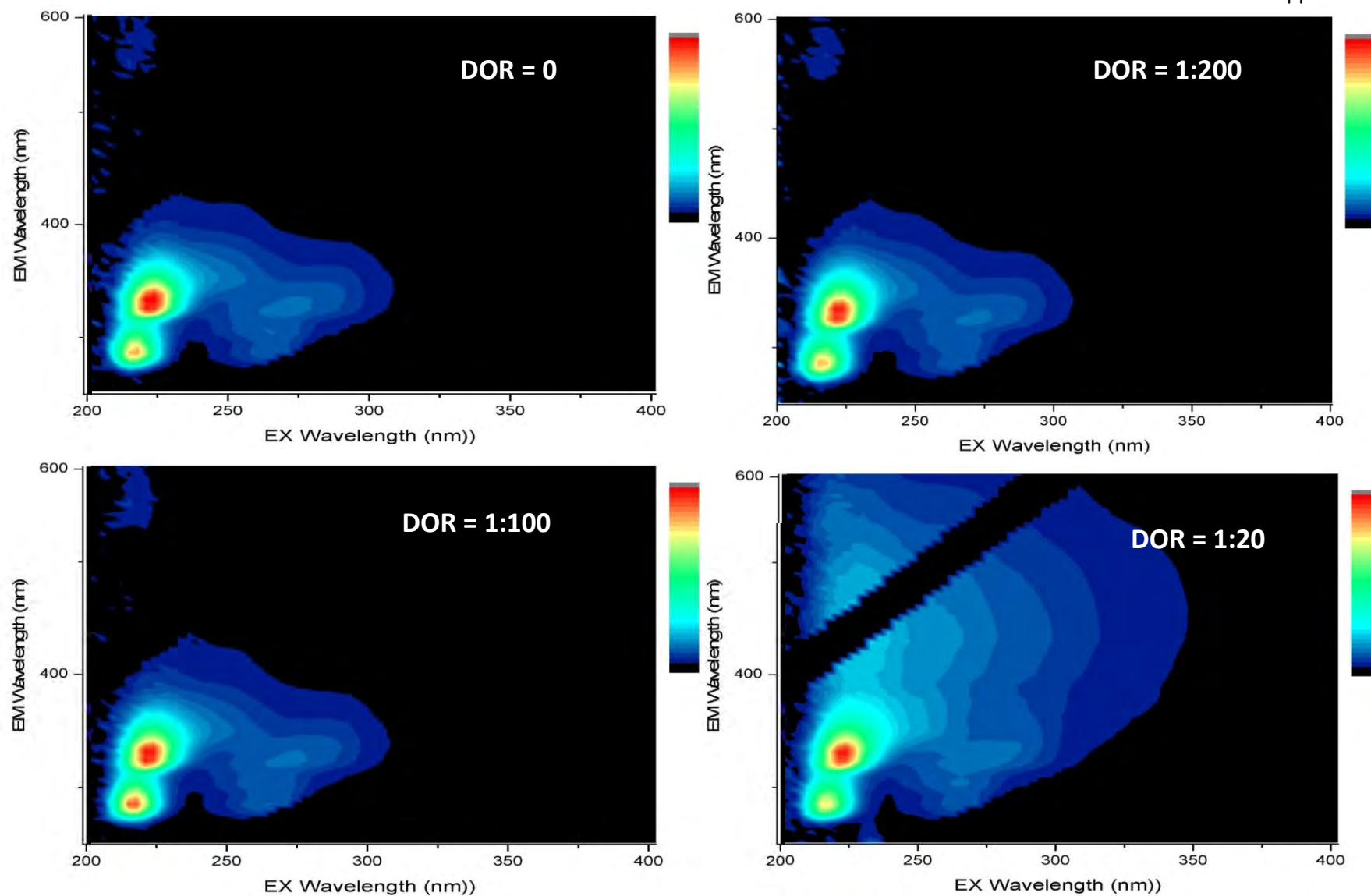


Figure F24. Dilbit Oil Category – Access Western Blend oil with dispersant EEMs. Colored contours represent intensity, scaled to maximum fluorescence peak (red).

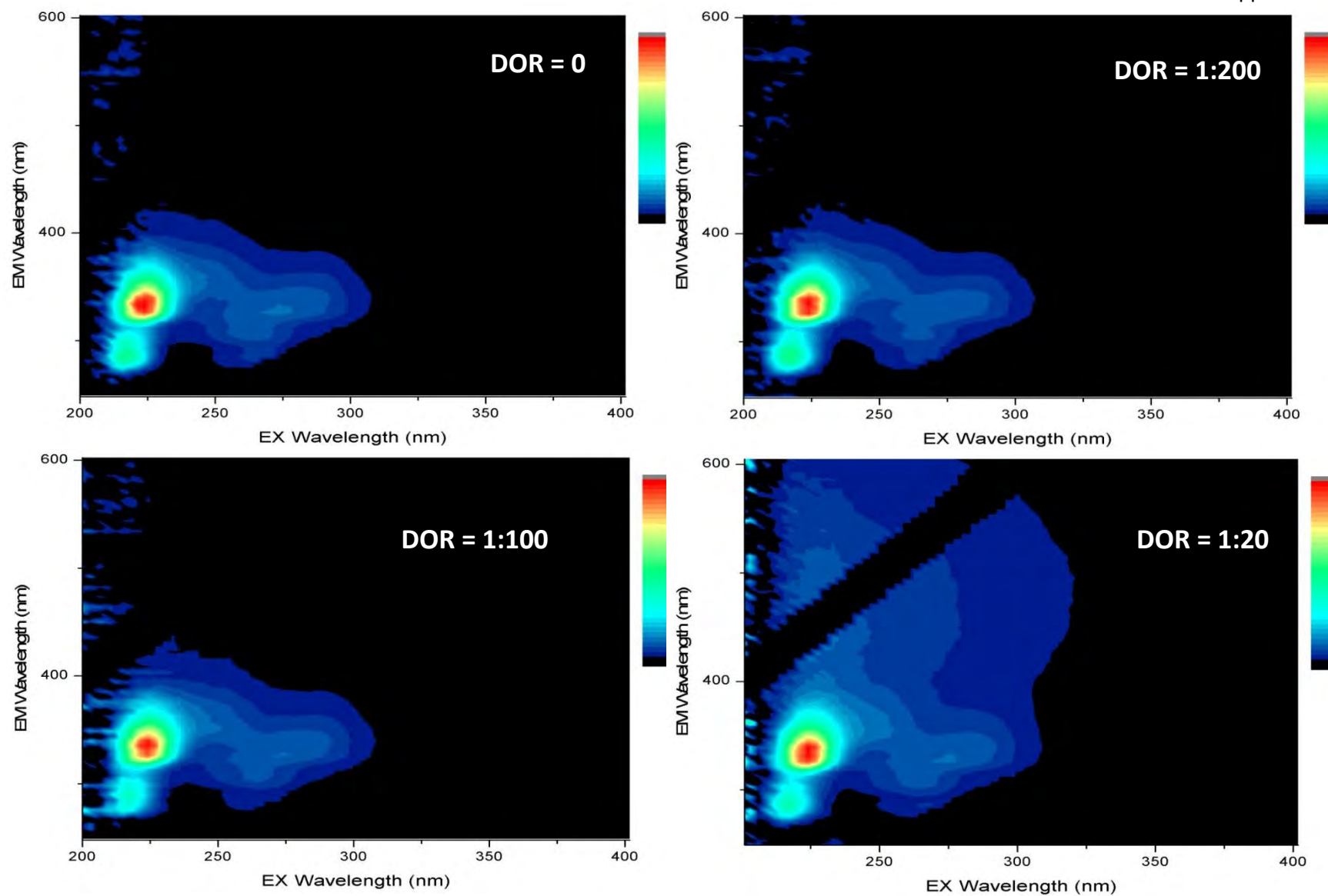


Figure F25. Dilbit Oil Category – Cold Lake oil with dispersant EEMs. Colored contours represent intensity, scaled to maximum fluorescence peak (red).

IAA No. E12PG00037

Final Report

Dispersant Effectiveness, In-Situ Droplet Size Distribution and Numerical Modeling to Assess
Subsurface Dispersant Injection as a Deepwater Blowout Oil Spill Response Option
and
Evaluation of Oil Fluorescence Characteristics to Improve Forensic Response Tools

APPENDIX G VDROP-J and JETLAG Numerical Plume Modeling

Report on Simulated Oil Plume Advanced Numerical Modeling using VDROP-J and JETLAG

Prepared by:

Michel C. Boufadel, PhD, PE and Feng Gao

**New Jersey Institute of Technology
Civil and Environmental Engineering
University Heights, Newark, NJ 07102
973-596-5657
Michel.boufadel@njit.edu**

Introduction

The goal was to develop the needed tools to simulate the horizontal release of oil from a horizontal orifice. The models were to be calibrated (i.e., trained) by simulating the release of oil from a 2.4 mm orifice in the BIO tank (32 m long, 0.6 m wide, and 2.0 m tall, but contains water at a depth of 1.5 m). The BIO tank contains also currents at an approximate speed of 5.0 cm/s along the duration of the jet.

The orifice had an elevation of 0.25 m from the inside bottom of the tank, and thus the distance between it and the water surface is 1.25 m. The diameter of the orifice was 2.4 mm. The oil was Alaskan North Slope (ANS) whose density $\rho = 866 \text{ kg/m}^3$, dynamic viscosity $\mu = 11.5 \text{ cp}$, and interfacial tension with water $\sigma = 0.02 \text{ N/m}$. The oil mass flow rate was 58g (approximately 0.06 liter per second, 3.6 liter per minute, around 1.0 gpm). The oil temperature in the canister was 80 °C while the water temperature in the tank was 15 °C. Due to the short duration of the experiments and the relatively small volume of released oil, it is unlikely that the oil temperature raised the water temperature by a measurable amount.

Based on the volumetric oil flow rate and the diameter of the orifice, the average oil exit velocity is 13.3 m/s. In the absence of dispersant, the Reynolds and Weber numbers are:

$$\text{Re} = \frac{\rho V D}{\mu} = \frac{(866)(13.3)(0.0024)}{0.0113} \cong 2,500$$

(1)

$$\text{We} = \frac{\rho V^2 D}{\sigma} = \frac{(866)(13.3)^2(0.0024)}{0.02} \cong 18,000$$

(2)

Another important number is the Ohnsorge number given as:

$$\text{Oh} = \frac{\text{We}^{0.5}}{\text{Re}} = \frac{\mu}{(\rho \sigma D)^{0.5}} = \frac{(0.0115)}{(866 \times 0.02 \times 0.0024)^{0.5}} \cong 0.055$$

(3)

Based on Figure 1 of Johansen et al. (2013), the resulting jet is in the atomization regime (the blue dot in the graph).

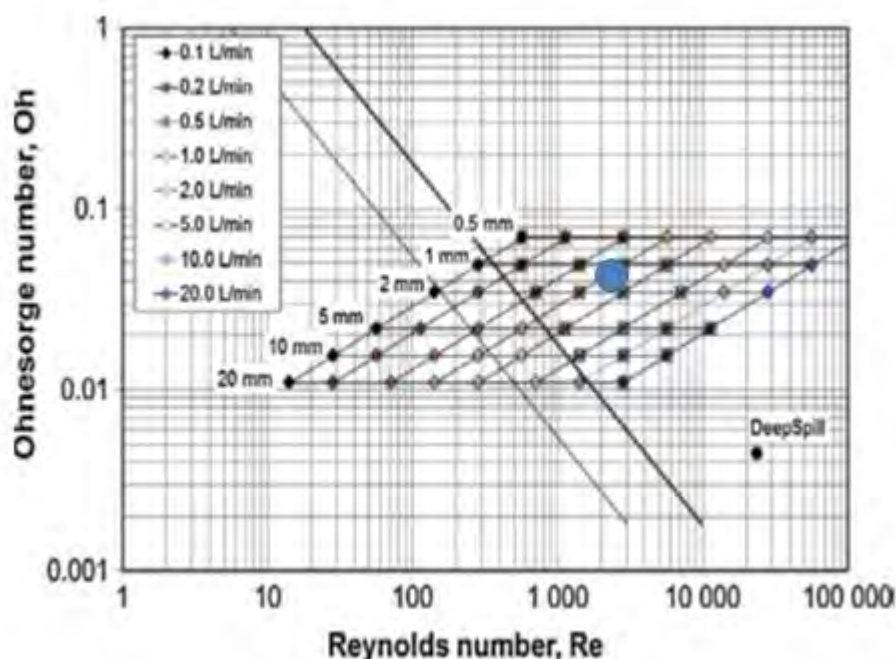


Figure 1: Experimental conditions plotted in the diagram of the Ohnesorge vs. Reynolds number as obtained by Johansen et al. (2013). The injection rate varied from 0.1 to 20 L/min, with nozzle diameters varied from 0.5 to 20 mm. The oil viscosity is presumed to be 5 cP. The thick line in the diagram shows the boundary between transitional and atomization breakup. The blue disk represents the experimental conditions of the BIO tank (this study).

Technical Approach

There are two major challenges with modeling oil jets. The first is the hydrodynamics of the jet and the other is the formation of droplets. However, we approach this problem first from an engineering point of view where we attempt to understand the engineering properties of the jet, and then by zooming in on the hydrodynamics of the jet and the movement of oil droplets. For this purpose, we use first the models VDROP-J and JETLAG, which provide the average hydrodynamics properties along the centerline of the jet. The model VDROP-J provides also the centerline droplet size distribution. In the second step, we use the models Fluent a Computational Fluid Dynamics (CFD) model and the model NEMO3D for tracking the individual oil droplets.

The layout of the document is as follows: The next Section addresses the modeling using the engineering approach. The following section addresses the detailed hydrodynamics of the plume and the movement of individual oil droplets as they interact with their surroundings. In that Section, we address the droplet size distribution within the plume, which would help to design future experiments.

Engineering Properties of Jet Hydrodynamics

For jet hydrodynamics, we use herein the models VDROD and JETLAG to capture the behavior of the plume. While the model VDROD provides the centerline velocity based on correlations from the literature, the model JETLAG provides the average velocity within the plume. To allow comparison, we used the Gaussian approximation for the velocity profile across the jet, and we computed the peak (centerline) velocity from JETLAG. The resulting velocity along the centerline of the plume is reported in Figure 2 for VDROD and for JETLAG in the presence of a current $U_a=3.0$ cm/s and in the absence of current ($U_a=0$ cm/s). The agreement is very good between the two cases lending further credence that VDROD-J is compatible with numerical models of plumes such as JETLAG.

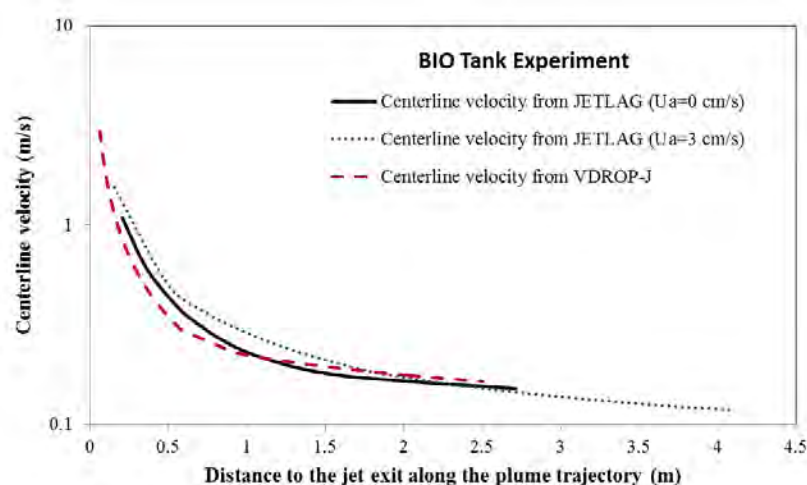


Figure 2: The velocity along the centerline of the jet/plume using VDROD-J and JETLAG. The velocity along the centerline of the jet/plume using VDROD-J and JETLAG. Note that the agreement was particularly good considering that no fitting was conducted, rather each model was run with the parameters stated in the Problem Statement Section.

The holdup is defined as the ratio of the volume of oil at a particular location in the plume to the total volume (oil+water) at that location. The value of the holdup affects the droplet size distribution, and reflects the intensity of water entrainment into the jet/plume; a large holdup value results in a high rate of coalescence between droplets. Figure 3 reports the holdup along the centerline using VDROD-J and JETLAG, and one clearly notes that the agreement is good further reflecting the compatibility of VDROD-J with JETLAG for evaluating the mass of oil in the jet/plume. The holdup decreased sharply from around 10% at few centimeters from the pipe exit to almost 0.5% after 2.5 m. Thus at 2.5 m, 99.50% of the fluid in the plume is made up of water.

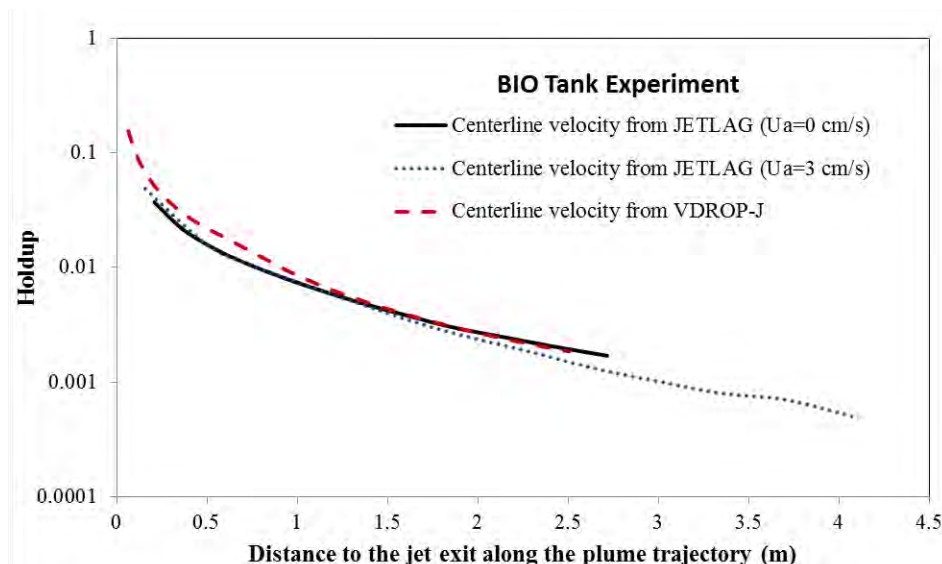


Figure 3: Holdup (ratio of oil volume to total volume of fluid) as function of distance from the pipe exit. Note the rapid decrease, which required a logarithmic scale for the holdup.

Figure 4 shows the simulation results from JETLAG for the shape of the plume. It shows the centerline along with the lower and upper bound of the plume along the vertical plan (note that the plume is circular, and thus three dimensional). The location of the LISST used in the experiments is also reported, and its results will be discussed later in this document.

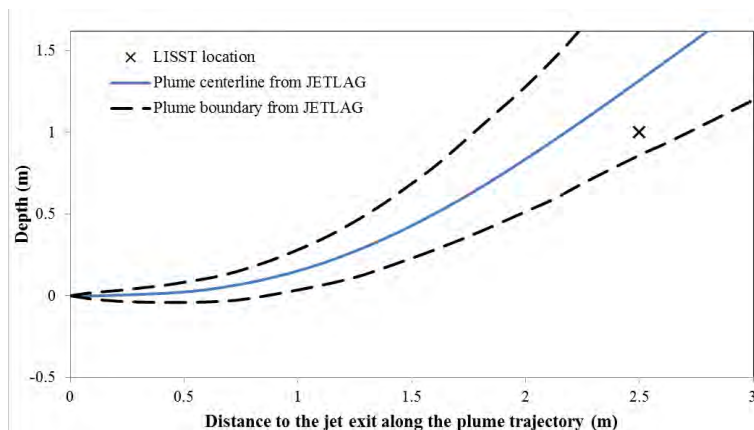


Figure 4: Plume centerline and boundaries based on the model JETLAG. The LISST was located within the plume near the lower edge of the plume.

Droplet Size Distribution

Using only the parameters from the Problem Statement, we obtained the breakage constant $K_b=0.1$ from the correlation in Zhao et al. (2014). We then used VDROD-J to predict the droplet size distribution at the location of the LISST (given in Figure 5), and we compared it to the observed data from the LISST in Figure 4, which shows an exceptional agreement. The only adjustable parameter was the initial droplet size, selected at 500 microns herein. The initial size of the droplets results from the so-called primary breakup, and it depends on shear flow near the orifice and thus cannot be predicted by VDROD-J, which relies on turbulence away from boundaries.

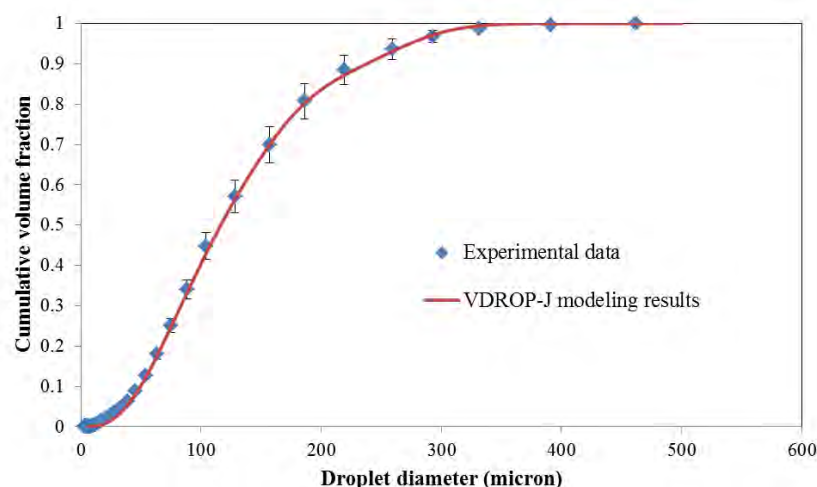


Figure 5: Droplet size distribution obtained from VDROD-J and from the LISST (location reported in Figure 3) in the absence of dispersant.

Based on the good agreement between the model VDROD-J and experimental data, one can predict the DSD at various locations in the plume, as illustrated in Figure 5; it is clear that the DSD changes drastically in the first meter of its trajectory, and the DSD does not change much afterward. This is reasonable as the mixing energy decreases rapidly with distance from the orifice (to the power “-4”).

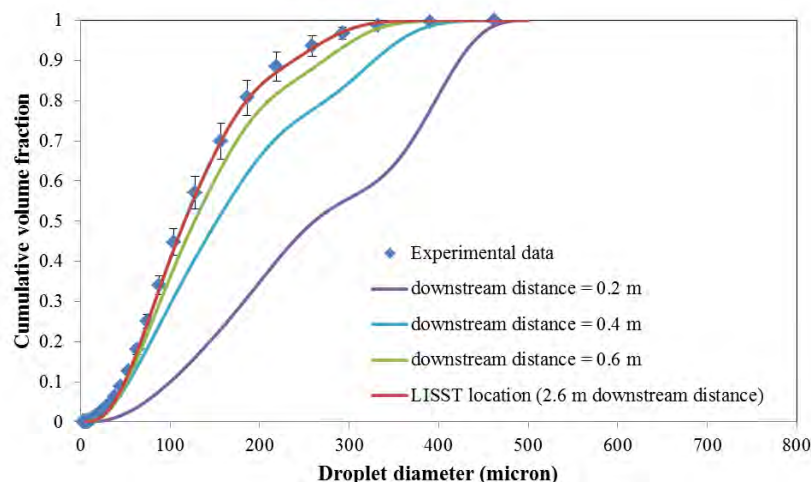
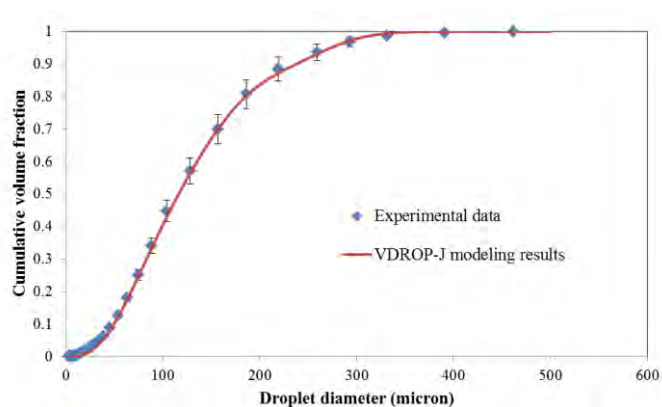


Figure 6: The droplet size distribution at various locations from the orifice along the centerline. The DSD essentially reached the steady state distribution within less than a meter.

The impact of dispersant was evaluated by premixing the oil with dispersant at the DOR of 1:20, and releasing oil at the same rate as before (see Problem Statement). The experimental and modeling results are reported in Figure 7. In the VDROP-J model, the same parameters used earlier were used again with the exception of the interfacial tension, which was calibrated to be 0.0013 N/m, a reduction of 15 folds. The results in Figure 6 show a reasonable fit of the model to the data. The fit is good for larger sizes, but it is relatively poor at the smaller sizes. To better illustrate this discrepancy, we used a different scale in the lower panel of Figure 7. The discrepancy is due to the fact that the oil and dispersants were premixed resulting in the so-called tip-streaming, whereby the oil peels off from the droplet without the action of mixing. It is a pure chemical process that VDROP-J is not designed to handle.



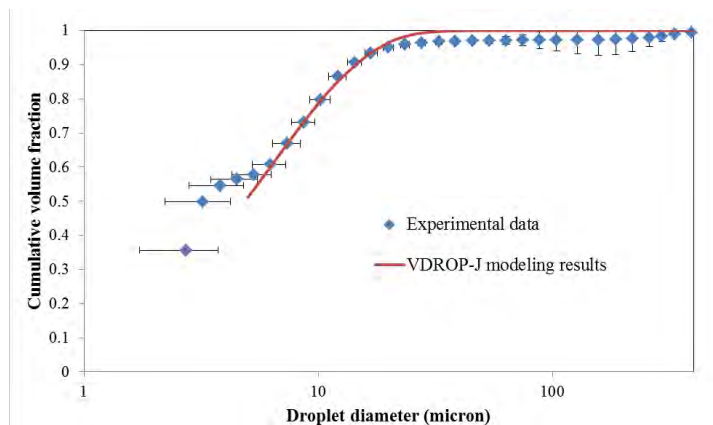


Figure 7: Droplet size distribution in the presence of dispersant obtained at the location of the LISST in Figure 4. The difference between the two graphs is that the lower one has a logarithmic scale for the size axis.

Computational Fluid Dynamics

Evaluating the hydrodynamic properties of an oil jet (e.g., a blowout) is very difficult for a variety of reasons including: 1) The oil jet velocity is very large at the orifice (e.g., around 15 m/s for our experiment), and drops sharply with distance, and 2) there are multiple phases present, namely oil, water, and oil droplets in water, and 3) the turbulent energy and the presence of eddies prevents accurate evaluation of average speeds. For example, when using an acoustic Doppler velocimeter (ADV), one obtains different readings depending on the phase passing in front of the ADV. Hence, one needs a robust method to study the oil jet underwater numerically to complement experimental measurement.

We used computational fluid dynamics (CFD) to simulate the experiment of oil jet carried out at Bedford Institute of Oceanography in Canada. In the CFD simulation, the computational domain consisted of 2,777,029 nodes. The turbulence model $k - \varepsilon$ was selected, as it is most appropriate for such problems because of its usefulness of application in free-shear layer flows, calculation stability, and relative easiness of convergence (Aronson et al., 2000; Pope, 2000; Wilcox, 1998). The model relies on solving two equations to model the turbulent kinetic energy and the turbulence dissipation rate. The $k - \varepsilon$ model belongs to the family of RANS (Reynolds Average Navier Stokes) models, which aim to solve for the average flow field of turbulent flow (Eaton and Johnston, 1981).

In the present simulation, the achievement of steady state was observed based on monitoring the conservation of mass (e.g. the inflow rate of the oil equates the rate of the outflow of oil) with a maximum of 1% difference. A mesh independent study was performed to ensure that the simulation results does not change with the further refinement of mesh. This was done by

monitoring the average pressure at the outlet to see whether it changes with mesh refinement. After approximately 10,000 iterations, the simulation reached steady state with first order of accuracy as the mass conservation information was monitored. All simulations were run in parallel on 20 processors located on the NRDP Computational Laboratory.

Figure 8 shows results of CFD where the profile of the plume that was modelled based on an oil flow rate of 1.0 L/second. The purple lines represent the contours of the holdup, which is equal to the volume of oil divided by the volume of fluids in a given control volume. The holdup at the exit is 1.0, and one notes that it decreases to a few percent and even lower with 0.5 m. The contours of the velocity magnitude show velocities larger than 0.2 to 0.3 m/s within the plume but a sharp decrease at the edge of the plume. One also shows the velocity vectors outside of the plume reflecting the entrainment of fluids (i.e., water) to the plume, especially near the exit to the tank.

Figure 9 shows the edge of the plume (delineated using 10% of the velocity) along with three locations for obtaining cross sections. Figures 10, 11, and 12 show cross sections of the holdup (lines) and velocity magnitude.

Figure 10 shows that the cross section is more or less circular as the exit point to the tank was circular. The lack of perfect circularity is due mesh discretization. It appears that the bottom of the tank, which was at 25 cm below the exit, has an effect on the general flow circulation, as the flow vectors below the jet are different from those above it. But it is not sure if the bottom has any measurable effects on the hydrodynamics within the plume.

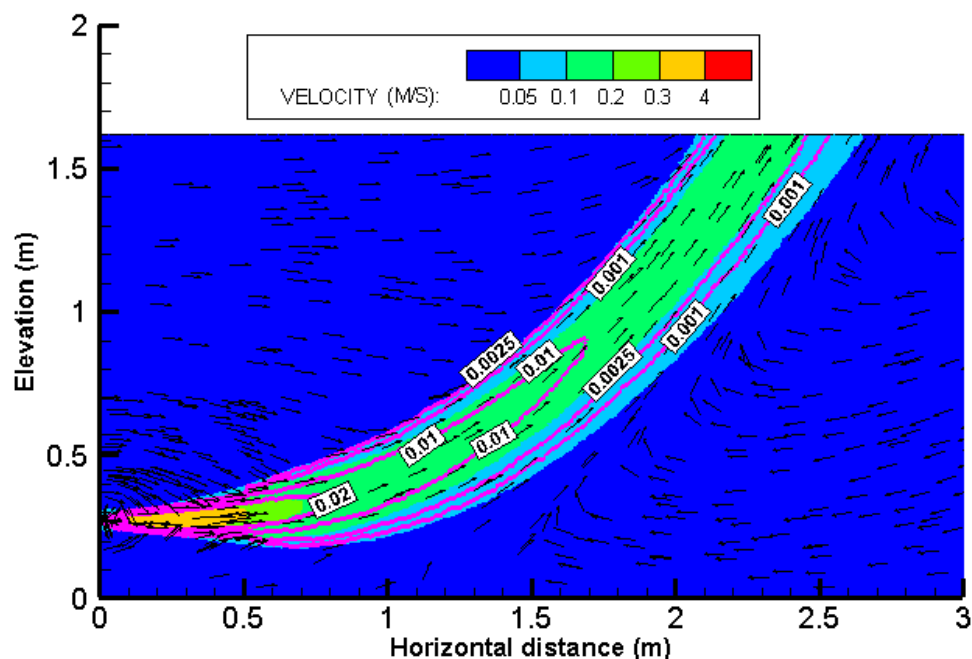


Figure 8: The profile of the plume through a vertical plane passing through the center axis. The figure shows the contour of the velocity magnitude (flooded colors) and the holdup (volume of oil to total liquid volume), using purple lines. The arrows indicate the velocity component in the plan of the figure. The length of the velocity vector does not represent the magnitude but only represents the direction.

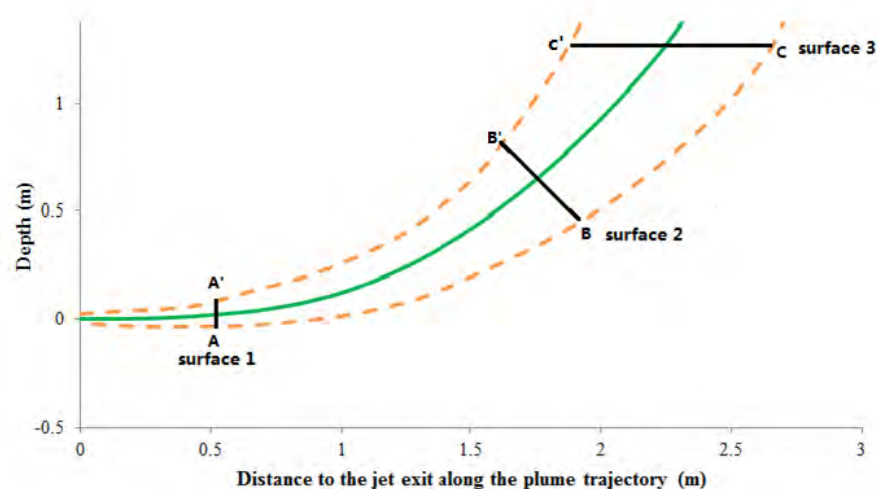


Figure 9: The locations of cut cross sections along the plume trajectory. The cross sections are numbered as surface-1, surface-2 and surface-3 as they are distant away from the orifice. “Surface-1” is 0.5 m away from the orifice and perpendicular to the horizontal direction. “Surface-2” is centered at 0.81 m above the jet orifice and 45° to the tank bottom. “Surface-3” is parallel to the horizontal, and 10 cm below the water surface. The green curve denotes the center line of the jet plume and the dotted orange lines denote the edge of the plume (which is defined by 10 % of the centerline velocity magnitude). The cross sections are cut while being at downstream locations (i.e., one sees the jet coming toward them).

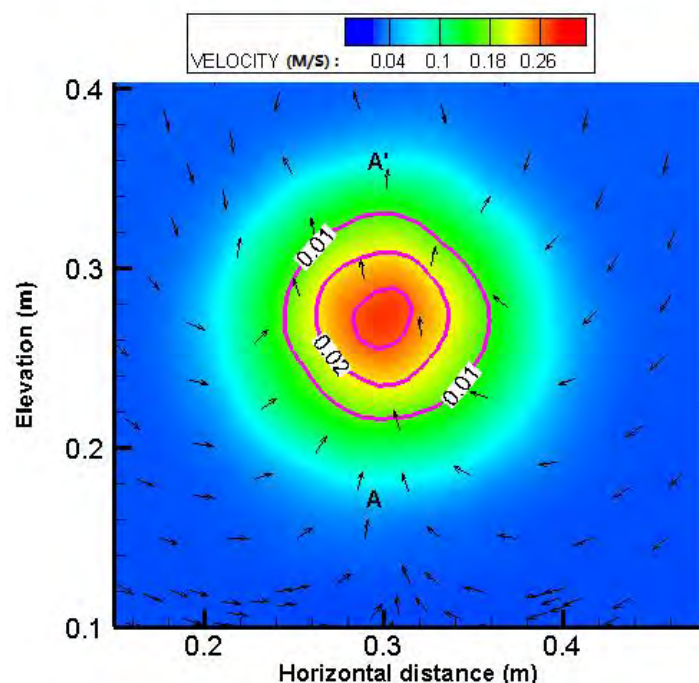


Figure 10: Surface-1 (Purple lines indicate the contour of the holdup, continuous flood contour indicates the velocity magnitude. The arrow vectors indicate the velocity vectors that parallel to the present surface)

Figure 11 shows the cross section B-B' (see Figure 9). One notes that the plume is no longer circular in comparison to Figure 10. Also, the center of the plume is closer to the top portion of the plume than it is to the bottom of the plume. First, note that the velocity in this cross section is going in the direction of B-B', which means it is upward. We believe the non-circular shape of the plume in Figure 11 is due to two complementary processes: 1) The close distance to the top portion of the plume is most likely due to buoyancy which has more effects on the center of the plume than on the edge of the plume because the center of the plume has more oil in it. Therefore, the buoyancy of the center of the plume is larger than that of the top, causing the center to be closer to the top of the plume. The converse occurs for the bottom of the plume. 2) As buoyancy pulls the plume upward, we believe that the lower edge of the plume is carried further out due to inertia.

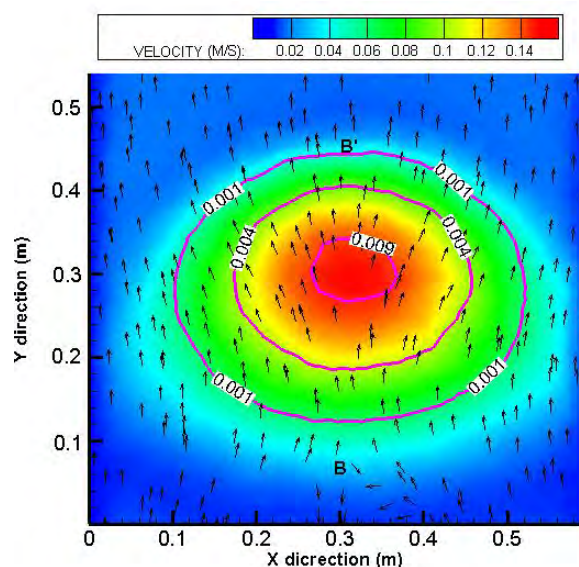


Figure 11: Surface-2 (Purple lines indicate the contour of the holdup, continuous flood contour indicates the velocity magnitude. The arrow vectors indicate the velocity vectors that parallel to the present surface)

Figure 12 shows the cross section C-C' where the velocity vectors are outward (i.e., away from the plume). Notice that the width of the plume is determined by the width of the tank (i.e., 0.60 m). Notice also that the velocity magnitude did not drop a lot from Figure 11, which is probably due to the fact that the plume reached the water surface and is thus confined to move horizontally. In this figure, the effect of inertia discussed for Figure 11 is more prevalent, as one notes that the distance between the center of the plume and the downstream edge of the plume (i.e., toward B) is much larger than in the opposite direction. Note that the downstream edge of the plume here is the lower edge of the plume of Figure 11.

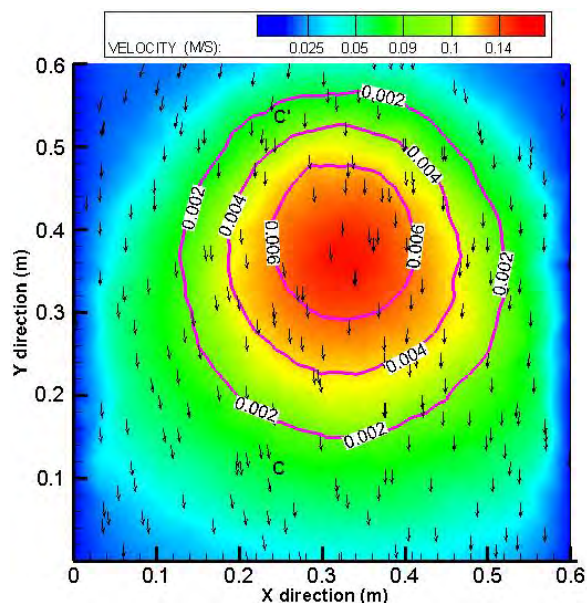


Figure 12: Surface-3 (Purple curve indicates the contour of the holdup, continuous flood contour indicates the velocity magnitude. The arrow vectors indicate the velocity vectors that parallel to the present surface)

The eddy diffusivity is defined as:

$$D = 0.9 \frac{k^2}{\varepsilon} \quad (4)$$

where k is the kinetic energy due to turbulence per unit mass and ε is energy dissipation rate per unit mass (watt/kg), and it reflects the intensity of turbulent mixing. The unit of D is m^2/s .

Figure 13 shows the eddy diffusivity profile in a vertical plane passing through the center axis of the plume. The eddy diffusivity is important for the mixing of oil and water within the plume, and it was used later to predict the movement of individual oil droplets. One notes that the plume has a core of high mixing surrounded by a layer of relatively small mixing. This is probably due to the fact that the edge of the plume is “constrained” by the entrainment of water into it, a process

that tends to reduce mixing. However, the entrainment does not seem to affect the core of the plume.

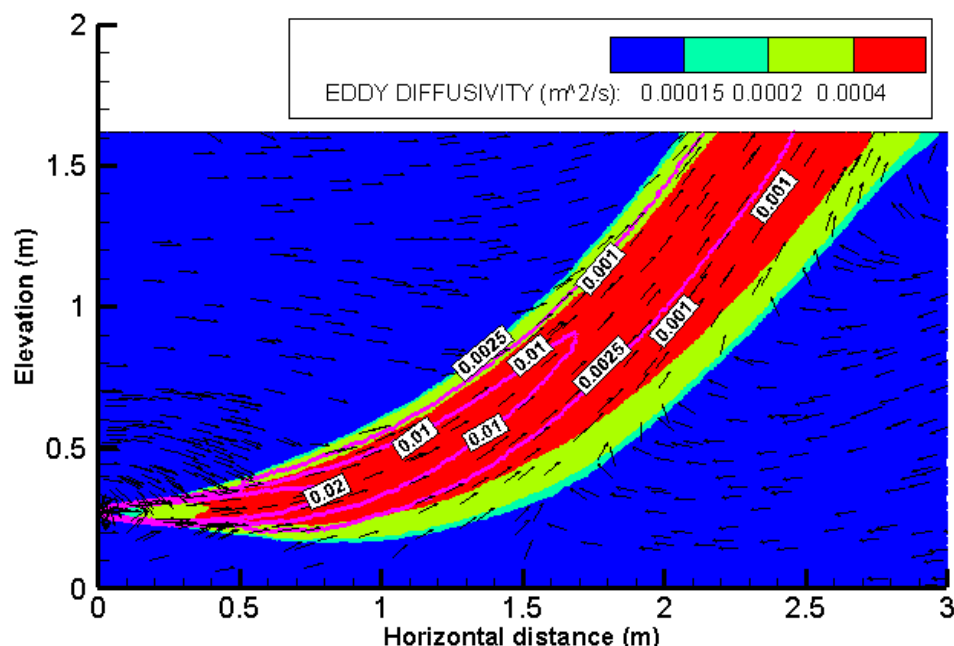


Figure 13: The profile of eddy diffusivity of the plume (Purple lines indicates the contour of the holdup, flood contour indicates eddy diffusivity. The arrow vectors indicate the velocity vectors that parallel to the present surface. The length of the velocity vector does not represent the magnitude but only represent the direction.

Figures 14, 15, and 16 report the eddy diffusivity at the cross sections used earlier (see Figure 9). One notes that the eddy diffusivity magnitude in Figure 14 (cross section 1) and Figure 15 (cross section 2) is comparable. However, one notes a large decrease for Figure 16 (cross section 3). This is probably because the eddy diffusivity is due to the $k - \varepsilon$ turbulence model, and turbulence was unhindered between cross section 1 and cross section 2. However, cross section 3 was only 0.10 m below the water surface where turbulent eddies were quashed by the water surface, which acted as a boundary.

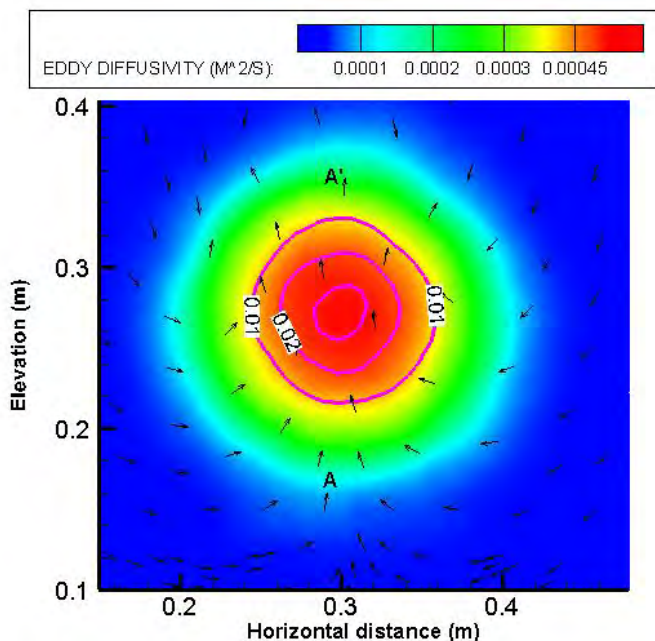


Figure 14: Surface-1, purple lines indicate the contour of the holdup, continuous flood contour indicates eddy diffusivity. The arrow vectors indicate the velocity vectors that parallel to the present surface

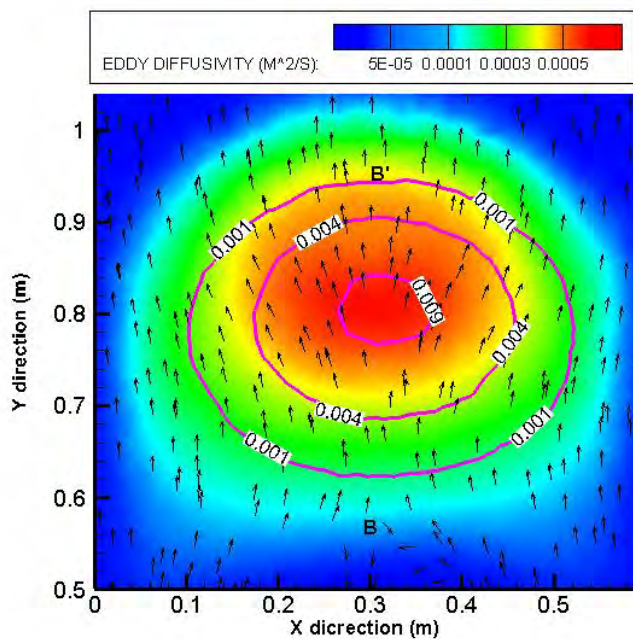


Figure 15: Surface-2 (Purple lines indicate the contour of the holdup, continuous flood contour indicates eddy diffusivity and the arrow vectors indicate the velocity vectors that are parallel to the present surface)

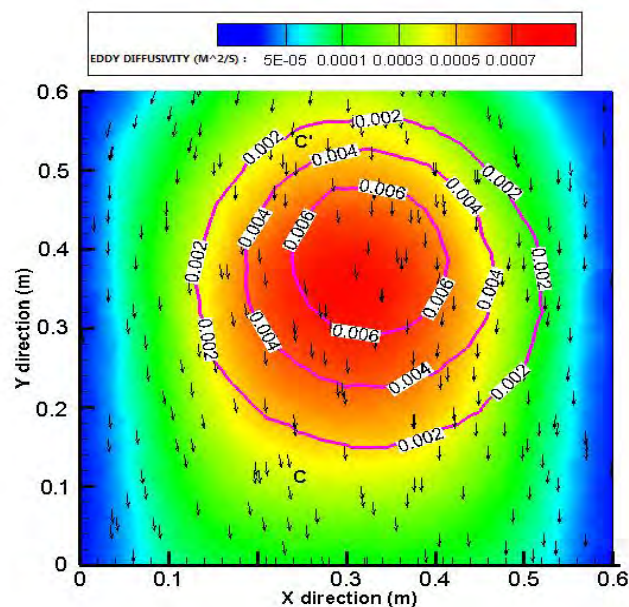


Figure 16: Surface-3 (Purple lines indicates the contour of the holdup, flood contour indicates eddy diffusivity and the arrow vectors indicate the velocity vectors that parallel to the present surface)

The value of the energy dissipation rate ε (watt/kg) is commonly needed to determine the breakup of oil droplets and their coalescence. Although, we have not conducted the breakup of oil droplets within the current framework, we provide herein the values of ε for future (imminent) application. Figure 17 shows the profile contour of ε , where the values drop sharply with the centerline distance (note the logarithmic scale of the contours).

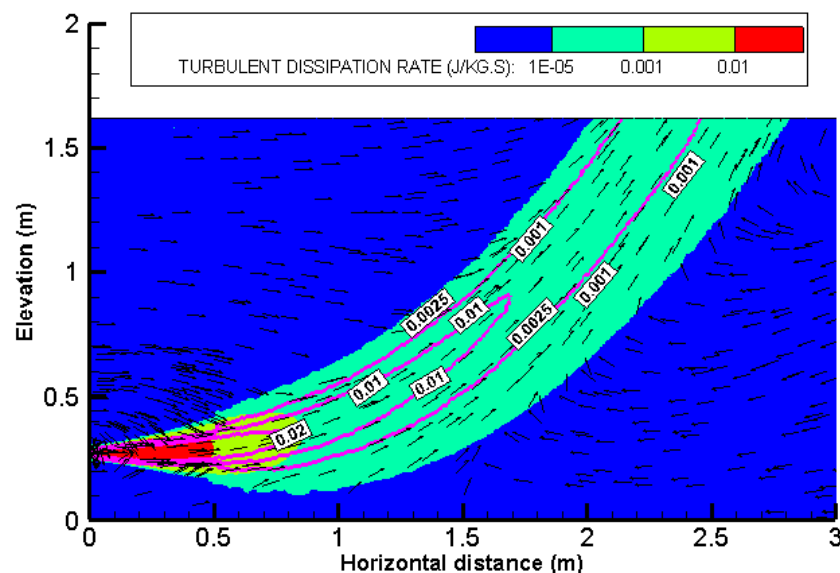


Figure 17: The profile of turbulent dissipation rate in the plume. Purple lines indicates the contour of the holdup, continuous flood contour indicates turbulent dissipation rate. The arrows indicate velocity vectors components that are parallel to the page surface. The length of the velocity vector does not represent the magnitude but only represent the direction.

Figure 18, 19, and 20 show the contours of ε in cross sections 1, 2, and 3, respectively (see Figure 9 for reference). While the maximum value is at or near the center, one notes a sharp decrease of ε between cross sections. The decrease is much sharper than that of the eddy diffusivity, which is probably because the turbulent kinetic energy k behaved more or less similar to ε , and thus the ratio in Eq. 4 remained more or less uniform with distance from the source.

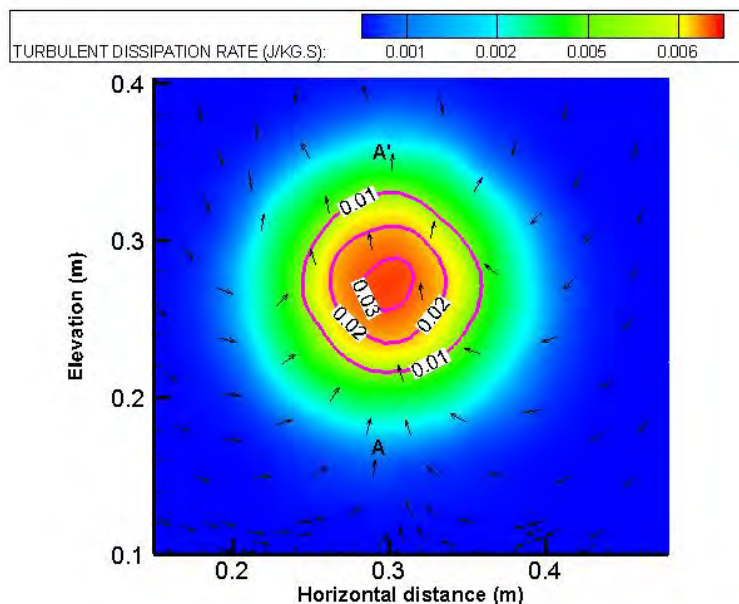


Figure 18: Surface-1 (Purple lines indicates the contour of the holdup, continuous flood contour indicates eddy diffusivity. The arrow vectors indicate the velocity vectors that parallel to the present surface)

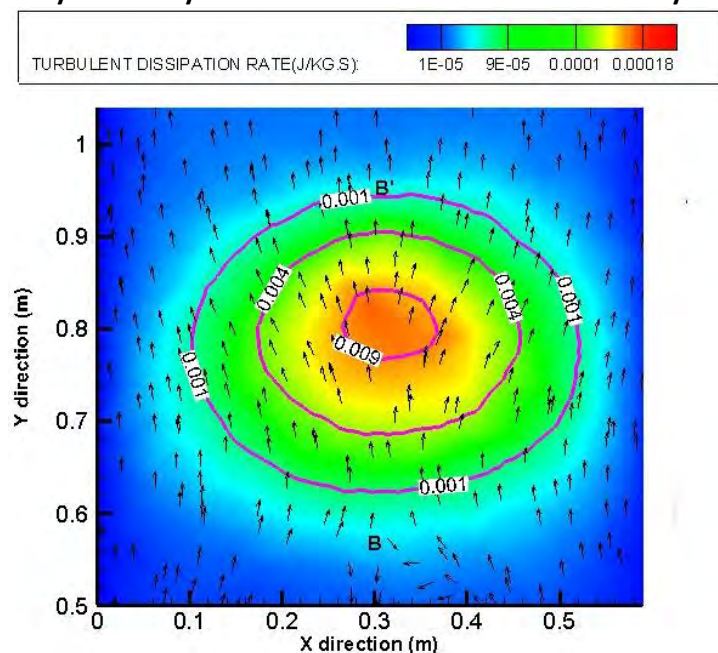


Figure 19: Surface-2 (Purple lines indicates the contour of the holdup, continuous flood contour indicates turbulent dissipation rate. The arrow vectors indicate the velocity vectors that parallel to the present surface)

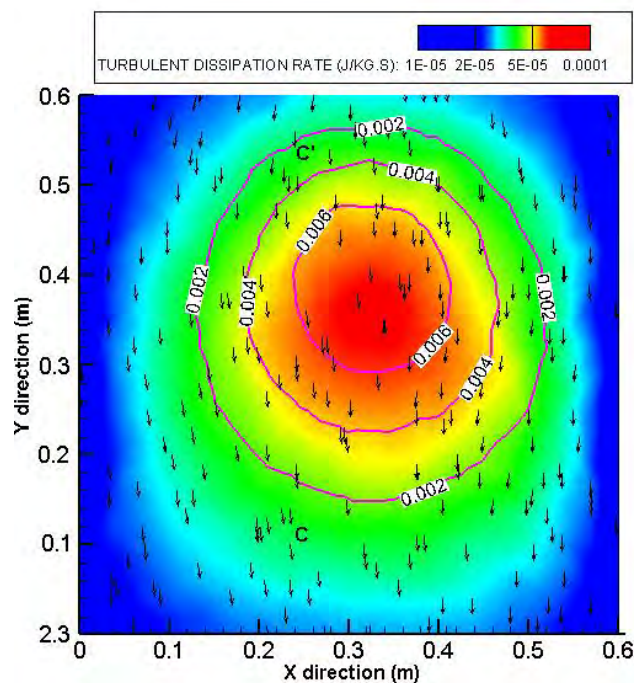


Figure 20: Surface-3 (Purple lines indicate the contour of the holdup, continuous flood contour indicates turbulent dissipation rate. The arrow vectors indicate the velocity vectors that parallel to the present surface)

Figure 21 reports the variation of ε along the centerline of the plume, where one notes a sharp decrease with distance (note the logarithmic scale on the vertical). Theoretical arguments in water jets revealed that ε decreases proportional to x^{-4} , where x is the centerline distance from the source.

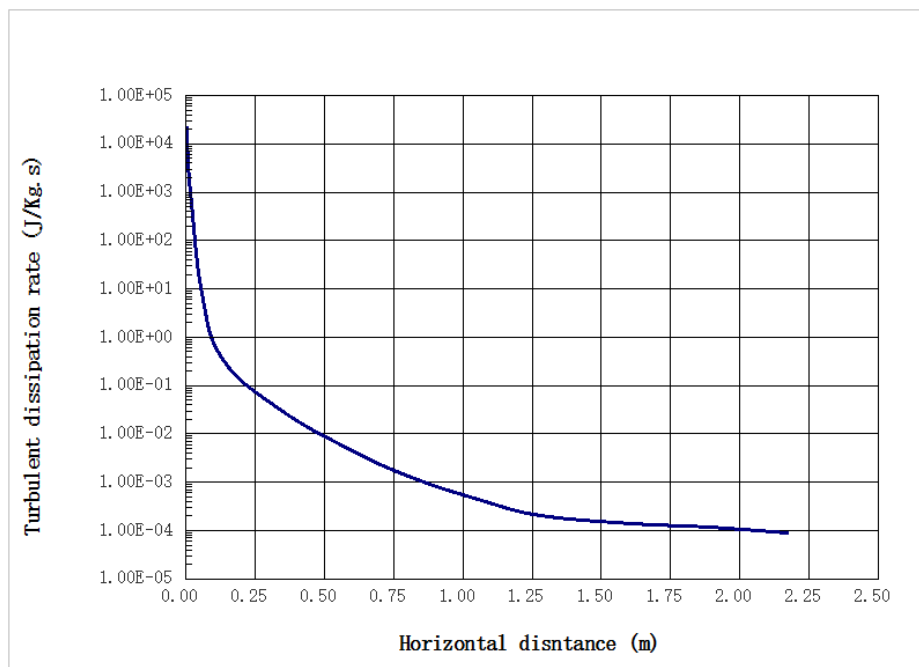


Figure 21: Turbulent dissipation rate along the centerline of the plume (The turbulent dissipation rate decreases sharply when exiting the orifice.)

Particle tracking using Lagrangian method coupled with CFD

In the experiment of oil jet underwater, we observed that some oil droplets exit the plume and rise up individually. This interesting phenomenon gives rise to how the oil droplets behave when exiting the jet orifice. In the present model, we aim to understand how oil droplets behave after exiting the orifice (e.g., how the large oil droplets exit the plume and oil droplets of which diameters remain within the plume. However, CFD (Computational Fluid Dynamics) does not consider the behavior of single droplets. For example, RANS (Reynold Averaged Navier Stokes Equations) in CFD considers the oil and water fully mixed, which is different from the real situation, where they are in different phases: oil droplets in water.

We modelled herein the trajectories of oil droplets using a Lagrangian method coupled with CFD data. The flow field was obtained from the CFD simulations (Section I), and used as input to our particle tracking model NEMO3D.

The velocity of water is:

$$\vec{U} = u.\vec{x} + v.\vec{y} + w.\vec{z} \quad (5)$$

The velocity of the particle is:

$$\vec{U}_p = u_p \vec{x} + v_p \vec{y} + w_p \vec{z} \quad (6)$$

For particle tracking:

$$\frac{d\vec{S}_p}{dt} = \vec{U}_p + R\sqrt{2D\Delta t} \quad (7)$$

Where

$$\vec{S}_p = X_p \vec{x} + Y_p \vec{y} + Z_p \vec{z} \quad (8)$$

Equation (3) is thus written in each of the coordinate directions:

$$\frac{dX_p}{dt} = u_p + R\sqrt{2D_x\Delta t} \quad (9a)$$

$$\frac{dY_p}{dt} = v_p + R\sqrt{2D_y\Delta t} \quad (9b)$$

$$\frac{dZ_p}{dt} = w_p + R\sqrt{2D_z\Delta t} \quad (9c)$$

Where D_x , D_y , and D_z are the eddy diffusivities computed in Section I (Eq. 4). The velocities u_p , v_p and w_p are given based on the momentum equation. In the x direction:

$$\frac{du_p}{dt} = \left(\frac{f_1}{\tau_d}\right) * (U \cos \beta - U_p \cos \alpha) = \left(\frac{f_1}{\tau_d}\right) * (u - u_p) \quad (10)$$

Momentum equation in the y direction:

$$\frac{dv_p}{dt} = \left(\frac{f_1}{\tau_d}\right) * (U \sin \beta - U_p \sin \alpha) = \left(\frac{f_1}{\tau_d}\right) * (v - v_p) \quad (11)$$

Momentum equation in the z direction:

$$\frac{dw_p}{dt} = \left(\frac{f_1}{\tau_d}\right) * (w - w_p) + \frac{\rho_w - \rho_o}{\rho_w} * g \quad (12)$$

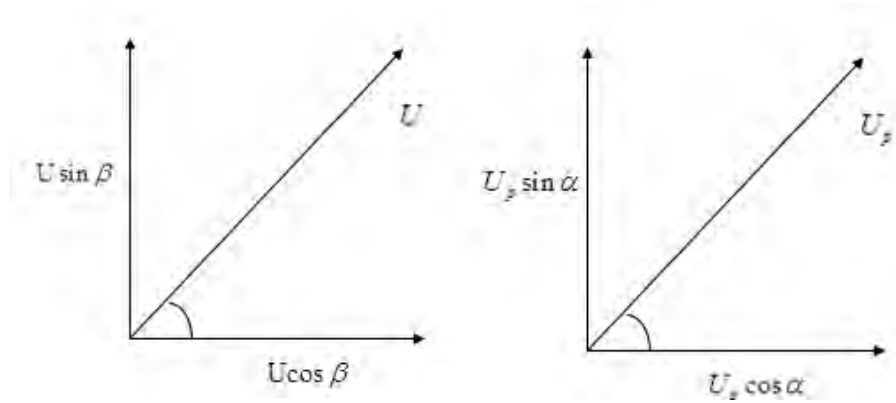


Figure 22: The angles of the velocities in cylindrical coordinates for the water velocity U (left panel) and for the oil droplet velocity U_p (right panel).

The parameter τ_d is the Stokes drag coefficient given as:

$$\tau_d = \frac{\rho_o * D^2}{18 * \mu_o} \quad (13)$$

The parameter f_1 is a correction for the Stokes coefficient to account for situations where the flow is not laminar, but when the droplet Reynolds number $Re = \frac{\rho_w * u_s * D}{\mu_w}$ is less than 100. It is calculated based on the following equations (Miller et al., 1998):

$$f_1 = 1 + 0.0545 Re + 0.1 * Re^{\frac{1}{2}} (1 - 0.03 * Re) \quad (14)$$

The slip velocity for the calculation of the Reynolds number is given by the Euclidean norm:

$$u_s = \|\vec{U} - \vec{U}_p\| = \left[(u - u_p)^2 + (v - v_p)^2 + (w - w_p)^2 \right]^{1/2} \quad (15)$$

By putting equation (5)-(14) into the NEMO 3D code, one can obtain the trajectories of the oil droplets with different diameters.

The oil droplets with different diameters rise up not only because of the flow field velocity, but also due to the individual velocities of its own. As shown in Figure 23, oil droplets with larger diameters rise ahead of the centerline of the plume, and oil droplets with a 1000 microns exist the plume at around 0.5 m from the orifice in the horizontal direction. The present method can predict at which point the oil droplets will exit the plume. In addition, when combined with LISST data, one can also estimate how much percentage of oil droplets with large diameters will exit the plume after released.

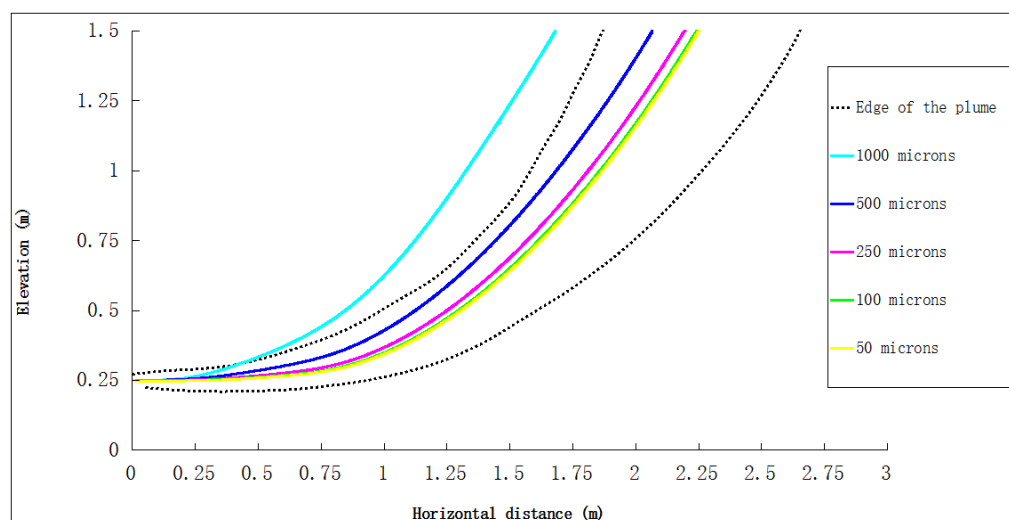


Figure 23: The trajectories of oil droplets with different diameters. The edge of the plume is defined by 10 % of the centerline velocity.

When the inertia terms are not estimated for oil droplets, the buoyancy effect is estimated by terminal velocity directly (e.g., the right hand side of Equation (9a), (9b), (9c) is zero) while the present method uses equation (5)-(14) to consider the effect of inertia and buoyancy.

Figure 24 shows the evaluation of the combined effect of inertia and buoyancy effect on oil droplets when rising; the oil droplet trajectories rise faster when the inertial effects are not accounted for. This is because the jet is horizontal and tends to propel the droplets horizontally.

Thus, not accounting for the inertia of droplets overestimate their rise rate. The difference becomes more pronounced for the large oil droplets, such as 500 and 1000 microns, which is because the large droplets have a higher buoyancy (due to their large volume) and have larger inertia due to their large mass. The results in Figure 24 demonstrate that one needs to account for both the effects of inertia and buoyancy when considering the movement of oil droplets in jets.

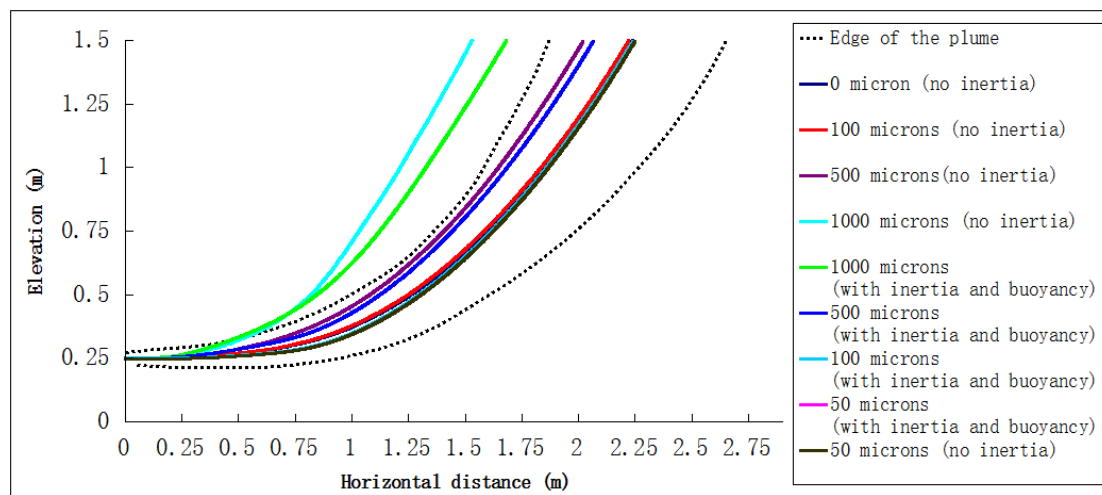


Figure 24: Evaluation of the effects of inertia and buoyancy on oil droplets trajectories. In the absence of inertia, oil droplets rise faster.

Figures 25 through 28 show the trajectories of oil droplets of various sizes. Figures 25 and 26 show identical results, which suggests that the mixing due to eddy diffusivity was large enough to minimize the effect of buoyancy between 50 and 100 microns. However, the effect of buoyancy seems to become important for droplets of size 500 microns (Figure 27) and 1,000 microns (Figure 28). For the latter, the droplet trajectories were outside of the 10% boundary of the plume.

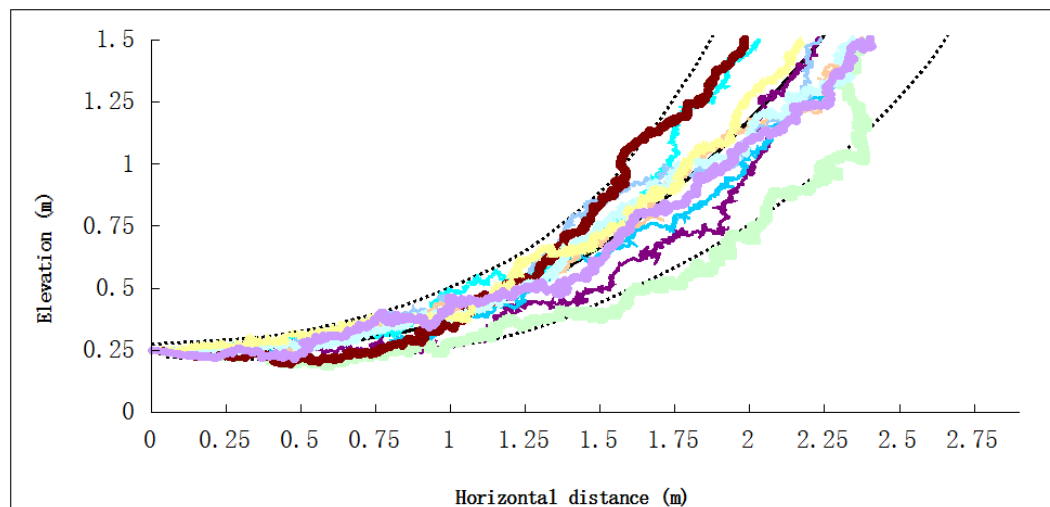


Figure 25: The trajectories of oil droplets when the diameter is 50 microns (with inertia and turbulent diffusion)

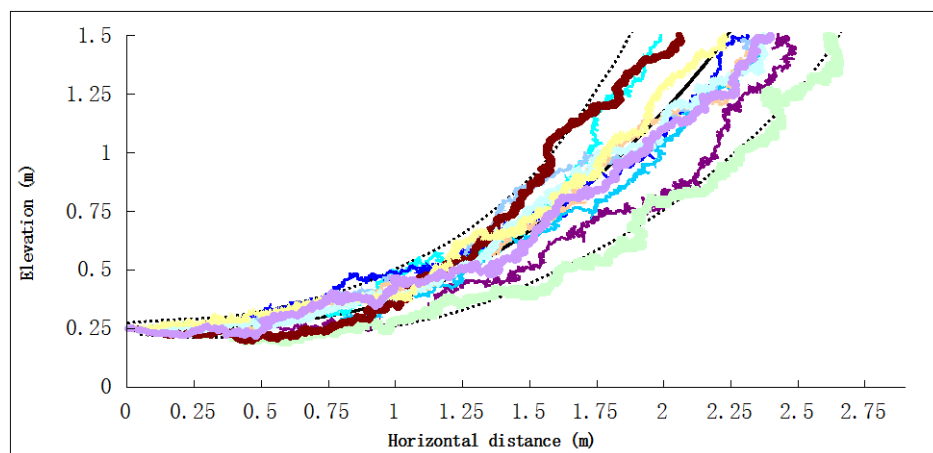


Figure 26: The trajectories of oil droplets when the diameter is 100 microns (with inertia and turbulent diffusion)

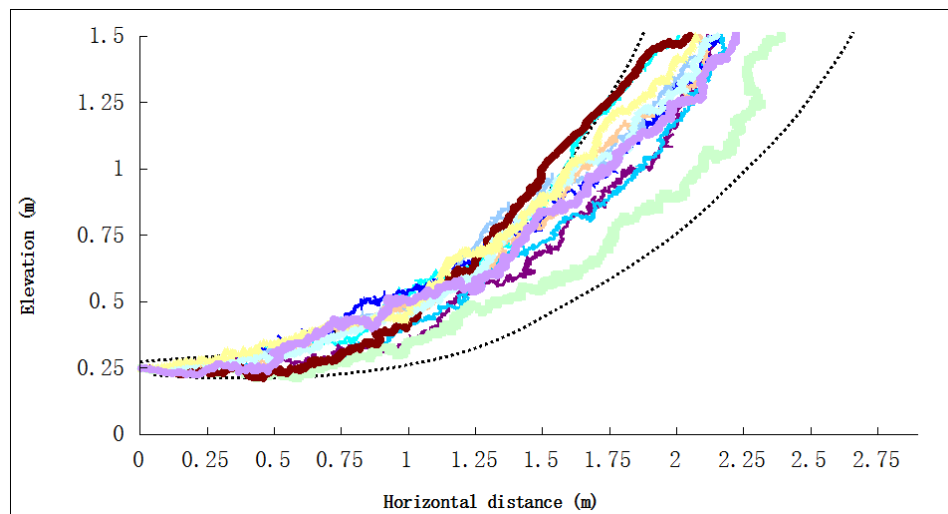


Figure 27: The trajectories of oil droplets when the oil droplet diameter is 500 microns with inertia and turbulent diffusion.

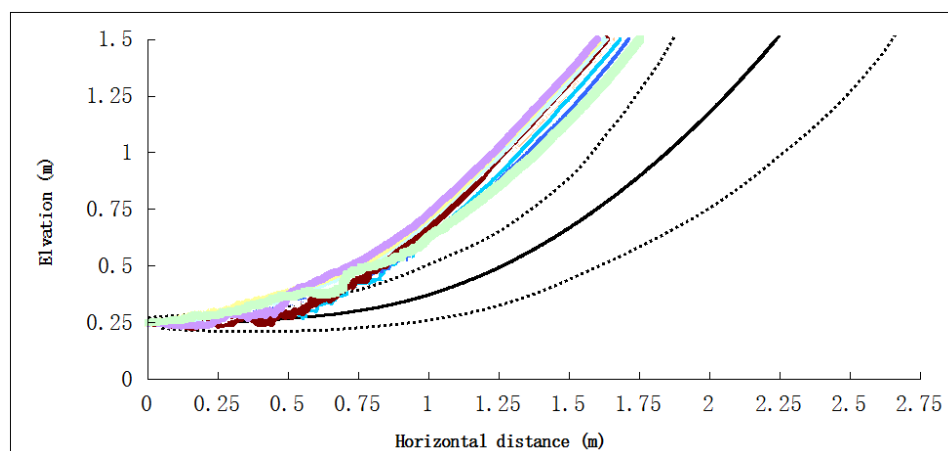


Figure 28: The trajectories of oil droplets when the diameter is 1000 microns, with inertia and turbulent diffusion.

References

- Aronson, D., Chroner, Z., Elofsson, P., Fellbom, H., 2000. Comparison between CFD and PIV measurements in a passenger compartment. SAE Technical Paper.
- Eaton, J., Johnston, J., 1981. A review of research on subsonic turbulent flow reattachment. AIAA journal 19, 1093-1100.
- Johansen, Ø., Brandvik, P.J., Farooq, U., 2013. Droplet breakup in subsea oil releases – Part 2: Predictions of droplet size distributions with and without injection of chemical dispersants. Mar Pollut Bull 73, 327-335.
- Miller, R., Harstad, K., Bellan, J., 1998. Evaluation of equilibrium and non-equilibrium evaporation models for many-droplet gas-liquid flow simulations. International Journal of Multiphase Flow 24, 1025-1055.
- Pope, S.B., 2000. Turbulent flows. Cambridge university press.
- Wilcox, D.C., 1998. Turbulence modeling for CFD. DCW industries La Canada, CA.
- Zhao, L., Boufadel, M.C., Socolofsky, S.A., Adams, E., King, T., Lee, K., 2014. Evolution of droplets in subsea oil and gas blowouts: Development and validation of the numerical model VDROD-J. Marine pollution bulletin 83, 58-69.

IAA No. E12PG00037

Final Report

Dispersant Effectiveness, In-Situ Droplet Size Distribution and Numerical Modeling to Assess
Subsurface Dispersant Injection as a Deepwater Blowout Oil Spill Response Option
and
Evaluation of Oil Fluorescence Characteristics to Improve Forensic Response Tools

APPENDIX H

**Weber Number Scaling Numerical Modeling Prediction of Droplet Size Distribution from
Subsurface Oil Releases with and without Chemical Dispersants**

By

Haibo Niu and Linlu Weng

Water Studies Laboratory

Department of Engineering

Dalhousie University (Truro Campus)

Truro, NS, Canada



1 Introduction

The increased in offshore oil and gas exploration in deep waters increases the risk of deepwater oil spills. One recent example is the Deepwater Horizon (DWH) incident in the Gulf of Mexico. Oil released from subsurface blowouts breaks up into droplets and the sizes of these droplets have strong impacts on the subsequent fate of oil in the marine environment (Chen and Yapa, 2007; Bradvik et al., 2013; Johansen et al., 2013). With a density smaller than that of the ambient seawater, larger oil droplets will rise to the sea surface more rapidly than smaller droplets and will reach surface closer to the spill location than the smaller droplets. Better knowledge on droplet size distributions resulting from subsurface oil releases will help us predict whether the oil will surface and if so, when and where and what the oil slick thickness be (Chen and Yapa, 2003).

Currently, both our knowledge on the droplet size distributions and our capability to predict the distributions are limited. Before the DWH incident, only very few experimental work have been conducted to measure droplet size distribution from subsurface releases and only few studied the effects of chemical dispersant on droplet sizes. Topham (1975) was probably the earliest work studying droplets from subsurface releases and he has reported droplet size ranging from 0.5 mm (detection limit) to 3 mm for Norman Wells crude and a peak diameter of 15 μm for Swan Hills crude. The field experimental data from the Canadian Arctic gathered by Dome Petroleum gave a range from 50 μm to 2.1 mm (Buist et al., 1981). Masutani and Adams (2001) conducted jet experiments on an oil-water system using four types of crude oil and studied the different modes of jet breakup. Johansen et al. (2003) was the only full-scale deep water experiment, they observed that droplet sizes resulting from the release of diesel at 844 m depth were from 1 to 10 mm.

While DWH is the first oil spill occurring at significant depth (~1500m), it is also the first time where chemical dispersants were directly injected into the subsurface oil release to enhance the dispersion of oil over a large water column (Louis et al., 2011). A total of 18,379 barrels of dispersant were used at the DWH incident (The Federal Interagency Solutions Group, 2010). When a chemical dispersant is added at the depth of the wellhead, the surfactant is expected to break the oil into small droplets. The only available data on the effects of dispersant on droplet sizes is Brandvik et al. (2013). Brandvik et al (2013) have studied the effects of dispersant by using seven different dispersant-oil-ratios (DORs) and the peak droplet sizes were found strongly affected by DORs.

Very few publications are available on predicting the droplet sizes. Chen and Yapa (2007) developed a method based on the maximum entropy formalism using the “deepspill” experimental data. Currently, this method is mainly applied to subsurface releases without chemical dispersant. However, the feasibility of this method is yet to be validated in the case of subsurface release with chemical dispersant. More recently, Johansen et al. (2013) have incorporated new experimental data for the subsurface release cases with chemical dispersant application developed a modified Weber number approach to predict the droplet sizes. Zhao et al. (2014) used the same data set with a droplet breakup rate approach. However, all of these available approaches were based on one single set of experimental data on subsurface oil-dispersant interaction (Brandvik et al., 2013) by using one type of oil (Oseberg Blend). There is an urgent need to validate these models with extensive experimental data on more oil types.

Furthermore, although it appears likely that subsurface *in-situ* use of chemical dispersants may be very effective for countering deepwater oil spills, many uncertainties still exist. For example, assumptions of the optimum DOR are based on empirical data mostly obtained from bench-scale experimental protocols that have been designed for testing at standard temperatures and pressures (STP), whereas conditions at a wellhead on the ocean floor or anywhere along a riser beneath the ocean surface could be significantly different. Dispersant effectiveness as a function of dispersant type, oil type, and DOR must be better understood for application in deepwater environments. Furthermore, the interaction of dispersant and crude oil at depth under different turbulence regimes may also have significant implication in optimizing operational performance of subsurface dispersant injection. Improved understanding of these issues should provide better support in decision-making for subsurface dispersant application.

To fill the existing knowledge gaps, extensive experimental studies have been conducted in a flow-through wave tank located at the Bedford Institute of Oceanography (BIO) with an underwater high flow rate oil release system. Accordingly, the objective of this project is to: 1) analyze these newly gained experimental data from BIO; 2) develop a method that can effectively predict the droplet size distributions of oil released from subsurface, with and without application of chemical dispersant; and 3) incorporate the newly developed method with an oil spill model to study its effects on fate and transport of oil from subsurface releases.

2 Methodology

2.1 Maximum Entropy Formalism (MEF) Approach

Probability density function (PDF) such as Rosin-Rammler or Nukiyama-Tanasawa distribution, are established correlations for the droplet size distribution. However, more theoretical foundations were needed for these correlation. Maximum entropy formalism (MEF) approach was used by Chen and Yapa (2007) to develop model for estimating oil droplet size distribution.

To estimate a droplet spectrum, the probability density function (PDF) needs to be connected to a characteristic size (e.g. δ_{max} , δ_{30} , or δ_{32}) (Chen and Yapa, 2007). δ_{max} is the maximum droplet size, δ_{30} is the mass mean volume equivalent diameter, and δ_{32} is the Sauter mean (volume surface) diameter. δ_{max} is determined by diameter of the nozzle D and the Weber number (We) as follows:

$$\delta_{max} = kDWe^{-3/5} \quad (1)$$

By knowing δ_{max} , δ_{30} and δ_{32} can be estimated as follows:

$$\delta_{30} = \left(\int_0^{\delta_{max}} f \cdot \delta^3 d\delta \right)^{1/3} \quad (2)$$

$$\delta_{32} = \left(\int_0^{\delta_{max}} f \cdot \delta^2 d\delta \right)^{-1} \delta_{30}^3 \quad (3)$$

where f is PDF defined as:

$$f = 3\delta_1^2 \exp\left[-\lambda_0 - \lambda_1\delta_1 - \lambda_2\delta_1^3 u_1 - \lambda_3(\delta_1^3 u_1^2 + \delta_1^2 B)\right] \quad (4)$$

Where δ_1 is nondimensional droplet diameter. u_1 is nondimensional droplet velocity. After solving the Lagrangian multiplier λ_i ($\lambda_0, \lambda_1, \lambda_2, \lambda_3$), which are evaluated by several nonlinear constraint equations, mentioned in the Chen and Yapa (2007) the droplet size number based distribution can be obtained in

$$\text{Equation } f_N = \frac{dN}{d(\delta/\delta_{30})} = A \exp\left[-\frac{\delta_{30}}{\delta} - B\left(\frac{\delta}{\delta_{30}}\right)^C\right] \quad (5 \text{ (Chen and Yapa,$$

2007). It indicates that the droplet distributions are controlled by two tuning coefficients B and C :

$$f_N = \frac{dN}{d(\delta/\delta_{30})} = A \exp\left[-\frac{\delta_{30}}{\delta} - B\left(\frac{\delta}{\delta_{30}}\right)^C\right] \quad (5)$$

Where f_N is a number based probability density function, N is the droplet number, δ_{30} is the volume mean diameter, A is a term that accounts for normalization conditions. Their result seems to be less biased. Due to the limited data, the effects of oil properties were neglected. The applicability of the formulation for chemically dispersed oil will be tested in future study.

2.2 Droplet Breakup Approach

Maximum Entropy Formalism (MEF) Approach was widely used in flow atomization and spray; there is less of consideration of oil property. Zhao et al. (2014) has developed a VDROD-J model which considers the effects of both oil viscosity and oil-water interfacial tension (ITF). In a liquid-liquid dispersion system, a population balance equation is proposed as follows:

$$\begin{aligned} \frac{\partial n(d_i, t)}{\partial t} = & \underbrace{\sum_{j=i+1}^n \beta(d_i, d_j) g(d_j) n(d_j, t)}_{\text{droplet breakup}} \\ & + \underbrace{\sum_{j=1}^n \sum_{k=1}^n \Gamma(d_j, d_k) n(d_j, t) n(d_k, t) - n(d_i, t) \sum_{j=i+1}^n \Gamma(d_i, d_j) n(d_j, t)}_{\text{droplet coalescence}} \end{aligned} \quad (6)$$

Where n is number concentration of droplets of diameter d_i at a given time t . The term $\beta(d_i, d_j)$ is the breakage probability density function (dimensionless) for the creation of droplet of diameter d_i due to breakage of droplets of (a larger) diameter d_j , and $g(d_j)$ is the breakage frequency of droplets of diameter d_j . The first term represents the birth of droplets d_i resulting from the breakup of droplets d_j , while the second term represents the death of droplets d_i due to breakup into smaller droplets. For droplets coalescence, the term $\Gamma(d_k, d_j)$ is the coalescence rate (m^3/s). The first term of droplet coalescence represents the birth of

droplets d_i as a results of coalescence events occurring between droplets d_k and d_j to form drops with the size of d_i , while the second term represents deaths of droplets d_i due to the coalescence of drops d_i with all other drops (including drops of size d_i themselves) to form larger drops.

The breakage rate $g(d_i)$ is given by:

$$g(d_i) = K_b \int_{n_e} S_{ed} (u_e^2 + u_d^2)^{1/2} BE \cdot dn_e \quad (7)$$

where S_{ed} represents the collisional cross section of eddy and droplet (m^2), u_e is the turbulent velocity of an eddy (m/s), u_d is droplet velocity (m/s), n_e is number concentration of eddies (number of eddies/ m^3), BE is the breakup efficiency which is related with the IFT, dn_e is the number of eddies of size between μ_e and μ_d are the velocities of eddies and droplet and K_b is a system-dependent parameter for droplet breakup, and would need to be obtained by calibration to experimental data. Based on experimental data, the K_b was found can be approximated by (Zhao et al., 2014):

$$K_b = 3.57(\rho U^2 D)^{-0.63} \quad (8)$$

where ρ is density (kg/m^3), U is velocity (m/s), and D is droplet diameter (m) In Figure 1, an example is given for the comparison of VDROD-J with the experimental data (Brandvik et al., 2013). For a given release condition (e.g., same oil type, discharge nozzle size, and exit velocity), same K_b (0.11 in this case) will be obtained. Therefore, Equation 8 does not consider the effects of chemical dispersant on droplet sizes or shape of the curves. To fit the droplet size distributions with model, other parameters such as ITF or known dispersion efficiency must be used to adjust the shape of the curve. Both Zhao et al. (2014) and Johansen et al. (2013) indicated IFTs (15.5, 0.05 and 0.09) from three experiments based on DOR of 0, 1:50, and 1:25, respectively. The measured IFT (0.09) for DOR=1:25 is actually higher than the IFT (0.05) for DOR=1:50. This is against to the IFT fitting produced by Zhao et al. (2014) which indicated that the higher IFT would lead to a closer curve to the untreated condition (DOR = 0). The author may use estimated efficiencies of 10% and 80% for the case of DOR=1:50 and 1:25 during the fitting, respectively.

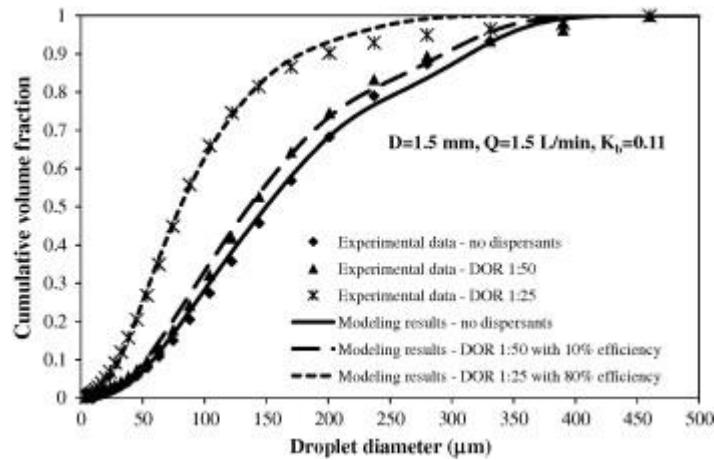


Figure 1: Comparison of oil droplet size distribution between VDROD-J and experimental data.

(Source: Zhao et al. 2014)

2.3 Modified Weber Number Approach

There is no validation conducted for the MEF and droplet breakup approaches for droplet size prediction with chemical dispersant application. However, chemical dispersion is one of the important technologies in offshore oil spill response, and promising in responding to deepwater release. Thus, an approach in predicting droplet size with chemical dispersant is desired.

Johansen et al. (2013) has proposed a modified Weber number approach for such purpose based on the conventional Weber number approach by Wang and Calabreses (1986). In Johansen et al. (2013), Weber number scaling law was used to fit their experimental data, expressed as:

$$d'/D = AWe^{-3/5} \quad (9)$$

where d' is characteristic droplet diameter (m) D is the nozzle diameter (m), A is a factor of proportionality and $We = \rho U^2 D / \sigma$ is the Weber number; ρ is density of the liquid in the jet (oil) (kg/m^3) U is the exit velocity (m/s), and σ is the interfacial tension between oil and water (N/m or kg/s^2). However, this simple Weber scaling law only fit well on DOR=0, for other DOR experiments, this scaling law do not fit it. Based on these available data, a new prediction model (modified weber number) is used for oil droplet size distribution with and without chemical dispersant.

The modified Weber number, We^* , is defined as follows:

$$We^* = \frac{We}{1 + BVi(d_{50}/D)^{1/3}} \quad (10)$$

where We is the Weber number, $Vi = We/Re$ is the viscosity number, d_{50} is the median droplet diameter (m), D is the nozzle size (m), B is an empirical coefficient determined by experimental analysis. The relative droplet size d_{50}/D can be expressed as:

$$(d_{50}/D) = A(We^*)^{-3/5} \quad (11)$$

where A is an empirical constant. Based on the data from Brandvik (2013) and Johansen et al. (2013) the value of A and B can be determined as $A = 15.0$ and $B = 0.8$.

Once d_{50} is determined, the droplet size distribution can be estimated using either lognormal or Rosin-Rammler distribution. Johansen et al. (2013) has concluded that Rosin-Rammler (Equation 12) distribution gives better fit of experimental data overall.

$$V(d) = 1 - \exp\left[-0.693(d/d_{50})^\alpha\right] \quad (12)$$

where $V(d)$ is the cumulative distribution, and α is the spreading-parameter.

Although the mathematical formulations of three methods described above are of different level of complexity, all three methods require two or three tuning coefficients determined from regression. It seems that the efficiency and accuracy of droplet size prediction from these three methods are more or less the same. Comparatively, the complexity of the modified Weber number approach is lower than the other two, leading to advantage in real-world application. Therefore, the modified Weber number approach is selected in this study to fit the new experimental data with performance validation.

3 Prediction of Droplet Size Distribution

3.1 Experimental settings

A series of experiments of droplet size measurement for two types of oils (IFO-120 and ANS) have been conducted by the COOGER in BIO. The current flow rate for the experiments is set to 1 cm/s and the oil temperature is set to 80 °C. The detailed settings of the other parameters (i.e., oil amount, water temperature, injection time, and flow in the tank) are listed in Tables 1 and 2. 24 experiments were conducted for each types of oil by consideration of seasonal conditions (spring and summer). As shown in Tables 1 and 2, the experiment No.1 to 12 were set based on spring condition with slightly lower water temperature (mostly lower than 10°C) . In contrast, the experiments of No. 13 to 24 were set based on summer condition with warm water temperature (mostly higher than 10°C). The “R” marked in the experiment No. denoted a repeated experiment with slightly adjusted conditions (e.g., different DOR). In addition, some of the repeated experiments (i.e., 6R, 7R, 10R and 11R), which were scheduled in spring but not conducted due to abnormal weather conditions with rising water temperature, were actually conducted late fall.

There were four dispersant-oil ratios (0, 1:250, 1:100, and 1:25) for the spring condition. Comparatively, the settings of dispersant-oil ratios are slightly different from which in the spring condition, which are 1:200 and 1:20.

Table 1: Experimental settings for droplet size analysis for IFO-120

No.	Factors		Measurements					Injection Pressure (psi)
	Oil	DOR	Date	Oil Amount (g)	Water Temperature (°C)	Injection Time (sec)	Flow in the Tank (gpm)	
1	IFO-120	0	9-Jun-14	145.2	13.0	5	600	40
2	IFO-120	1:250	20-Jun-14	199.6	12.2	7	600	62
2R	IFO-120	1:200	04-Dec-14	208.2	6.7	7	600	60

3	IFO-120	1:100	20-Jun-14	213.9	13.2	7	600	62
4	IFO-120	1:25	11-Jun-14	179.1	12.8	9	600	40
4R	IFO-120	1:20	05-Dec-14	219.6	5.6	10	600	30
5	IFO-120	0	17-Jun-14	275.1	12.0	7	600	62
6R	IFO-120	1:200	04-Dec-14	215.6	6.6	8	600	60
7R	IFO-120	1:100	10-Dec-14	239.3	7.5	8	600	60
8	IFO-120	1:25	11-Jun-14	255.8	13.2	9	600	40
8R	IFO-120	1:20	05-Dec-14	243.3	5.4	10	600	60
9	IFO-120	0	17-Jun-14	359.6	12.7	7	600	62
10R	IFO-120	1:200	04-Dec-14	221.7	6.6	8	600	60
11R	IFO-120	1:100	17-Dec-14	N/A	4.9	10	600	60
12	IFO-120	1:25	16-Jun-14	354.8	12.5	9	600	62
12R	IFO-120	1:20	10-Dec-14	204.8	6.8	9	600	60
13	IFO-120	0	12-Sep-14	256.8	14.9	7	600	60
14	IFO-120	1:200	15-Sep-14	279	13.5	8	600	60
15	IFO-120	1:100	16-Sep-14	336.2	14.0	8	600	60
16	IFO-120	1:20	17-Sep-14	315.9	14.7	7	600	60
17	IFO-120	0	12-Sep-14	293.3	14.7	8	600	60
18	IFO-120	1:200	15-Sep-14	331.8	13.8	8	600	60
19	IFO-120	1:100	16-Sep-14	353.8	14.7	7	600	60
20	IFO-120	1:20	17-Sep-14	345.6	15.2	7	600	60
21	IFO-120	0	12-Sep-14	303.6	15.2	8	600	60
22	IFO-120	1:200	15-Sep-14	363.3	14.0	8	600	60
23	IFO-120	1:100	16-Sep-14	352.6	14.7	7	600	60

24	IFO-120	1:20	17-Sep-14	380	16.0	7	600	60
----	---------	------	-----------	-----	------	---	-----	----

Note: R indicates repeated experiment.

Table 2: Experimental settings for droplet size analysis for ANS

No.	Factors		Measurements					
	Oil	DOR	Date	Oil Amount (g)	Water T (°C)	Injection Time (sec)	Flow in the Tank (gpm)	Injection pressure (psi)
1	ANS	0	22-May-14	208.0	11.4	4	600	40
2	ANS	1:250	23-May-14	280.0	10.6	5	600	40
2R*	ANS	1:200	02-Dec-14	290.5	6.4	5	600	40
3	ANS	1:100	23-May-14	284.5	11.2	5	600	40
4	ANS	1:25	26-May-14	283.0	8.4	5	600	40
4R	ANS	1:20	03-Dec-14	287.2	6.8	5	600	40
5	ANS	0	26-May-14	279.3	8.4	5	600	40
6	ANS	1:250	30-May-14	279.7	7.7	5	600	40
6R	ANS	1:200	02-Dec-14	335.0	6.1	5	600	40
7	ANS	1:100	30-May-14	276.3	8.5	5	600	40
8	ANS	1:25	02-Jun-14	277.4	9.4	5	600	40
8R	ANS	1:20	03-Dec-14	297.2	7.0	5	600	40
9	ANS	0	02-Jun-14	281.4	9.7	5	600	40
10	ANS	1:250	06-Jun-14	281.0	10.3	5	600	40
10R	ANS	1:200	17-Dec-14	344.5	5.4	5	600	40
11	ANS	1:100	06-Dec-14	276.8	10.7	5	600	40

12	ANS	1:25	09-Jun-14	280.6	12.5	5	600	40
12R	ANS	1:20	10-Dec-14	295.7	7.3	5	600	40
13	ANS	0	05-Sep-14	303.7	17.7	5	600	40
14	ANS	1:200	08-Sep-14	295.2	16.0	5	600	40
15R	ANS	1:100	10-Sep-14	304.3	13.8	5	600	40
16	ANS	1:20	10-Sep-14	291.9	14.7	5	600	40
17	ANS	0	05-Sep-14	299.6	18.1	5	600	40
18	ANS	1:200	08-Sep-14	297.7	16.2	5	600	40
19	ANS	1:100	09-Sep-14	283.4	15.3	5	600	40
20	ANS	1:20	11-Sep-14	289.6	14.1	5	600	40
21	ANS	0	08-Sep-14	297.1	15.1	5	600	40
22	ANS	1:200	09-Sep-14	281.8	14.2	5	600	40
23	ANS	1:100	10-Sep-14	284.4	13.4	5	600	40
24	ANS	1:20	11-Sep-14	285.8	13.6	5	600	40
25	ANS	1:50	11-Sep-14	316.2	17.6	6	600	40

Note: R indicates repeated experiment.

3.2 Measured Droplet Size Distributions

The droplet size distributions of IFO-120 based on different DOR and seasonal conditions are shown in Figures 2 to 10. In addition, the droplet size distributions of ANS are listed in Figures 11 to 21. The ranges of DOR for the ANS experiment (Figures 11 to 20) were the same as which for the IFO-120. A series of experiments with DOR = 1:50 are currently conducting by COOGER (one set of result is listed in Figure 21), further analysis will be conducted for this case.

As shown in Figure 2, the distribution and corresponding median of the droplet size distribution from experiment No. 1, 5, and 9 based on same type of oil (IFO-120), DOR = 0, seasonal condition (spring, similar water temperature) but different oil amount, injection time, and injection pressure. In addition, the first two experiments (No. 1 and 5) have the same peak diameter ($d_p = 259 \mu\text{m}$), but slightly different d_{50} ($258 \mu\text{m}$ in No. 1 and $176 \mu\text{m}$ in No. 5). The third experiment showed smaller d_{50} ($186 \mu\text{m}$) and d_p ($100 \mu\text{m}$). This may be caused by relatively large plume or more smaller droplets caught by LISST.

In summer condition, the experiment 13 and 21 has same d_p (391 μm) and very similar d_{50} (263 μm in No. 13 and 264 in No. 21), while the experiment 17 has a slightly smaller d_{50} (192 μm) and d_p (293 μm) with similar settings from which in spring condition. However, the droplet size distributions from No. 13 and 21 are not completed due to the limited measuring window of the LISST. Thus, the data from these two experiments will not be included in the further analysis. Comparing results from summer and spring, the d_p and d_{50} from summer is relatively higher than which from spring. Since the only significant different setting from summer to spring is the water temperature, which may be another factor that affecting the oil droplet size.

The droplet size distributions with similar conditions but different DOR in spring are listed in Figures 4, 5, 7, and 9. By comparing the d_p and d_{50} in the experiments with different DOR, it indicates that the change of droplet size is relatively insignificant with DOR from 0 to 1:100 (Figures 2, 5, and 7). However, a significant decrease droplet size is observed with DOR increasing from 1:100 to 1:20. Therefore, there are may be a threshold of DOR dosage that significantly changes the effects of dispersant on droplet size.

The droplet size distributions with similar conditions but different DOR in summer are listed in Figures 6, 8, and 10. For the warm cases (14, 18, and 22), experiment No.18 showed strong effects of truncation due to the maximum diameter can be measured by LISST instrument was 500 μm . Both experiments 14 and 22 have similar but slightly smaller d_{50} compared with untreated cases (No.13 and 21), but the d_p from warm water are much smaller. This indicates that dispersant started to play a role in this case but the effects are not very strong.

For the case of DOR=1:100 with spring condition, the shape of the distribution and calculated d_{50} and d_p in experiment No.3 are very similar to the untreated case and DOR=1:250 cases of experiment No.5 and No.2, and the dispersant did not show a strong effects on the droplet distribution (Figure 7). Similar as experiment No. 18, experiment No.7R also showed strong effects of truncation. For the summer condition cases (Figure 8), although d_{50} and d_p for experiment No.15 does not change significantly compared with DOR=1:200 cases (e.g. No.14), d_{50} from experiment No. 19 and 23 are much smaller and the overall oil concentration are much higher. This indicates high dispersant effectiveness.

For the case of DOR=1:25 (or 20) with spring condition (Experiment No. 4, 8, and 12), while the first experiment showed very low oil concentration compared with the other two experiments. The second and the third experiments repeated very well with much higher oil concentration and smaller d_p (128 μm for No. 8 and 104 μm for No. 12) and d_{50} (99 μm for No. 8 and 93 μm for No. 12) (Figure 9). Similar trends can be observed for the summer condition cases (Figure 10).

Compared the droplet size distributions from spring to summer conditions with same DOR, the droplet sizes from the results in summer experiment are significantly smaller than which in winter condition. The only known parameter that is different from the spring and summer condition with same DOR is the water temperature. Therefore, temperature may help facilitate the effect of dispersant on reduction the droplet size. In general, the results from the cases with spring and summer conditions indicate very high effectiveness of chemical dispersants.

Compared with the droplet sizes of IFO-120, the droplet sizes of ANS are significantly smaller. The droplet size distributions from three experiments (No. 1, 5 and 9) with untreated ANS in spring conditions are shown in Figure 11. The d_p (75 - 88 μm) and d_{50} (68 - 81 μm) are different but not significant in these

three experiments. However, there is an abnormal peak observed in No. 5, which may due to unknown effects (further experiments and analyses shall be needed). The droplet sizes from the experiments with summer condition (No. 13, 17 and 21) (Figure 12) are similar ($d_p = 104 - 128 \mu\text{m}$ $d_{50} = 89 - 101 \mu\text{m}$) and higher than which from experiments with spring condition.

For the case of DOR=1:250 with spring condition, three experiments (No. 2, 6 and 10) have been conducted (Figure 13). In addition, three repeated experiments (No. 2R, 6R and 10R) with DOR=1:200 have also been conducted (Figure 14). Experiment No. 2 shows two d_p in one distribution which may due to influences from environment, and thus is difficult to be analyzed. Nevertheless, the droplet size distributions from No. 6 and 10 are highly similar with same d_p ($75 \mu\text{m}$) and similar d_{50} ($63 \mu\text{m}$ for No. 6 and $66 \mu\text{m}$ for No. 10). The repeated experiments with DOR=1:200 show similar situation, the shape of the distribution and calculated d_{50} and d_p are very similar between No. 2R and 6R; while the situation of No. 10R is similar to which of No. 2. Compared with the untreated case ($d_p = 75 - 88 \mu\text{m}$), the smaller d_p ($< 75 \mu\text{m}$) in DOR=1:200 (or 250) show the effect of dispersant on oil droplet distribution. The droplet size distributions from the experiments (14, 18, and 22) based on summer condition are highly similar with identical d_p ($75 \mu\text{m}$) and very close d_{50} ($64 - 65 \mu\text{m}$). Experiments with DOR=1:200 (or 250) have slightly smaller d_{50} ($64 - 65 \mu\text{m}$) compared with untreated cases (13, 17 and 21) ($d_{50} = 68 - 81 \mu\text{m}$), as well as the d_p ($75 \mu\text{m}$ for DOR = 200 or 250 and $75 - 88 \mu\text{m}$ for DOR = 0). This indicates that the effect of dispersant on ANS is more significantly than which on IFO-120 with very insignificant change of droplet size from DOR = 0 to 1:200.

Three experiments have been conducted for DOR=1:100 with spring condition (Figure 16). The d_{50} ($55 - 58 \mu\text{m}$) in experiment No.3, 7 and 11 are smaller than the DOR=1:200 (or 250) cases ($d_{50} = 64 - 65 \mu\text{m}$) while d_p ($75 \mu\text{m}$) are same. For the summer condition cases (Figure 17), d_{50} and d_p for experiment No.15R does not change significantly compared with DOR=1:200 cases (e.g. No.14), while the ones from experiment 19 and 23 are relatively smaller.

For the case of DOR=1: 25 with spring condition, the d_p ($12 \mu\text{m}$) and d_{50} ($3 - 10 \mu\text{m}$) from corresponding experiments (No. 8 and 12) are significantly lower than which from the experiments with DOR=1: 200 and 1: 100; while data from experiment No.4 appears abnormal distribution and could not be analyzed (Figure 18). The situations from the repeated experiments (No. 4R, 8R, and 12R) with DOR = 1:20 (Figure 19) are very similar to the original one (DOR = 1:25). Furthermore, similar trends can be observed for the summer condition cases (Figure 20). Figure 21 is a trial experiment of DOR=1:50 which is done in the summer of 2015, which indicate the droplet size of ANS is steadily decrease with increase DOR. It should also be noted that the droplet size distributions are significantly different from the experiments with DOR = 1:20 or 25 to the others. This may be cause by over dose of chemical dispersant. The other peaks in the distributions (Figures 18, 19 and 20) may be caused by the over-dosed dispersant or the unknown background components that were affected by the dispersant.

In general, the chemical dispersant plays an importance role in reduce the droplet size of ANS no matter in spring or summer conditions. The effectiveness of dispersant in reducing droplet size is higher on ANS than which on IFO-120. There may be thresholds for the dose of chemical dispersant to some oils (e.g., IFO-120) but will need further experiments to analyze. There may also be over dose of dispersant to some oils (e.g., ANS) when the DOR is high, eventually affecting the droplet size distribution. Future experiment will also need for this particular issue.

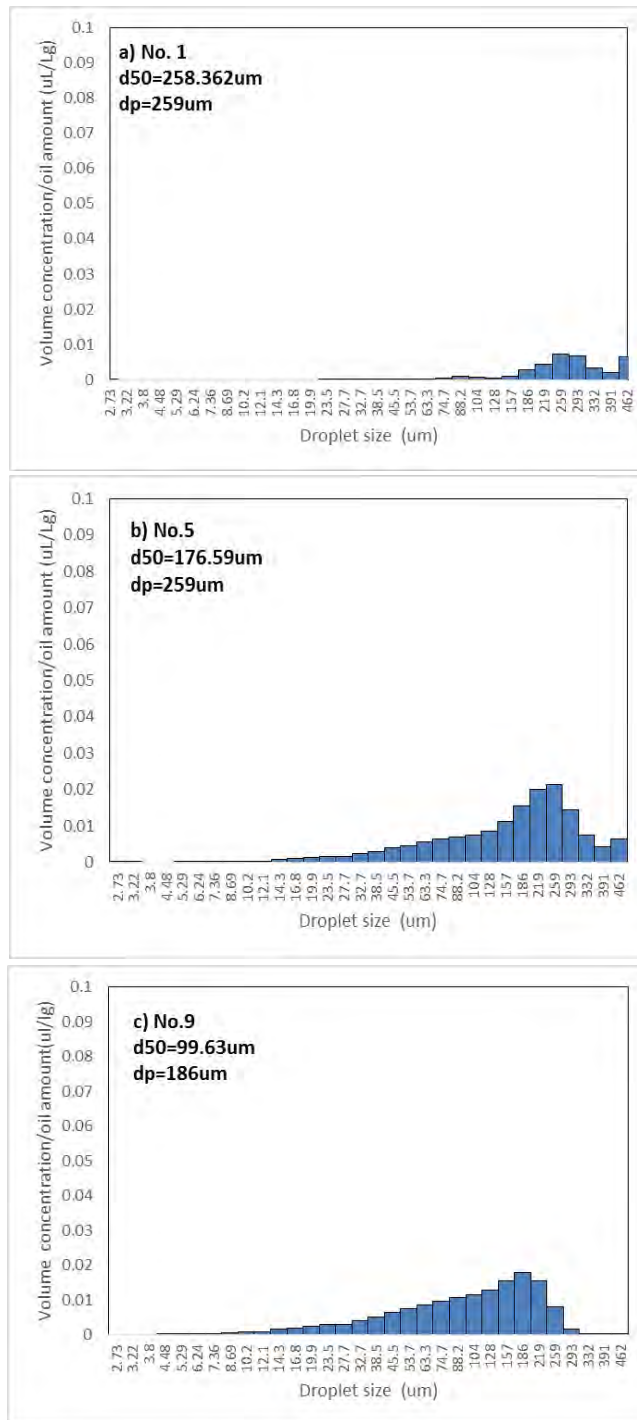


Figure 2: Experimental droplet size distribution of IFO-120 based on experiment a) No. 1, b) No. 5, and c) No.9 with DOR = 0 in spring condition

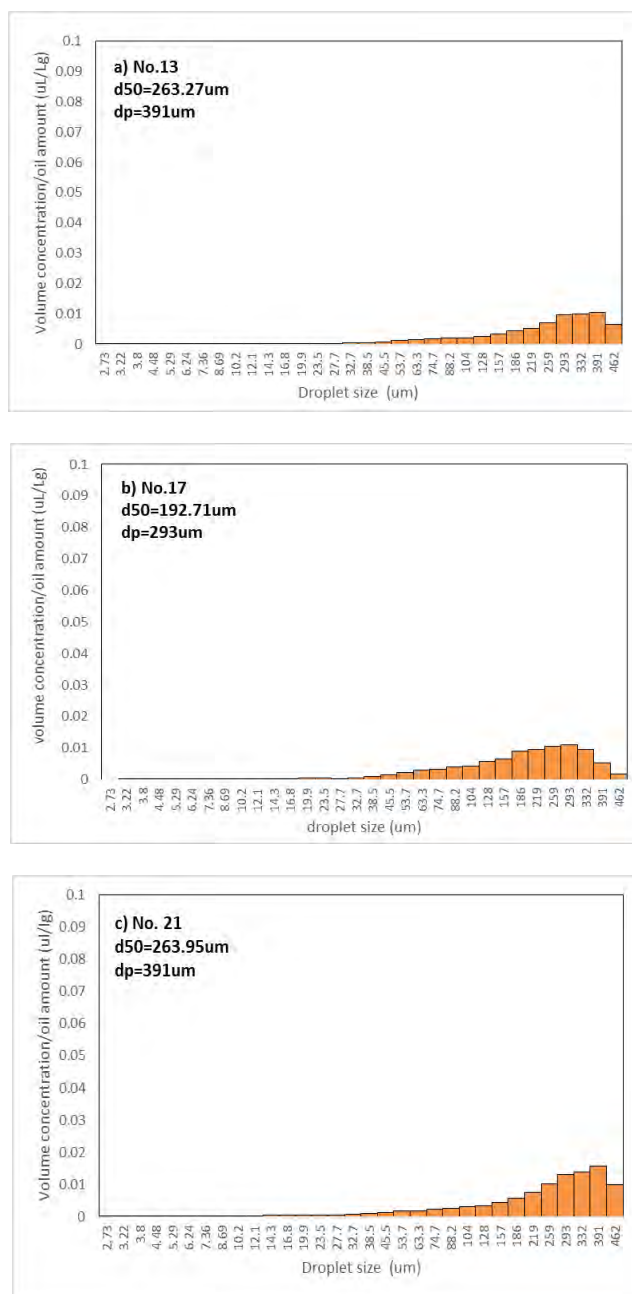


Figure 3: Experimental droplet size distribution of IFO-120 based on experiment a) No. 13, b) No. 17, and c) No. 21 with DOR = 0 in summer condition

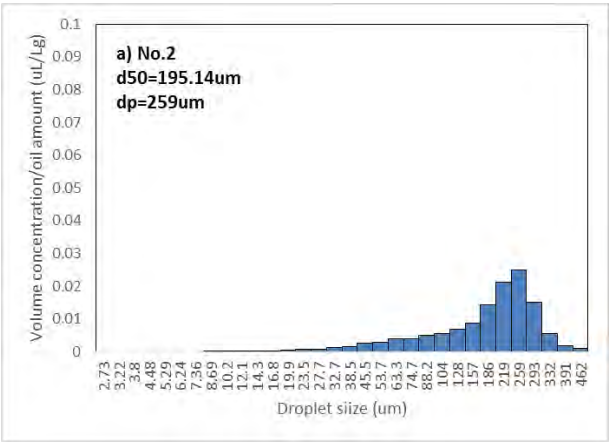


Figure 4: Experimental droplet size distribution of IFO-120 based on experiment a) No. 2 with DOR = 1: 250 in spring condition

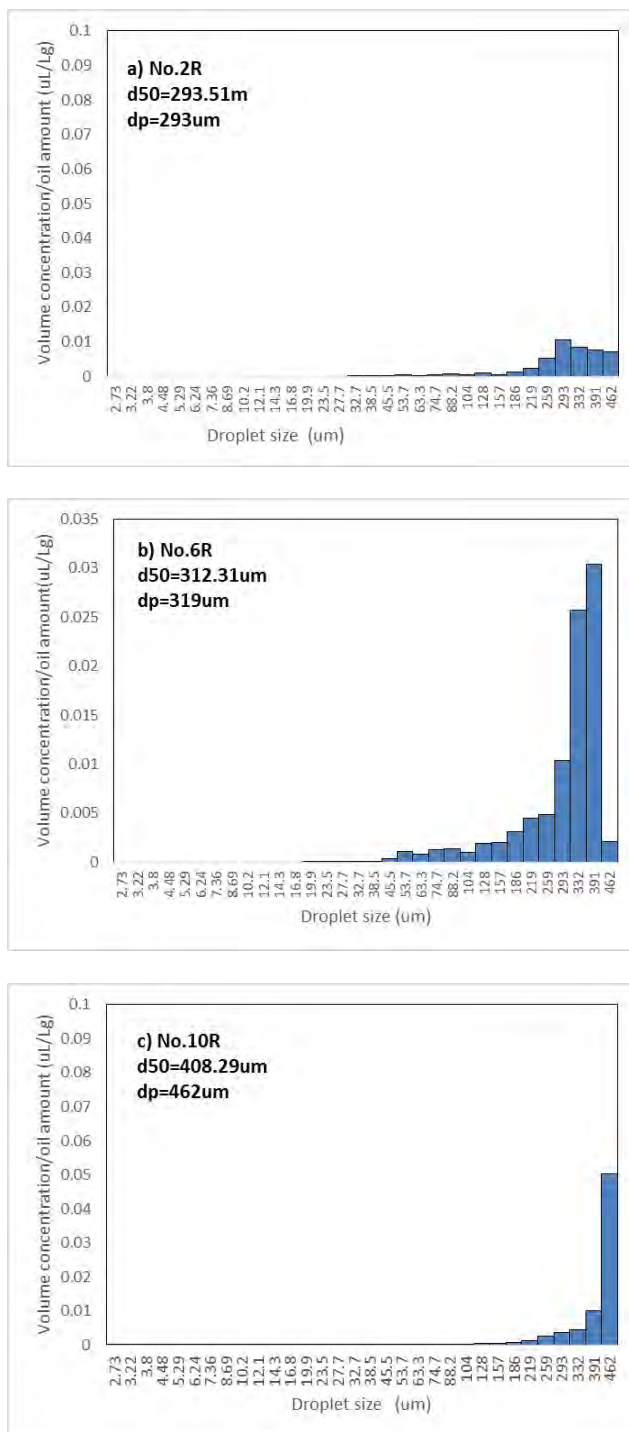


Figure 5: Experimental droplet size distribution of IFO-120 based on experiment a) No. 2R, b) No. 6R, and c) No.10R with DOR = 1: 200 in spring condition

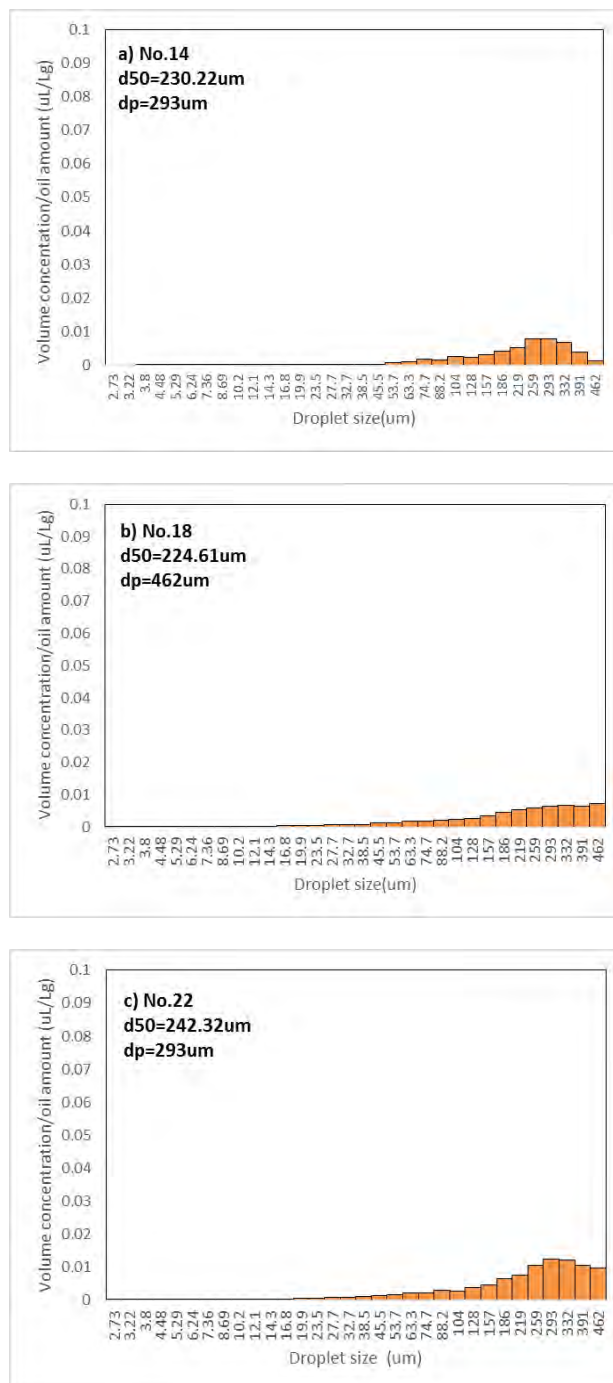


Figure 6: Experimental droplet size distribution of IFO-120 based on experiment a) No. 14, b) No. 18, and c) No. 22 with DOR = 1:200 in summer condition

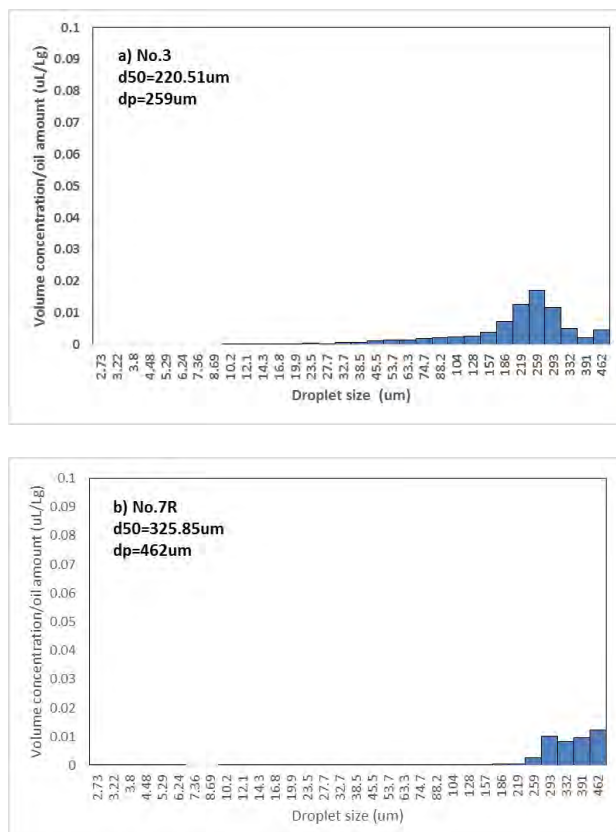


Figure 7: Experimental droplet size distribution of IFO-120 based on experiment a) No. 3, and b) No. 7, with DOR = 1:100 in spring condition

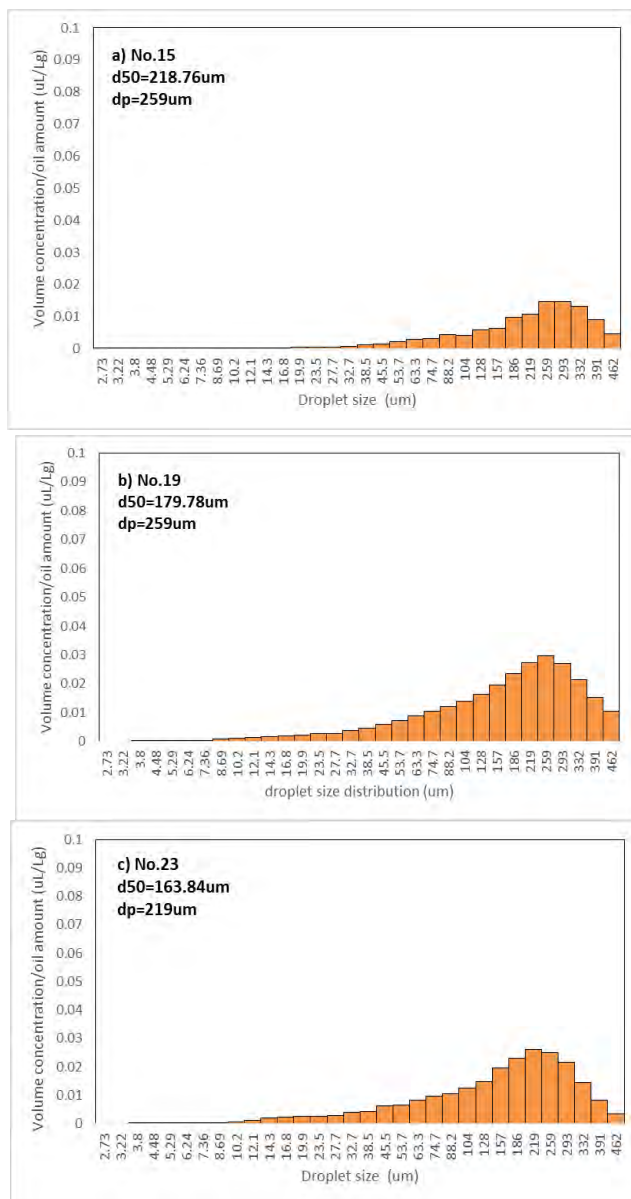


Figure 8: Experimental droplet size distribution of IFO-120 based on experiment a) No. 15, b) No. 19, and c) No.23 with DOR = 1:100 in summer condition

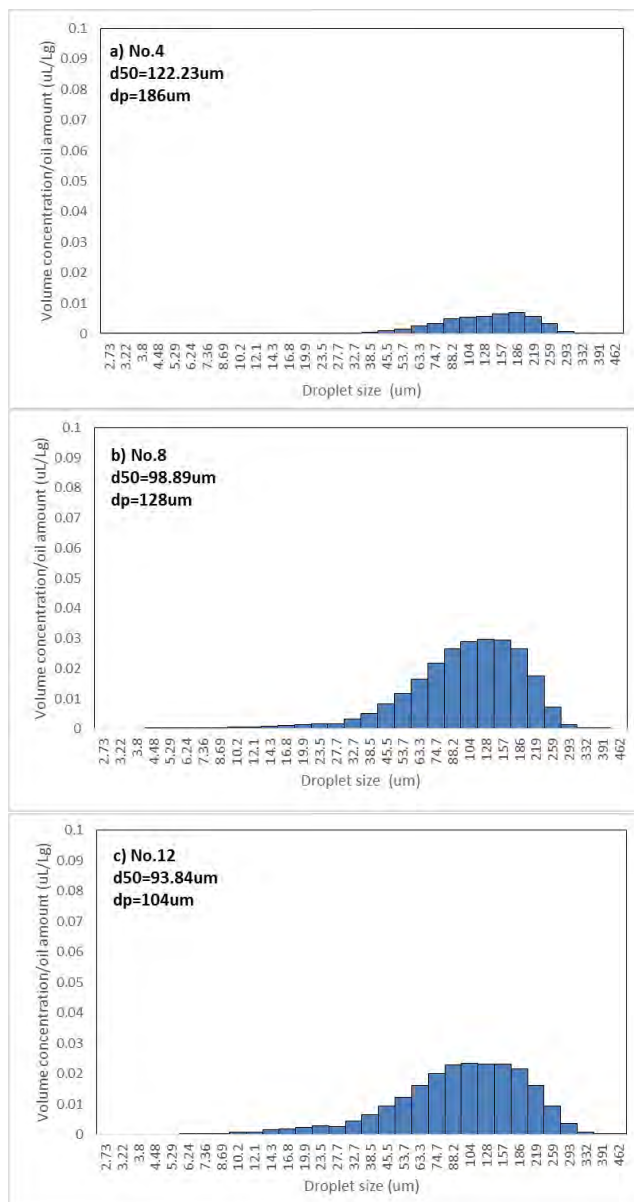


Figure 9: Experimental droplet size distribution of IFO-120 based on experiment a) No. 4, b) No. 8, and c) No.12 with DOR = 1:25 in spring condition

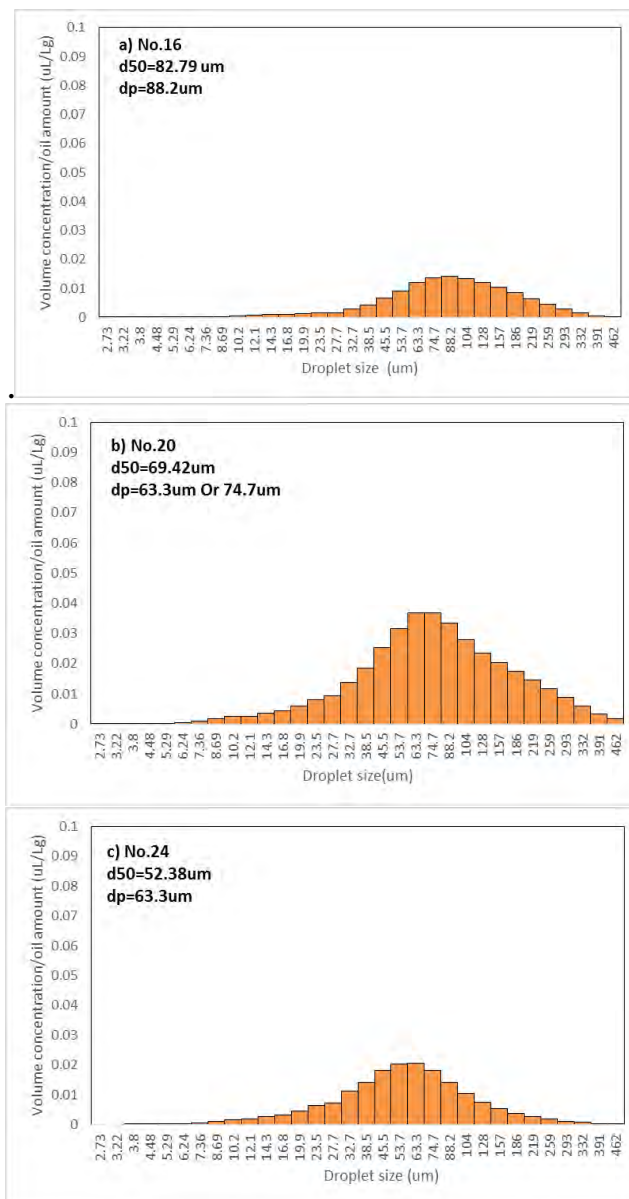


Figure 10: Experimental droplet size distribution of IFO-120 based on experiment a) No. 16, b) No. 20, and c) No.24 with DOR = 1:20 in summer condition

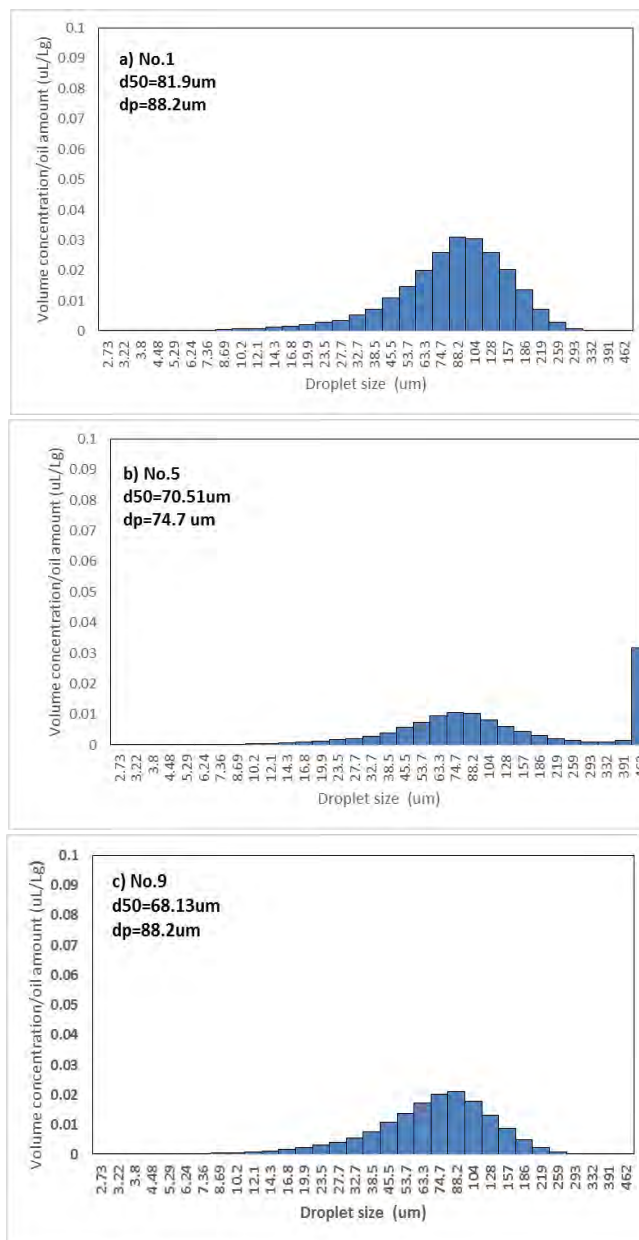


Figure 11: Experimental droplet size distribution of ANS based on experiment a) No. 1, b) No. 5, and c) No. 9 with DOR = 0 in spring condition

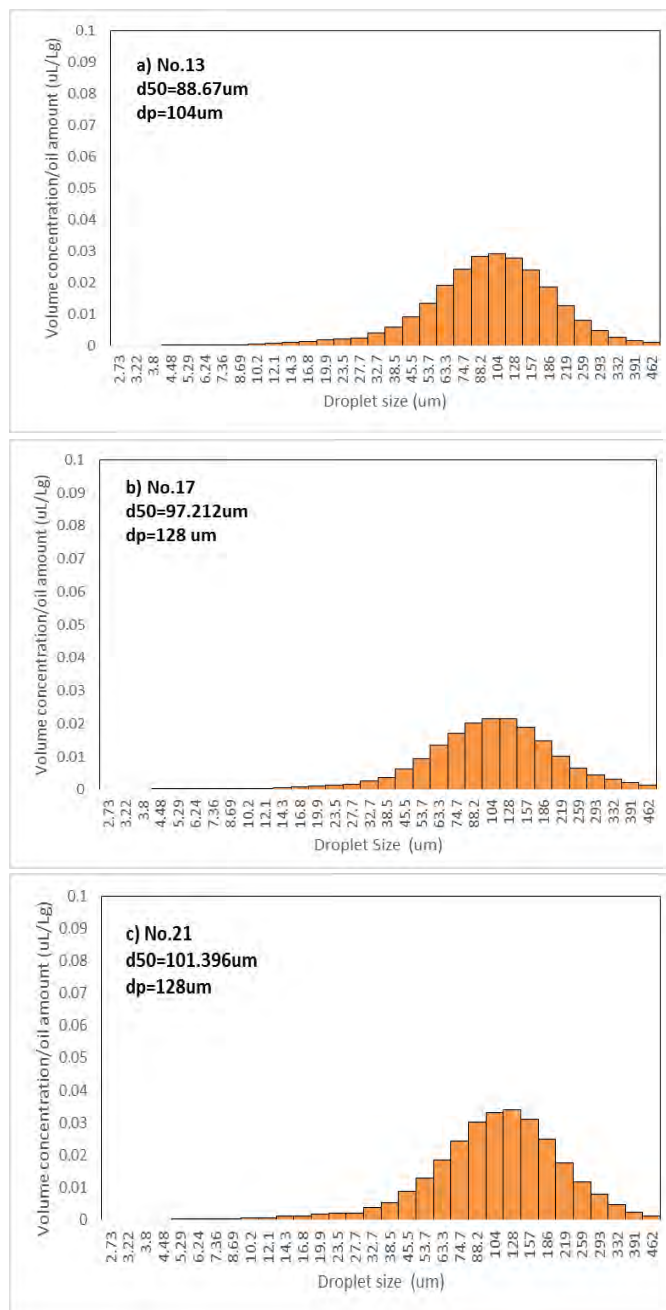


Figure 12: Experimental droplet size distribution of ANS based on experiment a) No. 13, b) No. 17, and c) No. 21 with DOR = 0 in summer condition

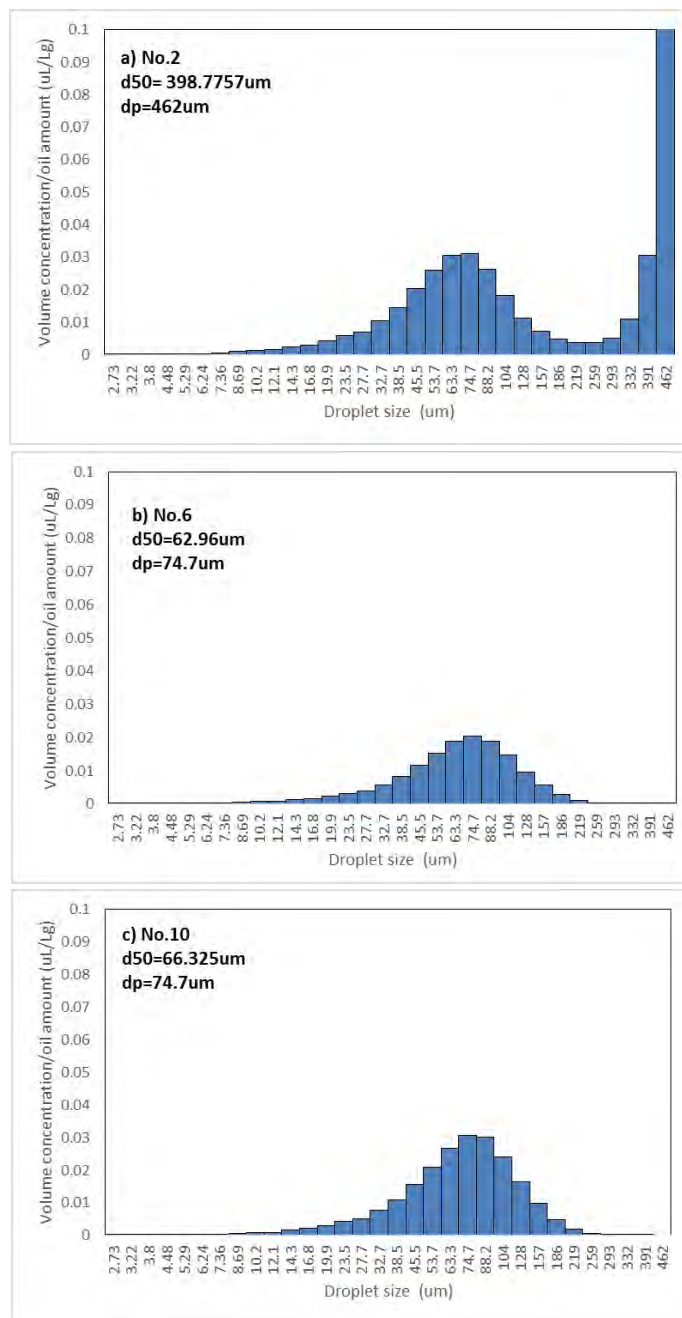


Figure 13: Experimental droplet size distribution of ANS based on experiment a) No. 2, b) No. 6, and c) No. 10 with DOR = 1:250 in spring condition

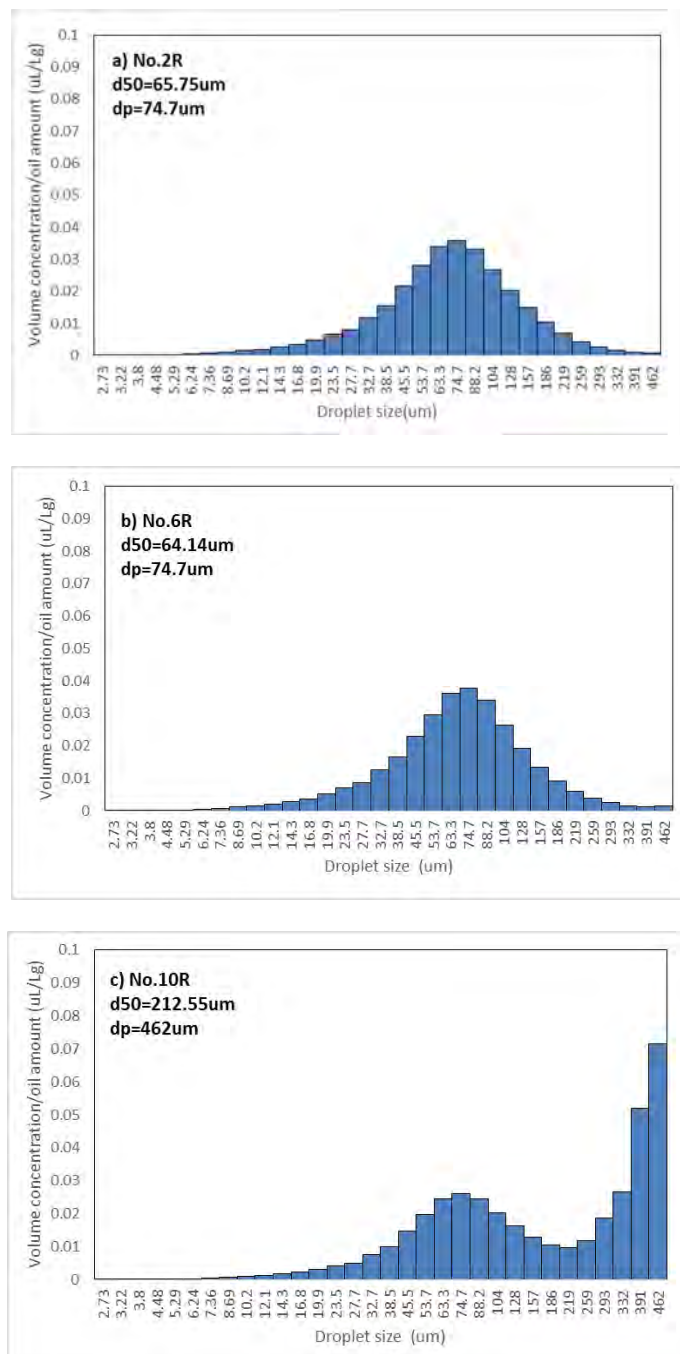


Figure 14: Experimental droplet size distribution of ANS based on experiment a) No. 2R, b) No. 6R, and c) No. 10R with DOR = 1:200 in spring condition

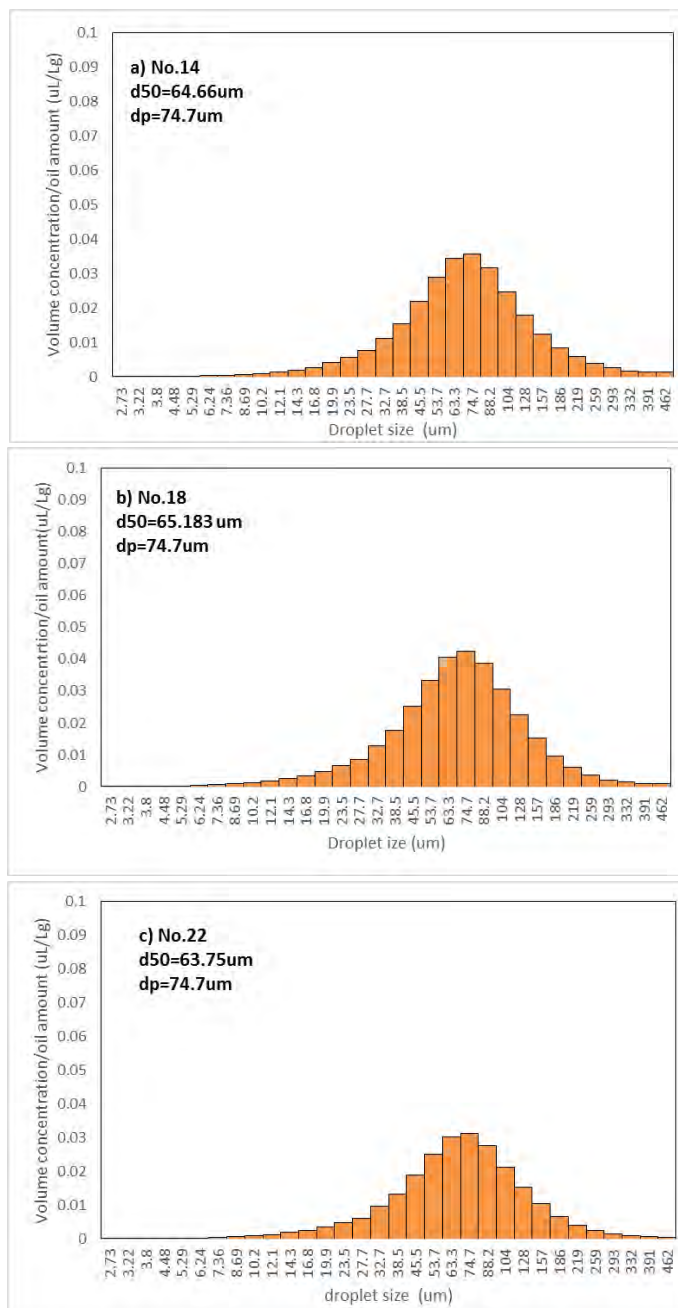


Figure 15: Experimental droplet size distribution of ANS based on experiment a) No. 14, b) No. 18, and c) No. 22 with DOR = 1:200 in summer condition

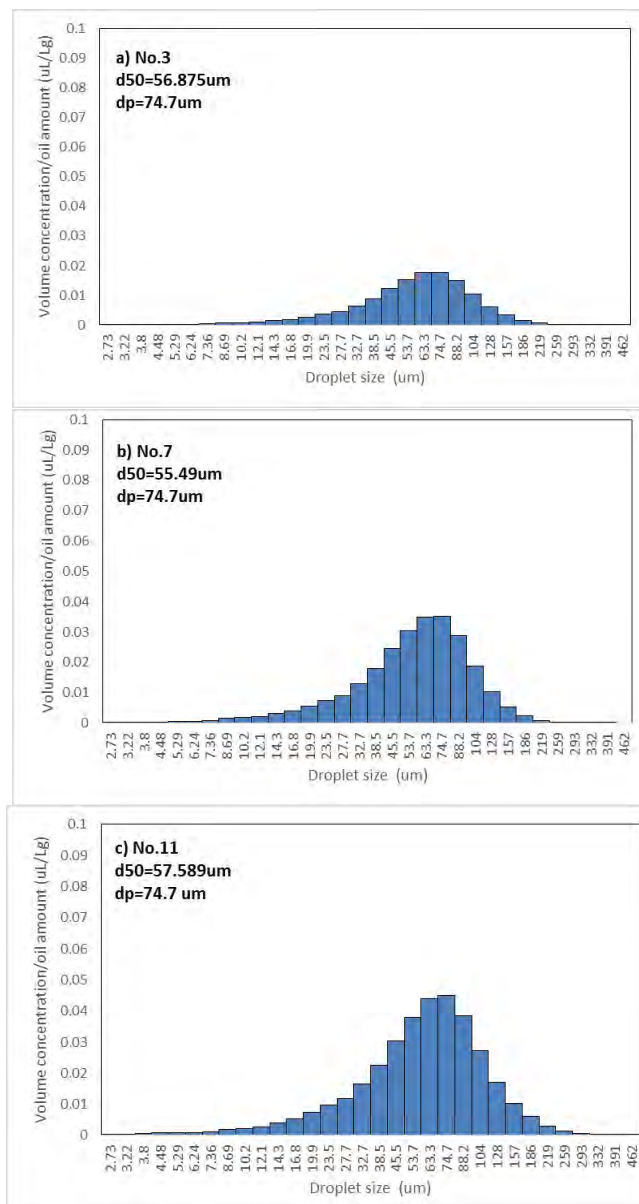


Figure 16: Experimental droplet size distribution of ANS based on experiment a) No. 3, b) No. 7, and c) No. 11 with DOR = 1:100 in spring condition

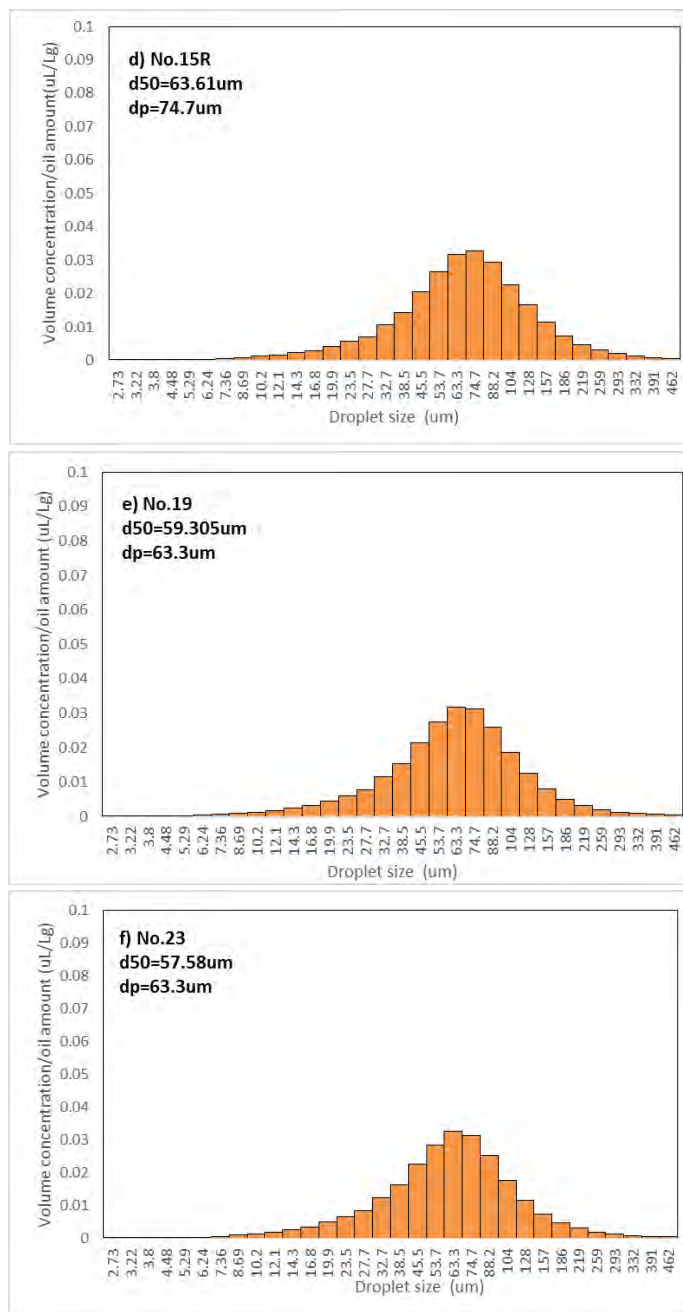


Figure 17: Experimental droplet size distribution of ANS based on experiment a) No. 15R, b) No. 19, and c) No. 23 with DOR = 1:100 in spring condition

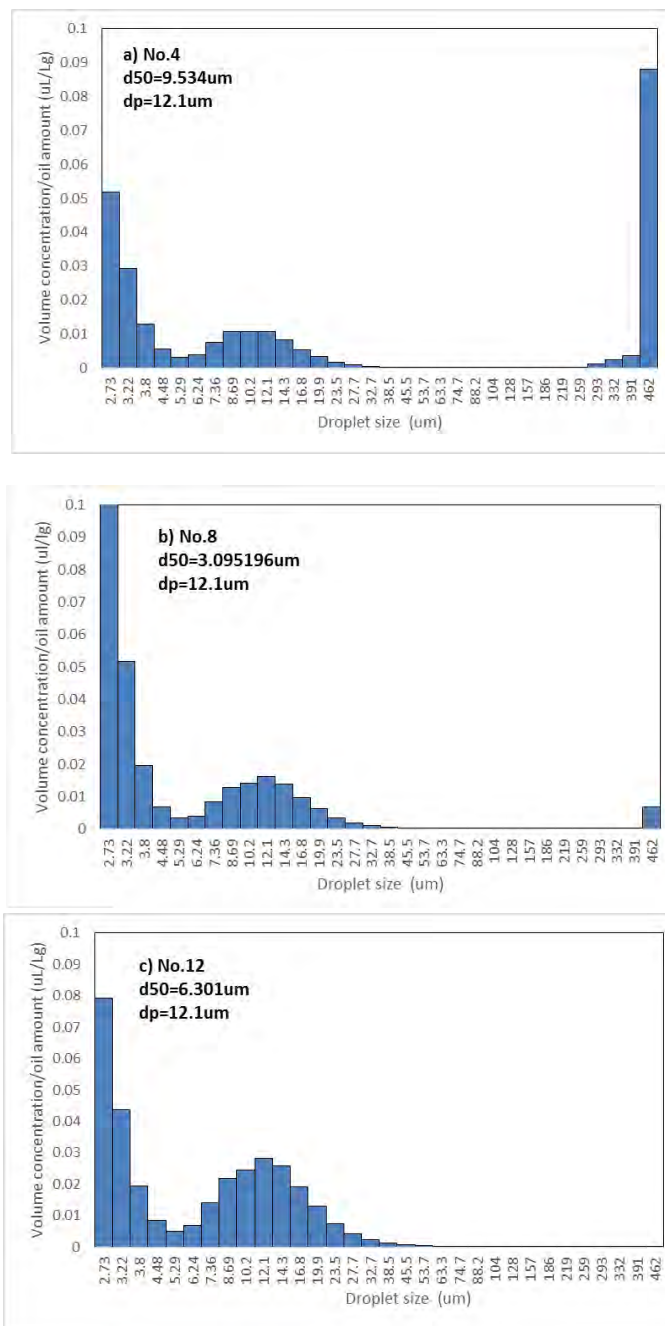


Figure 18: Experimental droplet size distribution of ANS based on experiment a) No. 4, b) No. 8, and c) No. 12 with DOR = 1:25 in spring condition

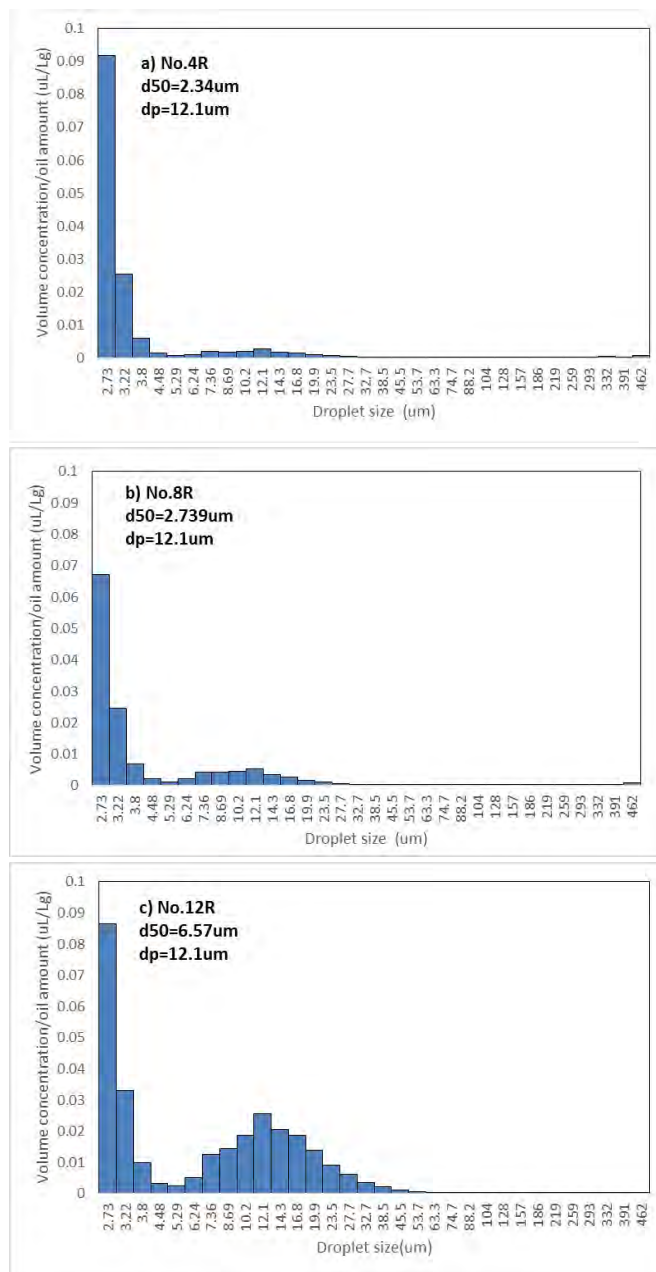


Figure 19: Experimental droplet size distribution of ANS based on experiment a) No. 4R, b) No. 8R, and c) No. 12R with DOR = 1:20 in spring condition

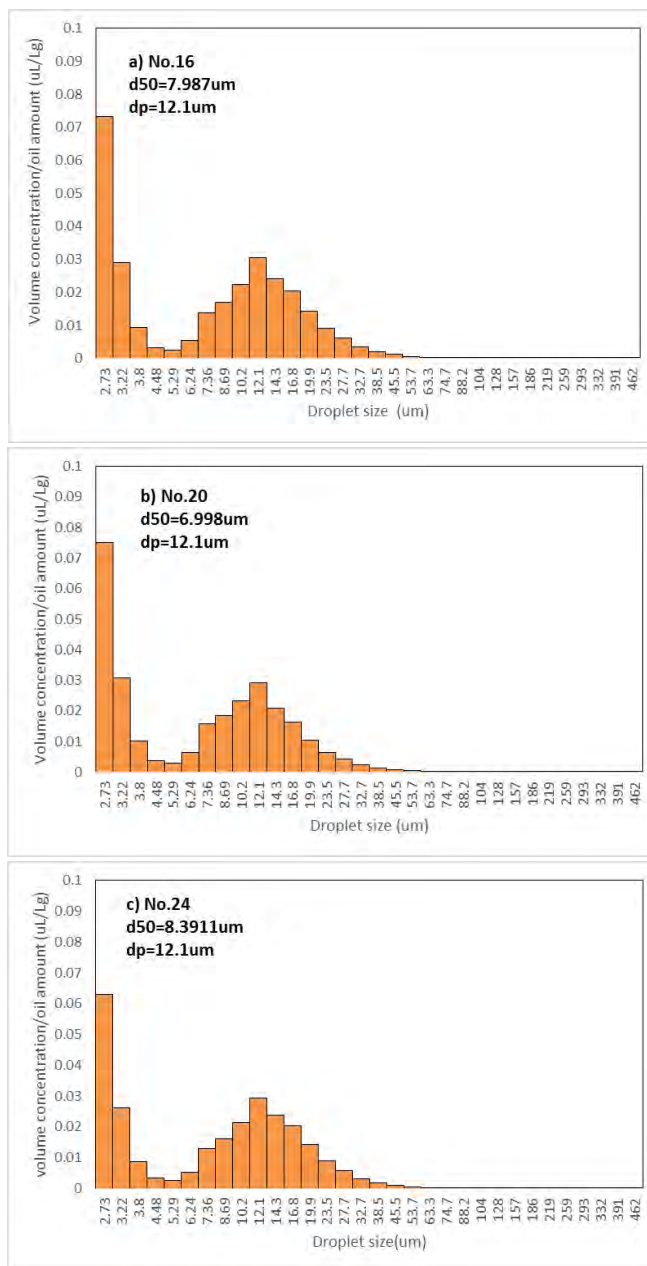


Figure 20: Experimental droplet size distribution of ANS based on experiment a) No. 16, b) No. 20, and c) No. 24 with DOR = 1:20 in Summer condition

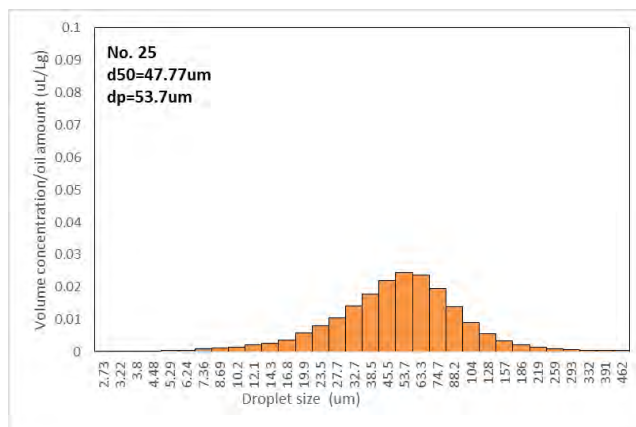


Figure 21: Experimental droplet size distribution of ANS based on experiment with DOR = 1:50 in summer condition

3.3 Data Fitting with Modified Weber Number Approach

Based on experimental settings (Table 1 and 2) and measured droplet size distributions (Figures 2 to 21), as well as the additional measurements on oil viscosity and IFT, the Weber number (We), Viscosity number (Vi) and Reynold number (Re) were calculated. The values of calculated and additional measured parameters for IFO-120 and ANS are listed in Tables 3 and 4. By normalize the d_{50} with the preset nozzle size in the experiments ($D = 2.387$ mm), the relationship between relative volume median droplet sizes (d_{50}/D) and modified Weber number (We^* in Equation 11) for corresponding oils can be determined as in Figures 22 and 23. In comparison purpose, the corresponding data for Oseberg Blend based on the SINTEF tower tank experiments are also included in these figures.

As shown in Figure 22, for the treated IFO-120 crude oil with $DOR \leq 1:100$, the modified Weber number approach fits the measured data IFO-120 well. The empirical constant A has been determined based on Equation 11 with regression approach. The empirical constant A for IFO-120 with $DOR \leq 1:100$ is $A = 5$ which is significantly lower than the one for Oseberg Blend ($A = 15$, Johnsen et al., 2013). In the case of $DOR > 1:100$, the value of regressed constant is $A = 2.54$ for IFO-120 and $A = 8.7$ for Oseberg Blend. It indicates an about 45% of A values for both oils from $DOR \leq 1:100$ to $DOR > 1:100$.

The regressions of constant A for ANS with different DOR conditions are listed in Figure 23. A reduction of 45% of A values is observed for ANS from $DOR \leq 1:100$ to $DOR > 1:100$. It can be seen that the fitting situation for the regression of IFO-120 is better than which of ANS. Nevertheless, the trends of A with the change of DOR are consistent for IFO-120, ANS, and Oseberg Blend. Furthermore, the change of A values may be caused by the significant reduction of IFT. For the Oseberg Blend, when the DOR changed from 0 to 1:100 to 1:25, the corresponding IFTs were reduced from 15.5 to 0.5 to 0.09 mN/m (Johansen et al., 2013). However, the change of IFTs measured in the COOGER's experiments are from 46.78 (mN/m) to 56.97 (DOR=1:100), and 49.09 (1:20), which are much less significant than which from Johansen et al., 2013. If similar magnitude of reduction as Johansen et al. (2013) is applied to IFO-120, the two fitted line could get much closer. Therefore, besides the oil properties, measured IFT played a significant role in determining the values of empirical constant A and it must be examined further.

Table 3: Data analyses for droplet size distribution of IFO-120

No.	Factors		Parameters								
	Oil	DOR	Q (L/min)	Viscosity (mPa·s)	d ₅₀ (μm)	dp (μm)	U (m/s)	IFT (mN/m)	We	Vi	Re
1	IFO-120	0	1.8063	44	230	259	5.6	46.78	1.55×10 ³	5.27	293.5
1R	IFO-120	0									
2	IFO-120	1:250	1.7729	45	197.3	259	6.6	57.84	1.74×10 ³	5.14	338.0
2R	IFO-120	1:200	1.849	45	293.510	293	6.887	57.84	1.89×10 ³	5.36	352.556
3	IFO-120	1:100	1.8999	42	223.1	259	7.1	56.97	2.02×10 ³	5.22	388.1
4*	IFO-120	1:25	1.2373	40	122.2	186	4.6	49.09	9.96×10 ²	3.75	265.4
4R	IFO-120	1:20	1.365	40	195.310	462	5.058	49.09	1.21×10 ³	4.14	292.84
5	IFO-120	0	2.4435	44	176.6	259	9.1	46.78	4.08×10 ³	8.56	476.4
6R	IFO-120	1:200	1.676	45	312.310	319	6.241	57.84	1.55×10 ³	4.86	319.451
7R	IFO-120	1:100	1.86	42	341.750	462	6.927	56.97	1.94×10 ³	5.11	379.893
8	IFO-120	1:25	1.7672	40	98.9	128	6.6	49.09	2.02×10 ³	5.36	379
8R	IFO-120	1:20	1.513	40	177.920	293	5.634	49.09	1.49×10 ³	4.59	324.444
9	IFO-120	0	3.1941	44	100.4	186	11.9	46.78	6.97×10 ³	11.19	622.7

10R	IFO-120	1:200	1.723	45	408.290	462	6.417	57.84	1.64×10 ³	4.99	328.489
11R	IFO-120	1:100	N/A	42	370.340	462	N/A	56.97	N/A	N/A	N/A
12	IFO-120	1:25	2.4511	40	93.8	128	9.1	49.09	3.91×10 ³	7.44	525.7
12R	IFO-120	1:20	1.415	40	211.340	293	5.27	49.09	1.3×10 ³	4.29	303.449
13*	IFO-120	0	2.281	44	263.3	391	8.5	46.78	3.13×10 ³	7.89	444.7
14	IFO-120	1:200	2.1684	45	230.2	259	8.1	57.84	2.29×10 ³	6.28	413.4
15	IFO-120	1:100	2.613	42	215.2	259	9.7	56.97	3.37×10 ³	7.17	533.7
16	IFO-120	1:20	2.8059	40	82.8	88.2	10.5	49.09	4.51×10 ³	8.52	601.8
17	IFO-120	0	2.2795	44	192.7	293	8.5	46.78	3.13×10 ³	7.99	444.5
18*	IFO-120	1:200	2.5788	45	224	462	9.6	57.84	3.24×10 ³	7.47	491.6
19	IFO-120	1:100	3.1426	42	179.8	259	11.7	56.97	4.88×10 ³	8.63	641.9
20	IFO-120	1:20	3.0697	40	69.38	74.7	11.4	49.09	5.40×10 ³	9.32	658.4
21*	IFO-120	0	2.3596	44	254.6	391	8.8	46.78	3.35×10 ³	8.27	460.1
22*	IFO-120	1:200	2.8236	45	245.9	293	10.5	57.84	3.88×10 ³	8.18	538.3
23	IFO-120	1:100	3.1319	42	167.8	219	11.7	56.97	4.85×10 ³	8.60	639.7
24	IFO-120	1:20	3.3753	40	52.6	63.3	12.6	49.09	6.53×10 ³	10.24	723.9

Table 4: Data analyses for droplet size distribution of ANS

No.	Factors		Parameters								
	Oil	DOR	Q (L/min)	Viscosity (mPa·s)	d ₅₀ (μm)	dp (μm)	U (m/s)	IFT (mN/m)	We	Vi	Re
1	ANS	0	3.617	7.2	81.9	88.2	13.471	63.97	5.84×10 ³	1.52	3852.38
2*	ANS	1:250	3.895	8.2	398.780	462	14.507	60.52	7.16×10 ³	1.97	3642.77
2R	ANS	1:200	4.041	8.2	65.750	74.7	15.051	60.52	7.71×10 ³	2.04	3779.38
3	ANS	1:100	3.958	8.3	56.875	74.7	14.740	55.94	8.00×10 ³	2.19	3656.72
4*	ANS	1:25	3.937	7.6	9.534	10.2	14.663	42.07	1.08×10 ³	2.64	3972.47
4R	ANS	1:20	3.995	7.6	2.340	12.1	14.880	42.07	1.08×10 ⁴	2.69	4031.43
5	ANS	0	3.885	7.2	70.512	74.7	14.471	63.97	6.74×10 ³	1.63	4138.34
6*	ANS	1:250	3.891	8.2	62.961	74.7	14.492	60.52	7.14×10 ³	1.96	3638.87
6R	ANS	1:200	4.66	8.2	64.140	74.7	17.357	60.52	1.02×10 ⁴	2.35	4358.32
7	ANS	1:100	3.844	8.3	55.487	74.7	14.316	55.94	7.54×10 ³	2.12	3551.38
8*	ANS	1:25	3.859	7.6	3.095	12.1	14.373	42.07	1.01×10 ⁴	2.6	3893.87
8R	ANS	1:20	4.134	7.6	2.739	12.1	15.398	42.07	1.16×10 ⁴	2.78	4171.8
9	ANS	0	3.915	7.2	68.131	88.2	14.580	63.97	6.84×10 ³	1.64	4169.46
10*	ANS	1:250	3.909	8.2	66.325	74.7	14.559	60.52	7.21×10 ³	1.97	3655.78
10R*	ANS	1:200	4.792	8.2	212.55	462	17.849	60.52	1.08×10 ⁴	2.42	4481.91

11	ANS	1:100	3.851	8.3	57.589	74.7	14.341	55.94	7.57×10 ³	2.13	355.76
12*	ANS	1:25	3.904	7.6	6.301	12.1	14.538	42.07	1.03×10 ⁴	2.63	3938.78
12R	ANS	1:20	4.144	7.6	6.570	12.1	15.321	42.07	1.15×10 ⁴	2.77	4150.74
13	ANS	0	4.225	7.2	88.870	104	15.735	63.97	7.97×10 ³	1.77	4499.9
14	ANS	1:200	4.107	8.2	64.661	74.7	15.295	60.52	7.96×10 ³	2.07	3840.5
15R	ANS	1:100	4.233	8.3	63.604	74.7	15.766	55.94	9.15×10 ³	2.34	3911.2
16	ANS	1:20	4.061	7.6	7.987	12.1	15.124	42.07	1.12×10 ⁴	2.73	4097.4
17	ANS	0	4.168	7.2	97.212	128	15.523	63.97	7.76×10 ³	1.75	4439.1
18	ANS	1:200	4.141	8.2	65.183	74.7	15.424	60.52	8.09×10 ³	2.09	3873
19	ANS	1:100	3.942	8.3	59.305	63.3	14.683	55.94	7.94×10 ³	2.18	3642.6
20	ANS	1:20	4.029	7.6	6.999	12.1	15.005	42.07	1.1×10 ⁴	2.71	4065.1
21	ANS	0	4.133	7.2	101.396	128	15.393	63.97	7.63×10 ³	1.73	4402.1
22	ANS	1:200	3.920	8.2	63.747	74.7	14.600	60.52	7.25×10 ³	1.98	3666.2
23	ANS	1:100	3.956	8.3	57.583	63.3	14.735	55.94	7.99×10 ³	2.19	3655.4
24	ANS	1:20	3.976	7.6	8.391	12.1	14.808	42.07	1.07×10 ⁴	2.68	4011.8

*Note: * mark means these data were not considered in the prediction of droplet size distribution due to incomplete measured distribution.*

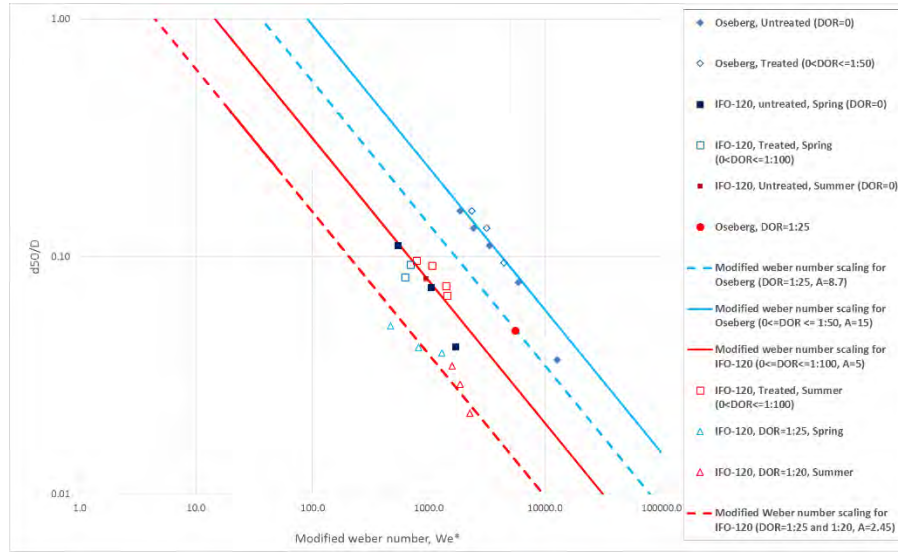


Figure 22: Data regression for constant A from modified Weber number and d_{50}/D for IFO-120

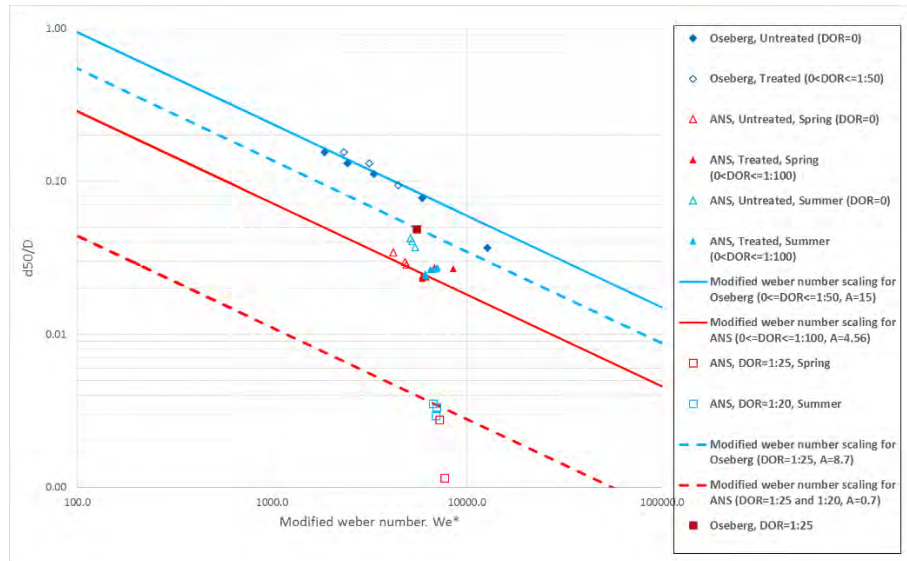


Figure 23: Data regression for constant A from modified Weber number and d_{50}/D for ANS

3.4 IFT and Reynolds Number Scaling

Due fact that the effects of oil/dispersant in water concentration affects IFT and in situ sampling may be impractical, as suggested by Johansen et al. (2013), some method for prediction of IFT related to a given DOR will be useful. IFT measurements with a variety of oils premixed with different dosages of dispersants might help to establish such relationships in more general terms. As demonstrated by MacKay and Hossain (1982), with same amount of oil and dispersant, the water volume affects the IFT significantly. In the direct sampling methods, the amount of oil/dispersant in 1L of sample from different experiments could vary significantly and therefore affects the IFT measurements. For example for Murban oil with DOR=1:1333, the IFT was 3.7 and 7.9 (mN/m) for 100 and 800 mL of water, respectively. Brandvik et al. (2013) provide a more advantage method for more consistent IFT measurement compared with the direct sampling methods. In this method, oil/water samples were collected at 1.5 m height above the nozzle in 1 L long necked measuring flask. Oil appeared as droplets in the water with size distribution depending on the DOR and method of dispersant application. The surface oil layer in the narrow neck of the bottle and was collected for IFT measurements after 24 h. using spinning drop method as described by Khelifa and So (2009), the Dataphysics Spinning Drop Tensiometer SVT-20N with control and calculation software SVTS 20 IFT was used. The IFT in this study were measured using a different method by premix 10 mg oil-dispersant in 100 mL seawater.

Before such a relationship is establish, we believe that the use of IFT should be avoided and the use of Modified Weber number approach should be re-considered. Wang and Calabrese (1986) have found that droplet breakup was governed by the Weber number scaling for small viscosity numbers ($Vi \rightarrow 0$), but that a Reynolds number scaling would apply for large viscosity number ($Vi \gg 1$):

$$(d_{50}/D) = C(Re)^{-3/4} \quad (13)$$

where $C = A^{5/4}B^{3/4}$, and the Re is the Reynolds number given by

$$Re = \frac{\rho U D}{\mu} \quad (14)$$

where ρ is the density of oil, U is the exit velocity, D is the nozzle diameter, and μ is the dynamic viscosity. Using of Reynolds scaling instead of modified Weber number scaling have the apparent advantage of avoiding the inconsistency IFT measurements and can make comparison of data from different sources easier.

The application of this concept for existing experimental data has been shown in Figure 24. The calculated and observed d_{50}/D correlates very well. In addition, the volume median diameters for IFO-120 are plotted against Reynolds number in Figure 25 together with data for Oseberg Blend by Brandvik et al. (2013). It can be seen from the plot that Reynolds scaling fits the data well. Values of empirical constants A were obtained for all IFO-120 combined (exclude DOR=1:25 (or 20)) and Oseberg Blend through regression analysis. A was 6.1 for combined data while the A for Oseberg Blend is 16.8. The data has shown that with the d_{50}/D is slightly bigger (higher A) for summer condition cases than winter condition cases

with same Reynolds number (Figure 25). The cases for ANS show quite difference compared with IFO-120 cases. The $DOR=0$ and $\leq 1:100$ experimental data points are more closed to Oseberg Blend data, the A for combined data of ANS (excluded $DOR=1:25$ (or 20)) is 10.5 (Figure 26). It is unclear if this is associated with uncertainties due to limited experimental data points or it is actually due to the effects of different water temperature. With more experimental data available, this observation will be revisited. Without considering the effects of temperature, the difference in A between IFO-120 and Oseberg Blend are considered to be the effects of oil type.

Furthermore, A has been reduced from 16.8 to 8.7 (49% reduction) for Oseberg, from 6.1 to 3.21 (47% reduction) for IFO-120 and 10.5 to 1.75 (83% reduction) for ANS (Figures 24 and 25). This is reduction can be used to model the effects of chemical dispersant on droplet size. Based on the experimental data on the three oils, it is proposed that a constant value A could be selected for Reynolds number scaling depending on oil types for cases of $DOR \leq 1:100$. For DOR of 1:25, a 50% reduction of A may be used and a linear interpolation may be used to estimate A values for other DOR greater than 1:100 but less than 1:25 for Oseberg Blend and IFO-120. However, the change A values for ANS does not follow the linear relation. Data points of $DOR = 1:50$ for ANS is close to the one of $DOR = 1:100$ but relatively far from which of $DOR=1:25$ (or 20). This may be caused by the effects of oil type and further interpolations for the relation of DOR and A value for ANS will be needed in future study.

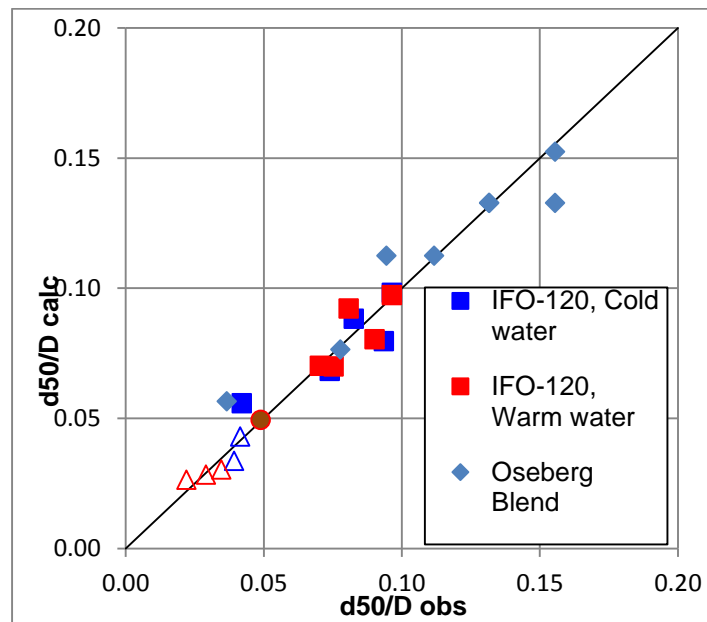


Figure 24: Measured (obs) and computed (calc) relative droplet sizes d_{50}/D from experiments with IFO-120 and Oseberg Blend

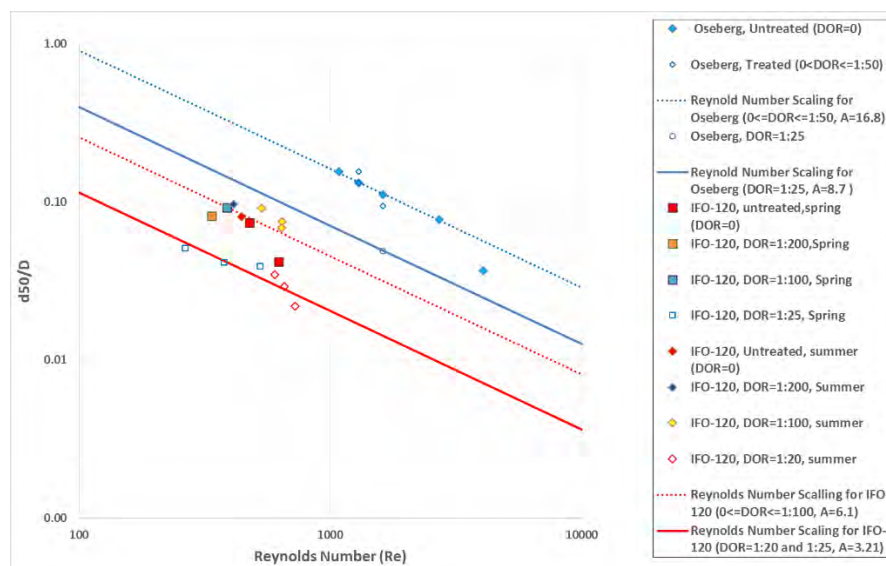


Figure 25: Data regression for constant A from Reynolds number and d_{50}/D for IFO-120

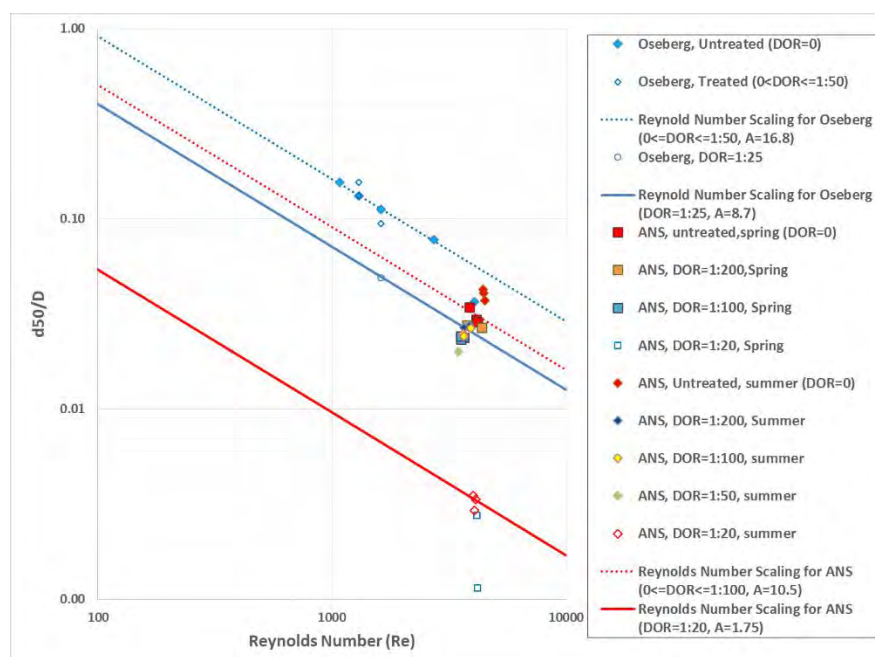


Figure 26: Data regression for constant A from Reynolds number and d_{50}/D for ANS

3.5 Determination of Distribution Shape using Two-Step Rosin-Rammler Method

The sections above described how to predict the characteristic diameter, d_{50} , for different types of oils (i.e., IFO-120 and ANS). Correspondingly, further prediction of the statistical distribution for the droplet sizes around the characteristic diameter will be conducted in this section. According to Lefebvre (1989),

two most commonly used distribution are lognormal and Rosin-Rammler distributions. Johansen et al. (2013) has also concluded that there is currently no theoretical basis for choosing the right distribution function and the choice of function must be based on empirical data.

Johansen et al. (2013) have found that Rosin-Rammler could provide better overall fit of the experiment data and they have derived a spreading coefficient $\alpha = 1.8$ for the corresponding distribution. In this study, Rosin-Rammler distribution was also selected and corresponding regression analysis has been conducted to calculate the best spreading coefficients (Tables 5 and 6).

The initial data analysis has indicated that the distributions of the data with $d/d_{50} \leq 1$ and $d/d_{50} > 1$ are significantly varied. Thus, it would be difficult and/or inaccurate to predict the measured IFO-120 and ANS data by only a single distribution.

In order to address this challenge, a two-step Rosin-Rammler approach was introduced by advancing from the Rosin-Rammler approach proved by Johansen et al. (2013). The proposed approach uses two separate spreading coefficients: α_1 for $d/d_{50} \leq 1$ and α_2 for $d/d_{50} > 1$, providing better fit of the data in all cases. The data distribution and the corresponding regression results are shown in Figures 27 to 42. Regressed based on the single Rosin-Rammler distribution, the overall spreading coefficient (α) for IFO-120 is 2.33 which is larger than that for Oseberg Blend (1.8). For ANS, $\alpha = 1.77$, is smaller than which for Oseberg Blend ($\alpha = 1.8$). According to the two-step Rosin-Rammler approach, the average α_1 for IFO-120 is 2.01 and α_2 is 2.74. In addition, the average α_1 for ANS is 1.78 and α_2 is 1.63. Furthermore, the regression coefficients (R^2) for the regressions based on single and two-step Rosin-Rammler distributions were also calculated for both IFO-120 and ANS under different DOR and seasonal conditions (Figures 27 to 42). The R^2 for two-step Rosin-Rammler are higher than which for the single one in most of the case, indicating the advantage of the proposed two-step Rosin-Rammler approach.

Table 5: Spreading coefficient for Rosin-Rammler distribution of IFO-120

			All Data			Average		
			Single	2-step		Single	2-step	
			α	α_1	α_2	α	α_1	α_2
Summer	Untreated	No.13*	/	/	/	1.86	1.53	2.20
		No.17	1.86	1.53	2.20			
		No.21*	/	/	/			
	1:20	No.16	1.75	2.13	1.44	1.72	2.04	1.37
		No.20	1.55	1.95	1.18			
		No.24	1.85	2.05	1.50			
	1:100	No.15	1.96	1.50	2.54			
		No.19	1.57	1.30	2.00			

		No.23	1.59	1.31	1.975	1.71	1.37	2.17
	1:200	No.14	2.39	1.85	3.10	2.39	1.85	3.10
		No.18*	/	/	/			
		No.22*	/	/	/			
Spring	Untreated	No.1*	/	/	/	1.60	1.41	1.89
		No.5	1.66	1.32	2.14			
		No.9	1.54	1.49	1.632			
	1:25	No.4	2.13	2.24	2.10	1.98	2.18	1.85
		No.8	2.05	2.31	1.83			
		No.12	1.77	1.99	1.62			
	1:100	No.3	2.61	1.98	3.31	2.61	1.98	3.31
		No.7R*	/	/	/			
		No.11R*	/	/	/			
	1:250	No.2	2.39	1.72	3.20	2.39	1.72	3.20
		No.6R*	/	/	/			
		No.10R*	/	/	/			
	Average					2.33	2.01	2.74

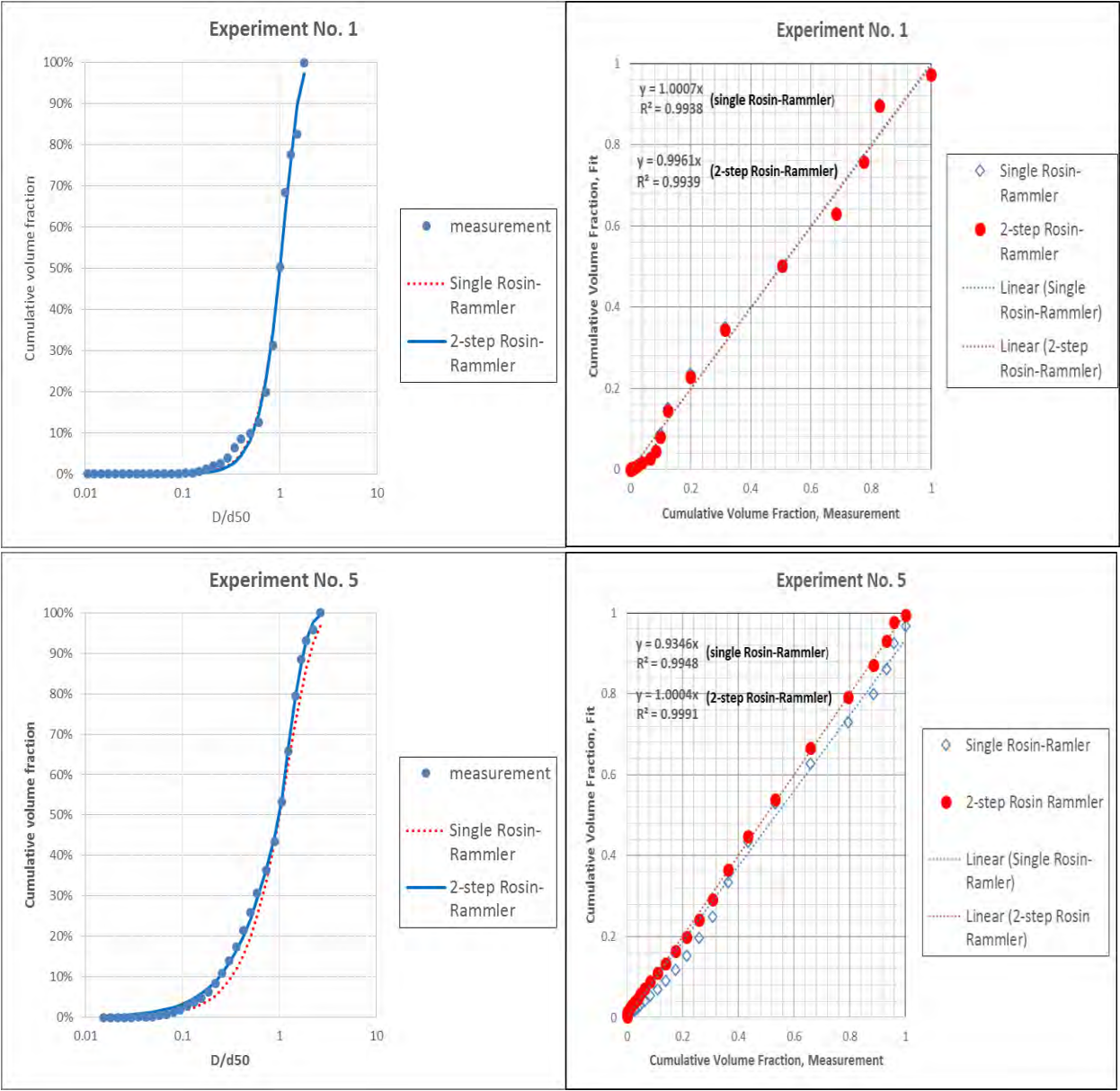
Note: “/” indicates that the data is unavailable due to incomplete droplet size distribution from measurement

Table 6: Spreading coefficient for Rosin-Rammler distribution of ANS

			All Data			Average		
			Single α	2-Step:		Single α	2-step	
			α	α_1	α_2	α	α_1	α_2
summer	Untreated	No. 13	1.93	2.32	1.57	1.90	2.30	1.55
		No. 17	1.87	2.29	1.51			
		No. 21	1.9	2.3	1.58			
	1:20	No. 16	1.12	0.62	1.39	1.14	0.64	1.41
		No. 20	1.12	0.61	1.34			
		No. 24	1.17	0.68	1.49			
	1:100	No. 15R	1.99	2.24	1.65			
		No. 19	2.05	2.24	1.67			

Spring	1:200	No. 23	2.03	2.20	1.66	2.02	2.23	1.66
		No. 14	1.96	2.26	1.49	2.02	2.27	1.57
		No. 18	2.03	2.29	1.61			
		No. 22	2.06	2.25	1.622			
	Untreated	No. 1	2.08	2.00	1.90	2.04	2.01	1.93
		No. 5*	/	/	/			
		No. 9	1.99	2.02	1.95			
	1:20	No. 4R*	/	/	/	0.98	0.49	1.10
		No. 8R*	/	/	/			
		No. 12R	0.98	0.49	1.10			
	1:100	No. 3	2.14	2.17	2.11	2.10	2.11	2.09
		No. 7	2.15	2.13	2.18			
		No. 11	2.00	2.03	1.97			
	1:200 (and 250)	No. 2R	1.87	2.11	1.50	2.01	2.19	1.73
		No. 6R	1.92	2.16	1.54			
		No. 10	2.23	2.30	2.15			
	Average					1.77	1.78	1.63

Note: "/" indicates that the data is unavailable due to incomplete droplet size distribution from measurement



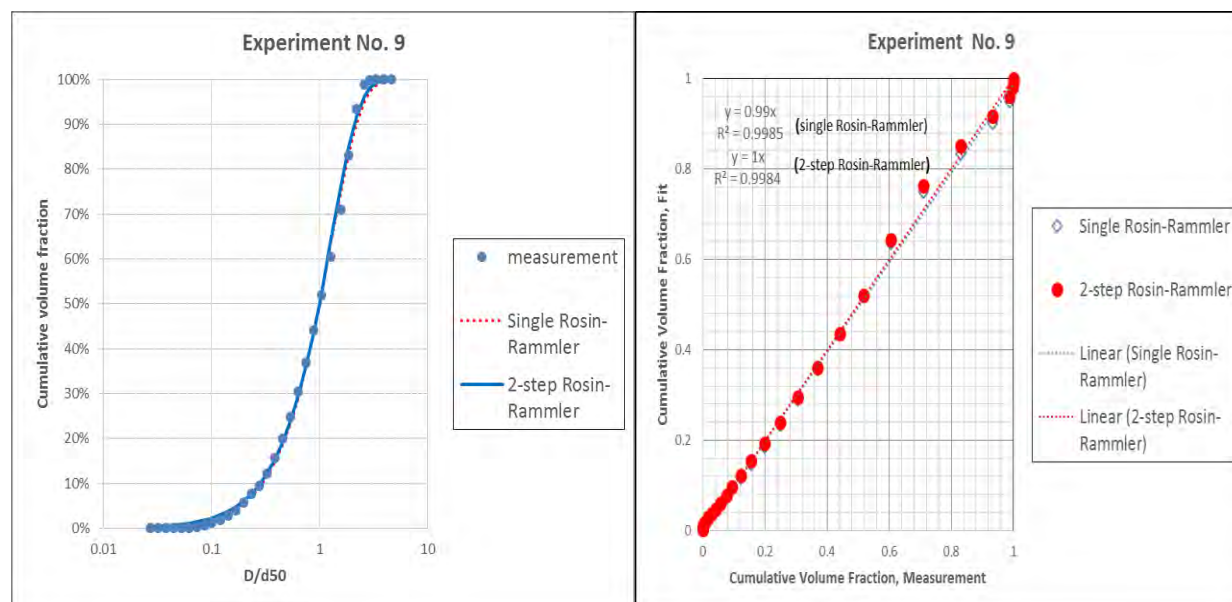


Figure 27: Cumulative distribution of d/d_{50} and regression results for IFO-120 with DOR = 0 in spring conditions

(Note: the left figures are distributions and the right ones are regression results)

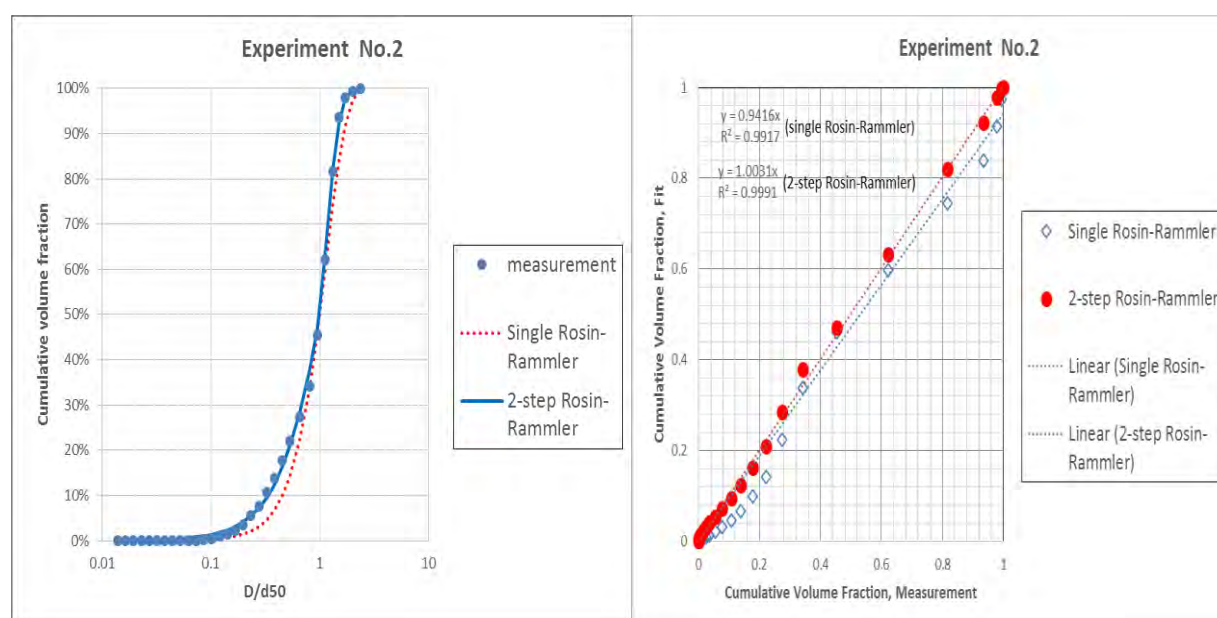


Figure 28: Cumulative distribution of d/d_{50} and regression results for IFO-120 with DOR = 1:250 in spring conditions

(Note: the left figures are distributions and the right ones are regression results)

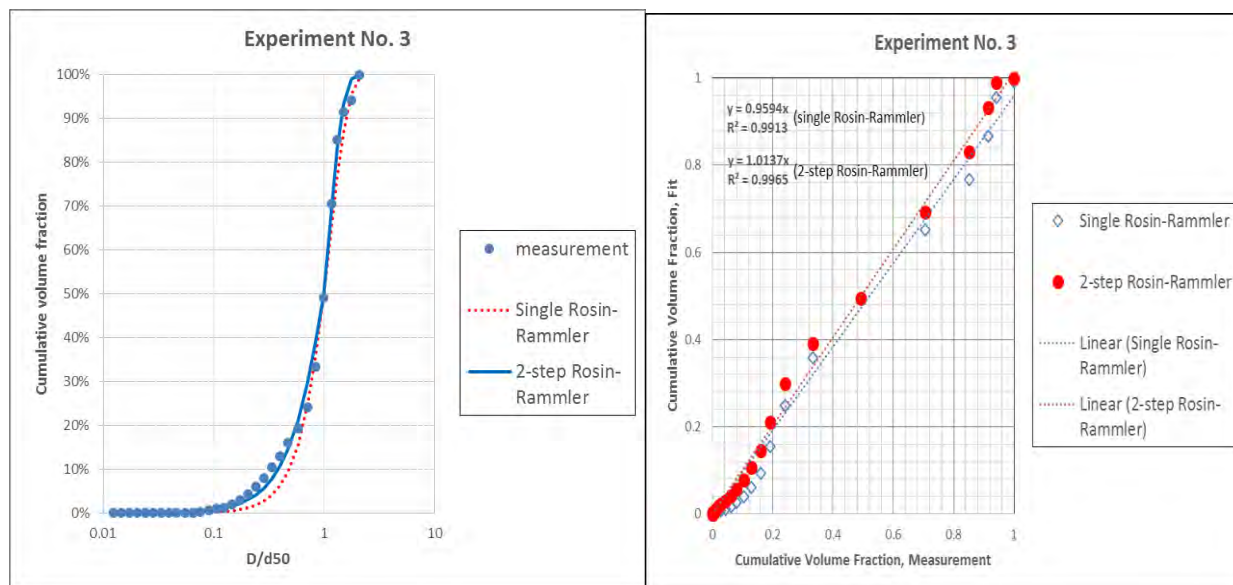
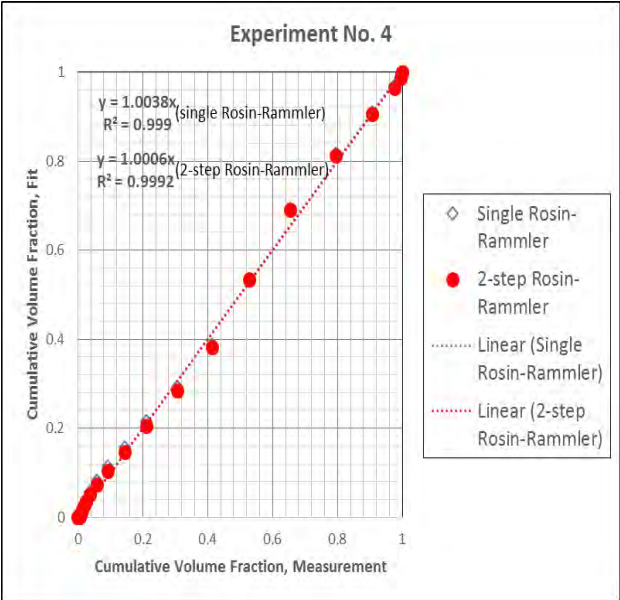
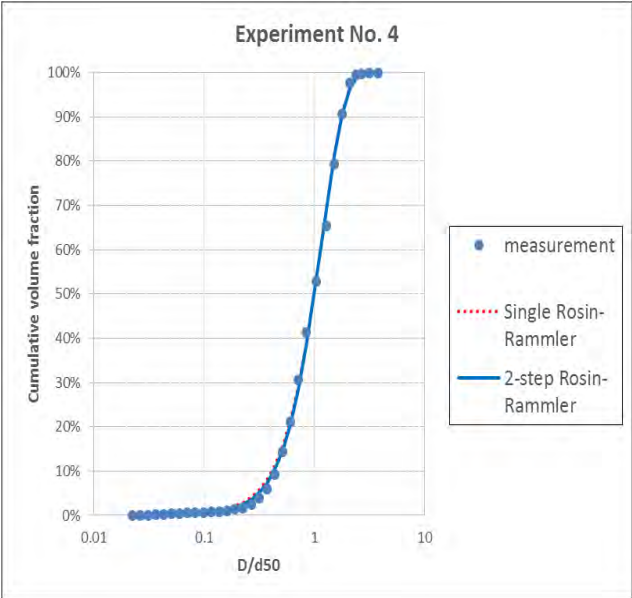
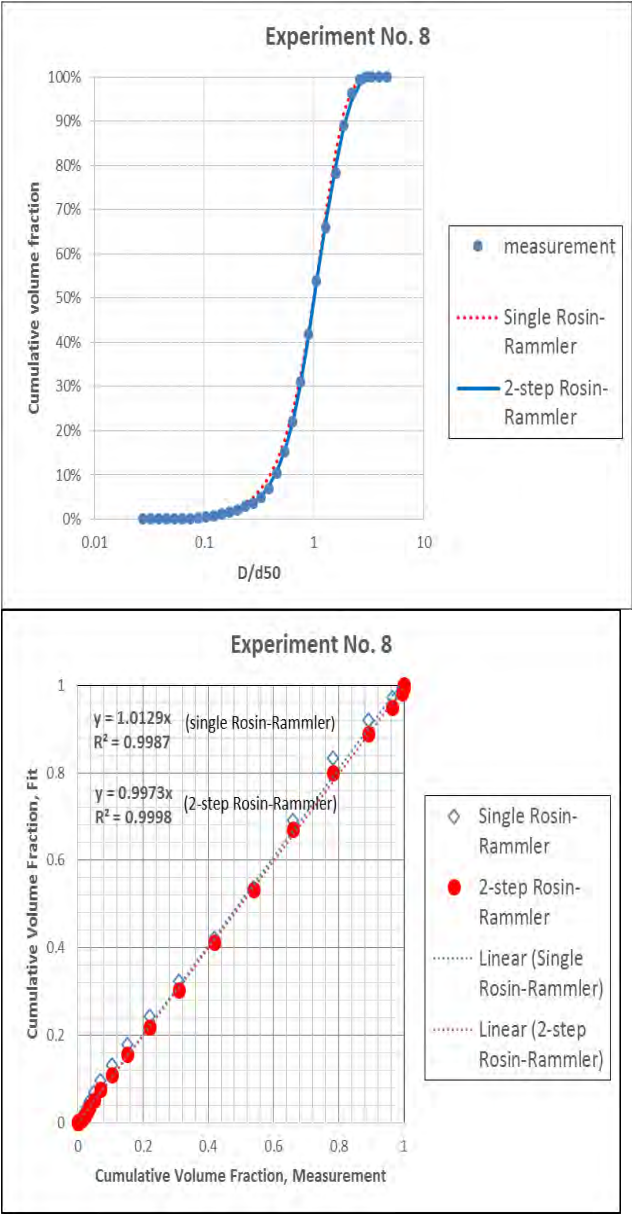


Figure 29: Cumulative distribution of d/d_{50} and regression results for IFO-120 with DOR = 1:100 in spring conditions

(Note: the left figures are distributions and the right ones are regression results)





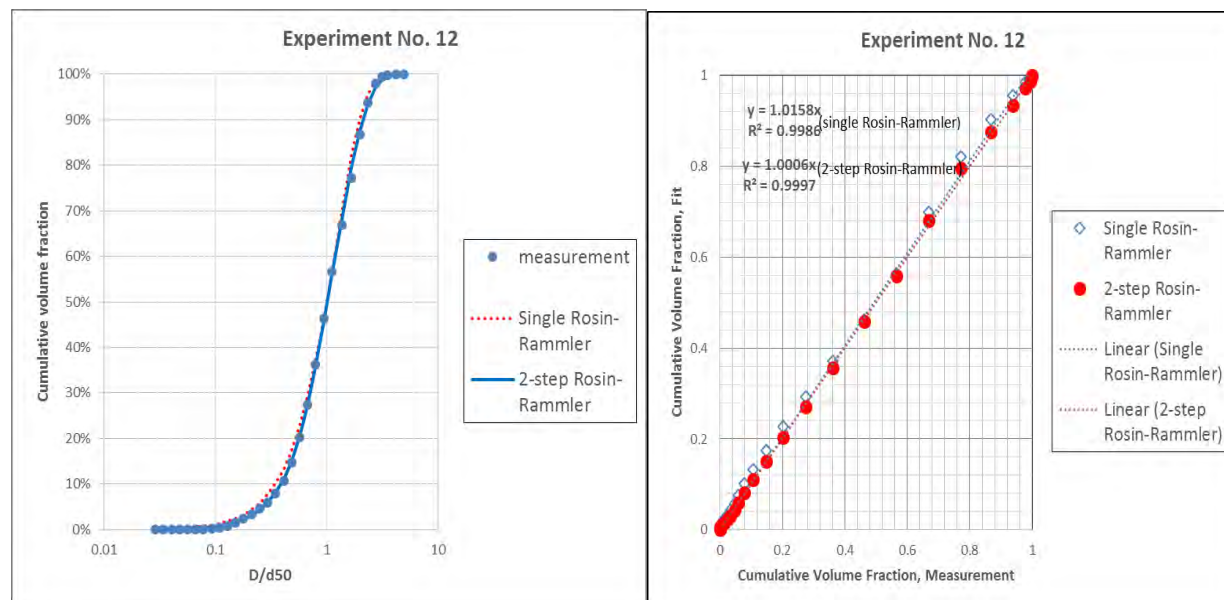


Figure 30: Cumulative distribution of d/d_{50} and regression results for IFO-120 with DOR = 1:25 in spring conditions

(Note: the left figures are distributions and the right ones are regression results)

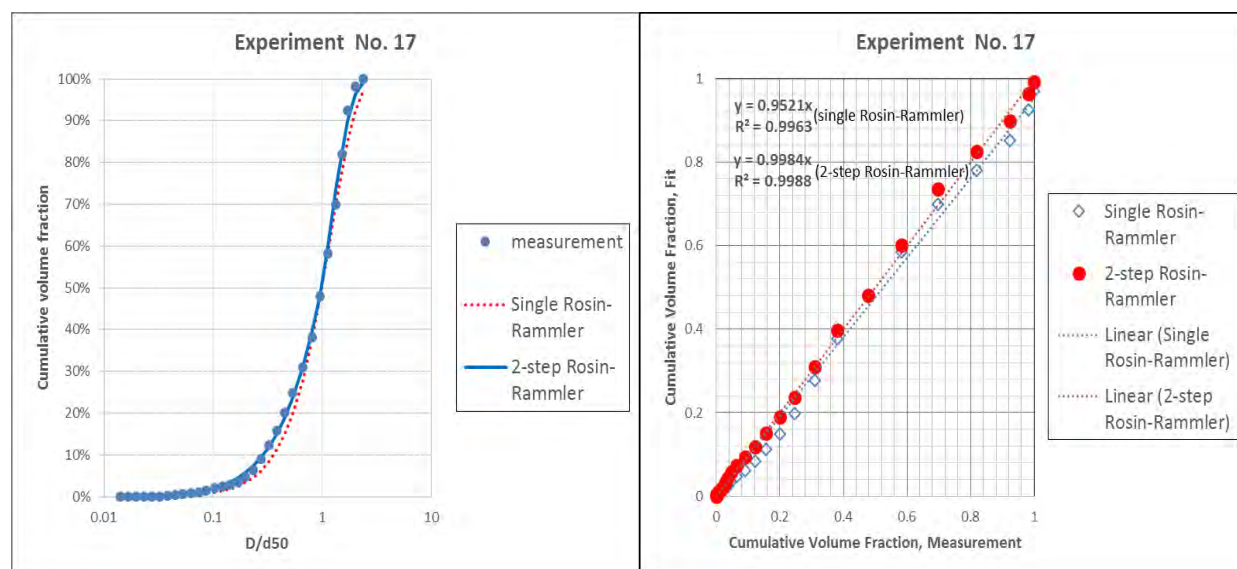


Figure 31: Cumulative distribution of d/d_{50} and regression results for IFO-120 with DOR = 0 in summer conditions

(Note: the left figures are distributions and the right ones are regression results)

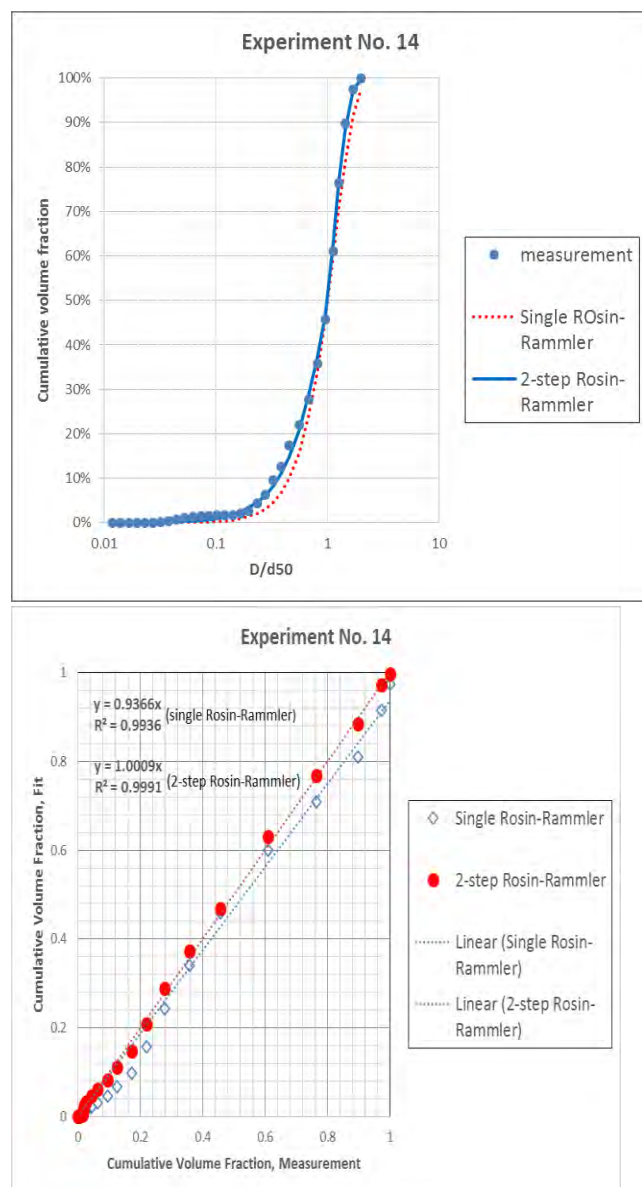
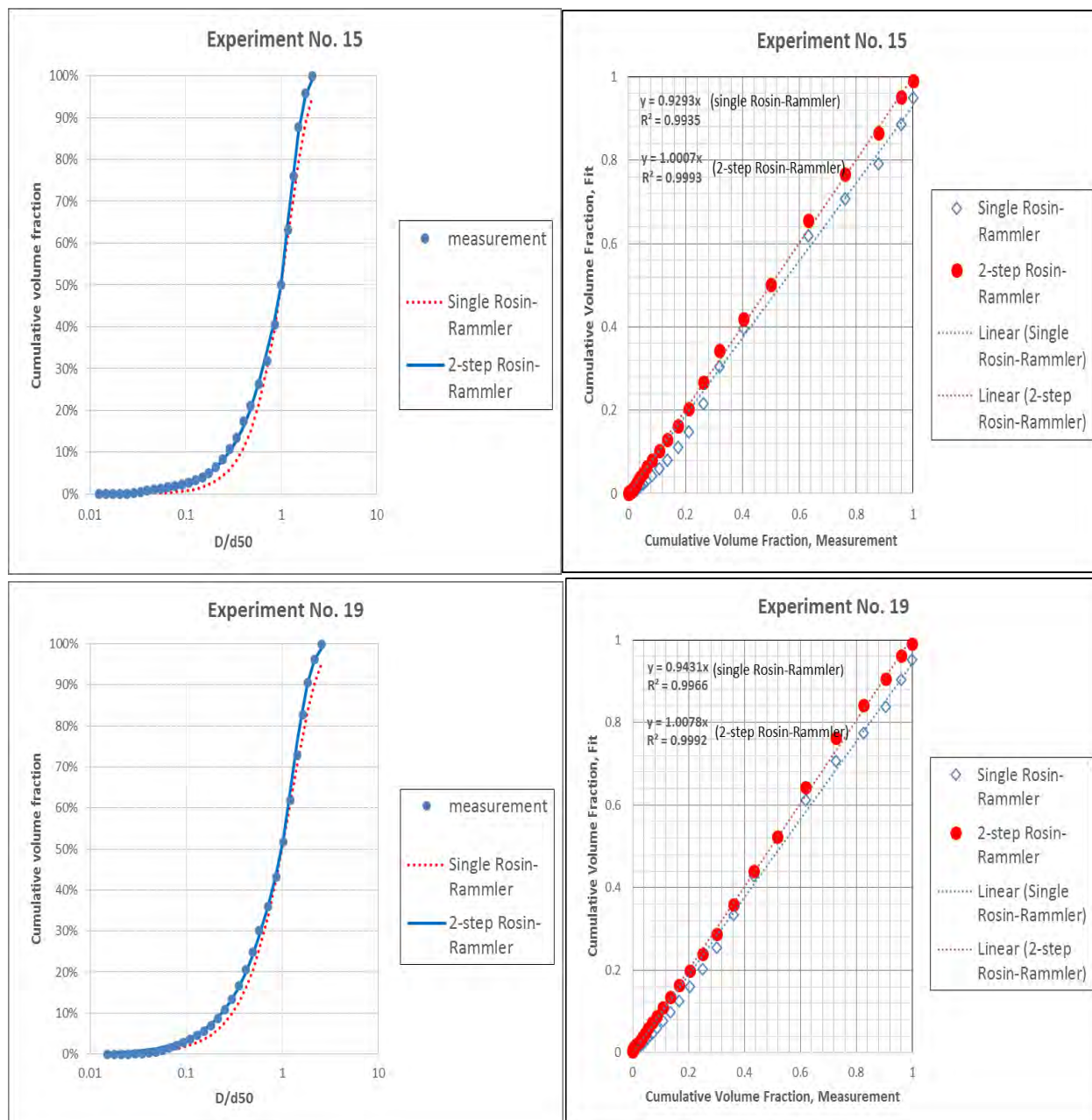


Figure 32: Cumulative distribution of d/d_{50} and regression results for IFO-120 with $DOR = 1.200$ in summer conditions

(Note: the left figures are distributions and the right ones are regression results)



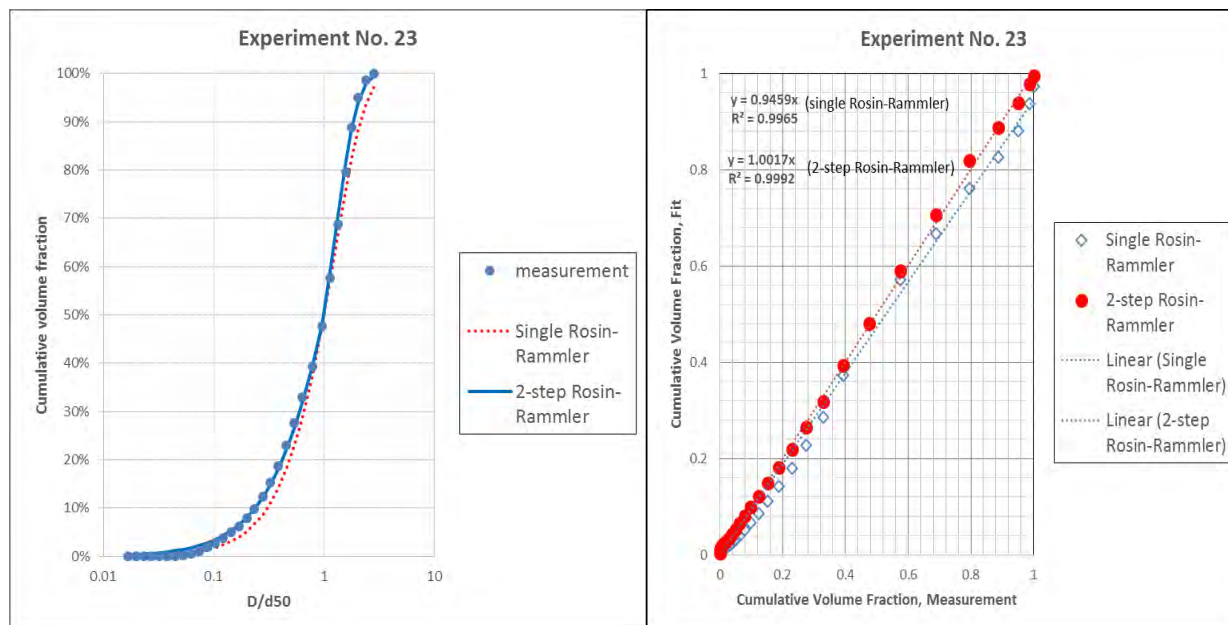
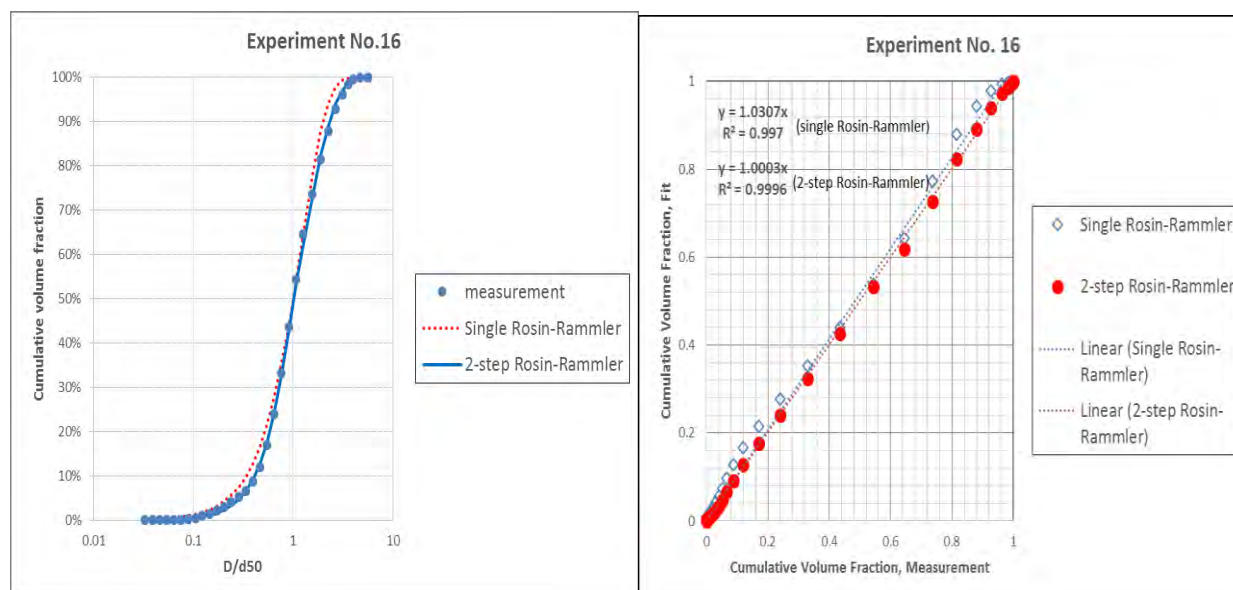


Figure 33: Cumulative distribution of d/d_{50} and regression results for IFO-120 with DOR =1: 100 in summer conditions

(Note: the left figures are distributions and the right ones are regression results)



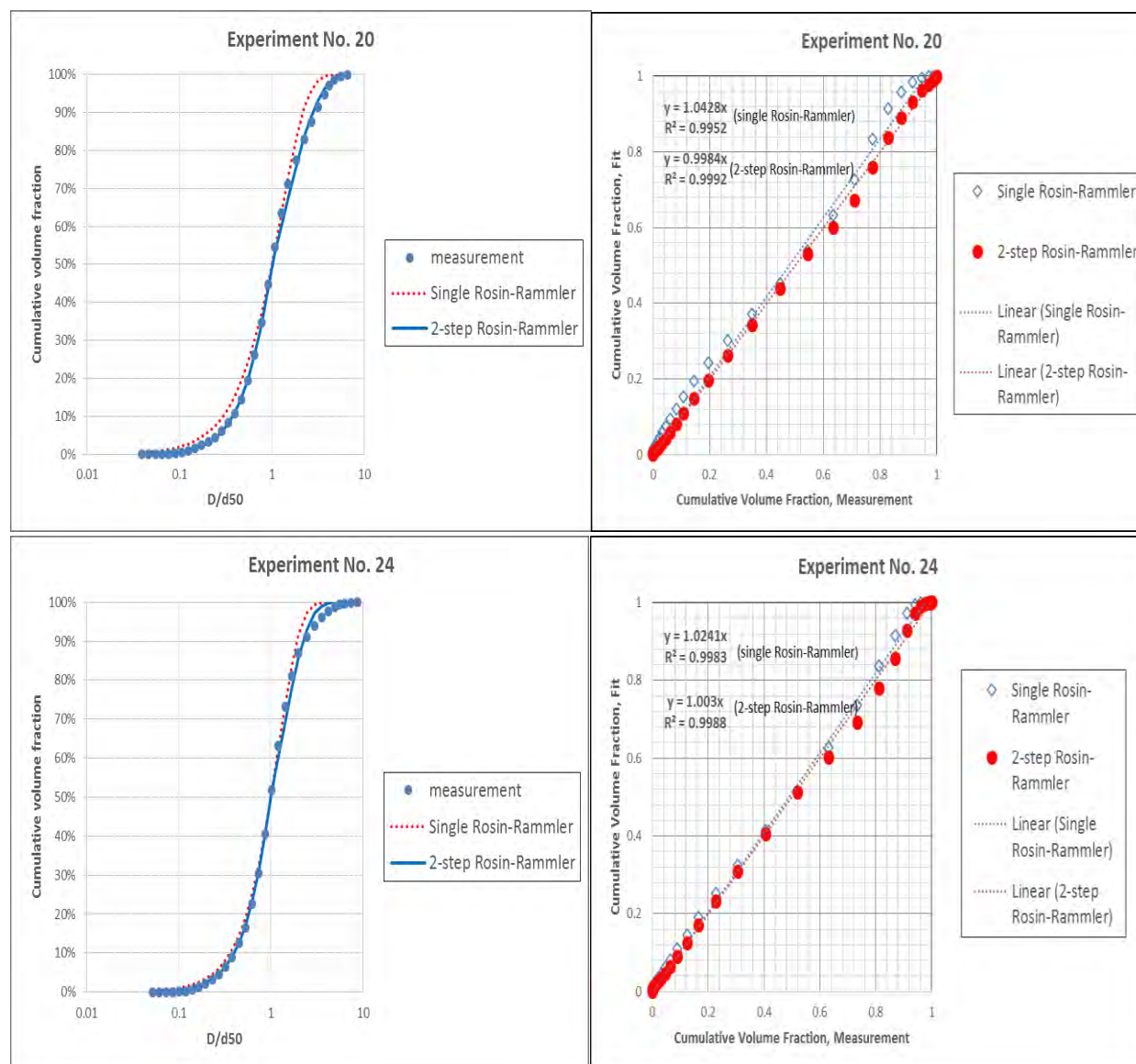


Figure 34: Cumulative distribution of d/d_{50} and regression results for IFO-120 with DOR = 1:20 in summer conditions

(Note: the left figures are distributions and the right ones are regression results)

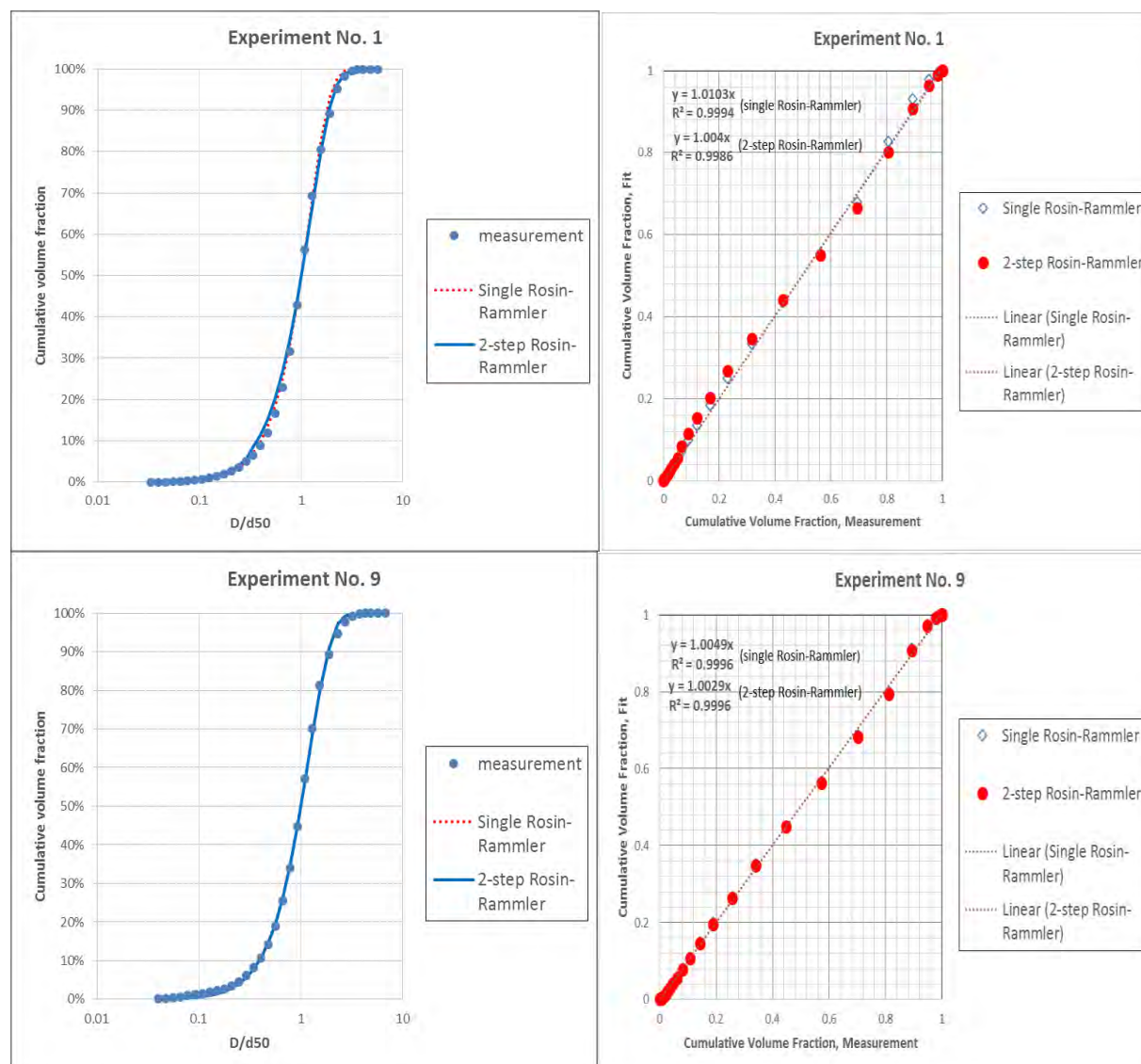
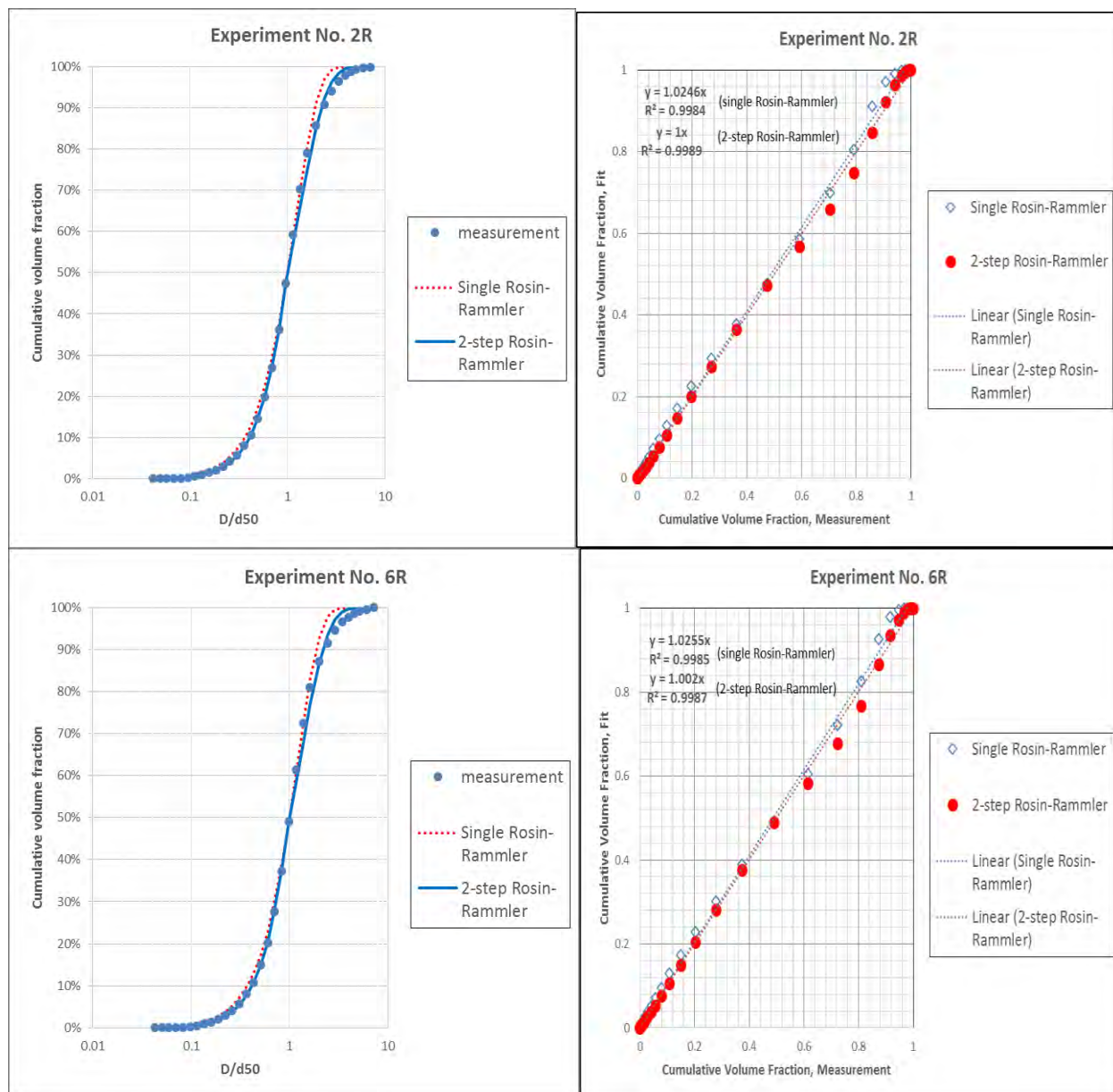


Figure 35: Cumulative distribution of d/d_{50} and regression results for ANS with DOR = 0 in spring conditions

(Note: the left figures are distributions and the right ones are regression results)



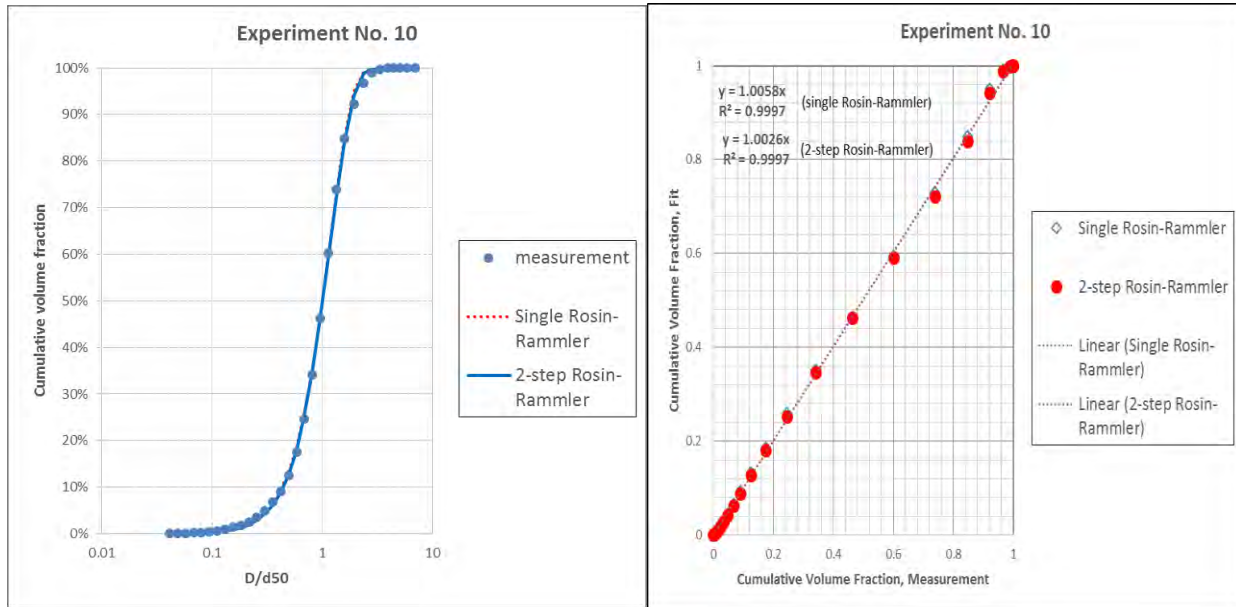
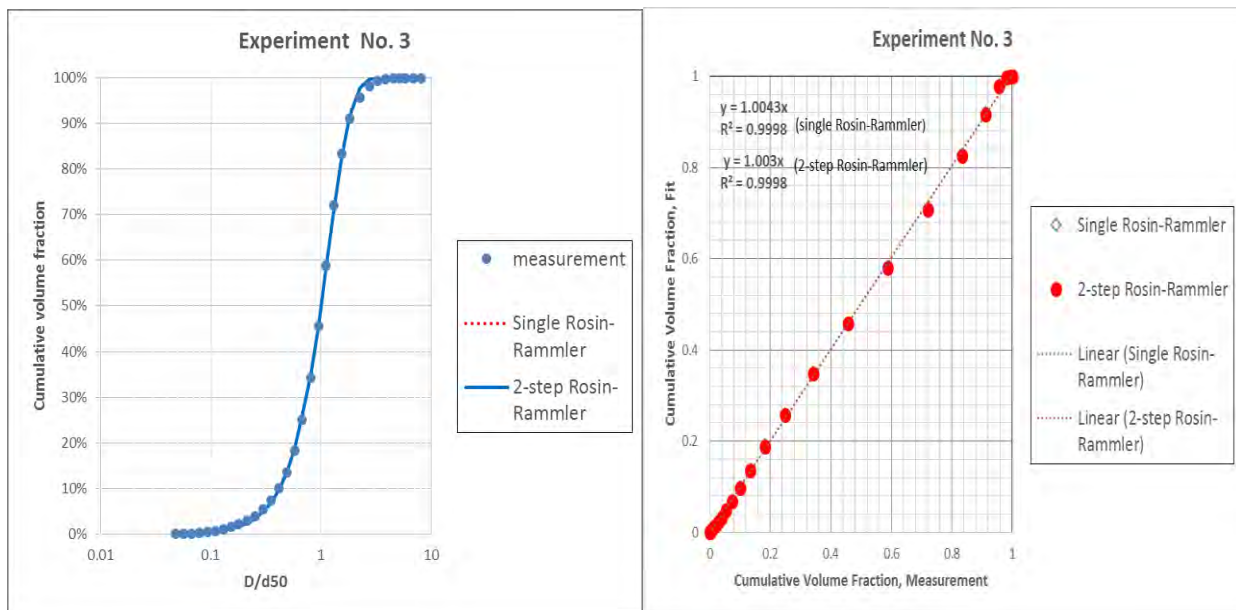


Figure 36: Cumulative distribution of d/d_{50} and regression results for ANS with DOR = 1:200 or (250) in spring conditions

(Note: the left figures are distributions and the right ones are regression results, Experiment No. 10 is DOR=1:250)



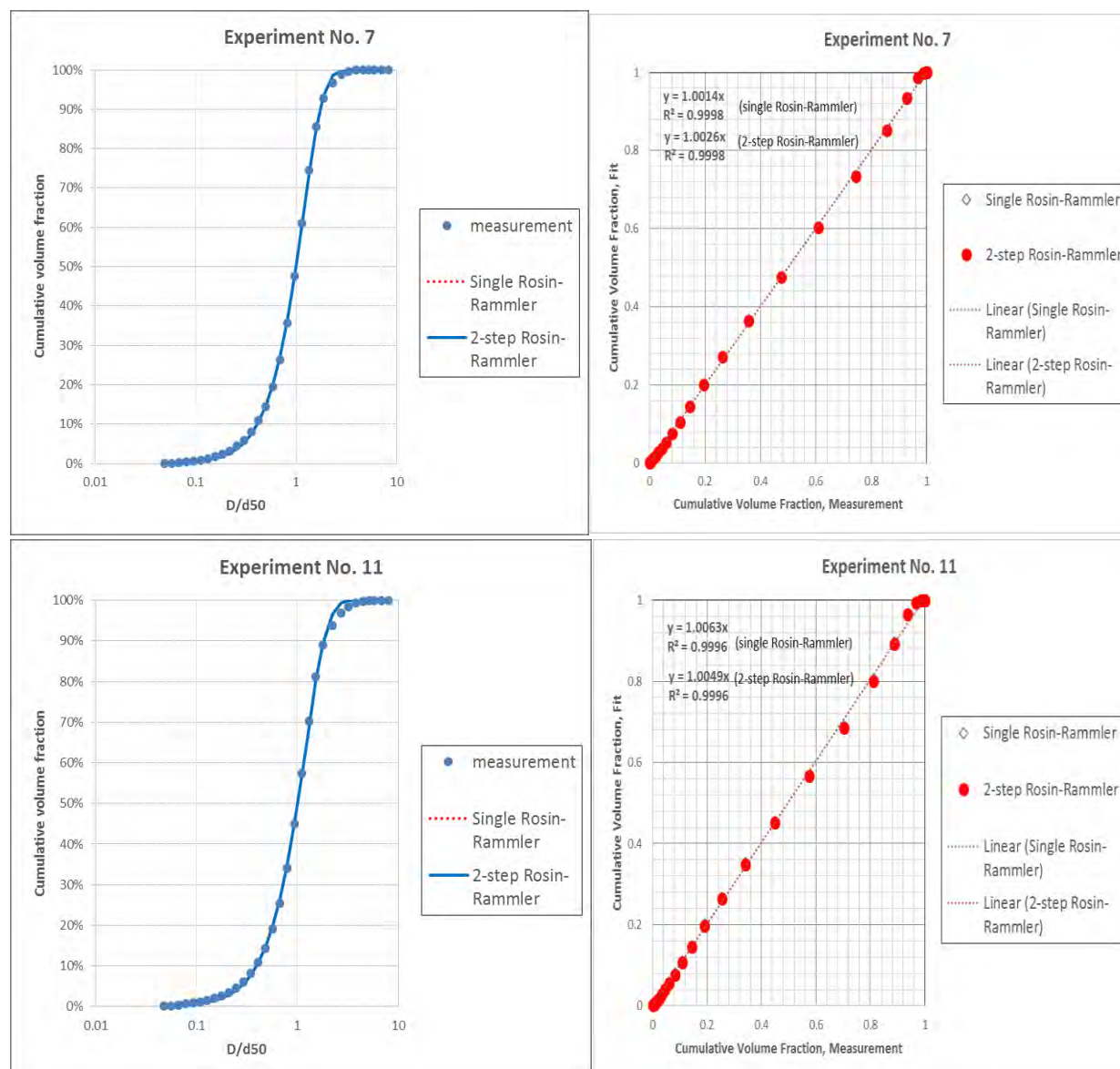


Figure 37: Cumulative distribution of d/d_{50} and regression results for ANS with DOR = 1:100 in spring conditions

(Note: the left figures are distributions and the right ones are regression results)

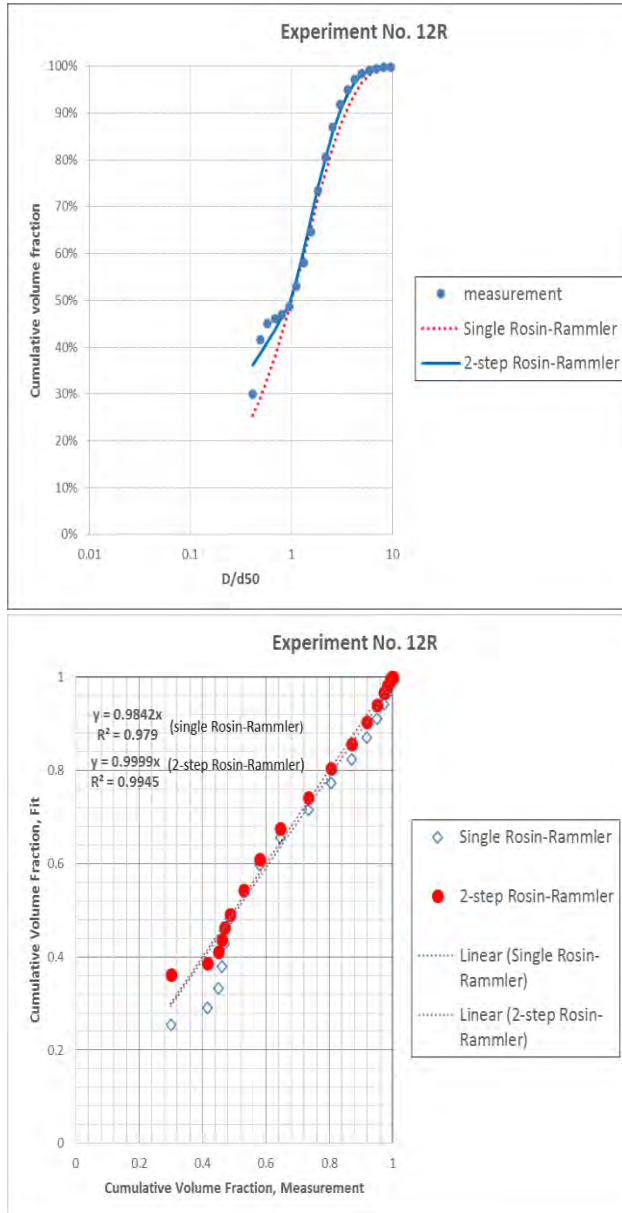
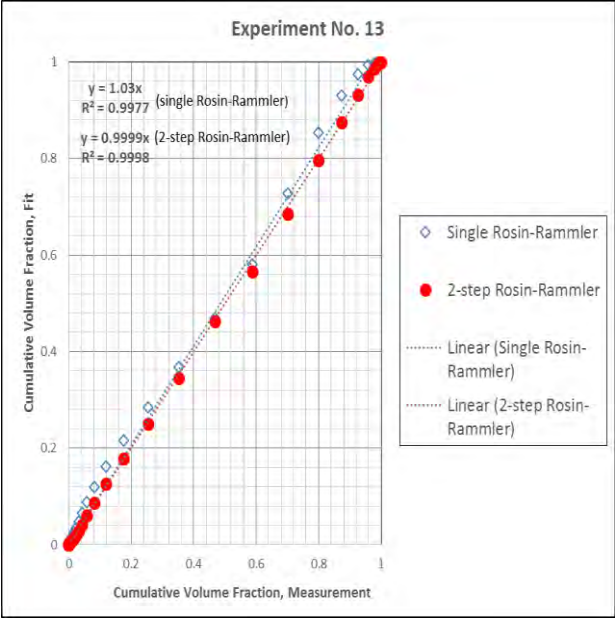
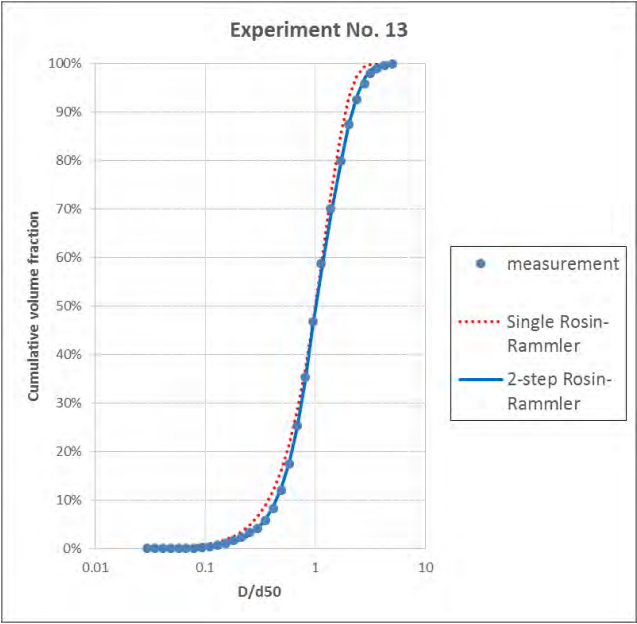


Figure 38: Cumulative distribution of d/d_{50} and regression results for ANS with DOR = 1:20 in spring conditions

(Note: the left figures are distributions and the right ones are regression results)



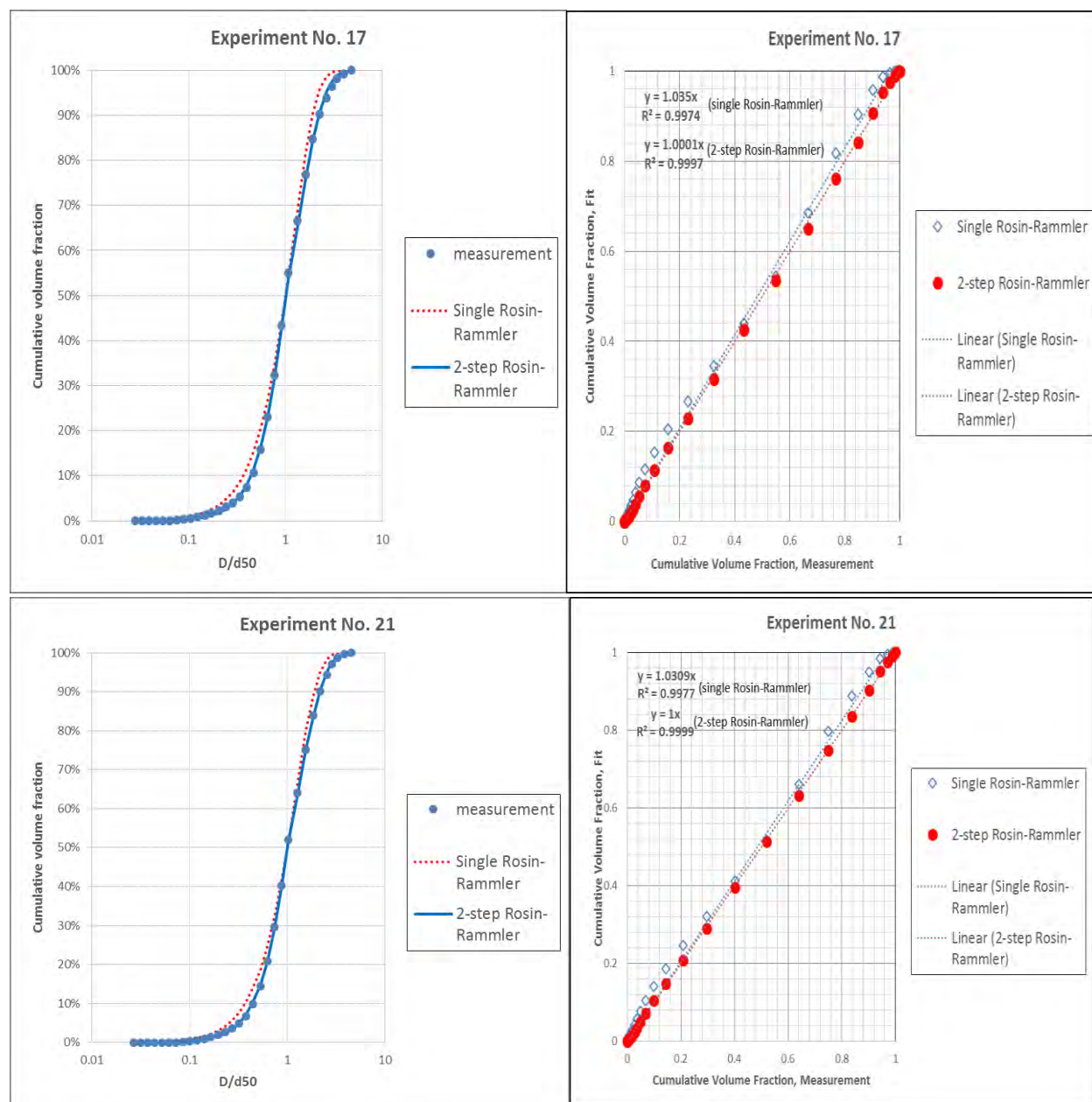
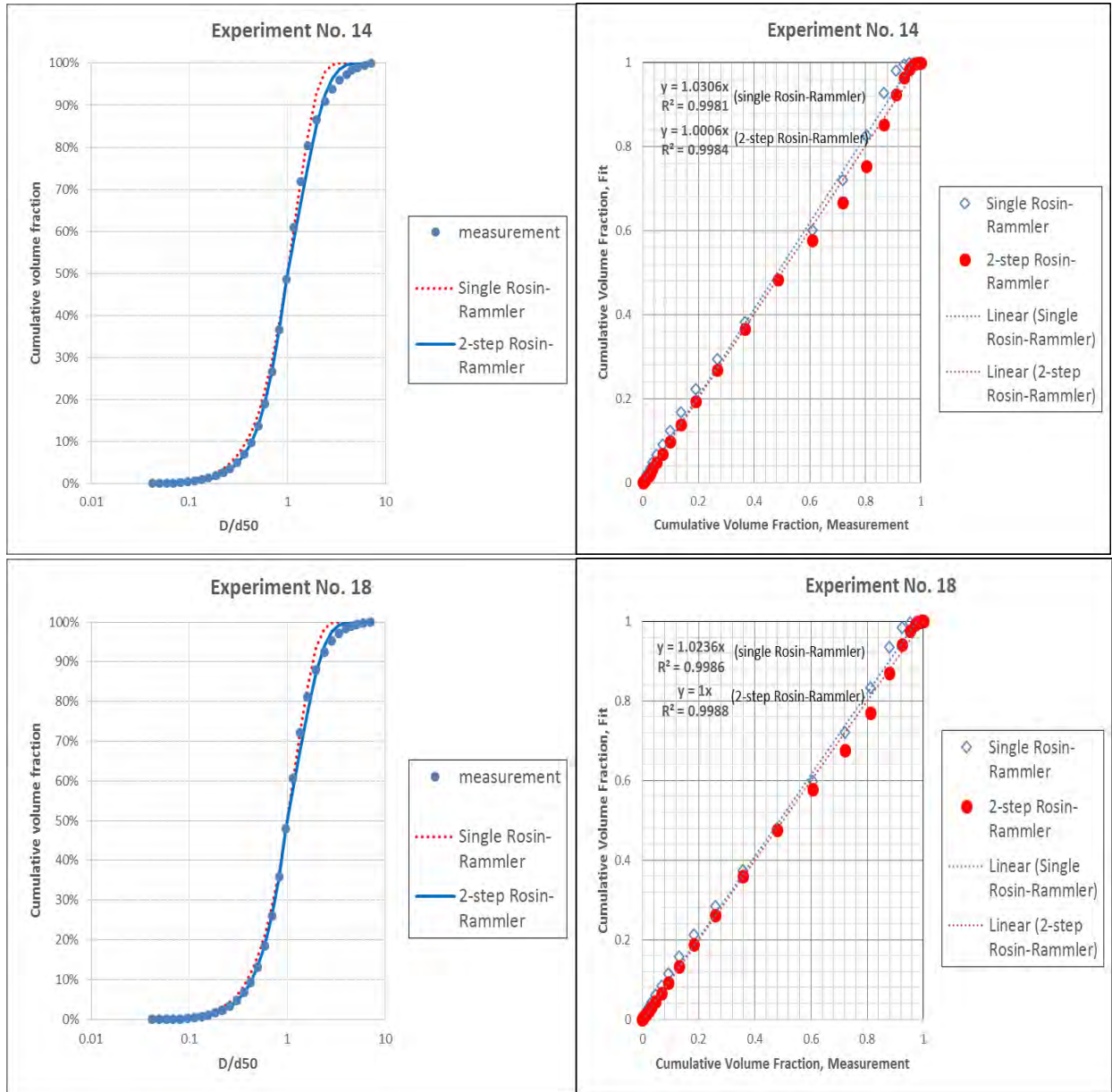


Figure 39: Cumulative distribution of d/d_{50} and regression results for ANS with DOR = 0 in summer conditions

(Note: the left figures are distributions and the right ones are regression results)



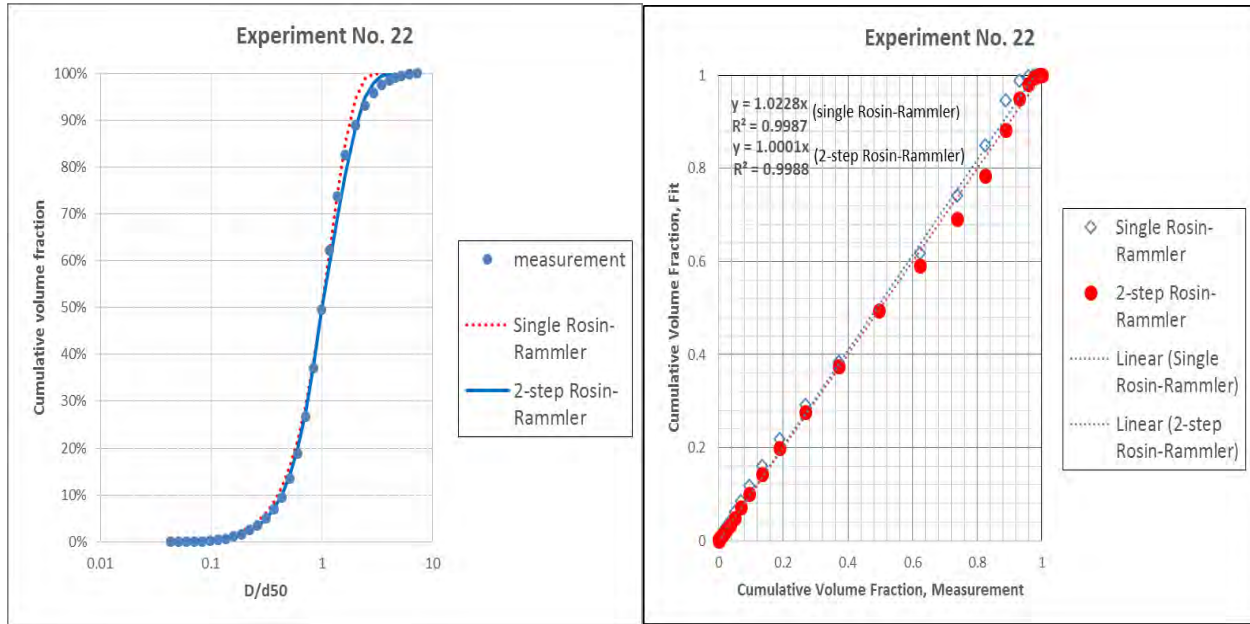
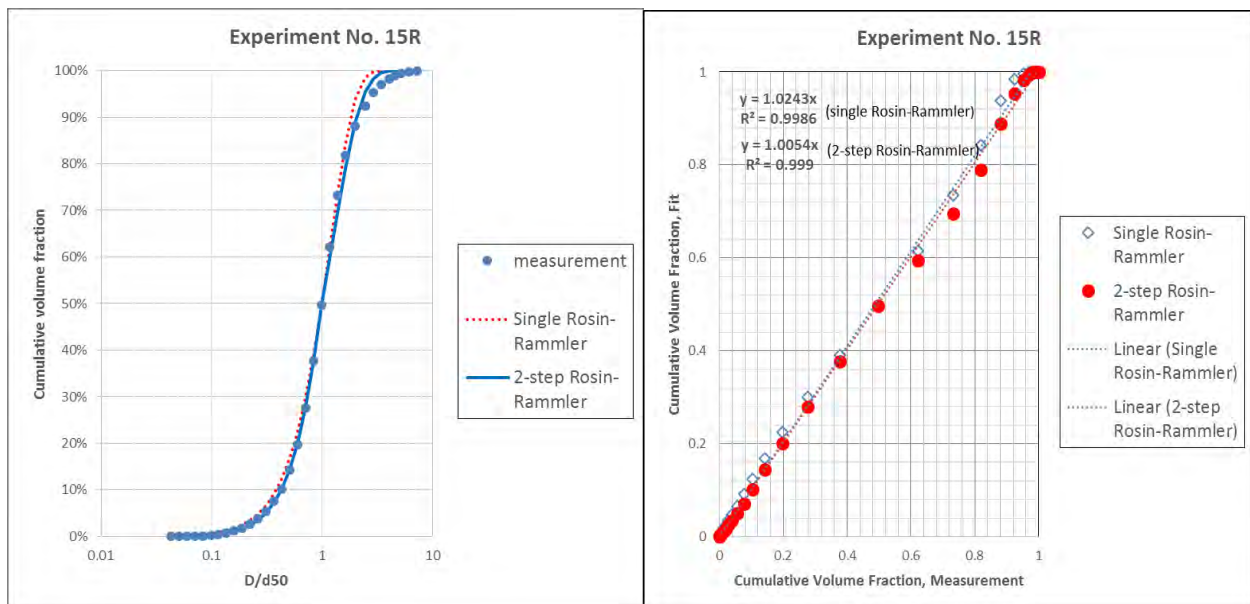
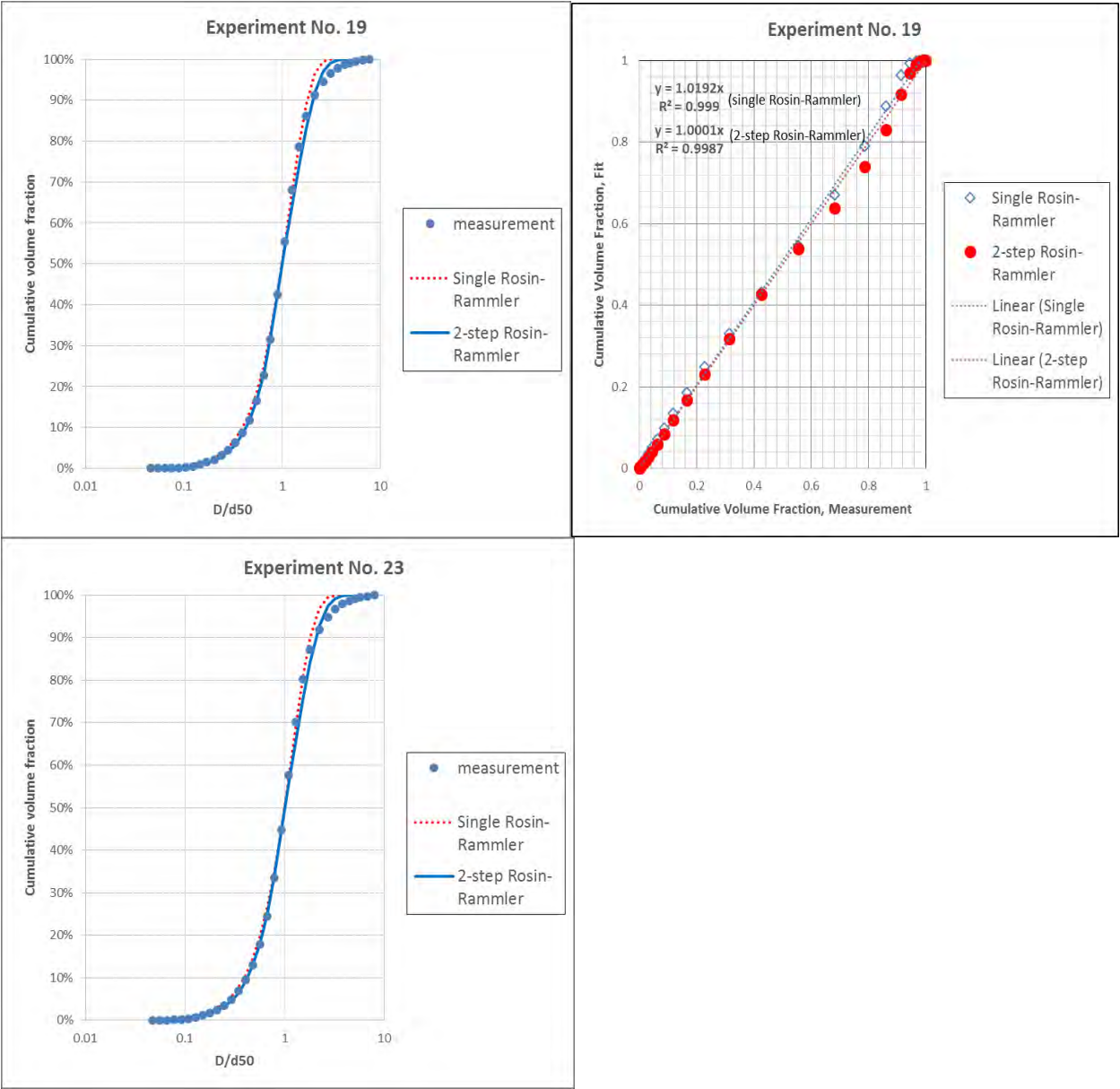


Figure 40: Cumulative distribution of d/d_{50} and regression results for ANS with DOR = 1:200 in summer conditions

(Note: the left figures are distributions and the right ones are regression results)





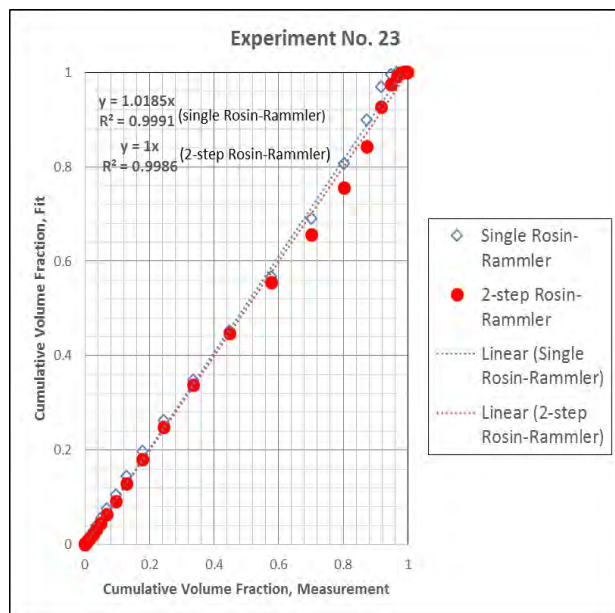
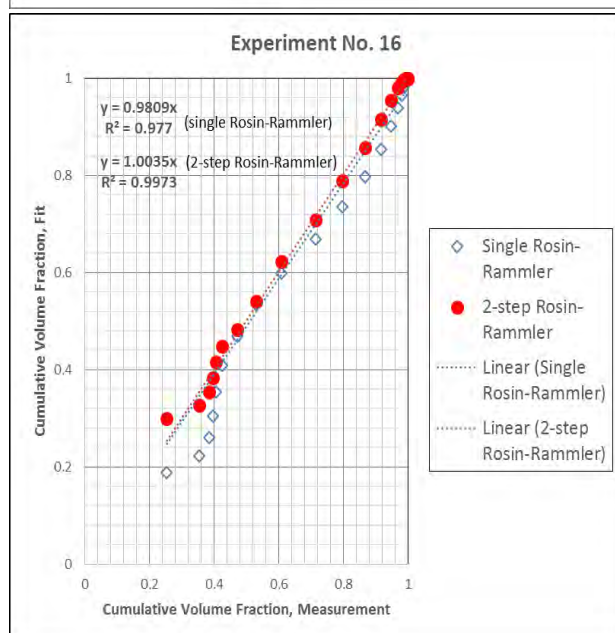
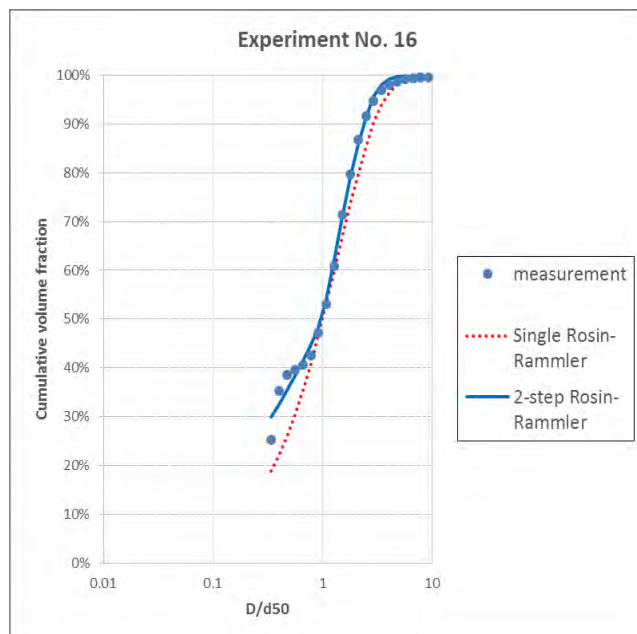
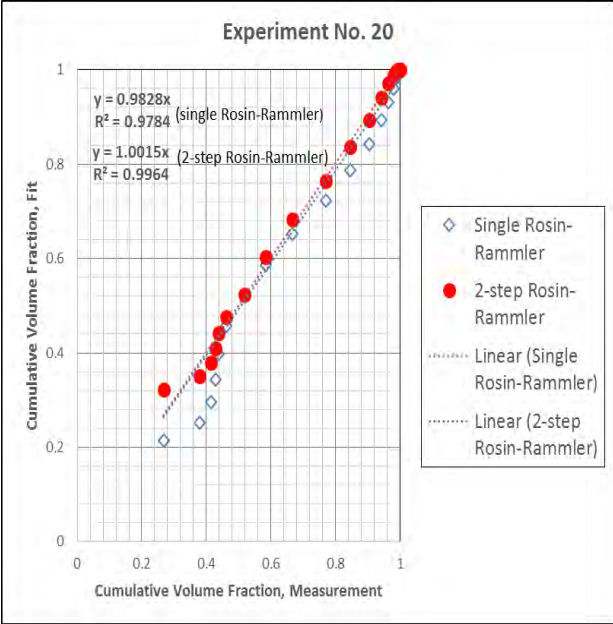
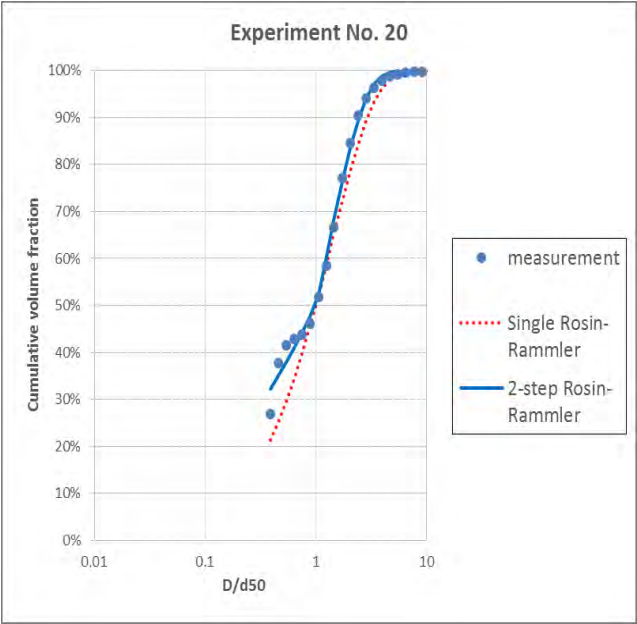


Figure 41: Cumulative distribution of d/d_{50} and regression results for ANS with DOR=1:100 in summer conditions

(Note: the left figures are distributions and the right ones are regression results)





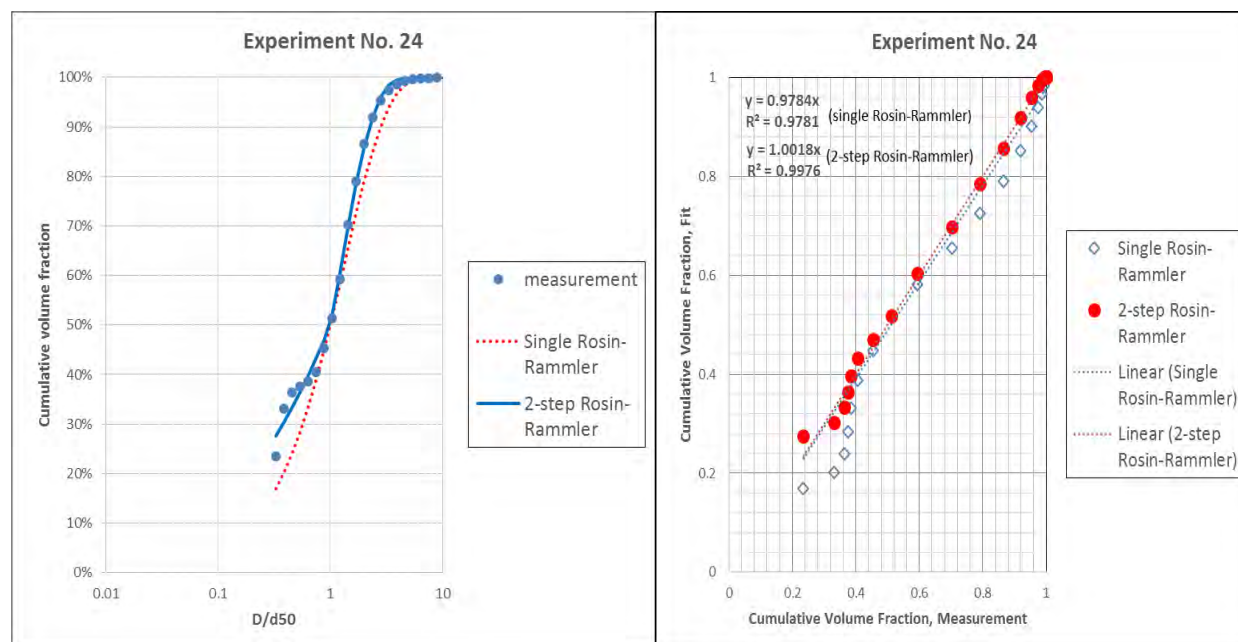


Figure 42: Cumulative distribution of d/d_{50} and regression results for ANS with DOR = 1:20 in summer conditions

(Note: the left figures are distributions and the right ones are regression results)

4 Summary

In this study, research has been conducted for the droplet size distributions of two types of oils (IFO-120 and ANS) release from subsurface injection with/without application of chemical dispersant in different seasonal conditions (i.e., spring and summer). Firstly, a series of experiments have been conducted via wave tank experiment by COOGER in BIO to measure the droplet sizes. These data were analyzed and utilized to determine the relative volume median diameter (d_{50}) and the peak diameter (d_p). Accordingly to the droplet size distribution and the modified Weber number approach, the Weber number (We), as well as the additional measurements on oil viscosity and IFT, the Viscosity number (Vi) and Reynold number (Re) were calculated. In addition, the relation between the droplet size distributions and dispersant-oil-ratios (DORs) has also been analyzed. Finally, the corresponding empirical coefficients have been determined for the droplet size prediction.

Furthermore, the data analysis has also indicated that the distributions of the data with $d/d_{50} \leq 1$ and $d/d_{50} > 1$ are significantly varied. Thus, it would be difficult and/or inaccurate to predict the measured IFO-120 and ANS data by only a single distribution. Therefore, a two-step Rosin-Rammler approach was introduced by advancing from the Rosin-Rammler approach proved by Johansen et al. (2013). The proposed approach uses two separate spreading coefficients: α_1 for $d/d_{50} \leq 1$ and α_2 for $d/d_{50} > 1$, providing better fit of the data in all cases. The regression coefficients for the two-step Rosin-Rammler are higher than which

for the original single one in most of the case, indicating the advantage of the proposed two-step Rosin-Rammler approach.

In general, the chemical dispersant plays an importance role in reduce the droplet size of ANS no matter in spring or summer conditions. The effectiveness of dispersant in reducing droplet size is higher on ANS than which on IFO-120. There may be thresholds for the dose of chemical dispersant to some oils (e.g., IFO-120) but will need further experiments to analyze. There may also be over dose of dispersant to some oils (e.g., ANS) when the DOR is high, eventually affecting the droplet size distribution. Future experiment will also need for this particular issue.

The measured IFT for the IFO-120 and ANS with different DORs appeared significant difference compared with the ones measured from SINTEF for the modified Weber number approach. This may due to the characteristics of different oil. Further experiments will be needed to address this issue.

Acknowledgement

This study was supported by the Centre for Offshore Oil, gas, and Energy Research, Fisheries and Oceans Canada, Bedford Institute of Oceanography and US Environmental Protection Agency (US EPA).

References

- Buist, I.A., W. M. Pistruzak, and D.F. Dickins, "DOME Petroleum's Oil and Gas Undersea Ice Study", in Proceedings of the Fourth Arctic Marine Oilspill Program Technical Seminar, Ottawa, ON, 1:647-686, 1981,
- Brandvik, P. J., et al. (2013). "Droplet breakup in subsurface oil releases - Part 1: Experimental study of droplet breakup and effectiveness of dispersant injection." *Marine Pollution Bulletin* 73(1): 319-326.
- Chen, F. H. and P. D. Yapa (2007). "Estimating the oil droplet size distributions in deepwater oil spills." *Journal of Hydraulic Engineering-Asce* 133(2): 197-207.
- Chen, F. H. and P. D. Yapa (2003). "A model for simulating deepwater oil and gas blowouts - Part II: Comparison of numerical simulations with "deepspill" field experiments." *Journal of Hydraulic Research* 41(4): 353-365.
- The Federal Interagency Solutions Group, Oil Budget Calculator Science and Engineering Team (2010). *Oil Budget Calculator: Deepwater Horizon*: 217.
- Johansen, O., et al. (2003). "DeepSpill - Field study of a simulated oil and gas blowout in deep water." *Spill Science & Technology Bulletin* 8(5-6): 433-443.
- Johansen, O., et al. (2013). "Droplet breakup in subsea oil releases - Part 2: Predictions of droplet size distributions with and without injection of chemical dispersants." *Marine Pollution Bulletin* 73(1): 327-335.

Louis J. Thibodeaux, et al. (2011). "Marine Oil Fate: Knowledge Gaps, Basic Research, and Development Needs; A Perspective Based on the Deepwater Horizon Spill." *Environmental Engineering Science* 28(2): 87-93.

Lefebvre, A. H. (1989). *Atomization and Sprays*, Taylor & Francis, P. 421

Stephen M. Masutani and E. E. Adams (2001). *Experimental Study of Multi-Phase Plumes with Application to Deep Ocean Oil Spills*. Deep Spill JIP, University of Hawaii (UH) and Massachusetts Institute of Technology (MIT). 147.

Topham, D.R., *Hydrodynamics of an Oilwell Blowout*, Beaufort Sea Technical Report #33, Department of the Environment, Victoria, BC, 52p., 1975

Wang, C. Y. and R. V. Calabrese (1986). "Drop Breakup in Turbulent Stirred-Tank Contactors .2. Relative Influence of Viscosity and Interfacial Tension." *Aiche Journal* **32**(4): 667-676.

Zhao, L., et al. (2014). "Evolution of droplets in subsea oil and gas blowouts: Development and validation of the numerical model VDROD-J." *Marine Pollution Bulletin* 83(1): 58-69.

Supplemental Material A. Fluorescence Analyses of 25 Oil Types at 4 Dispersant to Oil Ratios (listed in alphabetical order within oil type: Light, Intermediate, Heavy)
FWHM data in gray are estimates only as intensity did not return to half maximum before rising toward next adjacent peak.

Sample Name	API Gravity	Sulfur Content (weight %)	Point of Origin	DOR	overall maximum peak				Inner Filter Effect (IFE)	2nd intensity peak, lower ex/em*				minor peak, similar ex/higher em*				minor peak, higher ex/similar em*				F _{chelsea-R} 239/358 (RU)			F _{chelsea-C} 239/441 (RU)	F _{TriOS} 254/358 (RU)	F _{Cyclops-R} 254/349 (RU)	F _{Cyclops-C} 320/511 (RU)	F _{Eco} 371/460 (RU)	
					F _{Ex} ¹ (nm)	F _{Em} ¹ (nm)	F _{max} ¹ (RU)	F _{FWHM} ¹ (±4.5 nm)		F _{Ex} ² (nm)	F _{Em} ² (nm)	F _{max} ² (RU)	F _{FWHM} ² (±4.5 nm)	F _{Ex} ³ (nm)	F _{Em} ³ (nm)	F _{max} ³ (RU)	F _{FWHM} ³ (±4.5 nm)	F _{Ex} ⁴ (nm)	F _{Em} ⁴ (nm)	F _{max} ⁴ (RU)	F _{FWHM} ⁴ (±4.5 nm)									F _{281/340} (RU)
Arabian Light	Light (32.2°)	1.85	Saudi Arabia	0	224	335	400.4168	36.4960	1.1798	218	290	151.5028	31.7020	275	469	4.7933	248.7110	278	335	36.8206	41.0730	34.1437	4.6837	7.2898	28.8119	4.9367	16.8258	20.8790	3.5586	2.1712
				1:200	224	335	357.6249	36.4960	1.0714	218	285	148.2625	31.7020	284	478	2.6419	272.3370	275	335	33.5329	41.0730	30.9667	2.6676	11.6086	26.0505	3.8100	15.6252	19.1433	2.2830	1.3757
				1:100	224	335	426.8238	36.4960	1.2633	218	285	147.4888	31.7020	254	473	15.6626	233.8760	278	335	39.8975	41.0730	38.1081	14.1205	2.6988	36.0842	13.5018	22.3495	24.4236	12.2223	7.2024
				1:20	224	335	701.7454	41.0730	4.1859	218	290	224.3619	36.2160	236	441	236.8910	255.2810	278	335	82.6645	31.9220	78.7067	203.6622	0.3865	113.5339	231.9759	93.1478	73.9108	124.4251	53.3816
Brent	Light (38.2°)	0.40	East Shetland Basin, North Sea, UK (water depth 140 m)	0	224	335	646.1843	36.4960	1.1518	218	303	75.9188	31.7020	254	441	10.1605	144.8600	275	326	63.5367	45.6200	56.1012	7.3951	7.5863	40.2460	8.9941	31.0871	37.3653	5.6402	3.3604
				1:200	224	335	660.3712	36.4960	1.1618	221	290	63.9468	18.0940	248	432	11.6829	154.1170	275	326	65.5055	45.6200	58.2578	8.7661	6.6458	42.9915	9.3088	32.0393	38.7053	5.6408	3.7691
				1:100	221	335	708.1563	36.4960	1.3653	221	299	78.6673	27.1630	251	441	37.7209	205.3940	275	326	71.9189	50.2000	64.9403	32.8876	1.9746	58.0009	34.0570	44.3147	46.2510	22.0010	12.7049
				1:20	224	335	1098.4158	41.0730	3.0468	221	303	144.6971	22.6620	233	432	261.3387	200.2230	278	335	133.8242	36.4690	127.8678	189.0144	0.6765	173.4207	231.1604	146.2237	116.6535	85.0858	37.0050
Federated	Light (39.4°)	0.32	NW Alberta, Canada	0	224	335	574.3489	41.0730	1.1437	218	285	91.7448	27.1630	251	441	15.6750	144.7810	272	326	54.4863	50.2000	51.3190	13.8540	3.7043	68.2091	15.0958	46.4210	48.6704	9.2681	6.2912
				1:200	224	335	607.9723	41.0730	1.2130	218	290	112.8743	27.1630	248	441	30.9314	158.6540	272	326	57.8010	59.3710	55.3673	27.5293	2.0112	79.0319	29.2400	55.2828	54.6837	18.4455	12.0042
				1:100	224	335	645.2807	41.0730	1.3698	218	290	91.7746	27.1630	254	441	72.6915	181.3628	278	335	65.0589	50.2370	62.4421	66.5376	0.9384	99.7517	70.1628	71.2351	65.5325	39.0617	21.4244
				1:20	224	335	1223.1724	50.2370	4.3653	218	303	213.5284	27.1840	233	436	661.2244	226.9050	275	340	165.3826	27.3510	163.8397	460.6894	0.3556	371.8531	614.1385	289.5725	207.3393	168.2464	67.0266
Gullfaks	Light (32.7°)	0.31	North Sea, Norway (water depth 230 m)	0	221	335	937.0018	36.4960	1.2434	218	290	97.9804	22.6270	257	441	15.8195	219.6830	275	326	90.0457	41.0430	77.5575	13.4001	5.7878	44.3429	12.4754	37.0081	45.7345	10.1643	6.3561
				1:200	221	335	934.4237	36.4960	1.2715	218	290	96.3758	18.0940	251	436	18.0573	224.5310	275	326	91.9918	41.0430	80.0347	14.3665	5.5709	43.6717	14.9723	37.1213	46.3369	10.3233	8.3937
				1:100	221	335	933.0803	36.4960	1.3451	218	294	96.5534	27.1410	257	436	28.6241	219.5650	275	326	93.8404	45.6200	80.6821	24.8691	3.2443	46.8422	25.7671	39.3444	47.9996	18.4141	9.9173
				1:20	221	335	1524.2070	41.0730	3.7319	215	281	179.2527	9.0400	233	441	352.3552	200.4510	275	335	193.9621	31.9220	179.7879	253.8018	0.7084	212.7369	324.5520	187.2627	146.4968	122.7369	50.1927
Hibernia	Light (35.6°)	0.41	Newfoundland, Canada (water depth 80 m)	0	221	335	938.0775	36.4960	1.2390	218	285	173.3257	36.2160	290	492	11.2138	224.2920	275	326	87.9497	41.0430	74.9422	10.8507	6.9067	42.8229	10.5048	33.8845	44.5846	8.2628	4.5030
				1:200	221	335	951.4881	36.4960	1.3366	218	290	168.1463	36.2160	260	483	27.3287	224.2920	275	326	93.5200	45.6200	81.0861	25.1700	3.2215	48.8423	23.7015	41.7274	51.5979	22.5015	11.8736
				1:100	221	335	978.6157	36.4960	1.4740	215	281	170.8232	22.6080	254	478	55.8991	210.1160	275	326	96.1672	45.6200	85.2278	50.5145	1.6872	55.1197	50.2643	47.7291	56.0714	40.6007	19.1972
				1:20	221	335	1812.4055	41.0730	4.0175	218	290	305.6178	22.6450	225	422	567.3160	186.1020	275	335	201.2828	41.0430	182.7473	374.9851	0.4873	236.6556	480.2082	199.5141	152.8903	192.4787	68.6181
MC252 (Discoverer Enterprise)	Light (37.2°)	<0.1	Louisiana, US (water depth up to 1500 m)	0	221	335	998.4975	36.4960	1.2686	218	290	181.4689	31.6770	257	474	17.8789	224.2920	272	326	94.8271	41.0430	76.9368	15.3431	5.0144	46.3171	15.2539	40.7658	50.3429	15.0873	8.3661
				1:200	221	331	1009.1816	36.4960	1.3728	215	290	196.1398	31.7020	260	473	31.0582	214.8390	275	326	99.4748	50.1630	82.3071	26.9270	3.0567	53.4529	28.4331	45.5031	53.5737	25.1354	12.7483
				1:100	221	335	1085.5377	36.4960	1.4799	218	285	189.5899	22.6080	254	473	81.0433	228.5220	272	326	106.1992	45.6200	88.2869	72.3715	1.2199	64.3268	72.8640	55.0190	63.5313	59.5572	27.6216
				1:20	221	331	1998.5995	36.4960	4.7580	221	308	437.3233	31.7270	230	487	744.6895	200.4510	275	335	231.8561	50.2000	203.9413	527.5106	0.3866	229.0701	670.7186	200.3698	175.3657	268.1784	89.7799
MC252 (generic)	Light (35.2°)	0.21	Louisiana, US (water depth up to 1500 m)	0	221	335	857.3517	36.4960	1.2351	215	285	159.8695	22.6270	251	441	16.8587	167.7920	269	326	80.8431	45.5860	65.0029	14.7138	4.4178	36.3515	15.9277	33.1775	41.2382	10.0270	5.3895
				1:200	221	335	877.7767	41.0730	1.2462	215	303	108.8697	9.0750	254	450	26.8996	173.0670	272	326	83.4356	45.6200	68.4320	19.2422	3.5563	42.3193	21.1766	34.9381	46.2312	16.2865	9.5183
				1:100	221	335	964.0212	41.0730	1.5711	215	290	92.4174	22.5900	260	446	92.3028	218.8310	275	331	93.3841	54.7840	79.1424	83.1330	0.9520	62.4186	89.9889	56.6115	58.4282	52.7589	25.1734
				1:20	221	331	1795.1270	41.0730	4.7317	218	303	376.3732	22.6800	233	441	704.3134	204.5770	272	335	212.5289	31.8980	193.3704	483.6686	0.3998	260.6423	622.6480	217.6143	178.0065	199.9642	75.7345
Scotian Shelf Condensate	Light (51.Light																													

(White Rose)	(29.8°)		Canada (water depth 100 m)	1:200	221	335	1223.9796	36.4960	1.3272	218	290	202.7941	27.1630	--	--	--	--	275	326	115.3793	41.0430	93.9090	12.3688	7.5924	50.1617	14.9794	42.3903	56.7183	9.6724	5.1417
				1:100	221	335	1236.6347	36.4960	1.5486	215	294	159.5234	22.6270	260	441	50.7172	205.2810	275	326	116.7994	45.6200	98.9043	45.3497	2.1809	63.0618	47.2371	54.5822	63.8962	31.4917	15.6276
				1:20	221	335	1973.5528	36.4960	3.5550	218	303	280.6617	9.0750	233	441	359.0106	171.7950	278	335	211.3166	54.7840	186.5334	261.0755	0.7145	182.6322	322.1702	163.5870	147.7333	124.8090	49.8540
Vasconia	Intermediate (26.3°)	0.56	Colombia	0	224	335	844.9348	36.4960	1.1536	215	303	100.6205	31.7020	--	--	--	--	275	326	79.9347	41.0430	68.0535	1.9690	34.5629	45.3441	4.3971	36.3864	45.3699	1.0751	0.6805
				1:200	224	335	828.3719	36.4960	1.1583	218	303	97.9280	31.7020	--	--	--	--	272	326	80.8601	41.0430	67.4266	1.5176	44.4299	44.2001	4.0596	35.4004	46.8488	0.5749	0.4581
				1:100	224	335	835.6222	36.4960	1.1724	218	290	98.3668	22.6270	--	--	--	--	275	326	80.5851	41.0430	67.9124	1.9921	34.0901	43.5892	4.6579	37.7414	46.1524	1.1150	0.6503
				1:20	221	335	935.7946	36.4960	1.6723	215	308	139.7536	27.2050	--	--	--	--	272	326	92.7718	45.6200	80.0346	23.4436	3.4139	60.3238	33.0451	52.4788	59.7833	12.6010	5.4375
Access Western Blend Dilbit	Heavy (21.3°)	3.91	Athabaska region, Alberta, Canada	0	221	335	39.5805	41.0730	1.0197	218	285	33.2874	36.2160	215	558	2.4487	56.3880	272	326	4.9297	77.4050	4.1833	0.3668	11.4056	7.2683	0.8325	4.6137	4.4813	0.1885	0.1454
				1:200	221	335	46.5153	41.0730	1.0204	215	285	38.9976	36.2160	218	567	2.9473	51.7750	272	326	5.3889	77.4050	4.6291	0.3983	11.6208	7.7770	1.0395	4.5552	4.5711	0.0901	0.0734
				1:100	221	335	49.8423	45.6200	1.0266	218	285	45.8912	36.2160	215	571	2.9107	51.7510	272	326	5.9759	77.4050	5.1332	0.6010	8.5418	8.7321	1.3962	5.2585	5.1513	0.1711	0.1227
				1:20	224	335	60.1881	45.6530	1.0777	218	285	47.3804	40.7590	233	441	13.3766	148.9860	272	326	7.8131	109.5590	7.1753	6.3520	1.1296	15.7712	11.7630	9.8247	8.5862	2.5057	0.9710
Belridge Heavy	Heavy (13.6°)	1.03	San Joaquin Valley, California, US	0	230	344	118.6885	50.2740	1.0688	221	294	25.0773	18.1090	--	--	--	--	290	353	20.8257	68.6540	17.6309	3.5970	4.9016	67.1562	7.8788	37.7229	30.6641	1.1081	0.8613
				1:200	230	344	161.7504	50.2740	1.0812	218	294	34.0575	22.6450	--	--	--	--	290	353	27.5169	68.6540	23.7155	4.5438	5.2193	88.9294	10.7576	48.5595	39.1353	1.2513	1.1570
				1:100	227	344	140.9613	50.2740	1.0744	221	308	33.8168	31.7270	--	--	--	--	290	353	25.1983	73.2570	21.4500	4.6412	4.6216	82.0319	9.3816	45.6629	36.5600	1.2524	0.9988
				1:20	227	340	147.0897	50.2740	1.1216	221	290	31.8670	18.1090	--	--	--	--	290	353	27.1402	73.2570	22.3664	6.7721	3.3027	86.7568	13.2676	50.2330	39.1433	2.4427	1.6384
Cold Lake Dilbit	Heavy (21.5°)	3.77	NE Alberta, Canada	0	224	335	120.6093	41.0730	1.0503	218	285	55.0742	36.2450	--	--	--	--	275	326	13.9909	63.8180	12.5727	0.6645	18.9218	17.8324	2.0608	11.2944	11.8179	0.2705	0.2268
				1:200	224	331	120.6515	41.0730	1.0454	218	285	50.9834	40.7590	--	--	--	--	275	326	13.4098	63.8180	12.3240	0.7111	17.3317	17.8461	1.7589	10.9085	11.6320	0.2531	0.2152
				1:100	224	335	125.8546	41.0730	1.0587	218	285	44.4385	31.7020	--	--	--	--	275	326	14.3305	63.8180	13.2762	1.1542	11.5027	21.0296	2.6073	12.3514	12.9223	0.4954	0.2521
				1:20	224	340	133.1499	41.0730	1.1657	218	285	55.7758	40.7590	233	441	15.7453	158.4750	275	326	15.3840	72.9890	14.0151	7.2938	1.9215	23.0364	13.6412	15.1511	14.9083	3.6527	1.4960
Hondo	Heavy (19.5°)	4.41	Santa Barbara Channel, California, US (water depth 260	0	221	331	283.0362	41.0730	1.0889	215	290	55.1274	31.7020	--	--	--	--	278	335	27.6105	54.7840	27.0154	1.4698	18.3809	43.2085	5.8964	26.0841	26.9209	0.4113	0.2916
				1:200	221	335	312.2745	41.0730	1.0758	218	290	62.6687	36.2160	--	--	--	--	275	335	30.6188	54.7840	29.9090	1.9443	15.3831	50.0240	6.6702	30.1853	31.3212	0.3143	0.3773
				1:100	221	335	274.7955	41.0730	1.0745	215	285	49.9639	36.2450	--	--	--	--	278	335	26.6222	54.7840	26.0164	1.4917	17.4407	39.2872	5.2774	25.4749	25.4756	0.3729	0.3969
				1:20	221	335	288.0102	41.0730	1.0747	215	285	51.1261	31.6770	--	--	--	--	278	335	27.9249	54.7840	27.6591	1.6937	16.3307	44.4916	6.3517	27.1693	27.9998	0.3853	0.3321
IFO-40	Heavy (21.9°)	2.51	unknown	0	224	335	1173.9084	41.0730	1.2005	221	303	120.4664	31.7020	--	--	--	--	275	335	114.0423	50.2000	109.7049	3.9261	27.9426	155.5248	7.4990	103.6229	111.3150	1.6747	0.8991
				1:200	221	335	1246.6349	41.0730	1.2208	218	303	130.7611	27.1630	--	--	--	--	275	335	119.5841	50.2000	115.7084	2.4241	47.7317	160.5839	6.8963	105.1693	115.5723	0.9567	0.4653
				1:100	224	335	1338.5599	41.0730	1.2469	218	303	144.2245	31.7020	--	--	--	--	278	335	128.8407	50.2000	126.7588	3.5465	35.7420	181.6527	7.1909	118.8126	128.3301	2.0773	0.8103
				1:20	224	335	1458.7885	41.0730	2.2908	218	303	168.9769	18.1230	248	520	54.9662	224.9950	278	335	151.8776	54.7840	148.7639	32.5496	4.5704	222.4382	41.1861	153.5833	156.2830	36.6263	13.9537
IFO-120	Heavy (18.4°)	2.89	unknown	0	221	335	3030.6917	36.4960	1.6769	218	299	356.9362	27.1630	--	--	--	--	275	326	288.5176	45.6200	253.8040	2.3142	109.6730	238.3292	10.3519	156.8753	198.5147	0.6383	0.7026
				1:200	221	335	2903.2101	36.4960	1.6130	221	299	284.1346	18.1230	--	--	--	--	275	335	278.0117	45.6200	245.6221	2.4122	101.8258	216.1829	14.6200	151.8306	189.2919	1.0311	0.7444
				1:100	221	335	3090.2251	36.4960	1.6501	218	303	372.9288	27.1840	--	--	--	--	275	335	289.7281	45.6200	260.1135	3.0331	85.7579	229.2055	6.2012	156.3515	190.8314	1.2379	0.4351
				1:20	221	335	2527.7304	41.0730	1.6704	215	299	362.2292	18.1230	--	--	--	--	278	326	236.1044	45.6200	215.0700	6.2661	34.3231	189.9474	15.3716	139.1934	165.5095	4.2343	1.3665
IFO-180	Heavy (14.1°)	1.54	unknown	0	224	335	1263.0471	41.0730	1.2176	221	294	93.4542	18.1090	--	--	--	--	278	335	118.9519	45.6530	115.4168	3.4277	33.6718	155.2826	9.0125	105.8880	114.2930	1.5280	0.7810
				1:200	224	335	1394.4230	41.0730	1.2311	221	303	126.8108	22.6450	--	--	--	--	278	335	131.1659	45.6530	126.7468	3.5129	36.0808	172.7134	10.4629	122.5754	123.2982	1.5977	0.8673
				1:100	224	335	1703.5484	45.6530	2.3720	218	303	158.7036	22.6620	--	--	--	--	278	335	164.8318	50.2370	158.9337	4.3777	36.3057	229.6268	43.9836	166.9271	164.3761	20.2543	7.7073
				1:20	224	335	1532.9881	41.0730	1.6277	218	303	148.5740	22.6450	--	--	--	--	275	335	149.2341	54.7840	144.6928	11.8678	12.1921	213.5766	20.6104	148.9958	150.1388	8.5394	3.8566
IFO-300	Heavy (11.9°)	1.72	unknown	0	224	335	720.5500	41.0730	1.1149	221	299	58.8131	18.1090	--	--	--														